

Proceedings of the XIII Space Photovoltaic Research and Technology Conference (SPRAT XIII)

*Proceedings of a conference held at
NASA Lewis Research Center
Cleveland, Ohio
June 14-16, 1994*



National Aeronautics and
Space Administration

Office of Management

**Scientific and Technical
Information Program**

1994

1. The first part of the document is a list of the names of the persons who have been appointed to the various positions of the Board of Directors of the Corporation.

2. The second part of the document is a list of the names of the persons who have been appointed to the various positions of the Board of Directors of the Corporation.

3. The third part of the document is a list of the names of the persons who have been appointed to the various positions of the Board of Directors of the Corporation.

4. The fourth part of the document is a list of the names of the persons who have been appointed to the various positions of the Board of Directors of the Corporation.

5. The fifth part of the document is a list of the names of the persons who have been appointed to the various positions of the Board of Directors of the Corporation.

6. The sixth part of the document is a list of the names of the persons who have been appointed to the various positions of the Board of Directors of the Corporation.

7. The seventh part of the document is a list of the names of the persons who have been appointed to the various positions of the Board of Directors of the Corporation.

8. The eighth part of the document is a list of the names of the persons who have been appointed to the various positions of the Board of Directors of the Corporation.

9. The ninth part of the document is a list of the names of the persons who have been appointed to the various positions of the Board of Directors of the Corporation.

10. The tenth part of the document is a list of the names of the persons who have been appointed to the various positions of the Board of Directors of the Corporation.

FOREWORD

David M. Wilt
NASA Lewis Research Center

The Thirteenth Space Photovoltaic Research and Technology (SPRAT) Conference gathered representatives from 26 commercial corporations, 8 universities and 7 governmental agencies, including Europe, for two and a half days of presentations and discussions regarding the status and future of space photovoltaics. The conference was well attended, with over 100 attendees, and included 38 technical papers, 6 program reviews and 5 workshop discussions.

The effects of shrinking research and development budgets were evident in the focus and tone of this SPRAT. Most attendees appeared to be oriented toward near term, system oriented projects and fewer were involved in long term, high risk research. It was generally agreed that space power requirements would continue to move toward smaller (<2 kW) power levels. Most future applications are believed to be in traditional orbits (LEO, GEO) although interesting opportunities may be found in high radiation, mid-altitude orbits useful for global communication networks. New solar cell devices and materials will be difficult to introduce unless they are mission enabling, or offer significant cost and/or performance benefits. The attendees were unable to come to a consensus regarding the type of array (eg. rigid, concentrator, flexible) suitable for specific missions. Many factors outside the realm of photovoltaics influence the selection process. These topics and many more are covered in the following pages of this record.

Organizing and conducting the SPRAT conference requires a dedicated committee. The members of my team were: Navid Fatemi as logistics chairman, George Rybicki as publications chairman, Dennis Flood as conference mentor and Pat Nicewander as (the glue that holds everything together). The committee was also assisted by Karen Wester who organized the social functions. Their efforts and attention to detail were responsible for the success of this conference and the maintenance of my mental health.

TABLE OF CONTENTS

Goddard Space Flight Center Solar Array Missions, Requirements, and Directions Edward Gaddy and John Day, NASA Goddard Space Flight Center	1
BMDO Photovoltaics Program Overview Leonard H. Caveny, Ballistic Missile Defense Organization, and Douglas M. Allen, W.J. Schafer Associates	13
Air Force Activities in Space Photovoltaic Power System Technology Kelly Gaffney, U.S. Air Force	23
An Update on the Department of Energy's Photovoltaic Program John P. Benner and Mark Fitzgerald, National Renewable Energy Laboratory	31
Europe's Space Photovoltaics Programme Klaus P. Bogus, European Space Agency	35

SESSION I—InP CELL DEVELOPMENT

High-Efficiency, Deep-Junction, Epitaxial InP Solar Cells on (100) and (111)B InP Substrates R. Venkatasubramanian, M.L. Timmons, and J.A. Hutchby, Research Triangle Institute, and R. Walters and G. Summers, U.S. Naval Research Laboratory	43
Chemical Beam Epitaxy for High Efficiency Photovoltaic Devices A. Bensaoula, A. Freundlich, M.F. Vilela, N. Medelci, and P. Renaud, University of Houston	53
Status of Diffused Junction p+n InP Solar Cells for Space Applications Mircea Faur, Cleveland State University; Maria Faur, NYMA, Inc.; D.J. Flood and D.J. Brinker, NASA ; C. Goradia, Cleveland State University; N.S. Fatemi and P.P. Jenkins, NYMA, Inc.; D.M. Wilt and S. Bailey; NASA Lewis Research Center; M. Goradia and J. Moulot, Cleveland State University	63
High Quality InP-on-Si For Solar Cell Applications Zane A. Shellenbarger, Thomas A. Goodwin, Sandra R. Collins, and Louis C. DiNetta, AstroPower, Inc.	81
P/N InP Solar Cells on Ge Wafers Steven Wojtczuk and Stanley Vernon, Spire Corporation, Edward A. Burke, Private Consultant	91

SESSION II—THIN-FILM AND HIGH EFFICIENCY CELL DEVELOPMENT

Status of Flexible CIS Research at ISET B.M. Basol, V.K. Kapur, A. Minnick, A. Halani, and C.R. Leidholm, International Solar Electric Technology (ISET)	101
Development of a Lightweight, Light-Trapped, Thin GaAs Solar Cell for Spacecraft Applications Margaret H. Hannon, Louis C. DiNetta, Michael W. Dashiell, John R. Cummings, and Allen M. Barnett, AstroPower, Inc.	107
Advances in Polycrystalline Thin-Film Photovoltaics for Space Applications Bruce R. Lanning, Joseph H. Armstrong, and Mohan S. Misra, Martin Marietta Corporation	115
Amorphous Silicon Thin Films: The Ultimate Lightweight Space Solar Cell G.J. Vendura, Jr., M.A. Kruer, H.H. Schurig, M.A. Bianchi, and J.A. Roth TRW Space and Technology	125
Modeling of High Efficiency Solar Cells Under Laser Pulse for Power Beaming Applications Raj K. Jain, NASA Lewis Research Center, and Geoffrey A. Landis, NYMA, Inc	135
Calculation of Near Optimum Design of InP/In _{0.53} Ga _{0.47} As Monolithic Tandem Solar Cells P. Renaud, M.F. Vilela, A. Freundlich, N. Medelci, and A. Bensaoula	141

SESSION III—RADIATION DAMAGE AND ENVIRONMENTAL TESTING

Performance, Defect Behavior and Carrier Enhancement in Low Energy, Proton Irradiated p+nn+ InP Solar Cells I. Weinberg and G.C. Rybicki, NASA Lewis Research Center, C. Vargas-Aburto, Kent State University, R.K. Jain, University of Toledo, and D. Scheiman, NYMA, Inc.	149
Electron-Irradiated Two-Terminal, Monolithic InP/Ga _{0.47} In _{0.53} As Tandem H.L. Cotal, R.J. Walters, and G.P. Summers, U.S. Naval Research Laboratory, and S.R. Messenger, SFA, Inc.	159
Radiation Effects on p+n InP Junctions Grown by MOCVD S.R. Messenger, SFA, Inc.; R.J. Walters, U.S. Naval Research Laboratory; M.J. Panunto, University of Maryland Baltimore County; and G.P. Summers, U.S. Naval Research Laboratory	167
Design of High-Efficiency, Radiation-Hard, GaInP/GaAs Solar Cells Sarah R. Kurtz, K.A. Bertness, A.E. Kibbler, C. Kramer, and J.M. Olson, National Renewable Energy Laboratory	181
Investigation of the Stability and 1.0 MeV Proton Radiation Resistance of Commercially Produced Hydrogenated Amorphous Silicon Alloy Solar Cells Kenneth R. Lord II, Michael R. Walters, and James R. Woodyard, Wayne State University	187

The Use of Displacement Damage Dose to Correlate Degradation in Solar Cells Exposed to Different Radiations Geoffrey P. Summers, U.S. Naval Research Laboratory; Edward A. Burke, Philip Shapiro, Richard Statler, and Scott R. Messenger, SFA, Inc.; and Robert J. Walters, U.S. Naval Research Laboratory	197
Annealing of Irradiated n+p InP Buried Homojunctions R.J. Walters and G.P. Summers, U.S. Naval Research Laboratory, M.L. Timmons, R. Venkatasubramanian, J.A. Hancock, and J.S. Hills, Research Triangle Institute	203
Qualification Test Results for Blue-Red Reflecting Solar Cell Covers W.T. Beauchamp, OCLI	213
UV Testing on INTELSAT-VII, VIIA, and VIII Solar Cells A. Meulenbergh, COMSAT Laboratories	223
Parasitic Current Collection by Solar Arrays in Leo Victoria A. Davis and Barbara M. Gardner, S-Cubed Division of Maxwell Laboratories	227

SESSION IV—FLIGHT RESULTS

Final Results of the Advanced Photovoltaic Experiment David J. Brinker, NASA Lewis Research Center, and John R. Hickey, The Eppley Laboratory, Inc.	239
Preliminary Results from the Flight of the Solar Array Module Plasma Interactions Experiment (SAMPIE) Dale C. Ferguson and G. Barry Hillard, NASA Lewis Research Center	247
Photovoltaic Electric Power Applied to Unmanned Aerial Vehicles (UAV) Jack Geis, Wright Patterson Air Force Base, and Jack H. Arnold, Rockwell International	257
Post-Flight Investigation Programmes of Recently Retrieved Solar Generators Lothar Gerlach, European Space Agency-ESTEC (XPG)	269

SESSION V—BLANKET AND ARRAY DEVELOPMENT

High-Performance, Flexible, Deployable Array Development for Space Applications Russell N. Gehling, Joseph H. Armstrong, and Mohan S. Misra, Martin Marietta Astronautics	287
Static Stability Of A Three-Dimensional Space Truss John F. Shaker, NASA Lewis Research Center	299
An Update on the Development of a Line-Focus Refractive Concentrator Array Michael F. Piszczor, NASA Lewis Research Center, Mark J. O'Neill, Entech, Inc., and Lewis M. Fraas, JX Crystals	313
An Introduction to the Astro Edge Solar Array B.R. Spence and G.W. Marks, Astro Aerospace Corporation	323

SESSION VI—NON-SOLAR ENERGY CONVERSION

Rare Earth Garnet Selective Emitter Roland A. Lowe, Kent State University, and Donald L. Chubb, Serene C. Farmer, and Brian S. Good, NASA Lewis Research Center	335
InGaAs PV Device Development for TPV Power Systems David M. Wilt, Navid S. Fatemi, and Richard W. Hoffman, Jr., Essential Research, Inc.; Phillip P. Jenkins, David J. Brinker, and David Scheiman, NYMA, Inc.; Roland Lowe, Kent State University; and Donald Chubb, NASA Lewis Research Center	341
Pulsed Laser Illumination of Photovoltaic Cells Jane A. Yater, NASA Lewis Research Center, Roland Lowe, Kent State University, and Phillip Jenkins and Geoffrey A. Landis, NYMA, Inc.	353
P/N In(Al) GaAs Multijunction Laser Power Converters Steven Wojtczuk and Themis Parodos, Spire Corporation, and Gilbert Walker, NASA Langley Research Center	363
High Efficiency GaP Power Conversion for Betavoltaic Applications Paul E. Sims, Louis C. DiNetta, and Allen M. Barnett, AstroPower, Inc.	373

SESSION VII—CELL/MATERIAL PROPERTIES

Review of Solar Cell Temperature Coefficients for Space Geoffrey A. Landis, NYMA, Inc.	385
Effects of Plasma Hydrogenation on Trapping Properties of Dislocations in Heteroepitaxial InP/GaAs S.A. Ringel and B. Chatterjee, The Ohio State University	401
Nucleation, Growth, and Strain Relaxation of Lattice-Mismatched III-V Semiconductor Epitaxial Layers R.E. Welser and L.J. Guido, Yale University	409

WORKSHOP SUMMARIES

Summary of Workshop on InP: Status and Prospects R.J. Walters, U.S. Naval Research Laboratory, and I. Weinberg, NASA Lewis Research Center	419
Systems, Arrays and Applications Workshop 1 G.J. Pack, Lockheed Missiles and Space Company, and Lothar Gerlach, ESA/ESTEC	423
Future Directions In PV Cell Development: Summary of the Workshop at SPRAT-XIII Geoffrey A. Landis, NYMA, Inc.	425
Array Technologies Workshop I Douglas Allen, W.J. Schafer Associates, and Andrew Meulenberg, Comsat Laboratories	431

Workshop Summary	
Thermophotovoltaics and Non-Solar Energy Conversion	
Donald L. Chubb, NASA Lewis Research Center, and Larry C. Olsen,	
Washington State University	437

GODDARD SPACE FLIGHT CENTER SOLAR ARRAY MISSIONS, REQUIREMENTS AND DIRECTIONS

Edward Gaddy and John Day
NASA Goddard Space Flight Center
Greenbelt, Maryland

ABSTRACT

The Goddard Space Flight Center (GSFC) develops and operates a wide variety of spacecraft for conducting NASA's communications, space science, and earth science missions. Some are "in house" spacecraft for which the GSFC builds the spacecraft and performs all solar array design, analysis, integration, and test. Others are "out of house" spacecraft for which an aerospace contractor builds the spacecraft and develops the solar array under direction from GSFC. The experience of developing flight solar arrays for numerous GSFC "in house" and "out of house" spacecraft has resulted in an understanding of solar array requirements for many different applications. This presentation will review those solar array requirements that are common to most GSFC spacecraft. Solar array technologies will be discussed that are currently under development and that could be useful to future GSFC spacecraft.

BACKGROUND

The GSFC both purchases and manufactures spacecraft. For the purchased spacecraft, GSFC supplies a spacecraft specification to a manufacturer who then purchases or fabricates the array. The spacecraft specification usually has in it a general specification which covers the power system and the solar array. Such spacecraft under development by the GSFC are: Total Ozone Mapping Spectrometer (TOMS), National Oceanic and Atmospheric Administration Spacecraft (NOAA)-J, NOAA-K, NOAA-L, NOAA-M, NOAA-N, and NOAA-N prime, Global Geospace Science (GGS)-WIND, GGS-POLAR, Geostationary Operational Environmental Satellite (GOES)-J, GOES-K, GOES-L, Tracking and Data Relay Satellite (TDRS) F-7, Landsat-7, Advanced Composition Explorer (ACE), Earth Observing Spacecraft (EOS)-AM, EOS-PM, SPEC, CHEM, TDRS H, I J, and Hubble Space Telescope (HST) Servicing Mission Replacement Array. Some of the characteristics of the arrays on these spacecraft is summarized in Table I.

The GSFC also manufactures some spacecraft. In these cases, GSFC and specifically the Space Power Applications Branch develops and purchases solar arrays. GSFC has a greater influence on the specifics of these solar arrays as opposed to the arrays on the out of house spacecraft. These arrays have provided us with knowledge of the requirements for spacecraft solar cells and some insight into what technologies will be most helpful for the future. Spacecraft in this group include the Small Explorer (SMEX)- 2 also known as the Fast Auroral Snapshot (FAST), the X-Ray Timing Explorer (XTE), SMEX -3 also known as the Submillimeter Wave Astronomy Satellite (SWAS), the Tropical Rainfall Measuring Mission (TRMM), SMEX 4, 5, and 6; and the Far Ultraviolet Spectroscopic Explorer (FUSE). Table II summarizes some of the array characteristics of the spacecraft in this category.

The GSFC also operates spacecraft. Some of the spacecraft the center currently operates include: the International Ultraviolet Explorer (IUE), the International Sun Earth Explorer subsequently renamed the International Cometary Explorer (ICE), the Earth Resource Budget Spacecraft (ERBS), the Cosmic Origins Background Explorer (COBE), the Hubble Space Telescope (HST), the Gamma Ray Observatory (GRO), the Upper Atmosphere Research Satellite (UARS), the Extreme Ultraviolet Explorer (EUVE), and the Solar Magnetospheric Particle Explorer (SAMPEX). Table III summarizes some of the array characteristics of the spacecraft arrays in this category.

Table I
GSFC Out of House Solar Arrays Currently in Development

S/C	Launch	Life (yrs)	Orbit	Array Type	Cell Type	Array/Cell Manufacturer
TOMS	1994	3	LEO	rigid, deployable	BSFR, silicon	TRW, ASEC
NOAA-J	1994	2	LEO	rigid deployable, tracking	BSR, silicon	MM, ASEC
GG5 WIND	1994	3	sun earth libration	rigid, body mount, electrostatically clean	BSFR, silicon	MM, ASEC
GG5 POLAR	1995	3	elliptical	rigid, body mount, electrostatically clean	BSFR, silicon	MM, ASEC
GOES-J	1995	5	GEO	rigid, deployable, tracking	BSR, silicon	Loral, Spectrolab
TDRS-7	1995	10	GEO	rigid, deployable, tracking	BSR, silicon	TRW, ASEC
Landsat -7	1998	5	LEO	rigid, deployable, tracking	BSR, silicon	MM, TBD
ACE	1997	2	sun earth libration	rigid, deployable	BSFR, silicon	APL, Spectrolab
EOS- AM	1998	5	LEO	flexible, deployable, tracking	5.5 mil GaAs/Ge	MM, TRW, ASEC
NOAA K, L, M	1996- 1999	2	LEO	rigid, deployable, tracking	BSR, silicon	MM, TBD
HST Servicing	1999	5	LEO	TBD	TBD	TBD
EOS-PM SPEC CHEM	1998- 2003	TBD	TBD	TBD	TBD	TBD
TDRS H, I, J	1999- 2001	TBD	TBD	TBD	TBD	TBD

Table II
GSFC In House Solar Arrays Currently in Development

S/C	Launch	Life (yrs)	Orbit (km)	Array Type	Cell Type	Array/Cell Manufacturer
FAST	1994	1	350 x 4200	rigid, body mount, faraday cage	GaAs/Ge	TRW, ASEC
XTE	1995	2	600	rigid, deployable, tracking	BSFR, silicon	Spectrolab
SWAS	1995	3	600	rigid, deployable	GaAs/Ge	Spectrolab
TRMM	1997	3	350	rigid, deployable, tracking	GaAs/Ge	TRW, ASEC
SMEX 4, 5, 6	1996 - 1999	TBD	TBD	TBD	TBD	TBD
FUSE	2000	TBD	TBD	TBD	TBD	TBD

REQUIREMENTS FOR SOLAR CELLS

A solar cell of a given type must have undergone the following tests before we will consider it for use on a in house spacecraft solar array. Except as noted below, existing silicon and gallium arsenide and gallium arsenide on germanium solar cells meet these requirements almost flawlessly. These requirements are frequently not explicitly stated by GSFC specifications, but in one way or another they are present.

1. The solar cell's beginning of life current versus voltage characteristics must be determined as a function of temperatures from -80C to +80C for low earth orbits. Ideally, this range is extended to -180C to +80C to cover geosynchronous orbits.
2. The solar cell's current versus voltage characteristics must be determined as a function of amount and kind of hard particle radiation. In other words, the solar cell must be exposed to electrons and protons of varying energies and of varying amounts in ground tests to determine suitability for use on spacecraft. This exposure must generally be thorough enough so that the radiation in space can be converted into an equivalent number of 1 Mev electrons and to determine the solar cell's end of life current versus voltage characteristics as a function of temperature from -100C to +100C.
3. The solar cell's performance must be determined as a function of its degradation due to the exposure to sunlight, particularly the ultraviolet component. The equivalent of a one year's exposure on an accelerated basis is considered to be satisfactory.

Table III
In - Orbit Spacecraft Currently Operated by GSFC

Spacecraft	Launched	Orbit Altitude (km) and Inclination (°)	Solar Array Type	Solar Cell Type	Array/Cell Manufacturer
IUE	1/78	30,210 x 41,343, 33.8°	rigid, deployable, fixed	BSR, silicon	GSFC, ESA AEG
ISEE-3 later known as ICE	8/78	sun earth libration point, followed by lunar swing by and cometary encounter	rigid, body mounted	BSFR, silicon	GSFC, Spectrolab
ERBS	11/84	590, 57	rigid, fixed		Ball, Spectrolab
COBE	11/89	873 x 885, 99	rigid, deployable, fixed	BSFR, silicon	GSFC, Solarex
HST	4/90	600, 28.5	flexible, roll out, tracking	BSFR, silicon	Marshall, ESA, BAe, AEG
GRO	4/91	370, 28.5	rigid, deployable, tracking	BSR, silicon	TRW, ASEC
UARS	9/91	570, 57	rigid, deployable, tracking	BSFR, silicon	GE, ASEC
EUVE	6/92	520, 28.4	rigid, deployable,	BSFR, silicon	GSFC, FSC Solarex
SAMPEX	7/92	509 x 679, 82	rigid, deployable fixed	GaAs/Ge	GSFC, FSC Spectrolab

4. The solar cell's performance must be determined after exposure to thermal cycling. Generally, a solar cell in a low earth orbit will be exposed to on the order of 5,500 cycles from -80C to +80C each year. Most GSFC spacecraft have a lifetime of two years or more, and the cell must be tested to such a flight environment. Further, the test showing competence in this area should have the solar cell fixed to a panel as this is the condition under which the solar cell must actually perform. The condition of making electrical connection to the solar cell and mounting it to a substrate makes this test significantly more strenuous than just cycling the solar cell. If the solar cell is to be used in a geosynchronous orbit, it must be able to withstand very roughly eighty cycles per year as extreme as -180C to +80C.

5. The solar cell must not degrade due to the humidity in an air-conditioned room over many years. The solar cell must not degrade due to humidity exposure in an unconditioned atmosphere for several days, such as at launch and during shipment. The solar cell's resistance to humidity is traditionally proven by exposing the solar cells to 90% relative humidity at 45C for 30 days with the requirement that the solar cell not degrade more than 2% in peak power. This test is to some degree arbitrary. Exactly how well a cell must do in the test to show that it performs well under the conditions of the real world is not well determined. Consequently, this test could be weakened if it a cell manufacturer could show that it made an unduly pessimistic prediction for a new type of solar cell.

6. The solar cell's absorptance must be measured.

7. The solar cell's weight density must be determined.

8. The GSFC occasionally has missions with magnetic specifications that require no magnetic materials be used in the fabrication of the solar cell.

9. A darkened solar cell must be able to withstand reverse bias to approximately 10 percent more current than its short circuit current or to a voltage, typically around 50 volts, that is determined by a combination of the power system and array performance. Whichever of the requirements is least severe governs. This requirement is not met flawlessly by gallium arsenide or gallium arsenide on germanium solar cells unless they are first screened.

10. Although GSFC frequently does not specify cell size, sizes under 2 cm by 4 cm are not practical due to laydown cost. This requirement is of course flexible if the benefits of a small solar cell can be shown to outweigh the cost penalty. For example, we would gladly fly 50% efficient 2 cm by 2 cm solar cells.

11. It must be possible to fix an interconnect strongly enough to a cell so that it can take small bumps and thermal cycling without coming off. To prove this, the contacts on the solar cell must withstand a 1.5N pull test before and after being exposed to humidity. As in the case of the humidity test, this requirement is somewhat arbitrary and can be modified if it can be shown that it is too severe for a particular solar cell.

12. A completely new type of solar cell must be flown on a balloon to determine its output.

13. Very likely, a completely new type of solar cell would have to be flown on a limited basis in space before using it as a primary source of power.

15. Any organization manufacturing solar cells must have a significant quality assurance effort and be financially stable. In terms of quality, this means that the organization should meet or come close to meeting the requirements of MIL-Q-9858.

REQUIREMENTS FOR GSFC IN HOUSE SOLAR ARRAYS

In addition to the above for solar cells, the following requirements for solar arrays apply. These requirements are explicitly stated in GSFC specifications.

The array must meet configuration, maximum weight, minimum beginning of life power, insulation resistance, cleanliness, outgassing, mechanical, and miscellaneous requirements such as temperature sensor accuracy. The array must also meet specifications on resistance to accidental damage, resistance to damage by storage temperature and humidity, and resistance to: ultraviolet radiation, atomic oxygen, micrometeoroids and space debris and shadowing.

The array's performance after thermal cycling must be proven in a life test which includes samples of every component which will be mounted on the flight arrays. Although solar arrays have been manufactured for many years, this requirement is still frequently not met flawlessly. The array's performance test must be proven after exposure to vibration or acoustic. This test is generally met without difficulties.

The flight array must be acceptance tested by exposure to eight thermal vacuum cycles and exposure to acoustic. The thermal vacuum cycles again are frequently not flawless.

We occasionally require that no magnetic materials be used on the solar array and/or that the array be electrostatically clean. This usually means that the upper surface of the array be conductive. The requirement is sometimes tightened to the extent that virtually every surface on the array be conductive.

GALLIUM ARSENIDE VERSUS SILICON

Table IV summarizes the array characteristics of the spacecraft for which GSFC or its contractors did a trade off between GaAs solar cells and silicon solar cells. The GaAs arrays cost approximately 70% more on a per watt basis than silicon solar arrays, but because of the benefits they provide, their system level cost is actually lower than silicon. For each spacecraft array in Table IV, but with emphasis on TRMM, we summarize below the factors used in determining whether to use GaAs or silicon.

Table IV
Summary of GSFC Solar Arrays with a GaAs versus Silicon Tradeoff

Spacecraft	Cell Type	Array Cell Area (m ²)	Lifetime (yrs)	Altitude (km)	Equivalent 1 Mev Electrons	Array Delivery Date
SAMPLEX	GaAs/Ge	1.7	3	450 x 830	1.1×10^{13}	Launched
XTE	Silicon	15.5	2	600	4.6×10^{12}	Aug. 94
FAST	GaAs/Ge	2.6	1	350 x 4200	1.5×10^{14}	May 94
TRMM	GaAs/Ge	18.1	3	350	1.7×10^{12}	May 95
SWAS	GaAs/Ge	3.6	3	600	9.6×10^{12}	Sept. 94
EOS	GaAs/Ge	35	5	705	5.4×10^{13}	Feb. 96

SAMPEX

The solar array for SAMPEX is very small. A silicon array could not meet the power requirements for the spacecraft. This solar array and its cells were supplied by Spectrolab.

XTE

The solar array for the X-Ray Timing Explorer is fully designed and a contract has been let to Spectrolab for its fabrication. The solar array consists of silicon solar cells on an aluminum face sheet honey comb core substrate. Silicon solar cells were selected for this spacecraft primarily because of the difficulties in obtaining accurate prices for gallium arsenide solar arrays. We had limited pricing experience with the cells and most of the panel manufacturers had limited experience working with the cells and hence a high price uncertainty. Had the array used gallium arsenide solar cells, it would have been the first GSFC spacecraft array of a moderate size, approximately 2,000 watts, to do so. The advantage of the gallium arsenide solar cells was that their use would have prevented the necessity of a tracking solar array which would have increased spacecraft reliability and removed the substantial costs associated with the tracking mechanisms.

FAST

The solar array for FAST has been fabricated through a contract with TRW. The solar array for the Fast Auroral Snapshot satellite is gallium arsenide. This array is area limited and the silicon solar array of the required size could not supply the needed power. The cells are on an aluminum face sheet honeycomb core that forms the outside of the spacecraft body.

As an aside, this array is particularly interesting in that it has no magnetic materials, has magnetic compensation wiring directly under the solar cells and has a Faraday cage over its entire surface. The Faraday cage primarily consists of covers with conductive indium oxide coatings. The covers are interconnected in such a way that interconnects completely cover any insulating area on the array.

TRMM

The solar array for the Tropical Rainfall Measuring Mission is fully designed and a contract has been let to TRW for its fabrication. The solar array consists of gallium arsenide/germanium solar cells on an aluminum face sheet honeycomb core substrate. Both gallium arsenide and silicon solar cells were considered for the TRMM array. Table V provides a comparison of the resulting arrays. In Table V the delay actuator is a device which prohibits fouling by the premature deployment of one panel prior to deployment of another panel. The potentiometers are used to monitor the deployment of the various panels.

The silicon solar cell array is, from Table V, approximately 45% larger than the gallium arsenide array, a figure which G. C. Datum and S. Billets have also reported.¹ The smaller area reduced the spacecraft's fuel consumption and increased the probability of meeting a three year life. This was a particularly important consideration. Table II also shows that silicon array is 36% heavier. The areal and weight advantage of the gallium arsenide array results because the gallium arsenide solar cells offer approximately 40% more power on a per area basis at operating temperature. The GaAs solar cells greatly simplified the deployment of the solar array. This is important because deployables are historically among the less reliable components of spacecraft. Further, the array deployment would have to be tested on the ground and making a g-negation mechanism to allow the TRMM silicon array to deploy would have been difficult almost to the point of impracticality as each array wing would have consisted of six hinged panels.

Table V
TRMM Silicon versus GaAs Technical Factors Comparison

<u>Parameter</u>	<u>Si</u>	<u>GaAs</u>
Weight of Cell Stack, Wiring, Connectors and Miscellaneous	48 kg	47 kg
Array Area	26.2 m ²	18 m ²
Array Operating Temperature	74C	87C
BOL Efficiency @ Operating Temperature	11.3%	15.8%
EOL Efficiency	9.4%	13.3
Number of Individual Panels	12	4
Number of Panel Hinges	20	4
Number of Delay Actuators	2	0
Number of Potentiometers	12	2
Mechanical System Weight	144 kg	94 kg
Total Weight	192 kg	141 kg

SWAS

The solar array for the Submillimeter Wave Astronomy Satellite is gallium arsenide. This array is area limited and a silicon solar array of the required size could not supply the needed power. The solar array for SWAS is fully designed and a contract has been let to Spectrolab for its fabrication.

EOS

Although, most of the conclusions we draw below follow from our experience with in house arrays, we here mention our most technologically advanced array which is for the Earth Observing System, an out of house project. The EOS carries a flexible deployable array powered with 5.5 mil thick gallium arsenide solar cells. This represents the first such use of these cells on a flexible array. The trade which drove this array to the gallium arsenide solar cells was that the array is on one side of the spacecraft and tended to rotate the spacecraft in flight. Using the gallium arsenide array thereby enabled the attitude control system to use existing reaction wheels rather than developing new ones.

TRENDS

The gallium arsenide solar cell offers a substantial improvement over silicon. Silicon solar arrays are generally on the order of 40% larger when the operating temperature of the array is taken into account. In most cases, the gallium arsenide solar cell offers a dramatic weight reduction

compared to silicon even though the gallium arsenide cells are heavier than silicon. This is because reducing the array area reduces the size of the substrate, harnessing, number of covers, amount of adhesive etc. This reduction more than compensates the weight difference between the solar cell types. This is true in the overwhelming number of spacecraft solar arrays because they use aluminum face sheet over aluminum honeycomb core substrates. As the weight of the substrate decreases, the weight advantage of gallium arsenide solar cells becomes less. It is only with extremely lightweight solar arrays that gallium arsenide on germanium solar cells result in an array which approaches the weight of a silicon array for the same power. This happens on lightweight deployable solar arrays using the thinnest commercially available silicon, 55 microns thick, compared to the same array with gallium arsenide cells, 115 microns thick.² Because these arrays represent advanced technology they do receive a great deal of attention in the literature, however there are only a handful of them flying and therefore their practical effect on cell technology is limited.

The advantages of the GaAs solar cell, which derive primarily from its greater efficiency, suggest that spacecraft solar cells for future spacecraft will be driven primarily by a greater power density. With this statement in mind, the authors believe that the following solar cells offer the greatest opportunity to improve spacecraft performance.

MULTI JUNCTION SOLAR CELLS

The authors believe that the qualification and development for production of these cells would provide the greatest benefit at the least cost in the shortest time. Such solar cells have been produced in the laboratory^{3,4,5} with AM0 efficiencies of over 25%. If these solar cells are mass produced at 24 percent efficiency they represent over a 30 percent improvement in state of the art gallium arsenide solar cells. These cells will therefore multiply the considerable advantages the gallium arsenide cells have provided. Additionally, the method of manufacture of these solar cells suggests that the price will be competitive to gallium arsenide on germanium. This statement is based on the assumption that making the cascade cell primarily entails leaving it in the reactor which grows the various cell layers somewhat longer than is required for the gallium arsenide on germanium solar cell. During this time, the reactor will automatically control the flow of gasses to grow the additional layers. The time and labor involved in this additional processing is probably minimal. There will also be an additional yield loss.

Because of the improved power density is so welcome, because the solar cell is in many ways similar to gallium arsenide solar cells, because the cell is probably not significantly more expensive and because several organizations have successfully produced versions of the cell, we believe that the next most probable step in improving array performance is with the multi-junction solar cell.

IMPROVED GALLIUM ARSENIDE SOLAR CELLS

Gallium arsenide solar cells have been fabricated with air mass zero efficiencies in excess of 21 percent.⁶ These solar cells offer a significant improvement to spacecraft power systems using improved versions of existing solar cells. These are therefore a very valuable asset, if they can be put into production.

INDIUM PHOSPHIDE SOLAR CELLS

These solar cells have been fabricated with air mass zero efficiencies of over 19 percent.⁷ The effect of radiation on these solar cells is significantly less than that for gallium arsenide cells of approximately the same efficiency. Tobin reports that cells of this approximate efficiency degrade 4.7% after irradiation with 10^{14} 1 Mev electrons. GaAs cells degrade 9% after the same

irradiation.⁸ At this radiation level, these cells will therefore show about a 4% advantage over gallium arsenide solar cells, provided both cells have the same initial efficiency. At 10^{15} 1 Mev electrons, GaAs solar cells have a degradation of 26%. At these radiation levels, and presuming the InP cells retain an approximate 2 to 1 advantage over the GaAs cells in degradation means that the indium phosphide solar cell will have about a 13% advantage over the GaAs solar cell. However, the advanced GaAs solar cell has about a 10% advantage over the InP cell at beginning of life and the multijunction cell has an approximate 30% advantage over the indium phosphide cell at beginning of life. This means that only under the most extreme conditions of radiation will the InP cell show an advantage over an advanced gallium arsenide cell and that it will never show an advantage over a multi junction cell. As can be seen from Table I which is typical for most of our spacecraft, the radiation damage is generally under 10^{14} equivalent 1 Mev electrons.

ADVANCED SILICON SOLAR CELLS

A variety of high efficiency silicon solar cells have been developed.^{9, 10, 11, 12} These cells may find application in space as competitors to GaAs and production silicon solar cells. To do this, they must be tested to the cell requirements mentioned earlier, particularly because the cells may be quite sensitive to radiation. Even if they are resistant to radiation or can be made so, the authors believe that they do not overcome the advantage of the higher efficiency multi-junction solar cells even considering the greater expense of the later technology.

THIN FILM SOLAR CELLS

Thin film solar cells offer the advantage of an enormous power to weight gains over any of the solar cells discussed previously. To utilize this advantage a mechanism must be developed to deploy them and this mechanism must also be light enough to not cancel the cell's inherent advantage. These cells are at a disadvantage at lower altitudes because of their larger area, which is almost twice that of state of the art GaAs arrays. At these altitudes the large area creates an adverse impact on the spacecraft attitude control system and on the ability of the spacecraft to maintain altitude.

CONCENTRATOR SOLAR CELLS

The authors believe that concentrator solar cells are not useful to NASA spacecraft. This is because they have a significantly detrimental effect on spacecraft reliability. If non concentrating solar cells are used on a spacecraft, the spacecraft can lose its ability to drive the arrays or it can tumble for many hours and still be recovered. This is because arrays will supply about 30% of their rated power in a random spacecraft tumble, about enough to keep a powered down spacecraft going indefinitely. If concentrator arrays are used, the arrays will supply only small fraction of their rated power in a random spacecraft tumble. Under these circumstances the typical spacecraft batteries will discharge after about four hours or three orbits. In short, the concentrator arrays impose very strict requirements on the short term pointing reliability of the spacecraft attitude control system and the solar array drive. These requirements would be very difficult to convincingly achieve. The likelihood of ever using these cells is therefore small.

FLEXIBLE SOLAR ARRAYS

The development of flexible, deployable solar array such as the Advanced Photovoltaic Solar Array, (APSA)¹³, the Solar Array Flight Experiment (SAFE) and the Flexible Rolled Up Solar Array (FRUSA) have enabled NASA to enhance the capability of two of its larger spacecraft, namely EOS and HST. From the user's point of view these deployable arrays enable a large array to be packed in a small volume on the spacecraft. Unfortunately these arrays are very difficult to analyze mechanically, particularly with respect to the effect they have on the

spacecraft's attitude control system, they are mechanically complex and they are impossible to end to end test. For these reasons, we avoid them until their advantages become very large. However, as we gain experience with them, the authors believe that they will become more popular.

The weight advantage of these arrays is substantial, although not as great as the prototype arrays suggest. For example, the APSA has a power to weight ratio of 130W/kg. The EOS array, that derived from APSA but had to overcome various practical constraints, has a power to weight ratio of 32 W/kg. As an aside, this decrease is not due to the change from the thin silicon cells on APSA to the GaAs cells on EOS, if the EOS array had weightless cells and covers, it would have a power to weight ratio of only 43 W/kg. For reference the TRMM array has a power to weight ratio of 20W/kg, typical of many spacecraft.

FLIGHT TESTING ADVANCED SOLAR CELLS

To insure that advanced solar cells are flown as soon as practicable, it is necessary to fly them on spacecraft as soon as ground testing indicates that they are a promising candidate but before ground testing has fully qualified them. This is because even when solar cells are completely qualified through ground testing, many projects are reluctant to fly them unless they have flown before. The flight of small numbers of these cells on otherwise conventional arrays will provide experience to the manufacturers, will gain the confidence of spacecraft managers, and will complement ground based qualification. Such use of advanced solar cells will not generally enhance a given project's capability to meet its requirements and will therefore be resisted. However, the price to be paid by the project is small, provided only minimal telemetry is specified, and the benefits to the space program are large particularly in view of the several very promising advanced solar cells. The Space Power Branch at GSFC is therefore recommending that inexpensive low risk flight experiments be undertaken.

CONCLUSIONS

The GSFC has responsibility for a large number of solar arrays, some of which are powered by GaAs solar cells. These gallium arsenide solar cells have provided a wide variety of benefits including the preservation of spacecraft fuel, the enhancement of missions that would be severely power limited without them, the simplification of array deployment mechanisms, and the reduction of solar array weight. Because of the benefits these cells have provided are so useful, we believe that the further test and development of high efficiency solar cells, particularly multi-junction solar cells will further increase these already substantial benefits. These cells will provide additional power at a modest increase in price. We are recommending that the GSFC and other agencies start flying a small percentage of each of their state of the art arrays with advance solar cells so that experience can be gained with these cells even before they are fully qualified to be the primary source of power for spacecraft.

We have made the point that some areas of research seem to us to be less useful. In particular, the future development of concentrator solar arrays does not appear to be a fruitful avenue to pursue, at least for NASA spacecraft.

¹G. C. Datum *et al.*, "Gallium Arsenide Solar Arrays - A Mature Technology," Proceedings of the 22nd IEEE Photovoltaic Specialists Conference, October 7, 1991, Las Vegas, NV p. 1422.

²P. M. Stella *et al.*, "Thin Film GaAs for Space - - Moving Out of the Laboratory" Proceedings of the 23rd IEEE Photovoltaic Specialists Conference, May 10, 1993, Louisville, KY. Figure 1, p. 22.

-
- ³B. C. Chung *et al.*, "25.2%-Efficiency (1-Sun Air Mass 0) AlGaAs/GaAs/InGaAsP Three Junction Solar Cell," Proceedings of the 22nd IEEE Photovoltaic Specialists Conference, October 7, 1991, Las Vegas, NV p. 54.
- ⁴B. C. Chung *et al.*, "27.6% (1 Sun Air Mass 1.5) Monolithic Two Junction AlGaAs/GaAs Solar Cell and 25%(1 Sun, Air Mass 0) Three Junction AlGaAs/GaAs/InGaAs Cascade Solar Cell," Proceedings of the 21st IEEE Photovoltaic Specialists Conference, May 21 1990, Kissimmee, FL, p. 179.
- ⁵J. M. Olson *et al.*, "A 27.3% efficient Ga_{0.5}In_{0.5}P/GaAs tandem solar cell," Appl. Phys. Lett. 56(7) 12 February 1990, p. 623.
- ⁶S.P. Tobin, *et al.*, "Advances in High Efficiency GaAs Solar Cells," Proceedings of the 21st IEEE Photovoltaic Specialists Conference, May 21 1990, Kissimmee, FL, p. 158.
- ⁷C. J. Keavney, *et al.*, "Emitter Structures in MOCVD INP Solar Cells," Proceedings of the 21st IEEE Photovoltaic Specialists Conference, May 21, 1990, Kissimmee, FL, p. 141.
- ⁸B. E. Anspaugh, Addendum 1 to the Solar Cell Radiation Handbook," 1989, p. 37.
- ⁹M. A. Green, *et al.*, "Progress in High Efficiency Silicon Cell and Module Research," Proceedings of the 23rd IEEE Photovoltaic Specialists Conference, May 10, 1993, Louisville, KY, p.8.
- ¹⁰R. A. Sinton, *et al.*, "Large Area 21% Efficient Si Solar Cells," Proceedings of the 23rd IEEE Photovoltaic Specialists Conference, May 10, 1993, Louisville, KY, p.157.
- ¹¹J. Knobloch, *et al.*, "High-Efficiency Solar Cells from FZ, Ca, and MC Silicon Material," Proceedings of the 23rd IEEE Photovoltaic Specialists Conference, May 10, 1993, Louisville, KY, p.271.
- ¹²V. Garboushian, *et al.*, "Radiation Hardened High Efficiency Silicon Space Solar Cell," Proceedings of the 23rd IEEE Photovoltaic Specialists Conference, May 10, 1993, Louisville, KY, p.1358.
- ¹³P. M. Stella *et al.*, "Thin Film GaAs for Space - - Moving Out of the Laboratory," Proceedings of the 23rd IEEE Photovoltaic Specialists Conference, May 10, 1993, Louisville, KY. Figure 1, p. 22.

BMDO PHOTOVOLTAICS PROGRAM OVERVIEW

Leonard H. Caveny
Ballistic Missile Defense Organization
Washington, DC

and

Douglas M. Allen
W.J. Schafer Associates
North Olmsted, Ohio

Outline

BMDO advanced solar array program overview
Brilliant Eyes type satellites
Electric propulsion
BMDO photovoltaic programs
Why concentrators?
loffee concentrator and cell development
Entech linear mini-dome concentrators
Flight test update/plans
Conclusions

BMDO Advanced Solar Array Program Overview

**Primary need is for a better power source for Brilliant Eyes type
satellites**

**Lightweight and low cost systems are also needed to enhance
BMDO electric propulsion programs**

**Cooperation with other government agencies is important to address
broader needs and leverage capabilities**

- **NASA Lewis Research Center**
- **Phillips Laboratory**
- **Others**

**Commercial spin-offs to improve U.S. competitiveness in the global
marketplace are also important**

Brilliant Eyes Program Overview

BMDO Program for a low orbit constellation of satellites for surveillance and tracking of ballistic missiles for theater and national defense missions

Program is managed by the Air Force Space and Missiles Center for BMDO

Competition ongoing to select prime contractor

- **Rockwell and TRW selected from four original contractors last year**
- **Source selection in progress to select one contractor to build the first two satellites**
- **Both contractor's programs will be continued for a later downselect for the full satellite constellation**

First flight ~1997

Brilliant Eyes Type System Constellation Specs

Altitude <2000 km, high inclination & low inclination rings

In lower end of VanAllen radiation belts

Constellation of 10 to 40 satellites

Deployed on an MLV, multiple satellites per launch

Emphasis on achieving mission objectives at minimum cost

Conservative approach to non-critical satellite components

Brilliant Eyes Type System Spacecraft Specs

500 kg goal

**1 kW solar arrays for 500 W of orbital average power onboard
(end of life)**

5-7+ year lifetime

Rad hard parts required

Applications of Electric Propulsion

**Initial orbit positioning - primary application, major fuel savings
at a cost of weeks extra time for the deployment**

• **Extra satellites/launch vehicle (major \$ savings)**

or

• **Extra margin in launch mass (risk reduction)**

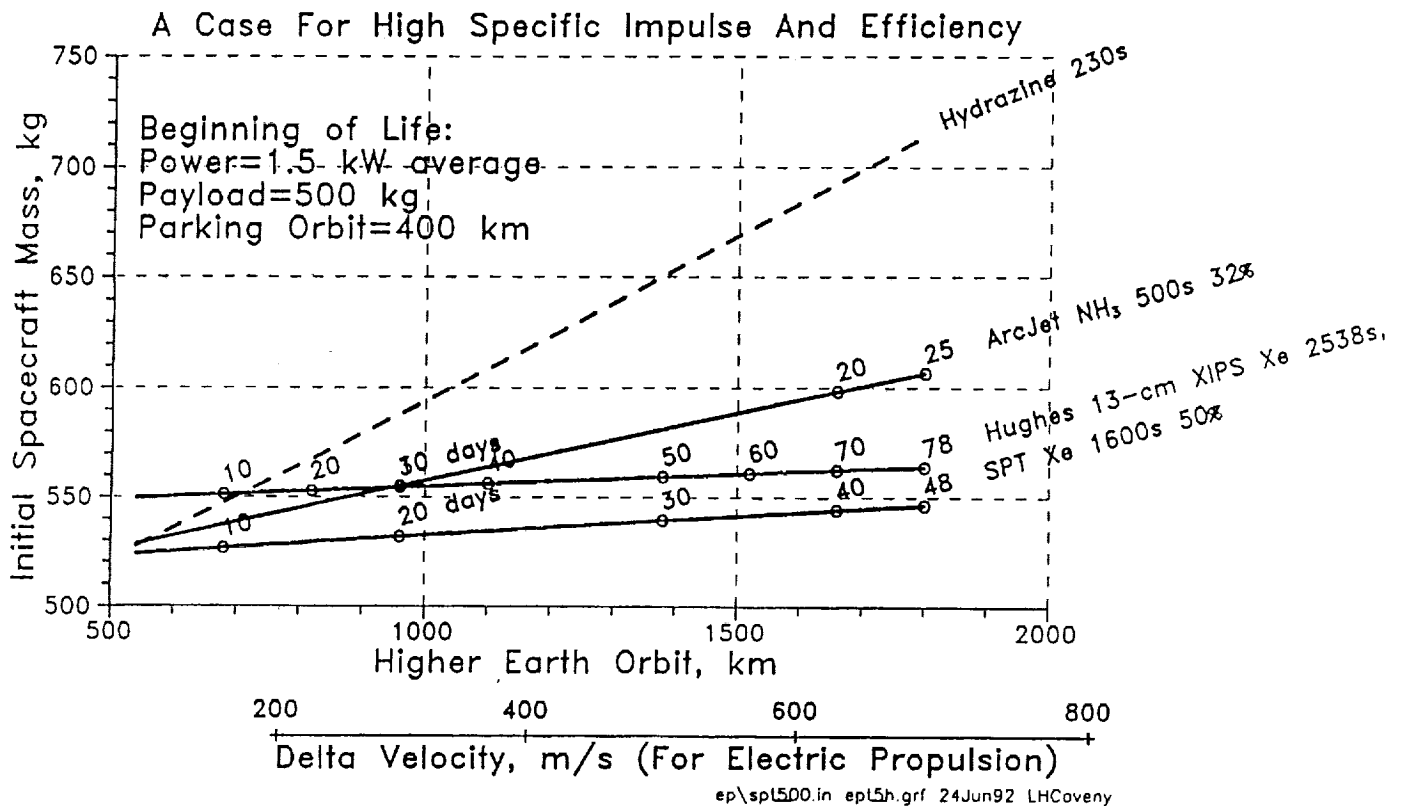
Strategic maneuvers and repositioning

Orbital maintenance

Deorbit satellite at end of life

**Primary Drawback of EP is longer trip times for positioning and maneuvers -
More solar array power (if affordable and mass efficient) helps a lot**

BRILLIANT EYES EARTH ORBIT TRANSFER



BMDO Photovoltaics Programs

Concentrator Solar Arrays

- Entech linear refractive concentrator
- Ioffe reflective and refractive concentrators and cells
- NASA Lewis agent for program management

Multiple-band-gap planar arrays

- Phillips Laboratory agent for program management

Other SBIR programs

Flight tests to demonstrate technology maturity

Why Concentrators?

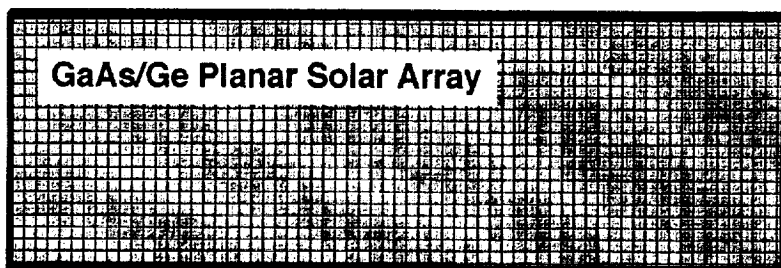
Concentrator solar arrays provide a pathway to major advances in satellite solar array parameters of interest

- Cost 2X lower than planar silicon
- Specific power of 100 W/kg or better - even for small satellites
- Very small penalty for incorporating radiation resistance

Technology development over the last decade has resulted in concentrator designs that are practical to integrate onto satellites

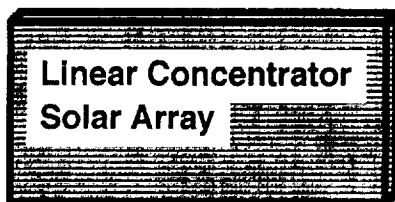
- Linear concentrators only require one critical axis for sun pointing
- Sun acceptance angles have been increased by nearly an order of magnitude
- Innovative optics designs allow low cost manufacturing approaches

Solar Array Technology Comparison for Brilliant Eyes Type Satellites



Array Specs:

1278 W (EOL)
2131 W (BOL)
12 m²
42 kg
\$6.39M (est.)



Array Specs:

1278 W (EOL)
1406 W (BOL)
4.5 m²
18 kg
\$0.84M (projected)

(note: drawings to scale)

Ioffee Concentrator and Cell Development

Mirrored and flat fresnel concentrator array development

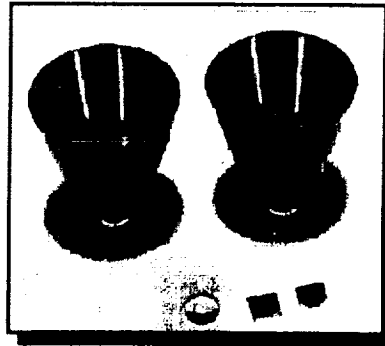
- Linear version of reflective concentrator now being developed
- Four fresnel modules being prepared for flight test

Advanced tandem and multi-junction solar cells

- GaAs/InGaAs
- GaAs/AlGaAs

Array goals are:

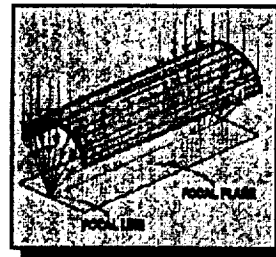
- 300 W/m²
- 100 W/kg
- 30% efficiency



Entech Linear Concentrator Technology Description

Concentrator solar arrays to provide power to satellites

Single axis convex fresnel concentrator concept



Technology nearing maturity for satellites

- Materials, cells, and lenses already space flight tested
- 2 axis mini dome concentrator module being prepared for launch on PASP+
- One axis version of concentrator ground demonstrated

Performance of arrays provides many operational benefits

- Efficiency = 1.5 x GaAs
- Recurring Cost = 0.3 to 0.5 x Si
- Array specific power = 1.5 to 2.5 x APSA for small arrays
- Radiation tolerance same as InP

Flight Test Update/Plans

Lear Jet concentrator module performance tests

LDCE-4, -5: Materials experiment, limited AO exposure

EOIM III: Small area lens materials and cells

Wakeshield (MATLAB-1): Materials experiment and two mini dome lenses (AO performance testing of lens coatings)

PASP-plus: First active experiment of advanced refractive concentrator array technology, long duration (1-3 yrs.), radiation damage, and high voltage plasma interaction

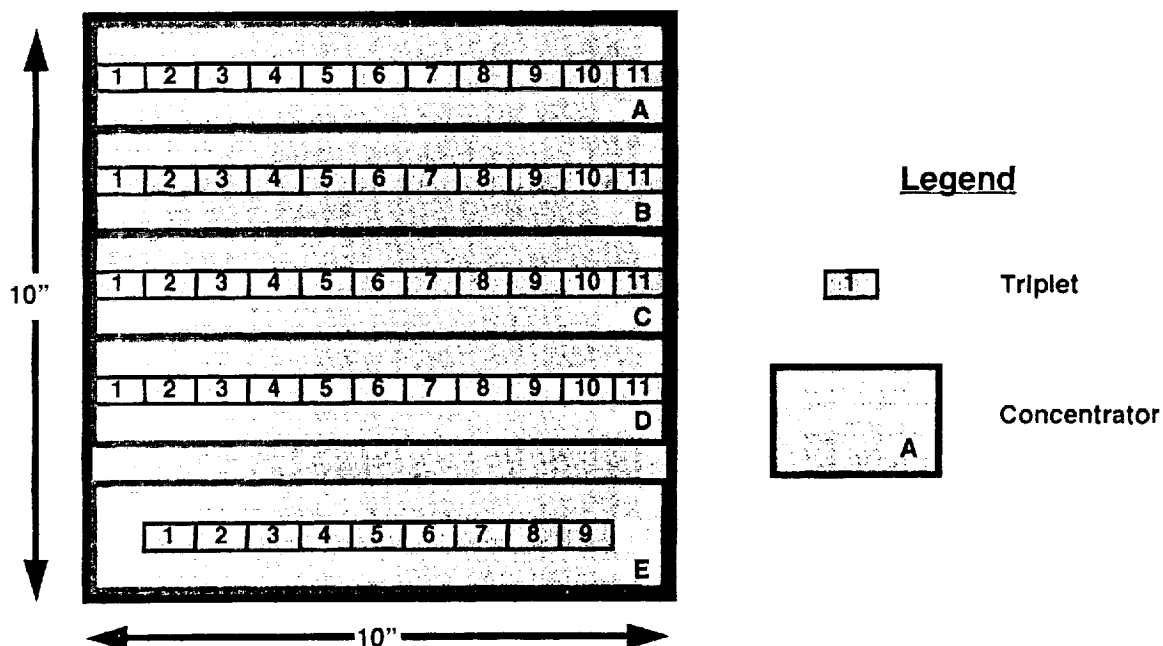
STRV-2: In planning stages, first active experiment of one axis concentrator module

Molniya flight experiment: 1995 test of four 16 element loffee fresnel concentrators

C-SAVE: Planned 1997 flight demonstration of a 1 to 1.5 kW linear concentrator array

STRV-2 Experiment Layout

Experiment Module



Molniya Concentrator Flight Experiment

Flight test of four loffee concentrator modules

- Flat fresnel concentrators
- 16 element modules
- Tandem solar cells

Mounted on outer wall of a Molniya communications satellite

Launch planned in summer 1995 on a Molniya launch vehicle
from Baikanour

Molniya orbit provides high radiation environment

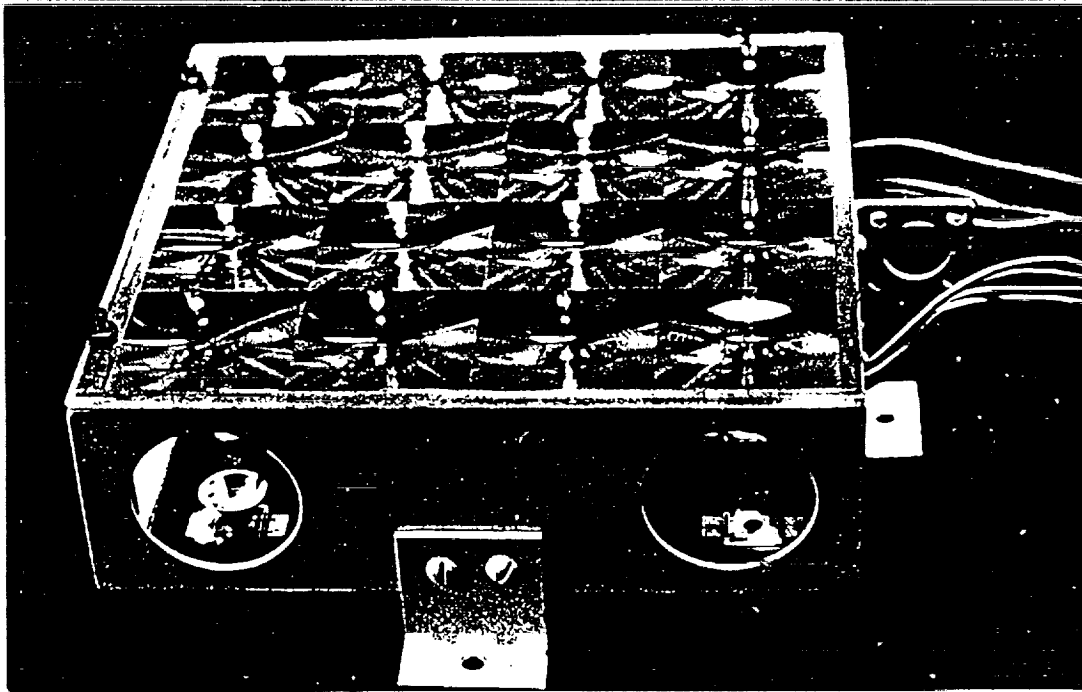
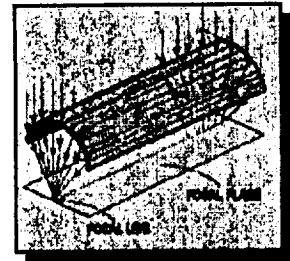


Photo of Fresnel lens concentrator panel on the basis
of 16 modules (input photoactive square 100 cm^2).

C-SAVE Concept

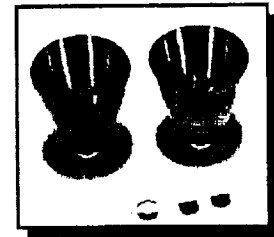
Objective

- Demonstrate and quantitatively measure the performance of a linear photovoltaic concentrator array
 - ✓ Array pointing
 - ✓ Off-axis tracking
 - ✓ Thermal distortion effects
- Space qualify concentrator solar arrays



Description

- Two solar arrays sized to approximately 500 w each (1 kw EOL total) - each array will be 1.5 m²
 - ✓ Either reflective or refractive optics
 - ✓ Sunlight focused onto a strip of high efficiency, multi-band gap photovoltaic cells
- Arrays will be deployed in space and will track the sun in one axis (when the experiment is operating)



Conclusions

Concentrator solar arrays provide significant benefits to future BMDO missions

- Low cost
- Light weight
- Radiation resistant

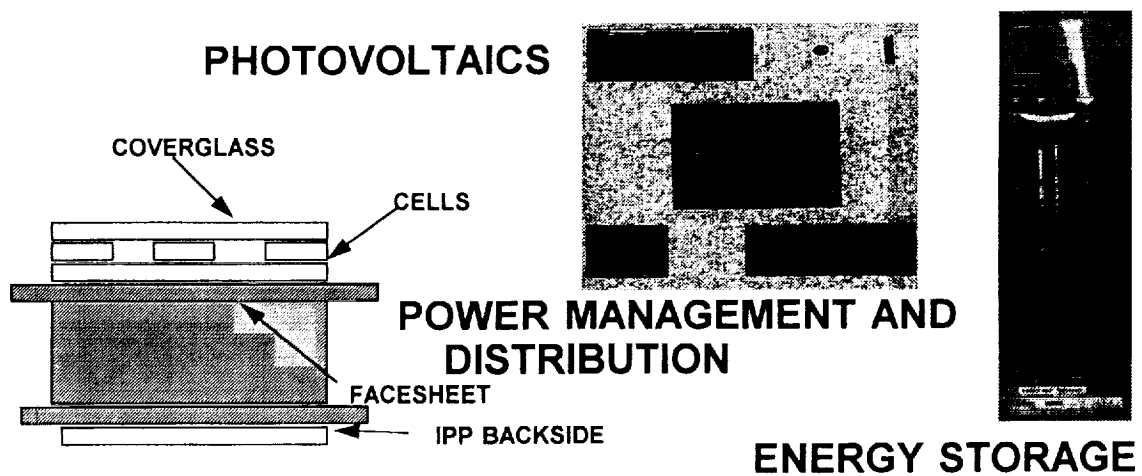
BMDO approach is to develop flight test modules and arrays to demonstrate technology maturity

Space concentrator arrays will provide significant cost and mass advantages to a range of commercial satellite programs

AIR FORCE ACTIVITIES IN SPACE PHOTOVOLTAIC POWER SYSTEM TECHNOLOGY

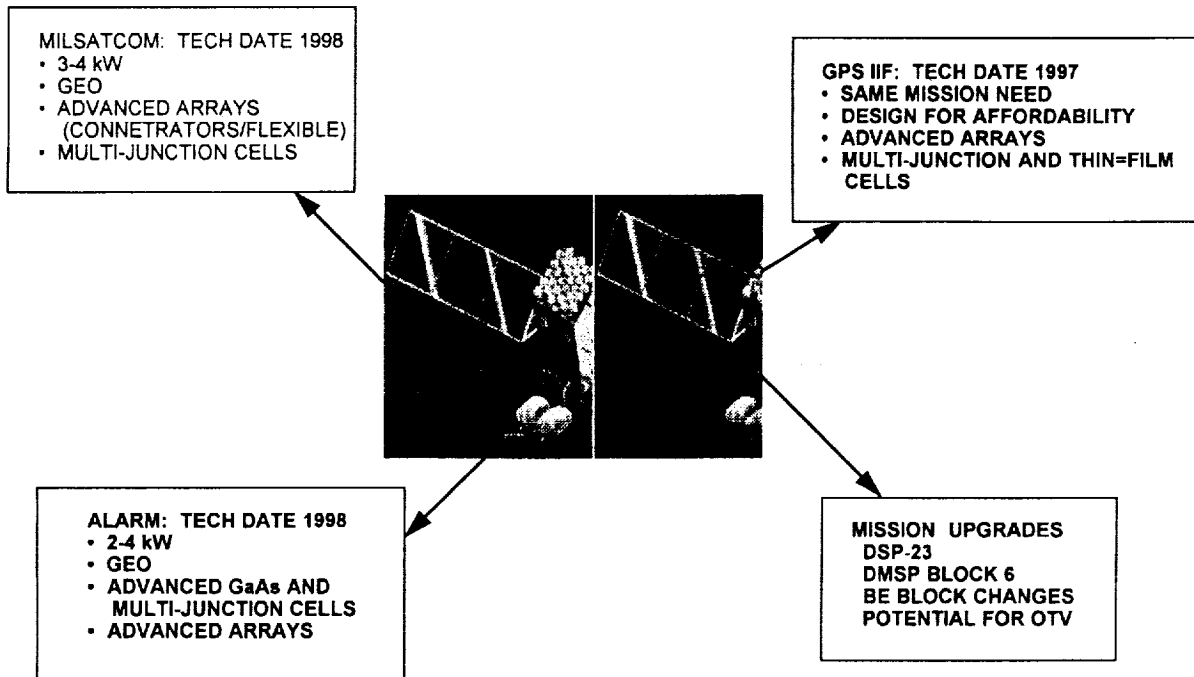
Kelly Gaffney
U.S. Air Force
Kirtland AFB, New Mexico

TECHNOLOGY FOCUS



**FULL TECHNOLOGY LIFE CYCLE DEVELOPMENT
HIGH RISK/HIGH PAYOFF
NEAR TERM SOLUTIONS
MARKET AND USER DRIVEN**

NEW AIR FORCE SATELLITES FOR THE YEAR 2000

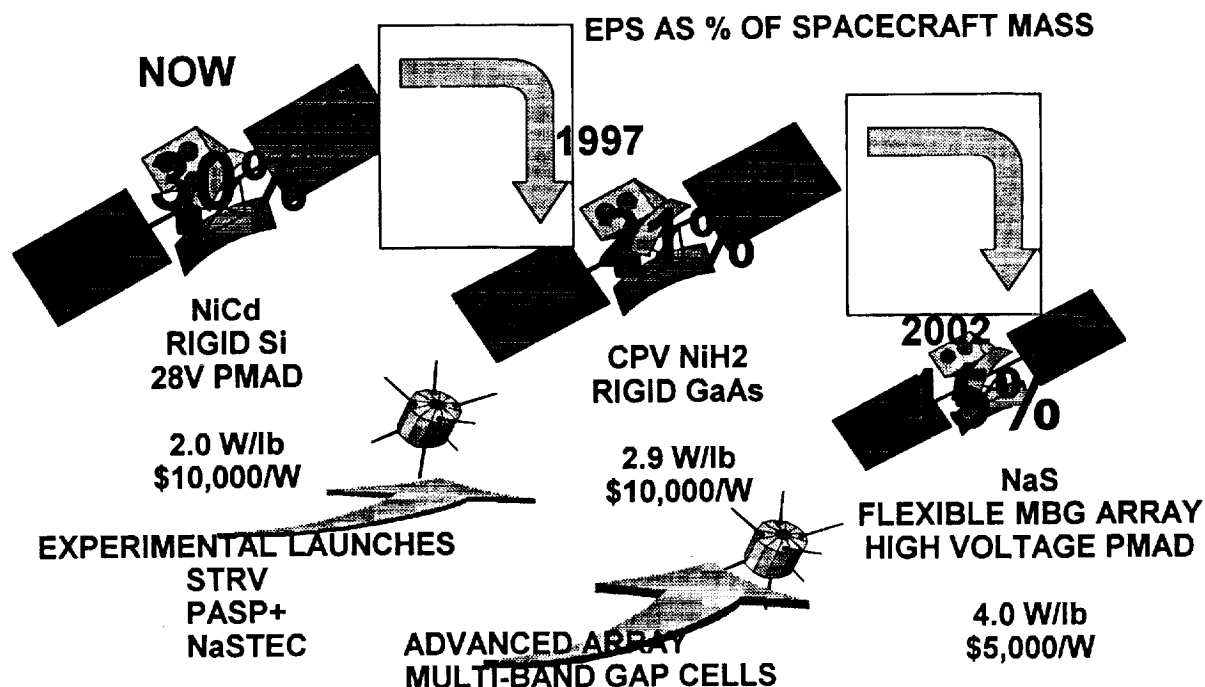


TECHNOLOGY CHALLENGES

SATELLITE/LAUNCH POWER TECHNOLOGY DRIVERS

<u>LAUNCH VEHICLE</u>	<u>SATELLITE</u>
ARRAY VOLUME (150W/M2)	NEED FOR MORE POWER
BATTERY/ARRAY MASS (15-25% OF SATELLITE MASS)	SOLAR CELL COST (\$1000/W)
SATELLITE LIFETIMES (NiCd BATTERIES--3 YEARS IN LEO) (SOLAR CELL DEGRADATION)	POWER SYSTEM MODULARITY & STANDARDIZATION .
PRIMARY BATTERY PERFORMANCE (10% OF LAUNCH PROBLEMS)	COMPONENT RELIABILITY (LATCHING RELAYS, BYPASS SWITCHES, ETC)

SYSTEM BENEFITS FROM TECHNOLOGY



TECHNOLOGY OPTIONS/BENEFITS

PHOTOVOLTAICS TECHNOLOGY IMPROVEMENTS

STATE OF THE ART: GaAs RIGID ARRAYS
18% EFFICIENT CELLS
50W/KG BOL, 250W/M2 BOL
STOWAGE PROBLEM

ADVANCED POWER OPTIONS:

LOW RISK: GaInP/GaAs/Ge RIGID ARRAY
27% EFFICIENT CELLS
85W/KG BOL, 400 W/M2 BOL
LESS OF A STOWAGE PROBLEM

MEDIUM RISK: CIS AND CdTe THIN FILM CELLS
12% EFFICIENCY, RAD-HARD
40% LIGHTER, LESS SUBSTRATE
SIGNIFICANTLY LOWER COST

MEDIUM RISK: ADVANCED FLEXIBLE BLANKET
OR CONCENTRATOR ARRAY
100-150W/KG BOL
SOME HAVE STOWAGE VOLUMES
OF 0.15M3



PHOTOVOLTAICS TECHNOLOGY OPTIONS/BENEFITS

GaAs CELL IMPROVEMENTS:

PREMISE: ULTRA LIGHTWEIGHT GaAs SOLAR CELL BY INCORPORATING LIGHT-TRAPPING FEATURES ON THE BACK OF THE CELL. HIGH CURRENTS CAN BE OBTAINED WITH A VERY THIN LAYER OF MATERIAL. GOAL IS A 24.5% CELL AT 1 SUN AMO

SUCCESS:

- IMPROVED LPE GROWTH LAYERS--2CM X 4CM CELL
- OPTIMIZED ANTI-REFLECTIVE COATING
- INCORPORATED LIGHT TRAPPING STRUCTURE TO THICK CELLS

FUTURE PLANS:

- CHOOSE METAL FOR USE IN BACK CONTACT
- IMPROVE FABRICATION PROCESS

BENEFITS:

- VERY LIGHT, HIGH EFFICIENCY GaAs
- GOOD RADIATION TOLERANCE BECAUSE OF THIN DEVICE STRUCTURE

PHOTOVOLTAICS TECHNOLOGY OPTIONS/BENEFITS

MULTI-JUNCTION SOLAR CELL:

PREMISE: DEVELOP 25% EFFICIENT, MONOLITHIC, MULTI JUNCTION SOLAR CELLS. CELLS SHOULD BE TWO-TERMINAL, STANDARD SIZE AND COST NO MORE PER WATT THAN GaAs

SUCCESS:

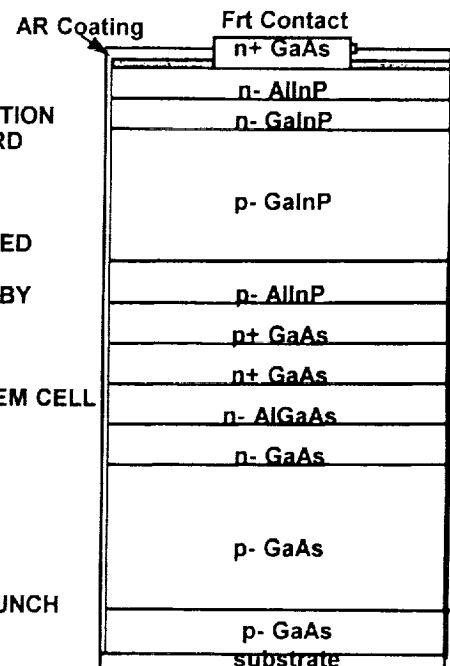
- 24.6% EFFICIENT, TWO JUNCTION GaInP/GaAs CELL DEVELOPED
- READY FOR FLIGHT TEST ON MIGHTYSAT
- 26.7% EFFICIENT GaInP/GaAs/Ge, 2 BY 2cm LAB CELL READY BY CHRISTMAS

FUTURE PLANS:

- THREE YEAR PLAN TO IMPROVE RELIABILITY/YIELD OF TANDEM CELL COLLABORATE WITH MANTECH AND NASA TO DEVELOP 6 BY 6, HIGH BATCH PRODUCTION
- GROUND AND RADIATION TESTING IN LATE 1996
- FLIGHT QUALIFICATION IN EARLY 1997

BENEFITS:

- 35-40% REDUCTION IN WEIGHT OVER GaAs
- 40% REDUCTION IN ARRAY CROSS-SECTIONAL AREA FOR LAUNCH
- COSTS SIMILAR TO GaAs



PHOTOVOLTAICS TECHNOLOGY OPTIONS/BENEFITS

THIN-FILM SOLAR CELLS

PREMISE: DEVELOP HIGH EFFICIENCY (12-15%), LARGE AREA DEPOSITION THIN-FILM PHOTOVOLTAIC DEVICES. FOCUS IS ON CIS AND CdTe

SUCCESS:

- DEPOSITION OF CIS ON 4 X 4 IN SUBSTRATE
- 12% CIS CELLS IN SMALL SIZES
- DEVELOPMENT OF 10% CIS ON 24 CM X 24 CM FLEXIBLE METAL FOIL BY DEC

FUTURE PLANS:

NEW PROGRAM TO DEVELOP REEL-TO-REEL DEPOSITION ON FLEXIBLE SUBSTRATES IN THE 12-15% RANGE

BENEFITS:

- SIGNIFICANT COST REDUCTIONS OVER CRYSTALLINE CELLS
- 30-40% ARRAY WEIGHT REDUCTION
- REDUCED STOWAGE VOLUME FOR ARRAY



PHOTOVOLTAICS TECHNOLOGY OPTIONS/BENEFITS

ADVANCED FLEXIBLE BLANKET ARRAY:

PREMISE: TO DEVELOP AND FLIGHT QUALIFY TWO FOLD-OUT ARRAYS WITH AT LEAST 150W/Kg EFFICIENCY, 0.15m³ STOWAGE VOLUME AND SYSTEM LEVEL COSTS OF LESS THAN \$500/W IN 1-3 KW POWER RANGE

SUCCESS: AWARDING OF TWO SEPARATE CONTRACTS

- ROLL-OUT FLEXIBLE BLANKET USING CIS THIN-FILM CELLS AND SHAPE MEMORY CONTROL
- RIGID, COMPOSITE, FOLD-OUT ARRAY USING ANGLED MIRRORS FOR SUN CONCENTRATION

FUTURE PLANS:

- DEVELOP AND FABRICATE ARRAYS
- FLIGHT TEST IN 1998
- POTENTIAL INTEREST BY POST-1999 SATELLITES

BENEFITS:

- 3-FOLD INCREASE IN ARRAY EFFICIENCY
- SIGNIFICANT DECREASE IN ARRAY STOWAGE VOLUME
- 50% COST SAVINGS ON ARRAY PROCUREMENTS

PHOTOVOLTAICS TECHNOLOGY OPTIONS/BENEFITS

INTEGRATED POWER SYSTEM: LOW RISK

PREMISE: TO DEVELOP AND DEMONSTRATE A MODULAR, STANDARDIZED POWER SYSTEM ARCHITECTURE USING SHUNT REGULATION MOUNTED TO THE GaAs SOLAR ARRAY USING A HYBRID PATCH AND RESISTOR STRIP. SYSTEM IS ABLE TO ACCOMMODATE GROWTH BETWEEN 100W -- 5KW WITH MINIMAL REDESIGN.

SUCCESSES:

PANEL DEVELOPMENT COMPLETE
PRELIMINARY GROUND TESTING OF COUPONS COMPLETE
FLIGHT TEST PROGRAM IN PLACE

FUTURE PLANS:

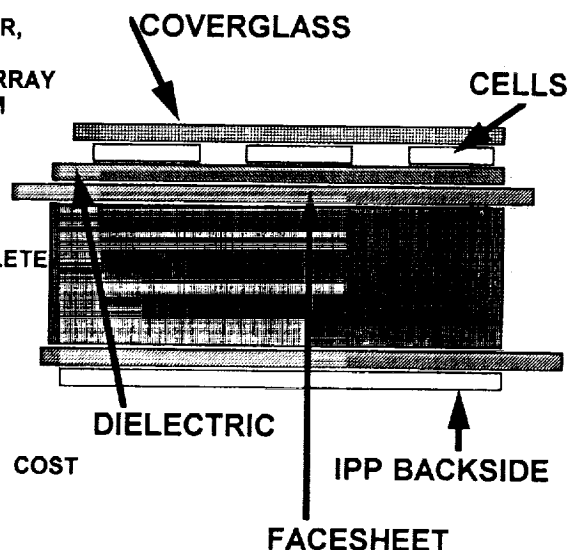
FLIGHT TEST ON STP MISSION IN LATE 1995

BENEFITS

MODULAR, STANDARD ARCHITECTURE MEANS LESS
REDESIGN AND MINIMUM REQUALIFICATION: LOWER COST

LESS SYSTEM WEIGHT: 12 W/KG

BETTER THERMAL CONTROL



PHOTOVOLTAICS FLIGHT EXPERIMENTS: NEW STARTS

LABSAT

FLIGHT TEST HIGH EFFICIENCY DUAL JUNCTION
CELLS AND TRIPLE JUNCTION CELLS ON COMPOSITE SUBSTRATES

HARDWARE DELIVERY DATE: 30 SEP 1995

CONDUCT DESIGN ANALYSIS FOR FUTURE LABSAT
POWER SYSTEM UPGRADES

UoSAT

COOPERATIVE EFFORT WITH UK, NASA, NRL, BMDO
TO FLIGHT TEST POWER SYSTEM COMPONENTS

PROBABLE AF EXPERIMENTS INCLUDE NaS LONG-TERM
FLIGHT TEST, ADVANCED ARRAY DEMO, TRIPLE JUNCTION
SOLAR CELL FLIGHT

LAUNCH DATE IS JUN 1996

PHOTOVOLTAICS FLIGHT EXPERIMENTS

STRV 1B

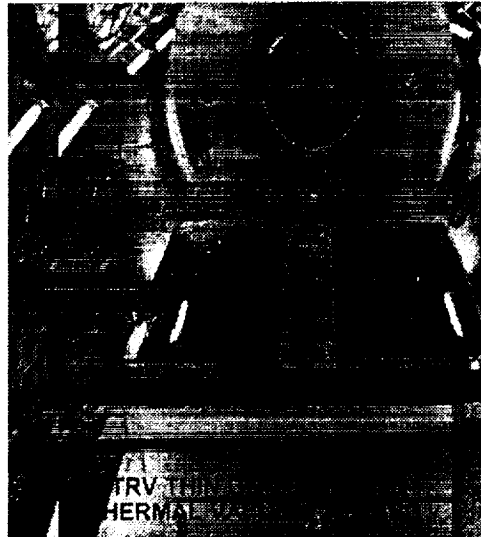
FLIGHT TEST OF ADVANCED CELL TECHNOLOGIES.
PRIMARY POWER PANELS ARE GaAs, 5.5MIL MANTECH
CELLS. EXPERIMENTAL PANELS HAVE 20 DIFFERENT
EMERGING CELL TYPES

PANELS WILL BE TESTED OVER THREE MISSION FOR
ELECTRICAL PERFORMANCE AND RADIATION
RESISTANCE.

PASP+

FLIGHT TEST OF 12 ADVANCED ARRAY DESIGNS:
FLEXIBLE BLANKETS, CONCENTRATORS, THIN-FILMS

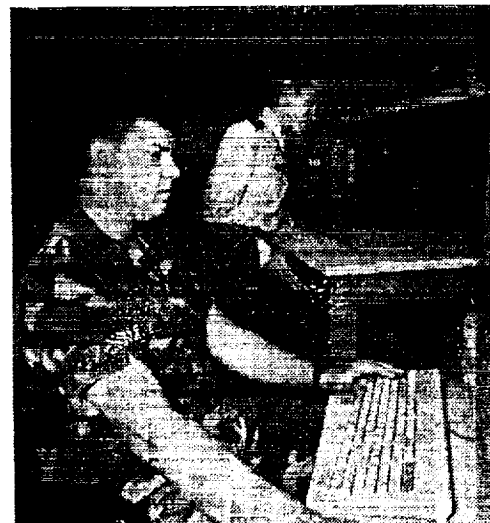
ARRAYS WILL BE TESTED FOR ENVIRONMENTAL AND
PLASMA INTERACTIONS, HIGH VOLTAGE PERFORMANCE
AND ELECTRICAL PERFORMANCE



LABORATORY PROGRAM

SOLAR CELL ASSESSMENT

- FULL LABORATORY CAPABILITY TO
CONDUCT MECHANICAL AND ELECTRICAL
TESTING OF SOLAR CELLS
- RADIATION DEGRADATION TESTING AT
UK DRA HARWELL FACILITY
- SOLAR CELL DATABASE TESTING WILL
START THIS YEAR (12 CELLS ALREADY
IDENTIFIED--TANDEM, THIN-FILMS, GaAs,
ADVANCED Si)
- DATABASE WILL BE OPEN TO ALL
- WILL TEST ANY CELLS UPON SPO REQUEST
AT NO COST



CONCLUSIONS

NEW AIR FORCE SYSTEMS ARE COMING ON LINE BY THE TURN OF THE CENTURY: LIFE CYCLE COST WILL BE THE BIG DRIVER

POWER TECHNOLOGIES AS BOTH COST AND WEIGHT REDUCTION TOOLS ARE OF INTENSE INTEREST TO OUR CUSTOMERS

TECHNOLOGY TRANSITION PATH FOR TANDEM CELLS AND ADVANCED ARRAYS IS IN PLACE

LABORATORY WILL CONTINUE ON THE PATH TO LIGHTER, CHEAPER CELL AND ARRAY TECHNOLOGIES

NEW PROGRAM INITIATIVES TO WATCH FOR: TANDEM CELL MANTECH, ADVANCED THIN-FILM CELL DEVELOPMENT, TANDEM CELL FLIGHT TEST SOLAR CELL ASSESSMENT, RENEWED INTEREST IN ARRAYS FOR OTV

AN UPDATE ON THE DEPARTMENT OF ENERGY'S PHOTOVOLTAIC PROGRAM

John P. Benner and Mark Fitzgerald
National Renewable Energy Laboratory
Golden, Colorado

Summary

Funding for the terrestrial photovoltaics program is \$78 million in 1994. This is more than double the minimum level reached in 1989 and runs counter to the general trend of decreasing budgets for Department of Energy (DOE) programs. During the past five years, the program has expanded its mission from research and development to also address manufacturing technology and commercialization assistance. These new activities are directed toward revitalizing the market to reinstate the rapid rate of sales growth needed to attract investment. The program is approaching balance among efforts in each of the three areas. This translates to a reduction in some of the R & D activities of most relevance to the space power community. On the other hand, some of the advancements in manufacturing may finally bring thin-film technologies to reality for space arrays. This talk will describe the status and direction of DOE program with an eye toward highlighting its impact on technology of interest for space.

Introduction

During the latter part of the 1980's, the growth rate in photovoltaic module shipments was more than 20%. Industry shifted from a condition of shipping from excess inventory to back-orders. During the last several years, world wide sales growth has slowed to less than 5%. This condition is attributed to the world wide recession. This condition does not help the industry attract capital needed for expansion of production or introduction of new products. The Department of Energy has addressed this problem by adding two programs focussed at helping industry to increase sales. First, the program directed support to manufacturing technology research to further improve competitiveness and open new applications by reducing product cost. The second initiative increased interactions with envisioned customers to enhance awareness of photovoltaic technology for applications where it is competitive today. The result on the total program budget can be seen in Figure 1.

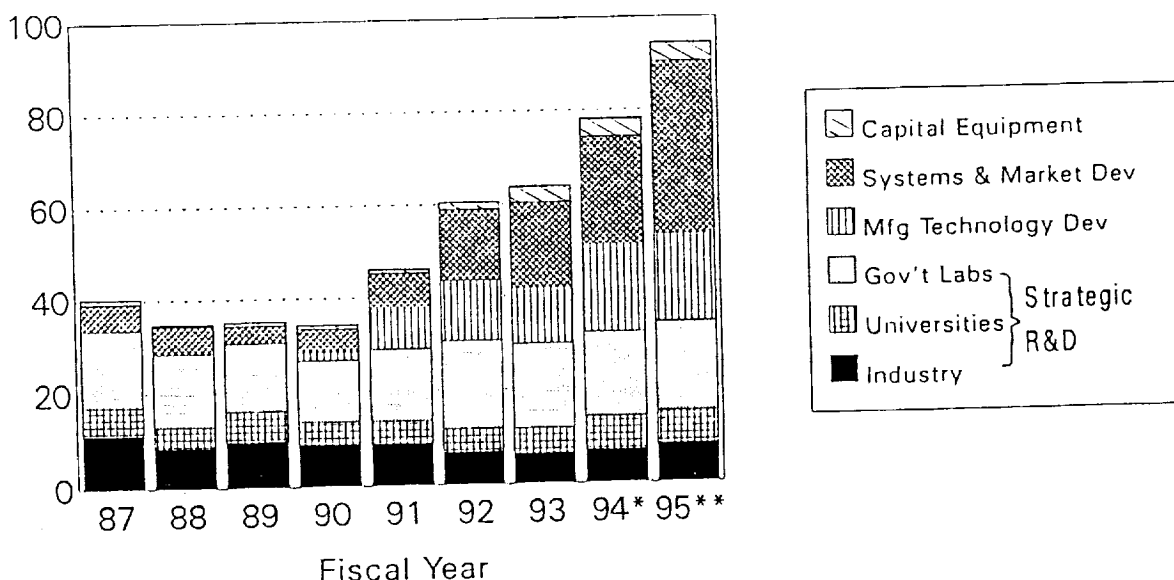


Figure 1. US DOE Photovoltaic Program Budgets

*FY94 Est. prior to rescissions

**FY95 Est. based on DOE budget request

Photovoltaic Manufacturing Technology

The Photovoltaics Manufacturing Technologies (PVMaT) project is a partnership between the U.S. Department of Energy and the U.S. PV industry. By working together to reduce costs, the partners ultimately hope to extend the U.S. leadership in manufacturing and developing commercial PV systems.

The PVMaT project is being conducted in three phases. Phase 1 identified and prioritized areas in the manufacturing processes where research and development were needed for major production cost reductions. Problem solutions began in 1992, under Phase 2A, while Phase 3A addresses generic module manufacturing needs common to the PV industry. Current industry partners, topic and award amounts are shown in Figure 2.

Company	Topic	Principal Investigator	Amount (\$M)
Phase 2A			
Siemens Soar Industries	Cz Silicon	Terry Jester	10.5
Solarex Corporation	Triple Junction a-Si Alloys	Robert Oswald	10.0
ENTECH, Inc.	Linear Focus Conc. Modules	Mark O'Neill	3.1
Astropower, Inc.	Silicon Film Technology	Sandi Collins	7.1
Utility Power Group	a-Si Modules	Michael Stern	4.7
Energy Conversion Devices	Roll-to-Roll a-Si	Masatsuga Izu	10.8
Phase 2B			
Golden Photon, Inc.	CdTe	Steve Johnson	9.8
Solarex Corporation	Cast Silicon	John Wohlgemuth	6.3
Solar Cells, Inc.	CdTe	Dan Sandwisch	7.4
Texas Instruments	Spherical Silicon	Jim Skelly	16.6
Phase 3A			
Springborn Laboratories	Improved Encapsulants	Bill Holley	1.5
Spire Corporation	Automated Cell Assembly	Mike Nowlan	1.4

Figure 2 PVMaT Industry Partners

Systems and Market Development

The DOE has established the PV Compact Coordinating Council as the focus of market development activities in the United States. PV Compact consists of utility representatives from the Utility Photovoltaic Groups (UPVG) and representatives from state energy offices and state Public Utility Commissions (PV4U). The DOE/NREL PV Program is supporting the development of a strategy to commercialize PV through UPVG. This is an organization of more than 70 utilities that work together to advance cost-effective and high-value uses of PV for utilities. UPVG activities include publishing a newsletter, sponsoring workshops, and supporting five active working groups working towards a goal to lead utilities into photovoltaic systems acquisitions of about 50 megawatts over five years with less than 30% government cost sharing. PV4U is a project to work with and assist state working groups involved with the development of PV systems by utilities.

Building Opportunities in the United States for Photovoltaics (PV:BONUS) is a DOE/NREL project to evaluate and implement innovative ideas for integrating PV into building systems. Twenty-nine teams proposed concepts, and, in FY 1993, five teams began work on the planned 5-year, \$25-million (from DOE) cost-shared project. Each of the five teams includes a lead contractor and up to 10 other organizations representing building-materials manufacturers, building contractors, PV suppliers, utilities, colleges and universities, systems designers, architectural and engineering firms, and building owners.

The DOE/NREL PV Program helps U.S. PV companies reach the growing international markets by leveraging funds and lowering institutional barriers to international trade in PV technology. DOE shares the cost of pilot installations, and PV Program personnel help perform site assessments, develop project evaluation criteria, write technical specifications for projects, and conduct workshops and training seminars.

In FY 1993, DOE and the Federal Republic of Brazil began working together to bring electricity to rural communities in Brazil using PV. The first phase began in December 1992 with the installation of lighting systems on 600 homes, schools, and public spaces in rural areas. Phase 2 of this project is now underway, with DOE contributing approximately \$1.3 million toward the estimated \$3 million cost of the project's second phase in FY 1994. Other project development efforts are underway in China, India, and Indonesia.

The guiding principal behind all of the market development activity is the establishment of expanded markets that are sustained by the competitiveness of photovoltaic products such that ongoing Federal support, in tax policy or direct funding, is not required.

Strategic Research and Development

The budget for photovoltaic research has been held flat during the period in which the new initiatives in manufacturing and market development were added. However, within the research program, priorities have changed substantially. The support for thin-film technologies has grown to keep pace with inflation. Other projects needed to be reduced to afford to maintain thin-films. Much of this reduction came from support of concentrator and high efficiency options. Currently, the newest element of the research program is the active request for proposals to form a Thin-Film Partnership. This single solicitation will draw in proposals from both the major industrial interests and well as the research teams from industry, universities and not-for-profit laboratories. The goals of the procurement are to: i) support the successful introduction of U.S. thin film products; and, ii) support advanced thin-film R&D needed for future product competitiveness. Since this is an active solicitation, no more can be described in this paper.

EUROPE'S SPACE PHOTOVOLTAICS PROGRAMME

Klaus P. Bogus
European Space Agency
Noordwijk, The Netherlands

SUMMARY

The current space PV technology development programme of ESA is described. The programme is closely coupled to the European space mission scenario for the next 10 year period and has as main objective to make the most effective use of the limited resources available for technology in the present economical climate. This requires a well-balanced approach between concentration on very few options and keeping the competition alive if more than one promising technology exists.

The paper describes ESA's main activities in the areas of solar array technology, solar cell technology, solar cell assembly technology, and special test and verification activities including the in-orbit demonstration of new technologies.

INTRODUCTION

Europe has had a very successful record in the field of space photovoltaics and has achieved a competitive position in the world market. For a large variety of European spacecraft systems photovoltaic solar generators are the exclusive source of electrical power and additionally, Europe has succeeded in exporting solar arrays across the Atlantic (e.g. IUE, Hubble Space Telescope, CTS-Hermes and INTELSAT).

The main purpose of the space photovoltaic technology development programme is to maintain the high standard of European solar array technology by carefully modernising the existing concepts in a step-wise approach. The smooth introduction of new technologies into flight programmes is achieved by close cooperation between technologists and project engineers.

The close coupling of the technology programme to the European mission scenario for the next 10 years is perfectly in line with the approach described above and leads to a fast application cycle of new technologies. A disadvantage of this approach is the resulting low priority for globally attractive new technologies which are not directly required in the ESA mission scenario with its limited scope.

DETAILS OF ESA'S SPACE PV TECHNOLOGY PROGRAMME

The programme is described in the 7 tables below according to a systematic division into solar array technology, solar cell technology, assembly technology, technology verification activities and supplementary activities.

The first column of each table contains the technology activity title, the second column indicates the present status of the activity. "Proposed" stands for a new activity which is not yet accepted in the budget planning, after acceptance it turns into "planned", and after initiation into "running". The 3rd column identifies the frame-programme under which the activity is funded: "Basic" is the general basic TRP (Technological Research Programme) of ESA, "ASTP" is the acronym for applied supporting technology programmes of the Telecommunications satellite area and "GSTP" is the newly introduced general supporting technology programme of ESTEC for all ESA missions. Additionally, several of the national activities in the ESA-member states are harmonised with ESA and run under common management arrangements. Schedule indications can be found in the 4th column. The last column contains summary descriptions.

SOLAR ARRAY TECHNOLOGY.

ESA's Solar Array Technology is based on a two main design concepts: Advanced lightweight rigid panel arrays and advanced flexible blanket arrays. With both concepts a high degree of maturity and flight experience has been accumulated in recent flight programmes: OLYMPUS-1, HST and ERS-1

are operating very successfully with flexible blanket arrays, whereas EURECA, HIPPARCOS and the ECS/MARECS satellites are supplied with rigid panel arrays.

The solar array technology development aims at the improvement of the present lightweight carbon-fibre face-sheet panels for specific future telecom-missions. Since the technology requirements are generally very mission specific it has become general practice to do these developments within the corresponding flight programmes and not in generic technology programmes.

Unfortunately EUROPE has presently no new programme requiring flexible blanket solar arrays so that this technology which has already reached a high degree of maturity, can not be further improved.

The development of alternative concepts was limited to studies on concentrator arrays (SARA-Louvre, Holographic Dispersive).

SOLAR CELL TECHNOLOGY.

This part of the programme comprises two main elements: Improvement of silicon solar cells and development of GaAs solar cells:

- Hi-ETA silicon cells with 16-17% efficiency have been pre-developed and are now approaching the pilotline production stage.
- Further improvement towards 18% efficiency are under pre-development using advanced passivation and optical confinement
- a demonstration of a 20% efficiency silicon cell is foreseen in a basic R&D study on small area, low quantity samples
- GaAs and GaAs-on-Ge cells have been pre-developed in Italy, Great-Britain and Germany.
- The next step will be a pilotline production of GaAs-on-Ge cells
- Further improvements of III-V-compound cells are expected in the area of ultra-thin (superstrate supported) GaAs cells and multi-junction/tandem cells.

SOLAR CELL ASSEMBLY TECHNOLOGY.

This part of the Programme covers :

- the development of improved Aluminium solar cell interconnectors (ATOX-resistant, low-cost)
- the development of ultrasonic welding for Si- and GaAs cells (long cycling life, low-cost)
- advanced cover-glass bonding (Direct Electrostatic bonding, Teflon Pre-preg bonding)
- Infra-red reflective coatings on cover-glasses (improved efficiency through lower Temp.)
- Development of integrated solar cell modules (GaAs-thin film and Silicon superstrate concepts).

TECHNOLOGY VERIFICATION TESTS.

Apart from the activities performed at SPASOLAB (ESA's solar cell laboratory in Madrid), the main activities are related to the investigation of space environmental effects on solar arrays. This includes investigation of synergistic effects, thermal cycle induced fatigue, plasma and atomic oxygen effects, micrometeorite impact effects and particle radiation damage in solar cells. Radiation damage investigations are required for two different reasons: One is the evaluation of new solar cells (e.g. advanced GaAs and Hi-ETA silicon cells), the other the planning of missions in different orbits (e.g. the new Telecom-missions in high-inclination, medium altitude orbits with equivalent fluences of more than 10^{16} One-Mev-electrons /sqcm).

SUPPLEMENTARY ACTIVITIES.

This segment contains mainly the preparation and evaluation of flight experiments and the Post-flight investigation programmes on the HST and EURECA solar arrays reported in another part of this conference.

SOLAR GENERATOR TECHNOLOGY PROGRAMME

1994 STATUS

1. ARRAY SYSTEM DEVELOPMENT
2. ASSEMBLY TECHNOLOGY
3. COMPONENT TECHNOLOGY
4. TECHNOLOGY VERIFICATION TESTS
5. SUPPLEMENTARY ACTIVITIES

SOLAR GENERATOR TECHNOLOGY PROGRAMME

1. ARRAY SYSTEM DEVELOPMENT

* SOLAR ARRAY FOR HIGH POWER APPL.	RUNNING	ASTP-4 9	94-95	ADAPTATION OF RIGID ARRAYS TO 5-7kW TELECOM APPLICATIONS
* ADVANCED RIGID PANEL ARRAYS	RUNNING	TELECOM HARMO	93-95	ARAFOM (FSS), HOTBIRD+ GSR(AS), MARK-3 (DASA)
* LILP ARRAYS	RUNNING	BASIC 4	91-93	LOW POWER/LOW INTENSITY ARRAYS FOR MARSNET
* SYSTEM ANALYSIS & ASSESSM. NOVEL CELLS	PLANNED	BASIC 9	95-96	EVALUATION OF NEW CELL TYPES ON ARRAY LEVEL

SOLAR GENERATOR TECHNOLOGY PROGRAMME

2. ASSEMBLY TECHNOLOGY

* ALUMINIUM INTERCON. TECHNOLOGY	RUNNING	BASIC 6	87-94	DEVELOPM. OF ULTASONICALLY WELDED ALU-INTERCONNECTORS
* SOLAR CELL ASSEMBL. TECHN. (SI & GaAs)	PROPOSED	ASTP-4 9	?	CONTINUE ASTP-3 DEVELOPM. FOR NEW CELL TYPES
* INT. ELEV. VOLTAGE MODULE	RUNNING	BASIC 6	93-95	DEV. OF INTEGRATED GAAS ULTRATHIN MODULES WITH DIODES
* I-R-REFLECTING COATING	RUNNING	ASTP-4 9	92-94	REDUCTION OF OPER. TEMPERATURE BY REFLECTOR ON COVER-GLASS
* TEFLON-BONDING OF GLASS ON CELL	RUNNING	ASTP-4 9	92-94	TEFLON BONDED CELL ASSEMBLIES WITH ESD-PROTECTION

SOLAR GENERATOR TECHNOLOGY PROGRAMME

3. COMPONENT TECHNOLOGY-A

* ALTERNAT. SOLAR CELL ASSESSMENT	RUNNING	BASIC 9	89-94	EVALUATION OF "3RD GENERATION" CELLS FOR SPACE
* GaAs-SOLAR-CELL DEVELOPMENT	RUNNING	ASTP-3 &HARMO	87-94	DEV. OF GaAs CELLS BY MOCVD ON GaAs AND GERMANIUM
* LILT SOLAR CELLS	RUNNING	BASIC 4	91-95	DEV. OF CELLS WITH 25%-EFF. IN DEEP SPACE (ROSSETTA)
* THIN-FILM CELLS	RUNNING	ASTP-4	92-94	PRE-DEVELOPMENT OF CIS-CELLS; SYSTEM-ASSESSMENT

SOLAR GENERATOR TECHNOLOGY PROGRAMME

3. COMPONENT TECHNOLOGY-B

* PILOTLINE HI-ETA SILICON CELLS	RUNNING	GSTP-1 9	94-96	END-DEVELOPMENT OF 16%-EFF. CELLS INCL. PILOT PROD.
* ADVANCED LIGTHW. GAAS CELLS	PLANNED	GSTP-1 9	94-96	CASCADE/TANDEM CELLS;>22% ULTRA-THIN
* GE-SUBSTRATES FOR GAAS CELLS	RUNNING	GSTP-1 9	93-95	DEVELOP IMPROVED SUBSTRATES IN PILOTLINE

SOLAR GENERATOR TECHNOLOGY PROGRAMME

4. TECHNOLOGY VERIFICATION TESTS

* S-A ENVIRONMENTAL INTERACTIONS	RUNNING	BASIC 6	93-94	IDENTIF. AND TEST OF SYNERGISTIC EFFECTS; MICROM. PROTONS/ATOX
* ESD-TEST SIMULATION	RUNNING	BASIC	93	MODEL OF ESD INTERACTIONS OF S-A's; REPR. TEST
* SPASOLAB	RUNNING	BASIC	93-95	TYPE APPROVAL TESTS (PSS-01-604)
* ARCHIMEDES	RUNNING	BASIC	94	p+ & e- TESTS OF NOVEL CELLS FOR MISSIONS WITH HIGH FLUX

SOLAR GENERATOR TECHNOLOGY PROGRAMME

5. SUPPLEMENTARY ACTIVITIES

*	FLIGHT EXPERIMENTS	RUNNING	TDP	94	IN-ORBT VERIFICATION OF NEW CELLS (STRV, HEALTHSAT,ETC.)
*	PORTABLE SUN SIMULATOR	RUNNING	GSTP-1	94-95	MINI-FLASHER FOR FIELD TESTS
*	EURECA SA	RUNNING	BASIC	93-94	POST-FLIGHT INVESTIGATIONS
*	HST SA-1	RUNNING	BASIC	94-95	POST-FLIGHT INVESTIGATIONS

SESSION I

InP CELL DEVELOPMENT

HIGH-EFFICIENCY, DEEP-JUNCTION, EPITAXIAL InP SOLAR CELLS ON (100) AND (111)B InP SUBSTRATES

R. Venkatasubramanian, M.L. Timmons, and J.A. Hutchby
Research Triangle Institute
Research Triangle Park, North Carolina

and

R. Walters and G. Summers
U.S. Naval Research Laboratory
Washington, DC

ABSTRACT

We report on the development and performance of deep-junction ($\sim 0.25\ \mu\text{m}$), graded-emitter-doped, n^+ -p InP solar cells grown by metallorganic chemical vapor deposition (MOCVD). A novel, diffusion-transport process for obtaining lightly-doped p-type base regions of the solar cell is described. The I-V data and external quantum-efficiency response of these cells are presented. The best active-area AM0 efficiency for these deep-junction cells on (100)-oriented InP substrates is 16.8%, with a J_{SC} of $31.8\ \text{mA}/\text{cm}^2$, a V_{OC} of 0.843 V, and a fill-factor of 0.85. By comparison, the best cell efficiency on the (111)B-oriented InP substrates was 15.0%. These efficiency values for deep-junction cells are encouraging and compare favourably with performance of thin-emitter ($0.03\ \mu\text{m}$) epitaxial cells as well as that of deep-emitter diffused cells. The cell performance and breakdown voltage characteristics of a batch of 20 cells on each of the orientation are presented, indicating the superior breakdown voltage properties and other characteristics of InP cells on the (111)B orientation. Spectral response, dark I-V data, and photoluminescence (PL) measurements on the InP cells are presented with an analysis on the variation in J_{SC} and V_{OC} of the cells. It is observed, under open-circuit conditions, that lower- V_{OC} cells exhibit higher band-edge PL intensity for both the (100) and (111)B orientations. This anomalous behaviour suggests that radiative recombination in the heavily-doped n^+ -InP emitter may be detrimental to achieving higher V_{OC} in n^+ -p InP solar cells.

INTRODUCTION

Epitaxial n^+ -p InP solar cells remain attractive for space photovoltaic applications as they have demonstrated a high AM0 conversion efficiency (~ 18 to 19%) [1]. These cell efficiencies have been obtained through material improvements by epitaxy as well as the use of a thin emitter ($\sim 0.03\ \mu\text{m}$). However, the absence of photon-assisted annealing of radiation-induced defects and the consequent lack of superior radiation resistance of these epitaxial thin-emitter cells stand in sharp contrast to that observed in diffused, deep-junction ($\sim 0.3\ \mu\text{m}$) cells [2].

This work aims to develop high-efficiency InP solar cells by MOCVD that replicate the diffused-junction structure, especially the deeper junction and the emitter surface doping gradient. The radiation resistance data from these cells are reported separately in a companion paper [3]. The goal is to improve the understanding of the radiation resistance of InP solar cells. In this work, we also present the first reported performance of InP solar cells on (111)B-oriented substrates.

The motivation for the study of cell performance on (111) orientation stems from the predicted advantages for hetero-epitaxial InP solar cells on Si substrates. There is about 8% lattice mismatch between InP and Si. This lattice mismatch can potentially introduce about $1.9 \times$

10^{14} dangling bonds per cm^2 at the interface of (100) InP-Si. However, the calculated dangling bond density for the (111) orientation is about 1.1×10^{14} per cm^2 . Thus, for similar growth conditions and defect control mechanisms, the (111) orientation potentially offers a 40% reduction in defect-density.

OMVPE GROWTH AND CELL STRUCTURE

The n^+ -p cell structures were grown on p-type InP substrates, doped to mid 10^{18} cm^{-3} . Fig. 1 shows the schematic of the cell structure. The best results of epitaxial growth on (100)-oriented substrates were obtained with use of no additional surface preparation to the customer-provided epi-ready InP wafers. However, it was found necessary to give a brief surface clean (consisting of a 1 min. etch in 1:1:5 = $\text{H}_2\text{O}:\text{H}_2\text{O}_2:\text{H}_2\text{SO}_4$ solution followed by a thorough rinse in deionized water) for the (111)B-orientation substrates prior to epitaxy. This cleaning step is critical to obtaining a smooth epitaxy of InP layers on the (111) oriented substrates. The growth was carried out in an atmospheric-pressure MOCVD system using ethyldimethylindium and phosphine as the Group III and Group V precursors, respectively. All the growths were carried out at 700°C , with typical growth rates of $0.05 \mu\text{m}/\text{min}$.

Diethylzinc (DEZn) bubbler source was used for obtaining Zn-doping. An important requirement for obtaining high-efficiency as well as radiation-resistant n^+ -p InP cells is that the base region be lightly-doped to mid 10^{16} cm^{-3} . This lightly-doped base also enables the evaluation of a larger portion of the quasi-neutral p-base by techniques such as deep level transient spectroscopy (by applying a larger voltage-bias without breakdown of the junction) to study radiation-induced defects.

Typically, a low concentration dimethylzinc-in-hydrogen gas source is used for obtaining lightly-doped p-base. At RTI and other laboratories [4], this gas source has been found to lead to very erratic doping levels. Hence, in this work, we have investigated a new approach to obtain lightly-doped p-InP using a diffusion transport process. In this technique, the inlet of an organometallic-Zn bubbler is closed and the outlet is kept open. H_2 gas flow is maintained through a bypass line, adjacent to the bubbler, to continuously carry the organometallic-Zn that diffuses out from the bubbler to the growth zone.

This approach avoids the possible residual moisture and oxygen contamination, frequently present in gas cylinders, that can scavenge the Zn, especially at low ppm levels. Also, this approach is likely to provide a constant molar ratio of organometallic-Zn to H_2 , as long as the organometallic Zn-source is kept at a constant temperature, unlike a high-pressure gas-mixture that can lead to inconsistent concentration levels over the lifetime of the source.

We show in Fig.2(a) the polaron profile of a Zn-doped base region, obtained with a flow of 1ccm through a diethylzinc (DEZn) bubbler causing a carrier concentration of $\sim 4 \times 10^{18} \text{ cm}^{-3}$, suggesting ultra-low flow rates to get a p-doping level in mid- 10^{16} cm^{-3} . In Fig. 2(b), we indicate that with a 10ccm H_2 flow and using the diffusion-transport process, and using the vapor pressure of dimethylzinc (DMZn), we obtain a doping level of $\sim 6 \times 10^{17} \text{ cm}^{-3}$. In Fig. 2(c), we indicate that with the same 10 ccm H_2 flow and using the diffusion-transport process with a DEZn bubbler, we obtain a doping level of $\sim 8 \times 10^{16} \text{ cm}^{-3}$. The lower doping level obtained with the DEZn source is consistent with the lower vapor pressure of DEZn, compared to DMZn, therefore leading to a lower concentration of Zn although the same 10ccm of H_2 is used to transport the diffused species.

H₂Se gas source was used for obtaining the heavily doped n⁺ emitter regions. Se is the same Group-VI n-type dopant as in S-doped InP diffused junctions, as opposed to the use of Si in some of the work [1] of epitaxial InP cells. The emitter was nominally linearly graded with increasing H₂Se flow rates, to obtain a surface doping of $\sim 3 \times 10^{18} \text{ cm}^{-3}$.

The cell structure in Fig. 1 also indicates the use of Ti/Au (30nm/300nm) contact for the p+ InP substrate. This contact was sintered at 415°C for one minute. The front emitter contact was a non-alloyed AuGe/Ni/Au (50nm/10nm/300nm) metallization. The InP cells on (100)-oriented substrates received a two-layer ZnS/MgF₂ anti-reflection coating (ARC) as indicated in Fig. 1. The ZnS/MgF₂ coatings were deposited by e-beam evaporation. However, the cells on (111)B-orientation received a single-layer ARC of plasma-deposited silicon nitride because the e-beam evaporated ZnS/MgF₂ coatings strongly deteriorated the performance of the cells on (111)B-oriented substrates. The cause for this behaviour is not exactly clear at this point.

CELL I-V AND SPECTRAL-RESPONSE CHARACTERIZATION

The I-V and external quantum efficiency (spectral response) data of the cells were measured using an InP standard cell characterized at the National Renewable Energy Laboratory (NREL). Relative external quantum efficiency data for a deep-junction cell are shown in Fig. 3. The cell indicates a good red response and a small roll-off in the short-wavelength response. This roll-off is attributed to some recombination of photo-generated carriers either in the emitter region or at the surface of the emitter. The surface recombination velocity of n⁺InP has been predicted to be low [5]. In addition, the electric field resulting from the graded doping in the emitter is expected to oppose the surface recombination of minority carriers (holes) and accelerate them towards the depletion layer. As discussed below, based on photoluminescence data, we believe that the roll-off is related to radiative recombination of minority carriers in the heavily-doped n⁺-emitter regions. The radiative recombination is attributed to lower radiative-lifetimes in the quasi-neutral regions of n⁺-InP.

The best active-area AM0 efficiency for these deep-junction cells on (100)-oriented InP substrates is 16.8%, with a J_{sc} of 31.8 mA/cm², a V_{oc} of 0.843 V, and a fill factor of 0.85. By comparison, the best cell efficiency on the (111)B-oriented InP substrates was 15.0%, with a J_{sc} of 31.3 mA/cm², a V_{oc} of 0.797 V and a fill factor of 0.815. These efficiency values for deep-junction cells are encouraging and compare favorably with performance of thin-emitter (0.03 μm) epitaxial cells as well as that of deep-emitter diffused cells.

The cell (efficiency) performance of a batch of ~20 cells, each on (100)- and (111)B-oriented InP substrates, are shown in Fig. 4. We can immediately observe the spread of cell efficiencies, for both the orientations, over a reasonably wide range. However, we note the tighter (and a more statistically expected Gaussian-like) spread of cell efficiencies on (111) substrates and a more random fluctuation on the (100) substrates.

ORIENTATION-EFFECTS ON REVERSE-BREAKDOWN VOLTAGES

Similar statistical behavior in the breakdown voltage of cells on (100) and (111)B substrates was obtained. Fig. 5 shows a histogram depicting the distribution of breakdown voltages of the cells on the two orientations. For a given base doping level, the breakdown voltages of nearly all the cells on (111) InP substrates were within 4.5-5.2 V, while the cells on (100) substrates had considerable variation. Two of the cells, from the same wafer of (100)

orientation, with very similar forward characteristics had completely different reverse-breakdown characteristics. In contrast, any two cells even from different wafers of (111) orientation had similar reverse characteristics.

The cause for this variance in behavior of reverse-breakdown characteristics is thought to be related to the more electronically-active (111)B InP surface than the (100) surface [6], leading to a more stabilized surface from a more-accelerated native-oxidation process. Thus the junctions on (111)-oriented substrates probably suffer from less surface-induced, soft-breakdown reverse-characteristics. In addition, it has been reported that under certain doping conditions, the (111) orientation can offer significantly higher breakdown voltages than the (100) orientation in GaAs [7].

In any case, the reproducibility of InP cell-efficiency and breakdown-voltage characteristics on (111)B-oriented substrates, compared to (100)-orientation, is noteworthy. This portends well for the investigation of InP cells on (111)-Si substrates.

PL CHARACTERIZATION OF InP CELLS

Band-edge photoluminescence (PL) from the InP cells were also evaluated at 300K to understand the variation in J_{SC} and V_{OC} of the cells. The PL excitation source was an Ar-ion laser operating at 515 nm. The PL measurements were conducted under open-circuit conditions and the laser radiation is expected to be fully absorbed within the 0.25- μ m-deep emitter region.

In Fig. 6, we indicate the PL data from two InP cells on (100) substrates, nominally grown with the same cell structure (shown in Fig. 1) and nearly identical J_{SC} values. The cell (1-1955-a-4), with a significantly higher V_{OC} (0.843 V), shows a much smaller band edge PL signal than the cell (1-1961-a-4) with a lower V_{OC} of 0.783 V. The same pattern is once again observed in cells grown on the (111)B orientation, and is shown in Fig. 7, i.e., the lower V_{OC} cells indicate higher band edge PL intensity. This leads us to suggest that the lower V_{OC} of n^+ -p InP cells is perhaps related to lower radiative lifetime in the n^+ -emitter regions. This argument would be consistent with the higher PL intensity and the well-documented low surface-recombination velocity of n-InP and n^+ -InP surfaces.

It has been known for some time that the open-circuit voltage of state-of-the-art n^+ -p InP solar cells are not as high as that one would expect for its bandgap [1], in relation to that observed in GaAs, especially considering that the surface recombination velocity of native n^+ -InP surfaces are comparable to those at high-quality GaAs-AlGaAs interfaces in GaAs solar cells. This discrepancy has not been resolved [1]. We believe that the high n-type doping level (~high 10^{18} cm^{-3} to low 10^{19} cm^{-3}) used in these cells probably result in low radiative lifetimes, leading to lower-than-ideal V_{OC} of cells. A lower emitter doping, in conjunction with a thicker emitter (like 0.1 μ m) to maintain low emitter sheet resistance, is worth an exploration. Recently at RTI, we have been able to improve the V_{OC} of the InP cells from above-mentioned 0.843 V to 0.875 V, one of the highest-reported values for InP cells under AM0 conditions, with the use of reduced doping levels in the emitter.

It may be worth pointing out that the J_{SC} levels in n^+ -p InP cells are less sensitive to any reduction in lifetime (from higher doping level) in the emitter-region as the combination of low surface recombination velocity of n^+ -InP and reasonable diffusion lengths can cause near-complete collection of photo-generated carriers from the emitter. This was evident in our deep-junction cells as well, where, the variation of V_{OC} was present in cells with very similar J_{SC} values. This effect was noticeable in both the orientations of InP substrates.

SUMMARY

In summary, we have developed and characterized the performance of deep-junction ($\sim 0.25\text{ }\mu\text{m}$), graded-emitter-doped, n^+ -p InP solar cells, grown by metallorganic chemical vapor deposition (MOCVD). A novel, diffusion-transport process for obtaining lightly-doped p-type base regions of the solar cell, was described. The best active-area AM0 efficiency for these deep-junction cells on (100)-oriented InP substrates is 16.8%, with a J_{sc} of 31.8 mA/cm^2 , a V_{oc} of 0.843 V, and a fill factor of 0.85. By comparison, the best cell efficiency on the (111)B-oriented InP substrates was 15.0%. The cell performance and breakdown voltage characteristics of a batch of 20 cells on each of the orientation were presented, indicating the superior breakdown voltage properties of InP cells on the (111)B orientation. Spectral response, dark I-V data, and photoluminescence (PL) measurements on the InP cells were presented with an analysis on the variation in V_{oc} of the cells. It is observed, under open-circuit conditions, that lower- V_{oc} cells exhibit higher band-edge PL intensity for both the (100) and (111)B orientations. This behaviour suggests that radiative recombination in the heavily-doped n^+ -InP emitter may be detrimental to achieving higher V_{oc} in n^+ -p InP solar cells.

REFERENCES

- 1) C.J. Keavney, V.E. Haven, and S.M. Vernon, Proc. of 21st IEEE Photovoltaic Specialists Conf., (IEEE, NY), 141 (1990).
- 2) M. Yamaguchi and K. Ando, J. Appl. Phys., 63, 5555 (1988).
- 3) R.J. Walters, G.P. Summers, M.L. Timmons, R. Venkatasubramanian, J.A. Hancock, and J.S. Hills, Paper Presented at this SPRAT Conference.
- 4) R. Venkatasubramanian and S.K. Ghandhi, Unpublished Results of work on low p-type doping of GaAs at Rensselaer Polytechnic Insitute, Troy, NY, 1983.
- 5) R. K. Ahrenkiel in *Properties of Indium Phosphide*, emis Datareviews Series No.6, INSPEC, p.80, 1991.
- 6) S.K. Ghandhi, *VLSI Fabrication Principles - Silicon and Gallium Arsenide*, John Wiley, NY, p.13, 1983.
- 7) M.H. Lee and S.M. Sze, Solid St. Electron. 23, 1007 (1980).

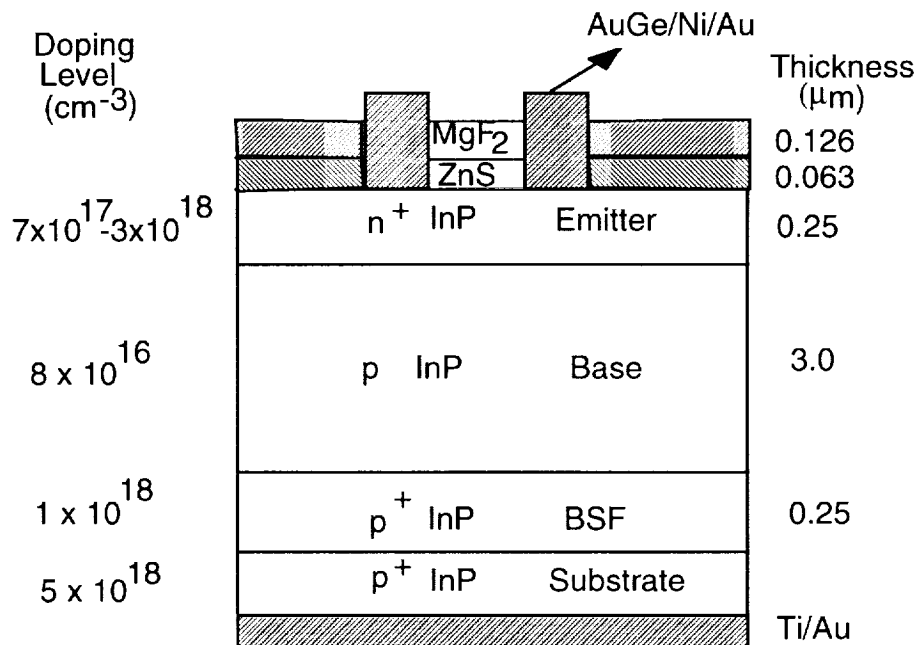


Fig. 1 Schematic of a n⁺-p InP solar cell structure indicating the graded emitter doping.

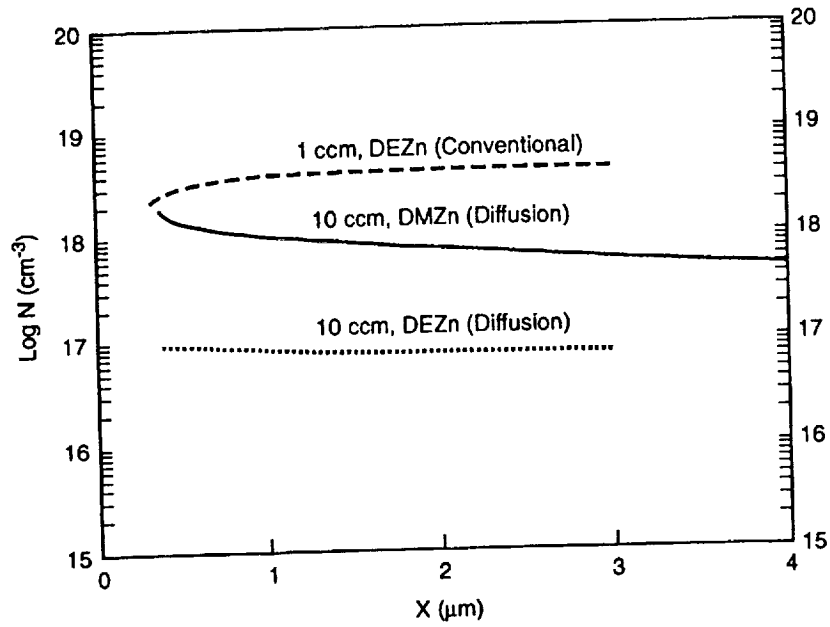


Fig. 2 Polaron doping profiles for (a) conventional Zn-doping with 1ccm H₂ bubbled through a DEZn bubbler, (b) diffusion-transport with 10ccm H₂ using the vapor pressure of DMZn and (c) diffusion-transport with 10ccm H₂ using the vapor pressure of DEZn.

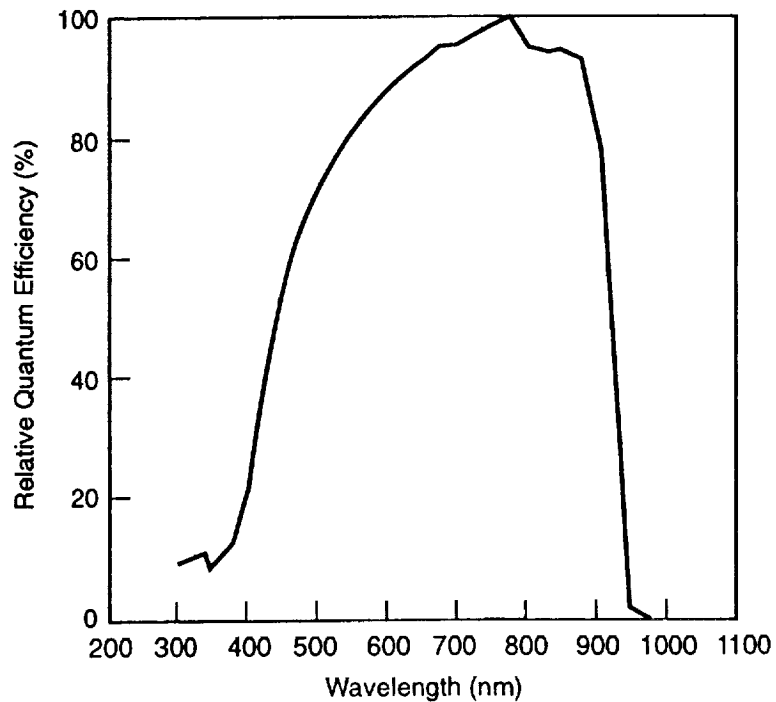


Fig. 3. External quantum efficiency of a deep-junction, n⁺-p InP cell measured at NREL.

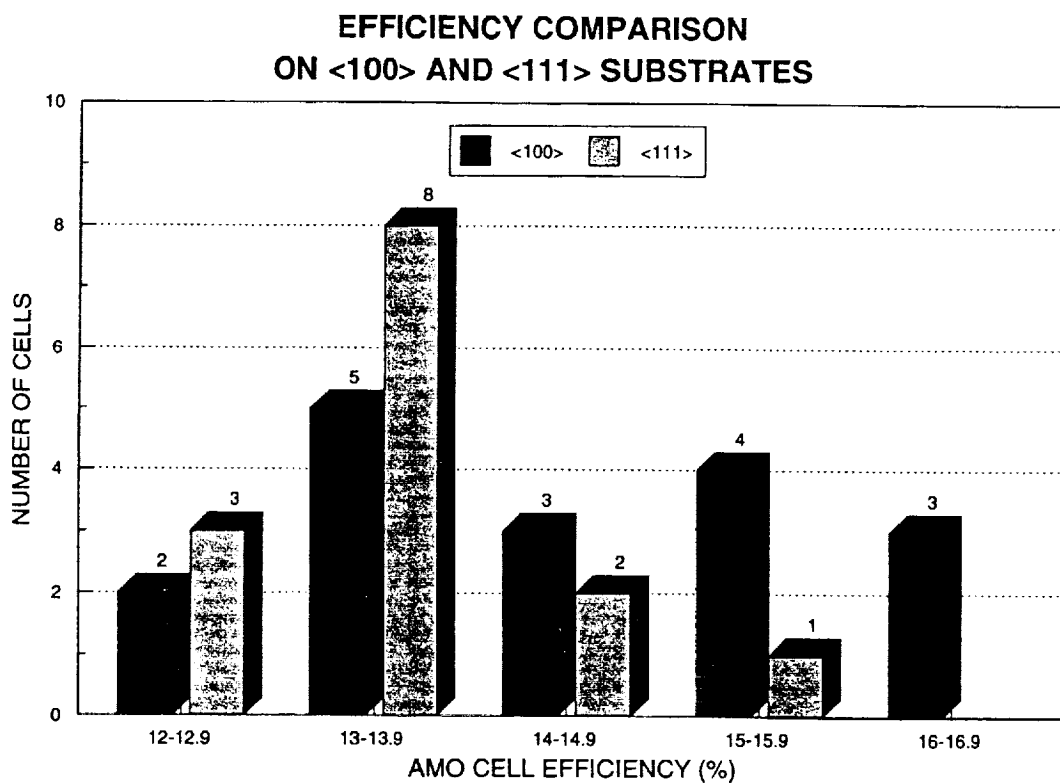


Fig. 4 Cell (efficiency) performance histograms for (100) and (111)-B InP substrate orientations.

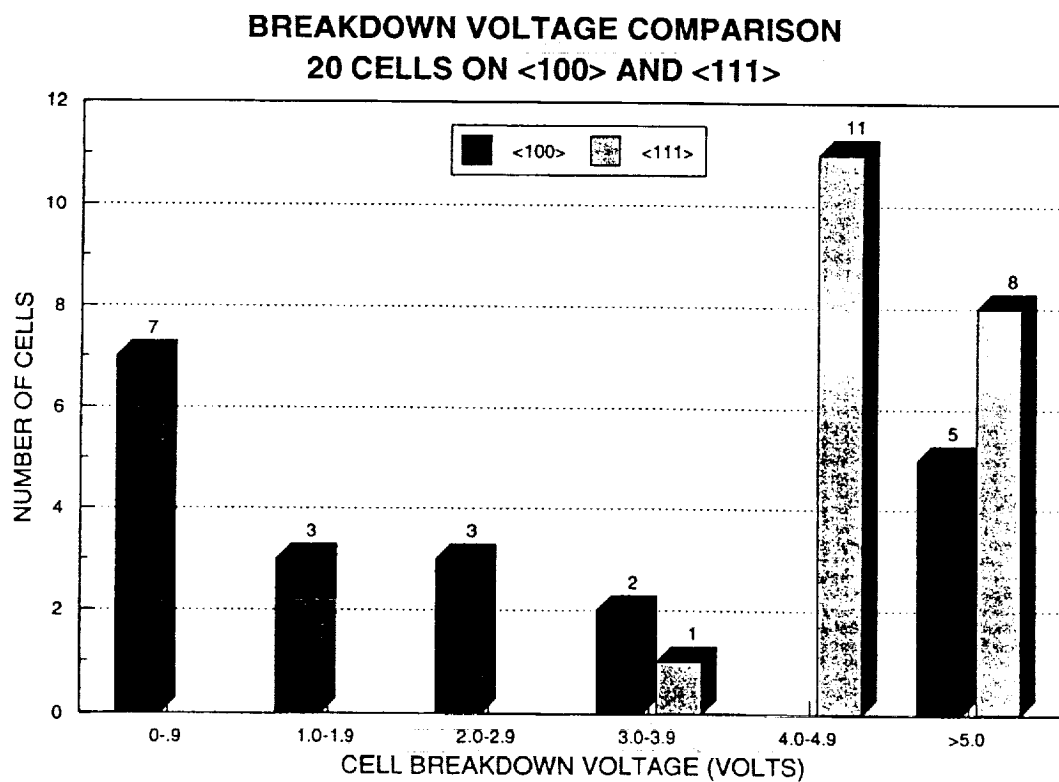


Fig. 5 Cell (reverse breakdown voltage) performance histograms for (100) and (111)-B InP substrate orientations.

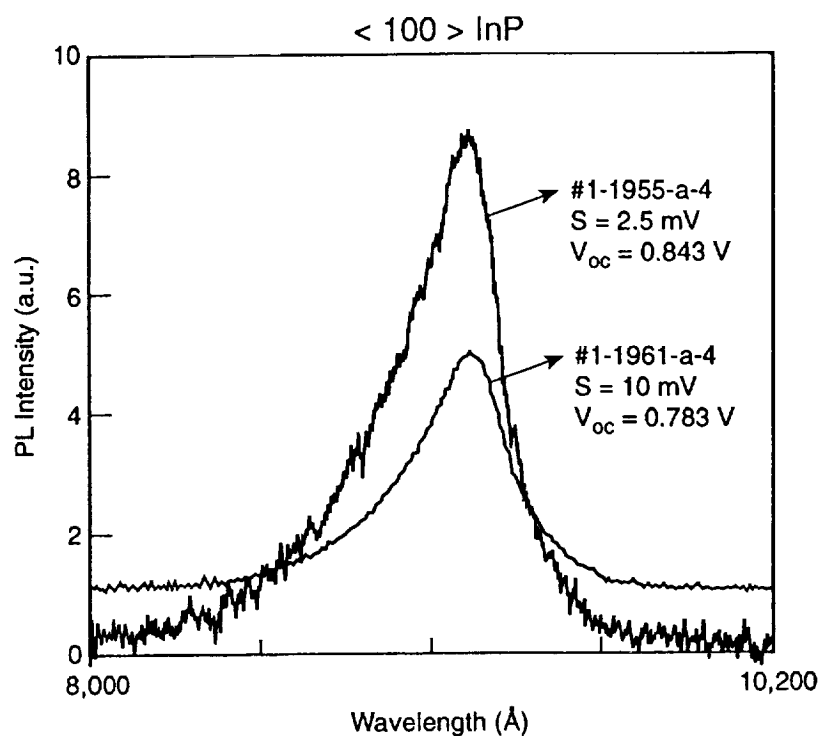


Fig. 6. 300K PL data (under open-circuit conditions) from two InP cells on (100)-oriented substrates, with nearly identical J_{sc} values, but different V_{oc} values.

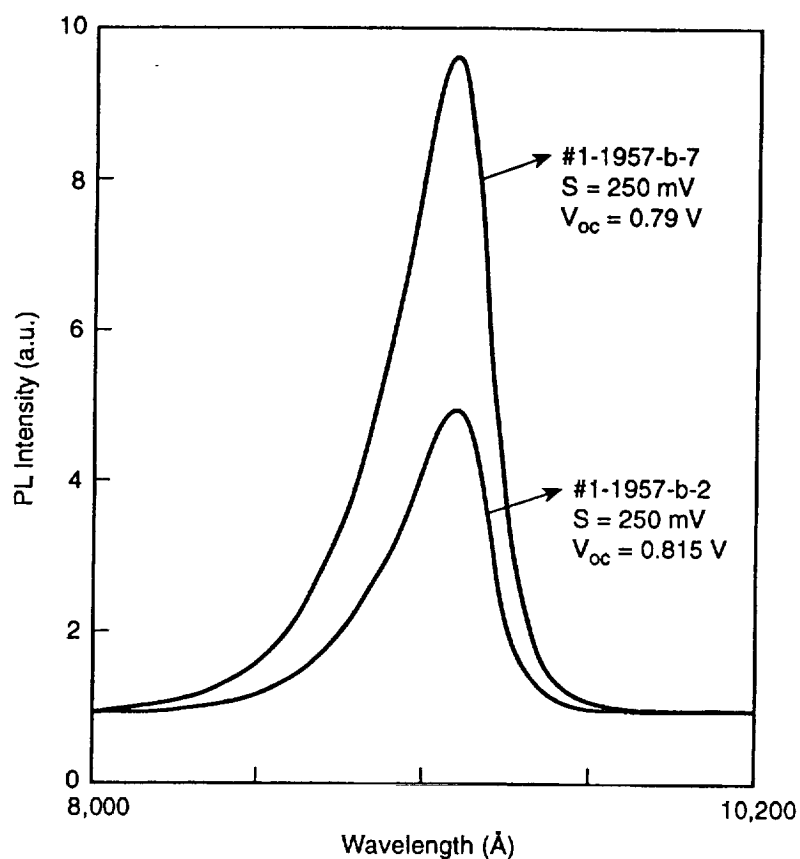


Fig. 7. 300K PL data (under open-circuit conditions) from two InP cells on (111)B-oriented substrates, with nearly identical J_{sc} values, but different V_{oc} values.

CHEMICAL BEAM EPITAXY FOR HIGH EFFICIENCY PHOTOVOLTAIC DEVICES

A. Bensaoula, A. Freundlich, M.F. Vilela, N. Medelci, and P. Renaud
University of Houston
Houston, Texas

INTRODUCTION

InP-based multijunction tandem solar cells show great promise for high conversion efficiency (η) and high radiation resistance. InP and its related ternary and quaternary compound semiconductors such as InGaAs and InGaAsP offer desirable combinations of energy bandgap values which are very suitable for multijunction tandem solar cell applications. The monolithically integrated InP/ $\text{In}_{0.53}\text{Ga}_{0.47}\text{As}$ tandem solar cells are expected to reach efficiencies above 30%. Wanlass et al. (ref. 1) have reported AM0 efficiencies as high as 20.1% for two terminal cells fabricated using atmospheric-pressure metalorganic vapor phase epitaxy (APMOVPE). The main limitations in their technique are first related to the degradation of the intercell ohmic contact (IOC), in this case the $\text{In}_{0.53}\text{Ga}_{0.47}\text{As}$ tunnel junction during the growth of the top InP subcell structure, and second to the current matching, often limited by the $\text{In}_{0.53}\text{Ga}_{0.47}\text{As}$ bottom subcell.

Chemical beam epitaxy (CBE) has been shown to allow the growth of high quality materials with reproducible complex compositional and doping profiles. The main advantage of CBE compared to metalorganic chemical vapor deposition (MOCVD), the most popular technique for InP-based photovoltaic device fabrication, is the ability to grow high purity epilayers at much lower temperatures (450°C - 530°C) (ref.2). In a recent report Yamaguchi et al (ref.3) have shown that cost-wise CBE is a breakthrough technology for photovoltaic (PV) solar energy applications. Through the research effort undertaken in our laboratory, we have seen a rapid progress in the energy conversion efficiency of InP-based solar cells fabricated using chemical beam epitaxy (ref.4). This communication summarizes our recent results on PV devices and demonstrates the strength of this new technology.

GROWTH TECHNIQUE

The realization of high performance solar cells and tunnel junctions requires extremely high purity layers, perfect control on hole and electron concentrations as well as low interdiffusion of dopant species across the junction during the device growth procedure. Therefore, a relatively low temperature growth process and a good control of the interface properties are required. CBE meets the above requirements since high quality GaAs, InP, GaP, InAsP, GaInP and InGaAs layers can be grown at lower temperatures than those used in more conventional techniques such as LPE, MOCVD, and even MBE. Moreover, it combines features from both MOCVD and MBE, allowing the growth of semiconductor heterostructures with monolayer abruptness and thickness control as well as easy multiwafer scale-up.

We have already demonstrated, using CBE, the growth of a variety of high quality heterostructures ranging from lattice matched (InGaAs/InP) and strained (InAsP/InP) to highly strained InAs/InP (ref. 5). In these studies the effect of growth temperatures and interruption schemes at the interfaces was demonstrated to be crucial. To illustrate the growth control capability of CBE we mention here our group latest results in the fabrication of perfectly balanced highly strained heterostructures GaP(under tension)/GaAs/InP (under compression) superlattices with thicknesses up to 1 μm (ref.6). These heterostructures are highly ordered and show very low defect densities as seen in Figure 1. High resolution x-ray diffraction (400) from these layers exhibit a residual strain of less than 8×10^{-5} ; by comparison residual strain in GaAs/AlAs structures is 1.38×10^{-3} .

CBE's flexibility in allowing the growth of such high quality complex heterostructures permits the implementation of novel PV design concepts with expected higher efficiencies at no added fabrication costs (sometimes lower). As an example we are investigating the use of internal Bragg reflectors and the addition of MQWs in a standard diode structure to enhance the photon absorption and increase the cell photocurrent, thus significantly improving the PV

efficiency. Preliminary results on adding MQWs in the intrinsic region of a P-I-N structures are very encouraging and will be published elsewhere.

All our Epitaxial growth runs were accomplished in a Riber CBE 32 system using trimethyl-indium (TMI), triethyl-gallium (TEG) and pre-cracked arsine (AsH_3) and phosphine (PH_3) as growth precursors. While research to date has included the growth of InP-based PV devices on both GaAs and GaAs/Si, we will restrict ourselves in this paper to homoepitaxial growths on InP substrates (mainly InP:S (100)). Reflection high energy electron diffraction (RHEED) was used to monitor the surface morphology during the growth process as well as calibrate an optical pyrometer focused on the substrate. This calibration uses the oxide desorption temperature (517°C) as the reference point. When this temperature is reached, the RHEED pattern changes from diffuse bulk type spots to clear bright lines. Due to the strong dependence of the InGaAs alloy composition on the substrate temperature, lattice matching with respect to InP was studied in the $450\text{--}530^\circ\text{C}$ temperature range. Lattice matching to better than 10^{-3} , as checked by High Resolution Double Crystal X-ray Diffraction, was achieved reproducibly, demonstrating excellent composition control for our ternary compounds.

DOPING STUDIES

Both the Be and Si doping behavior of InGaAs layers fabricated on InP:Fe (100) semi-insulating substrates at relatively low temperatures (450°C to 480°C) were investigated. Be and Si dopings were achieved using solid source effusion cells. Doping studies were carried out in lattice matched conditions. Be doped p-InGaAs with net hole concentrations (as determined from Hall measurements) varying from $2 \times 10^{17} \text{ cm}^{-3}$ to $2 \times 10^{20} \text{ cm}^{-3}$ were achieved. No surface degradation was observed, even at doping levels as high as $2 \times 10^{20} \text{ cm}^{-3}$. Si doping was investigated within a doping range of 10^{17} cm^{-3} to $2 \times 10^{19} \text{ cm}^{-3}$. No noticeable electrical compensation was detected and good reproducibility was achieved from run to run.

In order to investigate the cross-diffusion behavior and to further assess the cross-doping profiles, Secondary Ion Mass Spectroscopy (SIMS) experiments were carried out on InGaAs multilayered structures fabricated with a combination of different Be and Si doping levels and undoped spacers. SIMS experiments were performed in a Cameca IMS 4F system and both O^+ and Cs^+ profiles were taken for Be and Si respectively. Figure 2 represents compilation of O^+ and Cs^+ SIMS data. As it can be observed, the memory effects are in the range of 10^{16} cm^{-3} or less for both Be and Si doping. Furthermore, at the interface between Be and Si doped layers, observed cross-diffusions are within the experimental error. The sharp diffusion profiles between Be and Si are consistent with solar cells and tunnel junctions low inter-diffusion requirements. Our results indicate that p/n or n/p structure should exhibit similar behavior. We have chosen deliberately to study p/n type devices.

SOLAR CELL AND TUNNEL DIODE DEVICES

Figure 3 shows a diagram of a tandem solar cell structure. Besides achieving the proper electrical and structural quality for the individual layers, two issues stand out in the realization of these devices. The first relates to the fabrication of thin tunnel junctions with high current carrying capabilities and minimum resistivities. The second concerns the ability to grow a high quality InP solar cell on InGaAs at low enough temperature so as to preserve the characteristics of the underlying tunnel junction. Following we will describe the growth and fabrication of the individual tandem components.

$\text{In}_{0.53}\text{Ga}_{0.47}\text{As}$ solar cell

The cell fabrication process begins with the CBE growth of a structure as shown in Figure 3 (bottom cell). A summary of the characteristics under natural sunlight and without anti-

reflection coating is: $J_{sc}=30\text{mA/cm}^2$; $V_{oc}=0.27\text{V}$; $FF=57.8\%$; $\eta=5.1\%$, for an incident sunlight power of 91.4mW/cm^2 . A double anti-reflection coating (ZnS/MgF_2) was deposited and the new electrical characteristics under natural sunlight are (Figure 4): $J_{sc}=60\text{mA/cm}^2$; $V_{oc}=0.295\text{V}$; $FF=54.2\%$; $\eta=10.2\%$, for an incident sunlight power of 94.2mW/cm^2 (total area, 0.25cm^2). In this particular sample we note that a strong increase in the photocurrent after anti-reflection coating is observed. This increase cannot be explained solely by the addition of the anti-reflection layer. It is believed that this diode had a much lower shunt resistance before the dielectric deposition. A leakage current prior ARC coating was responsible for the lower photocurrent measured. Similarly after ARC the fill factor (FF) is smaller, a result of a higher series resistance.

The Spectral Response (SR) characteristics after ARC of this InGaAs cell are presented in Figure 5. A minimum at 680nm is clearly observed. This minimum is related to reflections at the InP window layer (we remind the reader that the ARC is optimized for the InGaAs material). We note that for wavelengths higher than 1100nm , the SR decreases noticeably, a result of a non optimized base layer. Both the base layer thickness and the minority carrier lifetime in this layer must be investigated to better understand the cause for this decrease. The high response at smaller wavelengths shows however the high quality of the emitter layer. In conclusion, while further improvements in the cell characteristics are expected through a better optimization of the base layer, the high photocurrent density already demonstrated in these cells (60mA/cm^2 , the highest ever reported) is very promising.

The dark I-V and short circuit current (I_{sc}) as a function of the open circuit voltage (V_{oc}) characteristics have been measured as well. The shunt resistance (R_{sh}) from dark I-V, the diode ideality constant (n) from I_{sc} - V_{oc} and the saturation current (J_s) from I_{sc} - V_{oc} were calculated. These values are shown in Table I. An ideality constant of 2.2 is expected for a small bandgap diode such as InGaAs. Both the shunt resistance ($42\ \Omega\cdot\text{cm}^2$) and the saturation current ($J_s = 0.6\text{mA/cm}^2$) can be improved through proper mesa passivation.

InP solar cell

Figure 3 shows the doping levels and thicknesses for the InP solar cell (top cell). Its electrical characteristics are shown in Figure 6. The characterization results performed under natural sunlight without anti reflection coating are: $J_{sc} = 20\text{mA/cm}^2$, $V_{oc} = 0.82\text{V}$, $FF = 77\%$, and $\eta=13\%$, for an incident sunlight power of 97mW/cm^2 . After the antireflection coating this solar cell presents 18% conversion efficiency under solar simulator. Its spectral response is shown in Figure 5. The flat SR from 450nm to 850nm shows the high quality of this material. The lower efficiency at smaller wavelengths ($<400\text{nm}$) is expected since this InP solar cell does not have any window layer. By using a window layer or decreasing the emitter thickness it is possible to improve the SR at lower wavelengths. In Table-1 the R_{sh} , I_s and n for this solar cell are given. It is expected that R_{sh} and the InP solar cell efficiency will increase after mesa passivation. A mesa passivation and a window layer should further increase the efficiency to 22%.

$\text{In}_{0.53}\text{Ga}_{0.47}\text{As}$ tunnel junction

p^+/n^+ $\text{In}_{0.53}\text{Ga}_{0.47}\text{As}$ tunnel junction structures with different active layer thicknesses (ranging from 0.2 to $0.8\ \mu\text{m}$) and growth temperatures (450 - $530\ ^\circ\text{C}$) were grown. Devices were made using a standard wet etching process with mesa openings of 100 and $200\ \mu\text{m}$ in diameter. Evaporated Au was used for front and back contacts. No high temperature annealing of the metallic contact layers was performed.

The net carrier concentrations as extrapolated from Hall measurement data for devices discussed here were varied from $N_A=1.3 \times 10^{19}$ to $N_A=5 \times 10^{19} \text{ cm}^{-3}$ in the p-type layers, and from $N_D=7 \times 10^{18}$ to $N_D=1.3 \times 10^{19} \text{ cm}^{-3}$ in the n-type layers. Thus, junctions with highly degenerate n type sides ($> 10 \text{ kT}$) and degenerate p type sides ($> kT$) were obtained, resulting in devices with effective dopings $N^*=N_A N_D/(N_A+N_D)$ ranging from 5.9×10^{18} to $8.3 \times 10^{18} \text{ cm}^{-3}$.

All our devices exhibit excellent I-V characteristics. Peak current densities obtained in this work are among the highest ever reported for epitaxial tunnel junctions. The best room temperature peak current density exceeds 1000 A/cm^2 (Figure 7); and specific resistivities lower than $10^{-4} \Omega \cdot \text{cm}^2$ were measured. Maximum resistivities R_{max} (peak current to peak voltage ratios) are in the 2×10^{-4} to $5 \times 10^{-4} \Omega \cdot \text{cm}^2$ range, making these junctions highly suitable as IOC's for the InP/InGaAs tandem solar cell. High peak to valley ratios are exhibited by many devices with room temperature peak to valley ratios of 9 and peak current densities greater than 550 A/cm^2 .

In order to investigate the evolution of the tunnel junction properties when incorporated in the InP/InGaAs tandem solar cell structure, an InGaAs tunnel junction with an effective doping of $7 \times 10^{18} \text{ cm}^{-3}$ was subjected to the growth of a thick ($> 3 \mu\text{m}$) InP solar cell. Prior to the solar cell growth, the tunnel junction coated wafer was cut in two pieces. One piece was processed as a reference sample. The InP solar cell regrowth structure was realized with standard parameters (doping and layer thicknesses) on the second piece of the wafer (ref. 7). Following the growth process, the InP solar cell was selectively etched using a HCl solution and mesa processing was accomplished. Even after more than 2 hours at 560°C , no degradation of the tunnel junction characteristics is observed. The device still exhibited very high peak current densities, up to 860 A/cm^2 as shown in Figure 8. Hence, our tunnel junctions are suitable for use in tandem structures either in a planar or the more demanding patterned electrical interconnect concept (ref. 8). With the above characteristics (tunneling currents and resistivities), the voltage drop across a patterned tunnel junction aligned with the top solar cell grid (e.g. 5% shadowing) at concentration of $100 \times \text{AM0}$ will be below 10^{-2} volts.

InP/InGaAs tandem solar cell with planar tunnel diode

A complete structure similar to that shown in Figure 3 was grown. In the following case the IOC for the tandem is realized with a planar tunnel diode. A very low photocurrent output for these type of structures under natural sun light illumination is characteristic. In Figure 9 we show the electrical characteristics of this tandem under concentrated light stimulation. The tandem's V_{oc} is equal to the sum of that from the InGaAs bottom cell (V_{oc1}) and that from the InP top cell (V_{oc2}) - $V_{\text{oc}} = V_{\text{oc1}} + V_{\text{oc2}} = 1.2 \text{ V}$ -. The SR was performed in order to investigate its low photo sensitivity (Figure 10). Despite the low overall photocurrent output, the InP top cell has a relatively good response. While the tandem responds fairly well for wavelengths less than 920 nm , for photons with wavelengths between 920 nm and 1650 nm the SR is near zero. As expected the $0.2 \mu\text{m}$ thick IOC tunnel diode absorbs nearly all the incoming photons thus totally blocking the irradiation of the bottom cell. The implications of this result is either the adoption of a tandem cell structure using a patterned tunnel concept, as proposed by Shen et al (ref. 8), or the use of ultra thin ($\sim 400 \text{ \AA}$) planar tunnel diodes. Both of these concepts are possible using CBE and are currently being investigated.

InP/InGaAs tandem solar cell with patterned tunnel diode

A structure similar to that of Figure 3 was grown but this time in a two-step process. First, the growth of the InGaAs solar cell followed by the InGaAs tunnel diode was performed. The sample was removed from the growth chamber and the tunnel diode was patterned with the same mask as the contact grid. Then, the sample was reloaded into the CBE chamber and the

InP solar cell was grown on top. Figure 10 shows the SR (after anti-reflection deposition) of this tandem. We see a noticeable improvement in the tandem photoresponse. The tunnel diode patterning has allowed a much higher illumination of the bottom cell. The InGaAs bottom cell however displays a higher SR compared to that of the InP top cell. This is mainly due to inhomogeneous etching during the patterning step and regrowth issues resulting in an inhomogeneous and poor quality InP material in the top cell. Nevertheless under light stimulations the patterned tunnel diode shows low resistivity and the tandem I-V characteristics display good ohmic IOC behavior even for high polarization. It is clear that regrowth procedures optimization will be necessary.

CONCLUSION

Chemical beam epitaxy has been shown to allow the attainment of high quality InGaAs and InP layers. InP and InGaAs solar cells have been obtained with high efficiency photoconversion, 10.2% for InGaAs solar cell and 18% for InP solar cell. The tunnel diodes obtained with this technique have very high peak current densities and show to be thermally stable during the top cell growth. This realization has permitted the fabrication of monolithically integrated tandem solar cells. The planar tandem device exhibits an open-circuit voltage equal to the sum of that of the individual sub-cells ($V_{oc} = 1.2$ V) demonstrating negligible voltage drop at the interconnect, but the InGaAs tunnel diode was shown to absorb highly thus blocking irradiation of the InGaAs bottom cell. By using patterned tunnel junctions we observe a significant improvement in the tandem photoresponse, but a lower spectral response for the top InP cell. Work underway is focusing on optimization of the regrowth procedures to address this problem.

**** Present address LPSES - CNRS, Valbonne - 06560 - France**

REFERENCES

1. M. W. Wanlass, J. S. Ward, K. A. Emery and T. J. Coutts; Proc. 23rd IEEE -PV Conf.; 1993; pp 621.
2. A. Freundlich, M. F. Vilela, A. Bensaoula, and N. Medelci; Proc. 23rd IEEE -PV Conf.; 1993; pp 644.
3. M. Yamaguchi, T. Warabisako and H. Sugiura, Journal of Crystal Growth; 136; 1994; pp.29.
4. A. Bensaoula, N. Medelci, M. F. Vilela and A. Freundlich; 6th International Conference on InP and Related Materials; Santa Barbara - CA - USA ; IEEE catalog #94CH3369-6, (1994), pp.280.
5. V. Rossignol, A. Bensaoula, A. Freundlich, and A. H. Bensaoula; 5th International Conference on InP and Related Materials; Paris - France ; IEEE catalog #93CH3276-3, (1993), pp.127.
6. A. H. Bensaoula, A. Freundlich, A. Bensaoula, V. Rossignol and A. Ponchet; J. Vac. Sci. Technol. B 12(2), 1994, pp. 1110.
7. A. Freundlich, M. F. Vilela, A. Bensaoula, and N. Medelci, Proc. 23th IEEE-PV Conf., 1993, pp. 644.
8. C. C. Shen, P. T. Chang and K. A. Emery; Proc. 22nd IEEE -PV Conf.; 1991; pp 381.

*This work was supported by the state of Texas advanced technology program 93-03652-260 , 93-003652-236 and 91-03652-243 and advanced research program 93- 003652-224 and partially supported by IST Inc. The authors would like to thank A. H. Bensaoula, E. Kim and V. Rossignol for their help in this project.

TABLES

Table I. - Shunt Resistance (R_{sh}), Saturation Current (J_s) and Ideality Constant (n) for the solar cells studied in this work.

Sample	InGaAs	InP	Patterned tandem	Planar tandem
R_{sh} ($M\Omega \cdot cm^2$)	4.2×10^{-5}	0.25	1.2×10^{-3}	2
J_s (mA/cm^2)	0.6	8×10^{-9}	0.7	8×10^{-4}
n	2.2	1.65	—	—

FIGURES

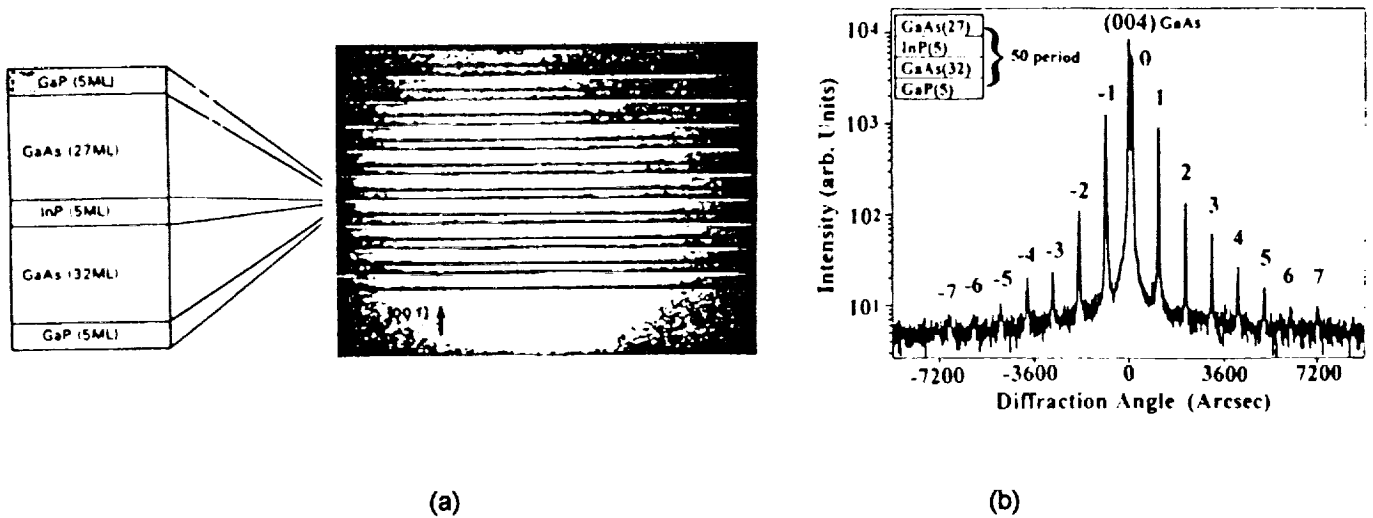


Fig. 1 - GaP/GaAs/InP superlattice, a 50-period GaP(5ML)/GaAs(32ML)/InP(5ML)/GaAs(27ML), (a) cross-sectional TEM and (b) High resolution x-ray diffraction patterns (ref. 6).

Dopant cross diffusion

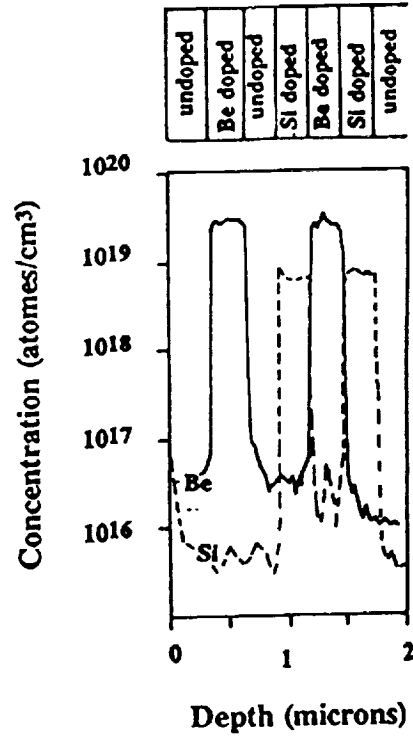


Fig. 2 - Secondary Ion Mass Spectroscopy of alternated dopant layers (Be and Si) and undoped spacers.

Top cell	InGaAs:Be Cap layer	$0.5-1 \times 10^{20} \text{ cm}^{-3}$	$0.5 \mu\text{m}$
	InP:Be Emitter	$1-3 \times 10^{18} \text{ cm}^{-3}$	$0.05-0.1 \mu\text{m}$
	InP:Si Base	$0.5-1 \times 10^{17} \text{ cm}^{-3}$	$1-2 \mu\text{m}$
	InP:Si BSF	$1-5 \times 10^{18} \text{ cm}^{-3}$	$0.2-0.5 \mu\text{m}$
Tunnel Junction	InGaAs:Si	$1-5 \times 10^{18} \text{ cm}^{-3}$	$0.1 \mu\text{m}$
	InGaAs:Be	$1-5 \times 10^{19} \text{ cm}^{-3}$	$0.1 \mu\text{m}$
Bottom cell	InP:Be Window	$3-5 \times 10^{18} \text{ cm}^{-3}$	$0.05-0.1 \mu\text{m}$
	InGaAs:Be Emitter	$1-3 \times 10^{18} \text{ cm}^{-3}$	$0.2-0.5 \mu\text{m}$
	InGaAs:Si Base	$0.5-1 \times 10 \text{ cm}^{-3}$	$2-3 \mu\text{m}$
	InGaAs:Si BSF	$1-5 \times 10^{18} \text{ cm}^{-3}$	$0.2-0.5 \mu\text{m}$
	InP:Si Buffer	$1-5 \times 10^{18} \text{ cm}^{-3}$	$0.5-1 \mu\text{m}$
	InP:S Substrate	$2 \times 10^{18} \text{ cm}^{-3}$	$400 \mu\text{m}$

Fig. 3 - InP/InGaAs tandem solar cell structure. Doping levels and thicknesses are shown.

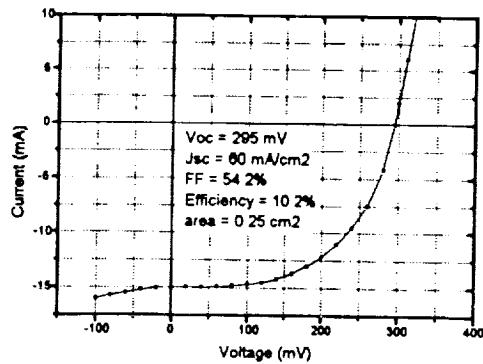


Figure 4 : Electrical characteristics of the InGaAs solar cell under natural sunlight, with anti reflection coating.

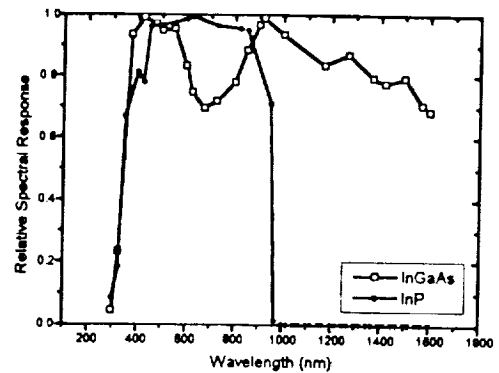


Figure 5 : Spectral Response of the InGaAs solar cell (opened squares) and InP solar cell (solid circles).

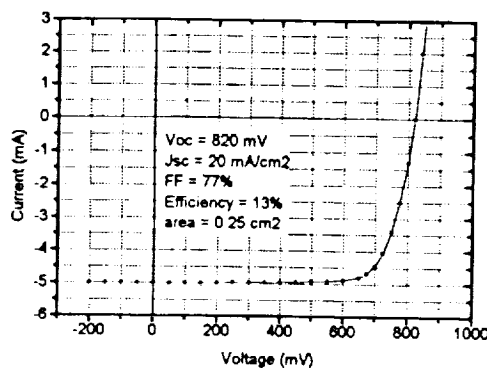


Figure 6: Electrical characteristics of the InP solar cell under natural sunlight (without anti reflection coating).

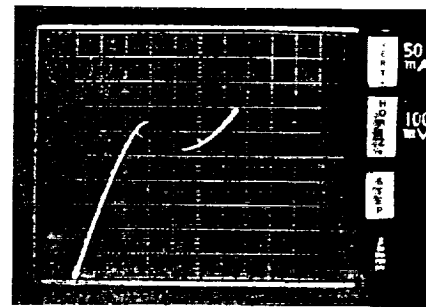


Figure 7: Room temperature I-V characteristics of InGaAs tunnel junction (mesa diameter = 200 μm) with a peak current of 1015 A/cm².

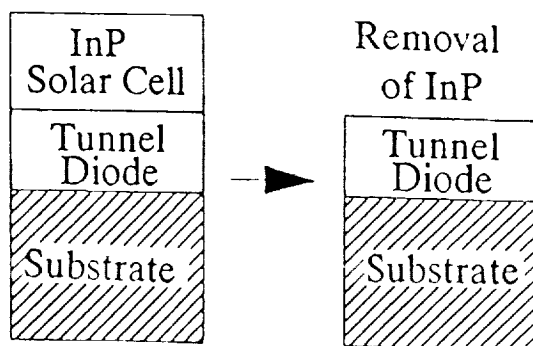


Figure 8: I-V characteristic of a InGaAs tunnel junction (mesa 200 μm in diameter) after solar cell growth. $J_p = 860 \text{ A/cm}^2$, $R_{max} = 2.9 \times 10^{-4} \Omega \cdot \text{cm}^2$.

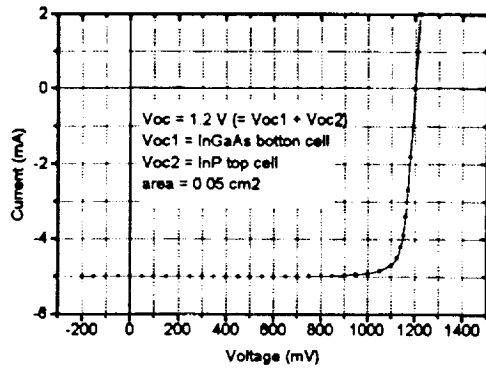


Figure 9 : Electrical characteristics of the tandem solar cell with a planar tunnel diode under concentrated light stimulation.

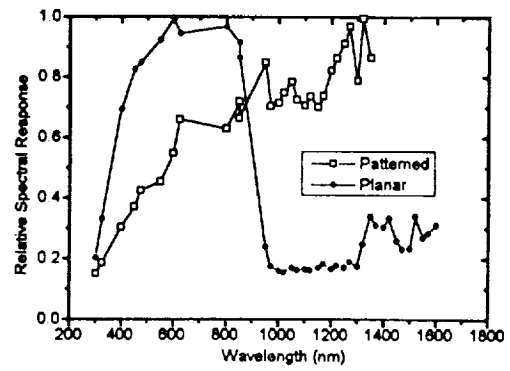


Figure 10 : Spectral Response of the InGaAs/InP tandem solar cell with a planar tunnel diode (solid circles) and InGaAs/InP tandem solar cell with a patterned tunnel diode (opened squares).

STATUS OF DIFFUSED JUNCTION p^+n InP SOLAR CELLS FOR SPACE APPLICATIONS

Mircea Faur
Cleveland State University
Cleveland, Ohio

Maria Faur
NYMA, Inc.
Brook Park, Ohio

D.J. Flood and D.J. Brinker
NASA Lewis Research Center
Cleveland, Ohio

C. Goradia
Cleveland State University
Cleveland, Ohio

N.S. Fatemi and P.P. Jenkins
NYMA, Inc.
Brook Park, Ohio

D.M. Wilt and S. Bailey
NASA Lewis Research Center
Cleveland, Ohio

M. Goradia and J. Moulot
Cleveland State University
Cleveland, Ohio

ABSTRACT

Recently, we have succeeded in fabricating diffused junction $p^+n(\text{Cd,S})$ InP solar cells with measured AM0, 25 °C open circuit voltage (V_{OC}) of 887.6 mV, which, to the best of our knowledge, is higher than previously reported V_{OC} values for any InP homojunction solar cells. The experiment-based projected achievable efficiency of these cells using LEC grown substrates is 21.3%. The maximum AM0, 25 °C efficiency recorded to date on bare cells is, however, only 13.2%. This is because of large external and internal losses due to non-optimized front grid design, antireflection (AR) coating and emitter thickness. This paper summarizes recent advances in the technology of fabrication of p^+n InP diffused structures and solar cells, resulted from a study undertaken in an effort to increase the cell efficiency. The topics discussed in this paper include advances in: 1) the formation of thin p^+ InP:Cd emitter layers, 2) electroplated front contacts, 3) surface passivation and 4) the design of a new native oxide/ $\text{Al}_2\text{O}_3/\text{MgF}_2$ three layer AR coating using a chemically-grown P-rich passivating oxide as a first layer. Based on the high radiation resistance and the excellent post-irradiation annealing and recovery demonstrated in the early tests done to date, as well as the projected high efficiency and low-cost high-volume fabricability, these cells show a very good potential for space photovoltaic applications.

INTRODUCTION

Owing to their excellent radiation resistance and annealing properties (refs. 1, 2), InP solar cells hold great promise for space power applications. In 1990, within a few short years after the renewed interest in the development of InP solar cells began in 1985, driven by early reports from NTT, Japan (ref. 4), an AM0, 25 °C efficiency of 19.1% was already achieved on a 4 cm² InP cell (ref.5). These $n^+pp^+(\text{Si,Zn})$ InP cells, developed by SPIRE Corp., were fabricated by MOCVD growth of the active layers on a heavily doped p^+ -InP:Zn substrate. The achievement of such a high efficiency in such a short period of time is particularly important since no special efforts were made to reduce external losses associated with an unpassivated surface and with the use of a ZnS/MgF_2 AR coating, developed for GaAs based solar cells. An unpassivated surface is suggested both by the low V_{OC} value of 876 mV, and the low blue response for an emitter thickness of only 30 nm. By passivating the front surface, the projected AM0, 25°C efficiency of 22% for these cells seems very realistic. Given this unprecedented short term success in developing high efficiency InP solar cells, and the relatively large accepted potential of these cells for high radiation environment space solar cells applications, it is rather odd that research funds from the space agency have continuously declined after 1990. A possible explanation of this, besides shrinking research funds, is the high cost of presently developed all-epitaxial high efficiency InP solar cells. For small power applications, where, beside radiation resistance, high BOL efficiency is required, the use of all-epitaxial InP solar cells grown on

InP substrates might be justified. However, their high wafer and processing costs, prohibit their large scale use in space solar cell arrays.

The cost of InP cells is due, to a significant extent, to the high cost of InP substrates. Hence, a large cost reduction might be achieved through heteroepitaxial InP solar cells grown on cheaper substrates such as Si or Ge. The increase in their AM0, 25 °C efficiency above presently achieved 7.1% (ref.6) for Si and 9% (ref. 7) for Ge substrates respectively is expected to come through the growth of GaAs based intermediate layers to accommodate the large lattice mismatch between InP and Si or Ge. Should these heteroepitaxial cells exhibit a BOL efficiency in excess of that of presently used Si space solar cells while retaining the radiation tolerance of homojunction InP solar cells, then, due to their lighter weight, lower substrate cost, and lower fragility, as compared to all-InP solar cells, they would have a very good potential for large scale use in space solar arrays, provided that the processing costs could be kept within reasonable limits.

A significant cost reduction over epitaxy can be achieved through the use of diffused junction InP cells. Until recently, the only InP solar cells fabricated by thermal diffusion were of the n^+p configuration. Cells fabricated by closed ampoule diffusion have yielded maximum AM0, 25 °C efficiency of 16.6% for a (S,Zn) cell (ref.8), 14.35% for non-optimized (S,Cd) cell (ref.9), and 15.2% for an open tube diffusion (S,Zn) cell (ref.10). The n^+p (S,Zn) InP cells made by closed ampoule diffusion have high radiation resistance (ref.1), and independent studies (e.g. refs. 11, 12) have shown much higher annealing rates after irradiation, under cell operating conditions, than high efficiency $n^+/n^+p/p^+p^+$ (Si,Zn) all-MOCVD InP cells (ref.5).

The drawback of the n^+p (S,Zn) diffused InP cells is that a large number of defects are present after diffusion both in the n^+ emitter and in the p-base, which, as shown above, makes the solar cell efficiency lower than that of all-MOCVD n^+p (Si,Zn) InP cells. Since, neglecting surface effects, of all solar cell performance parameters, V_{OC} can be regarded as the best measure of how low is the defect density within a given cell structure from among the different cell structures, its value can give useful information about the quality of each cell structure. For example, for the best n^+p (S,Zn) diffused cell with AM0, 25 °C efficiency of 16.6%, measured at NASA LeRC, the V_{OC} was only 828 mV as compared to 876 mV for the higher AM0 efficiency (19.1%) of the MOCVD-grown cell.

At the 11th SPRAT Conference, we predicted that for diffused solar cells, the p^+n configuration has a higher potentially achievable maximum efficiency than the n^+p configuration due especially to an increased V_{OC} (ref.13). The prediction was based on AM0, 25 °C V_{OC} values of 860 mV we measured for p^+n (Cd,S) InP solar cells as compared to experiment-based projected maximum V_{OC} of only 840 mV for our n^+p (S,Cd) InP cells. For our thermally diffused p^+n and n^+p structures, the ranking for projected maximum efficiency, in decreasing order, is: (1) p^+n (Cd,S); (2) n^+p (S,Cd); (3) n^+p (S,Zn), and (4) p^+n (Zn,S). The large structural and electrical-type defect density we found in the emitter and the base of structures (2) to (4) as compared to structure (1), explains V_{OC} , I_{SC} , and η limitations of the last three structures. This also explains why, although a large experimental effort was made by NTT to improve V_{OC} and efficiency of diffused n^+p (S,Zn) cells, the independently confirmed maximum efficiency was of only 16.6%. However, more recent work performed on NTT fabricated n^+p cells (ref.14) has shown that the AM0 efficiency of one such cell could be increased from 14.8% to 17.5% by plasma hydrogenation at 150 °C. The large gain in η is due to a sensitive increase in J_{SC} , which is thought to be due to a decrease in H2 and H3 trap center densities in the p-InP:Zn base, and the formation of a n^+-p-p^+ structure. A small increase in V_{OC} is thought to be due to a decrease by hydrogenation in surface and space charge recombination. For n^+p structures, we found Cd-doped substrates to be inherently superior to Zn-doped substrates (ref.10), and the experiment based practically achievable AM0 efficiency of diffused n^+p (S,Cd) InP solar cell using relatively large EPD ($\sim 5 \times 10^4 \text{ cm}^{-2}$) substrates is about 18.8%.

A preliminary investigation of p^+n and n^+p diffused structures and solar cells, prior to and after irradiation with 10^{13} cm^{-2} 3 MeV protons indicates that the same ranking should hold for structures (1), (2), and (4) with respect to radiation resistance as mentioned above for maximum efficiency. The p^+ emitter of p^+n (Cd,S) InP diffused structures exhibits very low radiation induced carrier removal rates (ref.16), which is thought to contribute to the increased radiation resistance of these cells as compared to other InP cell structures for which 3 MeV proton irradiation studies are available. Another interesting characteristic of

these cells is a remarkable annealing property at room temperature in the dark, which might be very attractive for other applications such as long-life alpha- or beta-voltaic batteries.

Recently, using a P-rich passivating layer grown by chemical oxidation, we have succeeded in fabricating diffused junction $p^+n(\text{Cd,S})$ InP solar cells with measured AM0, 25 °C V_{OC} of 887.6 mV (ref.16), which to the best of our knowledge is higher than previously reported V_{OC} values for any InP homojunction solar cells. Although the experiment based projected achievable efficiency of these cells using LEC grown substrates is 21.3% (ref.17), the maximum AM0, 25 °C efficiency recorded to date on bare cells is only 13.2%. This is because of large external and internal losses due to non-optimized front grid design, antireflection coating (ARC) and emitter thickness. This paper summarizes recent advances in the technology of fabrication of p^+n InP diffused structures and solar cells, resulting from a study undertaken in an effort to increase the cell efficiency. These advances include: 1) the formation of thin p^+ InP:Cd emitter layers, 2) electroplated front contacts, 3) surface passivation and 4) the design of a new native oxide/ Al_2O_3 / MgF_2 three layer AR coating using a chemically-grown P-rich passivating oxide as a first layer. The paper will also discuss some light instability problems associated with high Zn content front Au-Zn contacts and preliminary radiation resistance and post-irradiation annealing studies.

EXPERIMENTAL

Cd diffusion into n-InP:S ($N_D - N_A = 3.5 \times 10^{16}$ to $3.1 \times 10^{17} \text{ cm}^{-3}$) was performed by a closed ampoule technique using Cd_3P_2 as diffusion source (ref.18). Diffusion temperatures were from 560 to 660 °C. The substrates were Czochralski (LEC) grown with EPD of about $5 \times 10^4 \text{ cm}^{-2}$. Diffusions were performed through either P-rich chemically grown (ref.13) or MOVPE grown InGaAs cap layers.

The surface quality of diffused samples was monitored by either Nomarski or SEM microscopy. Electrochemical techniques (ref.19) were used for step-by-step characterization of these diffused structures during fabrication and after irradiation with high energy protons using a Polaron profiler PN4200, manufactured by BIORAD. We have recently developed a new electrolyte, which we call "UNIEL", for EC-V profiling of InP and GaAs based structures (ref. 19). In order to accurately locate the position of different defect levels derived from low frequency EG-V measurements, we have began, in parallel, photoluminescence measurements at 5 K on several Cd diffused samples. The excitation wavelength was 514 nm at a power density of 160 mW/cm^2 . Luminescence was dispersed in a 1.26 meter spectrometer and detected with cooled CCD array. The system resolution was about 0.5 meV.

Small area (0.48 cm^2) p^+n InP solar cells were fabricated using Zn- and Cd-diffused structures. Au was used for the back contact. The Au-Zn-Au (0.18 to $1.5 \text{ }\mu\text{m}$ thick) front contact grid was deposited by evaporation and defined using existing photolithographical masks, designed for n/p cell configurations. Au based contacts are known to penetrate into InP during sintering at 430 °C up to depths which are over three times the initial thickness of the evaporated Au-Zn-Au layer. Hence, we kept the thickness of the emitter at quite a high value (up to $5 \text{ }\mu\text{m}$) while keeping the thickness of the evaporated contacts below $0.2 \text{ }\mu\text{m}$. After sintering, the thick emitter was thinned down over the uncontacted area using a chemical etch (PNP), specially developed for this purpose (ref.20). Recently we were able to fabricate thin p^+ emitters using Cd-diffusion, by using either thicker P-rich oxides or InGaAs cap layers. New front contact schemes, employing electroplated Au and Au-Zn developed for thin emitters will be discussed in the following paragraph. We also propose a new optimized three-layer ARC for InP solar cells, which uses a P-rich chemical oxide as a first layer in a $\text{In}(\text{PO}_3)_3/\text{Al}_2\text{O}_3/\text{MgF}_2$ structure. This P-rich chemical oxide, which is described in more detail elsewhere (ref.16), is primarily designed as a surface passivation layer.

Unless otherwise mentioned, the performances of solar cells in this paper refer to non optimized single layer ARC using only the passivating layer. Dark and illuminated solar cell performances and their variation with illumination time or temperature were recorded at CSU using a computer controlled facility and an ELH lamp (assumed AM1.5 spectrum) as the light source. For selected cells, dark and illuminated I-V characteristics, and their variation with time, as well as reflectivity and spectral response measurements were performed at NASA LeRC.

RESULTS AND DISCUSSION

At the last SPRAT conference we reported an AM0, 25 °C, V_{OC} value of 880.3 mV for a diffused p^+n (Cd,S) InP solar cell. Since the maximum efficiency was only 12.57% as compared to projected achievable maximum efficiency of 21.3%, over the last year we have concentrated our efforts to reduce the large external and internal losses due to non optimized front grid contacts, AR coatings and emitter thickness, while further improving the diffused structure quality, by reducing the defect density in the emitter and junction area.

Since, of all solar cell parameters, V_{OC} can be regarded as the best measure of how low is the defect density within a given structure from among the different cell structures, its value can give useful information about the quality of each cell structure. Recently, using a P-rich passivating layer grown by chemical oxidation, we have succeeded in fabricating diffused junction p^+n (Cd,S) InP solar cells with measured AM0, 25 °C V_{OC} of 887.6 mV (Fig.1), which to the best of our knowledge is higher than previously reported V_{OC} values for any InP homojunction solar cells. The achievement of such a high V_{OC} value for a diffused junction cell with no AR coating, except for the thin passivating layer, is remarkable if one takes into consideration that the InP:S LEC grown substrates used have had a rather large EPD of $5-7 \times 10^4 \text{ cm}^{-2}$. From the dark I-V characteristic (Fig.2), the dark saturation current density J_0 ($A=1$) has a record low value of $1.38 \times 10^{-17} \text{ A/cm}^2$, which explains the high V_{OC} value.

The cell was fabricated by thinning the emitter from its initial thickness of about 4.5 μm to about 0.45 μm , after sintering the Au-Zn front contact. The relatively low short circuit current density (J_{SC}) of 26.3 mA/cm^2 and the low external quantum efficiency (EQY) of this cell can be explained by the large thickness of the emitter (0.45 μm , compared to the optimum thickness of $\sim 0.25 \mu\text{m}$) and the absence of an AR coating. Figure 3 shows the EQY of this cell. Worth noticing is the relatively high blue response for a p^+ emitter as thick as 0.45 μm , suggesting a large diffusion length in the Cd doped emitter and a well passivated surface. The cell had a high R_s of about $3.5 \Omega\text{-cm}^2$ due to relatively high contact and sheet resistance and non optimized front grid design (an existing photolithographical mask designed for n/p cell configurations was used), resulting in low FF of 69% and efficiency of only 11.98%.

Next paragraphs summarize recent advances in p^+n InP diffused structures and solar cell technology, undertaken in an effort to increase the cell efficiency. This includes the formation of thin p^+ -InP:Cd emitter layers, electroplated front contacts, surface passivation and the design of a new native oxide/ Al_2O_3 / MgF_2 three layer AR coating structure using a chemically-grown P-rich passivating oxide as a first layer. Also discussed are some light instability problems associated with high Zn content front Au-Zn contacts and preliminary radiation resistance and post-irradiation annealing studies.

Emitter Layer

As mentioned above, for cells such as that shown in Fig.1, thick emitters have been used. This adds a troublesome fabrication step, which affects the reproducibility of cell performances. Furthermore, as seen above, using thick emitters such as in Fig.4, thinning from over 4 μm to below 0.5 μm has the drawback of reducing the surface hole concentration in the thinned emitter, thereby increasing the series resistance (R_s) and lowering the fill factor (FF). A more step-like diffusion profile such as in Fig.5, was possible by optimizing the thickness of the $\text{In}(\text{PO}_3)_3$ -rich chemical oxide ($\sim 10 \text{ nm}$), used as a diffusion cap layer. To further decrease the R_s values of these cells, two avenues were undertaken:

- (a) Since the optimal emitter thickness is estimated at about 0.25 to 0.3 μm , we were able to fabricate thin emitters while maintaining the high surface acceptor concentration (see Fig.6).
- (b) Use low band gap diffusion cap layers such as InGaAs. Example: The EC-V diffusion profile in Fig.7(a) was realized using an intentionally undoped InGaAs cap layer. Curve (b) refers to a diffusion carried out under similar conditions (600 °C, 25 min., and same amount of Cd_3P_2 source material) using a thin $\text{In}(\text{PO}_3)_3$ -rich chemical oxide cap layer. As expected, the InGaAs cap, after Cd diffusion becomes highly doped, which should improve the contact

resistance. However, in this case, since InGaAs cap is not stable at higher temperatures, the hole concentration in the InP:Cd emitter is rather low, which should increase the sheet resistance.

Electroplated Front Contacts.

For thin emitters (0.5 to 0.75 μm) we first tried thin (0.1 μm) Au-Zn evaporated contacts, with an intent to then deposit thicker electroplated contacts after sintering. However, after sintering the contacts at 430 $^{\circ}\text{C}$, for 2 minutes, the contacts penetrated at depths greater than the emitter thickness, short-circuiting it. For lower sintering temperatures the contacts lifted during subsequent chemical treatments in PNP etch (ref.20) we are using both for surface passivation and thinning the emitter. For these samples, after removing the evaporated contacts, Au-Zn and Au-Cd front contacts were fabricated using conventional UV lithography and electroplating. The positive photoresist ($\sim 5 \mu\text{m}$ thick) was deposited on clean and chemically oxidized emitter surfaces. In both cases about 0.5 μm Au-Zn or Au-Cd were first electrodeposited by pulse plating at pulse current density of 0.5 to 2 mA/cm^2 , then 5 to 18 μm Au was deposited at a constant current density of 0.2 to 0.3 mA/cm^2 . When using clean surfaces the width of the contact grid fingers became up to 3 times the designed values, while their width have not increased significantly when a 20 to 50 nm chemical oxide was used. Electroplated Au-Zn or Au-Cd front contacts we found are well suited for deposition on thin emitters since they do not require sintering. For example, using $\sim 8 \mu\text{m}$ thick electroplated Au-Zn contacts, grown on a 0.6 μm thick emitter, using an oxidized surface, we recorded R_s values as low as 1.28 $\Omega\text{-cm}^2$, and FF values of over 80%, after thinning the emitter to about 0.3 to 0.4 μm . Since for p/n configuration the sheet resistance is a major contributor to R_s , we estimate that by using an optimized front grid mask, R_s values of less than 0.5 $\Omega\text{-cm}^2$ and FF greater than 84% can be achieved after thinning the p^+ emitter such as in Fig.6 to 0.25-0.3 μm .

Surface Passivation

One of the key factors limiting the performance of InP solar cells is their high surface recombination velocity (SRV), which is estimated, even for epitaxially grown cells to be as high as 10^7 cm/s (ref.21). Although not near to such an extent as the n^+p InP structures, p^+n InP structures fabricated by thermal diffusion have their surface stoichiometry destroyed. Therefore, it is important in the fabrication of high-performance InP solar cells in general and diffused InP cells in particular, to remove in a controlled manner the high defect density surface layer of the emitter and to passivate the surface. Calculations have shown that SRVs higher than $5 \times 10^5 \text{ cm/s}$ drastically reduce the efficiency of InP solar cells by lowering their blue response (ref.22). Simple chemical treatments of InP surfaces using HNO_3 and HF based etchants (ref.23) were found to decrease the SRV to below $5 \times 10^5 \text{ cm/s}$, e.g. 1.7×10^5 for $n^+-\text{InP}$ and $4.7 \times 10^5 \text{ cm/s}$ for $p^+-\text{InP}$, after rinsing the substrates in a HNO_3 (15%) solution (ref.24).

Using the PNP etch, based on HNO_3 , $\text{o-H}_3\text{PO}_4$, and H_2O_2 , we developed for thinning after contacting the $p^+-\text{InP}$ emitter (ref.20), from low frequency EG-V measurements, we recorded a surface state density minimum (N_{ss}) at the Cd-diffused $p^+-\text{InP}$ /passivating layer interface as low as $2 \times 10^{10} \text{ cm}^{-2} \text{ eV}^{-1}$. About 40 nm was removed from the surface of a the p^+n InP structure diffused at 660 $^{\circ}\text{C}$ (surface acceptor concentration: $\sim 4 \times 10^{18} \text{ cm}^{-3}$). Such a low N_{ss} value is in good qualitative agreement with the high measured V_{oc} and blue response values of solar cells fabricated on these structures.

AR Coating

The residual oxide grown on $p^+-\text{InP}$ using the PNP etch is composed of a thick In-rich outer layer and a P-rich layer at the interface with the emitter (Fig.8). From XPS investigation (ref.20), the interfacial oxide is rich in $\text{In}(\text{PO}_3)_3$. Since this oxide, as seen above, passivates the surface quite well, and it has a bandgap of $6.8 \pm 0.2 \text{ eV}$ (ref. 25), we proposed that it be used as a first layer AR coating (ref.16). The transparency of

this oxide over the measured 1.8 to 5.2 eV range (ref.25) and its low blue reflectivity, as compared to SiO, Sb₂O₃, shown in Fig.9, and optimized ZnS/MgF₂ double layer AR coating (not shown here), seem to make this oxide a very attractive candidate, indeed, for use as a first layer AR coating. In addition, when we deposited on our bare p⁺n InP cells either SiO or Sb₂O₃ or a double layer of ZnS/MgF₂, the V_{OC} dropped by as much as 50 mV, indicating a large increase in SRV. As shown in Fig.10, the two layered oxide (~ 130 nm) reduces the reflectance of an p⁺n InP solar cell from an average of 40% to slightly less than 20%. In this particular case, after removing the In-rich outer-oxide layer, the reflectance of the remaining thin In(PO₃)₃ oxide is about 25%.

Although the overall reflectance of the double-layered chemical oxide in Fig.9 is lower than that of SiO, it is still too high for use as a single layer AR coating. Furthermore, the outer In-rich oxide is unstable and quite conductive, which caused for our cells a noticeable drop in R_{sh}, and V_{OC}. Therefore, we removed it, and in our best design we add Al₂O₃ and MgF₂ as second and third layers of the three-layer coating. For the example in Fig.10, a three-layer AR coating composed of In(PO₃)₃ (45 nm) / Al₂O₃ (62 nm) / MgF₂ (41 nm), reduces the overall reflectivity (no grid fingers) to less than 2%. Details of this design will be given elsewhere (ref.26).

Progress in p⁺n InP Diffused Solar Cells

As mentioned above, our efforts over the last year or so were concentrated on designing: 1) thin p⁺-InP emitters, 2) front contacts, 3) passivating layer and 4) AR coating, so as to minimize the large external losses present in our cells. Therefore, since these efforts were made simultaneously, solar cells were only fabricated to check our progress and to correlate other measured parameters to solar cell parameters. Table 1 shows some preliminary results. As an example, by using a more step-like diffusion profile of Fig.5 for cell #3, instead of the more graded profile of Fig.4 for cell #1, the R_s value could be noticeably decreased, using the same n-type front grid design. An increased FF made it possible to increase the AM0 efficiency from 11.25% to 13.2%. The relatively lower V_{OC} for cell #3 is due to current leakage which occurs through the In-rich oxide (~ 110 nm) outside the mesa etched active area. This is confirmed by the data of cell # 4. As seen, upon removing the In-rich outer layer, although the J_{SC} value decreased, as expected from the reflectivity measurements such as shown in Fig.10, the V_{OC} value increased. The small increase in FF was due to an increase in R_{sh}. By depositing a non-optimized SiO (~ 85 nm) second AR coating layer, the cell current density increased by about 12%. To make sure that no current is collected from outside the active area of the cell, this particular cell was cleaved around the mesa etched defined lines, and no noticeable changes in cell AM0 parameters were observed.

From correlations between measured cell parameters, reflectivity, spectral response, dark saturation current densities and J_{SC}-V_{OC} plots, the projected AM0, 25 °C performance parameters of p⁺n (Cd,S) InP solar cells, using our state-of-the-art newly developed thin emitters, and optimal front grid (6% coverage), and the newly designed three layer AR coating, are: V_{OC}=910 mV, J_{SC}=37.85 mA/cm², FF=84%, and η =21.2%. These performances are predicted for an emitter thickness of 0.3 μm, a surface acceptor concentration of 3.5x10¹⁸ cm⁻³, base electron concentration of 7.5x10¹⁶ cm⁻³, front SRV of 10⁵ cm/s, and using LEC grown InP:S substrates with EPD=5x10⁴ cm⁻². Higher efficiency is possible by using better quality substrates, further improving the diffused structures and the cell fabrication sequences.

Some light degradation effects have been observed in our earlier p⁺n (Cd,S) cells, which we have attributed to excess Zn content (>10%) in the Au-Zn front contacts. Indeed, as seen in Fig.11 by lowering the Zn content to less than 10%, the relative degradation of cell parameters decreases from about 10% to less than 1%. We believe that by using lower Zn content (0.1 to 1%) Au-Zn front contacts, which recent studies indicate to offer a lower contact resistance, this problem can be eliminated. We observed similar degradation effects in our n⁺p (S,Zn) diffused cells with high base acceptor concentration (> 10¹⁷ cm⁻³). However, as seen in Fig.11 no light degradation is observed for a cell with lightly base doping (2.4 x 10¹⁶ cm⁻³).

Preliminary Radiation Resistance and Annealing Studies.

Preliminary results of radiation resistance studies of diffused p^+n (Cd,S) InP solar cells, such as shown in Table 2, indicate that the percent of remaining power (39%), after irradiation with 10^{13} cm^{-2} , 3 MeV protons is higher than that of other InP cell structures, including the all-MOCVD fabricated n^+p (Si,Zn) and diffused n^+p (S,Zn) InP cells, for which irradiation data using 3 MeV protons are available (ref.15). Furthermore, this cell shows a remarkable annealing property at room temperature (RT) in the dark. The AM0, 25 °C, performance parameters of this cell prior to irradiation and after about 1 year at RT in the dark, are shown in Table 3. Subsequent light soaking of this cell for 1 hour under AM1.5, 25 °C, raised its efficiency by about 2.5% (See Fig.11), indicating good annealing properties under illumination.

Preliminary radiation resistance studies and annealing studies of these cells have been started at Spire Corp., after irradiation with high energy alpha particles. For one such cell, for which data are available, after irradiation at an equivalent 1MeV e^- fluence of $1.06 \times 10^{17} \text{ e}^-/\text{cm}^2$, which corresponds to over 100 years in GEO, the remaining power output is 32% of the initial power (Table 4). As a result of a significant recovery of about 6%, after only 4 days at RT in the dark, and an expected higher recovery rate under the cell operating conditions (RT, under illumination), these cells are not expected to degrade significantly in high radiation environment orbits, even after such large fluences.

We attribute the high radiation resistance of diffused p^+n (Cd,S) InP cells to a very low carrier removal rate (Fig.12) in the emitter (ref.15). It is note worthy that the carrier removal in the InP:S base, after irradiation with 10^{13} cm^{-2} , 3 MeV protons has decreased by more than an order of magnitude. For a thick p^+ emitter, most of the cell current is not expected to come from the base or space charge region. Since, as seen, the more heavily doped Cd-diffused emitter degrades less than the low doped base, the superior radiation resistance of these cells, as compared to a thin emitter n^+p configuration with a thin emitter, should be expected.

Low Cost Processing Scheme for High Efficiency Radiation Resistant p^+n InP Diffused Solar Cells.

For InP solar cells to be commercially useful for practical space mission applications, their cost must be significantly reduced, and they should achieve high BOL and EOL efficiencies. For small to medium power requirements, the weight might not be a prime requirement, as long as the cells are intended for high radiation environments. Diffused structures InP cells in general, and p^+n (Cd,S) cell structures in particular, appear to be more radiation resistant than cells fabricated by epitaxy. A simplified processing scheme is proposed in Fig.13, for fabrication of high efficiency, radiation resistant p^+n InP diffused junction cell. The scheme we propose ensures not only a low fabrication cost, but also high throughput and reproducibility.

As shown in the previous paragraphs, preliminary results show that cells using Cd-diffused emitter have not only a good potential for achieving high BOL efficiencies, but they also appear to be more radiation resistant and to have better post irradiation annealing properties than other diffused cell structures. Since for the p^+n configuration, the Cd-diffused cells are more radiation resistant than the Zn-diffused emitter cells fabricated using similar S-doped substrates, it will be very interesting to see how the radiation resistance of epitaxial and diffused n^+p cells, with similar structures, e.g. (S,Zn) do compare. Also it would be interesting to compare p^+n InP homojunction or heteroepitaxial cell structures with the emitter diffused into a thin base grown epitaxially on heavily doped InP or cheaper substrates such as GaAs, Ge or Si with all-epitaxial grown similar cell structures.

CONCLUSIONS

- We have found the ranking in decreasing order of projected maximum efficiency of diffused junction InP solar cells to be: 1) p^+n (Cd,S), 2) n^+p (S,Cd), 3) n^+p (S,Zn), and 4) p^+n (Zn,S). Preliminary investigation indicates the same ranking holds for these structures with respect to radiation resistance.

- If further developed, the p^+n (Cd,S) InP solar cells, developed by CSU/NASA LeRC, offer the following significant advantages for space power applications:
 - Low processing cost
 - High throughput
 - Good reproducibility
 - High projected efficiency
 - High radiation resistance
 - Self annealing during operation
- The radiation resistance of these cells, combined with their annealing behavior under operating conditions, may eliminate the need for shunt circuits used in conventional satellites to dump excess power early in their missions.
- Although InP has about twice the density of Si, or Ge substrates, the ability of diffused InP to anneal under operating conditions allows the thickness of the protective cover glass to be reduced, compensating for the difference in the substrate weight.
- The technology of InP diffused structures, electroplated contacts, $\text{In}(\text{PO}_3)_3/\text{Al}_2\text{O}_3/\text{MgF}_2$ ARC, and improved electrochemical characterization techniques, developed in this work, can be applied to fabrication of other III-V solar cell and opto-electronic devices.

References

1. M.Yamaguchi and K.Ando, "Mechanisms for Radiation Resistance of InP Solar Cells," J.Appl. Phys. **63**, 5555 (1988).
2. I.Weinberg, C.K.Swartz, R.E.Hart, and R.L.Statler, "Radiation and Temperature Effects in Gallium Arsenide, Indium Phosphide, and Silicon Solar Cells," Proc. 19th IEEE PVSC, 1986, p. 548.
3. I.Weinberg, C.K.Swartz and R.E.Hart, "Potential for Use of InP Solar Cells in the Space Radiation Environment," Proc. 18th IEEE PVSC, 1985, p.21.
4. M.Yamaguchi, C.Uemura, A.Yamamoto and A.Shibukawa, "Electron Irradiated Damage in Radiation-Resistant InP Solar Cells," Jpn. J. Appl. Phys. **23**, 30 (1984).
5. C.J.Keavney, V.E.Haven and S.M.Vernon, "Emitter Structures in MOCVD InP Solar Cells," Proc. 21st IEEE PVSC, 1990, p.141.
6. C.J.Keavney, S.M.Vernon, V.E.Haven, S.J.Wojtczuk and M.M.Al-Jassim, "Fabrication of n^+/p InP Solar Cells on Silicon Substrates," Appl. Phys. Lett., **54**, 1139 (1989).
7. S.J.Wojtczuk and S.Vernon, " p/n InP Solar Cells on Ge Wafers," This Conference.
8. H.Okazaki, T.Takamoto, H.Takamura, T.Kamei, M.Ura, A.Yamamoto and M.Yamaguchi, "Production of InP Solar Cells for Space Power Generation," Proc. 20th IEEE PVSC, 1986, p.886.
9. M.Faur, M.Faur, C.Goradia, M.Goradia, N.Fatemi, D.J.Brinker and R.Thomas, "InP Solar Cells made by Closed-Ampoule Diffusion of Sulfur into Cadmium-Doped Substrates: Dependence of Cell Characteristics on Diffusion Temperature and Time," Proc.1st Int'l IPRM Conference, 1989, p. 459.
10. S.Bothra, H.G.Bhimnathwala, K.K.Parat, S.K.Ghandhi and J.M.Borrego, "Characterization and Modeling of Open Tube Diffused n^+p InP Solar Cells," Proc. 19th IEEE PVSC, 1987, p.261.
11. R.J.Walters, G.P.Summers and J.Bruening, "A Detailed Study of the Photo-Injection Annealing of Thermally Diffused InP Solar Cells," Proc. 12th SPRAT Conference, 1992, p.1.
12. S.R.Messenger, R.J.Walters and G.P.Summers, "High Temperature Annealing of Minority Carrier Traps in Irradiated MOCVD n^+p InP Solar Cell Junctions," *ibid.*, p.8.
13. M.Faur, M.Faur, D.J.Flood, I.Weinberg, D.J.Brinker, C.Goradia, M.Goradia and W.Thesling, "A Comparative study of p^+n and n^+p InP Solar Cells Made by Closed Ampoule Diffusion," Proc. 11th SPRAT Conference, 1991, p. 3-1.

14. S-K.Min, H.Y.Cho, W.C.Choi, M.Yamaguchi and T.Takamoto, "Hydrogenation Effects on $n^+ - p$ InP Solar Cells," Proc. 23rd IEEE PVSC, 1993, p.639.
15. M.Faur, M.Faur, D.J.Flood, I.Weinberg, C.Goradia, M.Goradia and C.Vargas-Aburto, "Low Carrier Removal Rates and Annealing Behavior of Thermally diffused p^+n (Cd,S) InP Structures After 10^{13} cm^{-2} 3 MeV Proton Irradiation," *ibid.*, p.1437.
16. M.Faur, M.Faur, D.J.Flood, D.J.Brinker, C.Goradia, S.Bailey, I.Weinberg, M.Goradia, D.T.Jayne, J.Moulot and N.Fatemi, "Effective First Layer Antireflecting Coating on InP Solar Cells Grown by Chemical Oxidation," Proc. 6th Int'l IPRM Conf. , 1994.
17. M.Faur, M.Faur, C.Goradia, M.Goradia, D.J.Flood, D.J.Brinker, I.Weinberg, C.Vargas and N.S.Fatemi, "Progress in p^+n InP Solar Cells Fabricated by Thermal Diffusion," Proc. 12th SPRAT Conf., 1992, p.23.
18. M.Faur, M.Faur, C.Goradia, M.Goradia and I.Weinberg, "High Quality Thermally Diffused p^+n InP Structures, " 3rd Int'l IPRM Conf., 1991, p.304.
19. M.Faur, M.Faur, M.Goradia, C.Vargas and D.M.Wilt, "Electrochemical Characterization of n^+p and p^+n InP Diffused InP Structures," Proc. 12th SPRAT Conf., 1992, p.33.
20. M.Faur, M.Faur, D.T.Jayne, S.Bailey and M.Goradia, " Etchant for Chemical Thinning of InP and its Applications in the Fabrication of InP Diffused Junction Solar Cells," Surface and Interface Analysis, 21, 110 (1994)
21. C.Keavney, " Improvement in InP Solar Cells," Proc. 20th IEEE PVSC, 1988, p.654.
22. C.Goradia, W.Thesling and I.Weinberg, "Key Factors Limiting the Open-Circuit Voltage of $n+pp^+$ InP Solar Cells," Proc. 22nd IEEE PVSC, 1991, p.386.
23. M.Faur, M.Faur, P.Jenkins, M.Goradia, S.Bailey, D.Jayne, I.Weinberg and C.Goradia, "Study of Surface Passivation of InP," Surface and Interface Analysis, 15, 745 (1990)
24. P.Jenkins, M.Goradia, M.Faur, S.Bailey and M.Faur, "Measurement of Surface Recombination Velocity on Heavily Doped Indium Phosphide," Proc. 21st IEEE PVSC, 1990, p.399.
25. J.Joseph, Y.Robach, G.Hollinger, P.Ferret and M.Pitval, "The Passivation of InP by $\text{In}(\text{PO}_3)_3$ for MISFET Applications," Proc. 1st Int'l IPRM Conf., 1989, p.268.
26. J.Moulot, M.Faur, M.Faur, C.Goradia, M.Goradia, S.Bailey and N.Fatemi, "Design of a Three-Layer Antireflective Coating for High Efficiency Indium Phosphide Solar Cells using a Chemical Oxide as First Layer," Review Abstract submitted to the 1st World Conf. on Photovoltaic Energy Conversion, Hawaii, Dec. 5-9, 1994.

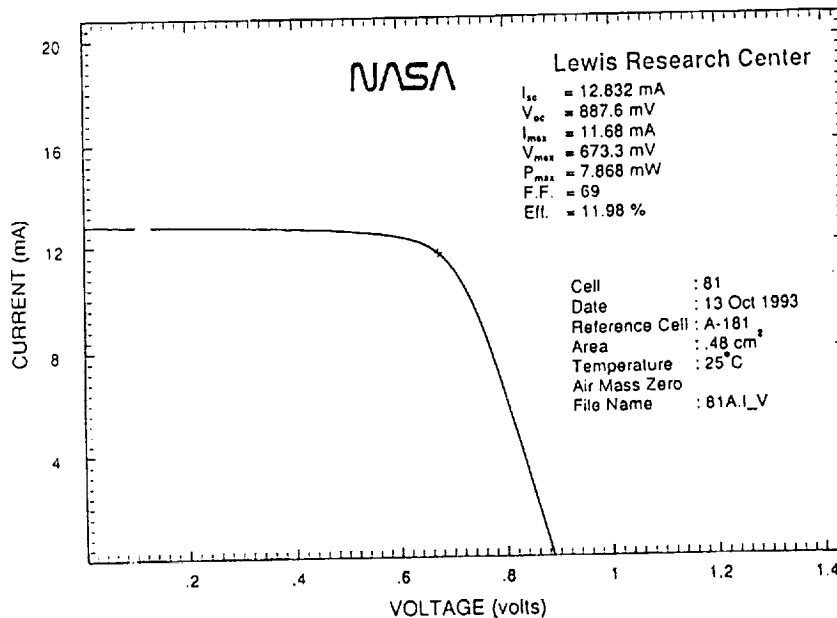


Fig.1. AM0, 25 °C illuminated I-V characteristic. Emitter thickness: ~ 0.45 μm ;
AR coating: ~ 30 nm $\text{In}(\text{PO}_3)_3$.

Table 1: AM0, 25°C performances of selected diffused junction p⁺n (Cd,S) InP solar cells measured at NASA LeRC

Cell #	Diffusion Profile such as in:	AR coating	Approx. emitter thickness (μm)	Rs (Ω-cm ²)	Jsc (mA/cm ²)	Voc (mV)	FF (%)	η (%)
1	fig. 4	In(PO ₃) ₃ ^b (~300Å)	0.35	4.92	27.6	886.9	62.8	11.25
2	fig. 5	In(PO ₃) ₃ ^b (~400Å)	0.45	3.24	27.5	884.6	73.7	12.95
3	fig. 5	In ₂ O ₃ ^a (900Å)/ In(PO ₃) ₃ ^b (~300Å)	0.4	3.35	28.2	881.7	72.6	13.2
4	fig. 4	In ₂ O ₃ ^a (1100Å)/ In(PO ₃) ₃ ^b (~400Å)	0.3	4.38	29.4	877.2	61.7	11.63
		In(PO ₃) ₃ ^b (~400Å)			27.6	886.6	62.8	11.25
		SiO (~850Å)/ In(PO ₃) ₃ ^b (~400Å)			30.95	887.3	61.5	12.36

The residual chemical oxide after dissolving the p⁺ InP emitter using the PNP etch [4], has two components: (a) a thick In₂O₃-rich surface layer, and (b) an interfacial In(PO₃)₃-rich layer.

Table 2: AM1.5, 25°C performance parameters of a diffused p⁺n (Cd,S) InP solar cell before (b) and after irradiation with 10¹³ cm⁻², 3MeV protons.

Time after irradiation (hours)	Voc (mV)	Jsc (mA/cm ²)	FF (%)	η (%)	Rs (Ω-cm ²)
0 (b)	871	27.42	72.64	12.65	3.27
8	664	15.48	64.00	4.86	5.33
90	676	16.37	65.10	5.25	5.19
206	682	16.85	65.50	5.49	4.88
857	708	18.47	66.00	6.29	4.85

(*) The cell was kept at RT in the dark except for 6 short exposures to light during illuminated I-V measurements

Table 3: AM0, 25°C performance parameters of a p⁺n (Cd,S) InP solar cell (same as in Table 2), before (b) irradiation and 1 year after irradiation (a) with 10¹³ cm⁻² 3MeV protons.

	Voc (mV)	Jsc (mA/cm ²)	FF (%)	η (%)
(b)	880.3	26.81	73.1	12.57
(a)	713.9	18.02	67.0	6.31

(*) Measurements performed at NASA LeRC. After irradiation, the cell was kept at RT in the dark except for 6 light exposures during the AM1.5, 25°C illuminated I-V measurements in Table 2.

Table 4: AM0, 25°C performance parameters of a CSU p⁺n (Cd,S) InP solar cell prior to and after alpha irradiation at 1MeV equivalent electron fluence of 1.06x10¹⁷ cm⁻². (*)

	Voc (mV)	Jsc (mA/cm ²)	FF (%)	η (%)	J01 (n1=1) (A/cm ²)	J02 (n2=2) (A/cm ²)	Rs (Ω-cm ²)	Rsh (x 10 ⁵ Ω)
Before irradiation	888	27.18	69.21	12.17	2.85 10 ⁻¹⁷	7.7 10 ⁻¹¹	3.66	5.1
Post irradiation	652	13.64	60.14	3.90	2.72 10 ⁻¹⁴	3.4 10 ⁻⁰⁸	6.04	2.8
After 4 days at RT in the dark	659	14.32	60.14	4.13	2.1 10 ⁻¹⁴	3.05 10 ⁻⁰⁸	5.91	2.6

(*) The measurements and irradiation were performed at SPIRE Corp., and presented here with permission from Dr. C. Blatchley.

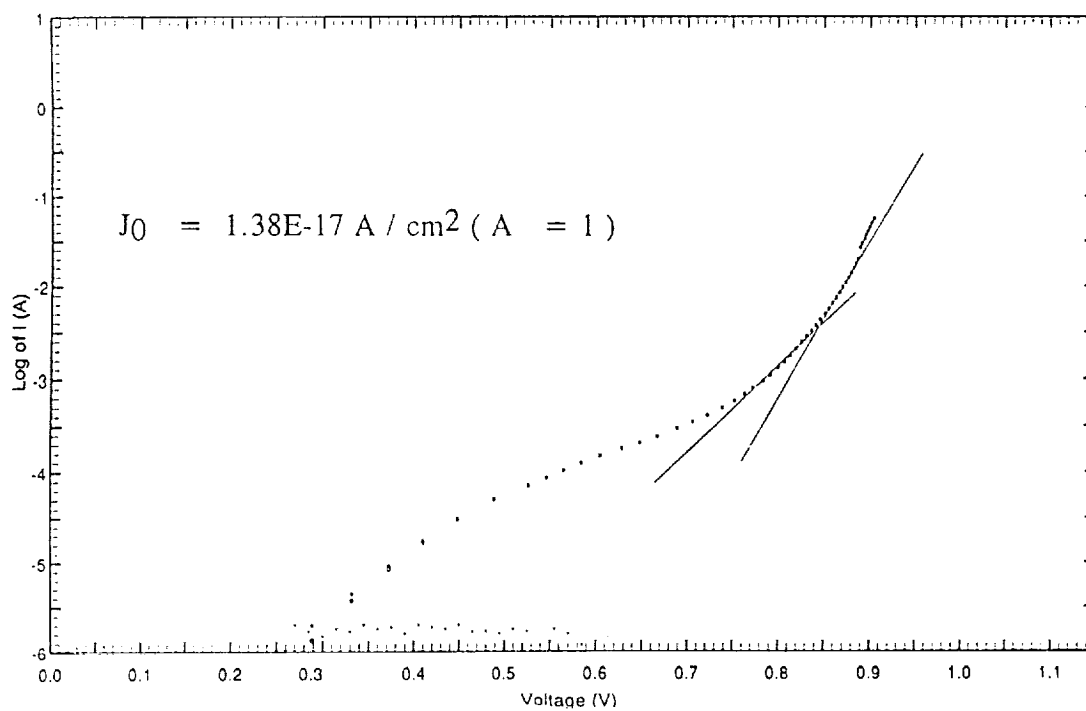


Fig. 2. Dark I-V characteristic of cell # 4 in Table 1.

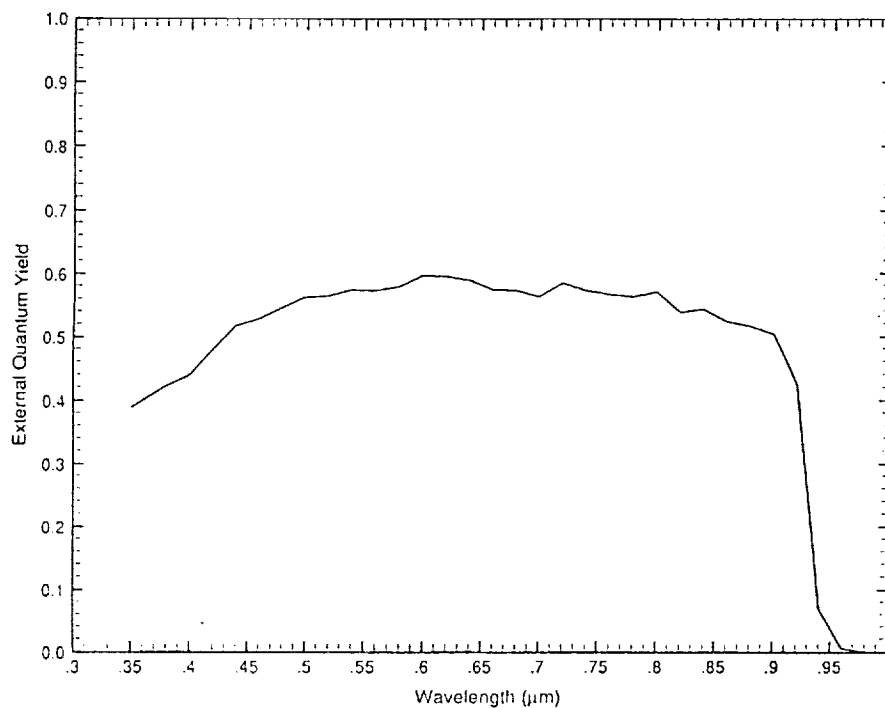


Fig. 3. Typical EQY plot of a cell with a thin $\text{In}(\text{PO}_3)_3$ (~ 30 nm) as an AR coating. Overall reflectivity: ~ 30%. Emitter thickness: ~ 0.45 μm .

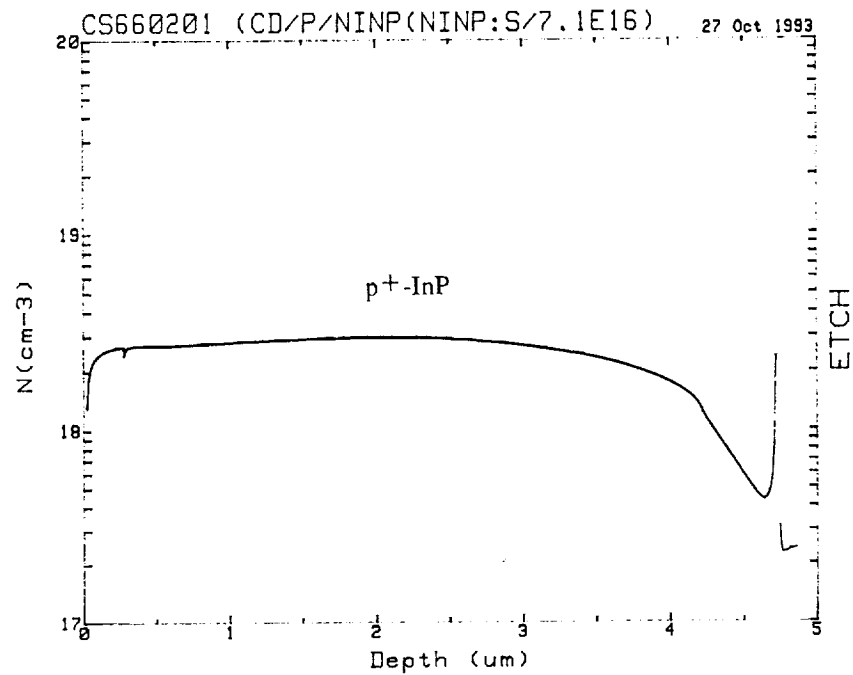


Fig.4. EC-V profile of a p^+n (Cd,S) InP structure diffused at 660 °C. Diffusion cap: $\text{In}(\text{PO}_3)_3$ (~ 3 nm).

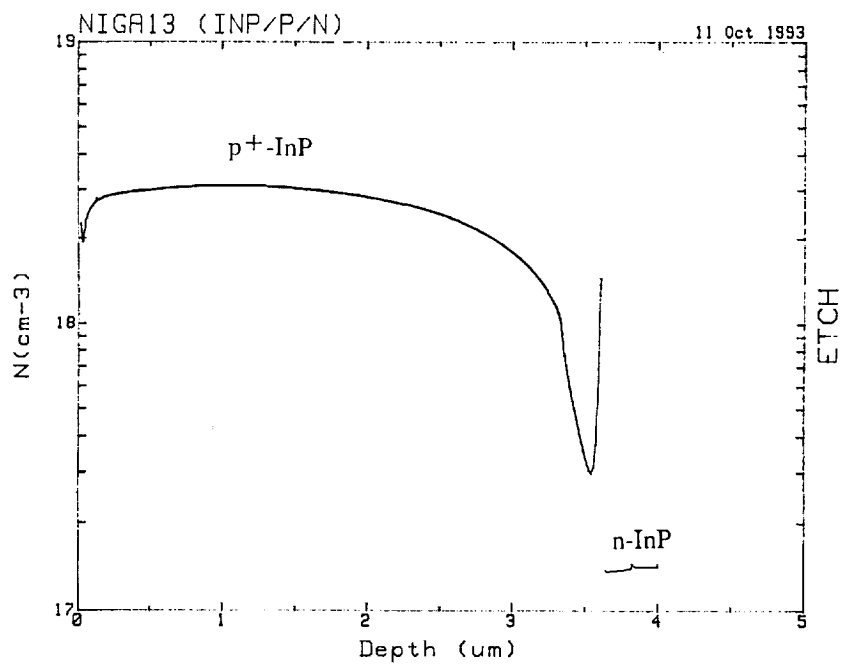


Fig.5. EC-V profile under similar conditions as in Fig. 4, but using ~ 10 nm thick $\text{In}(\text{PO}_3)_3$ diffusion cap .

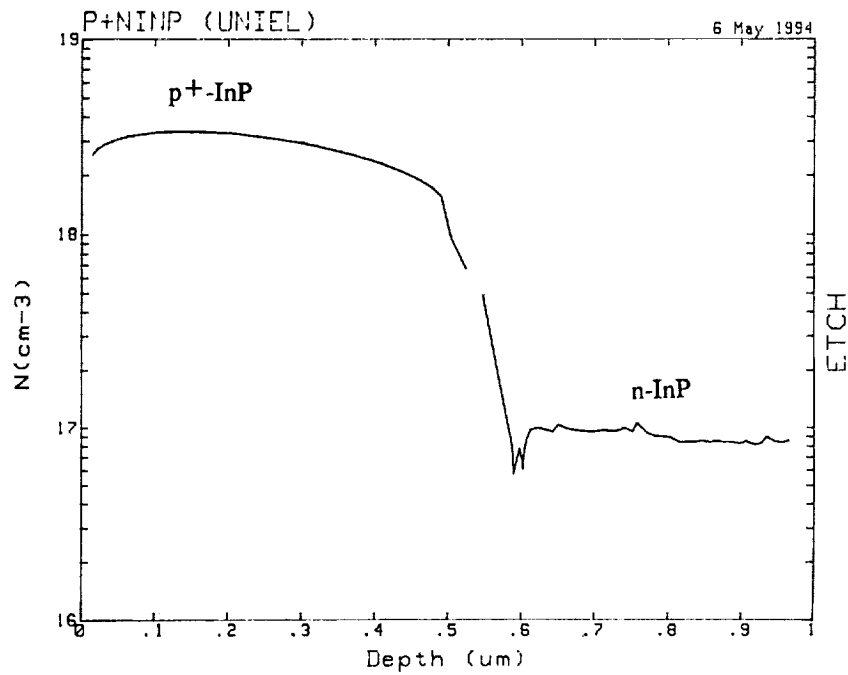


Fig.6. Thin emitter p^+n (Cd,S) InP EC-V profile, at 660 °C. using $\text{In}(\text{PO}_3)_3$ (~ 3 nm thick) diffusion cap.

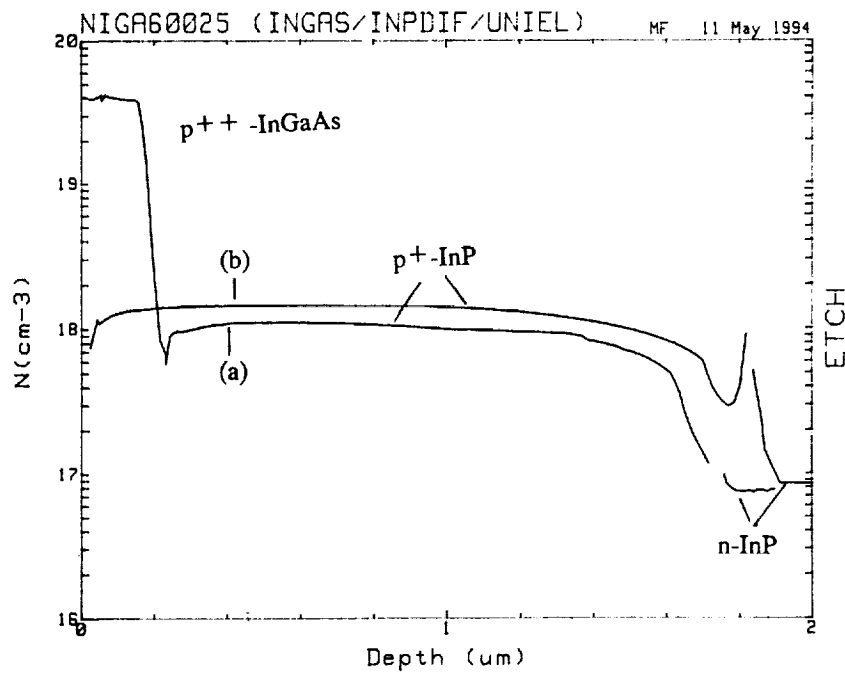


Fig.7. EC- V profiles of p^+n (Cd,S) InP structures, diffused in similar conditions at 600 °C through: (a) undoped InGaAs, and (b) $\text{In}(\text{PO}_3)_3$ cap layers.

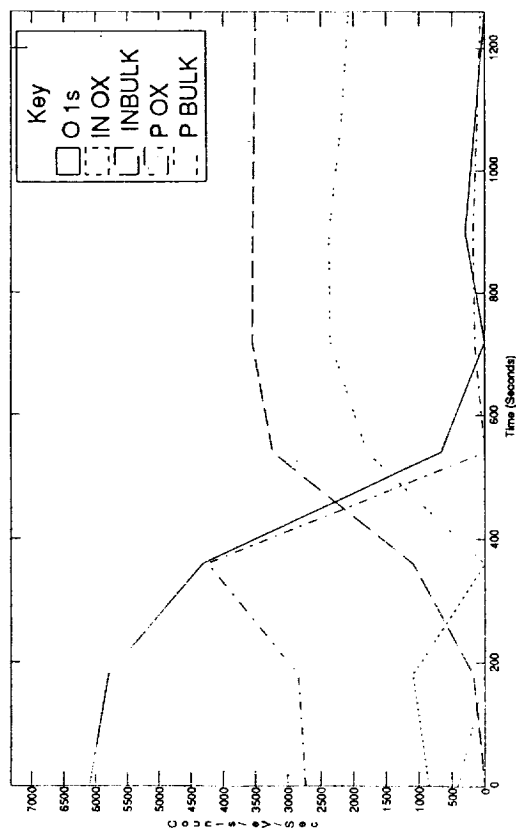


Fig.8. XPS profiles of an oxide grown on InP using the PNP etch.

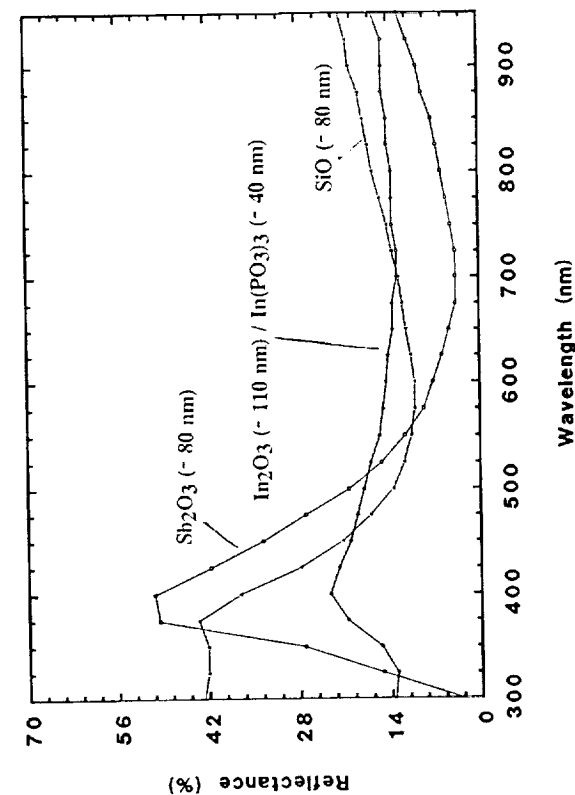


Fig.9. Surface reflectance of p+n InP using a single layer AR coating.

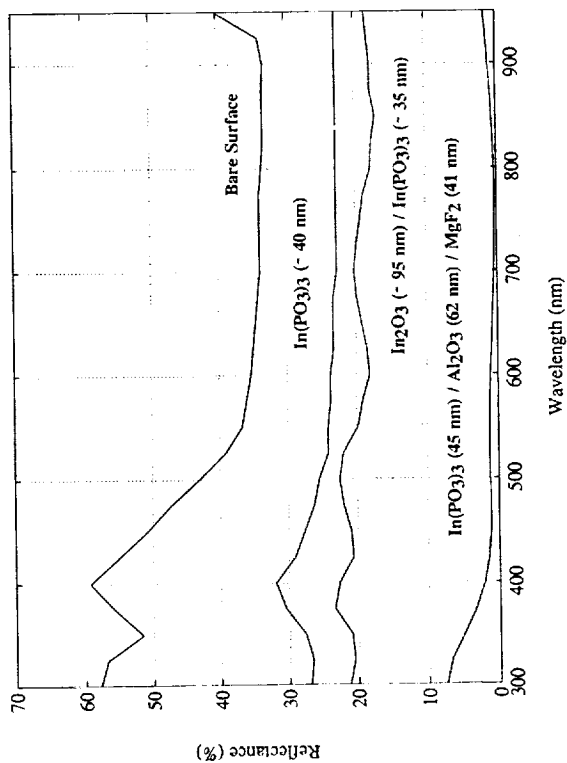


Fig.10. Surface reflectance of p+n solar cells using a double or single layer chemical oxide as compared to a bare surface and optimized three layer AR coating.

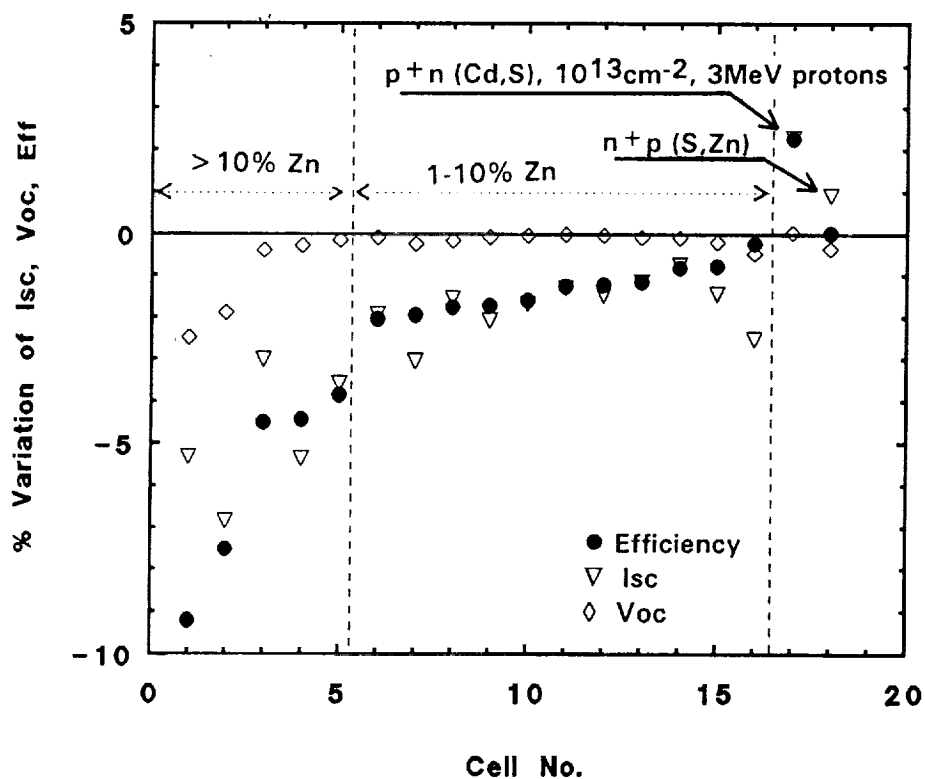


Fig.11. Relative degradation of p^+n (Cd,S) InP (cells # 1-17), and n^+p (S,Zn) InP (cell #18) parameters after 1 hour AM1.5, 25 °C illumination. For cells # 1-16, the Zn-content of evaporated Au-Zn front contacts is shown.

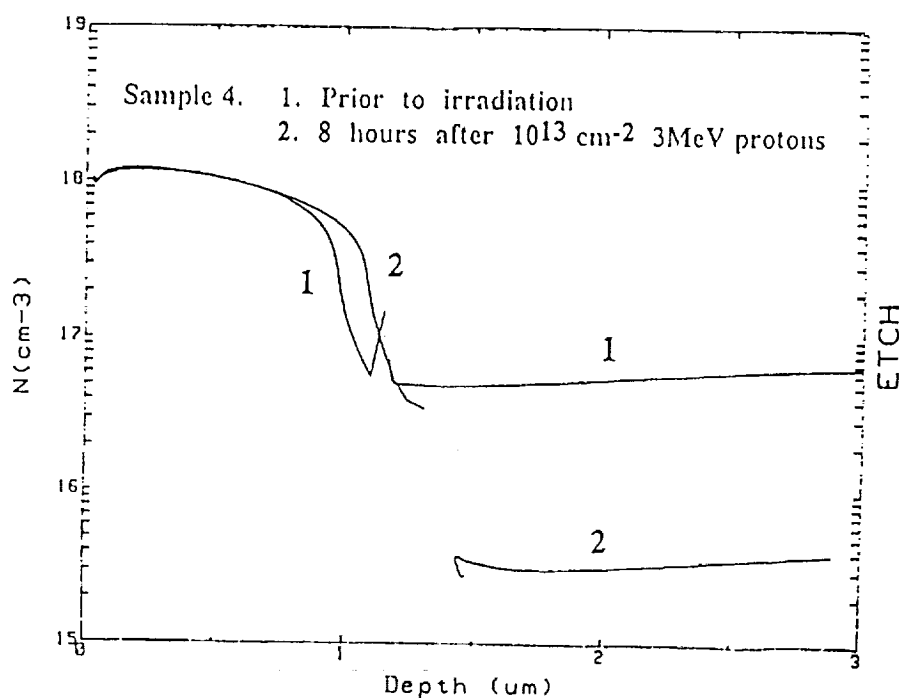
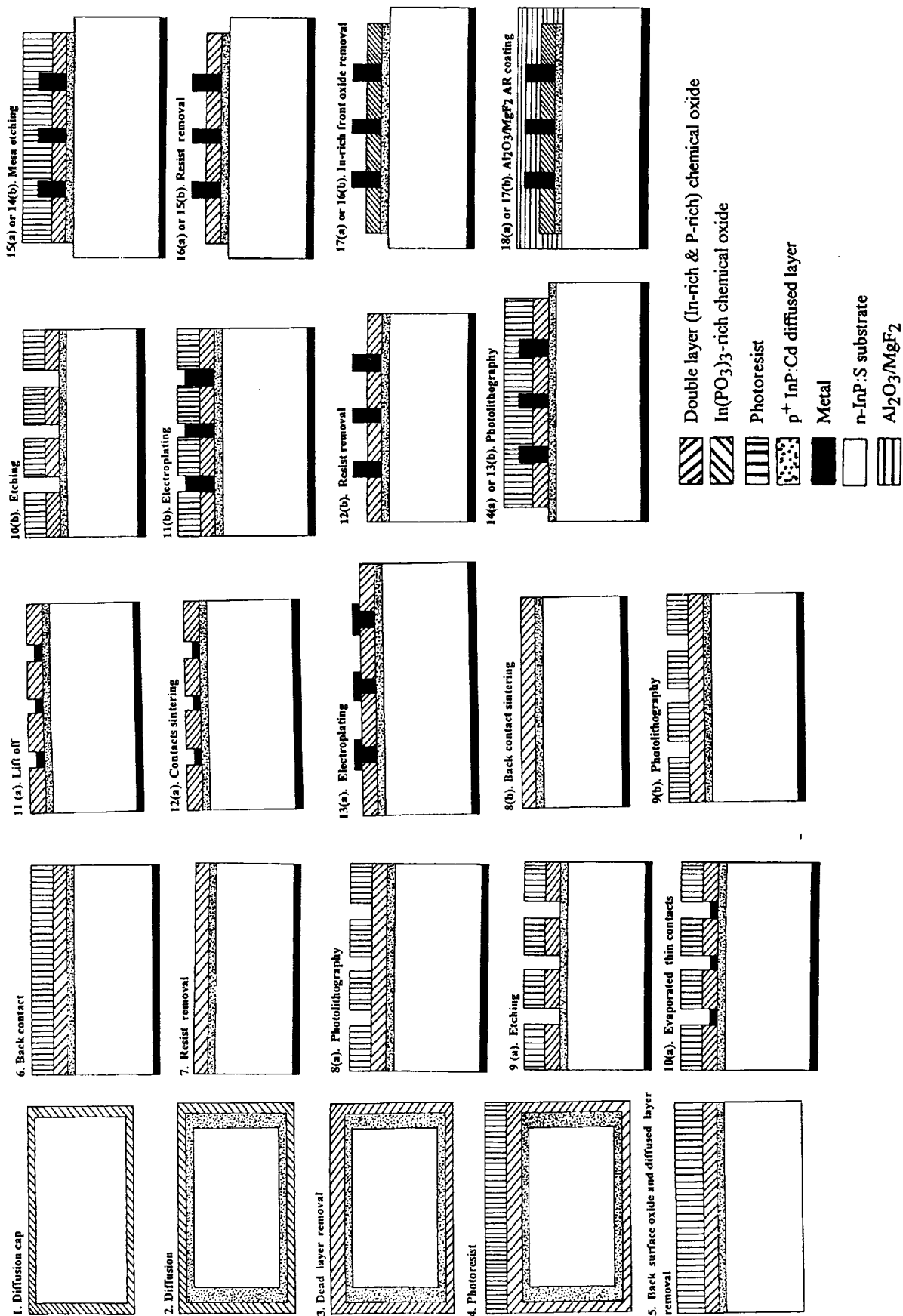


Fig.12. EC-V profiles of a p^+n (Cd,S) InP structure, prior to and after 10¹³ cm⁻² 3 MeV protons irradiation.

Fig. 13. Processing scheme of high efficiency p^+n (Cd,S) InP diffused-junction solar cell.



HIGH QUALITY InP-on-Si FOR SOLAR CELL APPLICATIONS

Zane A. Shellenbarger, Thomas A. Goodwin,
Sandra R. Collins, and Louis C. DiNetta
AstroPower, Inc.
Newark, Delaware

SUMMARY

InP on Si solar cells combine the low-cost and high-strength of Si with the high efficiency and radiation tolerance of InP. The main obstacle in the growth of single crystal InP-on-Si is the high residual strain and high dislocation density of the heteroepitaxial InP films. The dislocations result from the large differences in lattice constant and thermal expansion mismatch of InP and Si. Adjusting the size and geometry of the growth area is one possible method of addressing this problem. In this work, we conducted a material quality study of liquid phase epitaxy overgrowth layers on selective area InP grown by a proprietary vapor phase epitaxy technique on Si. The relationship between growth area and dislocation density was quantified using etch pit density measurements. Material quality of the InP on Si improved with both reduced growth area and increased aspect ratio (length/width) of the selective area. Areas with etch pit density as low as $1.6 \times 10^4 \text{ cm}^{-2}$ were obtained. Assuming dislocation density is an order of magnitude greater than etch pit density, solar cells made with this material could achieve the maximum theoretical efficiency of 23% at AM0. Etch pit density dependence on the orientation of the selective areas on the substrate was also studied.

INTRODUCTION

The material quality of InP films on silicon has not yet achieved acceptable levels. The critical issue is the reduction of dislocation density and residual strain. Yamaguchi (ref. 1) has estimated the material quality characteristics required for obtaining high performance devices using III-V films on silicon. A dislocation density of 10^6 cm^{-2} and a residual strain of 10^9 dyne/cm^2 are the estimated requirements for a solar cell. The lowest reported dislocation density of $3 \times 10^7 \text{ cm}^{-2}$ (ref. 2) for InP-on-silicon has not yet reached this level. Hence, state-of-the-art accomplishments are not within the high performance solar cell realm.

Both dislocation density and residual strain can be decreased by using a reduced growth area. It may be possible to improve the quality of InP on Si solar cells by exploiting this property. Instead of planar growth, a mosaic structure of closely spaced selective area growths can be grown. These mosaic units can then be monolithically interconnected to form a large area InP on Si solar cell structure.

Reductions in dislocation density resulting from reduced growth area have been reported by many groups for many different heterostructures. Noble (ref. 3) best described the reduction in dislocation density by the illustrations shown in Figure 1. Limiting the film area limits the effective dislocation length, which in turn reduces the probability of dislocation interaction and multiplication, and reduces the dislocation density of the material. Figure 1 illustrates the reduction in dislocation density as a function of effective dislocation length alone (dislocation interaction and multiplication are not illustrated).

Reductions in residual strain through limiting growth area have been reported by several groups for GaAs-on-silicon (refs. 4,5,6). Strain-relief in selectively grown films can be expressed by the bi-metal model as:

$$\varepsilon = \varepsilon_0 (1 - \exp [-k(w-x)])$$

where ε and ε_0 are residual strain for selective area growth and planar growth, respectively, w is half the patterned width, x is the distance from the center of the patterned film and k is the interfacial compliance parameter (ref. 4). This equation shows that a reduction in film area (i.e., a reduction in w) causes a reduction in residual strain ($\varepsilon < \varepsilon_0$). For selective GaAs films on silicon, residual strain has been reduced to zero by limiting film area to a 10 μm by 10 μm square (ref. 5).

The goal of this research was to quantify the benefits of reduced area InP films on silicon using a combined vapor phase epitaxy (VPE) and liquid phase epitaxy (LPE) growth process. Etch pit density measurements quantified the relationship between the growth area dimensions and dislocation density as well as the relationship between dislocation density and the orientation of the selective areas. On the basis of the demonstrated reduced area and combined technology benefits of GaAs films on silicon, we expected a significant reduction in etch pit density that would bring the quality of InP films on silicon within the device realm.

APPROACH

Single crystal n-type InP was grown on selectively masked on-axis (111) n-type Si substrates by a proprietary VPE technique. The average thickness of the VPE buffer layer was .5 μm . The growth areas were defined by chemically etching selective areas in a thermally grown SiO_2 masking layer. The growth geometry was evaluated using two different selective area patterns. Figure 2 displays the mask used to evaluate growth area size and aspect ratio. This pattern had selective areas ranging in size from 60 μm by 60 μm up to 4000 μm by 4000 μm . Figure 3 displays the mask used to test the orientation. This pattern had 400 μm wide selective areas oriented every 30°. On a (111) wafer the $\langle 110 \rangle$ and $\langle 112 \rangle$ equivalent directions are aligned in alternating 30° intervals. The masks were aligned with one edge parallel to the $\langle 110 \rangle$ edge. Therefore, on the mask in Figure 2 the selective areas were aligned with one dimension in the $\langle 110 \rangle$ direction and the perpendicular dimension in the $\langle 112 \rangle$ direction. On the mask in Figure 3 the selective areas were aligned in alternating $\langle 110 \rangle$ and $\langle 112 \rangle$ directions. The initial vapor phase growth produced stray InP crystals on the SiO_2 surface that created melt carryover problems during the LPE overgrowth. To prevent this, the selectively grown areas were masked with photoresist and any excess InP crystals were chemically etched from the substrate surface prior to LPE. In preparation for the LPE overgrowth, the substrates were cleaned in organic solvents and etched in $\text{H}_2\text{SO}_4\text{:H}_2\text{O}_2\text{:H}_2\text{O}$ (2:16:1000) for 30 sec.

The LPE growth system used for these experiments consisted of a quartz reactor tube, a 3-zone moveable furnace, a mechanical vacuum pump, and gas sources of nitrogen and palladium-diffused hydrogen. A graphite multi-well horizontal slider boat transported the substrate to the various growth melts. In order to protect the VPE InP layer from thermal degradation, a Sn-In-P overpressure melt as well as an InP polycrystalline cover wafer were used over the substrate prior to LPE growth. To enhance wetting of the growth area, the first growth melt contained In:Sn (3:1) solvent. Successive melts contained pure In solvent. The method of growth used was a two-phase ramp cool. Best results were obtained with a growth temperature of 694°C, a supercool of 6°C, and a cooling rate of 0.7°C/min for the first layer and 0.25°C/min for each subsequent layer. It is necessary to grow multiple layers to distribute the strain associated with the lattice mismatch of InP and Si. Growths with 3 and 5 layers exhibited good crystal quality, free of cracks. The average total thickness of the LPE growth layers was 5 μm . Figure 4 is an illustration of the growth structure. Figure 5 shows the surface of a typical growth.

The dislocation density of the growth surface was quantified with etch pit density (EPD) measurements. To reveal the etch pits, the growth surface was etched in $\text{HBr}:\text{H}_2\text{O}_2:\text{HCl}:\text{H}_2\text{O}$ (10:1:10:40) for 10 sec. The etch pits are visible as triangular wells or depressions as in Figure 6. The EPD was then determined by counting the etch pits in a known area on a photomicrograph. By analyzing several areas across the growth region, an average EPD was accurately determined.

RESULTS AND DISCUSSION

The first area of focus of this research was to determine the relationship between the selective area dimensions and film quality of the LPE overgrowth layers using the pattern shown in Figure 2. Etch pit densities of the selective area growths were determined using the method previously outlined. Most growths had EPD between 4×10^5 and $2 \times 10^6 \text{ cm}^{-2}$ for the different selective areas. The lowest etch pit density of $1.6 \times 10^4 \text{ cm}^{-2}$ was obtained for a selective area with dimensions of $80 \mu\text{m}$ by $2000 \mu\text{m}$. Figure 7 shows a graph of EPD versus selective area for a typical growth. As expected, the EPD decreased with decreasing area. The sets of two data points connected by vertical lines represent selective areas with the same dimensions but aligned perpendicular to each other. There was no substantial difference between selective areas oriented in the two different directions. The numbers next to the data points are the aspect ratios (length/width) of the selective areas. As seen in the graph, the data fall into two distinct groups. The group having lower etch pit densities consists of those selective areas with large aspect ratios (length/width). All of these selective areas have a short dimension of $500 \mu\text{m}$ or less. Figure 8 is a plot of the etch pit densities versus the short dimension of the selective area for three different long dimensions. Above a width of $500 \mu\text{m}$ there is little dependence on the short dimension. Below $500 \mu\text{m}$ there is a strong linear dependence on the short dimension. The etch pit density reduces at a rate of about 2000 cm^{-2} for every $1 \mu\text{m}$ reduction in the short dimension. Reducing the short dimension from $500 \mu\text{m}$ to $100 \mu\text{m}$ causes an order of magnitude reduction in etch pit density. Holding the short dimension constant and varying the long dimension shows almost no change. These results indicate that a long thin selective area will have substantially better material quality than a square selective area with the same total area. We believe the explanation for this lies in the fact the material quality improves near the edge of the selective area due to lateral overgrowth onto the masking layer. As the selective area becomes thin, this effect starts to become significant.

The second area of interest was dependence of material quality on substrate orientation. Si substrates were masked with the pattern shown in Figure 3. InP was then grown in these selective areas using our vapor phase InP overgrown with LPE InP. After growth, etch pit density measurements were performed on two of these samples. One had an average EPD of $4.05 \times 10^5 \text{ cm}^{-2}$ in the $\langle 110 \rangle$ directions and $7.64 \times 10^5 \text{ cm}^{-2}$ in the $\langle 112 \rangle$ directions. The other sample had an average EPD of $1.39 \times 10^6 \text{ cm}^{-2}$ in the $\langle 110 \rangle$ directions and $9.74 \times 10^5 \text{ cm}^{-2}$ in the $\langle 112 \rangle$ directions. This result, along with the lack of orientation dependence of the quality of growth in the first experiment, indicates that the material quality is independent of the orientation.

While the etch pit density was not dependent on the orientation, the growth morphology was. The selective area edges oriented in the $\langle 110 \rangle$ directions had jagged overgrowth while the selective area edges oriented in the $\langle 112 \rangle$ directions had very smooth growth. The photograph in Figure 9 shows this effect. We believe this is due to the fact that the InP growth nucleates in a triangular pattern that has its flat side in the $\langle 112 \rangle$ direction. Figure 10 shows a photograph of an InP growth with only partial nucleation. The triangular nucleation areas have a flat side parallel to the edge of the selective area oriented in the $\langle 112 \rangle$ direction. For most applications, having the long edge of the selective area in the $\langle 112 \rangle$ direction would be more desirable.

CONCLUSIONS

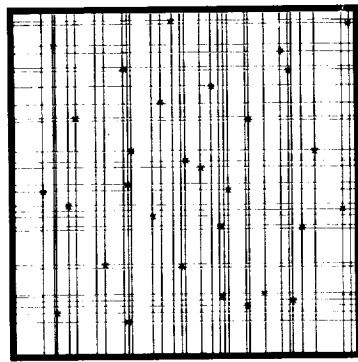
Using selective area growth is one method for improving the quality of heteroepitaxial InP on Si. Using a vapor phase buffer layer overgrown with LPE, etch pit densities as low as 1.6×10^4 were obtained. The following conclusions about the effects of selective area growth were reached.

1. The etch pit density of the InP/Si heteroepitaxial growth can be significantly reduced by reducing one dimension of the selective area below $500 \mu\text{m}$.
2. The etch pit density is not strongly dependent on the orientation of the selective area on the Si substrate.
3. Jagged overgrowth occurs on the selective area edges that are aligned in the $\langle 110 \rangle$ directions.

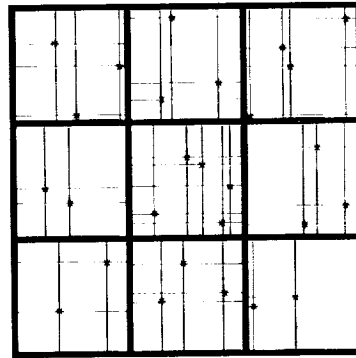
These results show it is possible to grow InP on Si by LPE with sufficient quality to support high performance solar cells. In order to make use of the benefits of selective area growth for high performance solar cells, methods to interconnect the individual areas must be developed.

REFERENCES

1. Yamaguchi, M., et al.: Dislocation Density Reduction in Heteroepitaxial III-V Compound Films on Si Substrates for Optical Devices. *Journal of Material Research*, vol. 6 (2), 1991, pp.376-384.
2. Wanlass, M.W.; Coutts T.J.; Ward, J. S.; Emery, K.A.; and Horner, G.S.: High-Efficiency, Thin Film InP Concentrator Solar Cells. Third International Conference on Indium Phosphide and Related Materials, April 1991, pp. 40-47.
3. Noble, D.B.; Hoyt, J.L.; King, C.A.; Gibbons, J.F.; Kamins, T.I.; and Scott, M.P.: Reduction in Misfit Dislocation Density by the Selective Growth of $\text{Si}_{1-x}\text{Ge}_x/\text{Si}$ in Small Areas. *Applied Physics Letters*, vol. 56 (1), 1990, pp. 51-53.
4. Yamaguchi, M.; Tachikawa, M.; Sugo, M.; Kondo, S.; and Itoh, Y.: Analysis for Dislocation Density Reduction in Selective Area Grown GaAs Films on Si Substrates. *Applied Physics Letters*, vol. 56 (1), 1990, pp. 27-29.
5. Yacobi, B.G.; Zemon, S.; Jagannath, C.; and Sheldon, P.: Strain Relief in Patterned GaAs Grown on Mismatched Substrates. *Journal of Crystal Growth*, vol. 95, 1989, pp. 240-244.
6. Sakai, S.; Matyi, R.J.; and Shichijo, H.: Selective liquid phase epitaxy and defect reduction in GaAs grown on GaAs-coated silicon by molecular beam epitaxy. *Applied Physics Letters*, vol. 51 (23), 1987, p. 1913.



a) Planar Film



b) Selective Film

Figure 1: The effect of growth area on dislocation density (ref. 4). Heavy lines represent oxide stripes, narrow lines represent dislocation segments, and stars represent dislocation nucleation sources.

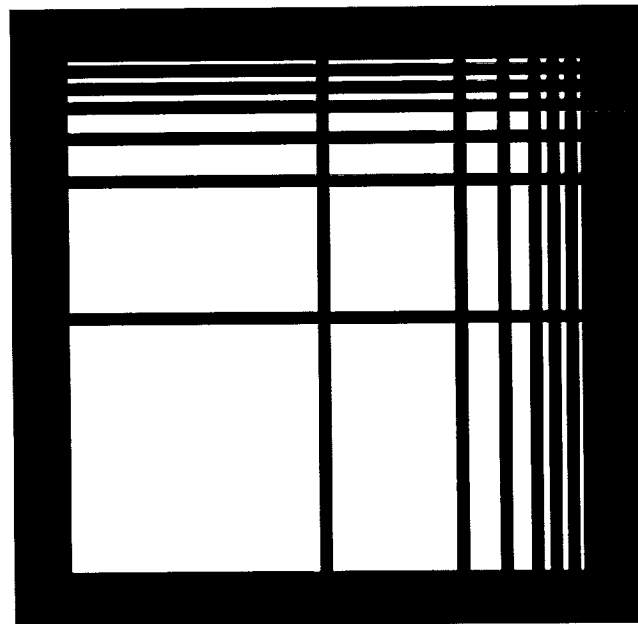


Figure 2: Mask design for film area vs. film quality study (scale = 10X).

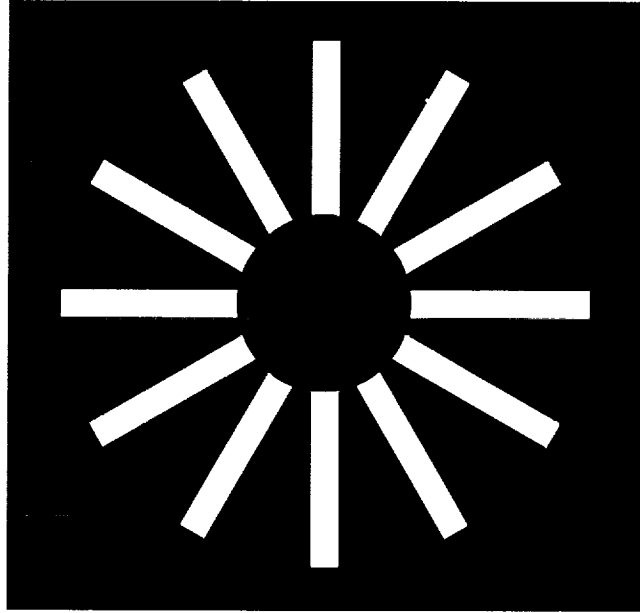


Figure 3: Mask design to determine optimum selective area orientation (scale = 10X).

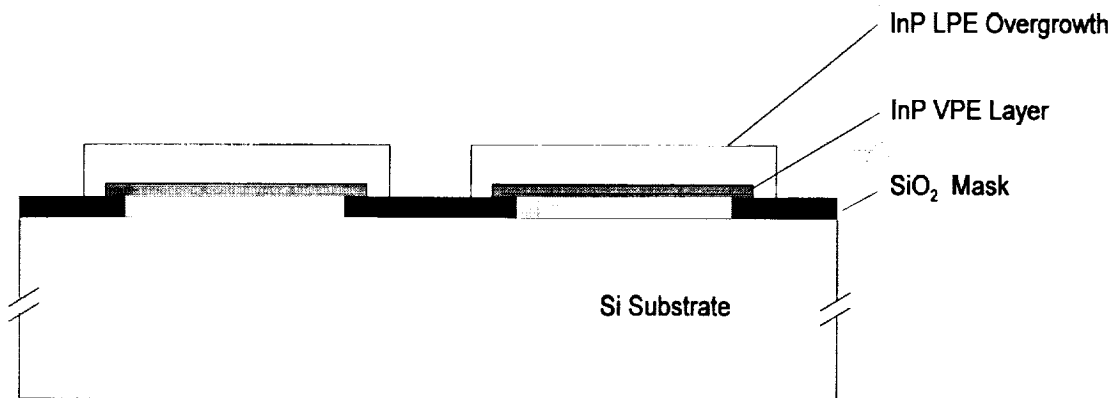


Figure 4: Growth structure.

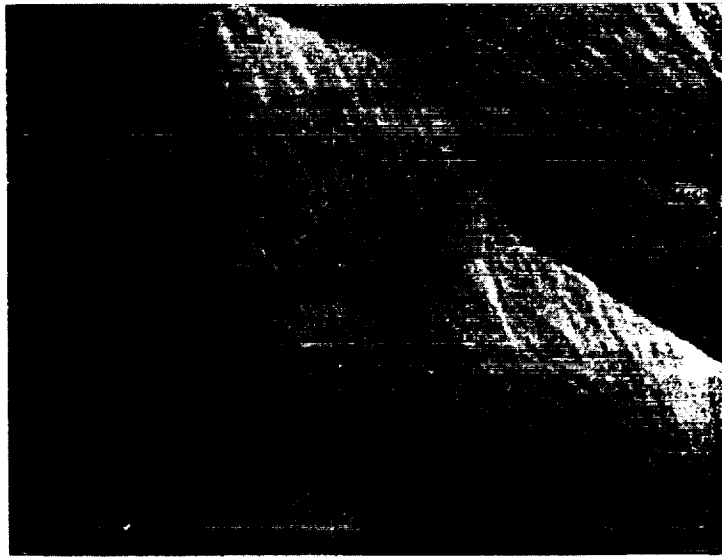


Figure 5: Typical LPE overgrowth surface (scale = 200X).



Figure 6: Typical LPE overgrowth surface showing etch pits (scale = 1000X).

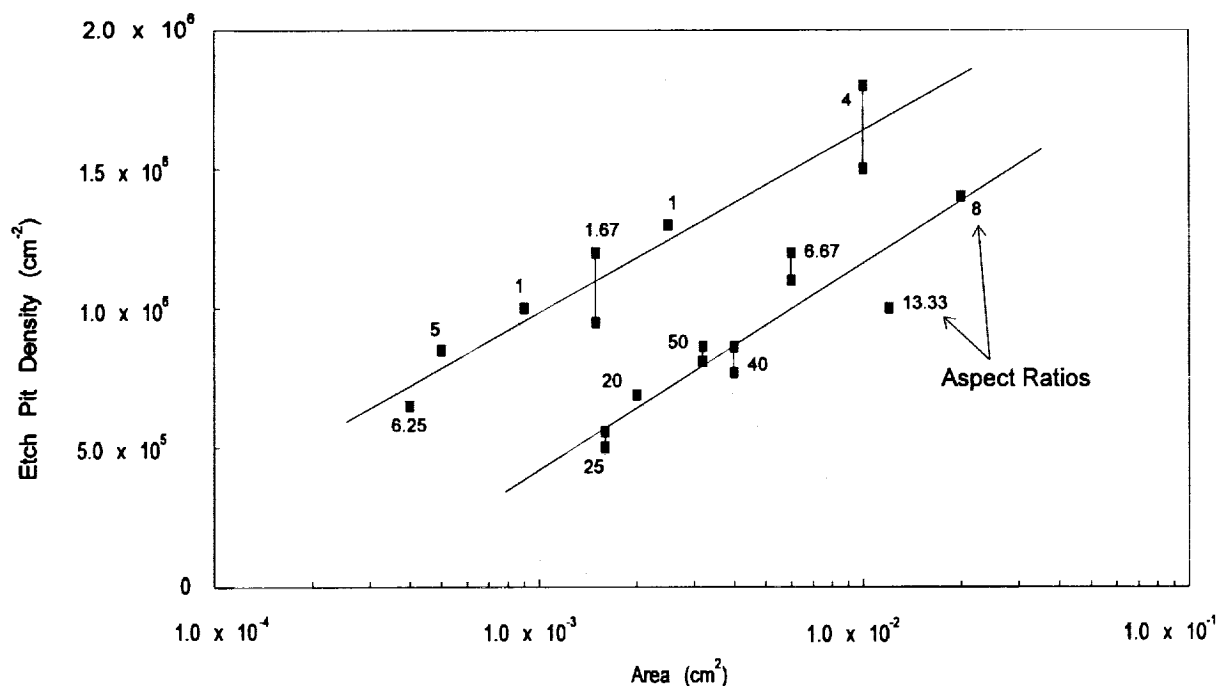


Figure 7: Graph of etch pit density vs. film area for growth J11605.

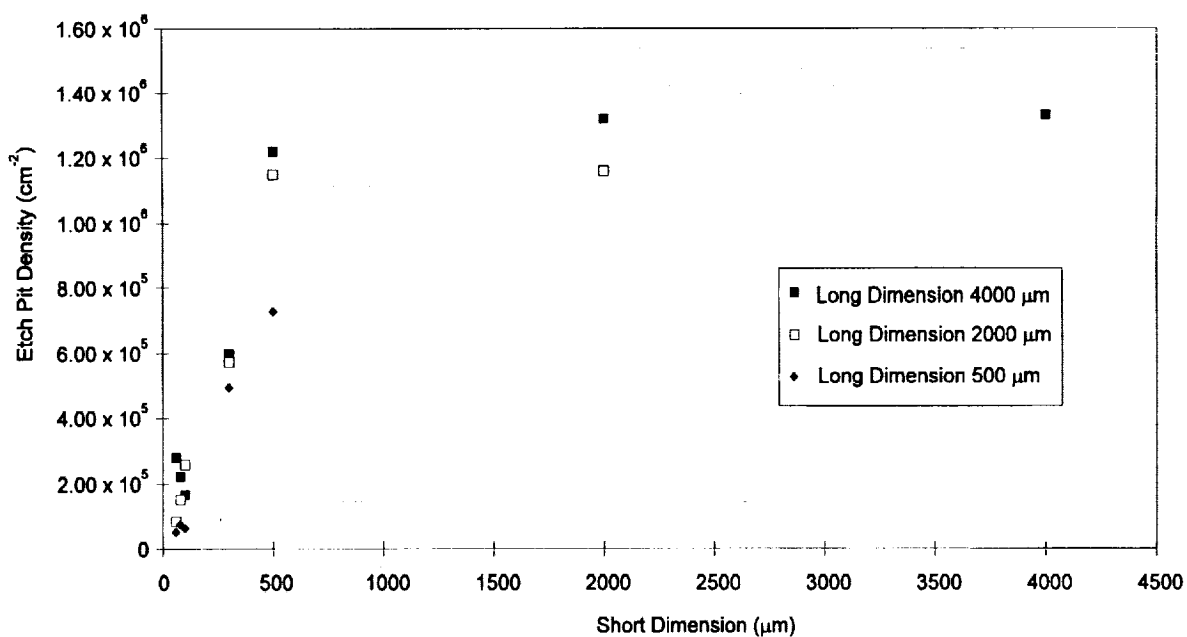


Figure 8: Graph of etch pit density vs. short dimension for growth J11707.

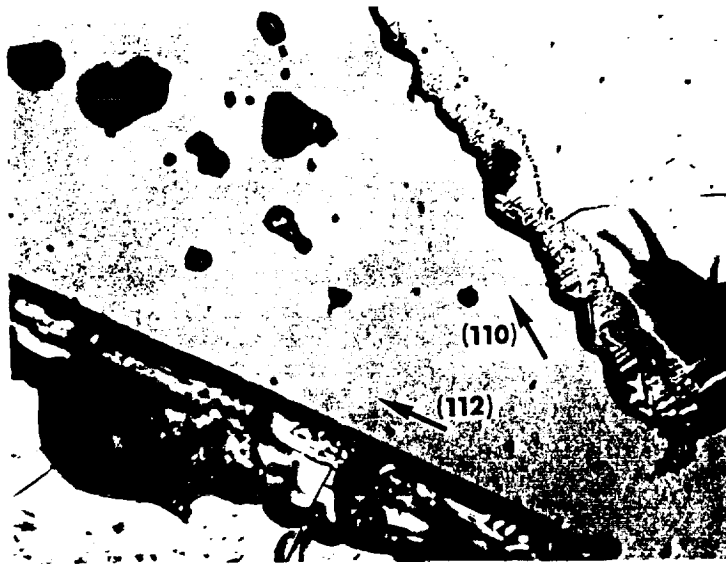


Figure 9: Edges of growth areas in $\langle 110 \rangle$ and $\langle 112 \rangle$ directions (scale = 100X).

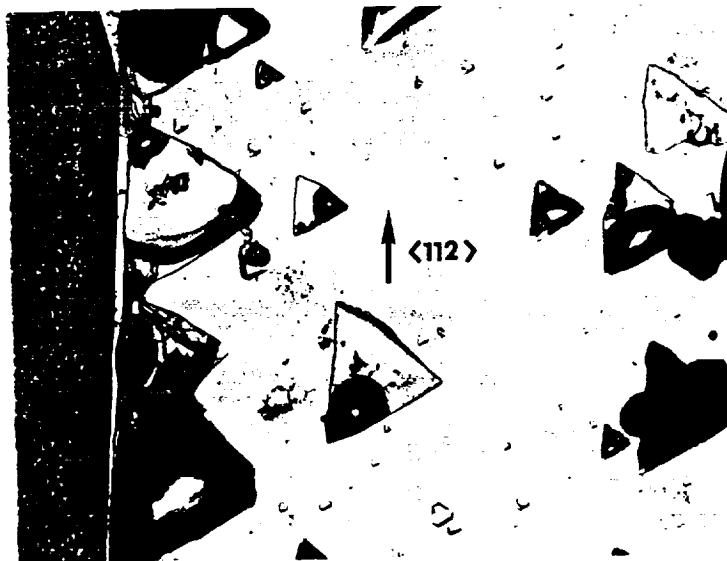


Figure 10: Nucleation areas near $\langle 112 \rangle$ oriented edge (scale = 100X).

P/N InP SOLAR CELLS ON Ge WAFERS

Steven Wojtczuk and Stanley Vernon
Spire Corporation
Bedford, Massachusetts

and

Edward A. Burke
Woburn, Massachusetts

SUMMARY

Indium phosphide (InP) P-on-N one-sun solar cells were epitaxially grown using a metalorganic chemical vapor deposition process on germanium (Ge) wafers. The motivation for this work is to replace expensive InP wafers, which are fragile and must be thick and therefore heavy, with less expensive Ge wafers, which are stronger, allowing use of thinner, lighter weight wafers. An intermediate $\text{In}_x\text{Ga}_{1-x}\text{P}$ grading layer starting as $\text{In}_{0.49}\text{Ga}_{0.51}\text{P}$ at the GaAs-coated Ge wafer surface and ending as InP at the top of the grading layer (backside of the InP cell) was used to attempt to bend some of the threading dislocations generated by lattice-mismatch between the Ge wafer and InP cell so they would be harmlessly confined in this grading layer. The best InP/Ge cell was independently measured by NASA-Lewis with a one-sun 25°C AM0 efficiency of 9.1%, open-circuit voltage of 790 mV, fill-factor of 70%, and short-circuit photocurrent 22.6 mA/cm². We believe this is the first published report of an InP cell grown on a Ge wafer.

Why get excited over a 9% InP/Ge cell? If we look at the cell weight and efficiency, a 9% InP cell on an 8 mil Ge wafer has about the same cell power density, 118 W/kg (BOL), as the best InP cell ever made, a 19% InP cell on a 18 mil InP wafer, because of the lighter Ge wafer weight. As cell panel materials become lighter, the cell weight becomes more important, and the advantage of lightweight cells to the panel power density becomes more important.

In addition, although InP/Ge cells have a low beginning-of-life (BOL) efficiency due to dislocation defects, the InP/Ge cells are very radiation hard (end-of-life power similar to beginning-of-life). We have irradiated an InP/Ge cell with alpha particles to an equivalent fluence of 1.6×10^{16} 1 MeV electrons/cm² and the efficiency is still 83% of its BOL value. At this fluence level, the power output of these InP/Ge cells match the GaAs/Ge cell data tabulated in the JPL handbook. Data are presented indicating InP/Ge has more power output than GaAs/Ge cells at fluences in excess of this value.

INTRODUCTION

The cost, weight, and fragility of InP wafers have impeded InP cell use in space. Therefore, InP cells on light, strong, inexpensive silicon (Si) or Ge wafers are of great interest (ref. 1). This paper reports the results of a Phase I Small Business Innovative Research program seeking to replace the InP wafer on which the InP solar cell is epitaxially grown with a Ge wafer which has better properties (Table I). Since InP is fragile, thick ~16 to 20 mil wafers are required for strength. Ge has become a leading substrate for GaAs space solar cells, and is inexpensive if bought in large quantities. Although the density of Ge (5.3 g/cm³) is similar to InP, Ge is stronger and therefore a thinner Ge wafer than InP wafer can be used to increase the power density (W/kg) and lower the launch weight.

Table I Comparison of III-V Space Cells on InP and Ge wafers.

	InP Cell on Ge Wafer	InP Cell on InP Wafer	GaAs Cell on Ge Wafer
High-Volume Wafer Cost (\$/2" wafer)	20-50	180-250	20-50
Wafer Density (g/cm ³)	5.32	4.81	5.32
Wafer Strength	Strong	Fragile	Strong
Typical Thickness (mils)	8	18	8
Wafer Weight (g/cm ²)	0.108	0.220	0.108
One-sun AM0 BOL Efficiency	9% (NASA)	18% (Typical)	18% (Typical)
BOL Cell Power Density (W/kg)	114 (Phase I)	112	229
AM0 EOL (10 ¹⁶ 1MeV e/cm ²) Efficiency	8% (Spire data)	12% (Spire data)	6% (JPL Handbook)
EOL Cell Power Density (W/kg)	102	75	76

InP cells have more defects when grown on Ge wafers, due to differences in crystal lattice constants of InP (5.87Å) and Ge (5.66Å). This lattice constant mismatch is 3.7% between InP and Ge. Mechanical stress in the InP film grown on the substrate is relieved through the formation of dislocation defects in the InP film. The dislocations act as recombination centers, and resulting in a lower beginning-of-life (BOL) efficiency for InP heteroepitaxial cells (~10%) on Ge wafers than InP cells (~20%) on InP wafers. However, the lower BOL efficiency of InP heteroepitaxial cells is compensated by the lighter weight of Ge wafers compared to InP wafers (Table I), so that the BOL power densities for InP/Ge and InP/InP are similar, and we expect a higher end-of-life (EOL) power density from these InP/Ge cells compared to GaAs or Si cells at high fluences.

The P/N InP/Ge cells have lower BOL efficiencies than Spire's InP cell record efficiency 19% N/P InP cells grown on InP wafers. However, we predict EOL efficiencies after high fluences will be similar for these two InP cell types, since radiation damage will dominate the diffusion lengths in both cell types, instead of dislocations dominating the diffusion length in InP/Ge cells, leading to similar EOL efficiencies in both types. Therefore, because of their lighter weight, InP/Ge cells should have an EOL power density about twice that of InP homojunction cells.

N-on-P InP-on-Si cells were investigated by Spire (ref. 2) with one-sun AM0 efficiencies of 9.9% the highest reported to date (ref. 3). Our Phase II goal in this program is to achieve 15% BOL efficiencies for P-on-N InP-on-Ge cells. We plan to work on lowering the dislocation density through an improved In_xGa_{1-x}P grading technique between the Ge wafer and the InP cell. By using a P/N design, the need for a tunnel junction in N/P heteroepitaxial InP cell designs is eliminated. The

tunnel junction is necessary in N/P designs due to outdiffusion of Si or Ge, N-type MOCVD dopants, from the Si or Ge wafers into the back P-layers of the N/P cell. P-on-N InP cells may more radiation resistant than even InP N-on-P cells, leading to higher EOL efficiencies (ref. 4). InP cells were grown on GaAs (ref. 5) at NREL with efficiencies of 14% BOL at one-sun AM0 (ref. 6). The NREL work shows that a 14% BOL efficiency can be achieved in a heteroepitaxial cell with significant dislocations. The dislocation density in the 9.9% AM0 Spire InP/Si cells is 10x higher than in the NREL work. If we can reduce the dislocation density in our InP-on-Ge cells to the level achieved by NREL in its InP-on-GaAs work, a similar efficiency to the NREL work should be achieved, since Ge (5.66Å) and GaAs (5.65Å) have similar lattice constants. The 15% Phase II InP/Ge goal therefore seems reasonable.

The power density of P-on-N InP/Ge cells at this early stage is already similar to the best N-on-P InP cells on InP wafers, which have undergone much more development. Beginning-of-life efficiency (9% AM0) of the P/N InP/Ge cells is limited partly by the new P-on-N InP cell technology used for the first time in Phase I. We are now making 17% P/N InP cells on InP wafers, but at the time of this program effort the P-on-N InP control cells on InP wafers, our first, had reached only 12% efficiency, mainly due to too thick (~2000Å) an emitter layer, compared to the 19% N-on-P InP cells on InP wafers with 300Å emitters achieved after long development. As the performance of the P/N InP cell on InP wafer baseline technology increases, so should the InP/Ge cell performance since we would be starting out with a higher efficiency InP cell on the Ge wafer. It is important to realize that the best efficiency the Phase I InP/Ge cells could possibly have is the ~12% efficiency of the control P/N InP cells on InP wafers. The BOL efficiency of the InP/Ge cell at time of the program was substantially limited by the P/N InP cell technology. This P/N InP cell technology should be improvable to levels approaching 20%.

CELL STRUCTURE

Table II shows the target epilayer structure used for the Phase I InP/Ge cells.

Table II *Epilayer structure of P-on-N InP cell on Ge substrate.*

Layer	Material	Doping cm ⁻³	Thickness μm	Comments
Contact Cap	InGaAs	P, ~10 ¹⁹ , Zn	0.3	InGaAs is selectively etched from photoarea, but left under front grid metal to form ohmic contact
Emitter	InP	P, ~10 ¹⁸ , Zn	0.2	Thickness tradeoff - thin better for QE; thick better for low resistance
Base	InP	N, ~10 ¹⁷ , Si	1.5	1.5 μm absorbs > 95% of AM0 light
Back Surf. Field	InP	N, ~10 ¹⁹ , Si	0.5	Reflects minority carrier holes, enhances QE
In _x Ga _{1-x} P Grading	InP to In _{0.49} Ga _{0.51} P	N, 10 ¹⁹ , Si	8	Lowers dislocation density due to InP/Ge lattice-mismatch
Nucleation	GaAs	N, 10 ¹⁹ , Si	1	Easier to grow on GaAs
Substrate	Ge	N, 10 ¹⁷ , Sb	300	Eagle-Picher epi-ready Ge wafers

The epilayers are grown by MOCVD using trimethylindium, triethylgallium, and phosphine at 76 torr and a low temperature, 600°C, to limit zinc diffusion and emitter junction depth. Dimethylzinc is being used for all P-type and silane for N-type doping, respectively. With an InP P/N cell design, we desire a thin emitter to limit surface recombination loss and increase photocurrent; on the other hand, the emitter must be thick enough so that along with increased cell gridline coverage (4% shadow loss), a reasonable emitter sheet resistance I^2R loss is obtained, compensating for the low maximum P-InP emitter doping ($\sim 10^{18} \text{ cm}^{-3}$, $\sim 10X$ lower than N-InP) and mobility ($\sim 20X$ lower than N-InP) of the P-InP emitter.

A P/N design is used to avoid a tunnel junction present in N/P designs. Germanium is an N-type dopant in III-V semiconductors in the metalorganic chemical vapor deposition (MOCVD) process, outdiffuses from the Ge wafer during epigrowth into the back of the cell. In an N/P design, Ge would create an opposing P/N junction in the P-type back layers of the cell. This parasitic junction must be a tunnel junction for the cell to pass current, increasing complexity in N/P cell designs. In a P/N design, the back N-type doping is simply increased by the Ge diffusion and is of little concern; no tunnel junction is needed. In addition, various NASA-Lewis papers indicate P/N InP cells may eventually be more efficient than N/P cells due to higher obtainable open-circuit voltages and amenability to surface passivation.

A high density of defects, mainly dislocations, form in the material to accommodate the lattice-mismatch (3.7%) between InP and Ge. If these defects thread upward into the cell through the junction, they increase the dark current and act as minority carrier recombination sites, lowering the cell efficiency. For lattice-mismatched heteroepitaxial cells, grading layers are used to attempt to bend the threading dislocations harmlessly away parallel to the plane of the cell junction. In this program we used an $\text{In}_x\text{Ga}_{1-x}\text{P}$ grading layer starting with $\text{In}_{0.49}\text{Ga}_{0.51}\text{P}$ lattice-matched to the GaAs-coated Ge wafer and ending with InP. This grading layer will be discussed more fully in future publications concerning InP/Si solar cells.

PRE-IRRADIATION CELL DATA

Table III shows verified (courtesy of I. Weinberg and D. Brinker of NASA-Lewis) preirradiation InP/Ge cell data of similar P/N InP cells on InP, GaAs, and Ge wafers. The 11.9% control cells on InP wafers represent an upper limit of what the InP cells on Ge could achieve at the time of the program. Recently 17% P/N InP cells on InP were made, so that if the new InP cell growth parameters were used, a higher InP/Ge cell efficiency would be obtained than presented in this paper. Series resistance from I-V data for all Phase I cells was $\sim 0.5 \Omega\text{-cm}^2$, causing $\sim 10 \text{ mV}$ drop in V_{MAX} for the $\sim 20 \text{ mA/cm}^2$ photocurrent. The series resistance is dominated by the emitter sheet resistance. If we half the emitter thickness, we will double the series resistance.

Table III AM0 one-sun data of Spire Phase I cells.

All one-sun AM0 25°C pre-irradiation Comments	η %	V_{oc} mV	J_{sc} mA/cm^2	FF %	Cell ID
P/N InP cell on InP wafer (control)	11.9	848	22.9	84.2	5668-2626-2-8
P/N InP cell on 8 μm InGaP grade on GaAs-coated Ge wafer (NASA-Lewis verified measurement)	9.1	792	22.6	69.8	5714-2795-1-8

CELL IRRADIATION

A second P/N InP/Ge cell, of a slightly lower BOL efficiency (7.5%) than the best cell shown in Table III was mounted in a special test fixture for the destructive alpha irradiation test (equipment courtesy of C. Blatchley and C. Colerico of Spire). An Am-241 alpha particle source was used to irradiate the cells to explore how performance varies with radiation damage. Equivalent 1 MeV electron exposures were determined by a non-ionizing energy loss (NIEL) calculation (ref. 7) for the alpha source for a 1.5 cm separation between the 1 cm² InP/Ge cell centered under the alpha source in vacuum. The calculation included effects of the angular incidence of particles at the cell edges offset from the centerline, so that the divergence of the alpha particle beam from its 0.5 cm aperture was taken into account. The alpha particle energy in the InP at the depth of interest is 3.643 MeV and the calculated NIEL value is 0.29 MeV-cm²/g. The equivalent 10 MeV proton flux is 4.18×10^7 protons/cm²-s. The equivalent 1 MeV electron flux is 3.55×10^{10} electrons/cm²-s or 1.28×10^{14} electrons/cm²-hour. AM0 efficiency data and quantum efficiency data were taken before irradiation, and after 1, 8, 32, and 126 hours. The final 126 hour data set was equivalent to a fluence of 1.6×10^{16} 1 MeV electrons/cm². One of the advantages of using the alpha source for these experiments is that it is possible to obtain high equivalent electron fluences in short times due to higher damage rate of the four heavy nuclei (two proton, two neutron) of the alpha particles versus the lighter electrons. AM0 data for this cell is at various fluences is shown in Table IV and Figure 1.

Table IV *InP/Ge cell (7.5% BOL) one-sun 25°C AM0 data at various equivalent electron fluences.*

(Alpha particle irradiation) Equivalent # of 1 MeV electrons/cm ²	η %	V _{OC} mV	J _{SC} mA/cm ²	FF %
1.3×10^{14}	7.5	774	23.4	57.1
1.0×10^{15}	7.4	768	23.5	56.2
4.1×10^{15}	7.0	751	22.7	56.8
1.6×10^{16}	6.3	708	21.6	56.8

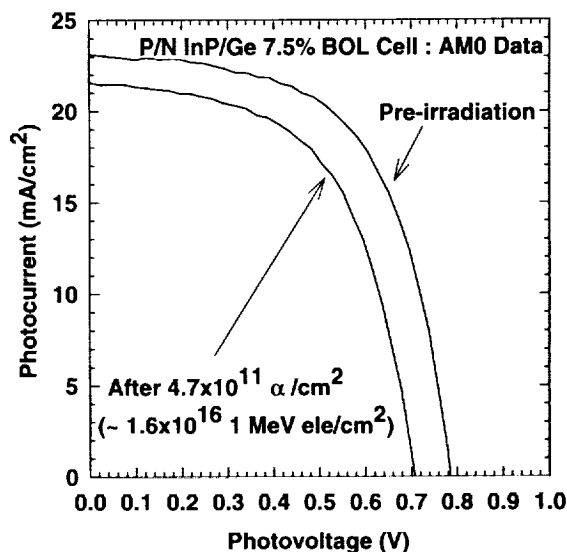


Figure 1 *AM0 I-V curves of an InP/Ge cell before and after alpha irradiation.*

Figure 2 shows measured absolute quantum efficiency of the cell before irradiation and after the maximum irradiation. As expected, most of the photocurrent loss seen in Figures 1 and 2 is due to lower quantum efficiency at the longer wavelengths, which are absorbed further from the cell junction and must diffuse to the junction to be collected. The radiation damage lowers the base (hole) diffusion lengths in these P/N cells slightly, as seen in Figure 2 near the InP cutoff wavelength (920 nm). The quantum efficiency at shorter wavelengths is affected very little, since, even though the diffusion lengths are lower in the emitter also, the emitter thickness ($0.2\text{ }\mu\text{m}$) is still small compared to the emitter (electron) diffusion lengths ($\sim 1\text{ }\mu\text{m}$).

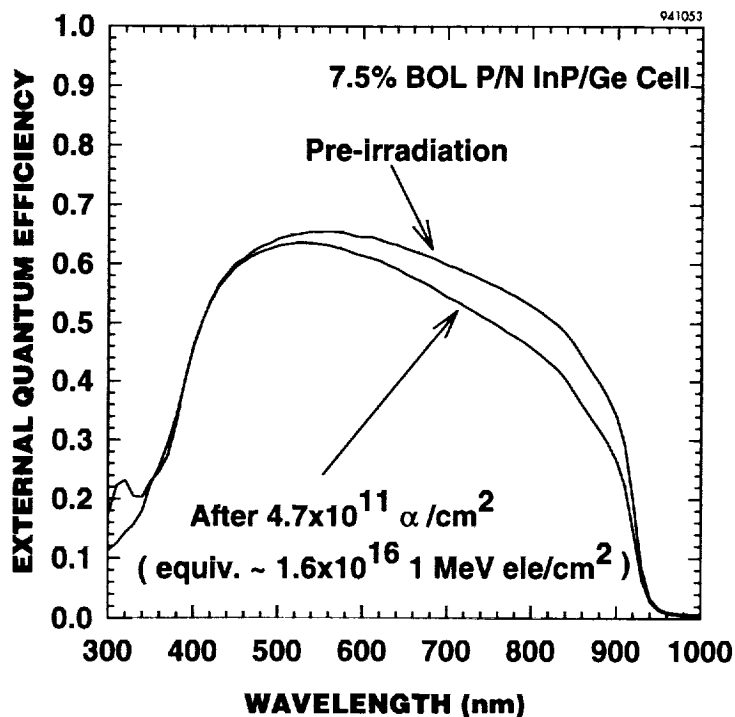


Figure 2 Absolute quantum efficiency of 7.5% BOL InP/Ge cell before and after irradiation. Drop in longer wavelength QE indicates lower base diffusion lengths.

CONCLUSIONS

We have presented experimental data on P/N InP/Ge solar cells which indicate that this technology is promising for space power use in long space missions or in very high radiation orbits. The use of Ge wafers eliminates the need for costly, fragile, heavy, InP wafers. Even in its primitive current state of development, these 9% BOL InP/Ge cells appear to have higher power output and cell power density than either 19% BOL InP cells on InP wafers or 18% BOL GaAs cells on Ge wafers after a fluence of $\sim 10^{16}$ electrons/cm² (Figure 3). Future work would center on increasing the InP/Ge cell performance so that it could compete with GaAs/Ge cells for space missions that do not require extreme radiation resistance.

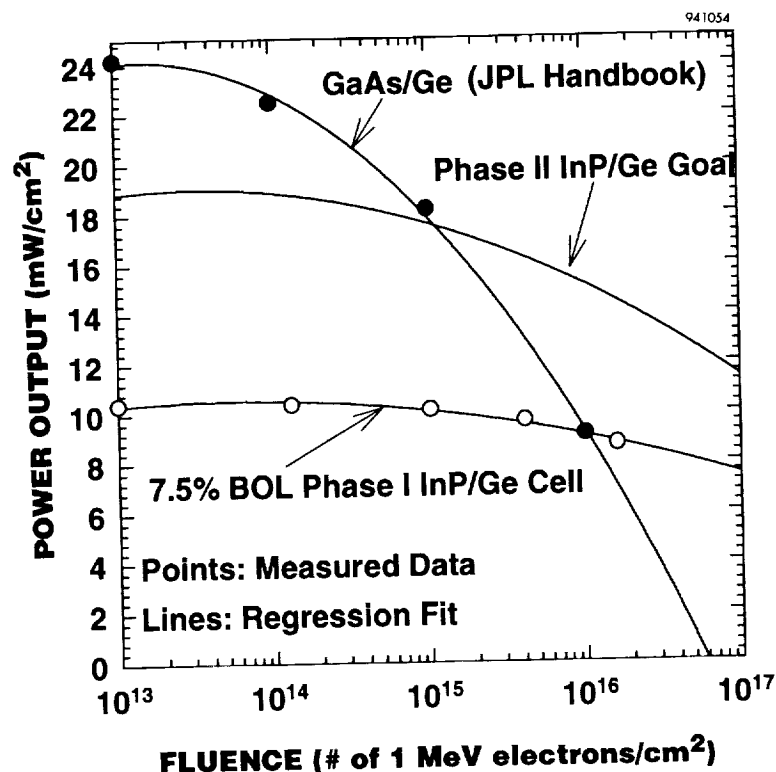


Figure 3

Measured AM0 power output versus electron fluence for P/N GaAs/Ge cells (from JPL Solar Cell Handbook) and P/N InP/Ge cells (this work). Points are measured data; lines through points are simple 2nd-order polynomial regression fit. Line labeled Phase II is simply a goal and is not measured data. This plot shows that even the primitive Phase I InP/Ge cells have more power output after a fluence of 10^{16} electrons/cm² than the current mainstay GaAs/Ge cells. However, this fluence is very high, and is likely only in high radiation (van Allen belt) orbits or for very long (~10 year or more) missions in more standard orbits. The Phase II goal shown indicates the point where these InP/Ge cells could compete with GaAs/Ge for more standard, low radiation missions.

REFERENCES

1. I. Weinberg and D.J. Flood, "Heteroepitaxial InP Solar cells for Space Applications," *Prog. in Photovoltaics: Research and Applications*, Vol. I, 1993, pp. 43-45.
2. C.J. Keavney, S.M. Vernon, V.E. Haven, S.J. Wojtczuk, and M.M. Al-Jassim, "Fabrication of n⁺/p InP Solar Cells on Silicon Substrates," *Appl. Phys. Lett.* **54** (12), 1989, pp. 1139-1141.
3. C. Keavney, S. Vernon, and V. Haven, "Tunnel junctions for InP-on-Si Solar Cells," *NASA Conf. Pub. 3121, 1991 Space Photovoltaic Research and Technology Conf.*, pp. 1-1 to 1-7.
4. R.K. Jain and D.J. Flood, "Design Modeling of High-Efficiency p⁺-n InP Solar Cells," *IEEE Trans. on Electron Devices*, Vol. **40**, No. 1, 1993, pp. 224-227.
5. M.M. Al-Jassim, R.K. Ahrenkiel, M.W. Wanlass, J.M. Olson, and S.M. Vernon, "The Heteroepitaxy of InP and GaInP on Silicon for Solar Cell Applications," *Mat. Res. Soc. Symp. Proc.* Vol. **198**, 1990, pp. 235-246.

6. M.W. Wanlass, T.J. Coutts, J.S. Ward, and K.A. Emery, "High-Efficiency Heteroepitaxial InP Solar Cells," *Rec. of the 22nd IEEE Photovoltaic Specialists Conf.*, 1991, pp. 159-165.
7. G.P. Summers, E.A. Burke, P. Shapiro, S.R. Messenger, and R.J. Walters, "Damage Correlations in Semiconductors Exposed to Gamma, Electron and Proton Radiations," *IEEE Trans. on Nuclear Science*, Vol. 40, No. 6, 1993, pp.1372-1379.

SESSION II

THIN-FILM AND HIGH EFFICIENCY CELL DEVELOPMENT

STATUS OF FLEXIBLE CIS RESEARCH AT ISET¹

B.M. Basol, V.K. Kapur, A. Minnick, A. Halani, and C.R. Leidholm
International Solar Electric Technology (ISET)
Inglewood, California

SUMMARY

Polycrystalline thin film solar cells fabricated on light-weight, flexible substrates are very attractive for space applications. In this work CuInSe_2 (CIS) based thin film devices were processed on metallic foil substrates using the selenization technique. CIS deposition method involved reaction of electron-beam evaporated Cu-In precursor layers with a selenizing atmosphere at around 400 °C. Several metallic foils such as Mo, Ti, Al, Ni and Cu were evaluated as possible substrates for these devices. Solar cells with AM1.5 efficiencies of 9.0-9.34 % and good mechanical integrity were demonstrated on Mo and Ti foils. Monolithic integration of these devices was also demonstrated up to 4"x4" size.

INTRODUCTION

Great advances have been made in polycrystalline thin film terrestrial solar cell technologies since early 1980's when the first promising laboratory devices with high efficiencies were demonstrated. These cells were fabricated on polycrystalline CdTe and CuInSe_2 (CIS) layers and they had AM1.5 conversion efficiencies of around 10%. During the last decade, the polycrystalline thin film solar cell efficiencies have improved to over 15% range and the stability data obtained from these devices has been very encouraging.

As the efficiency and the stability of the polycrystalline thin film solar cells have improved through the years, these devices have become more and more attractive for space applications where a reliable power source with high specific power is needed (refs. 1 and 2). Cells and modules fabricated on foil substrates also appeal to some specific terrestrial markets where flexibility is either required or preferred.

CIS and related compound thin film solar cells have already demonstrated terrestrial conversion efficiencies of over 16% (the highest efficiency reported is 16.4% by NREL for a Cu (In,Ga) Se_2 device). Preliminary tests also indicated that the radiation tolerance of CIS thin film cells was superior to that of single crystalline devices under high energy electron and proton irradiation.

Besides their radiation resistance and promise of high efficiency, CIS thin film devices also offer to the space power market a high specific power and low cost. If these devices could be fabricated on light-weight substrates and if they could be monolithically integrated to form modules, they would become very competitive with the existing single crystal technologies even if their beginning-of-life efficiencies were lower than those of the single crystalline cells (ref. 3). The typical substrate for a high efficiency terrestrial CIS solar cell is a 0.3 cm thick soda lime glass sheet. The main thrust of our effort in this program was the

¹ Work funded by NASA SBIR II contract No. NAS3-26615

fabrication of these devices on thin metal foil substrates using the selenization method.

EXPERIMENTAL

A "substrate" device structure with Foil/Mo/CIS/CdS/ZnO configuration was employed in this work. The 1-2 micron thick Mo layer was sputter deposited on the 1-2 mil thick foil substrate. CIS and CIGS ($\text{Cu}(\text{In,Ga})\text{Se}_2$) layers were grown by the selenization technique (refs. 4 and 5). In the first step of this process thin layers of Cu and In, and in some cases Ga, were deposited on the metallic foils by e-beam evaporation. Thicknesses of the Cu and In layers in these precursors were typically 0.2 microns and 0.47 microns, respectively. Ga content was varied from 0% to 20%. During the second step of the process the precursors were reacted in a selenizing atmosphere containing H_2Se gas at 400 °C to form the selenide compounds. The selenization profile and the selenization period were varied to optimize conditions so that films of good electrical and mechanical properties could be obtained.

Devices were completed by CdS and ZnO depositions. CdS layer was obtained using the chemical dip method. This technique utilizes a meta-stable solution containing a Cd source such as Cd-acetate, a sulfur source such as thiourea, and a complexing agent that controls the rate of release of the Cd^{2+} ions into the electrolyte. ZnO films were deposited by the MOCVD technique to a thickness of 1-1.8 microns. Further details of the processing steps can be found in our previous publications (refs. 4 and 5).

RESULTS AND DISCUSSION

Flexible Substrate Selection

We have evaluated various metallic foils as possible substrates for the growth of CIS layers. Some of the factors that were taken into consideration in these evaluations are indicated in Table I and they will be reviewed here.

The selenization technique for CIS film formation involves a reaction step during which the Cu-In precursor layer is annealed in a reactive atmosphere containing H_2Se gas. It is, therefore, essential that the substrates selected for CIS cells do not participate in the reaction between the Cu-In layers and the H_2Se gas and/or they do not themselves react extensively with the H_2Se atmosphere at elevated temperatures. We found Mo and Ti foils to be the best in terms of chemical stability in the reactive atmosphere of our selenization chamber. However, we also determined that Al and Ni foils could be utilized provided that a Mo layer of good mechanical integrity was interposed between the foil surface and the growing CIS film. This thin Mo layer was found to act as an effective diffusion barrier between the foil surface and the CIS film and between the foil and the selenization atmosphere. Any pinholes present in the thin Mo inter-layer deposited on the highly reactive foils of Al and Ni, however, would allow an interaction between the CIS film and the foil substrate through these defects. Such an interaction would give rise to the formation of areas in the growing film which were associated with undesirable Cu-In-Al-Se, or Cu-In-Ni-Se compounds. The parts of the CIS film with a defect free Mo inter-layer, however, were highly uniform suggesting that the Mo layer deposited over the Al and Ni surfaces was an effective barrier to selenization at 400 °C. The defect density of the Mo layers deposited on Ti and Mo foils was not a critical factor in determining the stoichiometric uniformity of the CIS films grown on such substrates with

limited reactivity. The main requirement for the Mo inter-layer in these cases was "good adhesion to the foil surface". Cu foils were extremely reactive and they could not be utilized in our application even if they were covered on both of their surfaces by Mo layers. Mo/Cu/Mo structures tested under selenization conditions quickly inter-diffused and Cu reacted with H_2Se forming copper selenides. More details of our studies on the reactivity of foil substrates can be found in references 4 and 5.

Handling of the thin foil substrates during processing is a practical factor that needs to be considered. Our experience showed that 1 mil thick Mo, Ti and Ni foils could easily be handled and they kept their mechanical integrity throughout the device fabrication steps. Al foils, on the other hand, tended to crease easily. Specially drawn "annealed" Al foils were better in terms of handling during the precursor deposition, but these substrates lost their "springy" nature after the high temperature selenization step and they again became susceptible to creasing.

In terms of specific power, Al and Ti are the two attractive choices as indicated in Table I. Both of these foils would contribute only 0.6-1 kg/kW to the overall specific power of CIS modules with 10W/ft² output. Thermal expansion coefficient match between the CIS film and the substrate is best for Ti and, to a certain degree, Mo foils.

Based on these factors and the experimental results, we first adapted Mo foil as the substrate because of our familiarity with this material as the back contact to CIS devices. Later we initiated work on Ti foil substrates which are more attractive in terms of their light weight and near-ideal coefficient of thermal expansion.

CIS Films and Solar Cells

It is very important to control the nature of the Cu-In precursor layers in the first stage of our CIS deposition process. The thickness uniformity, the degree of alloying between the Cu and In layers and the morphology of the resulting Cu-In precursor film are all factors that determine the quality of the CIS layer obtained after the selenization step. In films containing Ga, the place of this element in the precursor stack also affects the morphology of the resulting compound film. Adhesion is of utmost importance for CIS layers, especially for those deposited on flexible substrates. An important source of poor adhesion between a film prepared by the two-stage technique and its Mo coated substrate is the stresses generated in the CIS layer during the selenization process. We have eliminated this problem by carefully engineering the precursor layers (ref. 4) and have successfully deposited well adhering CIS layers on 6"x6" flexible Mo and Ti foil substrates.

Figure 1 shows the I-V characteristics of two CIS cells fabricated on flexible Mo (fig. 1a) and Ti (fig. 1b) foils. The area of these devices was 0.09-0.1 cm² and their AM1.5 efficiencies were 9% (active area), and 9.34% (total area) respectively. Witness cells fabricated on glass substrates utilizing the same Mo layers, the same Cu-In precursors and the same selenization procedures yielded efficiencies in the 11-12% range. Study of the flexible cell parameters indicated that these devices, on the average, gave 30-40 mV lower V_{oc} values compared to the glass based cells. The J_{sc} values were also lower but only by 1-2 mA/cm². However, the parameter that was consistently low in flexible solar cells was the fill factor. While the FF values of the glass based cells were typically in the 0.65-0.75 range, this range was only 0.5-0.6 for the flexible devices.

The SEM of figure 2 shows a cross sectional view of the CIS layer on a flexible Mo foil. There are certain characteristics of the flexible CIS films that we noted in studying such micrographs. The morphology of the CIS layers deposited on flexible foils are quite different than those grown on glass substrates. The dome-like features that are commonly observed in SEMs taken from the surfaces of flexible CIS layers originate from the dome-like pores that can be seen at the Mo/CIS interface in figure 2. The crystalline quality of the flexible films is also inferior to the crystalline quality of the glass based layers. This, we believe, is due to the different surface qualities of the two substrates. Foil substrate surfaces provide a large number of nucleation sites for grain growth and the resulting small crystals are not well oriented. CIS films grown on foil substrates do not show the columnar grain structure often observed in layers deposited on glass substrates. We have initiated work to address this issue and increase the flexible cell efficiencies to the 12-13% range.

Module Integration Studies

Monolithic integration of devices fabricated on metallic substrates requires deposition of an insulating layer over the metallic foil, and then a series of scribing steps to interconnect and isolate the adjacent cells (fig. 3). Glass based integration techniques which use mechanical scribes can not be utilized in the foil cell integration process because of the fragile nature of the thin insulator. Possible interaction of the insulating layer with the selenization environment is another factor that needs to be taken into account. We have carried out module integration work on 4"x4" size foils and monolithically integrated 16 cells on such a foil. Although these submodules demonstrated voltage addition the fill factor values are presently low and they limit the efficiency at this time to below 5%. Work is in progress to improve the efficiencies of these submodules to the 6-8% range by addressing the fill factor issue. It should be noted that the data reported in this paper represents the highest efficiency flexible CIS cells reported to date and the very first demonstration of monolithic integration of CIS cells on a flexible metal foil substrate.

REFERENCES

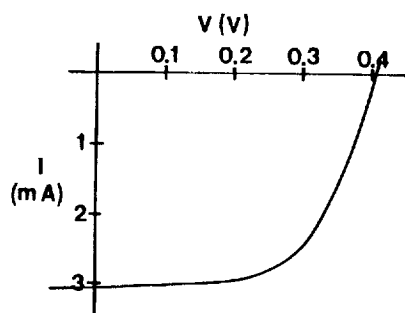
1. Landis G.A.; and Hepp A.F.: Applications of Thin-Film Photovoltaics For Space. 26th Intersociety Energy Conversion Engineering Conf., 1991, vol. 2, pp.256-261.
2. Boswell J.; Anspaugh B.; and Mueller R.: Thin Film PV Development at Phillips Laboratory. Proc. 23rd IEEE PV Specialists Conf., 1993, pp. 1324-1329.
3. Armstrong J.H.; Pistole C.O.; Misra M.S.; Kapur V.K.; and Başol B.M.: Flexible CIS Films and Devices For Space Applications. Proc. Space PV Research and Technology Conf., May 7-9, 1991, NASA Lewis Center, Cleveland, Ohio, p. 19-1.
4. Başol B.M.; Kapur V.K.; Halani A.; and Leidholm C.: CIS Thin Film Solar Cells Fabricated on Flexible Foil Substrates. Solar Energy Materials and Solar Cells, vol. 29, 1993, pp. 163-173.
5. Başol B.M.; Kapur V.K.; Halani A.; Minnick A.; and Leidholm C.: Modules and flexible cells of CIS. Proc. 23rd IEEE Photovoltaic Specialists Conf., 1993, pp. 426-430.

TABLE I. EVALUATION OF VARIOUS METALLIC FOILS AS A SUBSTRATE FOR FLEXIBLE CIS SOLAR CELLS

Foil Substrate	Reactivity with H_2Se	Ease of handling through process	Coeff. of thermal expansion* ($\times 10^6/^{\circ}C$)	Contribution to specific power** (kg/kW)
Mo	low	very good	4.8	2.29
Ti	moderate	very good	8.6	1.01
Al	high	poor (creases)	2.3	0.60
Ni	high	good	13.4	2.00
Cu	very high	very poor (reacts and becomes brittle)	16.5	2.01

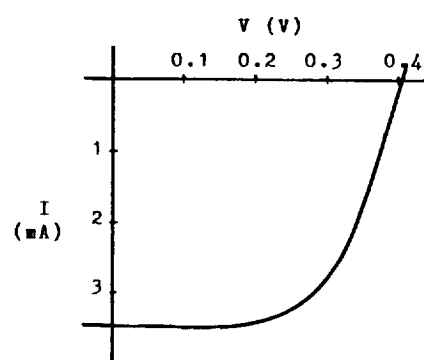
* CTE for CIS $\sim 7-9$ ppm/ $^{\circ}C$

** Assuming 10W/ft² modules on 1 mil thick foils



$V_{oc} = 0.405$ V
 $J_{sc} = 37.5$ mA/cm²
 FF = 0.597
 $\eta = 9.0\%$
 Area = 0.1 cm²

(a)



$V_{oc} = 0.4$ V
 $J_{sc} = 38.9$ mA/cm²
 FF = 0.6
 $\eta = 9.34\%$
 Area = 0.09 cm²

(b)

Figure 1. Illuminated I-V characteristics of two flexible cells fabricated on a) Mo foil, b) Ti foil. Measurements were made under AM1.5 illumination.

Figure 2. Cross sectional SEM of a foil/Mo/CIS/CdS/ZnO structure.

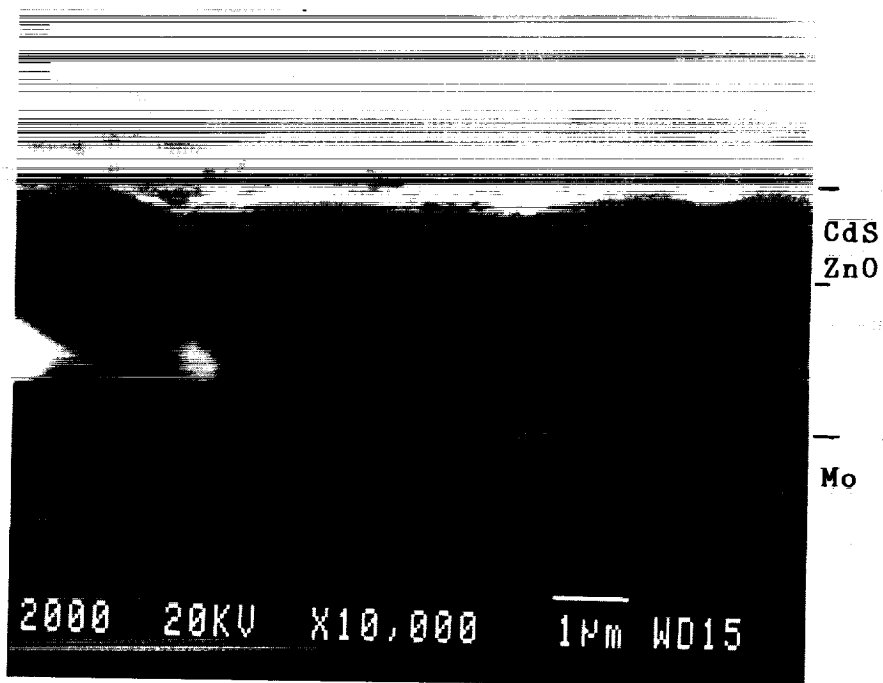
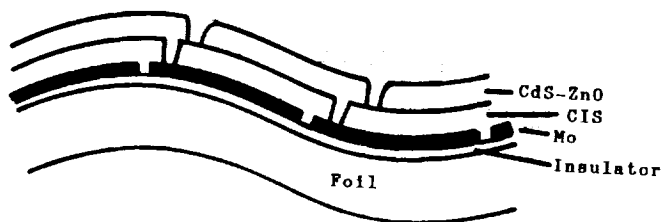


Figure 3. Structure of a monolithically integrated flexible CIS submodule.



DEVELOPMENT OF A LIGHTWEIGHT, LIGHT-TRAPPED, THIN GaAs SOLAR CELL FOR SPACECRAFT APPLICATIONS¹

Margaret H. Hannon, Louis C. DiNetta, Michael W. Dashiell,
John R. Cummings, and Allen M. Barnett
AstroPower, Inc.
Newark, Delaware

ABSTRACT

This paper describes ultra-lightweight, high performance, thin, light trapping GaAs solar cells for advanced space power systems. The device designs can achieve 24.5% efficiency at AMO and 1X conditions, corresponding to a power density of 330 W/m². A significant breakthrough lies in the potential for a specific power of 2906 W/kg because the entire device is less than 1.5 μm thick. This represents a 440% improvement over conventional 4-mil silicon solar cells. In addition to being lightweight, this thin device design can result in increased radiation tolerance. The attachment of the cover glass support to the front surface has been demonstrated by both silicone and electrostatic bonding techniques. Device parameters of 1.002 volts open-circuit voltage, 80% fill factor, and a short-circuit current of 24.3 mA/cm² have been obtained. This demonstrates a conversion efficiency of 14.4% resulting in a specific power of 2240 W/kg. Additionally, this new technology offers an alternative approach for enabling multi-bandgap solar cells and high output space solar power devices. The thin device structure can be applied to any III-V based solar cell application, yielding both an increase in specific power and radiation tolerance.

PERFORMANCE CAPABILITY

III-V materials such as GaAs make excellent candidates for thin devices because they are direct bandgap materials. The high absorption coefficient of such materials for light of an energy greater than the bandgap makes it possible to fabricate cells in which the thickness of the active region is considerably less than in indirect materials such as silicon. Light of photon energy greater than the bandgap is absorbed within the first few microns of entering a direct bandgap semiconductor, so an ultrathin device design is both feasible and advantageous. Conventional high performance GaAs solar cells are usually comprised of epitaxial layers of GaAs and $\text{Al}_x\text{Ga}_{1-x}\text{As}$ formed on a GaAs substrate. When GaAs devices are fabricated on a thick GaAs substrate, the substrate acts only as a support and does not contribute to the overall performance of the device.

The advantages gained from fabricating thin solar cells include a high power-to-weight ratio (specific power) which is important for space applications. In addition, with a sufficiently thin device structure (base thickness on the order of a diffusion length) the free carrier absorption is minimized and a light trapped device becomes feasible. Light trapping increases the effective optical path length with the use of a reflector and/or a textured surface. Incorporating light trapping into the device increases the performance by increasing the short circuit current, while the reduced GaAs base thickness lowers the reverse saturation current. Both of these effects enhance the open circuit voltage [ref. 1].

¹ This research was supported in part by the Ballistic Missile Defense Organization/Innovative Science and Technology branch and the Department of the Air Force and managed by Phillips Laboratory, Space Power and Thermal Management Division

Because the device is thin, back surface recombination becomes an important issue. Recombination of the carriers at the back surface is reduced by adding an $\text{Al}_x\text{Ga}_{1-x}\text{As}$ ($x > 0.5$) back surface passivation layer. This layer also reflects carriers back to the p-n junction due to the built-in electric field. Because the GaAs base is thin (< 2 microns), the carriers can reach the junction before they recombine. The front surface is also passivated by an $\text{Al}_x\text{Ga}_{1-x}\text{As}$ ($x = 0.85$) layer which has a large indirect bandgap. There is very little absorption in such a layer, allowing light into the underlying cell. Because of the good lattice match to the GaAs, this layer eliminates the surface states and other imperfections on the GaAs p-n junction surface that would ordinarily result in a high recombination velocity and decreased diffusion length.

The use of liquid phase epitaxy (LPE) to fabricate thin devices offers significant advantages over other techniques such as MBE and MOCVD. This technique produces high quality material while maintaining low cost and simplicity. Inherent to the LPE technique is the fact that the dislocation density of the epitaxial films produced is generally lower than the starting substrate. Therefore, the material is superior in terms of diffusion length and lifetime. These benefits are partly attributed to the tendency of impurities to segregate to the liquid (solvent) as opposed to the solid (epitaxial film). The ability to grow multiple layers of controlled electrical conductivity is also useful in the proposed device design. Segregation coefficients are well known so that the proper conductivity type and carrier concentrations can be obtained in the epitaxial films. Phase equilibria for the Al-Ga-As system have been extensively studied, resulting in the ability to precisely control composition.

The high efficiency and light weight of the cover glass supported GaAs solar cell can have a significant impact on space solar array technology. **Fig. 1** shows the specific power (power to weight ratio) and power density of several candidate solar cells. AstroPower's GaAs solar cell design offers a 440% increase in specific power over that of a 14.5% efficient silicon solar cell. The specific power is calculated assuming a 3-mil cover glass and a 1-mil silicone adhesive on the front surface of the solar cell.

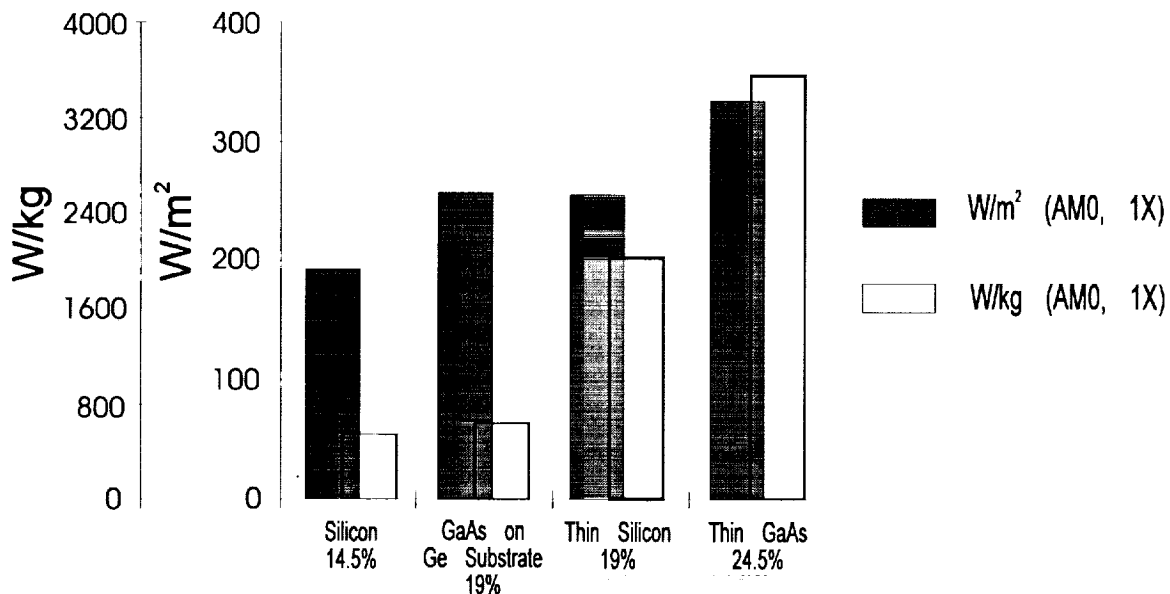


Fig. 1. Comparison of specific power and power density of candidate space solar cells.

AstroPower's approach combines the technology for a thin, light trapped GaAs solar cell with the electrostatic bonding of GaAs to glass and a coplanar back contact technology. Rather than working with p-type front contacts that interfere with the bonding of the glass to the solar cell, contact to the p-type layers is made from the back of the device. This all back contact design also eliminates grid shading

which further enhances the performance of the GaAs solar cell. Since both contact grids are located on the back surface, cell degradation from grid flattening and metals migration, associated with electrostatic bonding of raised contact devices, is eliminated. Also eliminated are the bonding difficulties and the low quality bond yields that typify electrostatically bonded, raised contact solar cells.

In order to obtain the highest efficiencies from thin (1.65 micron) GaAs solar cells it is necessary to incorporate a high degree of light trapping in the cells. To generate the same level of current from a thin device as is possible from a conventionally thick GaAs cell, the optical path length of the light must be extended beyond the physical thickness of the device. The light must travel obliquely and be internally reflected many times, allowing more of the light to be absorbed at a given thickness. Chemical micro-machining or random texturing can be achieved on the front or back surfaces to redirect the light at an oblique angle. Scattered light which is obliquely incident on the front surface at angles less than the critical angle (16° for GaAs), will be totally internally reflected. Such optical confinement leads to effective optical path lengths 2 to 10 times greater than the thickness of the active layers. The factor by which the optical path is increased due to light trapping is called the z-ratio. For example, when the z-ratio is equal to five, the optical absorption for confined light is equivalent to that of a solar cell with a thickness five times greater.

The optimum reflector should have the maximum reflection over the appropriate wavelength range. This aspect of light trapping is important since many reflector options (e.g. quarter-wavelength dielectric films or distributed Bragg reflectors) are optimized for maximum reflectance at one wavelength and exhibit high reflectance over only a narrow bandwidth. A 1-micron thick base requires a back reflector which is effective over the wavelength range of 730 to 880 nm [ref. 1].

Using the LPE technique to grow a thin structure, bonding to a cover glass, and ultimately removing the GaAs substrate allows for access to the back of the active region of the device. Thus an optical reflector (such as Au or Ag) can be applied directly to the back surface. This offers significant advantages over other techniques such as the use of Bragg reflectors grown by MOCVD on GaAs substrates. The spectral width of Bragg reflectors is restricted, and to achieve a z-ratio higher than 2, multiple Bragg reflectors must be used. As pointed out by Tobin et al., [ref. 2], "the added complexity of multiple Bragg reflectors" does not make this a practical approach. The use of the appropriate metal reflector on the back surface provides reflection over a broad spectral range. This technology also removes the excess weight of the substrate thus significantly increasing the specific power.

Modeling the thin GaAs solar cell shows benefits similar to those achieved in light trapped silicon. For silicon devices, reducing the thickness of the device decreases the reverse saturation current, while trapping the light leads to an increase in the short circuit current. In GaAs, however, the current gains are smaller and most of the increased performance is realized from enhanced open circuit voltage. The three most important features which lead to improvements in the efficiency of GaAs thin-film solar cells are: increased optical absorption, improved collection efficiency, and photon recycling [ref. 3]. Photon recycling is when photons generated by radiative recombination are optically confined so they can be re-absorbed to generate minority carriers again. The enhanced optical absorption and improved collection of minority carriers provide a modest increase in the short circuit current (I_{SC}). Because the solar cell volume is reduced by thinning the device, the bulk recombination is reduced which reduces the dark current. The reduced dark current and improved I_{SC} result in an increase in the open circuit voltage. Also contributing to an increase in the open circuit voltage is the fact that higher carrier concentrations can be used to further reduce the dark current since a low minority carrier diffusion length can be tolerated in a thin device. As light trapping increases for a given back surface recombination velocity, the solar cell efficiency increases. When light trapping is considered, the p/n structure is more efficient than an n/p structure since the long base diffusion length in the n/p structure is not as important when the solar cells are very thin.

RADIATION RESISTANCE

Radiation damage is the primary mechanism of degradation of GaAs solar cells deployed in space. This gradual degradation in solar cell performance is due to a reduction in the minority carrier lifetime that results from cumulative damage to the crystal lattice. As high energy particles bombard the cell, the number of recombination centers is increased, resulting in a decrease in the minority carrier lifetimes. The fact that light is absorbed in a shallow depth indicates that GaAs should have a better radiation resistance than silicon. Since the minority carrier transport is over much smaller distances, the diffusion length can be reduced by irradiation to much smaller values before having a significant effect on the carrier collection at the junction [ref. 4]. The thin light trapped GaAs solar cell design further enhances the radiation tolerance because damage created several microns into the material by high energy particles has no effect on photo current collection. The recombination region is thinner, thus increasing the resistance to high-energy radiation. The cover glass can be specified to screen out low energy particles corresponding to the chosen orbit, which normally cause damage at the surface [ref. 5].

Optimized emitter thickness and absorber layer doping can also contribute to radiation tolerance. The emitter thickness is kept below 0.5 microns in order to reduce the distance which minority carriers generated near the surface must travel to be collected. Because the entire device is less than 2 microns thick, carriers generated deeper in the material can still reach the junction before recombining. This becomes important when radiation has decreased the minority carrier diffusion length.

In conventional thick GaAs solar cells, the base layer carrier concentration is kept below $3 \times 10^{17} \text{ cm}^{-3}$ to improve the end-of-life (EOL) efficiency. In our thin device this effect is not as important because of the reduced dependence on diffusion length. Higher carrier concentrations are incorporated in order to reduce the dark current and thus enhance the open circuit voltage, while maintaining a radiation tolerant device.

EXPERIMENTAL RESULTS

A schematic cross-sectional representation of the AstroPower prototype thin GaAs solar cell design is shown in Fig. 2.

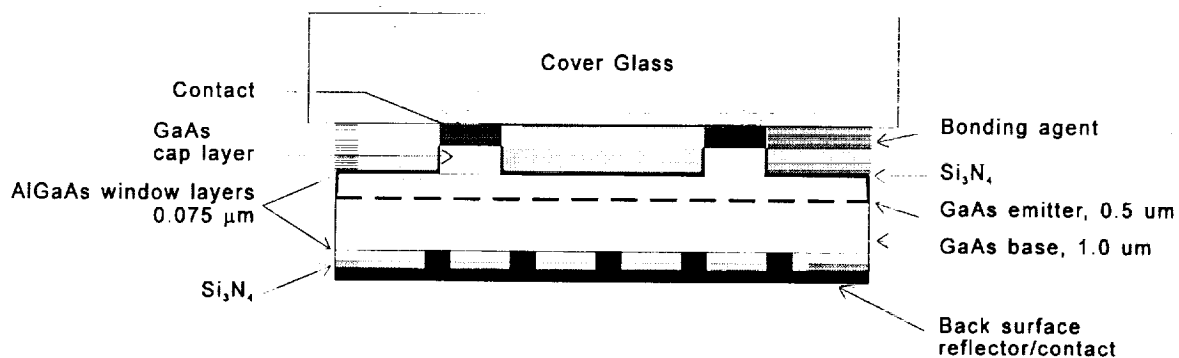


Fig. 2. Ultra-thin GaAs solar cell with light trapping.

A key requirement for high performance ultra-thin GaAs solar cells is the incorporation of light trapping into the devices. Light trapping was demonstrated by growing a thin (1.5 micron) GaAs base layer on an AlGaAs passivating layer using liquid phase epitaxy. The sample was then bonded to glass and the substrate was removed.

Comparisons were made between samples with and without a metal reflector, and the effectiveness of the reflector in projecting photons back toward a junction was determined. Silver was used as the reflector in this case. Reflection + transmission (R + T) measurements were performed before and after the substrate removal. The absorption can be obtained from the reflection and transmission data (absorption = $1 - (R+T)$). These results are shown in Fig. 3.

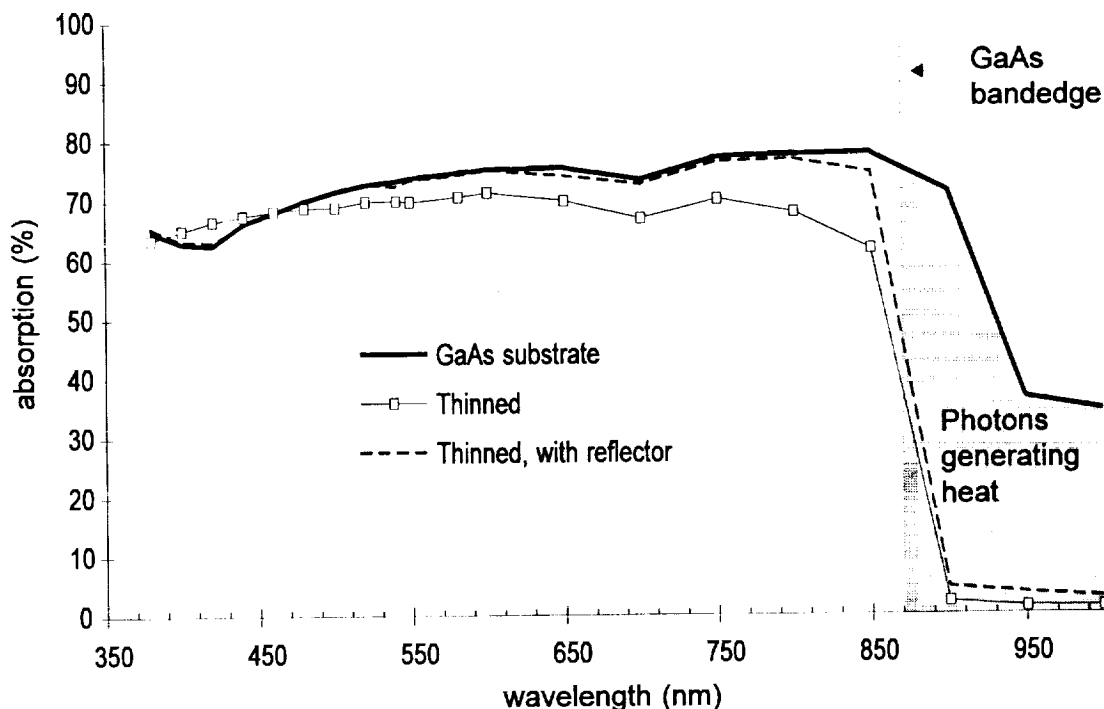


Fig. 3. Absorption results for: 1.5 μm GaAs LPE layer on a GaAs substrate; 1.5 μm glass bonded GaAs layer, and glass bonded 1.5 μm GaAs layer with a reflector.

As expected, the amount of light absorbed decreases as the GaAs structure is thinned, particularly over the 550 nm to 850 nm range where there is a higher flux density and the photons are more weakly absorbed. Application of a silver reflector resulted in increased absorption which closely matched the measurements of the thin material on the GaAs substrate. As much as 70% of the light is absorbed over the 550 nm to 850 nm range. By incorporating a silver reflector, we have been able to successfully light trap a 1.5 micron thick structure of GaAs. This will enable high short circuit currents to be obtained on a thin, ultra-lightweight GaAs solar cell.

Note that there is little absorption of sub-bandgap photons in the thinned material both with and without a reflector. This is advantageous for space solar cells because sub-bandgap photons that are absorbed generate heat in the device but do not contribute to the efficiency. As shown in Fig. 3, the structure on a GaAs substrate absorbs as much as 70% of the photons at 900 nm while the thinned structure with a reflector absorbs only 4% of the photons at 900 nm. Standard thick GaAs solar cells absorb these lower energy photons in the substrate.

Device layers are grown by liquid phase epitaxy (LPE) [ref. 6]. The front and back surfaces are passivated by an $\text{Al}_x\text{Ga}_{1-x}\text{As}$ window layer in order to reduce the surface recombination. The GaAs base layer is approximately 1 micron thick and the emitter layer is formed by diffusing the p-type dopant during the growth of the front passivating (window) layer. The junction depth is easily controlled by adjusting the window layer growth time.

Fig. 4 shows the quantum efficiency of a free-standing $1.65\ \mu\text{m}$, 1-cm^2 device. The short circuit current, as corrected for grid shading and reflection losses, was $29.13\ \text{mA/cm}^2$.

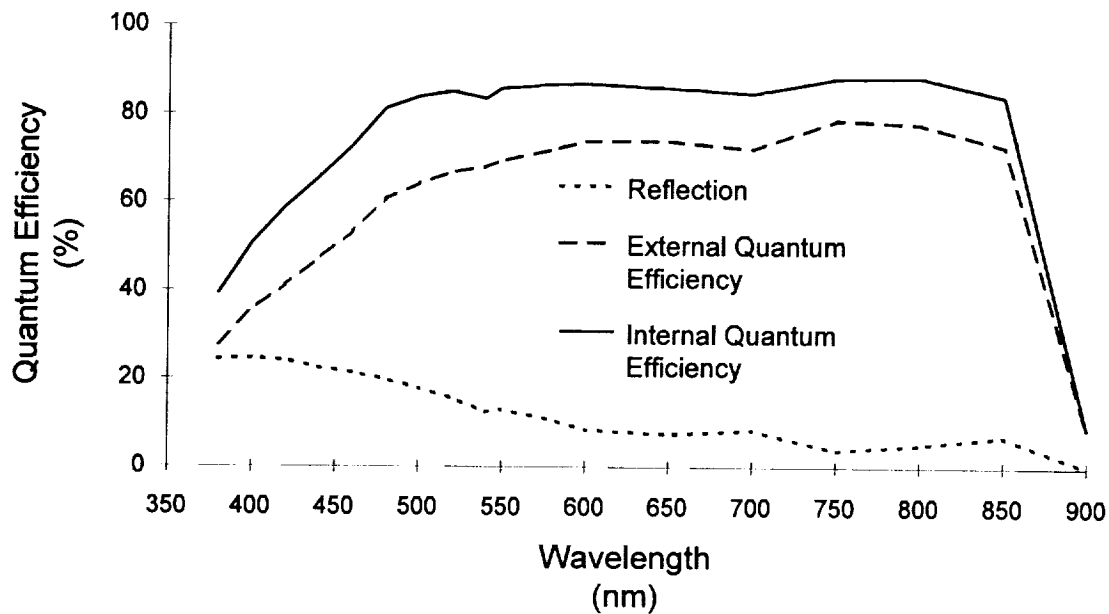


Fig. 4. Quantum efficiency results for free-standing device F12314B.

The results of the current-voltage measurement (F12314B) is shown in **Fig. 5**. This thin solar cell demonstrated an efficiency of 14.4%, as measured. From the quantum efficiency curves, it can be seen that the antireflection coating is not properly optimized and results in a lower than optimal current generation from 350 to 600 nm. When corrected for reflection losses, the potential of this material would yield a 17.3% efficiency at AM0.

Cell Data: F12314B	
V_{oc}	1.001 v.
J_{sc}	$24.3\ \text{mA/cm}^2$
Fill Factor	80%
Efficiency	14.4%

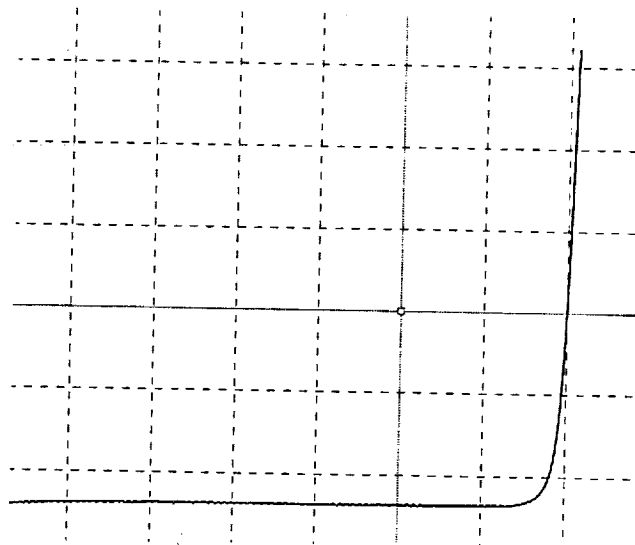


Fig 5. Current-voltage measurement results for free-standing device F12314B

The best parameters obtained from conventional GaAs devices fabricated at AstroPower were an open circuit voltage of 1.020 V, a short circuit current of 35.6 mA/cm², and a fill factor of 82.7%. This demonstrates the potential for a solar cell efficiency of 22.2%. As can be seen, the measured open-circuit voltages and fill factors are close to the best devices fabricated on GaAs substrates. Optimization of the thickness, doping, and antireflection coatings will yield an increase in the performance of the thin GaAs solar cell

The improved device design which utilizes electrostatic bonding and an all back contact technology is shown in Fig. 6. The p-type region is diffused from the back of the device to the emitter after thinning. The temperature required for this diffusion step necessitates a high temperature survivable electrostatic bond. This superior solar cell design solves many fabrication problems and enhances the manufacturability of the high performance GaAs solar cell. Development of this design is currently in progress.

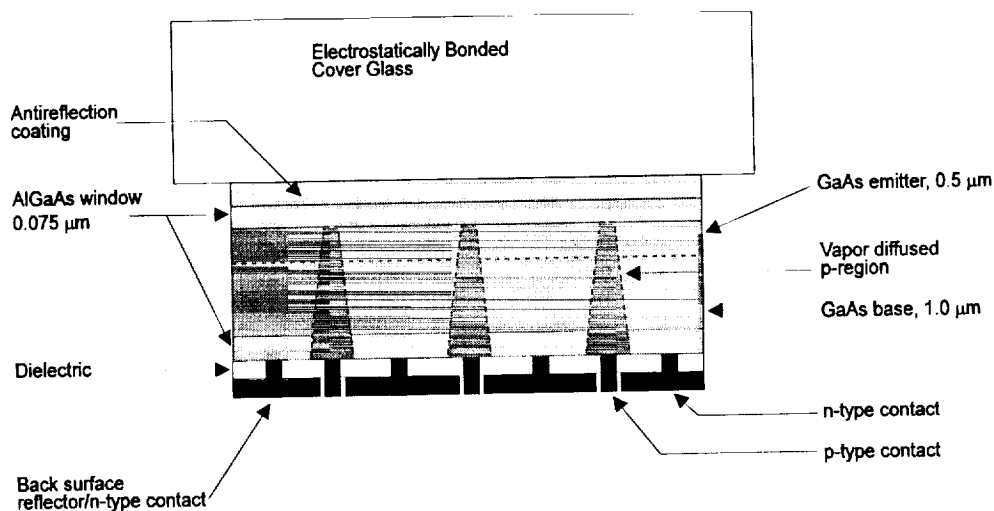


Fig. 6. *Electrostatically bonded, all back contact, ultra-thin GaAs solar cell.*

CONCLUSION

The results of this program have demonstrated the feasibility of the ultra-lightweight, high performance, thin, light trapping GaAs solar cell. This is a high payoff program and the resulting applications can have a dramatic positive effect on space solar power generation. Development of the thin light trapped GaAs solar cell will result in a new class of GaAs solar cell designs that can replace conventional GaAs solar cells because of their high specific power, radiation resistance, and durability.

REFERENCES

- [1]. Honsberg and A.M. Barnett, "Light Trapping in Thin Film GaAs Solar Cells", *Proc. 22nd IEEE Photovoltaic Specialists Conference*, Las Vegas, Nevada, (1991), pp. 262 - 267.
- [2]. TOBIN, S.M. VERNON, M.M. SANFACON, AND A. MASTROVITO, "Enhanced Light Absorption in GaAs Solar Cells With Internal Bragg Reflectors", *Proc. 22nd IEEE Photovoltaic Specialists Conf.*, Las Vegas, Nevada, (1991), pp. 147 - 152.

- [3]. LUSH AND M. LUNDSTROM, "Thin Film Approaches for High Efficiency III-V Cells", *Solar Cells*, 30 (1991).
- [4]. MARKVART, "Radiation Damage in Solar Cells", *Journal of Materials Science: Materials in Electronics*, Vol.1, No.1, pp. 1-12, (1990).
- [5]. FLOOD AND H. BRANDHORST, "Space Solar Cells", *Current Topics in Photovoltaics*, T.J. Coutts and J.D. Meakin ed., Harcourt Brace Jovanovich, Publishers, (1987).
- [6]. NELSON, *RCA Review*, 24 (1963).

ADVANCES IN POLYCRYSTALLINE THIN-FILM PHOTOVOLTAICS FOR SPACE APPLICATIONS¹

Bruce R. Lanning, Joseph H. Armstrong, and Mohan S. Misra
Martin Marietta Corporation
Denver, Colorado

INTRODUCTION

Polycrystalline, thin-film photovoltaics represent one of the few (if not the only) renewable power sources which has the potential to satisfy the demanding technical requirements for future space applications. The demand in space is for deployable, flexible arrays with high power-to-weight ratios and long-term stability (15-20 years). In addition, there is also the demand that these arrays be produced by scalable, low-cost, high yield, processes. An approach to significantly reduce costs and increase reliability is to interconnect individual cells series via monolithic integration.

Both CIS and CdTe semiconductor films are optimum absorber materials for thin-film n-p heterojunction solar cells, having band gaps between 0.9-1.5 eV and demonstrated small area efficiencies, with cadmium sulfide window layers, above 16.5% (Ref. 1,2,3). Both CIS and CdTe polycrystalline thin-film cells have been produced on a laboratory scale by a variety of physical and chemical deposition methods, including evaporation, sputtering, and electrodeposition. Translating laboratory processes which yield these high efficiency, small area cells into the design of a manufacturing process capable of producing 1-ft² modules however, requires a quantitative understanding of each individual step in the process and its (each step) effect on overall module performance. With a proper quantification and understanding of material transport and reactivity for each individual step, a manufacturing process can be designed that is not "reactor-specific" and can be controlled intelligently with the design parameters of the process.

Development of a thin-film, manufacturing process depends not only on the scalability of the process but on the overall fixed and operating costs, the environmental compatibility (i.e., material utilization/waste minimization with minimal health and safety risks), and the reproducibility/stability of the process. For this reason, the selection of deposition processes at MMC was influenced by: 1) cost; 2) environmental compatibility; and 3) reproducibility/stability of the process. In the development of CdTe and CIS devices at MMC therefore, CdTe films are being deposited by electrodeposition and CIS films are being deposited by DC, cylindrical magnetron sputtering. Both of these processes are scalable, low-cost processes with relatively minimal environmental impact and a discussion of the development of these processes is presented in this paper.

The objective of this paper is to present an overview of the current efforts at MMC to develop large-scale manufacturing processes for both CIS and CdTe thin-film polycrystalline modules. CIS cells/modules are fabricated in a "substrate configuration" by physical vapor deposition techniques and CdTe cells/modules are fabricated in a "superstrate configuration" by wet chemical methods. Both laser and mechanical scribing operations are used to monolithically integrate (series interconnect) the individual cells into modules. Results will be presented at the cell and module development levels with a brief description of the test methods used to qualify these devices for space applications. The approach and development efforts are directed towards large-scale manufacturability of established thin-film, polycrystalline processing methods for large area modules with less emphasis on maximizing small area efficiencies.

¹ This work is supported by Martin Marietta Independent Research and Development (IR&D) Project D-17R, "Photovoltaic Technologies"

CELL DEVELOPMENT

A part of the development of a commercial scale process for thin-film polycrystalline modules is an understanding of each of the individual processing steps and its correlation to device performance and reliability. In this section, a summary is presented of each of the processing steps for both CIS and CdTe devices.

Copper Indium Diselenide

CIS heterojunction cells are deposited onto flexible or rigid glass substrates in the "substrate configuration"; substrate, molybdenum back contact, CIS absorber, CdS window layer, ZnO transparent conductive oxide, with a metallized top grid contact. Conventional CIS devices have been optimized on molybdenum-coated glass substrates and little has been reported on the performance of CIS films on flexible substrates. The issue of flexible substrate requirements is discussed along with the current approaches and results for producing thin-film CIS

Substrate - For the rigid cells, borosilicate glass is an inexpensive substrate which matches well with the thermal characteristics of the semiconducting layers and is therefore the substrate of choice for a rigid module. Molybdenum can be uniformly sputtered onto glass substrates over 1 ft² areas and depending on the characteristics of the sputtering chamber (i.e., planar or cylindrical cathodes, oxygen level, etc.), the molybdenum will have a surface roughness similar to the glass substrate with a well-defined texture. Surface profile and texture have been observed to have an effect on overall device performance and the selection of the substrate can have an effect on the roughness and texture of molybdenum back contact.

Although flexible substrates offer inherent processing advantages in the development of a commercial scale process as well as meeting technical goals for space applications which are not obtainable with rigid substrates, substrate flexibility adds complexity to the fabrication process. Typical requirements for a flexible substrate in a CIS module would include such things as: 1) surface finish/profile; 2) high temperature stability (up to 550° C); 3) thermal compatibility (CTE); 4) insulating (dielectric breakdown voltage); 5) chemical/vacuum stability; 6) cost and availability; and 7) flexibility versus strength. Each class of materials, whether it be metal, ceramic, or plastic, has certain drawbacks as a flexible substrate although the leading candidates for flexible substrates are polyimide-type plastics, "metal organic-based" flexible glasses, coated metallic foils, and mica sheets.

Results from thermal gravimetric analysis have shown that nearly all the 'high-temperature' plastics tested out-gas to some degree above 400°C (this does not include evaporation of water above 100°C). This not only alters the properties of the material but can effect the adherence of the semiconductor films during deposition. CIS devices have been fabricated on polyimide films although efficiencies were not significant to report.

Because of their mechanical toughness, high temperature stability, cost, and availability, coated and uncoated metallic foils have been used in the development of flexible CIS devices. Unlike the smooth glass substrates which have been used to produce the highest efficiency cells reported by others, metallic foil substrates have a rougher surface profile which can effect device performance.

The differences between molybdenum coatings on the flexible foils and glass substrates were subtle. Peak to valley variations in the surface profile of the metallic foil were on the order of 200 nm whereas

the variation across a typical glass substrate is on the order of 10 nm. The molybdenum back contact films on metallic foils were highly textured with predominantly a (110) peak in the glancing incidence diffraction spectra. In comparison to single crystal molybdenum, the (110) peak of the sputtered molybdenum film on metallic foil broadened and shifted to higher d-spacings (i.e., residual tensile stresses after the molybdenum deposition and selenization processes). Molybdenum films on the glass substrate were also highly oriented although the (211) was the strongest peak and there was not any detectable broadening or shifting of the primary peaks.

Surface texture of the substrate is certainly a factor in the deposition, nucleation, and growth behavior of semiconducting films. This as well as other subtle factors, such as the surface emissivity/absorptivity of the substrate during thermal processing, can effect the photoresponse of a polycrystalline CIS device.

Molybdenum Back Contact - Depending on the substrate, a 200-1,000 nm thick coating of molybdenum is sputtered onto the surface. Substrate temperature, sputter rate and pressure are used to control the adhesion and stress state of the film; oxygen partial pressure is also used as a parameter to control the properties of the molybdenum film. To improve adhesion of the CIS absorber layer, a graded molybdenum structure can be deposited with copper to produce a pure molybdenum layer at the substrate/contact interface and a pure copper layer at the CIS/contact interface (as reported in the literature (Ref. 4), copper at the back surface of CIS would produce a "p+" structure in the CIS absorber layer and improve the ohmic contact).

CIS Absorber Layer - Reproducibility and uniformity of the CIS absorber layer is one of the most important factors in the performance and manufacturability of large-area modules. Since copper, indium, and selenium are three elements with considerably different properties (i.e., melting points, vapor pressures, oxygen solubility, conductivity, etc.), the formation of a single copper indium diselenide phase over large areas, both kinetically and thermodynamically, will depend on the processing order or deposition sequence and the uniformity of the film deposit(s) over large areas. Lateral compositional and thermal gradients across a large area can result in the formation and microsegregation of secondary phases and since these gradients/heterogenities are not significant in the "through-thickness dominated" growth behavior of a small area, the processing steps to produce high efficiency small area devices may therefore be limited over larger areas.

The approach in the development of a large scale process has been to select processing sequences for CIS which minimize the number of reaction pathways and secondary phase formation while at the same time, select deposition processes for each sequence which are reproducible and scalable. Two of these approaches are: 1) Cu/In Bilayer approach where copper and indium are successively deposited on a molybdenum back contact and then reacted with either elemental selenium or hydrogen selenide vapor; and 2) Selenized Bilayer approach where first, indium and selenium are deposited/reacted to form indium selenide, followed by copper and selenium deposition to form copper selenide, and finally, the two selenized bilayers are reacted to completion in a selenium atmosphere. The Cu/In bilayer is a low temperature (~400°C) approach with a small number of easily controllable, processing steps, demonstrated large-area scalability, and excellent substrate adhesion. Since a number of reaction pathways are possible with this type of approach, stable binary phases (as well as other types of microsegregation) can form along with the copper indium diselenide phase and degrade the performance of a large-area module.

The selenized bilayer approach on the other hand, reduces the total number of possible reaction pathways by the formation of essentially two stable intermediate binary phases which, when reacted to com-

pletion, can only form a single CIS phase (refer to a $\text{Cu}_{(2-x)}\text{Se}/\text{In}_2\text{Se}_3$ binary phase diagram). Although this type of approach minimizes formation of impurities by limiting the number of reaction pathways, the number of processing steps and substrate temperature are increased in comparison to the Cu/In bilayer approach. In addition, reported efficiencies for this type of approach have only been demonstrated on a small scale.

To evaluate emerging CIS technology, Martin Marietta (MMC), in cooperation with the National Renewable Energy Laboratory, designed and fabricated a CIS flight experiment with cells based on NREL's selenized bilayer process which has demonstrated 16.4% efficiency in AM1.5 insolation this year. In this case, gallium was added to the CIS to improve the bandgap as well as efficiency. The experimental array fabricated for the SAMMES flight experiment is scheduled for launch later this year. Active area efficiency for these devices calculated at 13.5% in AM0 as measured by a pulsed solar simulator at Spectrolab during final assembly. It is anticipated that there will be at least one year of data in orbit from this experiment.

CdS Window Layer - A thin, 40-60 nm - thick, CdS film is deposited onto the CIS absorber layer by the chemical bath deposition process. Cadmium to sulfur ratios in solution have been varied between 10 and 50 to optimize both film properties (i.e., adherence and uniformity) and yield from this batch process. Actual deposition occurs at 85°C in a buffered solution between 9.0 and 10.0 pH and processing time is less than 4 minutes. Reproducibility and uniformity of the thin CdS layer have been demonstrated over 1 ft² areas.

ZnO Top Contact - Since the approach for the molybdenum back contact and CIS absorber layers has been to utilize the potential scalability of a cylindrical, DC-magnetron sputtering process, a similar development strategy was used in the case of the ZnO top contact (ZnO can also be deposited by RF sputtering although the results presented in this paper are with a DC power source). ZnO films were sputtered from an 8" diameter, hot pressed target containing 98 w/o ZnO and 2 w/o Al_2O_3 and the transmittance response for a 902.5 nm-thick film is presented in Figure 1(a). The transmittance response for an uncoated substrate is included for reference.

With DC magnetron sputtering of ZnO, film properties are strongly dependent upon both the processing parameters and the target/substrate geometry. To determine the effect of substrate location with respect to the target source, glass witness coupons were positioned at increasing distances from the target source (normal to the target) and at positions away from the center of the target (parallel to the target surface). Results from this series of tests is shown in Figure 1(b) in which the film resistivity is plotted as a function of location relative to the target center. Within the region defined by the "racetrack" of the target (i.e., ~10 cm), the ZnO film resistivities are less than 1×10^{-3} ohm-cm for all but the 10 cm, target-to-substrate distance. In the fabrication of 10 cm x 10 cm CIS device therefore, processing parameters can be varied to first deposit a thin, high resistivity ZnO film on top of the CdS, followed by the low resistance film referred to above.

The "roll-off" in film resistivity for this 8" target occurs at around 15 cm relative to target center and there is a distinct increase in resistivity across the racetrack region. Degradation of film properties in the vicinity of the target racetrack is well documented in the literature and poor resistivities are said to result from bombardment by energetic neutral and negatively charged oxygen atoms. Such bombardment is believed to cause lower carrier mobilities and concentrations through a decrease in grain size, a mixed

crystalline orientation, and a higher defect density. An additional cause for the variations in resistivity may be due to the variations in the aluminum doping density. A plot of atomic ratio of Al/Zn as a function of the location relative to the target center is presented in Figure 2. Based on these results, the increase in resistivity across the racetrack zone correlates with the drop in Al/Zn ratio. By incorporating existing techniques to control neutral and negatively charged oxygen atoms and minimize racetrack effects, ZnO will then be uniformly deposited over a 30 cm diameter by DC magnetron sputtering.

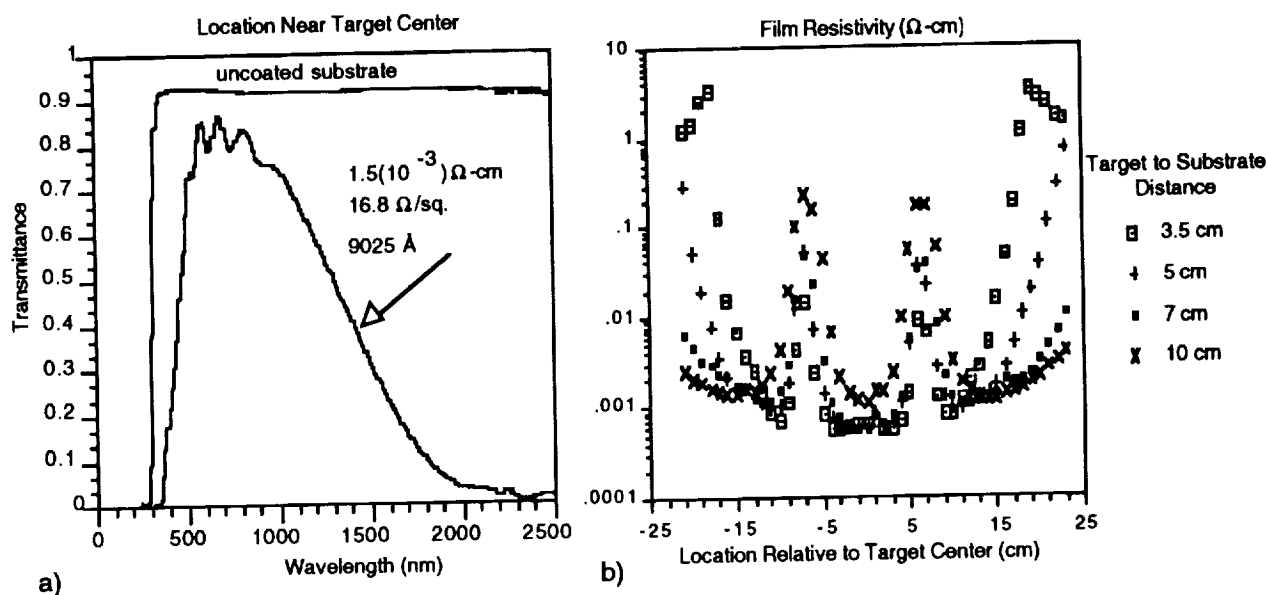


Figure 1 a) Transmittance Spectra for 902.5 nm-Thick ZnO Coating on Glass; b) Film Resistivity as a Function of Distance From the Target Center and Away From the Target

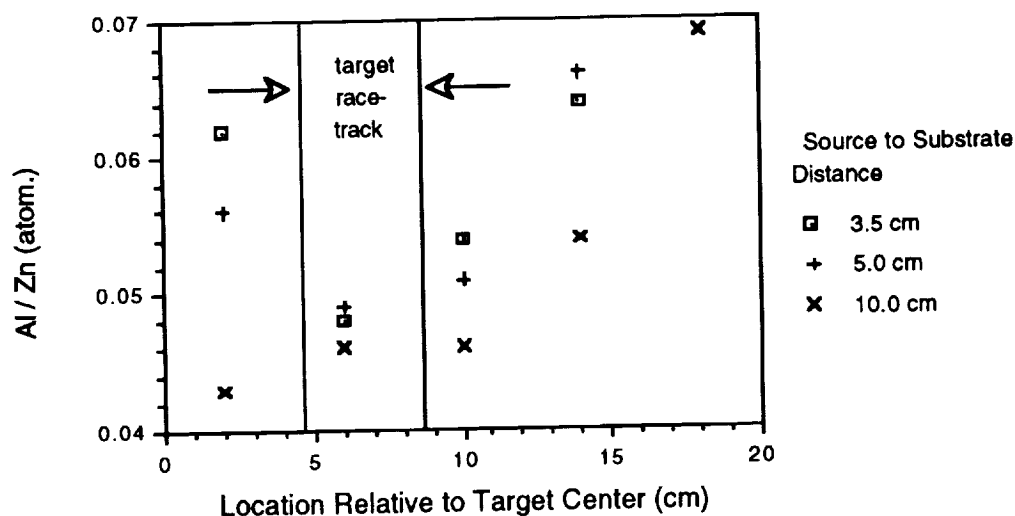


Figure 2 Aluminum/Zinc Ratio (Atomic Percent) as a Function of Distance Away From Target Center (Composition Measured by Wavelength Dispersive X-Ray Spectroscopy (WDS))

Cadmium Telluride

Unlike CIS thin-film devices, CdTe devices are fabricated in the superstrate configuration with entirely wet chemical deposition methods and no vacuum; device structure consists of glass superstrate, transparent conductive oxide, CdS window layer, CdTe absorber, and metal back contact. Using entirely wet chemical processes, thin-film CdTe cells have been fabricated with 6-7% (0.08 cm^2 active area) efficiencies on SnO_2 -coated glass. In this section, a brief overview is presented of the potential scale-up issues related to the CdS solution-growth and CdTe electrodeposition processes.

CdS Window Layer - The CdS deposition process for CdTe thin-film cells is similar to the process for CIS cells in that CdS films are heterogeneously nucleated onto activated surfaces from an aqueous solution containing cadmium salts and thiourea with ammonium as a complexing agent (reaction throttle). For CdTe however, the CdS films are grown on TCO-coated glass substrates with an average thickness between 250 - 320 nm and at a deposition rate of $\sim 180 \text{ nm/hour}$. With a proper selection of the cadmium-to-sulfur ratio and ammonium, which acts as a buffer and a complexing agent for cadmium, film properties can be optimized. CdS quality, in terms of surface adhesion, structure, and yield from a batch process, is directly related to the solubility/precipitation of $\text{Cd}(\text{OH})_2$ and the concentration of unassociated $[\text{Cd}^{2+}]$ cations.

CdS films are reproducibly and uniformly deposited onto 1 ft^2 substrates from a batch, solution-growth process with a $>90\%$ process yield; i.e., minimal waste. For optimum n-type carrier density, proper control of the oxygen/sulfur ratio, and surface activation for the subsequent CdTe electrodeposition step, CdS films are used in the as-deposited condition and are not post heat treated. A typical transmission spectra for CdS on an SnO_2 -coated soda-lime glass is shown in Figure 3. Although there is a shift in the heat treated CdS films to higher wavelengths, the absorption edge for these films is around 520 nm.

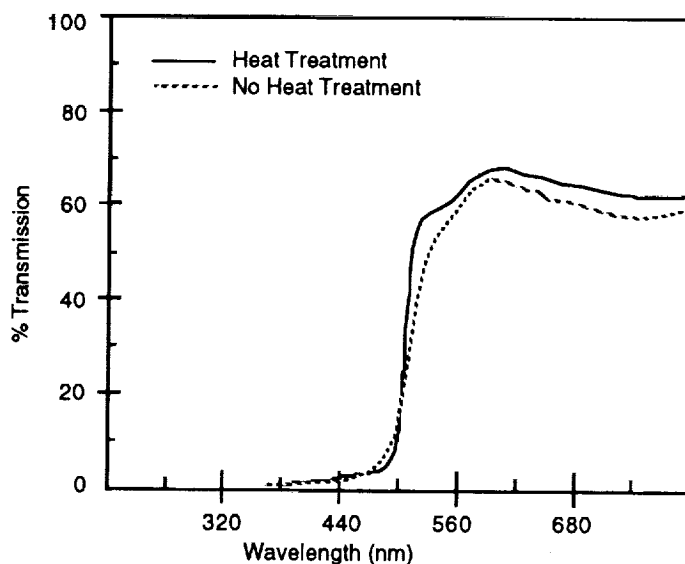


Figure 3 Percent Transmission of Heat Treated and As-Deposited, Solution Grown CdS

CdTe Absorber Layer - Optimally-doped CdTe films are produced by electrodepositing a $1.5 - 2.0 \mu\text{m}$ -thick CdTe layer from an acid bath containing cadmium salts and then heat treating these films at high temperature (400°C) in the presence of CdCl_2 . Although the electrodeposition process was selected

because of its low-cost and potential scalability to larger areas, a number of processing factors, such as cadmium to tellurium ratio in the electrolyte, transport/delivery of cadmium and tellurium to the electrode surface, electrolyte contamination, competing cathodic and anodic reactions, and film resistance of the as-deposited film, can all have a subtle effect on the final electrical quality of the CdTe films (not to mention what effect these factors will have on formation of the n-p junction). In contrast to CdTe films which are deposited by a vacuum, physical vapor deposition process, electrodeposited CdTe films are electrically coupled to the junction partner (i.e., CdS, which is also electrically coupled to a conductive oxide) as electrons are transported through the device during the deposition process. This inherent feature of electrodeposition provides an insitu monitor of CdTe film and device quality and can be used as active feedback control in a commercial scale process.

Through proper control of bath chemistry (pH, cadmium/tellurium ratio, temperature, deposition potential, etc.), CdTe films can be reproducibly deposited over small areas and all of these factors should translate to larger areas, however; as the deposition area increases, film resistivity becomes more critical. Film resistance has a direct effect on the deposition potential which in turn, effects the cadmium to tellurium ratio in the film. With increasing film resistance, the equilibrium potential becomes more noble (positive) and more tellurium is deposited with respect to cadmium. Through-thickness resistivity in the CdS, i.e., from the conductive oxide through the CdS to the CdTe film, is negligible compared to the drop in lateral resistivity which can occur in the TCO over large areas. For example, the voltage drop across a typical 20 ohms/square tin oxide was determined to be ~25 mv/cm. Over a 10 cm area then, the shift in deposition potential would be ~250 mv. A 250 mv shift would correspond to a change in the Cd/Te ratio from 1.0 to a ratio less than 0.8. Without reducing the resistivity of the TCO below 20 ohms/square, uniform films were deposited across 5 cm x 5 cm areas. Although a switch to more conductive TCO films can be made (at the expense of transmittance), lateral film resistivity will still be a significant factor as CdTe devices are fabricated over larger areas.

MODULE DEVELOPMENT

Other than the scaling issues presented above for the cell processing, the remaining issues limiting module and large area array development are the scribing operations which eliminate the hand touch labor of conventional series interconnects and the fabrication of reliable interconnects between modules. Results from the CIS scribing development efforts are presented in this section. A reliable method for bonding interconnects to a molybdenum film has been developed at MMC.

Scribing of the various coating layers of the photovoltaic cells is crucial in the fabrication of monolithically-integrated minimodules. Flow of current occurs from the overlayer transparent conductive oxide (TCO) to the Mo back contact. To enable this current flow in an isolated manner requires the fabrication of scribes in the Mo back contact layer, in the CdS/CIS multilayers to the Mo back contact, and in the ZnO:Al/CdS/CIS multilayers to the Mo back contact. Each of these materials exhibit different thermo-physical properties (absorptance = $f(\text{wavelength } \lambda)$) and mechanical properties, which affects their removal by scribing processes.

Candidate scribing processes that are being investigated at Martin Marietta include: 1) laser; 2) mechanical; and 3) chemical etching between photolithographically-deposited masks.

For removal of material by laser incidence, critical material properties include absorptance and emittance as a function of wavelength, and melting temperature. For the coatings Mo and CdS/CIS, absorptance generally increases as the incident wavelength is reduced. This suggests the use of lower wavelength lasers, such as a frequency-doubled (or quadrupled) YAG ($\lambda=0.54\text{ }\mu\text{m}$ for frequency-doubled) or excimer lasers will more effectively couple with these coatings, resulting in more efficient coating removal. Care must be exercised, however, not to couple with the underlying substrate material, which may result in substrate damage.

An example of a scribe in a $1\text{ }\mu\text{m}$ Mo coating on glass produced by a Q-switched YAG laser ($\lambda = 1.06\text{ }\mu\text{m}$) is shown in Figure 4(a). In general, the scribe edges appear clean and straight with a small amount of Mo cracking or delamination adjacent to the scribe. Excimer processing also resulted in clean scribe edges, although more cracking and flaking of the Mo was observed. Scribes produced by a pulsed Nd-YAG exhibited some glass substrate cracking and larger berms of material adjacent to the scribe than for the other laser methods.

Laser scribing of the combined CdS/CIS multilayers is more difficult, since the desire is to remove the CdS/CIS layers without damaging the Mo back contact. Of all the laser scribing methods, Excimer laser scribing shows the most promise for selective coating removal. Simple mechanical scribing using a synthetic diamond tool or a stainless steel blade has been found to be more effective for selective removal of CdS/CIS from the Mo back contact. Figure 4b shows an example of a scribe in CdS/CIS which shows removal of the multilayers, without extensive damage to the Mo back contact.

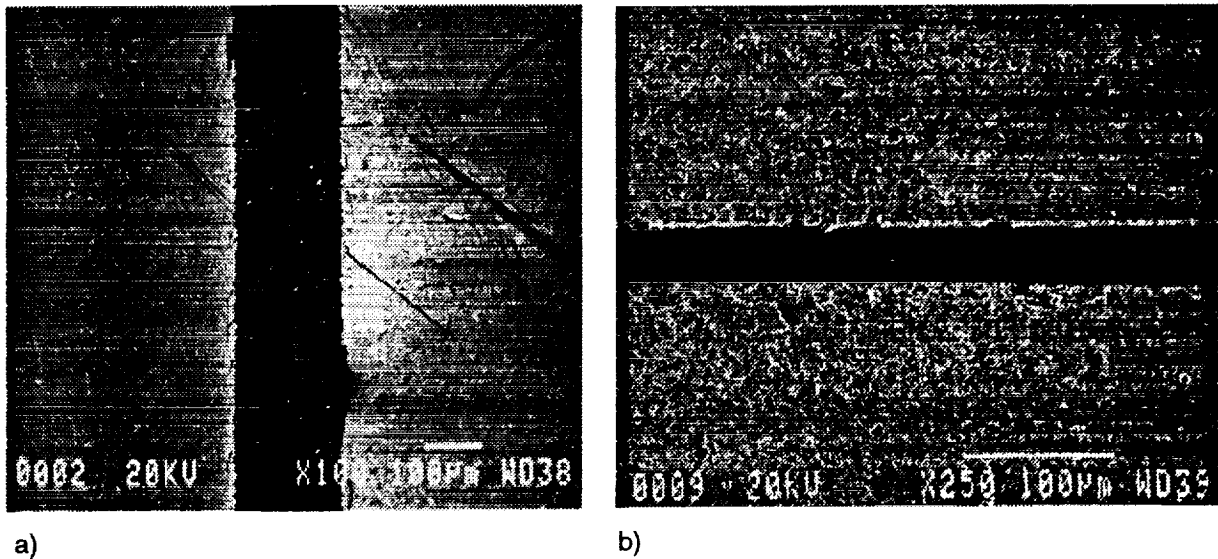


Figure 4 a) SEM Micrograph of Scribe in Mo Coating on Glass Produced by Q-Switched YAG Laser Showing Relatively Clean Scribe Edges and Minor Cracking of Adjacent Mo; b) SEM Micrograph of Scribe in CdS/CIS Coating on Mo-Coated Glass Produced by Mechanical Diamond Scribe Showing Selective Removal of CdS/CIS

QUALIFICATION TESTING

In order to survive the demanding 15-20 year lifetimes in space, thin-film cells and modules need to be first tested in thermal/vacuum and simulated radiation tolerance tests (i.e., solar, electron, proton, etc.). One distinct advantage of CdTe and CIS thin-film polycrystalline devices over silicon and gallium arsenide is the inherent radiation tolerance of the CdTe and CIS semiconducting layers. Long term radiation testing as well as thermal/vacuum cycling of CdTe and CIS cells is in progress.

Just as important as the environmental stability of these devices, however, is the mechanical stability of CdTe and CIS devices and particular, the effect of mechanical forces on the photoresponse of a flexible CIS module. Although preliminary data is available in the literature on the testing of rigid CdTe and CIS thin-film polycrystalline cells in simulated space environments and actual flight experiments, little is known of the effects of mechanical stresses and strains on the electrical behavior of a polycrystalline device. An effort is in progress to test the I-V and spectral response of flexible CIS cells before, during, and after the application of a cyclic bending force.

SUMMARY

An overview of the current efforts at MMC to develop large-scale manufacturing processes for both CIS and CdTe thin-film polycrystalline cells and modules is presented with an emphasis on those issues in each process that are critical to scalability/manufacturability. Except for the CdS window layer, all films in the CIS devices are being deposited by a DC magnetron sputtering system; large-area uniformity was also demonstrated for all the processing steps with the cylindrical magnetron sputtering system. CdTe cells were fabricated entirely by low-cost, wet chemical methods and small area efficiencies on SnO₂-coated soda-lime glass were on the order of 7%. Scalability issues were identified for the CdTe electrodeposition process.

Since a major concern in the fabrication of monolithically integrated modules is the scribing operation, results from laser scribing the CIS back contact and mechanically scribing the CIS/CdS layers are presented. To evaluate emerging CIS technology, Martin Marietta, in cooperation with the National Renewable Energy Laboratory, designed and fabricated a CIS flight experiment with cells based on NREL's selenized bilayer process which has demonstrated 16.4% efficiency in AM1.5 insolation this year.

REFERENCES

1. J. Hedstrom, H. Ohlens, M. Bodegard, A. Kylner, L. Stolt, D. Hariskos, M. Ruckh, H. Schock, 23rd IEEE PVSC, 364 (1993).
2. M. Conteras, J. Tuttle, D. Du, Y. Qi, A. Swartzlander, A., Tennant, and R. Noufi, Appl. Phys. Lett. 63e(13) (1993).
3. C. Ferekides, J. Britt, Y. Ma, and L. Killian, 23rd IEEE PVSC, 389 (1993).
4. L. Chung Yang and A. Rockett, J. Appl. Phys., 75(2) 1185 (1994).

AMORPHOUS SILICON THIN FILMS: THE ULTIMATE LIGHTWEIGHT SPACE SOLAR CELL

G.J. Vendura, Jr., M.A. Kruer, H.H. Schurig, M.A. Bianchi, and J.A. Roth
TRW Space and Technology
Redondo Beach, California

ABSTRACT

Progress is reported with respect to the development of thin film amorphous (α -Si) terrestrial solar cells for space applications. Such devices promise to result in very lightweight, low cost, flexible arrays with superior end of life (EOL) performance. Each α -Si cell consists of a tandem arrangement of three very thin p-i-n junctions vapor deposited between film electrodes. The thickness of this entire stack is approximately $2.0\mu\text{m}$, resulting in a device of negligible weight, but one that must be mechanically supported for handling and fabrication into arrays. The stack is therefore presently deposited onto a large area (12 by 13 in.), rigid, glass superstrate, 40 mil thick, and preliminary space qualification testing of modules so configured is underway. At the same time, a more advanced version is under development in which the thin film stack is transferred from the glass onto a thin (2.0 mil) polymer substrate to create large arrays that are truly flexible and significantly lighter than either the glassed α -Si version or present conventional crystalline technologies. In this paper the key processes for such effective transfer are described. In addition, both glassed (rigid) and unglassed (flexible) α -Si cells are studied when integrated with various advanced structures to form lightweight systems. EOL predictions are generated for the case of a 1000 W array in a standard, 10 year geosynchronous (GEO) orbit. Specific powers (W/kg), power densities (W/m²) and total array costs (\$/ft²) are compared.

INTRODUCTION

During the next ten years, spacecraft power requirements will grow significantly over the presently typical 1 to 4 kW EOL systems. Also, more interest will be focused upon smaller and lighter systems in the 0.1 to 1.5 kW range. Finally, the proliferation of small, less expensive launch vehicles will require low-mass, low cost, power sources. Current crystalline silicon technology using 8 mil thick devices is too heavy, costly and large to support higher power levels on satellites thrust into space by existing and planned vehicles. Thin, 13.5% efficient, silicon cells and even higher efficiency gallium arsenide and indium phosphide cells reduce weight and area but increase cost. New generation lightweight photovoltaic devices are required to meet this challenge (ref. 1). These new devices, by nature, are expected to be both enhancing and enabling: enhancing by offering advantages in power, weight and cost compared to traditional crystalline solar cells in existing satellite designs for conventional orbits; enabling by extending array and mission capability beyond the present limitations of such space systems.

For this reason, thin film solar cells are presently generating intense interest within the space community. Those technologies that have already enjoyed significant development for terrestrial applications are especially attractive. Both α -Si and copper indium diselenide (CIS) fall into this category, but of the two, α -Si is by far the more advanced (ref. 2-3). Very large area α -Si cells and integrated modules are already routinely manufactured for terrestrial applications with AMO efficiencies of 8 to 10%. Although this is considerably less than standard 13.5 and 18.5% Si and GaAs/Ge figures, the material's greater radiation resistance, ultra light weight, low cost, flexibility and the ability to be incorporated into existing, well-developed, lightweight, satellite array structures makes α -Si not only a viable but also a potentially superior alternative. Significantly, the cells can be interconnected in various series and parallel configurations by means of standard semiconductor monolithic integration techniques resulting in superior packing densities and the reduction in the yield and cost disadvantages associated with numerous discrete parts and corresponding handling operations.

α -Si SPACE SOLAR CELL APPROACH

The α -Si solar cell chosen for such space development, shown in Figure 1, is routinely fabricated by Solarex Thin Films and allows the maximum leverage of existing terrestrial technology (ref. 4). The active material consists of a stack of three individual α -Si p-i-n cells sandwiched between thin electrodes. The upper electrode of SnO_2 is transparent to incident light, while the back electrode of silver is opaque. The three α -Si cells are not compositionally identical. Instead, uppermost and lowermost devices are carbon and germanium alloys respectively to allow for increased collection efficiency by utilizing a broader segment of the solar spectrum. The entire stack has a total cross section of only $2.0\mu\text{m}$. However, the commercial product is deposited upon a 40 mil superstrate of either soda lime or borosilicate glass as a means of mechanical support during fabrication and handling. Although both single junction and double junction variations of this device are manufactured on superstrates as large as 4 square feet, the baseline space product considered in this study is limited to 12 by 13 in.

The effort to develop this terrestrial commercial product into a device suitable for space can be divided into two major phases:

I. Development and qualification testing of these glassed 12 by 13 in. terrestrial cells to create a usable, rigid space product. Although the superstrate contributes significantly to overall weight, results of early cost and power trades indicate advantages for certain missions.

II. Development of materials and additional processes for transferring 3 by 3 in. areas from the glass superstrate onto a thin, polymer substrate to demonstrate a flexible space product. Earlier stages will focus primarily on mechanical issues, while later stages will address both mechanical and electrical stability. A later phase will concentrate on the scaling up of these processes to transfer 12 by 13 in. and larger areas.

The most important aspects of the Phase I effort center on radiation and temperature effects and long term stability. Studies by Woodyard and co-workers indicate that radiation damage, in large part, may be reversed by annealing (ref. 5). Also, attention must be focused on the degradation of α -Si output due to photons (the Staebler Wronski effect) and its reduction (ref. 6-7). Significant adjustments in the manufacturing sequence have already been made by Solarex and will continue to be considered to minimize this effect.

ADVANCED PROCESSES

Phase II, addressed simultaneously with Phase I to save time, focuses on the materials and process development of two key additional processes required for transfer: release and liftoff. These processes are illustrated in Figure 2 on the right, while the standard commercial sequence is shown on the left. The release process consists of sputter deposition of carefully controlled thin film layers directly onto the glass superstrate to partially isolate it mechanically and chemically from the commercial device that is deposited subsequently. This limits the adhesive strength which, in turn, facilitates eventual separation. The liftoff process, on the other hand, involves the attachment of polymer and other films to the back surface of the commercial stack by means of a thermo-compression technique. The number and orientation of these backing layers are carefully balanced to create the right relative mismatch in the various coefficients of thermal expansion. As a result of differential contraction upon cooling, separation at the release interface is accomplished and the solar cell is thereby transferred from the rigid, glass superstrate onto the flexible, laminated substrate.

The release process is dependent upon very specialized, large-scale sputtering equipment. Either of two custom built sputtering machines can be used, depending upon solar cell size and quantity. Although cells of 12 by 13 in. are presently earmarked for the baseline process, individual device areas are expected to eventually increase to 4 and 8 ft^2 . It is advantageous to load large batches of such cells into a single machine for economy.

The chamber of the first unit is 6.0 by 6.0 by 6.0 ft. and can be evacuated to the low 10^{-7} torr range by a 16 in. cryopump. The machine can operate in RF or DC modes and is equipped with three 5.0 by 20.0 in. targets, capable of co-deposition onto three 20.0 by 20.0 in. substrates rotating via a planetary. Operation is computer driven and monitored to permit unattended deposition of multiple layers. Control devices include an in situ particle counter, a quartz crystal thickness monitor, a residual gas analyzer and an optical monitor to track reflective interference to a quarter of a wavelength.

The second sputtering machine consists of a chamber with a floor area 20 by 12 ft. and a ceiling 15 ft. high. Overnight evacuation to the low 10^{-7} torr is achieved by three 16 in. and one 48 in. cryopumps coupled to a Woods Root blower. The machine is fitted with three 5 by 40 in. planar cathodes that move in a raster pattern from 0.5 to 36 in. away from a substrate as large as 18 ft. long and 12 ft. high. Co-deposition is possible via two of the three targets. By means of another cathode assembly, 10 in. round, non-planar shapes can be coated. This machine can also operate in either RF or DC modes, is similarly computer controlled and monitored, and is fitted with a residual gas analyzer, a quartz crystal monitor and a particle counter.

An earlier version of the overall release process involved the deposition in the smaller machine of three separate layers, shown in Figure 3a. After cleaning, the glass superstrate was loaded into the chamber which was then evacuated to 10^{-6} torr. A 400Å layer of binder material was deposited. The purpose of this film was to promote adhesion between the glass surface and subsequent materials: a release layer of approximately 800Å followed by a 1.5 μm cap of SiO_2 . The purpose of the release layer is to provide a release interface (R.I.) - a plane of significantly weaker chemical and mechanical adhesion compared to all other interfaces - so that separation can eventually be achieved at this surface.

After deposition of these three layers, the treated glass was shipped to Solarex, where the α -Si solar cell components (Figure 1) were added. The device was then returned. Initial liftoff experiments, intended to separate the cell at the R.I., produced mixed results. In some cases the solar cell did not release at all; in others, release was uneven. EDAX and SEM investigations of suspect areas of the surface seemed to indicate atomic diffusion of the superstrate across the release layer resulting in pinning - localized areas of high adhesion - at the R.I. Since the commercial fabrication sequence involves SnO_2 and contact annealing processes that approach the softening point of glass, a high temperature mechanism was suspected.

To eliminate this pinning without affecting the solar cell manufacturing sequence, the release process was modified to include a 400Å diffusion barrier as shown in Figure 3b. An additional 800Å layer varying in composition from barrier to release layer materials was also necessary to ensure the R.I. remained the weakest link in the chain of interfaces in order to prevent separation at the barrier-release layer surface instead.

Again the treated glass was shipped to Solarex and returned with solar cells attached. Experiments demonstrated significantly improved results, although the process continues to be developed further.

The liftoff process involves the attachment of five plies of flexible material to the back surface of the cell in three stages. As shown in Figure 4, three layers of 1.0 mil polymer are interspersed with two 1.0 mil layers of fiberglass cloth. In the first stage, all but one polymer layer are aligned, placed in vacuum, degassed and subjected to a two step cure process. The second stage consists of surface preparation of the Ag contact on the back of the solar cell, followed by mechanical placement of the remaining polymer film. In the third stage, all parts are joined into a single unit by an additional vacuum, degas, and cure sequence. Under ideal conditions, upon cooling, the solar cell releases spontaneously and cleanly at the R.I. due to a differential in the coefficients of thermal expansion (CTE).

The CTEs are balanced by careful selection of layer composition, thicknesses and orientations. For example, the two fiberglass cloth plies are aligned in different directions, one at 0,90 degrees and the other at ± 45 degrees, as implied by the dissimilar slash patterns in Figure 4. Another key concern is the complete elimination of air bubbles during processing. Air bubbles result in voids - points of no adhesion between the flexible substrate and the solar cell. Thus, upon release of the bulk of the α -Si, areas under

the voids can remain behind, creating pinholes in the surface of the cell which in turn may result in shorting and power degradation.

Figure 4 is representative of one of several variations of the liftoff process still under development. Other variations use different quantities of layers or plies of different thickness. The objective, however, is to eliminate layers or to use thinner plies so that the total flexible substrate is approximately 2.0 mil.

LIGHTWEIGHT STRUCTURES

α -Si cells, both glassed (Phase I) and flexible (Phase II), are suitable for incorporation into conventional and low mass arrays. For the purposes of comparison, a 1000 W array was considered. In the first case a state-of-the-art 0.5 in. thick Al honeycomb with 5.0 mil graphite face sheets and a single layer of 2.0 mil Kapton to insulate the solar cells is assumed. In addition, two existing, well-developed lightweight structures were studied. The first is an adaptation of the Advanced Photovoltaic Solar Array (APSA) (ref. 8). The original APSA consisted of a 5.4 kW, 15.25 by 2.81 m, mast-deployed, 42 panel, prototype wing as shown in Figure 5 (ref. 9). This unit was populated by 2.2 mil thick crystalline silicon solar cells, 2.0 by 4.0 in. area, with 2.0 mil cover glasses. The efficiency of these cells was 13.5%. A key lightweight feature is the employment of a 2.0 mil carbon loaded Kapton substrate, accordion folded for stowage during launch. Despite this lightweight blanket, however, major contributions to mass resulted from the deployment mast, the frame and the stowage container. Since this study concerns an array less than 25% of the original APSA area, wherever possible, features such as this container size were scaled down accordingly.

Another advanced lightweight structure involved using a TRW developed and tested framed membrane technology. Main features of such a system, highlighted in Figure 6, include a rigid membrane solar cell support consisting of a very thin laminate with a foam core and high modulus, graphite fiber reinforced plastic (GFRP) face sheets. Kapton is used to insulate the solar cells from the membrane surface. The frame tubes are transfer molded from a mixture of high modulus and high strength GFRP materials. To create a panel structure subassembly, the various GFRP components are joined together through a precision bonding process without the need for mechanical fasteners. Such a panel design is adaptable for use with cells of various types, sizes and thicknesses and can be readily scaled up or down as required. An advanced version of the system involves lighter frame and substrate elements. Indeed, an adaptation of the system, using a different rigid laminate and no frame whatsoever, was incorporated in the Earth Observing System (EOS) program.

The ultimate lightweight array, the Ultra Light Film Array (ULFA), is presently limited to satellites ≤ 1000 W. It includes a 2.0 mil flexible Kapton blanket, but not the relatively heavy components of either the APSA or framed membrane designs. In this case, the blanket is deployed and supported by lightweight strain energy hinges. Although development of such a structure is not as mature as APSA and membrane technologies, it is nonetheless included in this study for comparison purposes.

RESULTS

Results are in the form of EOL performance predictions of satellite systems incorporating various α -Si and conventional crystalline solar cells populating the four structures described. In all cases, a standard, 10 year GEO mission is assumed for the nominal 1000 W array. Weight of stowage and deployment hardware is included. In the case of α -Si arrays, cell interspacing was set at 120 mil, while for crystalline devices it was 30 mils. Also, whenever possible, proven cell and system design factors were used. For example, empirical loss factors were applied to account not only for temperature and radiation degradation, but also for more obscure losses such as Staebler Wronski (SW), packing, wiring, installation, cycling, cover glass darkening, etc. All comparisons are thus at a system level of performance as opposed to often quoted device or cell level performance. It is noted, however, that all systems are not universally applicable to all cells, and in certain specific cases some overdesign and underdesign is inevitable. Therefore, the accuracy of results is estimated to be $\pm 10\%$.

Data are summarized in Table 1 for 13 different systems. Rows 1 through 4 present data for unannealed α -Si having 4 different cover glass thicknesses: 40 mils, 8 mils, 2 μ m and 1 mil. Systems 5 through 7 outline crystalline Si, while 8 and 9 highlight crystalline GaAs/Ge. Rows 10 through 13 examine the same α -Si systems as 1 through 4, but this time the systems are designed for self annealing, resulting in considerable radiation and Staebler Wronski loss recovery. Details such as cell type, size, device and cover thicknesses and BOL efficiency, η , are presented in the leftmost columns. For α -Si, BOL η was assumed to be a conservative 10.0% at AMO and 28°C. Crystalline η , on the other hand, varied from 12.2 to 18.2% as tabulated. Staebler Wronski degradation is assumed at 15% for unannealed α -Si and 5% for the same cells when annealed. In the table, honeycomb, membrane, APSA and ULFA data then follow in terms of three key parameters: specific power (W/kg), power density (W/m²) and areal density (lbs/ft²).

In generating these data for the systems involving α -Si, radiation degradation behavior in response to orbital environment was calculated from a model using the standard approach of equating ionization and displacement damage with P/Po power reduction. This technique uses existing data for P/Po from 1MeV proton fluences and extends it to other proton energies. P/Po is defined as a function of 1MeV protons similar to crystalline technology, using 1MeV electrons as the conversion parameter (ref. 10).

The α -Si comparison is presented graphically in Figure 7 in which the structural density (the sum of the system's areal density and the weight of peripheral hardware -hinges, booms, deployment hardware, etc.- spread over array area) is plotted as a function of specific power. As shown, even cells with 40 mil covers generate respectable powers when compared with the ~15 W/kg figure for a crystalline silicon system (not shown) using less than the state-of-the art honeycomb presented in this study. As expected, α -Si with 8 mil covers performs considerably better, especially in the case of APSA in which best results are 77.7 and 83.2 W/kg for unannealed and annealed cells respectively. Note that because of weight, only 2 μ m and 1 mil α -Si cells are appropriate for application to the ULFA structure. Here, results as high as 340.9 W/kg are indicated for the annealed 2 μ m cover system. Of note is the fact that 1 mil of cover glass and/or annealing makes a considerable difference over an unannealed 2 μ m α -Si array incorporated in any structure in the GEO environment.

In Figure 8, less-than-optimal 8 mil covered α -Si is compared to the best of the crystalline Si and crystalline GaAs/Ge systems. The crystalline Si cell used was a 2.5 x 5.0 cm, 2.7 mil thick device with both a back surface field and reflector (BSFR) and a 2.0 mil cover. The GaAs/Ge device was 4.0 x 4.4 cm, 5.5 mils thick, with a 3.0 mil cover. The curves demonstrate that both unannealed and annealed α -Si is superior at structural densities approaching APSA. At higher structural densities, however, α -Si and crystalline Si are comparable, while GaAs/Ge is superior.

In Figure 9, the same crystalline systems are compared with those for the α -Si cell covered with 1 mil of glass. Here the ULFA structure is inappropriate for all but the α -Si case. Best results are 266.5 and 288.3 W/kg for unannealed and annealed devices respectively.

Specific power alone, of course, is not the only major point of comparison. Depending on mission and program constraints, power density, and areal density can also be key considerations. Table 1 also offers these data for the 13 systems under study.

Another essential factor is cost. System cost, typically in \$/W, involves the sum of three separate figures: cell materials, structural materials and recurring fabrication labor. Only the first of these is presented in Table 1. The prices of the crystalline cells are well-established, while, admittedly, α -Si figures are rough estimates based upon current commercial terrestrial production prices. Depending on cover glass, these figures may be off by a factor as high as 5. Nevertheless, savings associated with α -Si compared to crystalline systems, depending on choice, readily approach an order of magnitude.

SUMMARY

An approach is described for developing very lightweight α -Si solar cells for space by leveraging progress of terrestrial devices. Glass and flexible versions are being addressed simultaneously. Critical release and liftoff processes for transferring such cells from a rigid 40 mil superstrate onto a flexible 2.0 mil substrate are presented. EOL performance predictions are generated based upon a 10 year GEO mission of a 1000W array incorporating different α -Si and crystalline cell configurations with four distinct structures. Results demonstrate that specific powers of 266.5 and 288.3 W/kg are achieved when α -Si cells with 1 mil covers, unannealed and annealed respectively, are combined with the ULFA structure. The specific power increases further, to 340.9 W/kg for annealed devices with a 2 μ m cover. These figures are two to five times better than the performance of conventional crystalline solar cells in similar systems for an identical mission.

REFERENCES

- 1) Vendura, Jr., G.J.; Malone, P.; and Crawford, L.: A Novel Lightweight Solar Array: Comparison with Conventional Systems. IEEE 23rd Photovoltaic Specialists Conference, Louisville, KY, May 1993, pp. 1381 - 1385.
- 2) Arya, R.R.; Yang, L.; Bennett, M.; Newton, J.; Li, Y.M.; Fieselmann, B.; Chen, L.F.; Rajan, K.; Wood, G.; Poplawski, C.; and Wilczynski, A.: Status, Progress and Challenges in High Performance Stable Amorphous Silicon Array Based Triple Junction Modules. IEEE 23rd Photovoltaic Specialists Conference, Louisville, KY, May 1993, pp. 790 - 794.
- 3) Basol, B.M.; Kapur, V.K.; Halani, A.; Minnick, A.; and Leidholm, C.: Modules and Flexible Cells of CuInSe_2 . IEEE 23rd Photovoltaic Specialists Conference, Louisville, KY, May 1993, pp. 426 - 430.
- 4) Carlson, D.E.: Market, Manufacturing and Technical Progress in Amorphous Silicon Photovoltaics in the U.S. IEEE 22nd Photovoltaic Specialists Conference, Las Vegas, NV, Oct. 1991, pp. 1207 - 1212.
- 5) Woodyard, J.R.; Landis, G.A.: Radiation Resistance of Thin-Film Solar Cells for Space Photovoltaic Power Solar Cells, 31, 1991, pp. 297 - 329.
- 6) Staebler, D.L.; and Wronski, C.R.: Appl. Phys. Lett. (1977) pp. 292.
- 7) Yamagishi, H.; Asaoka, K.; Nevin, W.A.; Yamaguchi, M. and Tawada, Y.: Light Induced Changes of Amorphous Silicon Solar Cells by Long Term Light Exposure. IEEE 22nd Photovoltaic Specialists Conference, Las Vegas, NV, Oct. 1991, pp. 1342 - 1346.
- 8) Kurland, R.M.; and Stella, P.M.: Demonstration of the Advanced Photovoltaic Solar Array. European Space Power Conference, Florence, Italy, Sept. 1991, pp. 675 - 680.
- 9) Stella, P.M.; and Kurland, R.M.: Operational Considerations of the Advanced Photovoltaic Solar Array. 27th Intersociety Energy Conversion Engineering Conference, San Diego, CA, 1992, pp. 6.29 - 6.34.
- 10) Tada, H.Y.; Carter, Jr., J.R.; Anspaugh, B.E.; and Downing, R.E.: Solar Cell Radiation Handbook, Third Edition, National Aeronautics and Space Administration, Jet Propulsion Laboratory, Nov. 1982.

TABLE 1: PERFORMANCE COMPARISON: CELLS, STRUCTURES & SYSTEMS

EOL, 10 Year, GEO									Rigid Honeycomb 0.433 lb/ft ² **			Framed Membrane 0.300 lb/ft ² **			APSA 0.133 lb/ft ² **			ULFA 0.032 lb/ft ² **		
No	Cell Type	Anneal	Cell Size	Cell Thick.	Cover Thickness	BOL η (%)	SW Loss	Cell* Cost (\$/W)	Spec. P. (W/kg)	P. Densit (W/m ²)	Areal D. (lbs/ft ²)	Spec. P. (W/kg)	P. Densit (W/m ²)	Areal D. (lbs/ft ²)	Spec. P. (W/kg)	P. Densit (W/m ²)	Areal D. (lbs/ft ²)	Spec. P. (W/kg)	P. Densit (W/m ²)	Areal D. (lbs/ft ²)
1	α -Si	N	12x13 in.	2 μ	40 mils	10.0	0.85	2.50	19.0	90.1	0.972	21.8	88.2	0.828	27.8	81.7	0.602	n/a	n/a	n/a
2	α -Si	N	12x6.5 in.	2 μ	8 mils	10.0	0.85	8.50	35.3	97.2	0.565	45.4	95.2	0.429	77.7	88.2	0.233	n/a	n/a	n/a
3	α -Si	N	12x13 in.	2 μ	2 μ	10.0	0.85	15.00	3.9	8.8	0.465	5.4	8.7	0.331	11.6	8.0	0.142	28.4	8.8	0.063
4	α -Si	N	12x13 in.	2 μ	1 mil	10.0	0.85	20.00	42.7	99.2	0.476	58.2	97.2	0.342	121.2	90.0	0.152	266.5	97.2	0.075
5	Si BSR	N	2.5x5.0 cm	8.0 mils	2 mils	12.2	1.00	247.00	33.3	89.6	0.551	42.3	88.3	0.428	59.7	81.0	0.278	n/a	n/a	n/a
6	Si BSFR	N	2.5x5.0 cm	8.0 mils	2 mils	14.6	1.00	269.00	32.3	87.0	0.551	41.1	85.8	0.428	57.6	78.2	0.278	n/a	n/a	n/a
7	Si BSFR	N	2.5x5.0 cm	2.7 mils	2 mils	13.5	1.00	526.00	37.7	92.7	0.503	49.3	91.3	0.379	73.3	81.9	0.229	n/a	n/a	n/a
8	GaAs	N	4.0x4.4 cm	5.5 mils	3 mils	18.2	1.00	1350.00	45.0	131.2	0.597	56.3	127.4	0.463	77.0	117.7	0.313	n/a	n/a	n/a
9	GaAs	N	4.0x4.4 cm	8.0 mils	4 mils	18.2	1.00	909.00	41.2	134.0	0.666	50.4	127.9	0.520	65.9	119.1	0.370	n/a	n/a	n/a
10	α -Si	Y	12x13 in.	2 μ	40 mils	10.0	0.95	2.50	20.3	96.5	0.972	23.4	94.5	0.828	29.8	87.5	0.602	n/a	n/a	n/a
11	α -Si	Y	12x6.5 in.	2 μ	8 mils	10.0	0.95	8.50	37.8	104.2	0.565	48.7	102.0	0.429	83.2	94.5	0.233	n/a	n/a	n/a
12	α -Si	Y	12x13 in.	2 μ	2 μ	10.0	0.95	15.00	46.9	106.3	0.465	64.4	104.1	0.331	139.5	96.4	0.142	340.9	105.2	0.063
13	α -Si	Y	12x13 in.	2 μ	1 mil	10.0	0.95	20.00	45.7	106.3	0.476	62.3	104.1	0.342	129.8	96.4	0.152	266.3	105.2	0.075

* = cell OR module

** = Areal Density + Peripheral Density

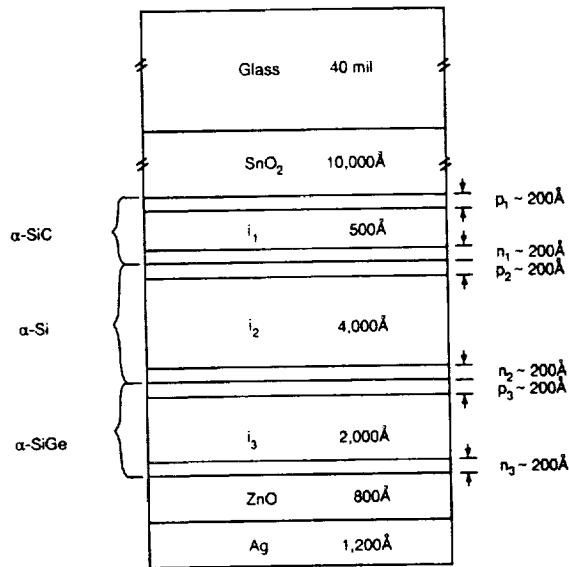


Figure 1: Cross Section of Triple Junction Solar Cell

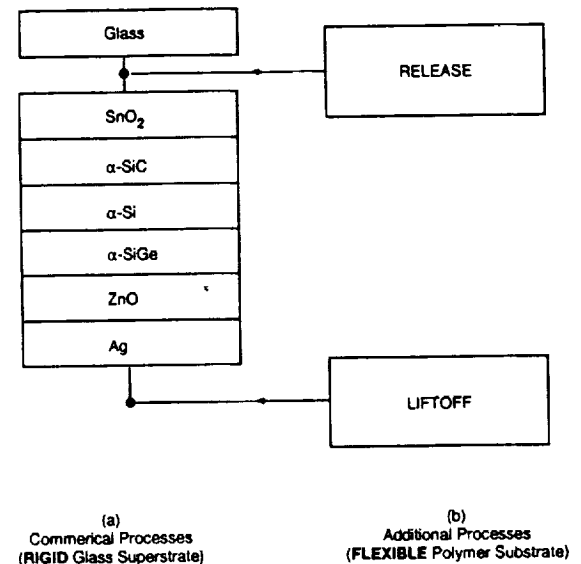
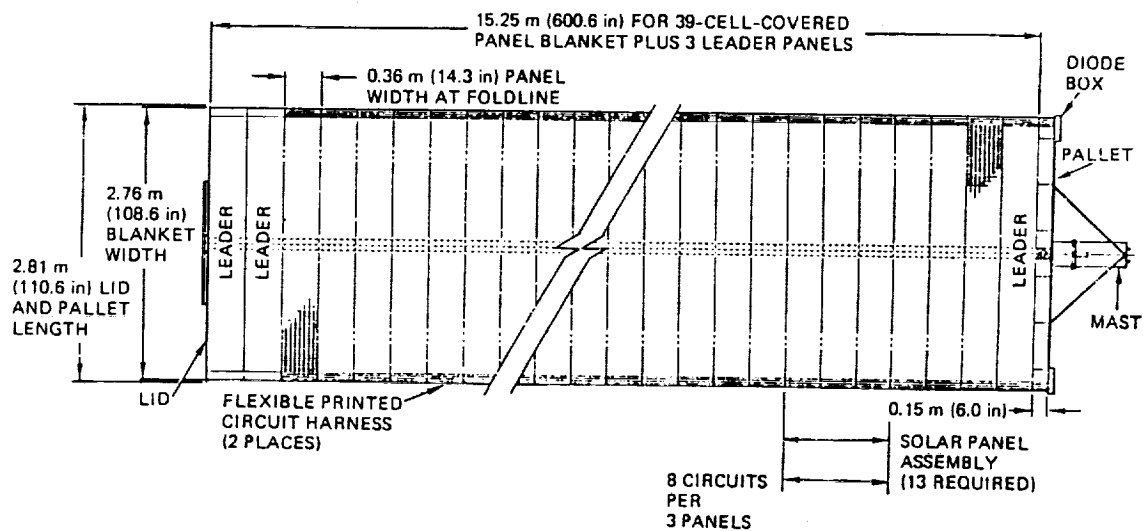
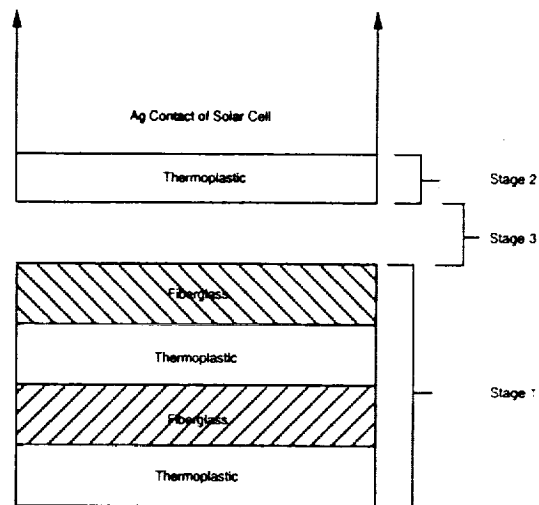
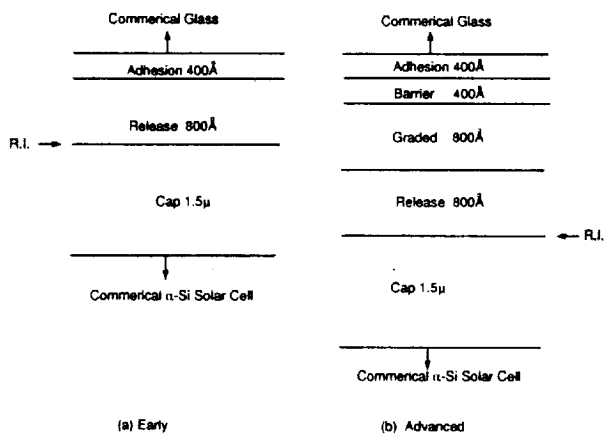


Figure 2: Total α -Si Processes



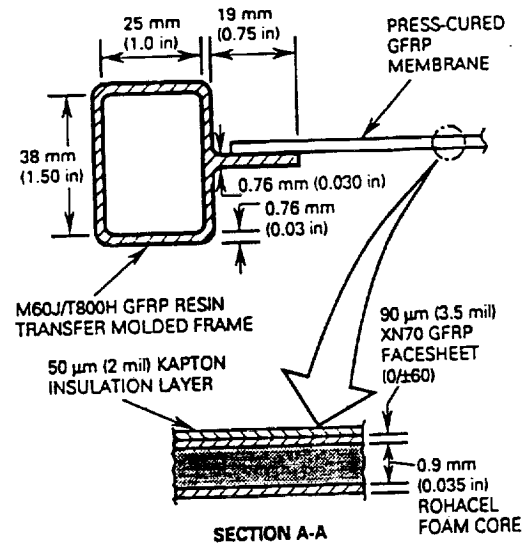


Figure 6: Framed Membrane Structure

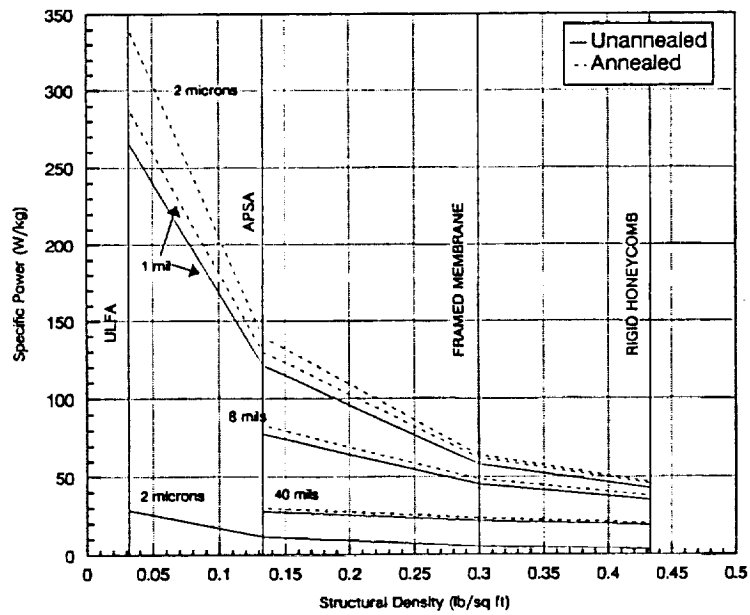


Figure 7: Comparison - α -Si vs. Structure

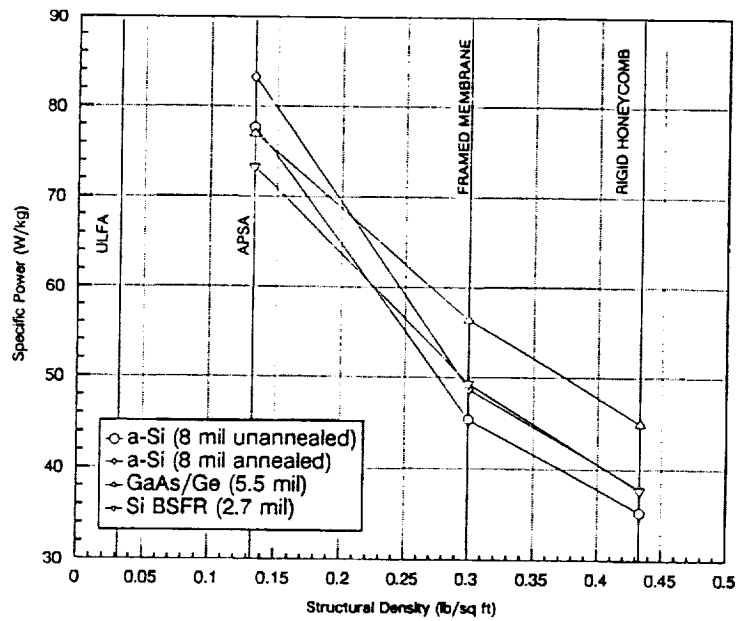


Figure 8: Comparison - Conservative α -Si with Best Crystalline vs. Structure

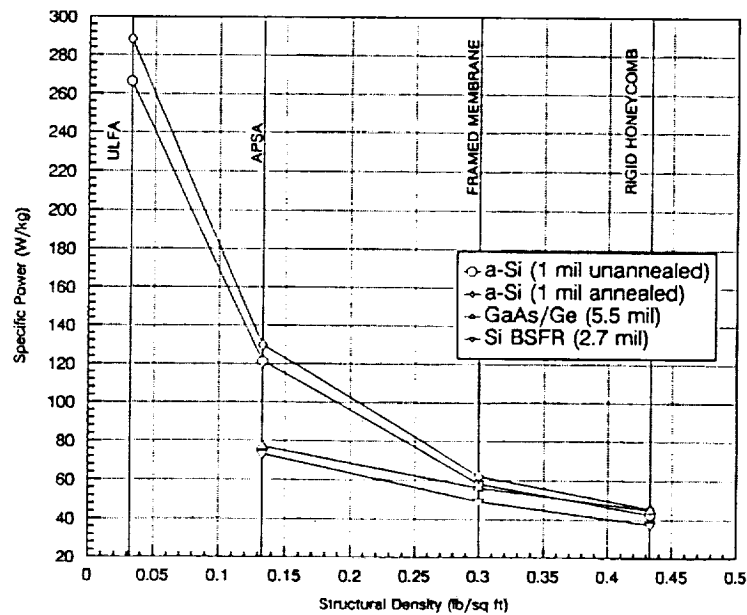


Figure 9: Comparison - Best Cases vs. Structure

MODELING OF HIGH EFFICIENCY SOLAR CELLS UNDER LASER PULSE FOR POWER BEAMING APPLICATIONS

Raj K. Jain¹
NASA Lewis Research Center
Cleveland, Ohio

and

Geoffrey A. Landis²
NYMA, Inc.
Brook Park, Ohio

SUMMARY

Solar cells may be used as receivers for laser power beaming. To understand the behavior of solar cells when illuminated by a pulsed laser, the time response of gallium arsenide and silicon solar cells to pulsed monochromatic input has been modeled using a finite element solar cell model.

INTRODUCTION

Solar cells have been used to convert sunlight to electrical energy for many years and also offer great potential for non-solar energy conversion applications. Their greatly improved performance under monochromatic light compared to sunlight, makes them suitable as photovoltaic (PV) receivers in laser power beaming applications. Laser beamed power to a PV array receiver could provide power to satellites, an orbital transfer vehicle, or a lunar base (ref. 1). Gallium arsenide (GaAs) and indium phosphide (InP) solar cells have calculated efficiencies of more than 50% under continuous illumination at the optimum wavelength (ref. 2). Currently high power free-electron lasers are being developed which operate in pulsed conditions. Understanding cell behavior under a laser pulse is important in the selection of the solar cell material and the laser.

An experiment by NASA Lewis and JPL at the AVLIS laser facility in Livermore, CA presented experimental data on cell performance under pulsed laser illumination (refs. 3 and 4). Reference 5 contains an overview of technical issues concerning the use of solar cells for laser power conversion, written before the experiments were performed. As the experimental results showed, the actual effects of pulsed operation are more complicated. Reference 6 discusses simulations of the output of GaAs concentrator solar cells under pulsed laser illumination. The present paper continues this work, and compares the output of Si and GaAs solar cells.

¹Work funded by the National Research Council - NASA Research Associateship Programs and a NASA Research Grant (NAG3-1466) at the University of Toledo.

²NYMA Inc. under a NASA Contract.

CELL SIMULATION RESULTS

Figure 1 shows the cell designs and the laser pulse simulated. For simplicity, the laser pulse was assumed to be square. Most of the results have been calculated for a peak intensity of 50 W/cm^2 , which corresponds to nearly 1000 suns concentration. The PC-1D computer code, a finite-element simulation of carrier transport in semiconductor devices (ref. 7), was used to analyze the cell current during and after the pulse for various conditions.

The GaAs solar cell simulated was a concentrator p^+n cell with an efficiency of 27.5% under AM1.5D, 1000 sun illumination. The current output was observed to be linear with laser intensity from 500 mW/cm^2 to 500 W/cm^2 . Figure 2 shows the cell short circuit current during and after the laser pulse, for a laser at three different wavelengths. The 511 nm wavelength corresponds to the available copper-vapor laser, 840 nm corresponds to the optimum wavelength for GaAs and also proposed operating wavelength in NASA SELENE project, and 870 nm is near the band edge of GaAs. The decay of the current can clearly be seen to have two distinct components: an initial rapid decay immediately following the laser pulse, followed by an exponential decay with much longer time constant. The amount of initial decay is greatest for the light with the strongest (hence, shallowest) absorption, 511 nm, and is least for the weakly absorbed light at 870 nm. Figure 3 shows this initial decay on a shorter time scale. Here the parameter varied is the operating voltage of the cell. Further results of this simulation can be found in reference 5.

Compared to GaAs, silicon solar cells have much longer minority carrier lifetimes and much weaker optical absorption, resulting in deeper absorption of the light and longer characteristic time constants. A typical silicon solar cell was modeled, with a diffused (erfc profile) n type junction. The efficiency is 17.2% under AM0 (space) illumination, slightly better than cells used in space today, but well below the best efficiencies observed in the laboratory. Efficiency increases to 31.8% for monochromatic light at 900 nm at an intensity of 50 W/cm^2 .

Figures 4 and 5 show the decay of short circuit current of the silicon cell compared with that of the GaAs cell. As expected, the silicon cell shows considerably slower response.

As in the GaAs cell, the decay has a rapid initial decay followed by a slower exponential decay. Figure 6 shows the fit of an exponential to the portion of the decay between 150 and 250 nS after the pulse. The characteristic time constant for this portion of the decay is 360 nS, which is intermediate between the base lifetime of $20 \mu\text{S}$ and the emitter surface lifetime of 11 nS.

Figure 7 shows the short circuit current at different wavelengths. Note that the currents have been normalized; the absolute response is best at 900 nm (peak of 31 A). The response at 1.06μ is poor (peak 3.6 A). As with the GaAs cells, the most weakly absorbed light has the least rapid initial fall-off, and the most strongly absorbed light the most rapid initial fall-off. The response drops by a factor of e over a time scale on the order of 25 nS.

For such a cell, then, we can expect that the silicon cell will tend to integrate the pulsed input into nearly CW output only if the time between pulses is short compared to 25 nS.

The capacitance of a Si cell at zero bias is typically about 100 nF. The series resistance of this 1 cm² cell was taken to be 4 mΩ. The RC time constant for the charge to be removed from the cell under short circuit is thus expected to be about 0.4 nS. This is much shorter than the time scale of the current decay. In actual operation, however, the cell would be connected to an external circuit with associated resistance, inductance, capacitance, and a battery-supplied bias voltage. This external circuit will considerably complicate the output characteristic (refs. 3 and 4).

REFERENCES

1. Landis, G.A.: Space Power by Ground-Based Laser Illumination. IEEE Aerospace and Electronics Systems Magazine, vol. 6, 1991, pp. 3-7.
2. Jain, R.K.: Calculated Performance of Indium Phosphide Solar Cells Under Monochromatic Illumination. IEEE Trans. on Electron Devices, vol. 40, 1993, pp. 1893-1895.
3. Anspaugh, B.; Mueller, R.; Lowe, R.; and Landis, G.: Results of Illuminating Various Solar Cells with Pulsed Laser Beams. JPL Publication 92-25, November 1, 1992.
4. Lowe, R.; Landis, G.A.; and Jenkins, P.: The Efficiency of Photovoltaic Cells Exposed to Pulsed Laser Light. 12th Space Photovoltaic Research and Technology Conference (SPRAT XII), NASA CP 3210, Oct. 1992, pp. 129-146.
5. Landis, G.A.: Photovoltaic Receivers for Laser Beamed Power in Space. Journal of Propulsion and Power, vol. 9, 1993, pp. 105-112; IEEE 22nd Photovoltaic Specialists Conference, Oct. 1991, vol. II, pp. 1494-1502.
6. Landis, G.A.; and Jain, R.K.: Approaches to Solar Cell Design for Pulsed Laser Power Receivers. 12th Space Photovoltaic Research and Technology Conference (SPRAT XII), NASA CP 3210, Oct. 1992, pp. 155-166; 1st Annual Wireless Power Transmission Conference, Feb. 1993, pp. 551-564.
7. Basore, P.A.: PC-1D Version 3: Improved Speed and Convergence. IEEE 20th Photovoltaic Specialists Conference, Sept. 1988, pp. 462-468.

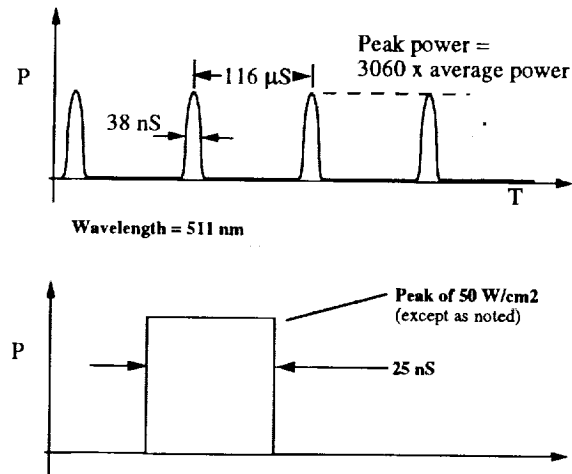


Figure 1A Pulse format of copper-vapor laser (top) and pulse used in computer model (bottom)

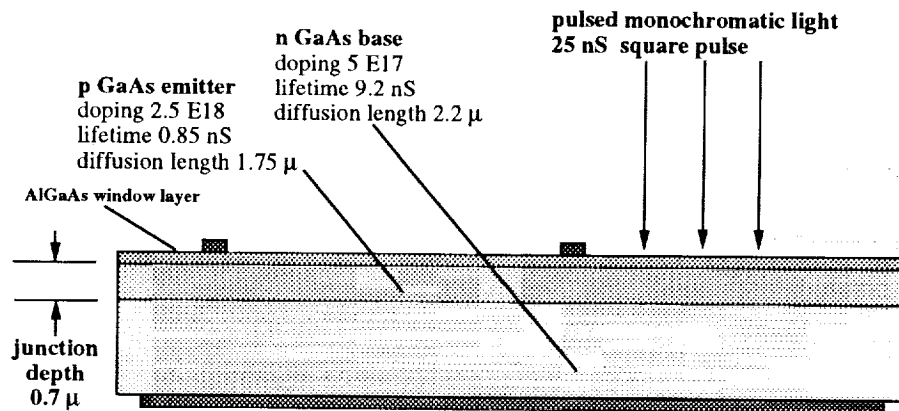


Figure 1B. GaAs solar cell model used for computer simulations.

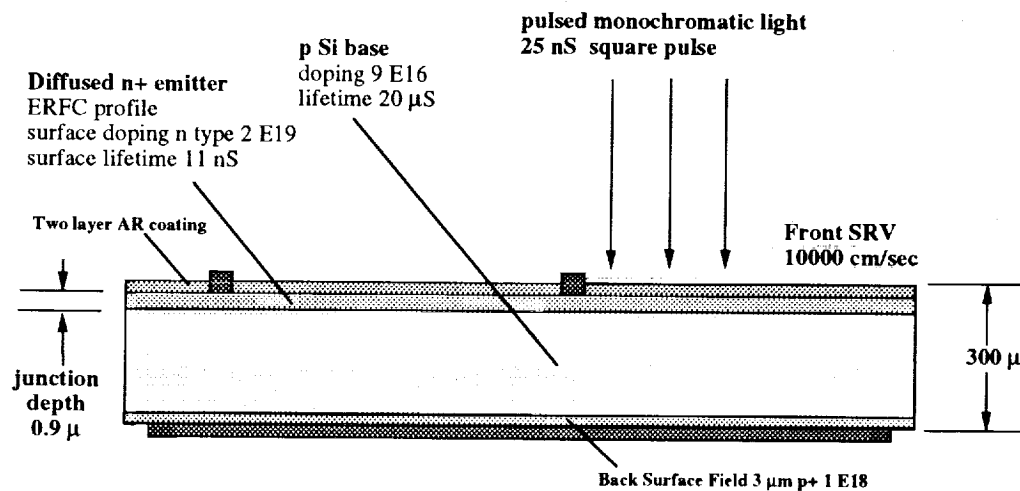


Figure 1C: Silicon solar cell model used for computer simulations.

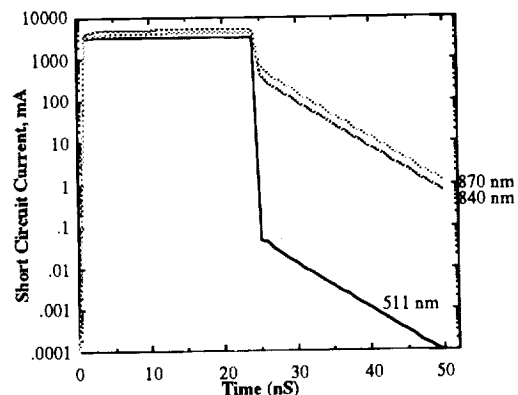


Figure 2. Short circuit current of GaAs cell during laser pulse with incident wavelength as parameter.

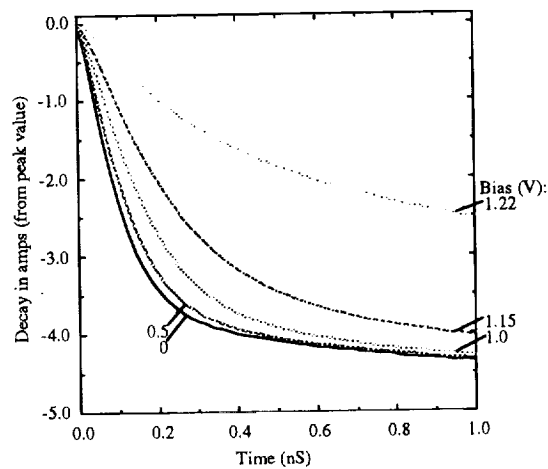


Figure 3. Current decay in first nanosecond of pulse as a function of bias (linear scale; current measured a decrease from illuminated value.) Wavelength 840 nm.

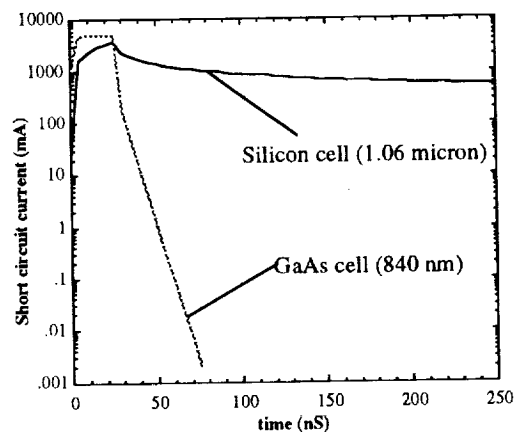


Figure 4: Comparison of Si and GaAs short-circuit current response to 25 nS pulse

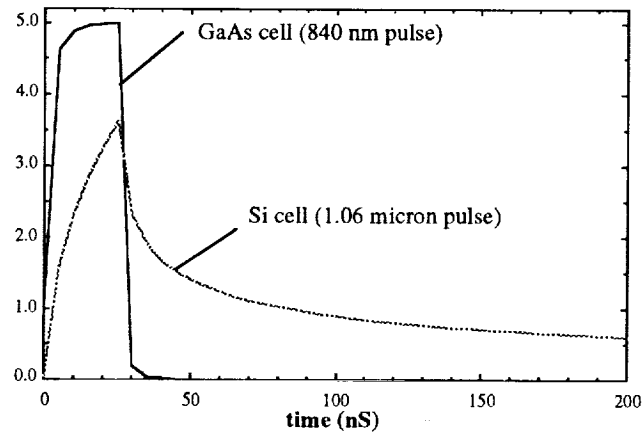


Figure 5: Comparison of Si and GaAs short-circuit current response to 25 nS pulse

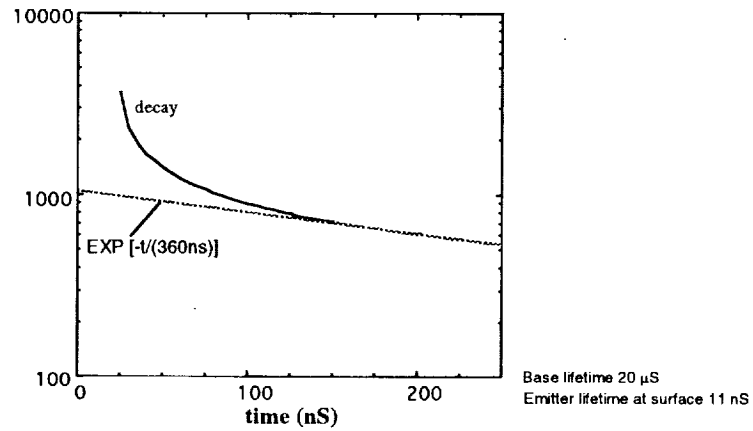


Figure 6: Exponential fit to decay of short circuit current for Si cell

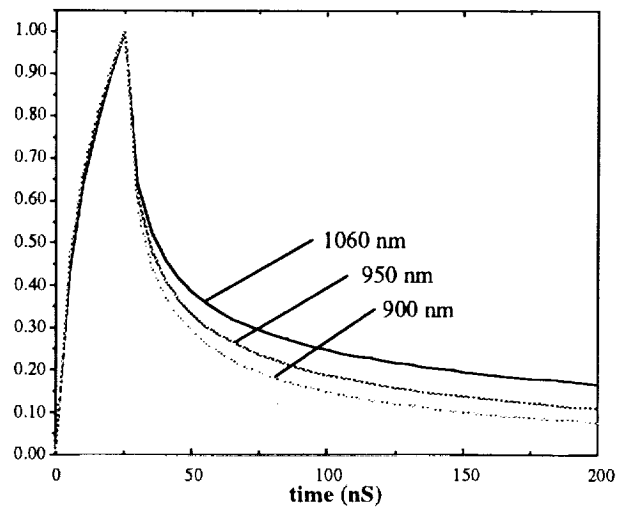


Figure 7: Decay of normalized short circuit current for Si cell at several wavelengths

CALCULATION OF NEAR OPTIMUM DESIGN OF $\text{InP/In}_{0.53}\text{Ga}_{0.47}\text{As}$ MONOLITHIC TANDEM SOLAR CELLS

P. Renaud, M.F. Vilela, A. Freundlich,¹ N. Medelci, and A. Bensaoula
University of Houston
Houston, Texas

SUMMARY

An analysis of InP/InGaAs tandem solar cell structures has been undertaken to allow for maximum AMO conversion efficiencies (space applications) while still taking into account both the theoretical and technological limitations. The dependence of intrinsic and extrinsic parameters such as diffusion lengths and generation-recombination (GR) lifetimes on N/P and P/N devices performances are clearly demonstrated. We also, report for the first time the improvement attainable through the use of a new patterned tunnel junction as the inter cell ohmic interconnect. Such a design minimizes the light absorption in the interconnect region and leads to a noticeable increase in the cell efficiency. Our computations predict 27% AMO efficiency for N/P tandems with ideality factor $\gamma=2$ (GR lifetimes $\approx 1\mu\text{s}$), and 36% for $\gamma=1$ (GR lifetimes $\approx 100\mu\text{s}$). The method of optimization and the values of the physical and optical parameters are discussed.

INTRODUCTION

The use of monolithic $\text{InP/In}_{0.53}\text{Ga}_{0.47}\text{As}$ tandem solar cells for space applications is still at the research stage. It has already been demonstrated that their band gap values are particularly adapted for maximum AMO performance levels (ref. 1) in addition to their particularly high resistance to radiation damage (ref. 2). Using chemical beam epitaxy (CBE) and new device processing techniques, we have already shown in our laboratory that high quality materials and devices can be obtained (ref. 3). Therefore, a detailed theoretical simulation is required in order to further optimize and refine the structures now possible with this new technology so that photovoltaic (PV) devices with maximum efficiencies can be achieved.

Regarding both top and bottom cell emitter and base thicknesses and doping levels, we calculate the conditions for maximum photocurrent matching. The dark current is evaluated from the intrinsic limitation where the saturation current is dominant (giving ideality factor $\gamma=1$), to the extrinsic limitation where GR current due to trap levels in the depleted region dominates (ideality factor $\gamma=2$). The trap level density, which is highly correlated to the epilayer quality, yield effective GR lifetimes in the microsecond range (ref. 4). Thus, their participation in the recombination processes of photo-excited carriers is negligible compared to band to band recombinations and does not affect minority carrier diffusion lengths. This is why most of actual photovoltaic devices show performances limited by the open circuit voltage and fill factor while still exhibiting an excellent photocurrent characteristic (ref. 5).

The present study is undertaken to set a near optimum design for a maximum internal efficiency. The effect of grid shadowing and light reflection which are directly relevant on technological processing are not taken into account.

¹Also at the LPSES-CNRS, Valbonne, France.

METHOD OF CALCULATION

The values of the radiative recombination coefficient and minority carriers mobility versus doping levels in high quality InP and GaInAs epilayers were extracted from references 6 and 7.

The expressions of the equations describing photovoltaic multi-junctions are well known (ref. 8) and will not be recalled here. Nevertheless, it is important to summarize those describing the bottom cell response and the dark current.

Let us write J_t and J_b as the top and bottom cell photocurrent. J_b is a single InGaAs solar cell response $J_{\text{InGaAs}}(E)$ reduced by the absorption of the top cell and the tunnel diode.

$$J_b = \int e^{-(\alpha_e(E)x_e + \alpha_b(E)x_b + \alpha_t(E)x_t)} J_{\text{InGaAs}}(E) \phi(E) d(E) \quad 1$$

Where x_e , x_b , x_t are the emitter, base and tunnel diode thicknesses; $\alpha_e(E)$, $\alpha_b(E)$ and $\alpha_t(E)$ are their absorption coefficients varying with doping levels, and $\phi(E)$ is the solar spectrum.

The top and bottom cell photocurrent matching is achieved by an appropriate choice of the individual layer thicknesses.

The expression of the dark current related to such diodes, is set by considering the saturation current I_s (ref. 8), the tunnel current I_{tun} (ref. 10), and the GR current I_{gr} (ref. 8) with $I_{\text{gr}} = qn_i W / \tau_{\text{gr}}$. Where q is the electron charge, n_i the intrinsic carrier density, W is the depletion region width, and τ_{gr} is the effective GR lifetime.

The I-V characteristic of a single cell is then expressed by (ref. 8),

$$I = J_{\text{cc}} - I_s (e^{V/u_t} + 1) - I_{\text{gr}} (e^{V/2u_t} + 1) - I_{\text{tun}} - V / R_{\text{sh}} \quad 2$$

Where $u_t = 0.026V$ at room temperature, $V = V_0 - R_s I$ (R_s : series resistance), and R_{sh} is the shunt resistance.

The output voltage of the tandem under illumination is the sum of that from the individual constituent cells reduced by the voltage drop in the tunnel junction. The tandem photocurrent however is controlled by the cell generating the lower photocurrent.

RESULTS AND DISCUSSION

Table 1 shows the parameters required to achieve a near optimum design of N/P and P/N tandem solar cells respectively.

The calculated performances are:

$n=1$	$n=2$
$J_{\text{cc}} = 33.3 \text{ mA}$	$J_{\text{cc}} = 33.3 \text{ mA}$
$V_{\text{ocInP}} = 1.17V$	$V_{\text{ocInP}} = 0.97V$
$V_{\text{ocInGaAs}} = 0.64 V$	$V_{\text{ocInGaAs}} = 0.5 V$
$\eta = 36.24\%$	$\eta = 27\%$

for a N/P structure and

$n < 2$ ($\tau_{\text{gr}} = 100\text{ms}$)	$n = 2$ ($\tau_{\text{gr}} = 1\text{ms}$)
$J_{\text{cc}} = 28 \text{ mA}$	$J_{\text{cc}} = 28 \text{ mA}$
$V_{\text{ocInP}} = 1.1V$	$V_{\text{ocInP}} = 0.9V$
$V_{\text{ocInGaAs}} = 0.62 V$	$V_{\text{ocInGaAs}} = 0.5 V$
$\eta = 30.5\%$	$\eta = 22\%$

for a P/N structure (because of a high series resistance we can not assume a idealiy factor equals to unity).

OPTIMIZATION

P/N or N/P ?

A priory P/N junctions may seem to be more suitable than N/P structures so as to take advantage of the absorption shift present in p doped compounds (ref. 9). N doped layers however have a lower sheet resistance and p type $\text{In}_{0.53}\text{Ga}_{0.47}\text{As}$ compounds show much better minority carriers mobilities (ref. 7). Furthermore the relatively low absorption coefficients in these materials will necessitate the use of thicker junction layers (of 4-5 μm) to minimize transparency losses. Thus a N/P structure is required for good carrier collection before recombination.

In this work the surface recombination velocities (SRV) values used are those found in InGaAs/InP double heterostructures and InPmonolayer.

Emitters

The top cell emitter thickness is calculated to allow an optimum performance through a compromise between a minimization of the surface recombination rate and a reduced sheet resistance (ref. 11).

The bottom cell emitter thickness is derived to achieve the best carrier collection before recombination. There is no sheet resistance and the SRV is small due to the presence of a window layer. Figures 2 shows for comparison the performances expected in the case of P/N and N/P tandems versus emitter width with optimum doping and base width shown in table 1. We can see that the different values of minority carrier mobilities versus doping level lead to a difference of 6% of absolute efficiency if a N/P rather than P/N structure is considered. Also p doped emitters need to be thicker due to high sheet resistance. Consequently, the base is required to be thin in order to allow the photocurrent matching. Therefore the optimum design of P/N tandem is a top cell inverted structure (emitter thicker than the base).

Bases

The base participation in the tandem performance can also be optimized by adjusting the width and the doping level. The high electron mobility in p doped InGaAs allows the use of a thicker bottom cell base without significant carrier recombination. The top cell base is therefore critical due to photocurrent matching constraints.

Figures 3 and 4 show the variation of the photocurrent and efficiency as a function of the InP base thickness assuming a perfect case of $\gamma=1$ ($\tau_{gr}=100\mu\text{s}$). We can see that light absorption in the InP base leads to an increase of the top cell photocurrent and a decay of the bottom cell photocurrent. The condition of equal currents (top cell thickness: 0.3 μm) corresponds precisely to the optimum conversion efficiency of the tandem shown in figure 4 (36% AM0). The high correlation between the photocurrent matching condition and the multi-junction efficiency is clearly demonstrated. Figure 4 shows also the case where a 100% internal efficiency is assumed in order to emphasize the influence of SRVs, lifetimes and diffusion lengths on the photo-response. These combined intrinsic and extrinsic limitations result in a 20% change in absolute efficiency between the two models.

The calculated internal spectral response of the near optimum design tandem solar cell is presented on figure 5. It emerges clearly that the device limitations are mainly due to the bottom cell characteristics. The limited values of diffusion lengths and low absorption do not permit better expectations.

Dark current

As mentioned previously, the dark current is controlled by three different processes. First the saturation current I_0 which varies with the square of the intrinsic carrier concentration (ref. 4) leads to an intrinsic limitation. Second is the band to band tunneling current which becomes non negligible only in highly doped junctions. Third is the Generation-Recombination current which is

the main factor to be minimized by the growth technique. The density of trap levels in the bandgap is taken into account in the I-V characteristics as an effective GR lifetime (equation 2). To describe the effect of this latter parameter on the cell performance, we have drawn in figure 6 the variation of the conversion efficiency of a tandem over a wide range of GR lifetimes yielding ideality factors ranging from 2 to 1. There is a non negligible 8 % in absolute efficiencies enhancement when GR lifetimes vary from $1\mu\text{s}$ to $20\mu\text{s}$.

Tunnel junction

In the case of a monolithic tandem structure, the electrical interconnect between the two cells is achieved by an InGaAs tunnel junction (ref. 12). An ideal tunnel junction should modify neither the electrical nor the optical properties of the tandem. It has been shown previously (ref. 12) that very thin and extremely low resistivity InGaAs tunnel junctions can be fabricated with CBE. In addition, through patterning of the tunnel junction we can further minimize light absorption in this region (ref. 13). The influence of light absorption in the tunnel junction area on the tandem efficiency is shown in figure 7.

CONCLUSION

The characteristics of an InP/InGaAs monolithic solar cell have been evaluated using a large range of geometric considerations. Our calculations demonstrate the influence of the emitter, base, and tunnel junction layer thicknesses and have allowed us to set a near optimum design for a maximum tandem efficiency. The minority carrier mobilities, especially in InGaAs, seem to suggest the superiority of N/P over P/N structures. Finally it has been demonstrated that photocurrent matching is the principal condition for a near optimum design and that high efficiency tandem solar cells require a low trap level density.

REFERENCES

- 1/ M. W. Wanlass, J. S. Ward, K. A. Emery, T. A. Gessert, C. R. Osterwald and T. J. Coutts; *Solar Cells*, 30 (1991) 363-371.
- 2/ M. W. Wanlass, J. S. Ward, K. A. Emery and T. J. Coutts;
- 3/ A. Bensaoula, N. Medelci, M. F. Vilela and A. Freundlich; 6th Int. Conf. on Indium Phosphide and Related Materials; (1994) Santa Barbara Ca. pp. 280.
- 4/ A. Zemel and M. Galland; *J. Appl. Phys.* **64** (11), pp. 6552 (1988).
- 5/ See as an example "A new structure of GaAs solar cell" M. F. Vilela, B. Beaumont, J. C. Guillaume, P. Gibart and C. Verie, 11th Eur. PV Energy Conf. (Montreux, Switzerland, 1992)
- 6/ Properties of Lattice-Matched and strained Indium Gallium Arsenide. 1993 INSPEC, (ed. London).
- 7/ Properties of Indium Phosphide 1991 INSPEC (ed. London and New York).
- 8/ H. J. Hovel. *Solar cells in Semiconductors and semimetals*. Vol. II (Ed. R. K. Willarson, A. C. Ber. Acad. Press, 1975
- 9/ H. Burkhard, H. W. Dinges, and E. Kuphal; *J. Appl. Phys.* **53** (1), 655 (1982).
- 10/ E. O. Kane, *J. Appl. Phys.* **32** (1), pp 83 (1961).

- 11/ C. Goradia, W. Thesling, I. Weinberg, 22nd IEEE PV. Specialists Conf.; Las Vegas (1991).
- 12/ M. F. Vilela, A. Freundlich, A. Bensaoula and N. Medelci; 5th Int. Conf. on InP and related materials, Paris, France, pp. 227 (1993).
- 13/ A. Freundlich, M. F. Vilela, A. Bensaoula, N. Medelci, Proc. 23rd IEEE-PV Conf. (1993), pp. 644.

Metallization, Contact layer	
Emitter	
Base	InP Top Cell
Tunnel junction	
Window	
Emitter	
Base	In _{0.63} Ga _{0.47} As Bottom Cell
Base wafer lattice matched to InP	

Figure 1: Schematic representation of the monolithic tandem solar cell.

Table 1.

	Top cell InP		Bottom cell In _{0.53} Ga _{0.47} As	
	N/P	P/N	N/P	P/N
Emitter				
SRV	$10^5 \text{ cm}^2 \text{ s}^{-1}$	$10^5 \text{ cm}^2 \text{ s}^{-1}$	$10^3 \text{ cm}^2 \text{ s}^{-1}$	$10^3 \text{ cm}^2 \text{ s}^{-1}$
Doping	$3.10^{18} \text{ cm}^{-3}$	$3.10^{18} \text{ cm}^{-3}$	10^{18} cm^{-3}	10^{18} cm^{-3}
Thickness	0.02 μm	0.15 μm	0.5 μm	1 μm
Lifetime	1 ns	1 ns	0.3 ns	0.3 ns
Diff length	0.45 μm	2.5 μm	0.4 μm	2.3 μm
Base				
SRV	$10^3 \text{ cm}^2 \text{ s}^{-1}$	$10^3 \text{ cm}^2 \text{ s}^{-1}$	$10^3 \text{ cm}^2 \text{ s}^{-1}$	$10^3 \text{ cm}^2 \text{ s}^{-1}$
Doping	$5.10^{17} \text{ cm}^{-3}$	$5.10^{17} \text{ cm}^{-3}$	10^{17} cm^{-3}	10^{17} cm^{-3}
Thickness	0.25 μm	0.05 μm	4.5 μm	3 μm
Lifetime	23ns	23ns	19 ns	19 ns
Diff length	13, 8 μm	1.35 μm	7 μm	1.5 μm
Series Resistance	0.97 Ω	2 Ω		
Shunt resistance	$10^4 \Omega$	$10^4 \Omega$		

The near optimum design has been calculated through a systematic variation of all the relevant cell parameters.

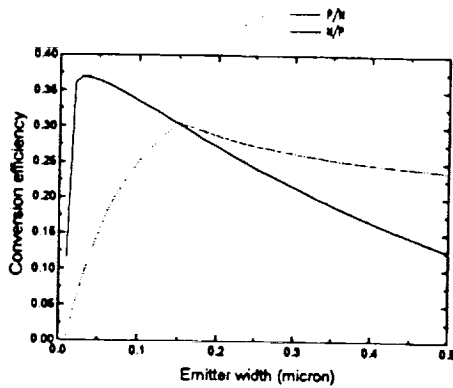


Figure 2 : Conversion efficiency of N/P and P/N tandem solar cell vs. top emitter width with optimum doping and base width.

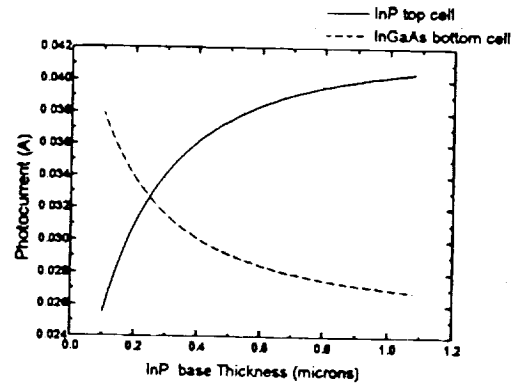


Figure 3: The effect of the top cell base thickness (emitter = 0.05 μm) on the photocurrent of a tandem cell with a patterned tunnel junction.

SESSION III

RADIATION DAMAGE
AND
ENVIRONMENTAL TESTING

PERFORMANCE, DEFECT BEHAVIOR AND CARRIER ENHANCEMENT IN LOW ENERGY,

PROTON IRRADIATED $p^{+}nn^{+}$ InP SOLAR CELLS

I. Weinberg and G.C. Rybicki
NASA Lewis Research Center
Cleveland, Ohio

C. Vargas-Aburto
Kent State University
Kent, Ohio

R.K. Jain
University of Toledo
Toledo, Ohio

and

D. Scheiman
NYMA, Inc.
Brook Park, Ohio

InP $p^{+}nn^{+}$ cells, processed by MOCVD, were irradiated by 0.2 MeV protons and their performance and defect behavior observed to a maximum fluence of 10^{13} cm^{-2} . Their radiation induced degradation, over this fluence range, was considerably less than observed for similarly irradiated, diffused junction $n^{+}p$ InP cells. Significant degradation occurred in both the cell's emitter and base regions the least degradation occurring in the depletion region. A significant increase in series resistance occurs at the highest fluence. Two majority carrier defect levels, E7 and E10, are observed by DLTS with activation energies at $(E_C - 0.39) \text{ eV}$ and $(E_C - 0.74) \text{ eV}$ respectively. The relative concentration of these defects differs considerably from that observed after 1 MeV electron irradiation. An increased carrier concentration in the cell's n-region was observed at the highest proton fluence, the change in carrier concentration being insignificant at the lower fluences. In agreement with previous results, for 1 and 1.5 MeV electron irradiated InP $p^{+}n$ junctions, the defect level E10 is attributed to a complex between zinc, diffused into the n-region from the zinc doped emitter, and a radiation induced defect. The latter is assumed to be either a phosphorus vacancy or interstitial. The increased, or enhanced carrier concentration is attributed to this complex acting as a donor.

INTRODUCTION

The highest AMO efficiency (19.1%) InP solar cell consisted of an $n^{+}pp^{+}$ structure epitaxially grown on a p^{+} InP substrate [1]. However, the high cost and relative fragility of InP served as motivation for research efforts directed at heteroepitaxial growth of InP on more viable substrates [2,3]. The highest AMO efficiency (13.7%) for this type of cell was achieved using a GaAs substrate [3,4]. Considering only cost and fracture toughness, Si would be the preferred substrate. The fact that Si is a donor in InP introduces complexities which are necessary in order to avoid the formation of an efficiency limiting counterdiode [5]. One method used to overcome this problem, lies in employing an $n^{+}p^{+}$

tunnel junction in contact with the cell's p region. A simpler method consists of using an n^+ substrate and processing the cell in the p^+nn^+ configuration. This eliminates the need for a tunnel junction. Unfortunately, the p/n configuration has received relatively little attention the best cell with this geometry having achieved an efficiency of 17% [6]. Irradiation of these homoepitaxial cells, with 1 MeV electrons, showed that they were slightly more radiation resistant than diffused junction n/p cells [7]. Additional p/n InP cells have been processed by closed ampoule diffusion [8]. Currently, there has been some activity aimed at producing heteroepitaxial p^+nn^+ InP cells using n^+ Ge substrates [9]. Since, like Si, Ge is an n-dopant in InP, use of this configuration obviates the need for a tunnel junction. Obviously, before attempting to process heteroepitaxial cells, one must produce a reasonably good homoepitaxial cell. In the present case we focus our attention on homoepitaxial p^+nn^+ cells processed prior to producing the cells heteroepitaxially on an n^+ Ge substrate [9].

EXPERIMENTAL DETAILS

The cells were processed by MOCVD, at the Spire Corporation, under contract to NASA Lewis. Cell configuration, dopants and concentrations are shown in fig. 1. Processing details can be found in reference 9. Irradiations by 0.2 MeV protons, to a fluence of $10^{13}/\text{cm}^2$ were performed at the University of Michigan's ion implantation facility. Cell performance was determined at NASA Lewis using a Spectrolab Mark II, xenon arc solar simulator with flight calibrated InP standard cell. Spectral response and Isc-Voc measurements were also performed before irradiation and at each step in the irradiation process. Carrier concentrations in the cell's p-base, near the junction were determined by capacitance-voltage measurements. Defect behavior was monitored by DLTS measurements.

RESULTS AND DISCUSSION

Performance

Pre-irradiation performance parameters are shown in table I. Considering the fact that theoretical modelling indicates possible efficiencies over 22%, the present efficiencies are excessively low [10]. This is attributable to the fact that the present cells were processed in an early stage of development. In fact, AMO efficiencies of 17% have subsequently been achieved at Spire [6]. Higher efficiencies can be anticipated with additional effort.

The results of the 0.2 MeV proton irradiations are shown in fig.2. Comparison of normalized efficiencies with 0.2 MeV proton irradiated diffused junction n/p cells is shown in fig.3. The n/p cells had the same junction depth as the present cells with AMO efficiency=15.1%, Voc=823 mV, Jsc=29.4 ma/cm², and FF=85.6% [11]. Comparison of normalized efficiencies indicates considerably more radiation resistance for the present cells at the higher fluences. Also, comparing numerical efficiency values, the present cells outperform the n/p cells at the higher fluences.

The external quantum efficiency, before irradiation and at a fluence of 10^{12} cm^{-2} , is shown in fig.4. The quantum efficiency at the highest fluence is lost in the system noise and is therefore not shown in the figure. Figure 4 indicates that considerable degradation occurs in both the emitter and base of the solar cell. A numerical estimate of the relative degradation is obtained using the relation

$$J_{sc} = \sum SR(\lambda_j) E(\lambda_j) \Delta \lambda_j \quad 1a$$

Where $SR(\lambda_j)$ the spectral response, in mA/mW, is obtained from the quantum efficiency using the relation

$$SR(\lambda_j) = Q_E(\lambda_j) \lambda_j / 1.24 \quad 1b$$

where $E(\lambda_j)$ in $\text{mW cm}^{-2} \text{ micron}^{-1}$ is the solar spectral radiance at wavelength λ_j in microns, $Q_E(\lambda_j)$ is the external quantum efficiency at λ_j , $\Delta \lambda_j$ is an appropriate wavelength interval and the summation is over all wavelengths covered by the quantum efficiency in fig.4. The junction depth is approximated by the optical path length $1/\alpha_j$ where α_j is the absorption coefficient at wavelength λ_j . Using 1a and 1b it is found that the degradation in short circuit current is approximately divided between the emitter and base. An estimate of the relative degradation in base and emitter is obtained from the I_{sc} - V_{oc} measurements obtained over a range of light intensities. The results before irradiation and at a specific fluence are shown in table II. Considering the reverse saturation currents J_{02} is attributed to recombination in the cell's depletion region while the major contribution to J_{01} arises from diffusion in the base of the cell. Hence, from the diffusion and recombination current densities in table II, it is concluded that the radiation induced degradation in the cell's base is much greater than that occurring in the depletion region.

Defects

The DLTS spectrum, at the highest fluence, is shown in fig.5 while defect parameters are listed in table III. No defect levels were observed prior to irradiation. The defect concentrations obtained from fig.5, and shown in the table, have been corrected for band bending and its effect on space charge when crossing the Fermi level [12]. The majority carrier defect levels labelled E7 and E10 have been observed previously after irradiation by 1 and 1.5 MeV electrons [13]. The broad signal observed between E7 and E10 appears to be due to the presence of one or more unresolvable defect levels. The present energy levels for E7 and E10 are in reasonable agreement with those previously reported for these defects [13]. However, the concentration ratio $N_T(E10)/N_T(E7) \sim 50$ in the previously electron irradiated case [13] while in the present case the ratio is 0.56. Hence, although E10 could reasonably be assumed to be the major radiation induced defect, observed by DLTS, in the n region of electron irradiated p^+n InP [13], the choice of major defect is not clear cut in the present case. It is noted that, after electron irradiation, E7 was observed, but not E10, in

the DLTS spectrum obtained using a Schottky barrier on n-type InP [13]. In fact, E10 was only seen when a p^+n junction was used, the p^+ region being heavily zinc doped. It was therefore initially concluded that E10 was a result of zinc diffusion into the n-region, the zinc complexing with an unidentified radiation induced defect [13]. Another possibility considered was the formation of a complex between a process induced and radiation induced defect [13].

Carrier concentrations in the n-region, measured over a range of fluences, indicated that at all but the highest fluence, the change in carrier concentration was negligible. However, at the highest fluence, the carrier concentration was significantly increased over the pre-irradiation value (table IV). This is in opposition to observations in the p-region of n^+p InP where both proton and electron irradiations produced decreased carrier concentrations [14,15]. Although this appears to be the first reported observation of carrier enhancement in proton irradiated InP, the effect has been observed before after 1 MeV electron irradiation [16]. It is significant that, in both cases, carrier enhancement is observed in the n-region of an InP p^+n diode where zinc is used as the p-dopant [16]. In agreement with the previous suggestion [13] it was argued that zinc diffuses into the n-region and complexes with a radiation induced defect [16]. In the latter case it was further argued that the defect was either a phosphorus interstitial or vacancy [16]. Furthermore, it was argued that the complex acts as a donor. In relation to the present solar cell parameters, the carrier enhancement does not appear to be a factor in improving cell performance or in decreasing series resistance. This is evident from fig. 1 and table V, the latter showing that cell series resistance, obtained from dark diode I-V data, increases significantly at the highest fluence. In any event, the present results indicate that, despite the anomolous increase in carrier concentration, the effects of radiation induced defects on transport properties, such as diffusion length are dominant in determining cell behavior under the present low energy proton irradiations.

CONCLUSION

Under irradiation by 0.2 MeV protons, it is concluded that;

The radiation induced degradation is considerably lower in the present cell when compared to diffused junction n^+p InP cells.

Considerable radiation induced degradation is observed in both the base and emitter of the present cells, both degradations being considerably greater than that occurring in the depletion region.

The relative concentration of defects E7 and E10, $N_T(E10)/N_T(E7)$, is considerably greater under 1 and 1.5 MeV electron irradiations than is the case for the present irradiations.

A significant increase in carrier concentration (carrier enhancement) occurs in the cell's n-region after irradiation by 0.2 MeV protons at a fluence of 10^{13} cm^{-2} . At the lower fluences, the change in carrier concentration is insignificant.

In concurrence with previous conclusions after electron irradiation, the defect level E10 is attributable to a donor complex formed between zinc and a radiation induced defect. The latter is assumed to be either a phosphorus interstitial or vacancy.

In the present case, the radiation induced carrier enhancement appears to have little or no effect on cell performance.

REFERENCES

1. C.J.Keavney, V.E.Haven and S.M.Vernon, "Emitter Structures in MOCVD InP Solar Cells," 21st IEEE Photovoltaic Spec. Conf., pp141-147 (1990)
2. C.J.Keavney, S.M.Vernon and V.E.Haven, "Tunnel Junctions for InP on Si Solar cells," Proceedings Space Photovoltaic Research and Technology Conf., pp1-1 to 1-7, NASA Conf. Publication 3121 (1991)
3. M.W.Wanlass, U.S. Patent No. 4,963,949 (1990)
4. T.J.Coutts, "Progress in InP-Based Solar Cells," Proceedings 3rd Int'l Conf. on InP and Related Materials, pp20-31, IEEE-LEOS, Piscataway N.J. (1991)
5. C.J.Keavney, S.M.Vernon, V.E.Haven, S.J.Wojtczuk and M.M.Al-Jassim, "Fabrication of n^+p InP Solar Cells on Silicon Substrates," Appl. Phys. Lett.54, pp1139-1141 (1989)
6. S.Wojtczuk, S.M.Vernon and E.A.Burke, "p/n InP Solar Cells on Ge Wafers," This Conference (1994)
7. I.Weinberg, C.K.Swartz and R.E.Hart Jr., "Radiation and Temperature Effects in Gallium Arsenide, Indium Phosphide and Silicon Solar Cells," Proceedings 19th Photovoltaic Spec. Conf., pp548-557, IEEE, Piscataway N.J. (1987)
8. Mircea Faur, Maria Faur, C.Goradia, M.Goradia, D.J.Flood, D.J.Brinker, I.Weinberg and N.Fatemi, "Progress in p^+n InP Solar Cells Fabricated by Thermal Diffusion," Proceedings, Space Photovoltaic Research and Technology Conf., pp23-32, NASA Conf. Pub. 3210 (1992)

9. S.Wojtczuk and S.Vernon, "p/n InP Solar Cells on Ge Wafers," Space Photovoltaic Research and Technology Conf. NASA Lewis Res. Center (1994)
10. R.K.Jain, I.Weinberg and D.J.Flood, "Comparative Modelling of InP Solar Cell Structures," Proceedings Space Photovoltaic R and T Conf., pp29-1 to 29-9, NASA Conf. Pub. 3121 (1991)
11. T.Takamoto, H.Okazaki, H.Takamura, M.Ohmori, M.Ura and M.Yamaguchi, "Radiation Effects on n⁺p Homojunction Indium Phosphide Solar Cells," Proceedings 2nd Int'l conf. on InP and Related Materials pp62-65, IEEE-LEOS, Piscataway N.J. (1990)
12. Y.Zohta and M.O.Watanabe, "On The Determination of the Spatial Distribution of Deep Centers in Semiconducting Films From Capacitance Transient Spectroscopy," J. Appl. Phys., 53, pp1809-1811 (1982)
13. J.L.Benton, M.Levinson, A.T.Macrander, H.Temkin and L.C.Kimerling, "Recombination Enhanced Defect Annealing in n-InP," Appl. Phys. Lett., 45, pp566-568 (1984)
14. I.Weinberg, R.K.Jain, C.K.Swartz, H.B.Curtis, D.J.Brinker, C.Vargos-Aburto and P.J.Drevinsky, "Proton Irradiated Heteroepitaxial InP Cells," Proceedings 23rd IEEE Photovoltaic Spec. Conf., pp1483-1486, IEEE, Piscataway N.J. (1993)
15. I.Weinberg, C.K.Swartz and P.J.Drevinsky, "Carrier Removal and Defect Behavior in p-type InP," J. Appl. Phys. 72, pp5509-5511 (1992)
16. A.Sibile, "Origin of the Main Deep Electron Trap in Electron Irradiated InP," Appl. Phys. Lett., 48, pp593-595 (1986)
17. K.Rajkanen and J.Shewchun, "A Better Approach to the Evaluation of the Series Resistance of Solar Cells," Solid State Electronics 22, pp193-197 (1979)

Table I: Cell Pre-Irradiation Performance Parameters

J _{sc}	V _{oc}	FF	Eff.
mA/cm ²	mV	%	%
23.6	851.4	84.7	12.4

Table II: Diffusion and Recombination Components
of Reverse Saturation Currents

$E_p = 0.2 \text{ MeV}$

Fluence	A_1	A_2	J_{01}	J_{02}
cm^{-2}			A/cm^2	A/cm^2
0	0.89	1.57	1.03×10^{-10}	3.9×10^{-12}
10^{12}	1.32	2.08	1.5×10^{-11}	5.5×10^{-8}

Table III: Characteristics of Majority Carrier Defect
Levels Obtained by DLTS in $p^+n n^+$ InP

$E_p = 0.2 \text{ MeV}$
Fluence = $10^{13}/\text{cm}^2$

DEFECT	ACTIVATION ENERGY	CAPTURE CROSS SECTION	CONCENTRATION	INTRODUCTION RATE
	eV	cm^2	cm^{-3}	cm^{-1}
E7	$E_c - 0.39$	4.1×10^{-17}	8.67×10^{15}	867
E10	$E_c - 0.74$	3.6×10^{-14}	4.88×10^{15}	488

Table IV: Electron Concentration in n-Region of 0.2 MeV
Proton Irradiated p^+nn^+ InP Cell

FLUENCE	ELECTRON CONC.	CHANGE IN ELECTRON CONC ^a
cm^{-2}	cm^{-3}	cm^{-3}
0	3.18×10^{16}	0
10^{13}	3.86×10^{16}	$+6.8 \times 10^{15}$

^a Change in carrier conc. was negligible at the lower fluence.

Table V: Series Resistance in 0.2 MeV Proton Irradiated Cell

FLUENCE (CM ⁻²)	0	2 X 10 ¹¹	10 ¹²	10 ¹³
SERIES RESISTANCE OHM - CM ²	0.49	0.36	0.56	1.7

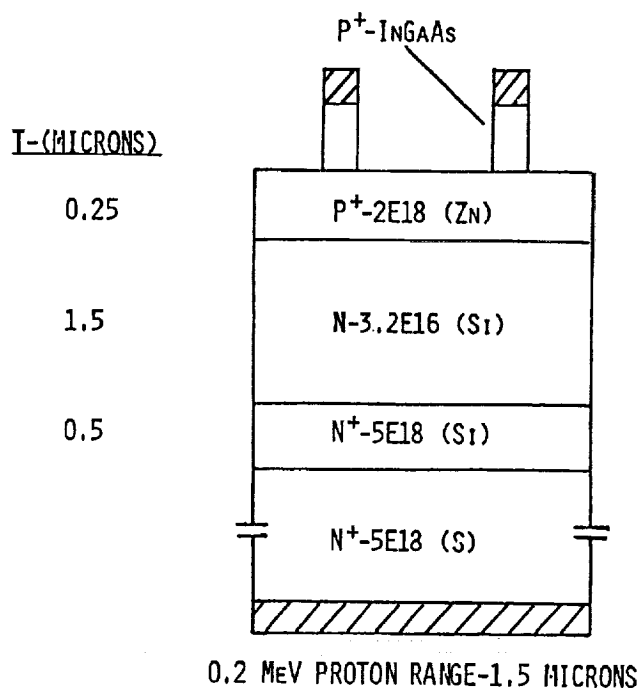


FIGURE 1. INP CELL DETAILS

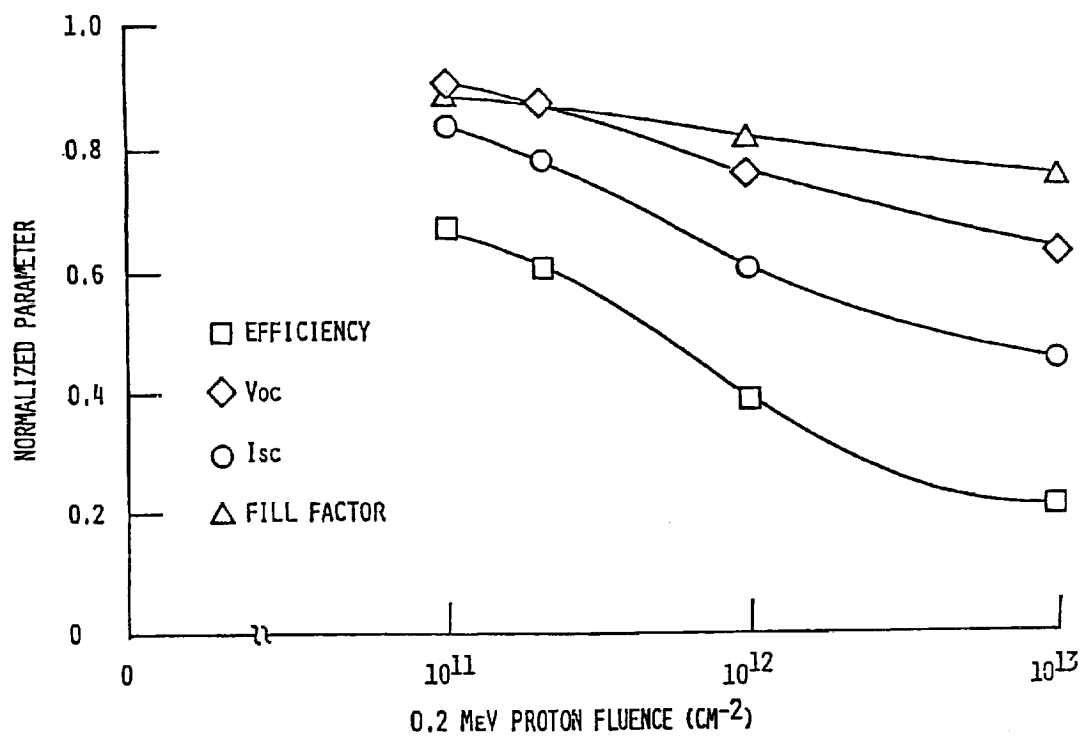


FIGURE 2. NORMALIZED INP CELL PARAMETERS AFTER IRRADIATION

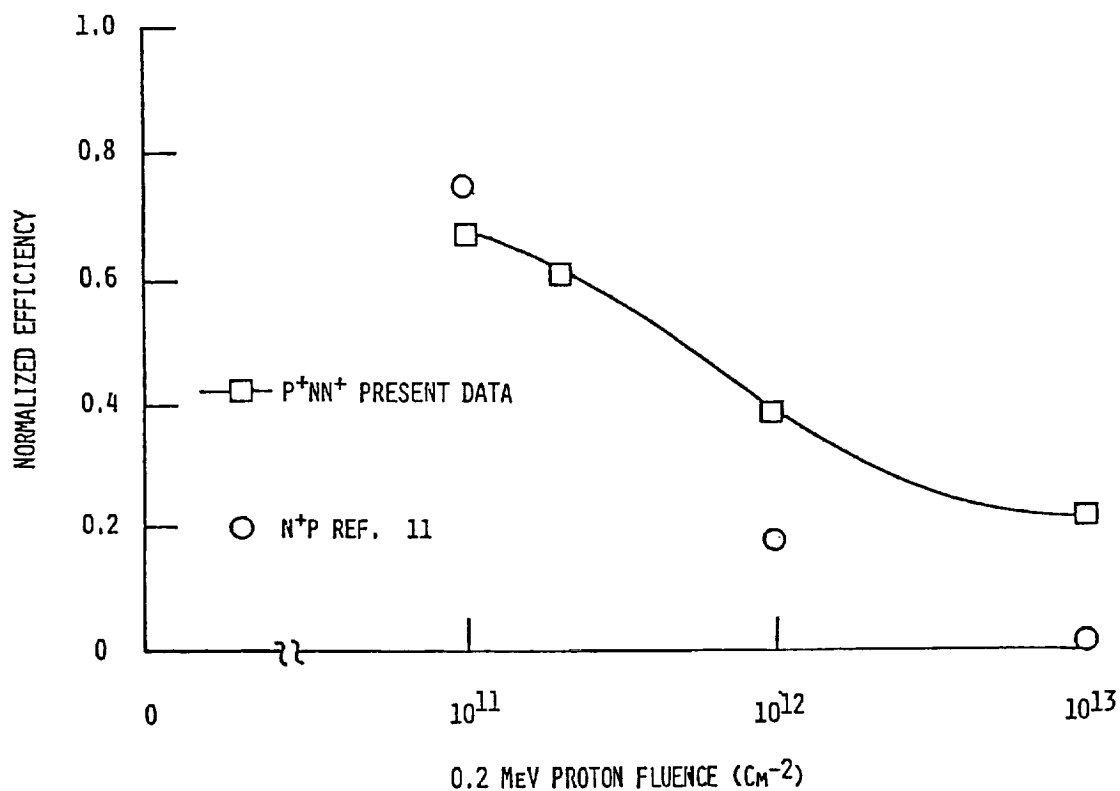


FIGURE 3. COMPARISON OF P^+NN^+ AND N^+P IRRADIATED INP SOLAR CELLS

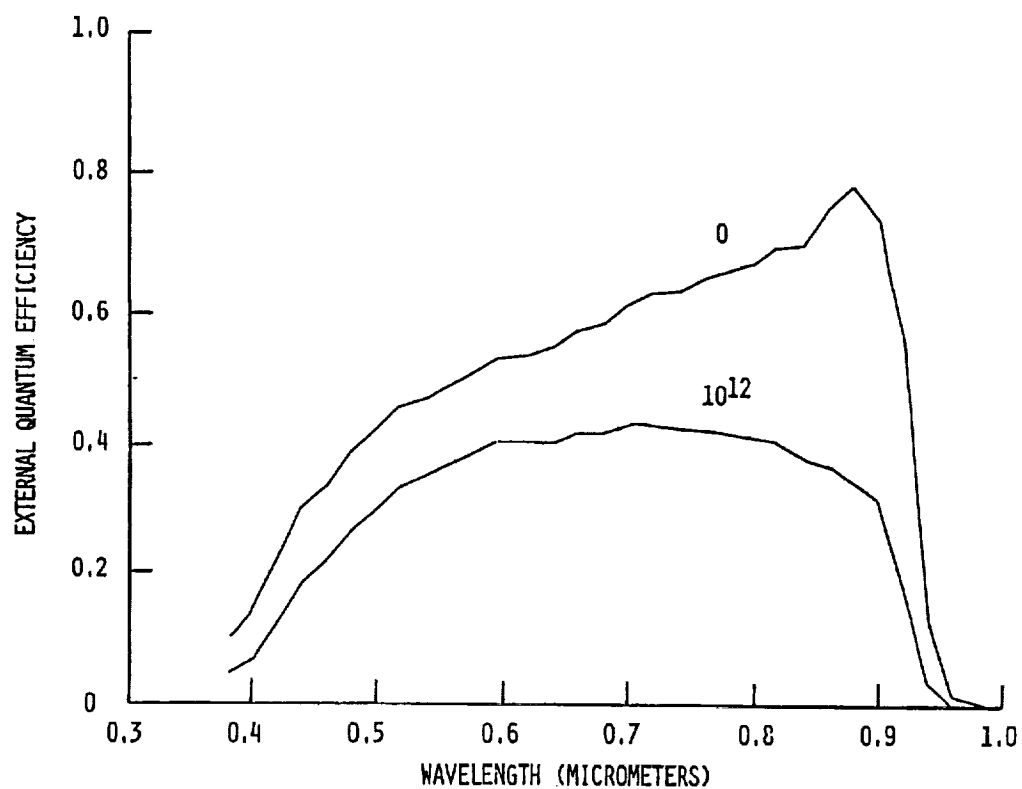


FIGURE 4. EXTERNAL QUANTUM EFFICIENCY, P^+NN^+ INP, $E_p=0.2$ MeV

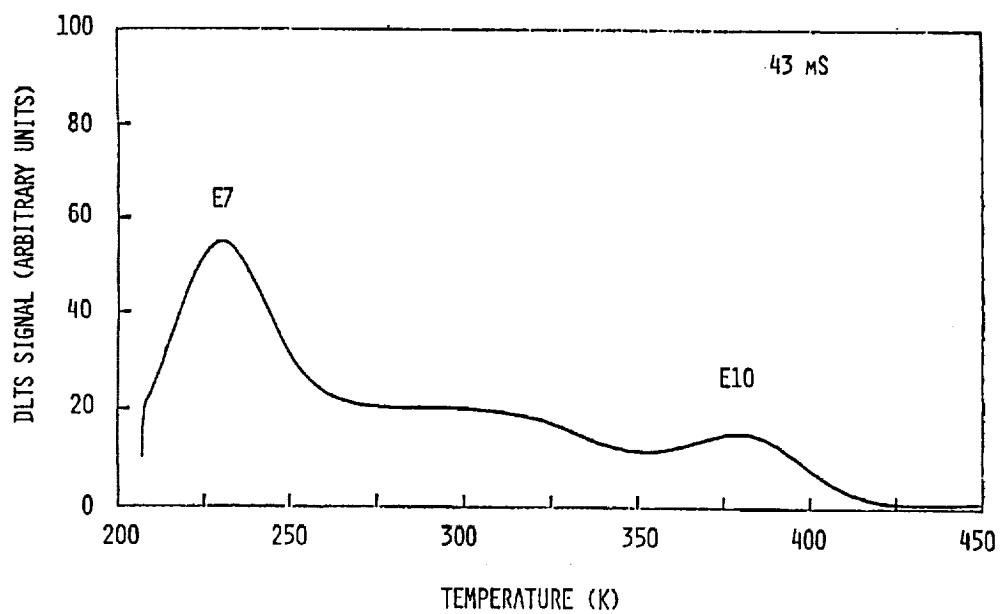


FIGURE 5. DLTS OF P^+NN^+ INP CELL, $E_p=0.2$ MeV, FLUENCE= 10^{13} cm^{-2}

ELECTRON-IRRADIATED TWO-TERMINAL, MONOLITHIC $\text{InP/Ga}_{0.47}\text{In}_{0.53}\text{As}$ TANDEM

SOLAR CELLS AND ANNEALING OF RADIATION DAMAGE

H.L. Cotal, R.J. Walters, and G.P. Summers
U.S. Naval Research Laboratory
Washington, DC

and

S.R. Messenger
SFA, Inc.
Landover, Maryland

ABSTRACT

Radiation damage results from two-terminal monolithic $\text{InP/Ga}_{0.47}\text{In}_{0.53}\text{As}$ tandem solar cells subject to 1 MeV electron irradiation are presented. Efficiencies greater than 22 % have been measured by the National Renewable Energy Laboratory from $2 \times 2 \text{ cm}^2$ cells at 1 sun, AM0 (25 °C). The short circuit current density, open circuit voltage and fill factor are found to tolerate the same amount of radiation at low fluences. At high fluence levels, slight differences are observed. Decreasing the base dopant level of the $\text{Ga}_{0.47}\text{In}_{0.53}\text{As}$ bottom cell improved the radiation resistance of J_{sc} dramatically. This in turn, extended the series current flow through the subcells substantially up to a fluence of $3 \times 10^{15} \text{ cm}^{-2}$ compared to $3 \times 10^{14} \text{ cm}^{-2}$, as observed previously. The degradation of the maximum power output from the tandem device is comparable to that from shallow homojunction (SHJ) InP solar cells, and the mechanisms responsible for such degradation is explained in terms of the radiation response of the component cells. Annealing studies revealed that the recovery of the tandem cell response is mostly dictated by the annealing characteristics exhibited by SHJ InP solar cells.

INTRODUCTION

In the past few years, tandem solar cells have been the center of much research as an alternate source of generating electrical power in space applications (refs. 1-4). However, for a solar cell to be suitable for this application, it must tolerate the harsh radiation environment of space. Such a cell is the two-terminal, monolithic $\text{InP/Ga}_{0.47}\text{In}_{0.53}\text{As}$ tandem solar cell grown by the National Renewable Energy Laboratory. In collaboration with the Naval Research Laboratory (NRL), the tandem cell program has been directed toward optimizing the radiation resistance of the tandem cells by improving the device structure. To date, this has lead to the fabrication of two-terminal, monolithic prototypes as large as $2 \times 2 \text{ cm}^2$ with beginning of life (BOL) efficiencies greater than 22% (1 sun, AM0, 25 °C). Several of these cells will be tested in the STRV 1 space experiment soon (ref. 5).

An InP-based approach has been integrated into the tandem technology mainly because of the proven higher radiation resistance of shallow homojunction (SHJ) InP cells than other types such as Si and GaAs (ref. 6). A key issue in the development of the two-terminal tandem device is to design each subcell so that the series current flow through both junctions is matched end-of-life (EOL) after irradiation. Preliminary studies on $\text{InP/Ga}_{0.47}\text{In}_{0.53}\text{As}$ tandem cells irradiated with successive fluences of 1 MeV electrons have already shown promising results (ref. 2). The subcell currents remained equal at relatively high fluences, and the degradation of the photovoltaic (PV) parameters occurred at a slow rate. By varying the base dopant level of the $\text{Ga}_{0.47}\text{In}_{0.53}\text{As}$ bottom cell, it was found that the rate of decay of the short-circuit current density (J_{sc}) and the open-circuit voltage (V_{oc}) is more pronounced for the heavily-doped case by the former parameter but less pronounced by the latter (ref. 7). As a first step in the optimization procedure for the tandem cell, the base dopant level of the bottom cell was reduced.

The ability of a solar cell to recover from radiation damage is also an important aspect of the overall cell performance. The recovery of irradiated tandem cells due to thermal annealing in the dark is presented, and the recovery is analyzed in terms of the annealing characteristics of the individual cells.

The tandem cells were tested with successive fluences of 1 MeV electrons. Illuminated current-voltage (I-V) measurements and annealing results are presented for $\text{InP/Ga}_{0.47}\text{In}_{0.53}\text{As}$ solar cells. The results are compared with previous studies on $\text{InP/Ga}_{0.47}\text{In}_{0.53}\text{As}$ cells and with each component cell, all with a similar structure.

CELL DESCRIPTION

The tandem cells were grown by the atmospheric-pressure metal organic vapor phase epitaxy (APMOVPE) technique for which the details have been described elsewhere (ref. 8). The cell structure consists of an InP top junction, a $\text{Ga}_{0.47}\text{In}_{0.53}\text{As}$ bottom junction and a $\text{Ga}_{0.47}\text{In}_{0.53}\text{As}$ tunnel junction to provide the electrical connection between the subcells, as shown schematically in Fig 1. The component cells are lattice-matched by adjusting the Ga and In compositions. The total area of the tandems in this study were $1 \times 1 \text{ cm}^2$.

EXPERIMENTAL PROCEDURE

The cells were irradiated with incremental fluences of 1 MeV electrons at NASA Goddard, and the fluence was measured with a Faraday cup. The irradiations were performed in ambient conditions at room temperature under open circuit. The beam current was usually kept in the nanoamp regime to avoid heating the device, and the electron fluence ranged from 1×10^{13} to $2.4 \times 10^{16} \text{ cm}^{-2}$. Measurements of the I-V characteristics were made within three hours after each irradiation. The results were obtained under one sun, AM0 at 25°C using a 2500 W SpectroLab, Mark III solar simulator. The efficiency is measured using an InP reference cell calibrated by NASA Lewis Research Center. Since the band gap of $\text{Ga}_{0.47}\text{In}_{0.53}\text{As}$ is 0.75 eV, it should be pointed out that the IR portion of the simulator in this energy region is somewhat stronger than what it should be. This is characteristic of the uncorrected Xe sources employed, and the overall effect this has on the I-V curve is to enhance the fill factor by a very small percentage (ref. 9). Annealing of the radiation damage was carried out in the dark and in the air up to 500 K.

RESULTS

The effects of radiation damage on the cell I-V curves are illustrated in Fig. 2. The main feature of importance from the I-V curve is the smooth kink which begins to develop at low voltages as a result of the current mismatch between the top and bottom cells. The kink appears at a fluence of about $3 \times 10^{15} \text{ cm}^{-2}$, and becomes more pronounced as the irradiation increases. This feature has been associated with the reverse-bias breakdown of the $\text{Ga}_{0.47}\text{In}_{0.53}\text{As}$ bottom cell, which has been observed before in InP/ $\text{Ga}_{0.47}\text{In}_{0.53}\text{As}$ devices (ref. 2). (Not related to radiation damage, however, a mismatch in the currents between the subcells at BOL has been seen due to the spectral content of different light sources (ref. 9).) This allows the larger generated current from the top subcell to pass through the tandem. The data also show excellent radiation resistance in these partially optimized cells despite the presence of a slight BOL current mismatch between the subcells.

Figure 3 depicts the change of the PV parameters with electron fluence for a tandem cell. At low fluences, the degradation of the maximum power (P_{max}) output of the cell was primarily due to the reduction of J_{sc} and V_{oc} . The power loss at a fluence of $1 \times 10^{15} \text{ cm}^{-2}$ was about 20% relative to the BOL power. An additional plot of the degradation of the efficiency of a SHJ InP solar cell is included in the figure for comparison. The degradation of the tandem cell efficiency is comparable to that of the SHJ InP cell. It should be noted that for GaAs/Ge solar cells the FF has been reported to be affected by the infrared portion of the excitation source (ref. 9). Since the infrared content of the Xe source used in this study has not been entirely suppressed to simulate the sun's true IR spectrum, the FF considered here is that of an effective FF. Although this should boost the cell efficiency by a small percentage, the radiation response and the annealing behavior of the solar cells are the issue of importance and not the absolute values of the PV parameters.

Illustrated in Fig. 4 are two I-V curves measured after irradiation with 1 MeV electrons at a fluence of $3 \times 10^{15} \text{ e/cm}^2$ for the tandem cell in this work, and a tandem cell from a previous study for comparison. The present cell is offset by 0.25 for clarity. At this fluence, P_{max} from the early tandem is suppressed by the radiation-induced kink which appears as a result of the current mismatch. The present tandem cell does not show a pronounced current mismatch at this fluence, and in consequence, P_{max} is considerably higher. Therefore, the devices studied here show a dramatic enhancement of the radiation resistance compared to the previous cell. This is known to be due to the reduced carrier concentration in the base of the bottom cell (ref. 2), and is discussed below.

A desirable feature of space solar cells is the ability to thermally anneal the radiation damage while being subject particle irradiation. Annealing of InP/ $\text{Ga}_{0.47}\text{In}_{0.53}\text{As}$ cells exposed to $2.4 \times 10^{16} \text{ cm}^{-2}$ electron

irradiation was carried out to examine the recovery of the cell response. Fig. 5 depicts a few I-V curves that were isochronally and isothermally annealed, both in 30-minute increments. As illustrated in the figure, the I-V curves gradually recover from the post-rad curve but fall short from recovering completely. The behavior of PV parameters as a function of annealing temperature is shown in Fig. 6. The pre-annealed value of each parameter is normalized with respect to the corresponding pre-rad value. Partial recovery of J_{sc} is seen to begin at 350 K and begins to level off near 450 K and stays constant up to 500 K. At this temperature, the sample was annealed isothermally to check whether more recovery was possible. All parameters except for Eff% showed no further appreciable recovery. At 500 K for 1.5 hours, P_{max} has recovered by 16% from its pre-anneal value.

DISCUSSION

Recent studies on prototype, two-terminal, monolithic InP/Ga_{0.47}In_{0.53}As solar cells demonstrated that these devices perform very well when exposed to 1 MeV electrons. It has been shown that the degradation of the PV response is similar to that observed in SHJ InP cells up to a fluence of 3×10^{14} e/cm². The results were very encouraging considering that the previous tandem cells were not optimized for radiation resistance. The present study reports on the work of a first step in optimizing the tandem cell structure for radiation resistance.

In an effort to optimize the InP/Ga_{0.47}In_{0.53}As tandem solar cells so that the subcell currents remain matched at EOL in a space environment, the PV response of the component cells must be adjusted. Particularly, J_{sc} must be designed to be highly tolerant to radiation. Work dealing with the effects of base dopant level on J_{sc} from Ga_{0.47}In_{0.53}As and InP solar cells suggest that the radiation hardness of J_{sc} is improved by decreasing the base dopant concentration (refs. 2, 7, 10). Similar results have been obtained from GaAs single junction solar cells (ref. 11). In view of this, the base dopant level of the bottom subcell was reduced by an order of magnitude (to about 10^{17} cm⁻³) which caused the resistance of J_{sc} to increase. In consequence, the onset of the current mismatch between the subcells was extended to substantially higher fluence levels. From previous tandem cells, the mismatch occurs at 3×10^{14} e/cm² whereas in this study it occurs at 3×10^{15} e/cm², which is a dramatic improvement. The improved current matching which is, in turn, due to the radiation-hardening of J_{sc} , is a result of the decreased sensitivity of charge collection to the radiation-induced degradation of the minority carrier diffusion length (or its lifetime) in the bottom cell (ref. 10).

It is interesting to note that the fill factor is only reduced by 8% relative to the BOL value at a fluence of 10^{15} e/cm². Using a technique developed by Handy (ref. 12), intensity-dependent measurements of the I-V curves for the tandem cells show that the series resistance is in the order of a few milliohms for the fluence range studied. In addition to this, analysis of dark I-V fits suggest that the series resistance may not even play a role in the degradation of Ga_{0.47}In_{0.53}As devices at a fluence of 10^{18} e/cm² (ref. 13). This would seem to suggest that the overall series resistance has almost a negligible effect on FF, and thus the device performance. The low series resistance is probably due to the heavily doped base of each subcell thus decreasing the overall material resistivities.

Partial recovery is seen in the irradiated tandem cells. The annealing characteristics exhibited by J_{sc} and V_{oc} are similar to those reported elsewhere (ref. 14) on SHJ InP solar cells and they seem to be consistent with this type of cell. Particularly, in that study, no notable recovery of J_{sc} , V_{oc} and P_{max} is further seen at temperatures above 400 K. This appears to be consistent with other SHJ InP cells where a similar trend is observed (ref. 15, 16). The annealing behavior of the tandem cell can be described in terms of the minority carrier diffusion length of each component cell. The recovery of J_{sc} under thermal annealing can be attributed to annealing of defects formed in the neutral regions of the device where J_{sc} is mostly affected. This, in turn, results in an increase of the minority carrier diffusion length thus allowing the collection of charge carriers to be more efficient. A point worthy of mention is that according to unpublished results obtained at NRL, the recovery of J_{sc} from the Ga_{0.47}In_{0.53}As bottom cell occurs at a faster rate than the InP top cell. This suggests that the recovery of J_{sc} from the tandem cell is mainly characteristic of the recovery from the InP top cell. Likewise, V_{oc} from InP solar cells does not recover as fast as that from Ga_{0.47}In_{0.53}As solar cells. This is an interesting result because it shows that unless the recovery rate of the PV response of the top subcell is the same as that of the bottom subcell, the tandem cell will not recovery effectively under thermal annealing.

A final remark about the degradation of J_{sc} and V_{oc} can be made on the basis of their normalized pre-annealed values in Fig. 6. At a fluence of 2.4×10^{18} e/cm², J_{sc} and V_{oc} have decreased to 62% and 78% from their pre-rad values, respectively. The modeling results from reference 10 combined with the results

of references 2 and 7 suggest that a more optimized cell design for the radiation resistance of J_{sc} and V_{oc} , the efficiency would be expected to increase by several percent at EOL.

CONCLUSIONS

High-performance, partly optimized InP/Ga_{0.47}In_{0.53}As tandem solar cells have been achieved, and have shown excellent radiation response. Efficiencies greater than 22% have already been obtained from 2x2 cm² cells. After 1 MeV electron irradiation, the tandem cells with a BOL efficiency of over 20% have shown an efficiency of approximately 10% at a fluence of 10¹⁶ e/cm². This is higher than Si and GaAs, both with efficiencies of about 7.5% at the same fluence. Furthermore, the results described here show that the radiation resistance of J_{sc} and V_{oc} can be further optimized by fine-tuning the device structure, specifically, the base dopant level of the Ga_{0.47}In_{0.53}As bottom cell.

The annealing results revealed that the tandem cell annealing characteristics are mainly controlled by the InP top cell. This indicates that if annealing of tandem solar cells are viable while in earth orbit, then not only is the degradation rate of importance but also the annealing rate. That is, J_{sc} in each subcell must recover at the same rate so that current matching can be maintained throughout the mission life.

REFERENCES

1. H.L. Cotal, G.P. Summers, and S.R. Messenger, "Radiation Effects of Two-Terminal, Monolithic InP/Ga_{0.47}In_{0.53}As Tandem Solar Cells," 6th IEEE International Conference on Indium Phosphide and Related Materials, March 1994, pp. 496-499.
2. R.J. Walters, S.R. Messenger, M.W. Wanlass, and G.P. Summers, "1 MeV Electron Irradiation of Monolithic, Two-Terminal InP/Ga_{0.47}In_{0.53}As Solar Cells," 23rd IEEE Photovoltaic Specialists Conference, May 1993, pp. 1475-78.
3. S.R. Kurtz, J.M. Olson, K.A. Bertness, D.J. Friedman, A. Kibbler, B.T. Cavicchi, and D.D. Krut, "Radiation Hardness of Ga_{0.5}In_{0.5}P/GaAs Tandem Solar Cells," 10th Space Photovoltaic Research and Technology Conference, May 1991, pp. 40-1 to 40-7.
4. P.R. Sharps, M.L. Timmons, R. Vankatasubramanian, R. Pickett, J.S. Hills, J. Hancock, J. Hutchby, P. Iles, C.L. Chu, M. Wanlass, and J.S. Ward, "Development of 20% Efficient GaInAsP Solar Cells," 23rd IEEE Photovoltaic Specialists Conference, May 1993, pp. 633-638.
5. C. Goodbody, and N. Monekoso, "The STRV-1 A & B Solar Cell Experiments," 23rd IEEE Photovoltaic Specialists Conference, May, 1993, pp. 1459-1464.
6. R.J. Walters, S.R. Messenger, G.P. Summers, E.A. Burke, and C.J. Keavney, "Proton and Electron Irradiation of MOCVD InP Solar Cells: Experimental Results and Radiation Modeling," 22nd IEEE Photovoltaic Specialists Conference, Oct., 199.
7. R.J. Walters, G.J. Shaw, S.R. Messenger, and G.P. Summers, "The Effect of Base Dopant Level and Thickness on the Radiation Response of GaInAs Solar Cells," 5th IEEE International Conference on Indium Phosphide and Related Materials, April, 1993, pp. 602.
8. M.W. Wanlass, J.S. Ward, K.A. Emery, and T.J. Coutts, "Monolithic, Series-Connected InP/Ga_{0.47}In_{0.53}As Tandem Solar Cells," 23rd IEEE Photovoltaic Specialists Conference, May 1993, pp. 621-625.
9. L.D. Partain, G.F. Virshup, and N.R. Kaminar, "Quantum Yield Spectra and I-V Properties of a GaAs Solar Cell Grown on a Ge Substrate," 20th IEEE Photovoltaic Specialists Conference, September 1988, pp. 759-763.

9. L.D. Partain, G.F. Virshup, and N.R. Kaminar, "Quantum Yield Spectra and I-V Properties of a GaAs Solar Cell Grown on a Ge Substrate," 20th IEEE Photovoltaic Specialists Conference, September 1988, pp. 759-763.
10. C.J. Keavney, R.J. Walters, and P.J. Drevinsky, "Optimizing the radiation resistance of InP Solar Cells: Effect of Dopant Density and Cell Thickness," J. Appl. Phys. **73**, 1993, pp.60-70.
11. M. Yamaguchi, and C. Amano, "Numerical Analysis for Radiation-Resistant GaAs Heteroface Solar Structures," J. Appl. Phys. **57**, 1985, pp. 537-544.
12. R.J. Handy, "Theoretical Analysis of the Series Resistance of a Solar Cell," Solid-State Electronics **10**, 1967, 765-775.
13. R.J. Walters, S.R. Messenger, G.P. Summers, E.A. Burke, and C.J. Keavney, IEEE Trans. Nucl. Sci. **N5-38**, 1991, pp. 1153.
14. N.M. Pearsal, N. Robson, H. Thomas, J.K. Luo, C.M. Hardingham, and T.A. Cross, "Annealing of Irradiation Damage in Epitaxial InP Homojunction Solar Cells," 23rd IEEE Photovoltaic Specialists Conference, May 1993, pp. 1442-1447.
15. R.J. Walters, Ph.D. Dissertation (University of Maryland Baltimore County, Baltimore, MD, 1994).
16. R.J. Walters, , G.P. Summers, M.L. Timmons, R. Venkatasubramanian, J.A. Hancock, and J.S. Hills, "Annealing of Irradiated n p InP Buried Homojunctions," 13th Space Photovoltaic Research and Technology Conference, June 1994, this vol.

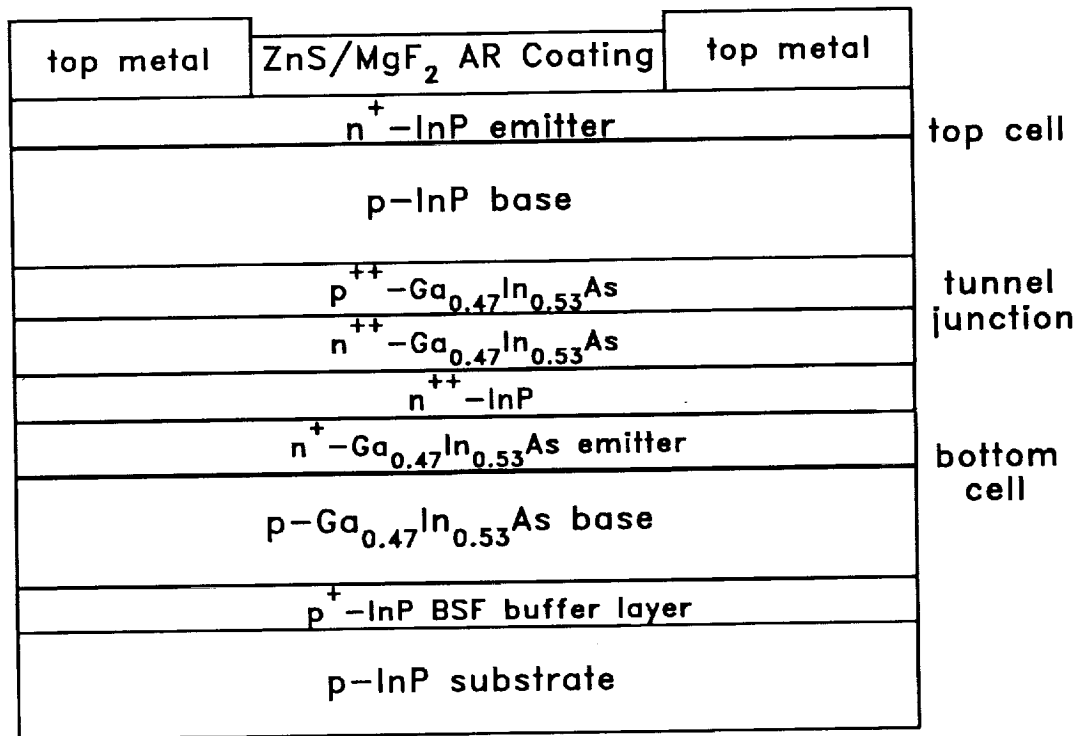


Figure 1: Schematic diagram of the InP/Ga_{0.47}In_{0.53}As tandem solar cell structure.

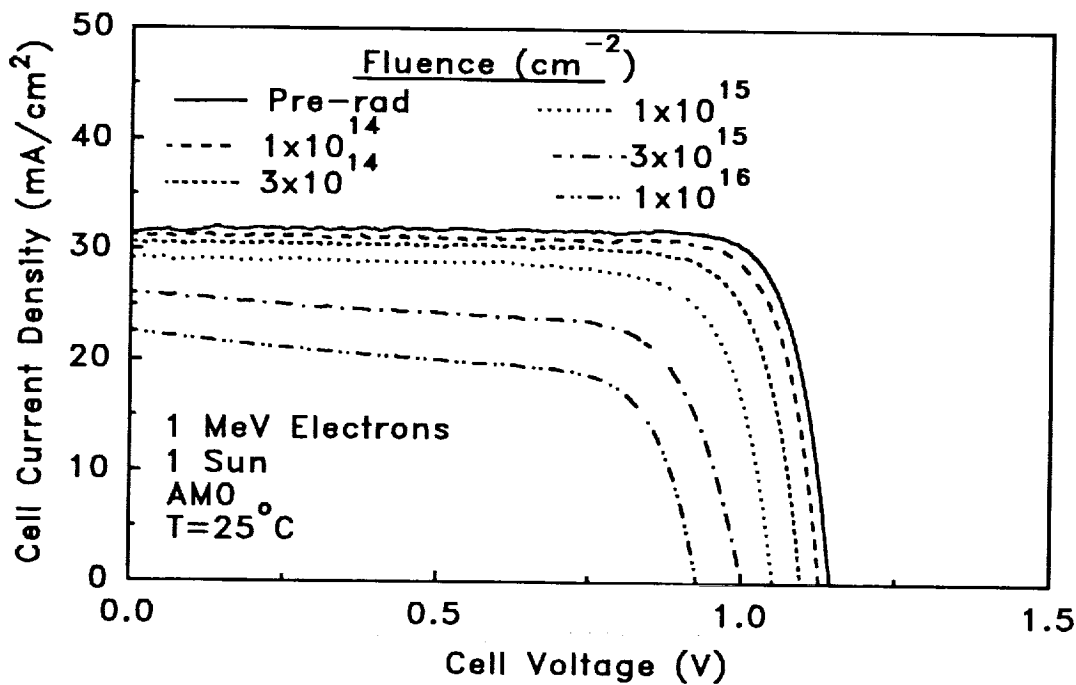


Figure 2: The effects of 1 MeV electron irradiation on the $\text{InP}/\text{Ga}_{0.47}\text{In}_{0.53}\text{As}$ tandem solar cell I-V curves. A kink is shown at low voltages.

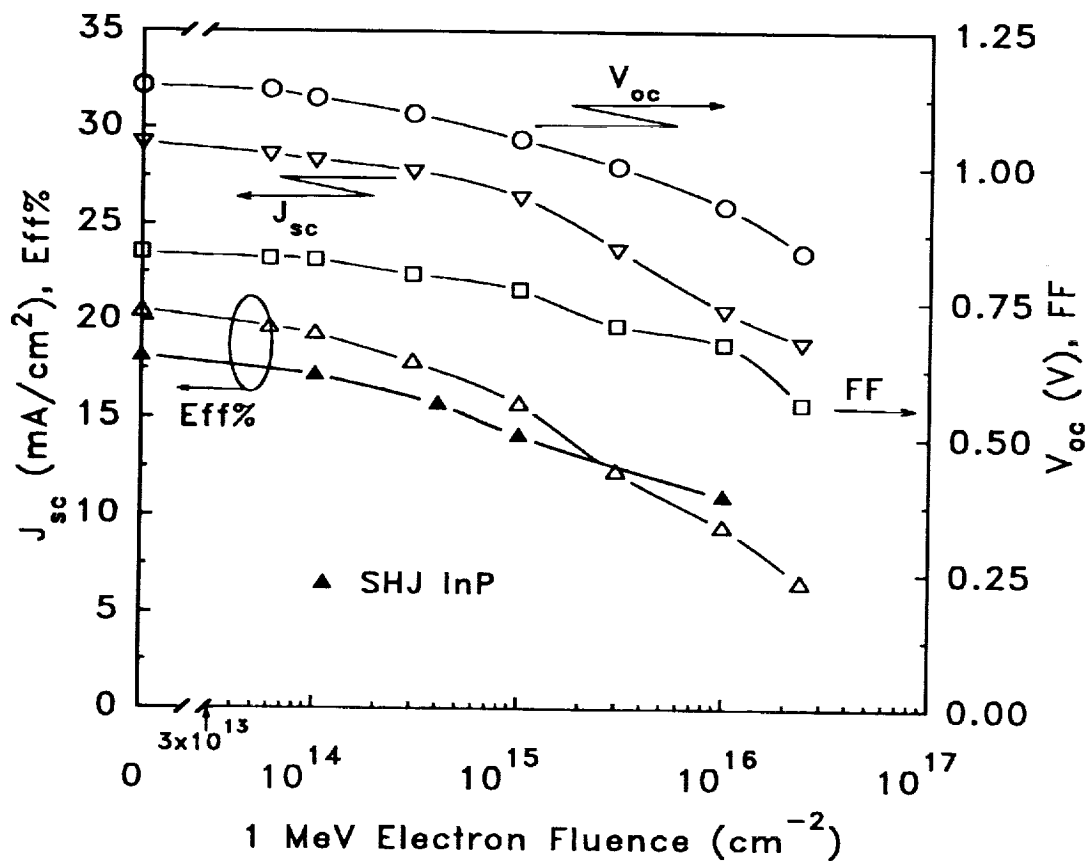


Figure 3: The degradation of the cell response for the $\text{InP}/\text{Ga}_{0.47}\text{In}_{0.53}\text{As}$ device shown in Fig. 2. The n p SHJ InP data was obtained from reference 15.

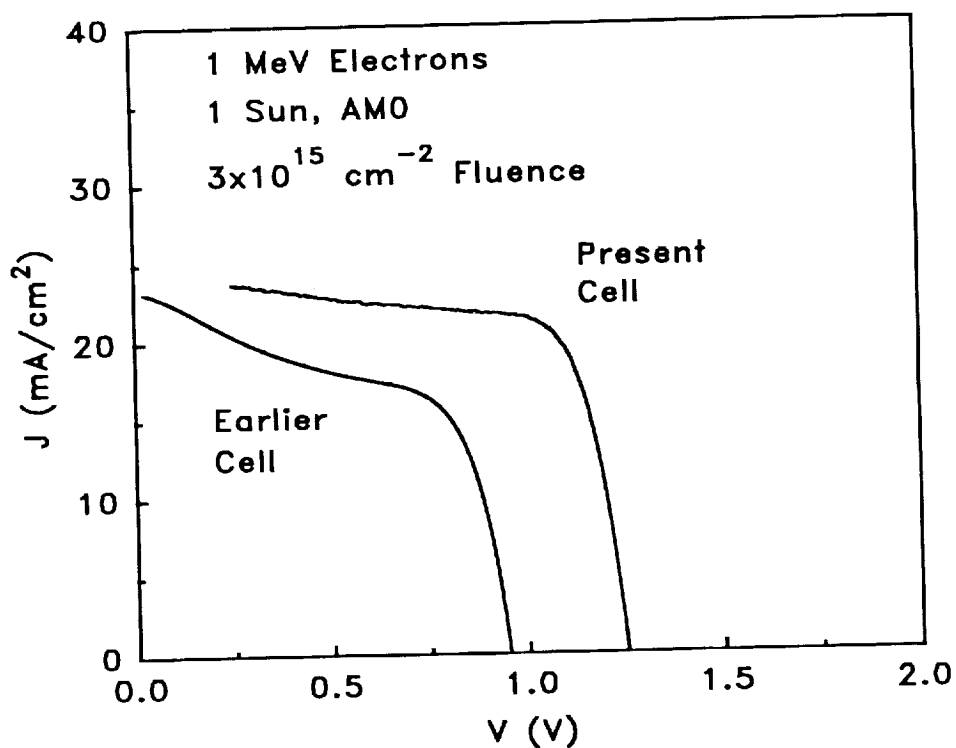


Figure 4: Comparison of the I-V curves for the tandem cell in this study with a tandem cell from a previous study (ref. 2). The present cell curve has been displaced by 0.25 V for clarity.

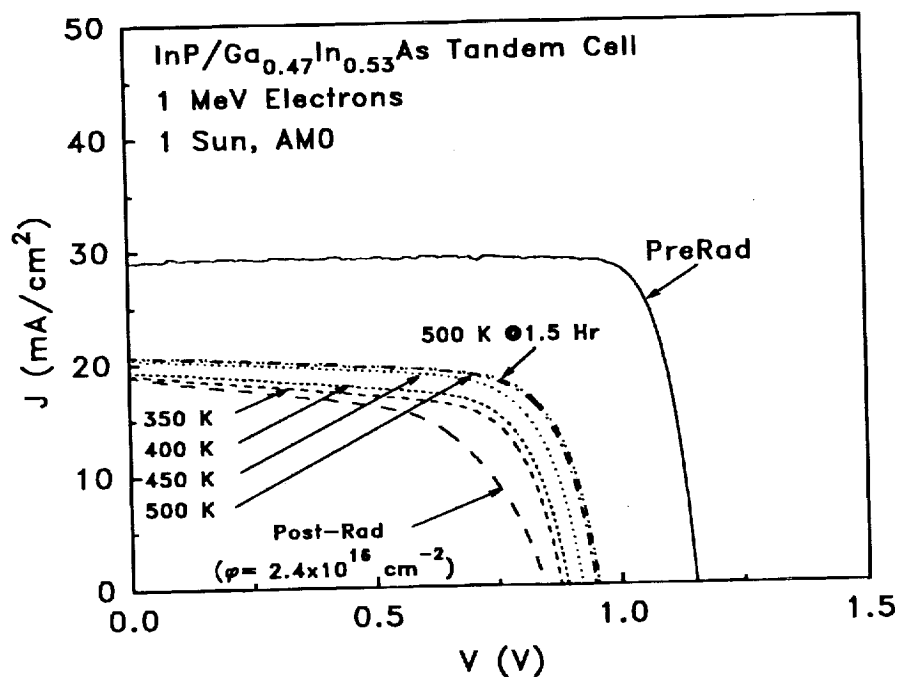


Figure 5: Annealing of 1 MeV electron-irradiated I-V curves for the InP/Ga_{0.47}In_{0.53}As tandem solar cell shown in Fig. 2.

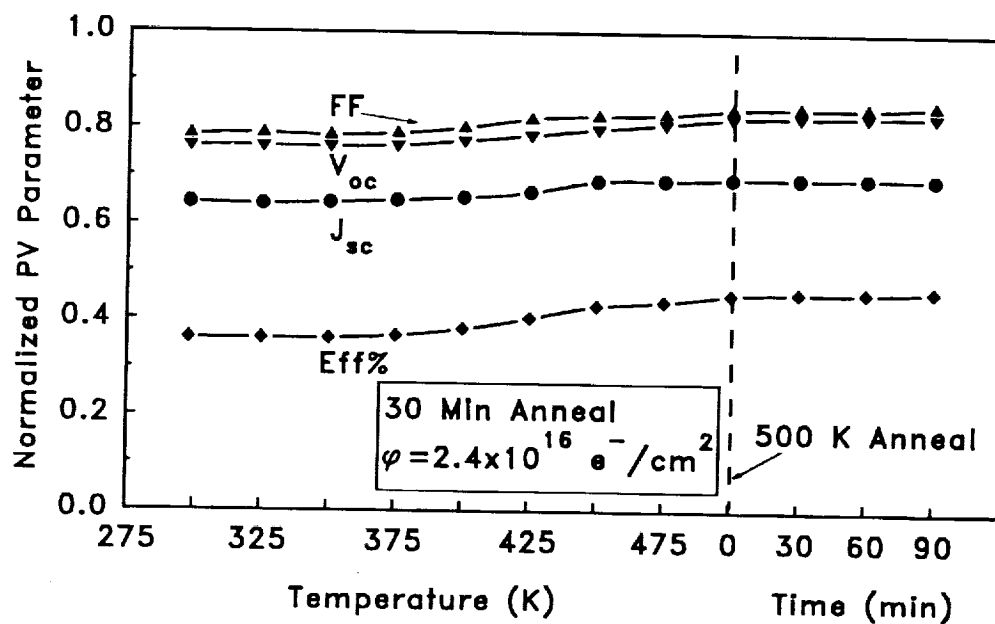


Figure 6: The recovery of the PV parameters of the InP/Ga_{0.47}In_{0.53}As solar cell irradiated with 1 MeV electrons. Partial recovery is seen up to 475 K. Only V_{oc} continues to recover gradually above this temperature.

RADIATION EFFECTS ON p+n InP JUNCTIONS GROWN BY MOCVD

S.R. Messenger
SFA, Inc.
Landover, Maryland

R.J. Walters
U.S. Naval Research Laboratory
Washington, DC

M.J. Panunto
University of Maryland Baltimore County
Baltimore, Maryland

and

G.P. Summers
U.S. Naval Research Laboratory
Washington, DC

INTRODUCTION

The superior radiation resistance of InP over other solar cell materials such as Si or GaAs has prompted the development of InP cells for space applications. The early research on radiation effects in InP was performed by Yamaguchi and co-workers who showed that, in diffused p-InP junctions, radiation-induced defects were readily annealed both thermally and by injection, which was accompanied by significant cell recovery.

More recent research efforts have been made using p-InP grown by metalorganic chemical vapor deposition (MOCVD). While similar deep level transient spectroscopy (DLTS) results were found for radiation induced defects in these cells and in diffused junctions, significant differences existed in the annealing characteristics. After injection annealing at room temperature, Yamaguchi noticed an almost complete recovery of the photovoltaic parameters, while the MOCVD samples showed only minimal annealing.

In searching for an explanation of the different annealing behavior of diffused junctions and those grown by MOCVD, several possibilities have been considered. One possibility is the difference in the emitter structure. The diffused junctions have S-doped graded emitters with widths of $\sim 0.3\mu\text{m}$, while the MOCVD emitters are often doped with Si and have widths of $\sim 300\text{\AA}$ ($0.03\mu\text{m}$). The difference in the emitter thickness can have important effects, e.g. a larger fraction of the total photocurrent is generated in the n-type material for thicker emitters. Therefore the properties of the n-InP material may explain the difference in the observed overall annealing behavior of the cells.

EXPERIMENTAL

In this study, n-InP solar cells and mesa diodes were irradiated with either 1 MeV electrons or 3 MeV protons, with both (current-voltage) IV and DLTS measurements being made. The IV measurements were performed both in the dark and under 1 sun AM0 illuminations using an Oriel 1000W portable Xe arc lamp simulator. A Kepco 50-2M bipolar amplifier, and two Keithley 617 electrometers were employed in the IV measurements, which were computer controlled through a GPIB interface. DLTS and capacitance-voltage (CV) measurements were performed using the Bio-Rad DL4600 system which uses the Boonton 72-B capacitance meter. The cryostat used in the DLTS system has a temperature range of 85-500K which allows annealing experiments to be performed directly in the cryostat. The cryostat window is made of sapphire which allows for cell illumination as well. All cell measurements were thus performed in the cryostat. This unique system provides a simple and convenient means for collecting cell data.

The samples were grown by Spire Corporation using Si as the n-type base dopant. Figure 1 gives a schematic description of the samples. The base dopant level was $\sim 3 \times 10^{16} \text{ cm}^{-3}$ and that of the emitter was $\sim 2 \times 10^{18} \text{ cm}^{-3}$, both of which were determined from CV measurements.

1 MeV electron irradiations were performed at a Van de Graaff accelerator at the NASA Goddard Space Flight Center in Greenbelt, MD. Incremental fluences were performed up to $\sim 10^{18}$

e/cm^2 . The beam currents were low enough ($\sim 150 \text{ nA}$) to avoid sample heating during the irradiations. Dosimetry is known to within 10-15%. The 3 MeV proton irradiations were performed at the Naval Surface Warfare Center in White Oak, MD on a Pelletron accelerator. One irradiation was performed giving a total fluence $\sim 3 \times 10^{12} \text{ p}/\text{cm}^2$ (15-20% accurate). The proton beam was rastered over a 2.4 cm^2 area, and the current on the target was $\sim 14 \text{ nA}/\text{cm}^2$.

RESULTS

DLTS Measurements:

Figure 2 shows the DLTS spectrum measured on a $\text{p}^+ \text{n}$ InP mesa diode after 1 MeV electron irradiation to a fluence $\sim 10^{16} \text{ cm}^{-2}$. Majority carrier traps EN1-4, and EB are formed during the irradiation. One minority carrier trap, HN1, appears in small concentrations and seems to be due to a composite defect. The "EN" refers to electron trapping in n-type InP. Similarly, "HN" refers to hole trapping in p-type InP. 3 MeV proton irradiation produces the same defect spectrum, except the relative peak heights are slightly different as shown in Figure 3. Trap EN1 is only seen using rate windows $> 1000/\text{s}$. As can be seen in Figs. 2 and 3, EB is the dominant DLTS signal in both cases. The activation energy, capture cross section, and annealing characteristics of this peak are similar to those of the EB peak measured in irradiated p-type InP as shown by McKeever et al. in reference 1. No clear relationship between the remaining peaks and peaks measured in irradiated p-type InP seems to exist. The activation energy of the EN2 defect is similar to that of the ED defect measured in irradiated p-type InP ($\sim 0.3 \text{ eV}$) as seen in reference 2, but the capture cross section of EN2 is about two orders of magnitude larger than that of ED. Also, the activation energy of HN1 is similar to that of the H4 defect (0.34 eV at this dopant level), but the capture cross section of HN1 is about an order of magnitude larger than that of H4. This may be due to the fact that HN1 is most likely several overlapping peaks. Tables I and II characterize each defect according to its activation energy, capture cross section, defect concentration, and introduction rate after 1 MeV electron and 3 MeV proton irradiations, respectively.

Introduction rates were calculated for the 1 MeV electron irradiations and are included in Table I. The errors are ~ 2 -4%. Figure 4 shows DLTS data for the introduction of defects with 1 MeV electron irradiation. The calculated introduction rate for EB of 0.15 cm^{-1} is much lower than the value of 0.7 given for the dominant defect H4 in p-type InP by Sibille in reference 3 and also by Levinson et al. in reference 4 (who measured a value of 1.0). The total trap introduction rate is 0.2 cm^{-1} which is also much lower than that found for p-type InP as stated in references 3-5. The introduction rates for the 3 MeV protons were obtained from only one data point assuming a linear dependence. This is justified due to the linear relationships found in the 1 MeV electron irradiated samples. The total trap introduction rate here is 52.5 defects per incident proton per cm which compares nicely with the data shown by Walters and Summers in reference 6. Overall, there are much fewer stable defects created in n-type InP than there are in p-type InP. This same result was also seen by Levinson et al. in references 4 and 7.

Forward bias injection annealing at any temperature did not change the DLTS defect structure. This is in contrast to the behavior of the H4 defect in irradiated p-type InP which injection anneals readily at room temperature. Isochronal thermal annealing was performed on the electron irradiated junctions and the results are shown on Figure 5. It is seen that the only defect which thermal anneals is EB. By a temperature of $\sim 400\text{K}$, EB is completely removed. It should be mentioned that the annealing experiments were performed with the sample under a reverse bias of -2V . It was found that open circuit anneals led to an enhanced annealing rate. Experiments are currently under way dealing specifically with this effect. Thermal annealing both with and without an applied forward bias produces the same results implying that the annealing is not injection sensitive. There is therefore only one thermal annealing stage occurring ~ 360 - 380K (for the case of $V_R = -2\text{V}$) where the EB peak is completely removed. This happens to be the same temperature where EB anneals in p-type InP as

discussed in reference 1. Isothermal annealing experiments on EB indicate a thermal activation energy to be 1.23 ± 0.02 eV in a first order process. This is for the case of annealing with a bias voltage of -2V. For zero bias, the thermal activation energy is 1.13 eV. These thermal energies are close to the value of 1.02 eV that Yamaguchi measured in p-type diffused InP junctions for the H4 defect as shown in reference 8. Reference 9 contains isothermal annealing data on LEC n-InP material. The 0.79 eV defect there has annealing behavior which is very similar to that of EB. First of all, it is insensitive to injection just as shown above. Also, its thermal activation energy is 0.98 eV which is also close to what was measured above.

Illuminated IV Measurements:

Due to the similarity in the defect spectra under both electron and proton irradiation, the IV data were performed on the 3 MeV proton irradiated cells only. The first experiment measured the recovery of the cells due to illuminations below room temperature. The IV curves were taken at 86K because, in p-type InP, it has been found that illuminated IV measurements taken at 86K do not cause injection annealing (ref. 10). The annealing experiment consisted of measuring the illuminated IV curve at 86K before and after the 3 MeV proton irradiation. The cell was then warmed to 200K and illuminated, at short-circuit, for 35 minutes before being cooled to 86K where another illuminated IV measurement was made. This same procedure was performed for an illuminated anneal at 300K for 30 minutes. The measured IV curves are shown in Figure 6 and the photovoltaic (PV) parameters are given in Table III. The cell shows some recovery due to the illuminations. The largest increase is in the short circuit current (I_{sc}), but even this increase is small. The fill factor (FF) also increases slightly after the 200K illumination but not after the 300K illumination. The increase in these two parameters caused an increase in the maximum power (P_{max}), but the recovery is inhibited because the open circuit voltage (V_{oc}) shows no recovery. The next experiment was an anneal at room temperature. The same sample was then left in the dark at 300K for one week. As is seen in Figure 6, there is more recovery in I_{sc} , but it is again only slight.

The same cell was then illuminated above room temperature. In these experiments, the illuminated IV curves could be measured at room temperature without altering the results. Figure 7 includes the IV curves measured after 1 week in the dark to indicate the final state of the cell after the $T \leq 300$ K annealing stages. The corresponding PV data is given in Table IV. Illuminating the cell at 350K for 4 hours caused significant recovery in all of the PV parameters. In particular, V_{oc} is seen to recover for the first time. Subsequently illuminating the cell at 400K for 3 hours caused increases in all of the parameters. Two hours of illumination at 450K only caused an increase in V_{oc} , but I_{sc} was unaffected.

The IV curve measured after the 450K illumination represents the maximum recovery of the cell. Significant recovery is evident, primarily due to the increase in I_{sc} . However, while the recovery is substantial, it is far from complete. In particular, almost none of the radiation-induced degradation of the FF has been removed. Also, V_{oc} shows only very little recovery.

Dark IV Measurements:

Measurements were also made of the dark IV characteristics. By fitting the measured dark IV data to the standard three-term diode equation, estimates of the diffusion term (I_{01}), the recombination term (I_{02}), and the shunt resistance term (R_{sh}) were determined. A commercially available curve fitting package, Peakfit, by Jandel Scientific was used. These fits were performed after each annealing step.

The forward bias dark current characteristics of the same cell used above were measured at room temperature before and after irradiation, as well as after the successive annealing treatments

described above. The measured data were fit to the following equation :

$$I(V) = I_{01} \left(e^{\frac{qV}{kT}} - 1 \right) + I_{02} \left(e^{\frac{qV}{2kT}} - 1 \right) + \frac{V}{R_{sh}}$$

where I_{01} , I_{02} , and R_{sh} are the diffusion, recombination, and shunt resistance fitting terms, respectively. In this equation, it was assumed that the energy level (E_i) of the dominant recombination center is located at the intrinsic Fermi Level (E_i). Attempts were made to fit the data with E_i as a free parameter, but the pre-irradiation recombination current in this particular cell was large enough that changes in E_i from E_i had virtually no effect on the fit. Some examples of the fits obtained are shown in Figure 8. The data for the fitting parameters are given in Table V for the annealing steps above. The fit to the pre-irradiation data does not seem to be very good. The reason for this is not known. Nevertheless, the fits to the post-irradiation and post-anneal data were excellent.

DISCUSSION

These results with p*n InP grown by MOCVD will now be compared with those obtained using n*p InP fabricated both by thermal diffusion and by MOCVD. The last SPRAT conference contains the data for the diffused junctions from reference 11. Figure 9 shows annealing data for all three of these cell types for the maximum power output. The scales are normalized to beginning-of-life (BOL). As seen on Fig. 9 the diffused junctions fully recover after a thermal anneal of 450K while both MOCVD cells do not recover even at 500K. Moreover, the slow recovery of both MOCVD cell types appears to be the same indicating similar behavior for n- and p-type InP. This trend is also apparent in Figure 10 where the same cell types are plotted this time for the normalized open circuit voltage. The fitted dark IV parameters I_{01} and I_{02} also follow this trend as can be seen on Figure 11. Figure 11 plots the data from Table V on scales normalized to BOL. The same slow recovery mentioned above occurs. It was also noticed at the last SPRAT conference from reference 12 that the radiation induced defects in p-InP did not anneal until thermal anneals at 650K were performed. It might be the case that the PV parameters also would anneal at such temperatures, but the experiments have not been performed successfully.

CONCLUSION

Defect introduction and annealing studies were performed on Spire-grown n*p InP solar cells and mesa diodes. The introduction rates of the defects formed were shown to be much lower than the p-type counterparts. The annealing characteristics were, however, the same. In comparing the MOCVD samples with the diffused junctions, the diffused junctions showed much better annealing characteristics. Full recovery of the PV parameters existed in the diffused junctions where only minimal recovery is seen in the MOCVD samples. Future studies will try to explain this important difference.

REFERENCES

1. McKeever, S.W.S.; Walters, R.J.; Messenger, S.R.; and Summers, G.P.: Deep Level transient spectroscopy of irradiated p-type InP grown by metalorganic chemical vapor deposition. *J. Appl. Phys.*, vol. 69, 1991, pp. 1435-1439.
2. Walters, R.J.; Messenger, S.R.; Summers, G.P.; Burke, E.A.; and Keavney, C.J.: Proton and electron irradiation of MOCVD InP solar cells: Experimental results and radiation modelling. *Proc. of the 22nd IEEE Photovoltaic Specialists Conference*, October 7-11, 1991, Las Vegas, NE, pp.1560-1565.
3. Sibille, A. and Bourgoin, J.C.: Electron irradiation induced deep levels in p-InP. *Appl. Phys. Lett.*, vol. 41, 1982, pp. 956-958.
4. Levinson, M.; Temkin, H.; and Bonner, W.A.: Electron bombardment induced defect states in p-InP. *J. Electron. Mater.*, vol. 12, 1983, pp.423-432.
5. Drevinsky, P.J.; Cafer, C.E.; and Keavney, C.J.: Processing- and radiation-produced defects in InP solar cells. *Proc. of the 3rd IEEE International Conference on Indium Phosphide and Related Materials*, Cardiff, Wales, April 8-11, 1991, pp. 56-59.
6. Walters, R.J. and Summers, G.P.: Deep level transient spectroscopy study of proton irradiated p-type InP. *J. Appl. Phys.*, vol. 69, 1991, pp. 6488-6494.
7. Levinson, M.; Benton, J.L.; Temkin, H.; and Kimerling, L.C.: Defect states in electron bombarded n-InP. *Appl. Phys. Lett.*, vol. 40, 1982, pp. 990-992.
8. Yamaguchi, M.; Ando, K.; Yamamoto, A.; and Uemura, C.: Injection-enhanced annealing of InP solar-cell radiation damage. *J. Appl. Phys.*, vol. 58, 1985, pp. 568-574.
9. Koyama, J.; Shirafuji, J.; and Inuishi, Y.: Annealing behaviour of gamma-ray-induced electron traps in LEC n-InP. *Electronics Letters*, vol. 19, 1983, pp.609-10.
10. Walters, R.J.:A study of the annealing of radiation-induced defects in InP solar cells. Doctoral dissertation, University of Maryland Baltimore County, May, 1994.
11. Walters, R.J.; Summers, G.P.; and Bruening, J.: A detailed study of the photo-injection annealing of thermally diffused InP solar cells. *Proc. of the 12th Space Photovoltaic Research and Technology Conference*, NASA Lewis, Oct. 20-22, 1992, pp. 1-7.
12. Messenger, S.R.; Walters, R.J.; and Summers, G.P.: High temperature annealing of the minority carrier traps in irradiated MOCVD n⁺p InP solar cell junctions. Same as ref. 11, pp. 8-15.

Table I DLTS defect parameters for 1 MeV electron irradiated n-InP diodes. The concentrations shown are for a 1 MeV electron fluence of 10^{16} cm^{-2} and a DLTS rate window of 2 s^{-1} .

Trap	Activation energy (eV)	Capture cross section ($\times 10^{-13} \text{ cm}^2$)	Concentration ($\times 10^{14} \text{ cm}^{-3}$)	Introduction rate (cm^{-1})
EN2	0.31	2.05	0.1	-
EN3	0.48	2.37	1.3	0.013
EN4	0.55	0.287	1.8	0.018
EB	0.76	15.6	14.5	0.22

Table II DLTS defect parameters for 3 MeV proton irradiated n-InP. The fluence was $3 \times 10^{12} \text{ cm}^{-2}$. The introduction rates were calculated assuming a linear dependence. The concentrations are for a rate window of 2/s.

Trap	Activation energy (eV)	Capture cross section ($\times 10^{-13} \text{ cm}^2$)	Concentration ($\times 10^{13} \text{ cm}^{-3}$)	Introduction rate (cm^{-1})
EN2	0.3	6.3	0.95	3.2
EN3	0.43	9.5	3.2	11
EN4	0.62	131	1.	4.7
EB	0.74	5	8.6	29
HN1	0.34	1.69	1.6	5.3

Table III Recovery of PV parameters of n-InP solar cell under short circuit illuminations from 200K to 400K. IV curves measured at 86K. Irradiation was 3×10^{12} 3 MeV protons cm^{-2} .

Condition	I_{sc} (mA)	V_{oc} (V)	P_{max} (mW)	FF	Eff(%)
Pre rad	21.88	1.270	29.90	0.9323	18.95
Post rad	17.71	1.229	17.82	0.8186	13.03
200K, 35 min.	17.84	1.231	18.12	0.8257	13.26
300K, 30 min.	18.03	1.230	18.29	0.8245	13.38
300K, 1 wk.	18.52	1.230	18.75	0.8230	13.71
350K, 4 hr.	18.58	1.231	18.74	0.8192	13.71
400K, 1 hr.	18.76	1.230	19.14	0.8293	14.00
400K, 3hr.	18.99	1.239	19.44	0.8259	14.22

Table IV Cell recovery under illumination from 300K to 450K. IV curves measured at 298K. Irradiation was 3×10^{12} 3 MeV protons cm^{-2} . "Post rad" data was taken after 35 min. illum. at 200K.

Condition	I_{sc} (mA)	V_{oc} (V)	P_{max} (mW)	FF	Eff(%)
Pre rad	25.13	0.8549	18.22	0.8480	13.33
Post rad	19.55	0.7633	11.21	0.7513	8.201
300K, 30 min.	19.58	0.7645	11.28	0.7537	8.251
300K, 1 wk.	20.03	0.7654	11.54	0.7528	8.443
350K, 15 min.	20.57	0.7662	11.87	0.7533	8.682
350K, 4 hr.	21.17	0.7731	12.40	0.7573	9.068
400K, 1 hr.	21.43	0.7761	12.61	0.7583	9.223
400K, 3 hr.	21.79	0.7806	12.95	0.7614	9.475
450K, 2 hr.	21.86	0.7875	13.10	0.7609	9.580

Table V Effect of illumination on the dark current parameters on n-InP solar cells irradiated with 3 MeV protons to a fluence of $3 \times 10^{12} \text{ cm}^{-2}$. Parameters are from fits of the dark IV data.

Condition	$I_{01} (\times 10^{-16} \text{ A/cm}^2)$	$I_{02} (\times 10^{-9} \text{ A/cm}^2)$	$R_{sh} (\times 10^5 \Omega)$
Pre rad	1.099	0.1717	4.390
Post rad	9.451	3.090	3.665
350K, 15 min.	8.645	3.057	3.452
350K, 1.75 hr.	8.507	2.736	3.149
350K, 4 hr.	7.229	2.766	2.678
400K, 3 hr.	6.906	2.370	2.998
450K, 2 hr.	5.603	2.205	3.385

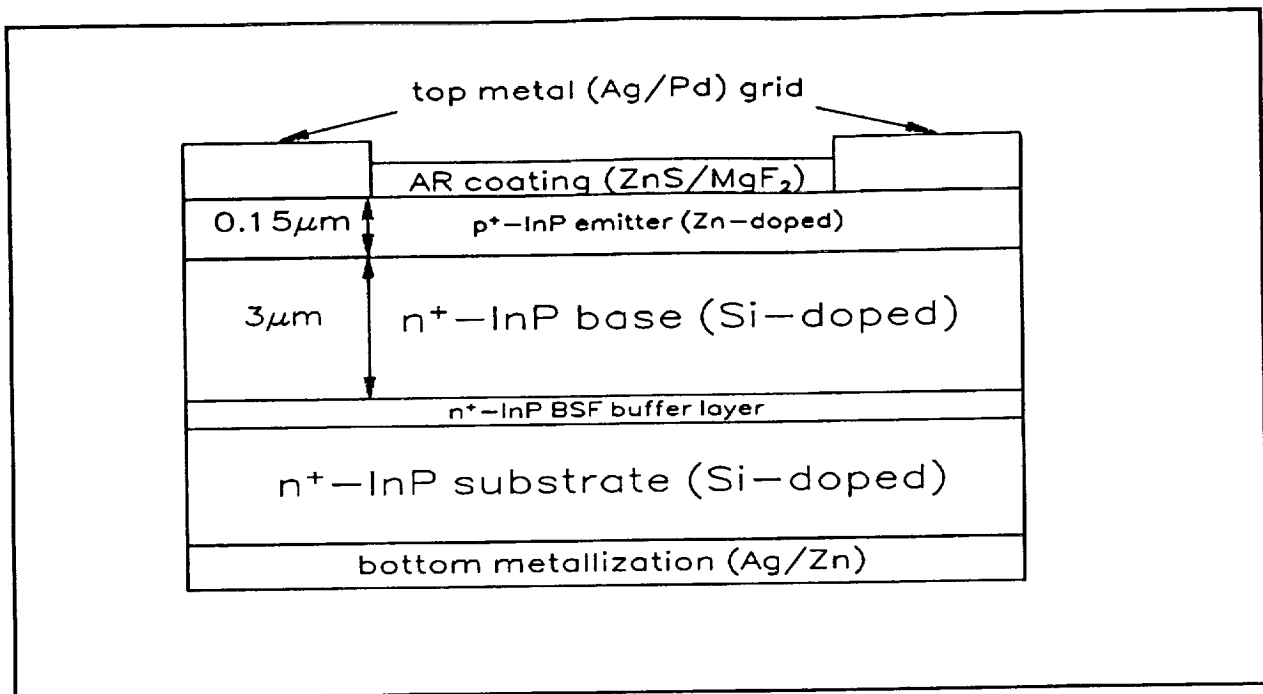


Figure 1 A schematic drawing of the p⁺n InP/InP cells.

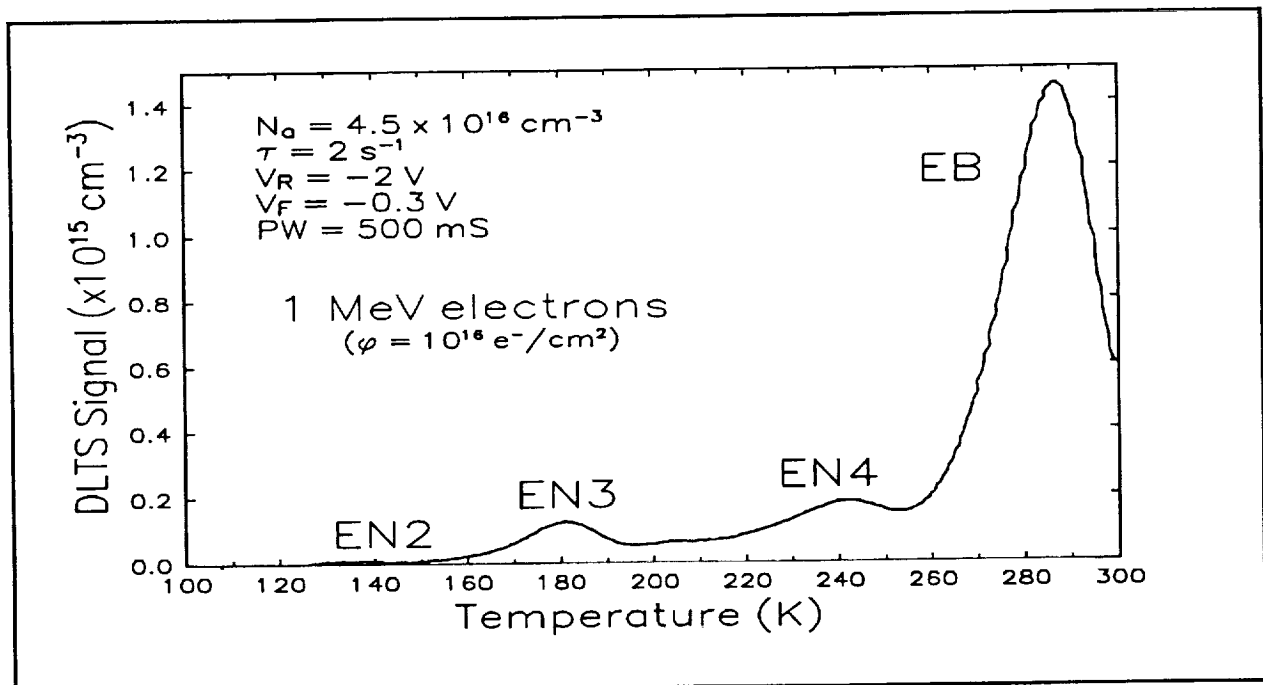


Figure 2 DLTS spectrum obtained after 1 MeV electron irradiation to a fluence of $1 \times 10^{16} \text{ cm}^{-2}$. The dominant peak, EB, is identified with the EB peak found in irradiated p-type InP.

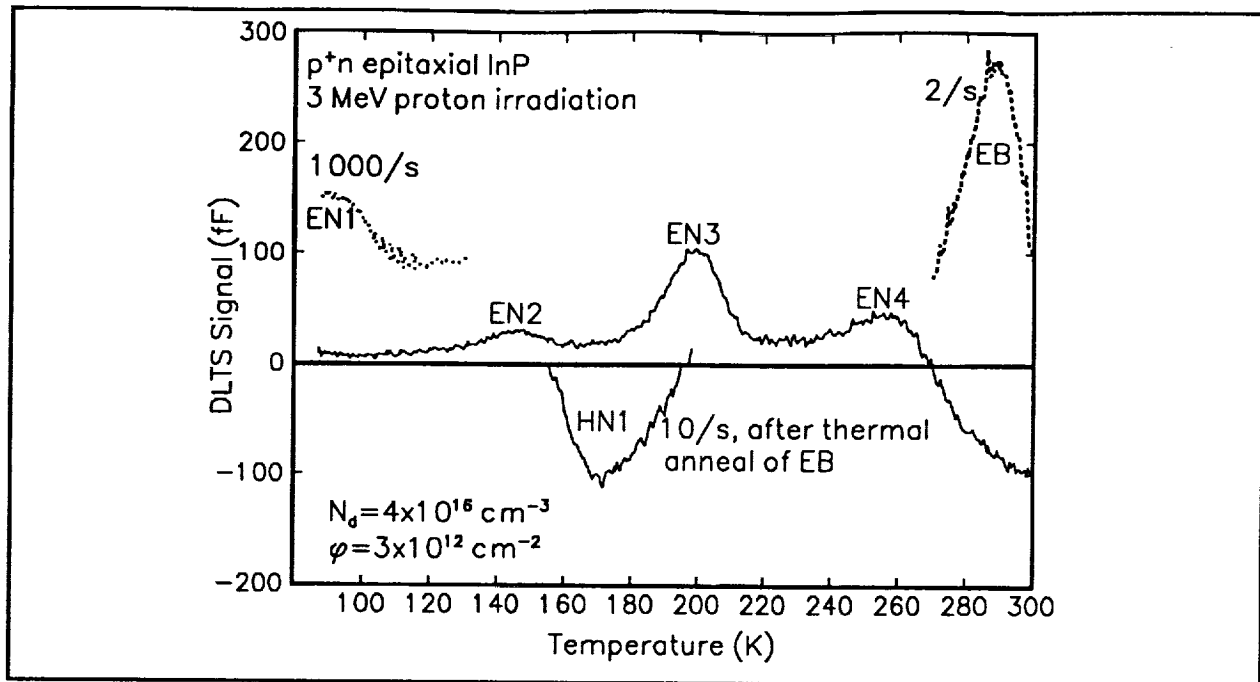


Figure 3 DLTS spectra obtained after 3 MeV proton irradiation to a fluence of $3 \times 10^{12} \text{ cm}^{-2}$. The HN1 peak is most likely two overlapping peaks.

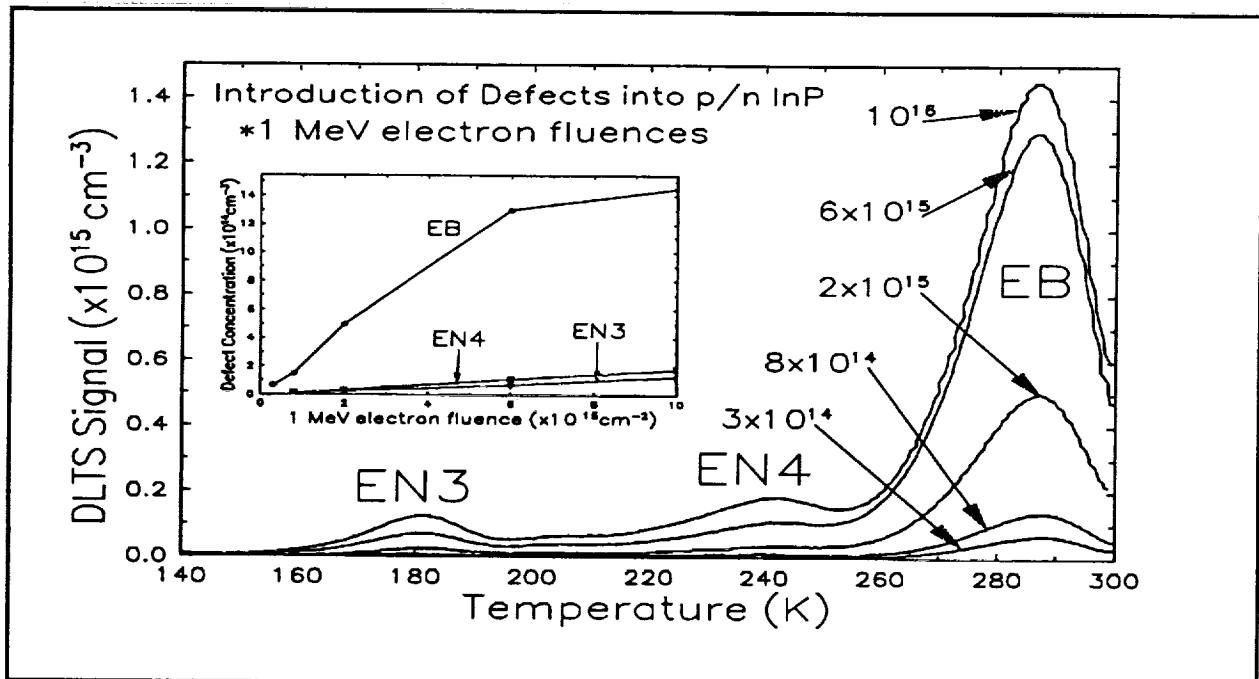


Figure 4 Introduction of defects resulting from 1 MeV electron irradiation. A linear dependence is found for all defects as shown in the inset.

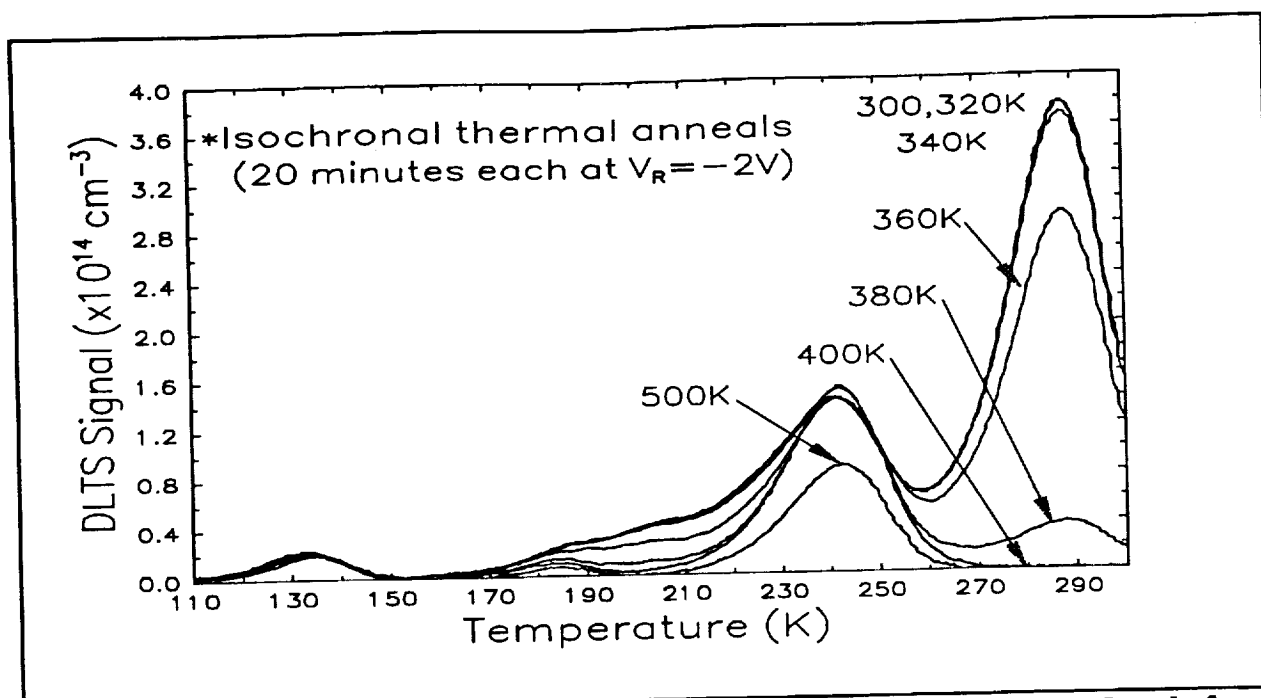


Figure 5 Isochronal annealing experiment. EB is the only defect which anneals. Holding the sample at $V_R = -2V$ during the anneals, the annealing stage occurs $\sim 380K$.

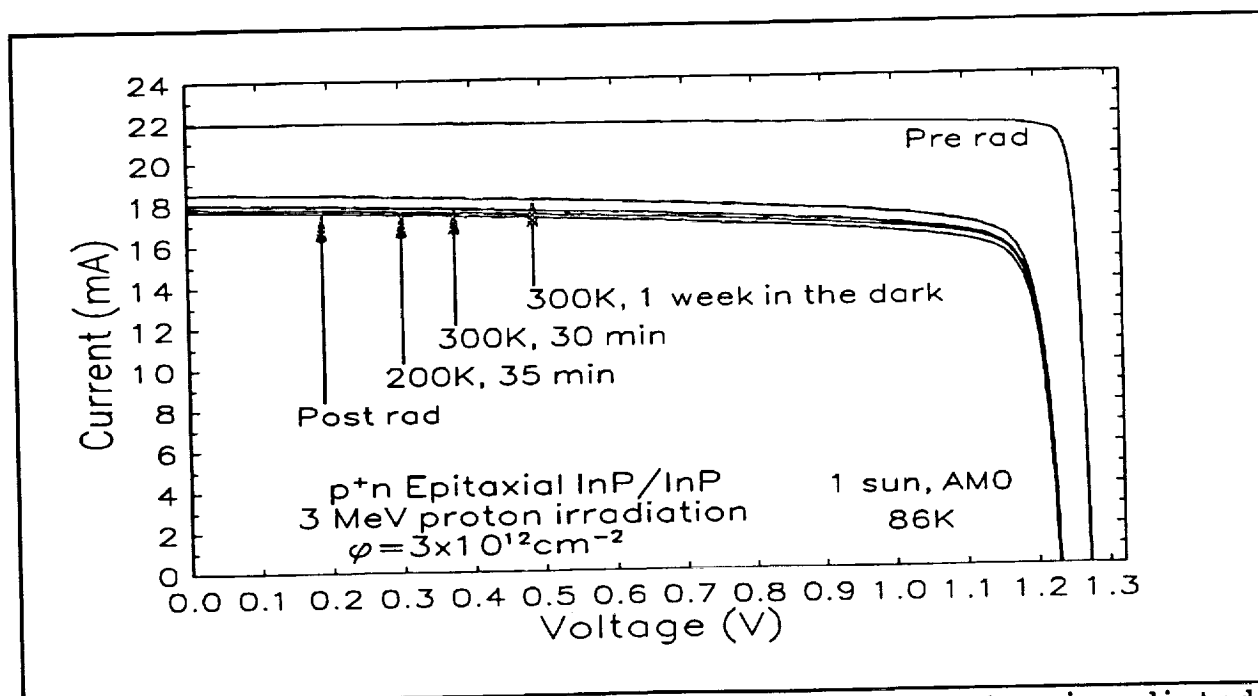


Figure 6 Photo-injection annealing of a 3 MeV proton irradiated n-InP cell. Illuminating the cell short circuited at 200K and then 300K caused a small increase in I_{sc} and FF, but V_{oc} did not change. The IV curves were taken at 86K.

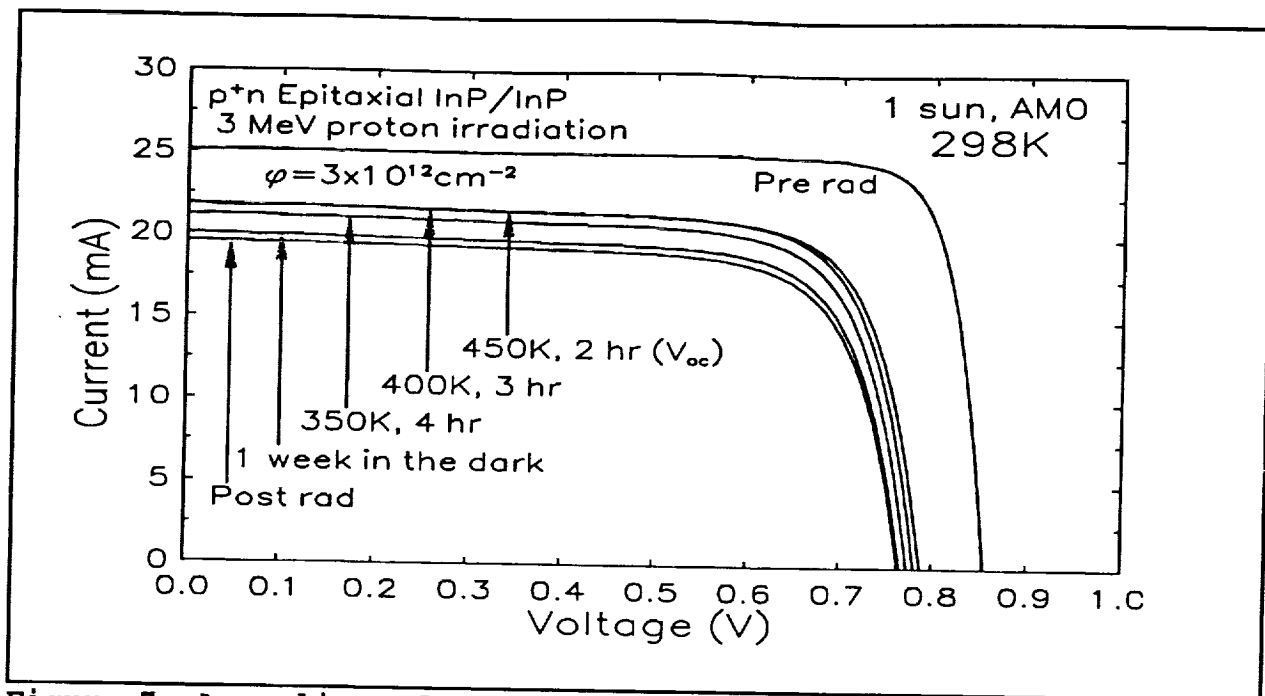


Figure 7 Annealing of the same cell above 300K. The IV curves were measured at 298K. All parameters recovered under illumination at 350K and 400K, but only V_{oc} showed more recovery at 450K.

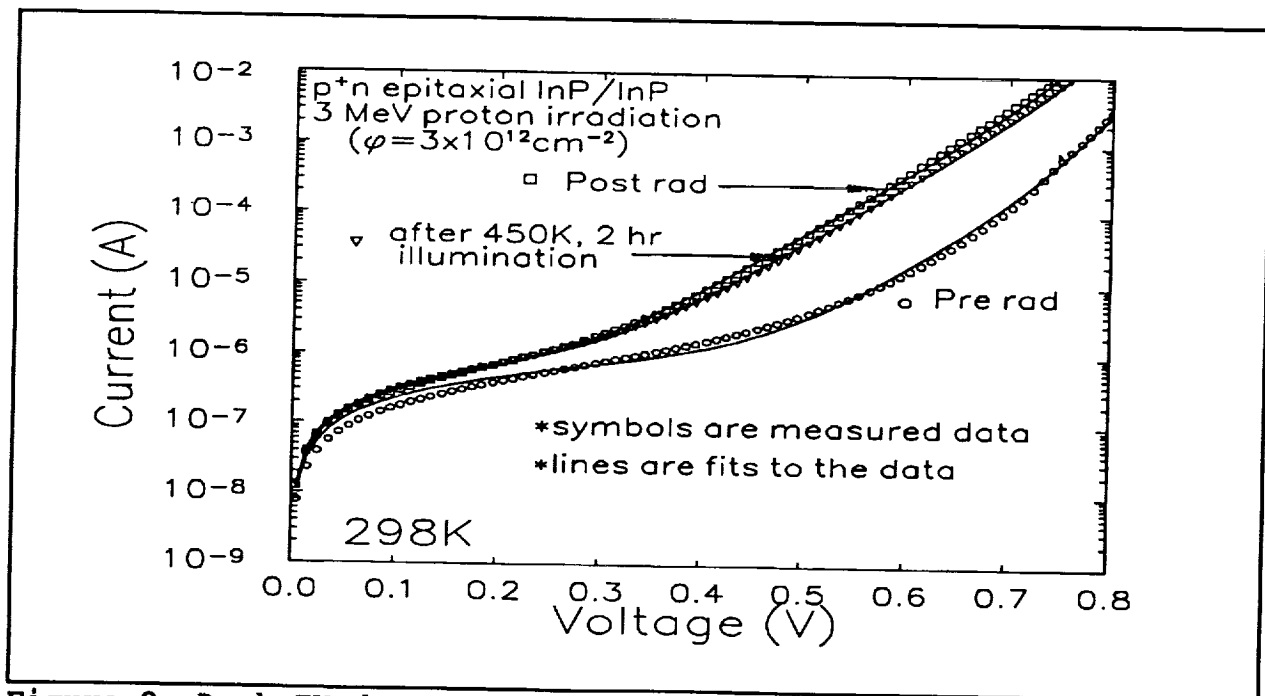


Figure 8 Dark IV data measured on the same cell. The irradiation increased both the recombination and generation currents, and the annealing caused only a small reduction.

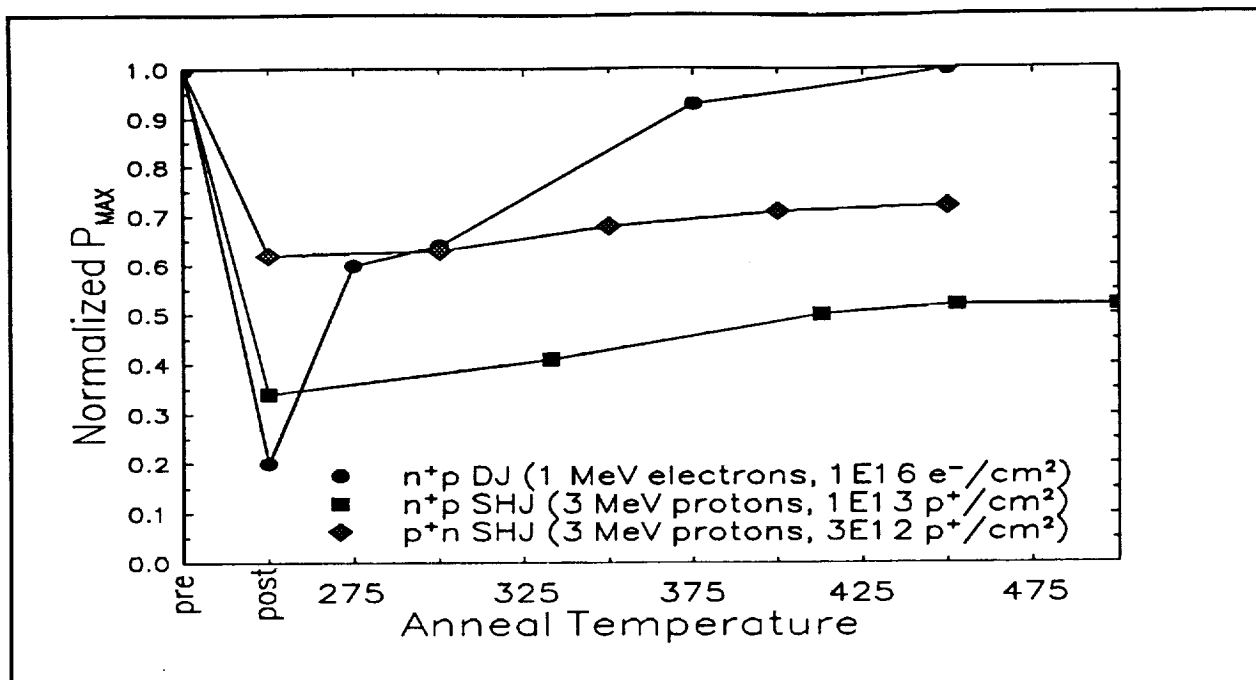


Figure 9 Comparison of P_{max} (normalized to BOL) between diffused junctions (DJ), and both p-type and n-type MOCVD junctions. P_{max} in the DJ cells recovered substantially while the MOCVD ones only recovered minimally.

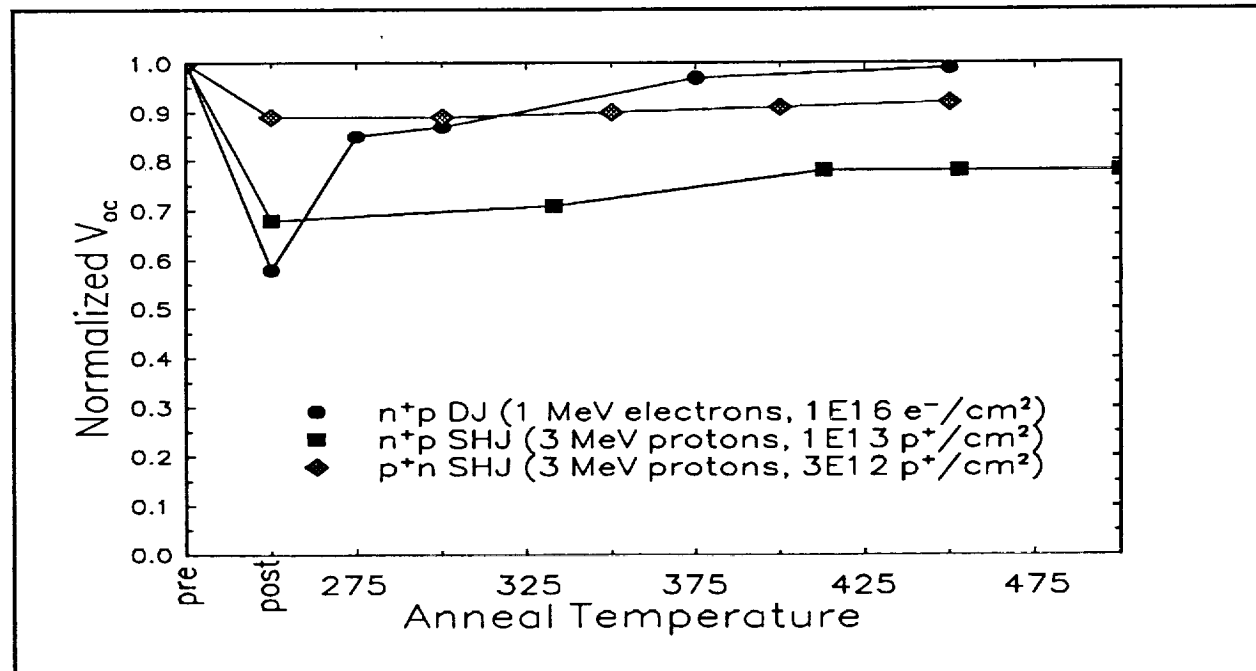


Figure 10 Same as Fig. 9 for normalized V_{oc} . The same trend exists for V_{oc} as for P_{max} above.

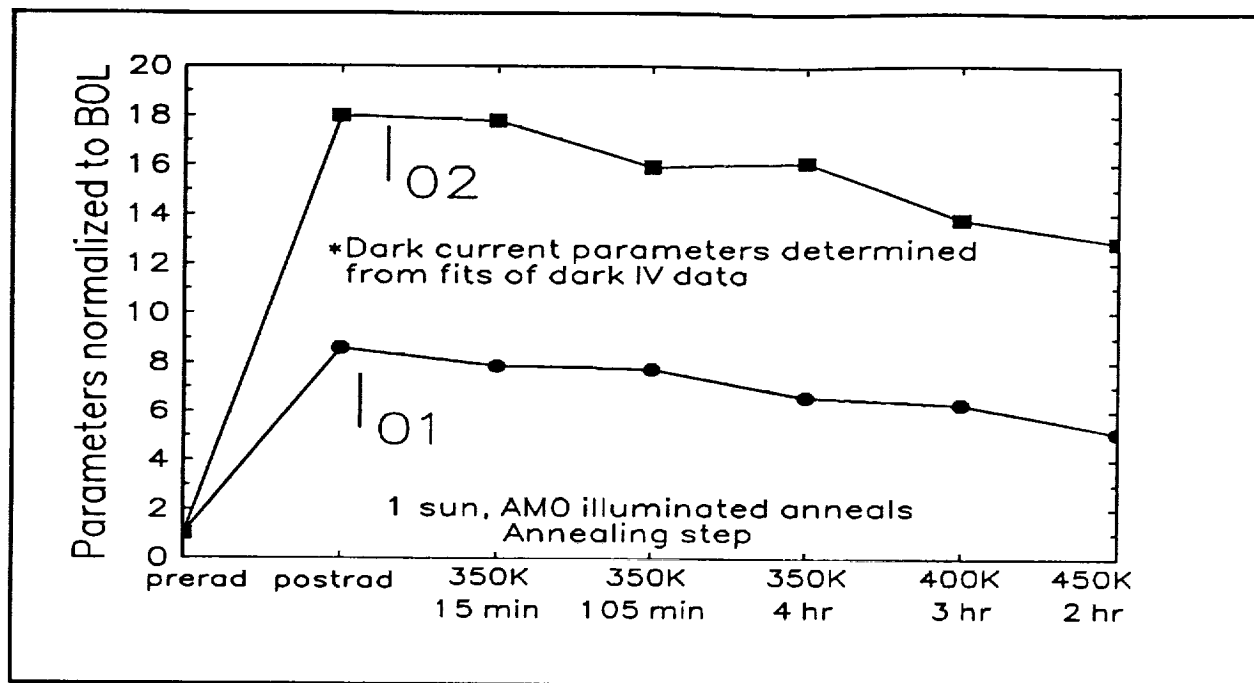


Figure 11 Diffusion (I_{01}) and recombination (I_{02}) terms plotted, normalized to the BOL to show relative changes. The increase in I_{02} dominates, but both terms show a decrease under illumination.

DESIGN OF HIGH-EFFICIENCY, RADIATION-HARD, GaInP/GaAs SOLAR CELLS¹

Sarah R. Kurtz, K.A. Bertness, A.E. Kibbler, C. Kramer, and J.M. Olson
National Renewable Energy Laboratory
Golden, Colorado

SUMMARY

Record air mass zero efficiency values are reported for Ga_{0.5}In_{0.5}P/GaAs devices before and after irradiation by 10¹⁵ cm⁻² 1 MeV electrons. The two-terminal, two-junction devices are grown monolithically with a high-conductance, GaAs tunnel-junction interconnect and an area of 0.25 cm². A device optimized for beginning-of-life (BOL) performance achieved BOL 25.7% (25.4%) efficiency, while devices optimized for end-of-life (EOL) performance achieved EOL efficiencies of 19.6% (19.8% and 20.0%). (The efficiencies noted in parentheses were measured at NASA Lewis) The effects of the thickness of the top cell and the doping level of the bottom cell were investigated in this study. A range of top-cell thicknesses and bottom-cell doping levels gave respectably high (greater than 18%) EOL efficiencies.

INTRODUCTION

In recent years, Ga_{0.5}In_{0.5}P/GaAs cells have drawn increased attention both because of their high efficiencies and because they are well suited for space applications. They can be grown and processed as two-junction devices with roughly twice the voltage and half the current of GaAs cells. They have low temperature coefficients, and have good potential for radiation hardness. We have previously reported the effects of electron irradiation on test cells which were not optimally designed for space. (ref. 1) From those results we estimated that an optimally designed cell could achieve 20% after irradiation with 10¹⁵ cm⁻² 1 MeV electrons. Modeling studies predicted that slightly higher efficiencies may be achievable. (ref. 2) Record efficiencies for EOL performance of other types of cells are significantly lower. Even the best Si (ref. 3) and InP (ref. 4) cells have BOL efficiencies lower than the EOL efficiency we report here. Good GaAs cells have an EOL efficiency of 16%. (ref. 5) The InP/Ga_{0.5}In_{0.5}As two-junction, two-terminal device has a BOL efficiency as high as 22.2% (private communication from M. Wanlass), but radiation results for these cells were limited. (ref. 6)

In this study we use the previous modeling and irradiation results to design a set of Ga_{0.5}In_{0.5}P/GaAs cells that will demonstrate the importance of the design parameters and result in high-efficiency devices. We report record AM0 efficiencies: a BOL efficiency of 25.7% for a device optimized for BOL performance and two of different designs with EOL efficiencies of 19.6% (at 10¹⁵ cm⁻² 1 MeV electrons). We vary the bottom-cell base doping and the top-cell thickness to show the effects of these two important design parameters. We get an unexpected result indicating that the dopant added to the bottom-cell base also increases the degradation of the top cell.

EXPERIMENTAL DETAILS

A schematic of the device structure is shown in Fig. 1. The devices were grown from trimethyl gallium, trimethyl indium, trimethyl aluminum, arsine, and phosphine in a hydrogen carrier gas. The dopant sources were diethyl zinc, hydrogen selenide, disilane, and carbon tetrachloride. Zinc and selenium were the p- and n-type dopant sources unless otherwise noted. The bottom-cell base doping levels were 1, 3, and 8 X 10¹⁶ cm⁻³, referred to hereafter as low, medium, and high, respectively. These doping levels could not be measured directly on the finished devices, but are estimated from calibration layers grown with similar diethyl zinc fluxes. Other details of the device structure and processing can be found elsewhere. (ref. 7, 8)

¹ Work funded by DOE contract No. DE-AC02-83CH10093

GRID			
0.5	GaAs	Si doping spike $n \approx 6 \times 10^{18}$	
0.025	AlInP	$n \approx 4 \times 10^{17}$ [Si]	(window)
0.1	GaInP	$n \approx 2 \times 10^{18}$	
0.5	GaInP (1.86 eV)	$p \approx 1.5 \times 10^{17}$	TOP CELL
0.05	GaInP (1.88 eV)	$p \approx 3 \times 10^{18}$	(BSF)
0.011	GaAs	$p \approx 8 \times 10^{19}$ [C]	
0.011	GaAs	$n \approx 1 \times 10^{19}$	TJ
0.1	GaInP	$n \approx 1 \times 10^{18}$	
0.1	GaAs	$n \approx 1 \times 10^{18}$	
3.5	GaAs	$p \approx 8 \times 10^{16}$	BOTTOM CELL
0.07	GaInP	$p \approx 3 \times 10^{17}$	(BSF)
0.2	GaAs	$p \approx 3 \times 10^{17}$	
substrate GaAs		Zn-doped	
Thickness (μm)	Doping (cm^{-3})		

Fig. 1. Device structure for the cell with high bottom-cell base doping, 0.65 μm -thick top cell and a BOL efficiency of 25.7%. The total top-cell thickness of 0.65 μm was varied by decreasing the thickness of the top-cell base layer (layer with $1.5 \times 10^{17} \text{ cm}^{-3}$ doping). The BSF layers serve to passivate the back surface of each individual cell and the TJ is a tunnel junction that makes an ohmic connection between the top and bottom cell.

All of the devices were measured before and after irradiation on the fiber-optics, two-source simulator in B. Sopori's lab at NREL. The efficiencies were measured by adjusting the simulator to obtain the correct currents on two (top and bottom) reference cells. The top- and bottom-cell photocurrents were measured by shining a NIR or visible laser, respectively, on the device in addition to the simulator light. The spectral responses of the top and bottom cells were measured using red and blue bias lights, respectively. The record efficiencies reported in Table I were measured by K. Emery and coworkers at NREL, then sent to NASA Lewis for confirmation. In most cases the efficiencies agree within 2% (relative). All of the cells are small: 5 mm X 5 mm. The cells are close to champion quality except that the anti-reflection (AR) coats were not well controlled and some variation was observed in the window layer of the top cell. EOL efficiencies of more than 20% would have been achieved if the AR coats had been optimal. The electron irradiation was done at JPL by Bruce Anspaugh and his staff.

RESULTS

A summary of the highest efficiency measurements is shown in Table I. A complete summary of all of the measured efficiencies, before and after irradiation, is shown in Fig. 2. Most of the data points in

Table I. Summary of measurements on highest efficiency devices. All measurements were completed using the AM0 spectrum and a cell temperature of 25°C.

Cell design	Irradiation	Measurement	V_{oc}	J_{sc}	FF	Efficiency
Base doping Top-cell thickness	(elec/cm ²)	place	(V)	(mAcm ⁻²)	(%)	(%)
high 0.65 μ m	None	NREL	2.393	16.55	88.7	25.7
	None	NASA	2.398	16.39	88.2	25.4
medium 0.45 μ m	10 ¹⁵	NREL	2.221	14.53	82.9	19.6
	10 ¹⁵	NASA	2.226	14.58	83.3	19.8
low 0.55 μ m	10 ¹⁵	NREL	2.198	14.72	83.0	19.6
	10 ¹⁵	NASA	2.198	14.90	83.4	20.0

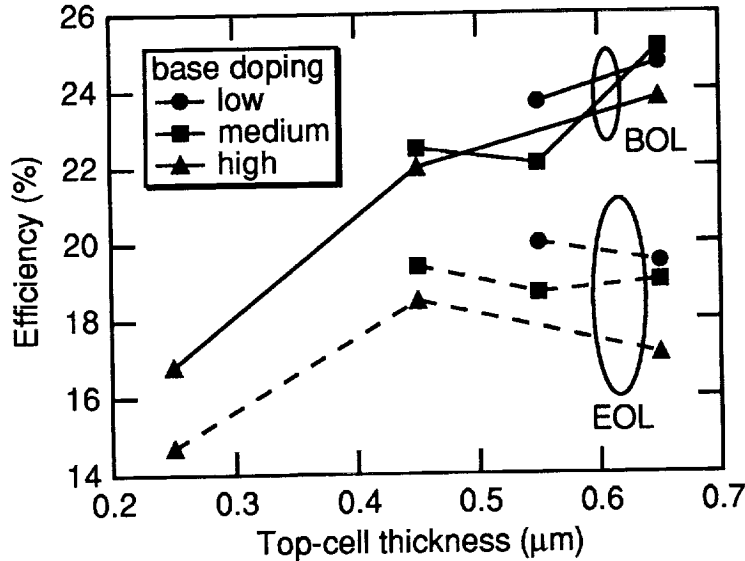


Fig. 2. The AM0 efficiencies of the devices before and after irradiation, as measured at NREL on the Sopori simulator.

Figs. 2–4 represent the averaged values for four 5 mm X 5 mm devices. Data is not included for a few cells that were badly shunted or damaged. The bottom-cell base doping had little effect on the BOL efficiency. The top-cell thickness has a very large effect on the efficiency because the thinner top cells generate less photocurrent and the device is limited by this smaller photocurrent. After irradiation, the cells with lower bottom-cell base doping tend to show higher efficiencies. The optimal top-cell thickness decreases after irradiation. This is because the current of the thick bottom cell usually degrades more than the current of the thin top cell. Fig. 2 shows that respectably high efficiencies (greater than 18%) are obtained for top-cell thicknesses between 0.45 and 0.65 μ m when the bottom-cell base doping is not too high.

The degradation of the photocurrents is shown in Figs. 3 and 4. The as-grown top-cell photocurrents show a very strong dependence on thickness, as expected. The device with top-cell thickness of 0.55 μ m has a lower photocurrent primarily because of a poor blue response, implying that some oxygen or carbon may have contaminated the window layer. After irradiation, the top-cell photocurrent shows a very significant dependence on bottom-cell base doping. This effect will be discussed below in more detail. The bottom-cell photocurrent decreases with top-cell thickness since a thinner top cell allows more light to penetrate to the bottom-cell junction. The larger decrease in photocurrent with higher base doping was expected from previous studies that showed the damage coefficient to increase with doping. The degradations of the V_{oc} and the FF ranged from 6%–9% and 2%–4%, respectively. The V_{oc} showed a slightly greater degradation (8%–9%) for the cells with the low bottom-cell base doping compared with those with high doping (6%–7%). This difference is not great

enough to compensate for the opposite trend in bottom-cell photocurrent degradation (10%–11% degradation for the lightly doped and 21%–23% for the highly doped cells).

In order to better understand the degradation of the photocurrents we plot the spectral response of the bottom and top cells in Figs. 5 and 6. The primary loss mechanism in both cases is a decreased minority-carrier diffusion length. The increase in damage coefficient with base doping for the GaAs bottom cells was reported previously. (ref. 1, 9) Similar changes in the degradation of the spectral response curve as a function of base doping have also been reported for InP n-on-p cells. (ref. 4) The increased radiation hardness of the $\text{Ga}_{0.5}\text{In}_{0.5}\text{P}$ top cell for low bottom-cell base doping is unexpected because no deliberate change was made in the top-cell doping. The similarities between the degradation of the top- and bottom-cell spectral responses imply that a memory or diffusion effect caused an unintentional change in the top-cell base doping. We are currently trying to confirm this hypothesis by using secondary mass ion spectroscopy to quantify the zinc levels in the top cells.

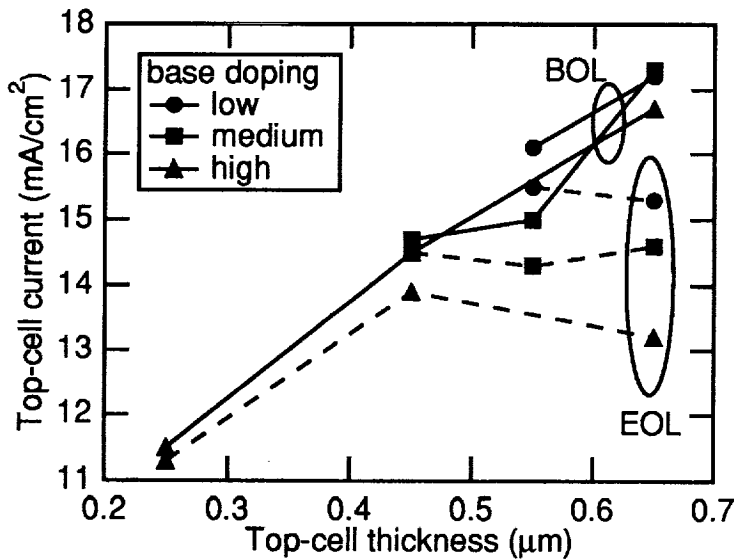


Fig. 3 Top-cell photocurrent before and after irradiation.

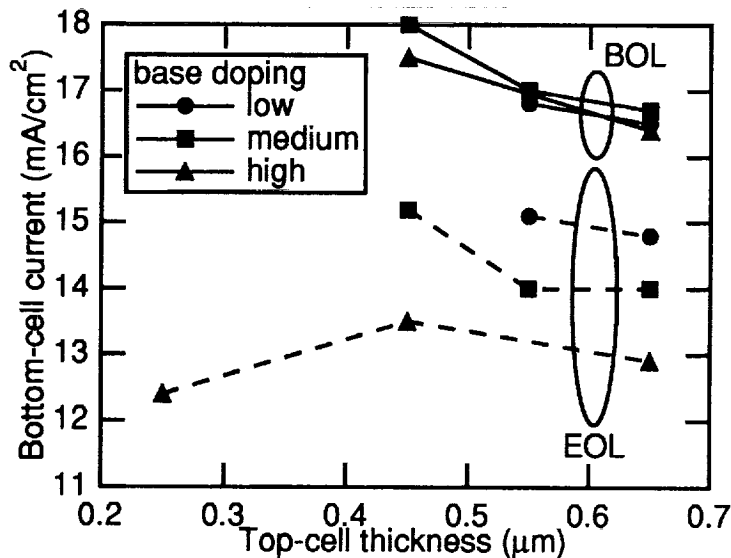


Fig. 4 Bottom-cell photocurrent before and after irradiation.

The results of this study are very consistent with our previous study (ref. 1) in which we predicted an EOL efficiency of 20% for an EOL optimized device. However, our previous study differed in one significant way: the photocurrent for a 0.75 μm -thick top cell degraded by only 2%, compared with 11% for the 0.65 μm -thick top cell with low bottom-cell base doping in this study. The results of both studies together may imply that the base doping of the 0.75 μm top cell was lower than that used in this study. Thus, if we had used a lower top-cell base doping in this study, we should have seen improved radiation resistance of the top cell, and, hence, of the tandem cell. A decreased doping of the top cell might increase the degradation of the V_{oc} . However, this is a small effect, and can be viewed as negligible since our previous study (with apparent low top-cell base doping) gave almost identical degradation of the V_{oc} compared with this report. Thus, we conclude that the device can be even further optimized for EOL efficiency.

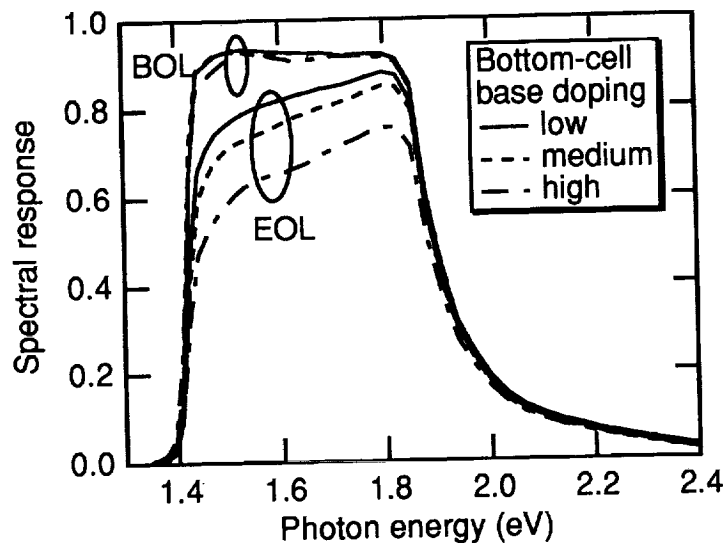


Fig. 5. The bottom-cell spectral response of tandem cells with 0.65 μm -thick top cells before and after irradiation.

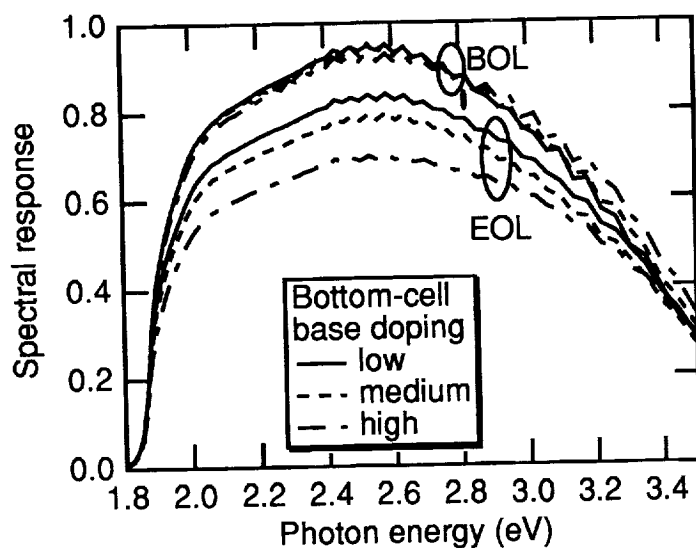


Fig. 6. The top-cell spectral response of tandem cells with 0.65 μm -thick top cells before and after irradiation. The small variations in the blue response may be caused by contaminants in the window layer of the top cell.

REFERENCES

1. Kurtz, S.R., J.M. Olson, K.A. Bertness, D.J. Friedman, A. Kibbler, B.T. Cavicchi, and D.D. Krut: Radiation hardness of $\text{Ga}_{0.5}\text{In}_{0.5}\text{P}/\text{GaAs}$ tandem solar cells. Space Photovoltaic Research and Technology, 1991, p. 40-1-40-7.
2. Cavicchi, B.T., D.D. Krut, D.R. Lillington, S.R. Kurtz, and J.M. Olson: The design and evaluation of dual-junction $\text{GaInP}_2/\text{GaAs}$ solar cells for space applications. 22nd IEEE Photovoltaic Specialists Conference, 1991, p. 63-67.
3. Garboushian, V., S. Yoon, and J. Turner: Radiation hardened high efficiency silicon space solar cell. 23rd IEEE Photovoltaic Specialists Conference, 1993, p. 1358-1362.
4. Keavney, C.J., R.J. Walters, and P.J. Drevinsky: Optimizing the Radiation Resistance of InP Solar Cells - Effect of Dopant Density and Cell Thickness. J Appl Phys, vol. 73, 1993, p. 60-70.
5. Bertness, K.A., M.L. Ristow, M.E. Klausmeier-Brown, M. Grouner, M.S. Kuryla, and J.G. Werthen: 16%-efficient GaAs solar cell after 10^{15} cm^{-2} , 1-MeV radiation. 21st IEEE Photovoltaic Specialists Conference, 1990, p. 1231-1234.
6. Walters, R.J., S.R. Messenger, M.W. Wanlass, and G.P. Summers: 1 MeV electron irradiation of monolithic, two-terminal $\text{InP}/\text{Ga}_{0.47}\text{In}_{0.53}\text{As}$ solar cells. 23rd IEEE Photovoltaic Specialists Conference, 1993, p. 1475-1478.
7. Olson, J.M., S.R. Kurtz, A.E. Kibbler, and P. Faine: A 27.3% efficient $\text{Ga}_{0.5}\text{In}_{0.5}\text{P}/\text{GaAs}$ tandem solar cell. Appl Phys Lett, vol. 56, 1990, p. 623-625.
8. Olson, J.M., S.R. Kurtz, A.E. Kibbler, K.A. Bertness, and D.J. Friedman: $\text{GaInP}_2/\text{GaAs}$ Tandem cells for space applications. Space Photovoltaic Research and Technology, 1991, p. 12-1-12-5.
9. Bertness, K.A., B.T. Cavicchi, S.R. Kurtz, J.M. Olson, A.E. Kibbler, and C. Kramer: Effect of base doping on radiation damage in GaAs single-junction solar cells. 22nd IEEE Photovoltaic Specialists Conference, 1991, p. 1582-1587.

INVESTIGATION OF THE STABILITY AND 1.0 MeV PROTON RADIATION RESISTANCE OF COMMERCIALLY PRODUCED HYDROGENATED AMORPHOUS SILICON ALLOY SOLAR CELLS¹

Kenneth R. Lord II, Michael R. Walters,
and James R. Woodyard
Wayne State University
Detroit, Michigan

ABSTRACT

The radiation resistance of commercial solar cells fabricated from hydrogenated amorphous silicon alloys is reported. A number of different device structures were irradiated with 1.0 MeV protons. The cells were insensitive to proton fluences below $1\text{E}12\text{ cm}^{-2}$. The parameters of the irradiated cells were restored with annealing at $200\text{ }^{\circ}\text{C}$. The annealing time was dependent on proton fluence. Annealing devices for one hour restores cell parameters for fluences below $1\text{E}14\text{ cm}^{-2}$ fluences above $1\text{E}14\text{ cm}^{-2}$ require longer annealing times. A parametric fitting model was used to characterize current mechanisms observed in dark I-V measurements. The current mechanisms were explored with irradiation fluence, and voltage and light soaking times. The thermal generation current density and quality factor increased with proton fluence. Device simulation shows the degradation in cell characteristics may be explained by the reduction of the electric field in the intrinsic layer.

INTRODUCTION

The goal of our research is to develop a model to predict EOL performance of thin-film solar cells in space environments. In order to achieve the goal we have irradiated and characterized a number of different thin-film solar cell device structures fabricated from hydrogenated amorphous silicon alloys (refs. 1-5). The radiation resistance of single, dual and triple junction cells has been determined for 1.0 MeV proton fluences in the $1\text{E}11$ through $1\text{E}15\text{ cm}^{-2}$ range. Both substrate and superstrate cell structures obtained from three companies producing commercial modules have been investigated. The p-n layers in the cells are made up of hydrogenated amorphous silicon alloys deposited using plasma enhanced chemical vapor deposition; the details of cell structures have been reported in references one through five. Cells were characterized using light I-V, dark I-V and quantum efficiency measurements.

Six cell structures have been investigated by our group. The results of 1.0 MeV proton irradiation on cell normalized power density are shown in Figure 1. Measurements on single and triple-junction cells with superstrate structures are shown. The triple-junction cells had two band gaps. The i-layers of the top two junctions were a-Si:H with the same band gap; the i-layer of the bottom junction was a-Si,Ge:H with a lower band gap than the top two junctions. Tandem and

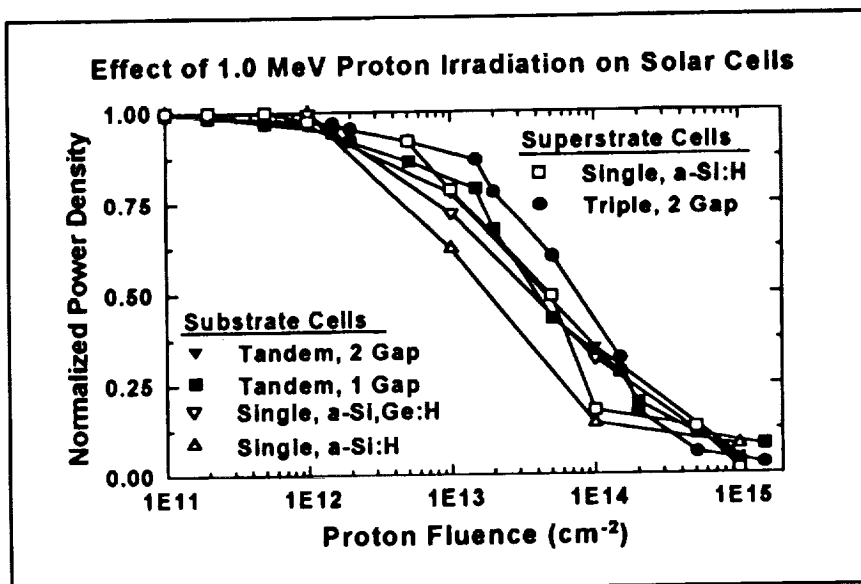


Figure 1: Plot comparing the effect of 1.0 MeV proton irradiation on the normalized power density of a-Si:H alloy based solar cells.

¹ Portions of this work were supported by NASA, the Spacecraft Technology Division of TRW, and the Wayne State University Institute for Manufacturing Research.

single-junction cells with substrate structures are also shown in Figure 1; tandems with single and dual gaps were investigated as well as single-junction cells with a-Si:H and a-Si,Ge:H i-layers. The cell efficiencies ranged between seven and eight percent under AM1.5 global irradiance; the radiation resistance of the cells has been reported in prior papers published by our group (refs. 1-5). Figure 1 shows 1.0 MeV proton irradiation degrades the normalized power density of all the cells by less than a few percent for fluences less than $1\text{E}12\text{ cm}^{-2}$. For fluences above $1\text{E}15\text{ cm}^{-2}$ the cell power degrades to less than 10% of the initial power. Reductions in the normalized power density in the $1\text{E}12$ through $1\text{E}14\text{ cm}^{-2}$ proton fluence range depends on cell structure. Cells with triple junctions have the best radiation resistance, dual-junction cells are next and single-junction cells have the lowest radiation resistance. Single-junction cells with a-Si,Ge:H i-layers have better radiation resistance than cells with a-Si:H i-layers; it is not clear whether the effect is due to the role of germanium in these cells or the differences in the thicknesses of the i-layers. The i-layers of the a-Si,Ge:H single-junction cells are thinner than the i-layers of the a-Si:H cells.

The effect of post-irradiation annealing at $200\text{ }^{\circ}\text{C}$ on the normalized power density of twenty-one solar cells fabricated from hydrogenated amorphous silicon alloys is illustrated in Figure 2. The data are for single-junction cells with a superstrate structure and 500 nm i-layer thickness. Three cells were irradiated at each fluence; the power densities following irradiation are shown by the open squares. The average power density of three irradiated cells at each fluence is shown by the filled squares. The power densities following a two-hour anneal at $200\text{ }^{\circ}\text{C}$ are shown by the open triangles with the averages represented by the filled triangles. Annealing the cells for one hour restores the normalized power density of cells irradiated with 1.0 MeV proton fluences less than $1\text{E}14\text{ cm}^{-2}$ fluences above $1\text{E}14\text{ cm}^{-2}$ require longer annealing times to restore the normalized power density. This is shown by the data in Figure 3. The average power density of the three single-junction cells irradiated with a fluence of $1.5\text{E}15$

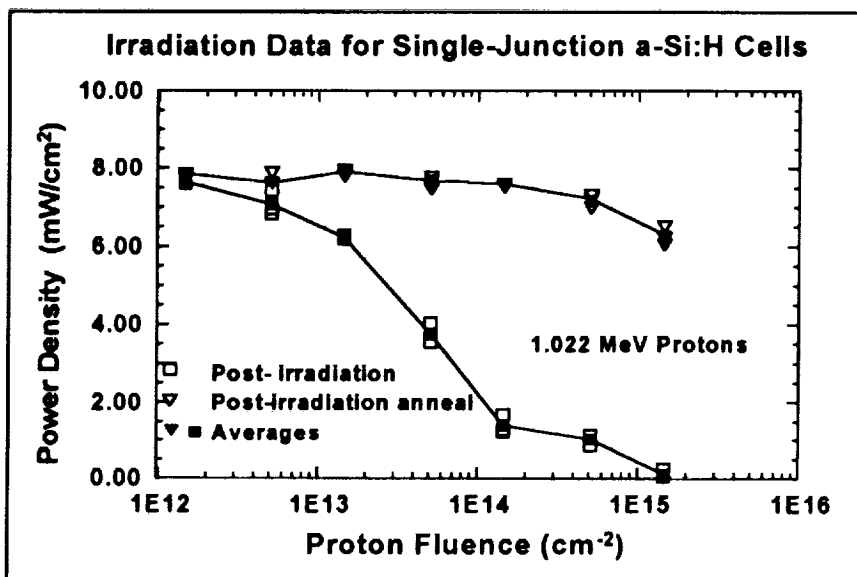


Figure 2: Power densities of twenty-one cells a-Si:H single-junction cells measured after 1.022 MeV proton irradiation and following a post-irradiation anneal at $200\text{ }^{\circ}\text{C}$ for two hours.

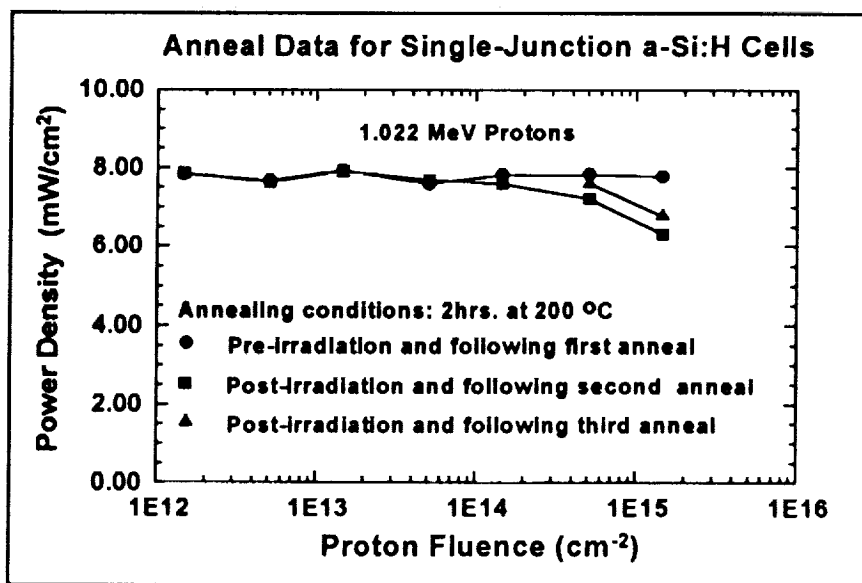


Figure 3: Average power densities following the first pre-irradiation anneal, and the second and third post-irradiation anneals of single-junction cells irradiated with 1.022 MeV protons.

cm^{-2} recovers to 6.2 and 7.0 mW/cm^2 with 2.0 and 4.0 hours annealing, respectively. The details of the time dependence of annealing have been reported in reference 6. In general, the higher the fluence for MeV protons, the longer the annealing time to restore the normalized power density.

The cross-over of the dual and triple-junction curves in Figure 1 at a fluence of $1\text{E}14 \text{ cm}^{-2}$ is believed to be due the difference in the irradiances of the simulators used to measure the light I-V characteristics of the cells. The dual-junction cells were measured with a simulator which was optimized to match an AM1.5 global spectrum. The triple-junction cells were measured with our simulator which is an ORC model SS1000. The spectral irradiance of the ORC simulator contains xenon lines above 800 nm and is deficient in the red. The thicknesses of the I-layers in the triple-junction cells were matched to an AM1.5 global spectrum. The mismatch between the ORC simulator spectrum and the triple-junction cells probably resulted in the bottom junction limiting the cell current. We have modified the ORC simulator by adding a cold mirror and tungsten-halogen lamp (ref. 7). We plan to repeat the triple-junction measurements with the dual-source simulator to determine the reason for the cross-over of the dual-and triple-junction curves in Figure 1.

The investigations summarized in Figure 1 must be extended to a range of proton and electron energies. It is our expectation that the measurements will provide the basic parameters for the development of a predictive model for determining the EOL performance of cells fabricated from hydrogenated amorphous silicon based alloys in a variety of space environments. We plan to apply the techniques learned from our investigations with hydrogenated amorphous silicon based alloys to other thin-film solar cells of interest for space-power generation.

PARAMETRIC FITTING MODEL

The first step in developing a predictive model for EOL performance is the determination of parameters from measurements which can be related to basic material properties of solar cells. We have elected to develop a parametric fitting model to characterize current mechanisms in single-junction cells. Single-junction cells were chosen because triple-junction cells are far more complex in structure. Dark I-V characteristics were selected for the initial modelling investigations because they showed the largest changes in parameters with 1.0 MeV proton irradiation.

Determination of solar cell parameters from measured dark I-V characteristics requires curve fitting a parametric model to measured dark I-V characteristics. The objective of curve fitting is to minimize the differences between measured and calculated dark I-V characteristics. The parametric model which we developed includes current mechanisms which are characterized by a sum of analytical functions with parameters. The parameters in the analytical functions are referred to as fitting parameters; they are varied to fit a calculated I-V characteristic to a measured dark I-V characteristic. The model was used for analysis of dark I-V characteristics in the forward-bias region. The parametric model used for curve fitting is:

$$I = I_0 \left[\exp\left(\frac{q(V - IxR_{se})}{nkT}\right) - 1 \right] + \frac{(V - IxR_{se})}{R_{sh}} + \alpha(V - IxR_{se})^m$$

where

I_0 = thermal generation current
 V = applied bias voltage
 q = electronic charge
 n = quality factor
 T = temperature

R_{se} = series resistance
 R_{sh} = shunt resistance
 α, m = constants
 k = Boltzmann constant

The parameters in the equation may be related to physical mechanisms which are responsible for carrier transport in a solar cell. Each mechanism requires one or two fitting parameters. The four mechanisms used in the forward-bias region of the dark I-V curve-fitting investigations are:

1. Injection current represented by the first term in the equation. The first term is the result of the simple diode equation. The model does not differentiate between injection and recombination current. It may be inappropriate to apply this expression to a p-i-n device, but it is useful for characterizing irradiation effects. The injection current parameters are I_0 and n .
2. Shunt current represented by the parameter R_{sh} in the second term.

3. Electric field and depletion effects in the intrinsic layer represented by the parameters α and m in the last term.
4. Series resistance represented by R_{se} in all three terms.

The results of curve fitting the dark I-V characteristic of a single junction cell in the forward-bias region is shown in Figure 4; the cell has a 500 nm thick intrinsic layer. The dark I-V characteristic was measured following the first two-hour anneal at 200 °C following receipt of the cell from the fabricator. Curve fitting was carried out using Matlab software which employs a Nelder-Mead simplex search subroutine. The measured I-V values and calculated results are represented by filled squares and open triangles, respectively. The symbols for the calculated values are plotted over the measured values, and because the fit is good, the filled squares are barely discernable.

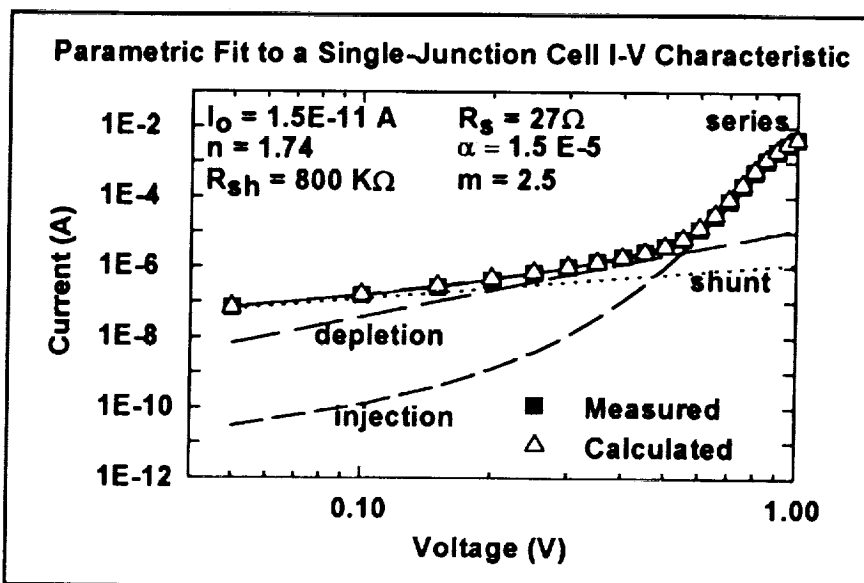


Figure 4: Typical curve fitting results for a single-junction cell showing the contributions of each of the four current mechanisms in a dark I-V characteristic.

The contributions of each of the four current mechanisms are plotted and identified with labels in Figure 4. The voltage ranges where the four mechanisms dominate in a major way are shown in Table I.

Table I

Voltage Range (V)	Dominant Mechanism	Corresponding Parameters
0-0.2	shunt	R_{sh}
0.20-0.60	depletion	α, m
0.60-1.00	injection	I_0, n
near 1.00	series	R_{se}

A parametric study was carried out using seven single-junction cells with 500 nm i-layers. The cells were annealed for two hours at 200 °C following delivery. I_0 was in the 1.5E-11 to 2.0 E-11 A range. The quality factor, n , ranged from 1.73 to 1.77. The series resistance, R_{se} varied from 25 to 37 Ω . The parameter, α , ranged from 1.0 to 1.4 E-5 $\text{A V}^{-2.5}$, m remained constant at 2.5. Agreement between the parametric model and measured I-V characteristic for the cells was <4% for the shunt and injection regions, and <8% in the depletion region.

The dark I-V characteristics of a-Si:H single-junction cells have been investigated to determine the effects of proton irradiation on cell behavior; the cells had 500 nm thick intrinsic layers. The parametric model was used to quantify changes in dark I-V characteristics resulting from 1.00 MeV proton irradiation. The cells studied were irradiated with 1.00 MeV proton fluences between 1.46E12 and 1.46E15 cm^{-2} . There were

twenty-one cells in the group, with three cells irradiated at each of the fluences. One cell was chosen for the parametric study from each of the fluences studied; the cell with lowest shunt current in the group of three cells was selected in order to determine fitting parameters with the best accuracy. Figure 5 shows the effect of 1.00 MeV proton fluences on the measured dark I-V characteristics for four of the seven fluences investigated. The figure shows increasing proton fluences result in lower currents in the 0.60 to 1.00 V range, the range associated with the injection current; it also shows the current in the 0.050 to 0.20 V range is lower for higher fluences; the current in this range is due primarily to the shunt current mechanism.

Significant changes occurred in the thermal generation current density, J_0 with irradiation and annealing. Figure 6 shows J_0 following anneal 1, the first anneal after receiving the cells and pre-irradiation. J_0 following anneal 1 is shown by open circles positioned on the graph at fluences the cells were to be irradiated. Following irradiation J_0 increased by a factor of two for a fluence of $1.5E12 \text{ cm}^{-2}$ and more than four orders of magnitude for a fluence of $1.5E15 \text{ cm}^{-2}$. After annealing for two hours at 200 °C, labeled anneal 2 on Figure 6, J_0 was restored to near pre-irradiated values for fluences less than $1.5E14 \text{ cm}^{-2}$. A third anneal further restored J_0 for the two highly irradiated cells. J_0 is much more sensitive to irradiation than power density. Figure 2 shows only a few percent change in power density at a fluence of $1.5E12 \text{ cm}^{-2}$ while Figure 6 shows a factor of two change in J_0 .

Changes in quality factor, n , were also observed. Figure

7 is a graph of fitted n values for pre-irradiation, post-irradiation and post-annealing conditions. For the same fluence range, n increased from 1.84 to 23.9 with irradiation. Subsequent anneals restored n to near pre-irradiated values as shown by the overlaid plots for these data; the open symbols essentially coincide for

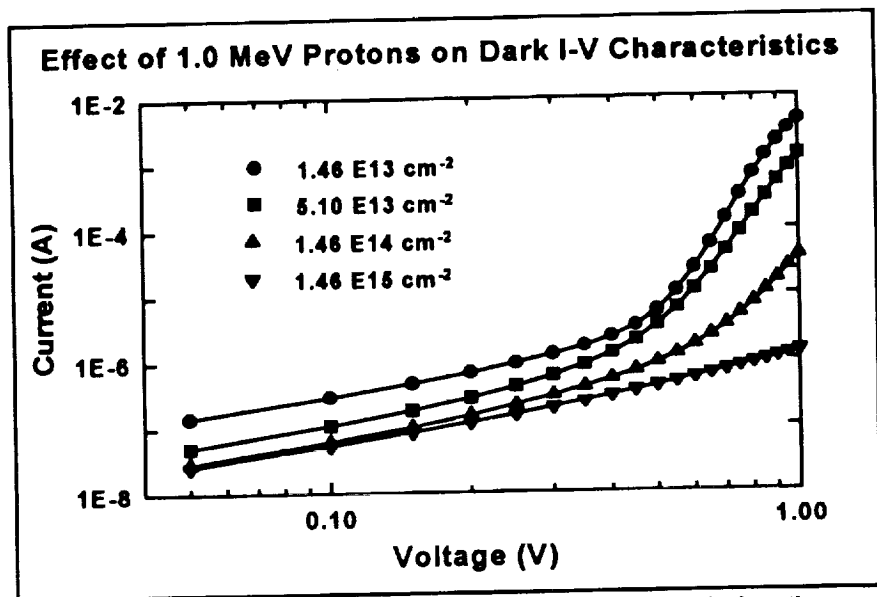


Figure 5: Plot of measured dark I-V characteristics for single-junction cells irradiated at various proton fluences.

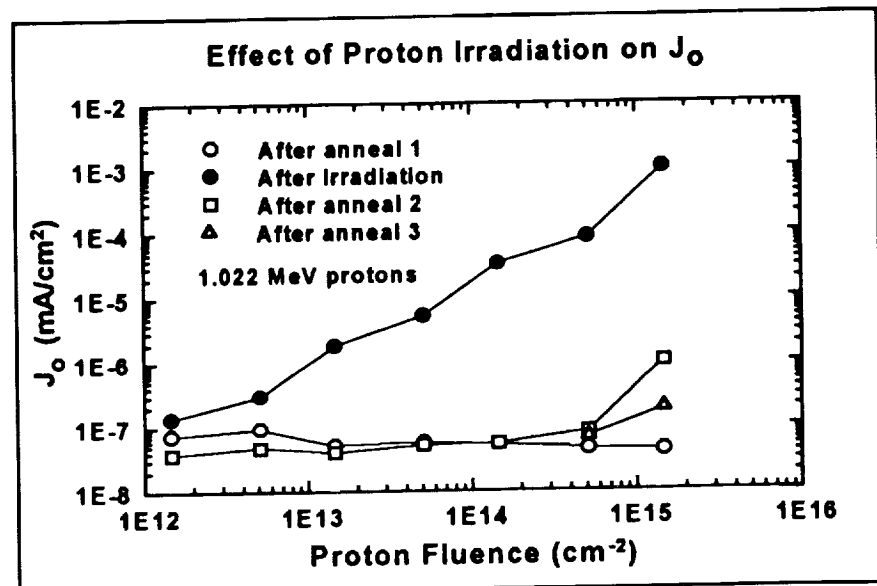


Figure 6: Plot showing the effect of proton irradiation at various fluences and subsequent annealing on reverse saturation current density, J_0 obtained from parametric fitting.

anneals one, two and three. These results are consistent with the literature which shows J_0 and n increase as the quality of device material degrades; degradation in the material is believed to be due to an increase in defect density.

R_{se} does not appear to be significantly influenced by irradiation. One exception was noted. R_{se} for one cell increased from 28 to 53 Ω following irradiation; it was restored to 32 Ω with annealing. The reasons for the large change in R_{se} for this cell are not understood. It is important to note that as the injection current decreases with increasing fluence, R_{se} becomes less of a factor in the I-V characteristic and parametric fitting of R_{se} becomes more difficult.

The depletion current fitting parameters, α & m , behave differently with fluence. α is influenced by irradiation, while m does not appear to change with irradiation. α decreases from its annealed pre-irradiated value, approximately $1E-5 \text{ A/V}^{2.5}$ to about $7E-7 \text{ A/V}^{2.5}$ with the largest fluence. It recovers to the $3E-6$ to $5E-6 \text{ A/V}^{2.5}$ range with annealing. We think it is significant that α does not recover to the annealed pre-irradiated value. m appears to remain constant at 2.5 with irradiation and annealing.

R_{sh} of the cells appears to increase with irradiation and decrease with annealing. Pre-irradiation R_{sh} values range between about 300 and 800 k Ω , and increase to about 2000 k Ω with irradiation. R_{sh} decreases with annealing to values which range between 300 to 900 k Ω . R_{sh} exhibits a switching behavior. R_{sh} of the twenty-one irradiated cells was determined under three conditions: pre-irradiation, post-irradiation, and post-irradiation annealing. The behavior of R_{sh} from the analysis of the cells was similar to above results. R_{sh} was calculated using the current at a forward bias of 0.050 V; the procedure assumes R_{sh} dominates the current. The average R_{sh} prior to irradiation was 417 k Ω . Of the twenty-one cells, sixteen exhibited an increase in R_{sh} after 1.00 MeV proton irradiation. Cells irradiated with the same fluences did not exhibit the same changes in R_{sh} and the reasons for this are not understood. The average R_{sh} increased to approximately 590 k Ω following irradiation. After annealing, seventeen of the twenty-one cells exhibited a decrease in R_{sh} . The average R_{sh} following post-irradiation annealing was about 300 k Ω . The analysis of twenty-one irradiated cells confirms the trend that R_{sh} is increased by irradiation and decreases with post-irradiation annealing.

We plan to pursue device simulation studies in an effort to explain the role of irradiation, in terms of fundamental material properties, on the parameters resulting from the fitting model.

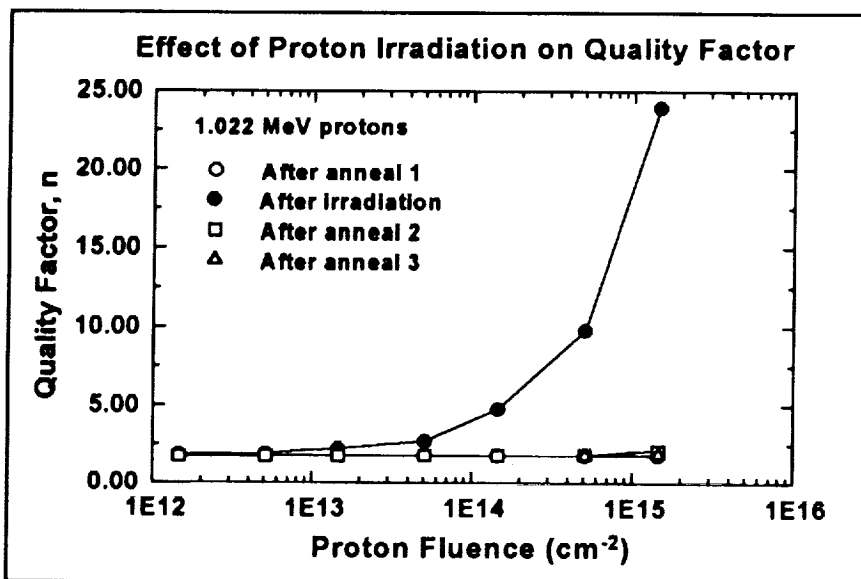


Figure 7: Plot showing the effect of proton irradiation at various fluences and subsequent annealing on quality factor, n , obtained from parametric fitting.

INSTABILITY STUDIES

Triple-tandem cells cut from a module had fill-factors ranging from 0.37 to 0.68 under as-received or virgin conditions. Figure 8 shows light I-V characteristics for a cell under two conditions; the filled circles are for virgin conditions and result in a fill-factor of 0.37. The virgin cell is characteristic of one of the poorer as-received cells. Note the current has an unexpected structure between 1.50 and 2.00 V; the structure is concave down instead of concave up as would be expected. Following a two hour anneal at 200 °C, a light I-V measurement produced the open squares in Figure 8; the corresponding fill-factor is 0.66. After annealing the cell, the light I-V characteristic was similar to one of the better as-received cells. The fabricator of the triple tandem cells indicated the module was annealed for one hour in air at 100 °C following fabrication; the annealing procedure

is employed by the fabricator as one of the steps in the fabrication of modules.

It is difficult to investigate current mechanisms in triple-junction cells because of their complex structure. For this reason, single-junction cells were investigated in an effort to determine if the behavior observed in Figure 8 is also characteristic of single-junction cells. Figure 9 shows light I-V measurements for a single-junction cell under light soaked and annealed conditions. The filled squares correspond to light I-V measurements for the cell annealed at 200 °C for two hours. I-V measurements following 32 hours of room temperature light soaking are represented by open circles. Annealing the cell following light soaking resulted in I-V measurements which are the same as before annealing. A comparison of Figures 8 and 9 shows there is similar structure in the light I-V characteristics, suggesting the current mechanisms resulting in the initially poor performance of this particular triple-junction cell may be elucidated with investigations of single-junction cells.

The effect of light soaking on the forward-bias dark I-V characteristic for a single-junction cell is shown in Figure 10 by open circles. The cell exhibits a switching effect in the region of the I-V characteristic where shunt current is the dominant current mechanism.

The switching effect has been observed in several cells; it occurs under both forward and reverse-bias conditions. An analysis of several cells shows the switching effect increases in frequency with light and forward-bias voltage soaking. It decreases with annealing and reverse-bias voltage soaking. The filled squares in Figure 10 represent a dark I-V characteristic measured following the application of a -2.00 V reverse-bias voltage for five minutes; this characteristic also corresponds to annealing at 200 °C for two hours. The figure clearly demonstrates the role the history of the cell plays in I-V characteristics.

Close inspection of dark I-V characteristics suggested the characteristics exhibited a time dependence. The role of time was investigated by including a delay time in the computer program. Measurements were taken with one and ten minute delays between the source-bias voltage steps. Time-dependent switching was observed in the reverse-bias voltage region of the dark I-V characteristics where the current switched from

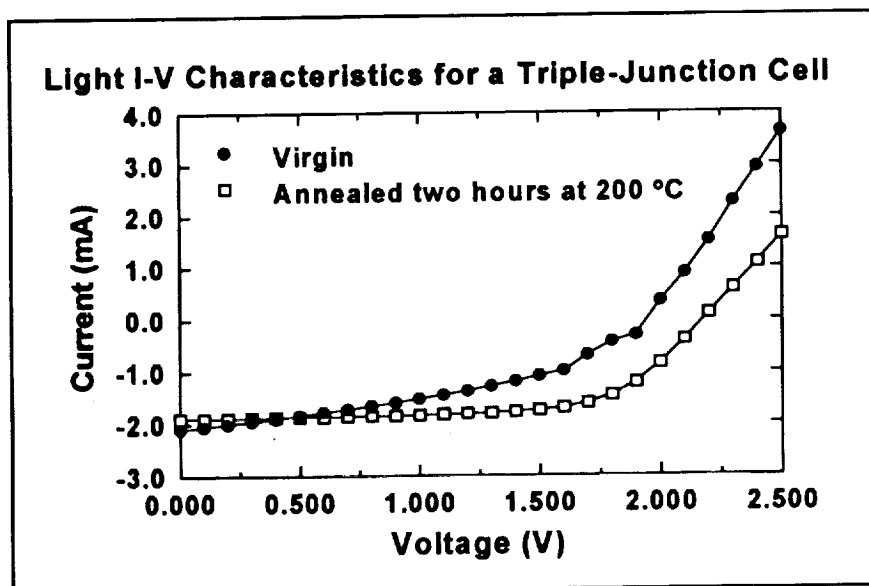


Figure 8: Light I-V characteristic for a triple-junction cell measured under virgin and annealed conditions.

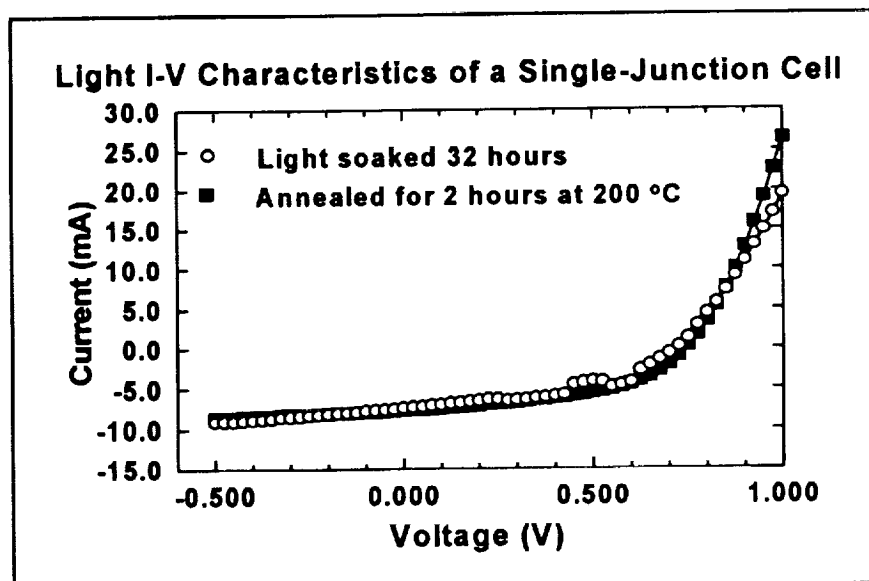


Figure 9: Light I-V characteristics of a single-junction cell under light soaked and annealed conditions.

shunt dominated to a current mechanism with a slope between two and two and one-half. Switching occurred at lower reverse-bias voltages as the delay time was increased, and the reverse-bias current was higher; the current mechanism is not understood. I-V characteristics exhibited another time dependence; as the voltage was scanned from the reverse-bias to the forward-bias region, the current decreased with increasing delay times. The observation suggests charge stored in a cell during reverse bias contributes to the current in the forward-bias region; however, the mechanism has not yet been fully characterized.

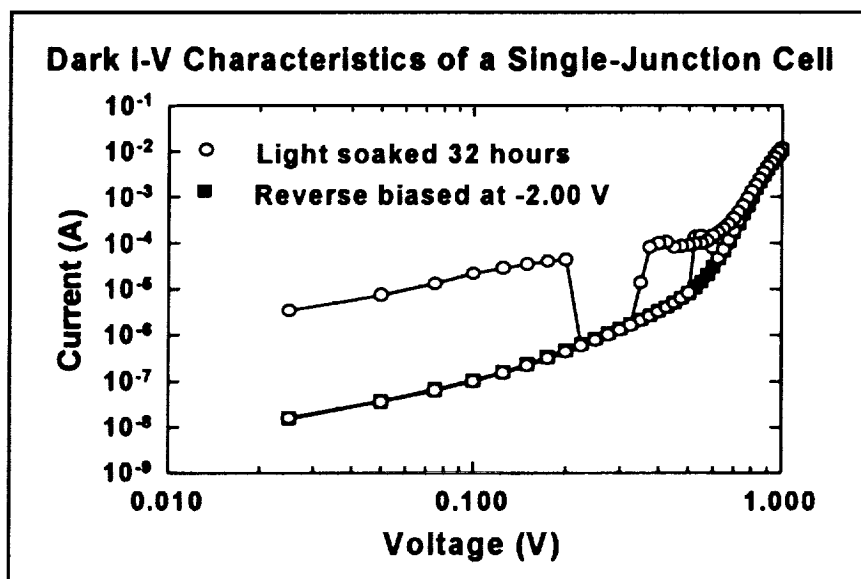


Figure 10: Dark I-V characteristics of a single-junction cell following light soaking and reverse-bias voltage soaking.

DEVICE SIMULATION

We have carried out device simulations with EPRI AMPS (ref. 8) in order to produce I-V characteristics. The simulated I-V characteristics may be compared with measured characteristics in an effort to determine fundamental material parameters. Changes were made in the material parameters for a simulation in order to produce an I-V characteristic similar to one obtained by measurement. Simulations were carried out and compared to I-V characteristics measured following irradiation of cells. The comparison provides information on the role of irradiation on fundamental material parameters. An understanding of the role of irradiation on the fundamental material parameters is necessary in order to develop a model for predicting EOL cell performance in a given space radiation environment. The work reported in this section represents our first efforts to use EPRI AMPS simulations to understand the effects of 1.0 MeV proton irradiation on hydrogenated amorphous silicon alloy based solar cells.

EPRI AMPS was used to simulate a PIN device structure using various i-layer thicknesses and sub-band-gap density of state, DOS, functions. Devices were simulated with i-layer thicknesses of 200, 500, and 800 nm; 20 nm thick n⁺-layers and p⁺-layers were used. Gaussian and U-shaped DOS functions were used in the simulations. Characteristics of devices were simulated with midgap DOS values of 5E15, 5E16, 5E17, and 5E18 cm⁻³ eV⁻¹. The effective DOS at the conduction and valence band edges was 1E19 cm⁻³. Devices were simulated under thermodynamic equilibrium conditions as well as light and voltage bias conditions. Light and dark I-V's and electric field distributions have been generated in these preliminary simulations.

The electric field is shown in Figure 11 for thermodynamic equilibrium conditions. The figure shows the spatial distribution of the electric field in a p⁺-i-n⁺ cell for a U-shaped DOS function with minimum DOS values of 5E15, 5E17, and 5E18 cm⁻³ eV⁻¹. For reference purposes, the cell layers are shown at the bottom of Figure 11. The n⁺-layer extends from 0 to 20 nm, the i-layer from 20 to 520 nm, and the p⁺-layer from 520 to 540 nm. The electric field decreases in the middle of the i-layer as the DOS is increased. The results suggest the reason for the decrease in cell power density with increasing 1.0 MeV proton fluence is the generation of defects in the i-layer. Defects in the EPRI AMPS model are represented by electron energy states in the sub-band-gap region. The effect of the defects is to trap charge carriers which increases the space-charge density. The increased space charge density in the i-layer reduces the electric field distribution which in turn reduces the collection of carriers. We plan to pursue the EPRI AMPS simulation in order to obtain the fundamental material parameters for the development of a predictive model.

CONCLUSIONS

The effect of 1.0 MeV proton irradiation is to degrade the normalized power density of cells with six different structures by less than a few percent for fluences less than $1\text{E}12\text{ cm}^{-2}$. For fluences above $1\text{E}15\text{ cm}^{-2}$ cell power degrades to less than 10% of the initial power. Reductions in the normalized power density in the $1\text{E}12$ through $1\text{E}14\text{ cm}^{-2}$ proton fluence range depends on cell structure. Cells with triple junctions have the best radiation resistance, dual-junction cells are next, and single-junction cells have the lowest radiation resistance. Single-junction cells with a-Si,Ge:H i-layers have better radiation resistance than cells with a-Si:H i-layers.

A parametric fitting model was employed to determine the effect on 1.0 MeV proton irradiation on cell parameters. Following irradiation J_0 increased by a factor of two for a fluence of $1.5\text{E}12\text{ cm}^{-2}$ and more than four orders of magnitude for a fluence of $1.5\text{E}15\text{ cm}^{-2}$. After annealing for two hours at 200°C , J_0 was restored to near pre-irradiated values for fluences greater than $1.5\text{E}14\text{ cm}^{-2}$. A third anneal further restored J_0 for the two highly irradiated cells. J_0 was found to be more sensitive to irradiation than power density. Changes in the quality factor, n , were also observed with irradiation. The quality factor increased from 1.84 to 23.9 with irradiation; annealing at 200°C restored n to near pre-irradiated values. The investigations show there is similar structure in the light I-V characteristics of triple and single-junction cells suggesting the current mechanisms resulting in the initially poor performance of a triple-junction cell may be elucidated with investigations of single-junction cells. Investigations of dark I-V characteristics show there is a switching effect in the region of the I-V characteristic where shunt current is the dominant current mechanism. The switching effect has been observed in several cells; it occurs under both forward and reverse-bias conditions. An analysis of several cells shows the switching effect increases in frequency with light and forward-bias voltage soaking; it was observed to decrease with annealing and reverse-bias voltage soaking. Time-dependent switching was observed in the reverse-bias voltage region of the dark I-V characteristics where the current switched from shunt dominated to a current mechanism with a slope between two and two and one-half. Switching occurred at lower reverse-bias voltages as the delay time was increased, and the reverse-bias current was higher; the current mechanism is not understood. Device simulation studies were carried to determine the role of the sub-band-gap density of electron states on the electric field distribution in the p^+i-n^+ layers. The electric field decreased in the middle of the i-layer as the density of states was increased. The results suggest the reason for the decrease in cell power density with increasing 1.0 MeV proton fluence is the generation of defects in the i-layer. The effect of the defects is to trap charge carriers which increases the space-charge density. The increased space charge density in the i-layer reduces the electric field distribution which in turn reduces the collection of carriers.

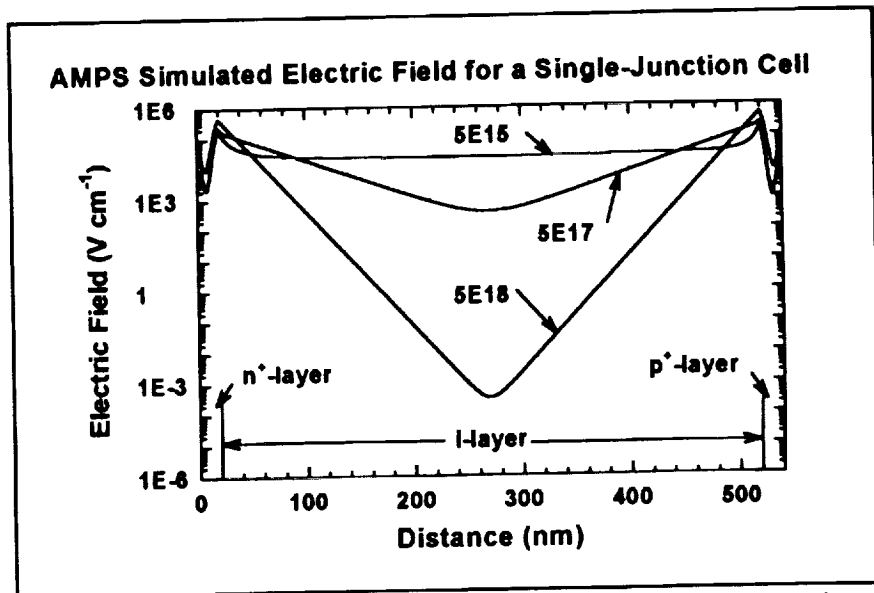


Figure 11: AMPS simulated thermodynamic equilibrium electric field for a 500 nm thick i-layer PIN device with $5\text{E}15$, $5\text{E}17$, $5\text{E}18\text{ cm}^{-3}\text{ eV}^{-1}$ midgap DOS.

REFERENCES

1. Geoffrey A. Landis and James R. Woodyard, Radiation Damage in Thin Film Solar Cells, Solar Cells, 1991, Volume 31, page 297.
2. James R. Woodyard, Dependence of 1.0 MeV Proton Radiation Resistance of a-Si:H Alloy Solar Cells on Cell Thickness, Amorphous Silicon Technology-1992, Materials Research Society Symposium Proceedings, Edited by Malcolm J. Thompson, Yoshihiro Hamakawa Peter G. LeComber Arun Madan and Eric Schiff, Volume 258, 1992, page 1151.
3. Kenneth R. Lord II, Michael R. Walters and James R. Woodyard, Investigation of the Radiation Resistance of Triple-Junction A-Si:H Alloy Solar Cells Irradiated with 1.00 MeV Protons, Space Photovoltaic Research and Technology 1992, NASA Conference Publication 3210, page 98.
4. Kenneth R. Lord II, Michael R. Walters and James R. Woodyard, Investigation of Light and Dark Characteristics of a-Si:H Alloy Cells Irradiated with 1.0 MeV Protons, Twenty Third IEEE Photovoltaic Specialists Conference-1993, page 1448.
5. Kenneth R. Lord II, Michael R. Walters and James R. Woodyard, Investigation of Shunt Resistances in Single-Junction a-Si:H Alloy Solar Cells, Amorphous Silicon Technology-1994, Materials Research Society Symposium Proceedings, Edited by Malcolm J. Thompson, Yoshihiro Hamakawa Peter G. LeComber Arun Madan and Eric Schiff, In Press.
6. S. Abdulaziz and J. R. Woodyard, Annealing Characteristics of Amorphous Silicon Solar Cells Irradiated with 1.00 MeV Protons, Eleventh Space Photovoltaic Research and Technology Conference-1991, NASA Conference Publication 3121, 1991, page 43-1.
7. M. Bennett and R. Podlesny, Two-Source Simulator for Improved Solar Simulation, Twenty-First IEEE Photovoltaic Specialists Conference-1990, page 1438.
8. J. K. Arch, P. J. McElheny, S. J. Fonash, and W. H. Howland. AMPS/1D: A One-Dimensional Device Simulation Program for the Analysis of MicroElectronic and Photonic Structures. Penn State University. November 2, 1990.

THE USE OF DISPLACEMENT DAMAGE DOSE TO CORRELATE DEGRADATION IN SOLAR CELLS EXPOSED TO DIFFERENT RADIATIONS

Geoffrey P. Summers
U.S. Naval Research Laboratory
Washington, DC

Edward A. Burke, Philip Shapiro, Richard Statler,
and Scott R. Messenger
SFA, Inc.
Landover, Maryland

and

Robert J. Walters
U.S. Naval Research Laboratory
Washington, DC

SUMMARY

It has been found useful in the past to use the concept of "equivalent fluence" to compare the radiation response of different solar cell technologies. Results are usually given in terms of an equivalent 1 MeV electron or an equivalent 10 MeV proton fluence. To specify cell response in a complex space-radiation environment in terms of an equivalent fluence, it is necessary to measure damage coefficients for a number of representative electron and proton energies. However, at the last Photovoltaic Specialist Conference (ref.1) we showed that nonionizing energy loss (NIEL) could be used to correlate damage coefficients for protons, using measurements for GaAs as an example (ref.2). This correlation means that damage coefficients for all proton energies except near threshold can be predicted from a measurement made at one particular energy. NIEL is the exact equivalent for displacement damage of linear energy transfer (LET) for ionization energy loss. The use of NIEL in this way leads naturally to the concept of 10 MeV equivalent proton fluence. The situation for electron damage is more complex, however. In this paper it is shown that the concept of *displacement damage dose* gives a more general way of unifying damage coefficients. It follows that 1 MeV electron equivalent fluence is a special case of a more general quantity for unifying electron damage coefficients which we call the *effective 1 MeV electron equivalent dose*.

INTRODUCTION

The most common way of specifying radiation environments for solar cells is in terms of their response to a fluence of 1 MeV electrons. The Solar Cell Radiation Handbook (ref.3) for example is full of such tables and figures showing the degradation of key photovoltaic parameters in a variety of space orbits. Although the effect of an electron or a proton *fluence* is the way displacement damage is generally determined, the *absorbed dose* is the parameter used to describe ionization effects in biological and microelectronic systems. Absorbed dose, which measures the energy deposited per unit mass as a result of ionization, was found to be so useful in comparing the effect of different radiations that a special unit was introduced to measure it. The original unit was the rad, but this has been superseded by the Gray (1 J/kg). Presumably the reason for determining displacement damage in terms of fluence originated in the way dosimetry is performed at particle accelerators. Conversely x-ray and γ -ray dosimetry is performed using techniques such as thermoluminescent emission, the magnitude of which is determined by the absorbed energy or dose. Unlike absorbed dose, fluence cannot be used to correlate the effect of different radiations. However, the product of fluence and NIEL gives the displacement damage

equivalent of absorbed dose, which we will show gives a sound physical basis for correlating both electron and proton displacement damage coefficients. The concept of equivalent fluence then follows in a straightforward way under certain conditions. In other cases it is necessary to introduce the concept of an effective 1 MeV electron equivalent dose in order to correlate electron damage coefficients.

DAMAGE CORRELATIONS USING ABSORBED DOSE

1. PROTONS

Figure 1 shows experimentally measured curves of the normalized power degradation for p/n GaAs solar cells produced by increasing fluences of incident monoenergetic protons with energies of 0.5, 1.0, 3.0, and 9.5 MeV. The data points plotted in figure 1 are taken from the original line figure given by Anspaugh in reference 2 and the lines are shown only to guide the eye. The displacement damage dose for each data point was then calculated from the product of the NIEL in GaAs $S(E)$ and the respective fluence $\phi(E)$ for the particular proton energy E , using the NIEL values given in reference 4. The data were replotted as shown in figure 2, where the abscissa is now the absorbed displacement dose given in units of MeV/g. As can be seen the data for all proton energies when plotted in this way collapse on to a single, universal line. This line, which represents the complete response of GaAs cells to protons of all energies, can be produced using protons of any single energy. Conversely, if degradation data exist for any one energy the experimental line for another energy such as 10 MeV protons could be readily obtained using the equation:

$$\text{Absorbed Dose} = \phi_1(E_1) \cdot S_1(E_1) = \phi_2(E_2) \cdot S_2(E_2) \quad (1)$$

Equation (1) leads naturally to the concept of 10 MeV proton equivalent fluence, which is widely used to simulate the effect of a complex proton environment given in terms of a differential proton spectrum $d\phi_p(E)/dE$. The 10 MeV proton equivalent fluence is calculated from the integral of the proton NIEL over the proton spectrum, divided by the NIEL for 10 MeV protons, i.e.,

$$\phi_p(10) = [1/S_p(10)] \cdot \int S_p(E) \cdot [d\phi_p(E)/dE] dE \quad (2)$$

It is usual to take damage correlation further than Eq.(2) by specifying radiation effects in terms of the effect of a 1 MeV equivalent electron fluence. This requires first reducing the 10 MeV equivalent proton fluence to 1 MeV equivalent electron fluence and then adding the result to the 1 MeV electron fluence equivalent to the total electron environment present. However, because of complexity in the way some semiconductors respond to electrons, such calculations require using the concept of equivalent damage dose in a modified way as we now show.

2. ELECTRONS

It has been found that a linear dependence of photovoltaic parameter change on absorbed dose as shown in figure 2 is always found for relatively high NIEL particles such as protons and helium ions. A linear dependence is also found for low NIEL particles such as electrons incident on n-type Si, GaAs and possibly other semiconductors. In these cases, Eq.(1) can be used directly to convert a 10 MeV proton fluence to a 1 MeV electron fluence from a ratio of the respective NIELs. Similarly, a 1 MeV equivalent electron fluence can be defined for an electron environment in the same way as discussed above for the 10 MeV proton equivalence, Eq.(2), by simply substituting the appropriate symbols.

However, for devices with p-type active regions electron-induced changes are often found to vary in a way which depends on the square of the NIEL of the electrons. This finding is analogous to the different response found for some biological systems to high and low LET ionizing radiations, which leads to the concept of the "quality factor, Q" of the radiation. The quality factor expresses the relative effect of a given radiation to the effect of x-rays, for which $Q = 1$. In the displacement damage case we will show

below that we can define a quantity called the "effective 1 MeV electron equivalent dose", which is obtained by multiplying the absorbed dose for electrons of energy E_j , i.e., $S(E_j) \cdot \phi(E_j)$, by the ratio $S(E_j)/S(1.0)$, where 1.0 refers to 1 MeV. This ratio is the displacement equivalent of the quality factor. The reason for the choice of normalizing energy is that the response to 1 MeV electrons is the traditional way of comparing the behavior of different kinds of solar cells.

As an example we consider the data of Yamaguchi and Amano (ref.5) for changes in minority carrier diffusion length in p-type GaAs irradiated with 0.8, 1.0, 2.0, and 4.0 MeV electrons and with Co^{60} gamma rays. The data were derived from in-depth profiles of short-circuit current changes measured in the emitter of a p/n GaAs cell using the EBIC method. The difference between the reciprocal square of the post- and pre-irradiation diffusion lengths, L_ϕ and L_0 , respectively is given by

$$1/L_\phi^2 - 1/L_0^2 = K(E) \cdot \phi \quad (3)$$

where $K(E)$ is the diffusion length damage coefficient for electrons of energy E . The NIELs for electrons in GaAs with energies of 0.8, 1.0, 2.0, and 4.0 MeV are 21.4, 26.5, 44.2, and 63.2 eV.cm²/g, respectively. The data points from figure 4 of reference 5 has been replotted in figure 3. The line for 4.0 MeV electrons is a least squares fit to the data. The other lines are calculated from this reference line using the ratio of the squares of the NIELs for the respective energies. Co^{60} gamma rays produce a spectrum of mostly Compton electrons and the average NIEL assuming a linear dependence on electron energy is 9.40 eV.cm²/g. Assuming a quadratic dependence gives 155.0 (eV.cm²/g)². Details of these calculations, which are somewhat complicated, have been discussed briefly in reference 3. As an example of the magnitude of the difference associated with the effect of a linear or a quadratic dependence on NIEL consider the data for 4.0 MeV electrons and Co^{60} gamma rays. With a linear dependence the 4.0 data would be calculated to shift to the right by a factor of $63.2/9.40 = 6.72$, which clearly would not coincide with the experimental data for Co^{60} . A quadratic dependence gives a shift of 45.2 and the agreement with the data can then be seen in figure 3 to be excellent.

The quadratic dependence of NIEL means that Eq.(1) must be modified for electrons on p-type GaAs to give.

$$\phi_1(E_1) \cdot [S_1(E_1)]^2 = \phi_2(E_2) \cdot [S_2(E_2)]^2 \quad (4)$$

which can be rearranged to give

$$\phi(E_1) \cdot S(E_1) = \phi(E_2) \cdot S(E_2) [S(E_2)/S(E_1)] \quad (5)$$

where the subscripts 1 and 2 for different types of particles has now been dropped because the discussion applies to electrons only. Eq.(5) can be written

$$\text{Dose}(E_1) = \text{Dose}(E_2) \cdot [S(E_2)/S(E_1)] \quad (6)$$

Eq.(6) shows how an effective 1 MeV electron equivalent dose can be defined, i.e.,

$$\text{Dose}(1.0) = \text{Dose}(E_2) \cdot [S(E_2)/S(1.0)] \quad (7)$$

Figure 4 shows the data in figure 3 replotted using Eq.(7) to calculate the effective 1 MeV electron equivalent dose for each point. As can be seen in figure 4, when plotted in this way, all the data collapses on to a single line. This line represents the general response of GaAs solar cells to electrons of all energies.

DISCUSSION

The results presented here show that the concept of displacement damage dose gives a more fundamental way of comparing the radiation response of solar cells to irradiation than the more commonly used particle fluence. A question that comes immediately to mind in comparing the radiation response of cells, however, is the cause of the general linear dependence of damage coefficients on NIEL found for protons in contrast to the quadratic dependence found for electrons on p-type Si, GaAs and possibly other semiconductors. This question is more complicated than is at first apparent because clearly there is a point at which a plot of the coefficients for p-type cells versus NIEL for protons and electrons, when extrapolated, must coincide. At this "critical" point a linear dependence would presumably be found, assuming there is a particle that actually has the corresponding value of NIEL. The answer to the question must lie in the nature of the stable defects caused by different particles. Higher LET particles such as protons produce defect cascades that have a tree-like structure with dense defect concentrations at the end of branches containing isolated defects (ref.6). Lower LET particles such as low energy (<~50 MeV) electrons produce mostly isolated point defects. It is the details of the formation mechanism of the point defects affecting the electrical properties of the solar cell that determine the dependence on NIEL. The "critical" value of the NIEL appears to correspond to the value at which the tree-like cascade structure becomes dominant.

REFERENCES

1. Summers, G.P., Burke, E.A., Walters, R.J., Shaw, G.J., Shapiro, P., Statler, R.L., and Messenger, S.R.: A General Method for Predicting Radiation Damage to Solar Cells in the Space Environment. IEEE 23rd Photovoltaic Specialists Conference, 1993, pp. 1426-1431.
2. Anspaugh, B.: Proton and Electron Damage Coefficients for GaAs/Ge Solar Cells. IEEE 22nd Photovoltaic Specialists Conference, 1993, pp. 1593-1598.
3. Tada, H.Y., Carter, J.R., Anspaugh, B.E., and Downing, R.G.: Solar Cell Radiation Handbook, 3rd edition. JPL Publication 82-69, 1982.
4. Summers, G.P., Burke, E.A., Shapiro, P., Messenger, S.R., and Walters, R.J.: Damage Correlations in Semiconductors Exposed to Gamma, Electron and Proton Radiations. IEEE Trans. in Nucl. Sci., vol., 1993, pp. 1372-1379.
5. Yamaguchi, M. and Amano, C.: Co⁶⁰ Gamma Ray and Electron Irradiation Damage of GaAs Single Crystals and Solar Cells. J.Appl. Phys., vol. 54, 1983, pp. 5021-5029.
6. Wood, S., Doyle, N.J., Spitznagel, J.A., Choyke, W.J., More, R.M., McGruer, J.N., and Erwin, R.B.: Simulation of Radiation of Damage in Solids. IEEE Trans. in Nucl. Sci., vol.28, 1981, pp. 4107-4112.

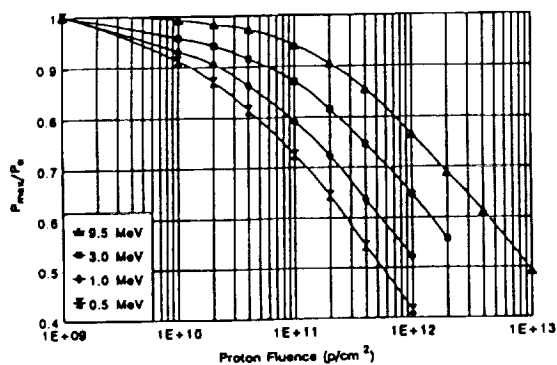


Figure 1-- Power loss of GaAs/Ge solar cells versus proton fluence from reference 2.

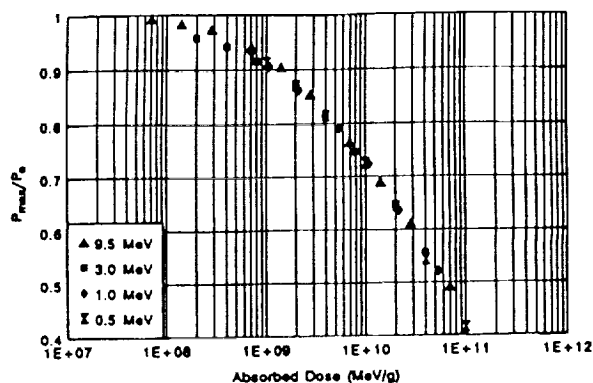


Figure 2-- Power loss of GaAs/Ge solar cells versus displacement damage absorbed dose using data from figure 1.

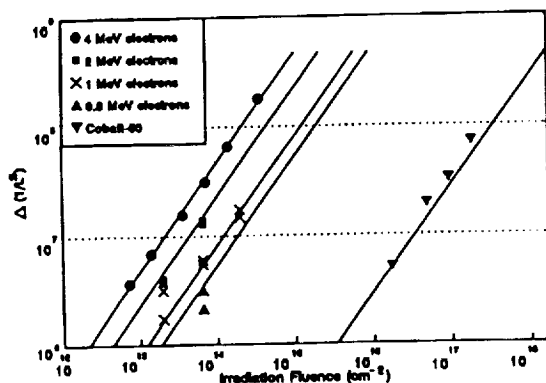


Figure 3-- Diffusion length damage coefficients versus electron fluence from reference 5. The line through the 4.0 MeV data is a least squares fit. The other lines are calculated from the 4.0 MeV line assuming a quadratic dependence on NIEL.

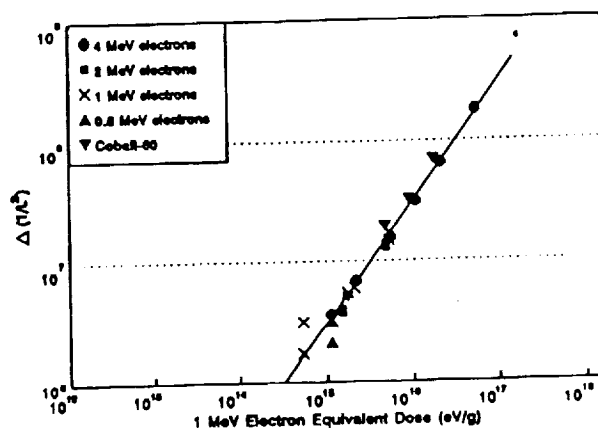


Figure 4- Diffusion length damage coefficients versus 1 MeV electron equivalent dose using the data from figure 3.

ANNEALING OF IRRADIATED n^+p InP BURIED HOMOJUNCTIONS

R.J. Walters and G.P. Summers
U.S. Naval Research Laboratory
Washington, DC

and

M.L. Timmons, R. Venkatasubramanian, J.A. Hancock, and J.S. Hills
Research Triangle Institute
Research Triangle Park, North Carolina

INTRODUCTION

At the last SPRAT conference, the Naval Research Laboratory (NRL) presented results from two experiments. One studied n^+p diffused junction (DJ) InP solar cells (ref. 1), and the other studied n^+p shallow homojunction (SHJ) InP mesa diodes grown by metalorganic chemical vapor deposition (MOCVD) (ref. 2). The former work showed that a DJ solar cell in which the maximum power (P_{max}) had been degraded by nearly 80% under irradiation recovered completely under short circuit illumination at 450K (fig. 1). The recovery was accompanied by the removal of all but one of the radiation-induced defect levels (fig. 2). The latter work, on the other hand, showed that the radiation-induced defects in the SHJ diodes did not anneal until the temperature reached 650K (fig 3). These results suggest that an irradiated DJ solar cell, under illumination, will anneal at a temperature 200K lower than an irradiated SHJ cell. This is an unexpected result considering the similarity of the devices. The goal of the present research is to explain this different behavior.

This paper investigates two points which arose from the previous studies. The first point is that the DJ cells were annealed under illumination while the SHJ diodes were annealed without bias. Given the known sensitivity of radiation-induced defects in InP to minority carrier injection-annealing (ref. 3), it is possible that the illumination is the cause of the lower annealing temperature. To test this, irradiated SHJ InP solar cells of the same structure as the diodes of ref. 2 have been annealed under illumination at temperatures ranging from 300-500K. The results of these experiments are presented here. The conclusion is that the illumination had no effect on the annealing, and the annealing follows that which was expected from the diode study of ref. 2 - i.e. the recovery is limited by a lack of defect annealing in this temperature range.

The second point investigated here is that the emitters of the DJ and SHJ devices were significantly different. The emitter of the DJ cells of ref. 1 were thick ($0.3\mu m$) and grown by diffusion which forms a graded carrier concentration profile. However, the emitter of the SHJ diodes of ref. 2 and cells studied here were thin ($0.03\mu m$) with a uniform carrier concentration profile. The thicker emitter means the DJ emitter current is much larger than that of the SHJ cells. Also, the different concentration profiles results in different spacial distributions of the junction electric field. These differences may impact the solar cell annealing characteristics. To investigate this, the Research Triangle Institute (RTI), under contract to NRL, used MOCVD to grow epitaxial cells with the structure of the DJ cells. The cells have a $0.25\mu m$ thick emitter with a graded dopant profile (fig. 4). The cells are referred to as deep homojunctions (DHJ). The growth of these cells is the subject of a companion paper given by RTI at this conference. The present paper reports the annealing characteristics of the DHJ cells following irradiation. Results of annealing both in the dark and under illumination in the temperature range of 175K-450K are presented. In general, the annealing characteristics of the DHJ cells was similar to that of the SHJ cells especially in terms of the defect spectrum. However, significantly more recovery of the short circuit current (I_{sc}) was seen in the DHJ cells than in the SHJ cells. Therefore, the thicker, graded

emitter seems to enhance the recovery of I_{sc} , but the overall cell recovery is incomplete due to a lack of defect annealing just as in the case of the SHJ cells.

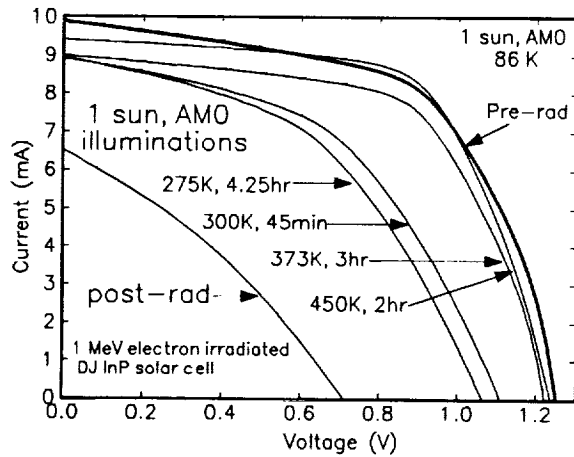


Figure 1: Photo-injection annealing of an irradiated DJ solar cell. Illumination at 275K causes substantial recovery, and full recovery is seen at 450K.

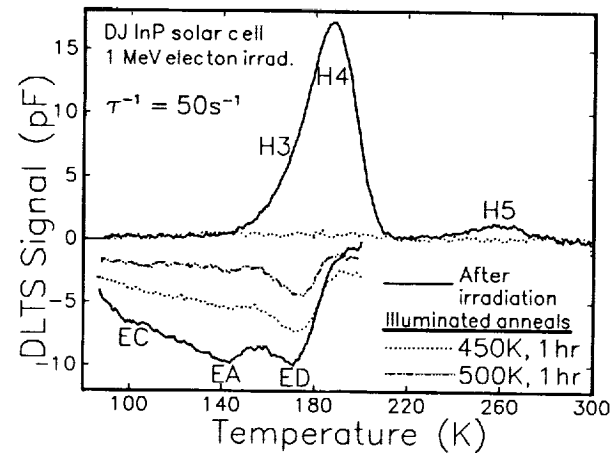


Figure 2: The defect annealing measured in the DJ cell of fig. 1. The illumination at 450K removed all but the ED defect.

EXPERIMENTAL DETAILS

Data measured on two n⁺p SHJ solar cells are presented. One cell was annealed in the dark, and the other was annealed under illumination. The data for the cell annealed in the dark has already been published in ref. 4, but the data is reproduced here to allow for direct comparisons. This cell was grown using MOCVD by Spire Corporation under contract to NRL and has the structure of fig. 5. The cell was part of run number 5414-7-1. Si was the emitter dopant, and Zn was the base dopant. The total cell area was 0.25cm² and BOL PV parameters were: I_{sc} =8.78mA, V_{oc} =0.883V, P_{max} =6.48mW, FF=0.836, Eff=18.95% (total area). The cell was 10 MeV proton irradiated up to a fluence of 10¹² cm⁻². Dosimetry was achieved through a faraday cup and current integrator circuit, and the fluence is known to within about 15%. Capacitance vs voltage (CV) measurements on a diode grown on the same wafer as the solar cell and irradiated simultaneously

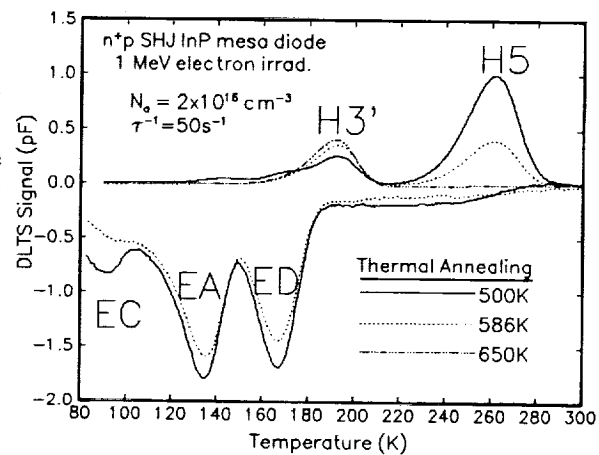


Figure 3: Annealing of an irradiated n⁺p SHJ diode. Only the H3 and H4 defects anneal below 500K. Not until 650K do the remaining defects anneal which is 200K higher than in the DJ cells (ref. 2).

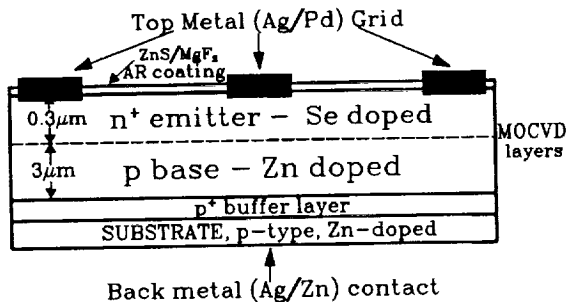


Figure 4: A schematic drawing of the DHJ cells grown by RTI. These are epitaxial cells grown to simulate the DJ cell structure, so the emitter is thick with a linearly graded dopant profile.

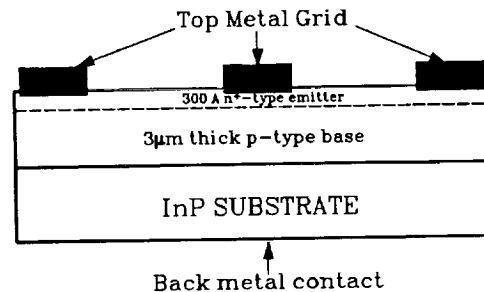


Figure 5: A schematic diagram of the n+p SHJ cells. The emitter of these cells is thin with a uniform carrier concentration profile. This is the same structure as the mesa diodes of ref. 2.

with the cell showed the base dopant concentration to be a uniform 10^{16} cm^{-3} before and after irradiation.

The second n+p SHJ solar cell studied here (the cell which was annealed under illumination) was also grown using MOCVD by Spire Corporation. This cell came from run number 2353-1-1. The cell structure was also that of fig. 5. Se was the emitter dopant, and Zn was the base dopant. The total cell area was 0.25 cm^2 and BOL PV parameters were: $I_{sc}=7.32 \text{ mA}$, $V_{oc}=0.850 \text{ V}$, $P_{max}=4.927 \text{ mW}$, $FF=0.792$, $Eff=14.4\%$ (total area). The cell was irradiated with alpha (α) particles from an Am-241 source. A special acknowledgement goes to Dr. Pascale Gouker of Spire for performing the irradiations and supplying NRL with this cell. The cell was irradiated up to a fluence of $8 \times 10^{11} \alpha\text{-particles/cm}^2$ which is equivalent to $5 \times 10^{16} \text{ 1 MeV electrons/cm}^2$ (the calculation of the 1 MeV electron equivalent fluence was done by E.A. Burke formerly of Spire). No pre-irradiation CV measurements of this cell were possible, but the target base carrier concentration was a uniform $5 \times 10^{16} \text{ cm}^{-3}$. CV measurements were performed on the cell after irradiation. The irradiation caused carrier removal near the junction (fig. 6).

Two of the RTI DHJ cells were studied. These cells came from RTI MOCVD run numbers 1955-a1 and 1955-a4. The total cell area was 0.25 cm^2 . Due to metal contact shadowing on top of the cells, the active area was 0.16 cm^2 . BOL PV parameters were: cell 1955-a1 - $I_{sc}=4.82 \text{ mA}$, $V_{oc}=0.833 \text{ V}$, $P_{max}=3.32 \text{ mW}$, $FF=0.828$, $Eff=15.2\%$ (active area) and cell 1955-a4 - $I_{sc}=4.85 \text{ mA}$, $V_{oc}=0.841 \text{ V}$, $P_{max}=3.40 \text{ mW}$, $FF=0.834$, $Eff=15.6\%$ (active area). The cells were irradiated with 3 MeV protons at the Naval Surface Warfare Center (NSWC) in White Oak, MD using a Pelletron Accelerator. The samples were mounted on a grounded plate, and the fluence was determined by measuring the target plate current. Unfortunately, due to incomplete charge collection and an obscuring aperture in the beam line which was not accounted for, the dosimetry was poor. The best guess at the fluence is $6.12 \times 10^{11} \text{ cm}^{-2}$, but this could be off by as much as 40%. The cells were mounted and irradiated separately. The beam

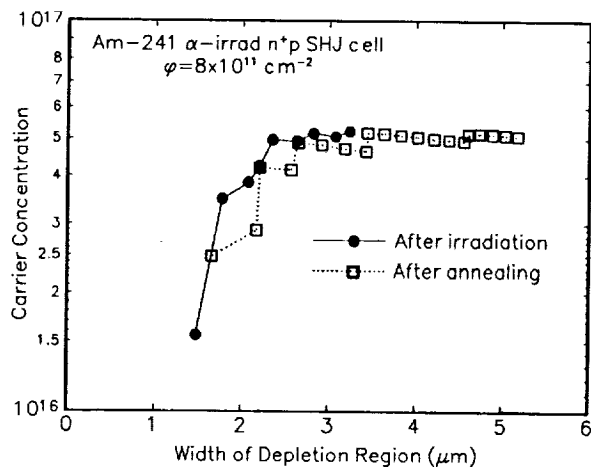


Figure 6: The carrier concentration profile of Spire cell 2353-1-1 after irradiation and after annealing. Carrier removal occurred near the junction, and the annealing had no effect.

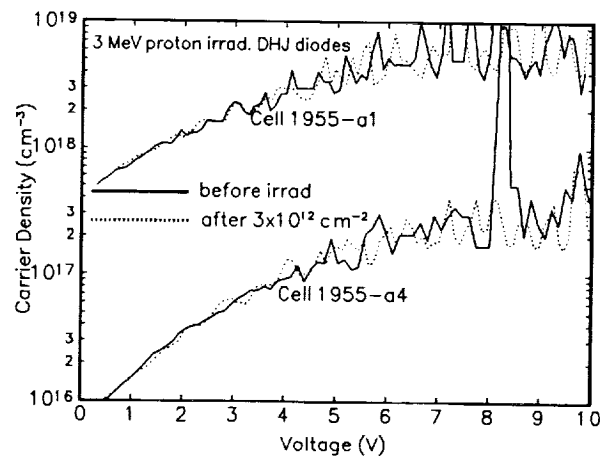


Figure 7: Carrier concentration profiles of the two DHJ cells studied here. The irradiation had no effect on the concentration. The inset scale indicates the depth relative to the junction.

current was $\leq 22 \text{ nA/cm}^2$, and the irradiations were completed in a matter of seconds. The irradiations were done in vacuum, at open circuit, and in the dark. CV measurements on diodes grown adjacent to the cells before irradiation showed the base dopant concentration of cell 1955-a1 to be about $3 \times 10^{18} \text{ cm}^{-3}$ and of cell 1955-a4 to be about 10^{17} cm^{-3} , but both profiles were somewhat graded (fig. 7). These diodes were irradiated simultaneously with the cells with no effect on the carrier concentration.

The solar cells were mounted in a continuous flow liquid nitrogen cryostat which is equipped with a sapphire window to allow for illumination. The temperature range of the cryostat is 86 - 500K. All of the experiments were performed using the cryostat including the annealing experiments. The chamber was under constant vacuum. An Oriel 1000W Xe arc lamp solar simulator with AM0 filtering was used. The lamp intensity was adjusted to one sun using an InP reference cell calibrated by Keith Emery at NREL. Illuminated IV curves were measured using two Keithly 617 electrometers and a Kepco 50-2M bipolar amplifier. The radiation-induced defect spectrum was characterized through deep level transient spectroscopy (DLTS). A Bio-Rad DL4600 spectrometer with a Boonton 72-B capacitance meter was used. The reverse bias for every DLTS measurement was -2V. A saturation fill pulse was consistently used to ensure complete trap filling. The same capacitance meter was used for the CV measurements.

EXPERIMENTAL RESULTS

Thermal Annealing of a SHJ cell in the Dark

One of the goals of this report is to compare the annealing characteristics of SHJ InP solar cells which have been annealed in the dark with those which have been annealed under illumination. NRL and Spire have published thermal annealing in the dark data in ref. 4, and that data is now reproduced for

comparison purposes. It should be noted that a similar experiment has been performed at NRL on a 1 MeV electron irradiated Spire MOCVD grown n⁺p SHJ InP solar cell which showed similar results.

Following irradiation with 10 MeV protons up to a fluence of 10^{12} cm⁻², cell 5414-7-1 was thermally annealed at 415 and then 500K. The cryostat was completely dark and no connections were made to the cell during the annealing. At 415K, the cell was annealed in incremental time steps beginning with 15 minutes and ending after 3 hours. After 3 hours at 415K, no further changes were observed, so the temperature was raised to 500K. The cell was again annealed in incremental time steps beginning with 15 minutes and ending after 1 hour and 15 minutes. After each time increment, the illuminated IV curve was measured at 298K (fig. 8). Also, both the majority and minority carrier trap DLTS spectra were measured after each time step (fig. 9). With the present DLTS system, a positive DLTS signal indicates majority carrier capture while a negative signal indicates minority carrier capture.

Considering the annealing at 415K, the only recovery of the PV parameters occurred after the first 15 minutes. The recovery consisted mainly of an increase in I_{sc} (about a 3.5% increase). The recovery of V_{oc} and the FF was 1% or less. The first 15 minutes at 415K also caused a small decrease in the concentration of all of the hole traps (fig. 9). The ED peak just became visible due to the decrease in the obscuring H3 peak. The continued annealing at 415K caused the complete removal of the H3 and H4 defects. Increasing the temperature to 500K caused another increase in I_{sc} , a very small one in V_{oc} , but none in FF. No changes in the DLTS spectra were seen. In total, the recovery was minimal - P_{max} , which was degraded by 25%, only recovered by 9.4%, and only the H3 and H4 defects showed annealing.

Thermal Annealing of a SHJ cell Under Illumination

One of the missing pieces in the current discussion is a study of the annealing of an irradiated SHJ cell under illumination. This data is now presented. Following the α -particle irradiation, Spire n⁺p SHJ InP solar cell number 2353-1-1 was illuminated short circuit at 350, then 400, and then 500K. As in the previous experiment, the annealing was carried out for progressively longer times at each temperature until no more changes were apparent. The temperature was then increased and the annealing repeated. After each time step, an illuminated IV curve was measured at 298K along with the full DLTS spectrum. The recovery of the IV curves is shown in fig. 10. The DLTS spectra are shown in fig. 11.

The illuminations at 350K had no effect on the IV curve or the DLTS spectrum. At 400K, all of PV parameters recovered a small amount except the FF which showed no change. Raising the temperature of illumination to 500K caused another moderate rise in V_{oc} , but I_{sc} and the FF did not show an increase. Overall, the IV curves showed only minimal recovery. In particular, the complete lack of increase in the FF significantly suppresses P_{max} . These results are similar in nature to the DLTS results. Illumination at 350K had no effect on the defect spectrum. At 400K, the H3 and H4 defects were completely removed, and at 500K, the H3' defect emerged (ref. 2). No other defect reactions were observed. The recovery of the IV curves is minimal and only two of the 6 radiation-induced defects show annealing stages.

Annealing of a DHJ Under Illumination

The second part of this study investigated the effect of the emitter structure on the annealing properties of irradiated InP solar cells. The first data set to be presented is the annealing of the RTI grown DHJ cell #1955-a4 under short circuit illumination. Since irradiated DJ cells showed substantial recovery due to short circuit illuminations below room temperature (ref. 1 and figs. 1 and 2), the first experiments were below room temperature illuminations. Initially, it was established through DLTS

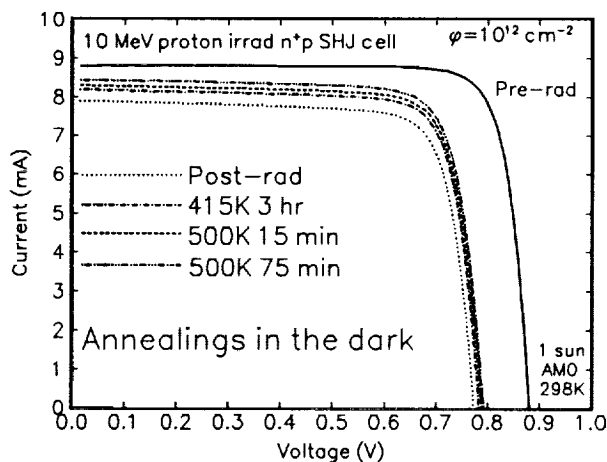


Figure 8: Thermal annealing in the dark of Spire cell 5414-1-7. Even at 500K, only limited recovery is seen especially in V_{oc} and the FF.

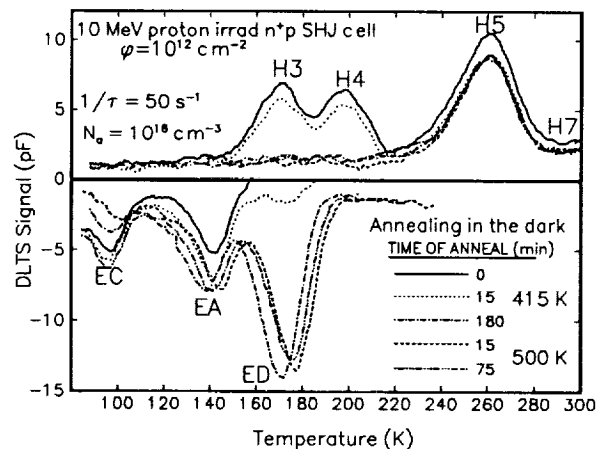


Figure 9: Defect annealing in the SHJ cell of fig. 8. Only the H3 and H4 defects anneal. Increase in negative signal is due to the removal of the positive signal and not an increase in defect concentration.

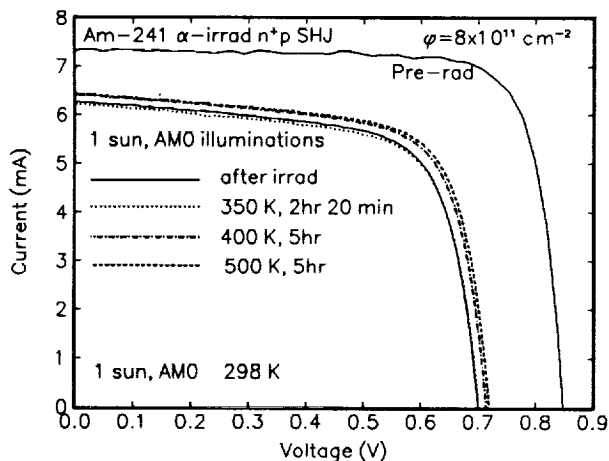


Figure 10: Illuminated thermal annealing of the α -irradiated SHJ cell. Only moderate annealing occurs even after 5 hrs at 500K. The lack of recovery in FF suppresses P_{max} .

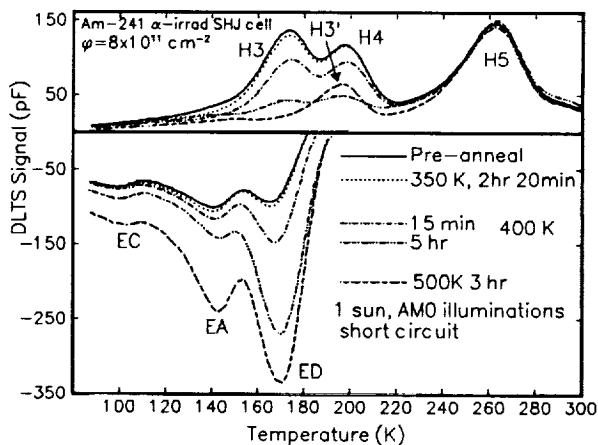


Figure 11: The defect annealing in the cell of fig. 10. As seen during thermal annealing in the dark, only the H3 and H4 defects show any annealing stages.

measurements that illuminated IV measurements at 86K did not cause annealing. Then the cell was held at 175K and illuminated short circuit for 1 hour. A subsequent illuminated IV measurement at 86K showed no change (fig. 12). A subsequent DLTS measurement also showed no change (fig. 13) which is a very unexpected result because independent of PV recovery, the H4 defect has always shown annealing at temperatures of 175K and above (1-5).

Following the 175K experiment, cell 1955-a4 was illuminated short circuit at 300K and above. As shown in fig. 13, illumination at 300K did cause the familiar reduction of the H4 peak height. The H5 peak is seen to grow concurrently which is characteristic of the SHJ cells, but not the DJ cells (refs. 1,2, and 5). A very small recovery stage of the PV parameters may be apparent (fig 14 -note that since the annealing temperature is 300K or larger, the IV measurements were taken at 298K). Illumination at 375K caused significant recovery in the IV curves, and illumination at 450K caused even more recovery which lead to complete recovery of I_{sc} . However, the recovery of V_{oc} is quite limited. The changes in the DLTS spectra are shown in fig. 13. The illuminations only affected the H3 and H4 defects which is very similar to the SHJ cell results.

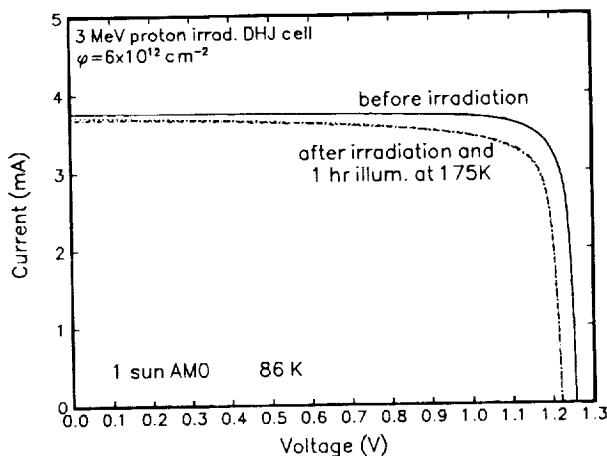


Figure 12: Low temperature illumination of RTI DHJ cell 1955-a4. One hour of short circuit illumination at 175K causes no recovery. IV curves measured at 86K to avoid annealing during the measurement.

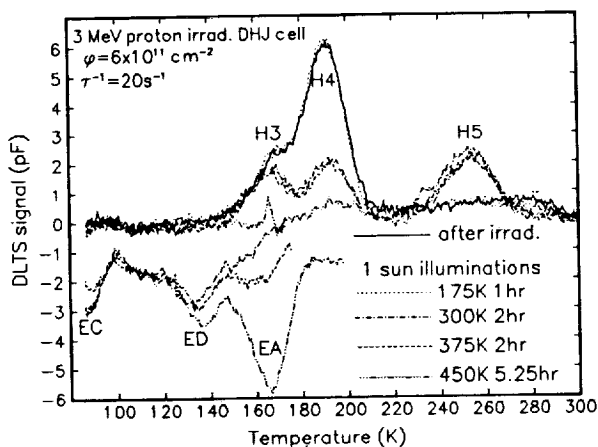


Figure 13: Illumination of RTI DHJ cell 1955-a4. At 175K, annealing of the H4 defect was expected but not seen. Above 300K, only the H3 and H4 defects anneal while the H5 peak grows.

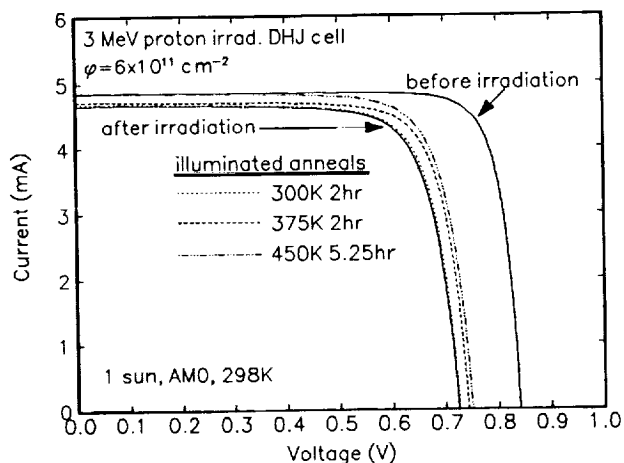


Figure 14: Continued illumination of RTI DHJ cell 1955-a4 at $T \geq 300K$. Some recovery seems evident at 300K. I_{sc} completely recovers at 450K. V_{oc} limits the cell recovery.

Thermal Annealing of a DHJ in the Dark

The final data sets to be presented are the thermal annealing of an irradiated DHJ cell in the dark. The DHJ cell #1955-a1 was annealed in the dark (and unbiased) at 375 and 450K. Initially, the cell was illuminated at 300K to ensure all room temperature annealing stages were complete. The recovery of the cell is shown in fig. 15. All of the PV parameters recovered with I_{sc} recovering the most. The effect on the DLTS spectrum is shown in fig 16. The annealing removed H3 and H4 but did not affect the remaining defects. These results follow the same trends as the illuminated annealing data.

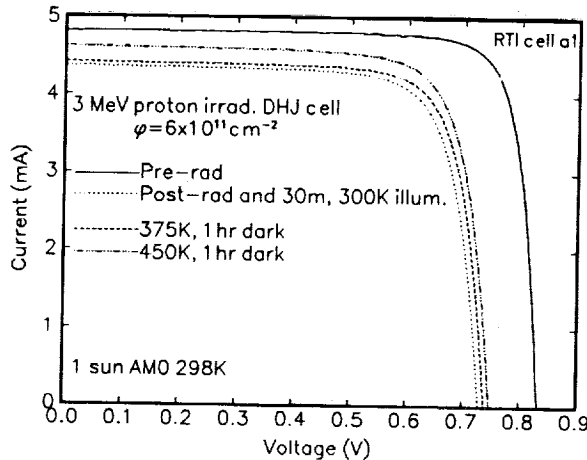


Figure 15: The effect of thermal annealing in the dark on RTI DHJ cell 1955-a1. The recovery stages are similar to those seen during the illuminated annealing of cell 1955-a4.

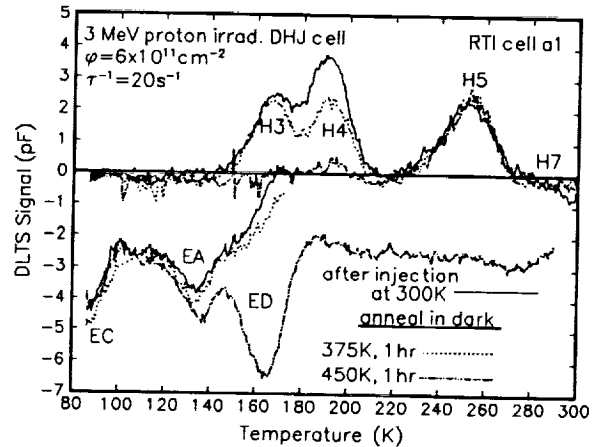


Figure 16: The effect thermal annealing in the dark on RTI DHJ cell 1955-a1. Basically the same defect reactions are seen as in the illuminated annealing of cell 1955-a4.

DISCUSSION

The first question under investigation was - would illuminating an irradiated SHJ cell above room temperature enhance the cell annealing characteristics? The answer is no. Essentially the same amount of annealing of the PV parameters was seen following annealing under illumination and in the dark, and the recovery is far from complete. Furthermore, the residual defect spectra measured at the end of both annealing experiments are essentially the same. As was predicted by the results of ref. 2, very little solar cell recovery is seen in the SHJ cells after annealing at temperatures below 500K, regardless of the illumination.

These results provide a better understanding of the cause of the different annealing behavior in DJ and SHJ solar cells. In a DJ cell, illumination at 450K removed all of the radiation-induced defects from the cell junction except for the electron trap, ED, which only partially annealed after 2 hours at 450K. In a SHJ cell, on the other hand, below 500K, none of the defects show annealing stages except the H3 and H4 defects. These two defects are removed in the range of 375-450K, but all others remain.

Therefore, the enhanced annealing evident in the DJ solar cells can be attributed, at least in part, to the enhanced defect annealing in the cell junction. Considering these results with those of ref. 2, it is expected that the defects in the junction of a SHJ cell will anneal if the temperature is raised to 650K. Therefore, it may be concluded that a SHJ solar cell will show complete recovery after annealing at 650K. If this is the case, then it can also be concluded that, irradiated n⁺p InP solar cells grown by S diffusion will completely recover at a temperature which is 200K lower than an irradiated n⁺p InP SHJ cell grown by MOCVD. This is a strong possibility given the present results, but since data from an irradiated n⁺p SHJ cell annealed above 500K do not yet exist, no definite conclusions can be drawn.

The second question under investigation was if the difference in emitter structure between the SHJ and DJ cells was responsible for the different cell annealing behavior. The enhanced annealing of the DJ cells was above shown to be, in part, due to enhanced defect annealing. Since the radiation-induced defects in SHJ InP have been shown to be sensitive to an electric field (ref. 6), this enhancement may be an electric field related effect. The DHJ cells were grown to simulate the DJ cells, so the junction electric field is expected to be similar in both cell types. However, the residual defect spectrum measured in both DHJ cells (i.e. in both the cell annealed in the dark and the cell annealed under illumination) was essentially the same as that of the SHJ cells. Therefore, the difference in the junction electric field of the DJ and SHJ cells most likely is not the cause of the enhanced defect annealing. However, it should be noted that the exact structure of DHJ and the DJ cells has not yet been analyzed. Therefore, these conclusion can only be tentative. A more precise determination of the structure of these devices is the next step in the NRL/RTI research project.

The annealing of the DHJ cells is also similar to that of the SHJ cells in terms of the recovery of V_{oc} . V_{oc} shows almost no recovery in both of these cell types. The DJ cells, on the other hand, have shown complete recovery in V_{oc} . This is almost certainly due to the fact that most of the radiation-induced defects in the base of the DHJ cells are not removed by the present annealing experiment while in the DJ cells, all but the ED defect are removed. The persistence of the radiation-induced defects in the epitaxial cells following these annealing experiments inhibits the recovery of V_{oc} while the annealing of the defects in the diffused junctions induces full recovery of V_{oc} in the DJ cells.

While the annealing of the defect spectrum in the DHJ cells is similar to that of the SHJ cells, the recovery of the PV parameters shows a significant difference. Annealing a DHJ cell for 5.25 hrs under illumination at 450K caused complete recovery of I_{sc} , and annealing a DHJ for 1 hour in the dark at 450K showed substantial I_{sc} recovery. The SHJ cells did not show this much recovery, so it does seem that the emitter structure of the DHJ cells has enhanced the annealing characteristics of I_{sc} . The DLTS results suggest that this is not due to enhanced defect annealing in the base (DLTS samples only the base region), so the enhanced recovery is most likely due to an annealing mechanism in the n-type emitter. This result is consistent with work presented at this conference by Messenger et al. on irradiated p⁺n InP solar cells. Those results show recovery in I_{sc} due to short circuit illumination at room temperature and below. It seems, now, that a possible explanation has emerged for why I_{sc} in the DJ cells recovers under illumination at $T < 300K$ and I_{sc} in the SHJ cells does not. It may be that the I_{sc} recovery is caused by an increased carrier collection efficiency in the n-type InP due to the illumination and only the DJ cells have enough n-type material for the effect to be seen.

CONCLUSIONS

The present research has shown that illuminating an irradiated n⁺p SHJ InP solar cell during thermal annealing above 300K does not enhance the recovery of the PV parameters or the defect annealing rate. The results strongly suggest that irradiated n⁺p DJ solar cells will anneal at a temperature

200K lower than an irradiated n⁺p SHJ cell with or without illumination. The measured full recovery of I_{sc} in an irradiated DHJ cell has indicated that illumination may be only affecting the current collection in the n-type InP material, so only n⁺p cells with thick emitters, i.e. the DJ and DHJ cells, show recovery of I_{sc} under illumination. However, the fact that the I_{sc} of the DHJ cells did not recover under illumination below room temperature shows that the present DHJ cell structure still lacks qualities of the DJ cell structure which are essential for optimizing this effect. Furthermore, the lack of recovery of V_{oc} and the lack of defect annealing in the DHJ cells indicates that there is still a major difference between the epitaxial and diffused cell structures which inhibits the epitaxial cells from obtaining full recovery of radiation-induced damage.

These points clearly indicate that while the present investigation of the effects of the cell structure on the cell annealing characteristics has indicated the importance of the n-type emitter, more research into the device structure needs to be done to fully understand the mechanism for the enhanced annealing properties of the DJ solar cells.

REFERENCES

1. Walters, R.J., G.P. Summers, and J. Bruening, "A Detailed Study of Thermally Diffused InP Solar Cells", XII Space Photovoltaic Research and Technology Conference, p.1, Oct 20-22, 1992
2. Messenger, S.R., R. J. Walters, and G.P. Summers, "High Temperature Annealing of Minority Carrier Traps in Irradiated MOCVD n⁺p InP Solar Cell Junctions", XII Space Photovoltaic Research and Technology Conference, p.8, Oct 20-22, 1992
3. Walters, R.J. and G.P. Summers, "Deep Level Transient Spectroscopy Study of Proton Irradiated p-type InP", J. Appl. Phys. **69** (9), 6488, 1 May 1991 and references therein
4. C.J. Keavney, R.J. Walters, and P.J. Drevinsky, "Optimizing the Radiation Resistance of InP Solar Cells: The Effect of Dopant Density and Cell Thickness", J. Appl. Phys., **73** (1), 1 Jan. 1993 p 60-70
5. Walters, R.J., "A Study of the Annealing of Radiation-Induced Defects in InP Solar Cells", Ph.D. Dissertation, University of Maryland Baltimore County, May 1994
6. S.R. Messenger, R.J. Walters, G.P. Summers, "Effect of Carrier Concentration on the Properties of Irradiation-induced Defects in p-type Indium Phosphide Grown by Metalorganic Chemical Vapor Deposition", J. Appl. Phys. **71**, p.4201-4207, 1 May 1992.

QUALIFICATION TEST RESULTS FOR BLUE-RED REFLECTING SOLAR CELL COVERS

W.T. Beauchamp
OCLI
Santa Rosa, California

Recent market forces and design innovations have spurred the development of solar cell covers that significantly reduce the solar absorptance for a cell array. GaAs cells using Ge as the substrate host material, can have a significantly higher output if the solar absorptance of the cell array is reduced. New optical coating design techniques have allowed the construction of covers that reflect the ultraviolet energy (below 350 nm) and the near infrared energy (above 900 nm) resulting in the beneficial reduction in absorptance. Recent modeling¹ suggests three or more percent output increase due to the lowered temperature with such a device.

Within the last several months we have completed the testing of production samples of these new covers in a qualification series that included the usual environmental effects associated with the routine testing of solar cell covers and the combined effects of protons, electrons and solar UV as would be encountered in space.

For the combined effects testing the samples were exposed to 300 sun days equivalent UV, $5 \times 10^{14}/\text{cm}^2$ of 0.5 MeV protons and $10^{15}/\text{cm}^2$ of 1.0 MeV electrons. Measurements of the reflectance, transmission, emittance and other appropriate parameters were made before and after the testing. As measured by the average transmission over the cell operating band, the change in transmission for the samples was less than or about equal to 1%.

The details of the testing and the results in terms of transmission, reflectance and emittance are discussed in the paper.

Key Words:

Space Power, Photovoltaic System, Space Qualification, Solar Reflector, Reduced Solar Absorptance, Temperature Reduction, Output Efficiency

INTRODUCTION

The results of this series of tests give quantitative data on the nominal performance of blue-red reflecting (BRR) solar cell covers designed for use on GaAs and silicon solar cells before and after exposure to the normal environmental tests for such devices, as well as the stability of that performance in simulated space environmental effects testing. The tests performed included the normal application specific performance parameters and environmental exposures that are important to the use of the devices in service.

The test program used samples prepared using standard production methods and procedures. The samples were manufactured in production lots from at least two different coating runs for each coating type and were divided into test groups in a randomized manner with each group being exposed to a specific series of tests and analyses. Many of the tests and characterizations were performed at OCLI. However, the space environmental exposure testing using UV and high energy protons plus electrons, was done at the *Boeing Corporation*. Low energy proton exposures and evaluations were done by the *Hughes Aircraft Co., Space and Communications Division*, and by the *Martin Marrietta, Astro Space Division*. Samples prepared for this test series were mostly² characterized at OCLI for the appropriate performance parameters before testing and after testing to assess the changes induced by the environmental exposures.

¹ See *Blue/Red Reflecting Solar Cell Covers for GaAs Cells*; Proceedings of the Twenty Third IEEE Photospecialist Conference; Louisville, KY; May 1994

² Some pre and post measurements of performance, as well as, the particle exposures were done by Martin Marrietta for the low energy series.

Product Descriptions and Codes

The products explicitly tested were blue-red reflecting solar cell covers for GaAs and silicon cells. For OCLI, the basic code used to designate a blue-red reflecting cover is BRR. If the cover is intended for use on a GaAs cell then a (g) is appended to this code to result in the BRR/g designation. If the cover substrate material is Corning 0213 glass - a cerium doped micro sheet material - then the designation becomes BRR/g-0213. Similarly, if the application requirements dictate the use of fused silica as the substrate material and the cell will be GaAs the designation would be BRR/g-FS. A BRR cover for use on a silicon solar cell would be designated as a BRR/s-0213 or BRR/s-FS. Another version of the basic conceptual design for these products deletes the UV reflection feature and substitutes an AR. This version would be designated as an AR-RR/g-0213, etc.

In this qualification series, samples of the BRR/g-0213 and the BRR/s-0213 covers were tested and evaluated.

Product Descriptions

The function of coatings on a reflecting solar cell cover is to reduce the solar absorption of the array with little or no change in the electrical output of the system. The reduction in solar absorption is accomplished by reflecting as much as possible of the incident solar energy that is at wavelengths outside of the response wavelength band for the cell. GaAs solar cells are responsive to energy at wavelengths from about 350 nm to about 900 nm. For silicon solar cells the response region is from about 350 nm to about 1100 nm. If the cover is designed to reflect both the UV energy below 350 nm and the near-infrared energy above 900 nm or 1100 nm, the lower solar absorbance will allow the system to remain cool and the cell efficiency will be less degraded by temperature effects. Of course, the reduction in solar absorbance will result in a lower temperature only if there is no significant change in the emittance of the array surface due to the cover and coating.

A typical BRR cover reflectance for both types of cover - for GaAs and silicon cells - is shown in Fig. 1. In the response regions of the cells, the transmission is very high. In the out of band regions above 900 nm or 1100 nm and below 350 nm, the reflectance is as high and as broad as practical.³ If the solar absorbance is measured for a BRR cover adhered to a typical GaAs cell, the nominal solar absorbance is on the order of 75% with this BRR/g-0213 design. (The absorption of the cell and the back contacts, as well as the glass, coating, and cement are included in the solar absorbance value for the complete cell-cover system.)

By comparing the spectral plots in Figure 1, the difference between a GaAs BRR and a silicon BRR can be seen to be in the breadth of the transmission band. The position of the reflector for the NIR wavelengths is independent of the position of the reflector for the UV wavelengths. In addition, for the changes necessary to adapt from a reflector for use on GaAs to one for use on silicon, the transmission at wavelengths in the cell response bands can be kept very high. Therefore, the transition edge - from transmitting to reflecting - can be independently placed at a best position for each cover. The value of 1100 nm for silicon and 900 nm for GaAs on the long wavelength side of the transmission band and 350 nm for the short wavelength edge for both cell types was chosen based on extensive testing of cell/cover combinations for use on pointing arrays⁴.

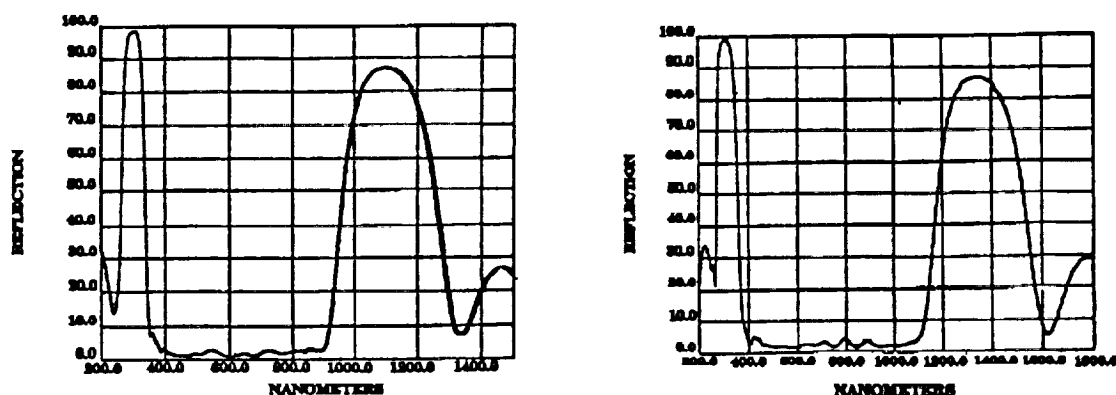
The typical construction for a BRR cover is to place the UV reflector on the front surface of the cover and the red reflector on the rear surface. Because the 0213 glass is highly absorbing at wavelengths less than 350 nm, the UV reflector must be on the front to be functional. The red reflector could also be on the front of the cover (under the UV reflector) but this might result in a significant reduction in the emittance for the cover. The coating(s) on the front surface will modify the emittance due to the optical properties of the materials in the far infrared. In particular the materials in the coating can add to

³ There is a great flexibility in the width of the reflectance band for the cover in both the UV and the NIR. What is practical is determined by a host of factors including the reduction in solar absorbance for broader reflectance measured against increased cost of manufacture, the possible effect on transmission over the cell response region associated with the more complex design, and possible greater warpage of the cover due to stress in the coatings as well as other technical factors.

⁴ For the use of a BRR on a spinner satellite power system, the effects of angle of incidence on the coating must be taken into account. This results in the use of a NIR reflecting band positioned slightly farther out in wavelength than for the pointing array case.

Reststrahlen reflectance or Fresnel reflectance in the infrared resulting in a reduced emittance. This is particularly true for moderately thick coatings⁵ such as the red reflector.

Figure 1. Nominal Reflectance as a Function of Wavelength for a BRR/g-0213 Solar Cell Cover (a) and for a BRR/s-0213 Solar Cell Cover (b).



Note: These scans have different wavelength scales.

The covers evaluated in this test series were all constructed on 0.006 inches (6 mils) thick Corning 0213 cerium doped microsheet. The 0213 glass was taken from stock material used at OCLI for routine manufacturing of solar cell covers and qualified for space use as a cover material, uncoated and in conjunction with a UVR coating on the front, in a qualification test discussed in the 1989 OCLI Qualification Report APD 89011.

Part Preparation and Sample Selection

The parts tested for this qualification were prepared using manufacturing procedures for the particular design, and were deposited in equipment regularly used for manufacturing of covers as well as other products. The samples were, as much as practical, selected at random from two separate lots and/or two separate coating runs for each coated surface on the covers. Control samples in the tests included uncoated 0213 glass and the UVR covers. These control samples showed changes consistent with, and in statistical agreement with, the data contained in the OCLI qualification test report for the UVR's and Corning 0213 microsheet glass (report APD 89011).

TESTS PERFORMED AND QUALIFICATION TEST GROUPS

The parameters measured and the environmental tests performed are shown in Table 1. This list of evaluations dictated the sequence of tests for each group and the data to be gathered.

Because of limited space in the test facilities at Boeing, the number of samples that could be exposed to combined space effects was further limited. To insure statistical validity in the results, a minimum of 5 samples of each design type were tested in two independent sets.

Facilities and Equipment Used for the Testing and Exposures.

For the measurements of the optical performance properties of the covers before and after the exposures, a Shimadzu 160 spectrophotometer was the primary instrument used. For measurements of the infrared reflectance, a Perkin Elmer 983 was used (this was primarily for the emittance determination). The regular environmental exposures for humidity and other durability tests were performed in the OCLI testing laboratory to the military specifications pertinent to the individual tests.

⁵ The red reflector is of the order of 5 to 6 times as thick as the UVR.

Table 1 Qualification Test Matrix for the BRR/g-0213 (GaAs BRR) and the BRR/s-0213 (Silicon BRR) Qualification Series.

REQUIREMENT	Test Group								
	A	B	C	D	E	F	G	H	I
QTY	5+5	5+5	5+5	5+5	5+5	5+5	5+5	4+4	
SIZES	2 cm x 4 cm	2 cm x 4 cm	2 cm x 4 cm	2 cm x 4 cm	2 cm x 4 cm	2 cm x 4 cm	2 cm x 4 cm	2 cm x 4 cm	tested by others
Surface Quality; Workmanship; 80-50 requirement	X	X	X	X	X	X	X	X	X
Coating Orientation	X	X	X	X	X	X	X	X	X
Normal Emittance (1- R 5 to 50 microns)								X	X
Cuton/Cutoff Wavelength	X	X	X	X	X		X	X	X
Ultraviolet Relection- $\geq 85\%$ @ 300 nm +/- 20 nm	X	X	X	X	X		X	X	X
Transmittance	X	X	X	X	X		X	X	X
Humidity A-72 hours @120°F; $\geq 95\%$ R.H.	X								
Humidity B-10 days per MIL-STD-810B		X							
Thermal Shock-LN2 1 hr. & 350°F 1 hr.			X						
Temperature Cycle-1000 cycles; -180°C to +195°C				X					
Salt Fog-48 hours					X				
Ultraviolet Exposure-300 sun days								X	
Radiation Resistance-20 to 30 KeV protons									X
Radiation Resistance-500 KeV protons								X	
Radiation Resistance-1 MeV electrons								X	
Abrasion Resistance-20 rub	X		X		X				
Adhesion-Slow tape	X					X			
15' Bolt/Slow tape							X		
Transmittance & Cuton	X	X	X	X	X		X	X	X

The radiation and UV exposures were done at the *Boeing Company Physical Sciences Laboratories* using their X-200 Solar Simulator (at Organization 9-5574, Boeing, Renton, WA) and the Dynamitron Accelerator at the *Physical Sciences Research Center* (Seattle, WA.). The 1200 total hours UV exposure started on November 1, 1993 and finished on December 23, 1993. The UV exposure was done at about 6x the solar intensity (Air Mass Zero (AM0) Solar Spectrum) for a resultant 300 sun days equivalent exposure. This was followed by the exposure at the Dynamitron to 0.5 MeV protons to $> 5 \times 10^{14}/\text{cm}^2$ and then to 1 MeV electrons to $> 10^{15}/\text{cm}^2$.

Radiation exposure at low energies (20 KeV to 30 KeV) for protons was done by the *Astro Space Division of the Martin Marietta Co.* and the *Space and Communications Division of the Hughes Aircraft Co.*

During exposure the radiation test samples were kept at or near room temperature by actively cooling the mounting plates with flowing water.

Measurement Error Analysis

Repetitive measurements of known wavelength and photometric standards have established the following measurement errors for transmission:

	Accuracy	Repeatability
Wavelength:	$\pm 0.5 \text{ nm}$	$\pm 0.1 \text{ nm}$
Photometric:	0.05%	0.02%

QUALIFICATION TEST RESULTS FOR THE BRR/GaAs COVERS

All parts were measured for transmittance, UV reflectance, and NIR reflectance before test and met the OCLI Product Specification No. 6067001-08.

Before and after measurements of transmittance were done for all test groups except group F. Group F only involved observations of the surface quality and coating orientation for the samples. Measurements of reflectance are included in the data after testing for completeness, but no data was taken for this group before.

Only the samples in test group H were measured before and after the test for emittance as well as for the transmittance values. The values for the emittance of the covers were calculated as one minus the reflectance in the range 5 μm to 50 μm .

Summaries of the before measurements of transmittance for the BRR/g-0213 test samples are shown in Table 2. The values of the arithmetic average transmission for various wavelength ranges are shown in the table. Data is presented for each of the test groups (however, the thermal cycle tests - Group D - have not been completed as of this writing).

The after exposure transmittance measurements for each of the test groups is shown in Table 3. In this data set the values for the transmittance of the group F samples are also included, as measured after test, for reference. The changes in transmittance, absorbance, reflectance and emittance for the test sample sets in each group are given in Table 4.

The surface quality of all test parts in the test groups was \leq 80-50 per MIL-O-13830A.

The normal spectral emittance for the BRR/g covers was found to be unaffected, well within the accuracy of determination of the emittance, by the combined effects testing. Nominal values for the normal spectral emittance as determined by these measurements, were in the range of 86% to 87%. The average transmittances in the 400 nm to 900 nm wavelength band were also unaffected by the normal environmental exposures.

The 50% cut-on wavelengths (transmission) of all BRR/GaAs coatings were $359.5 \text{ nm} \pm 1.7 \text{ nm}$ at the UV position and $972 \text{ nm} \pm 7 \text{ nm}$ at the near infrared position. All measured BRR/g-0213 parts had less than 1% average transmission between 200 nm and 320 nm before and after testing.

The BRR/g-0213 parts in test group H were subjected to combined UV exposure for 300 AM0 UV sun days equivalent (at 6x sun intensity), followed by proton irradiation (0.50 MeV) to $5 \times 10^{14}/\text{cm}^2$, in a vacuum of 1×10^{-6} torr and then electron irradiation (1.0 MeV) to $1.0 \times 10^{15}/\text{cm}^2$. The average transmission from 400 nm to 900 nm was lowered an average of 1.12%. This change is a little higher than was expected. However, it is near the change limit specified for other cover products such as the UVR only. The specification limit for change in solar transmittance is usually set at less than 1%. The change in the cut-on edge at the UV was about 5.6 nm on average and at the NIR edge was 0.69 nm on average.

Summary of Qualification for the BRR/GaAs

For all qualification test groups discussed above, transmission changes due to the testing were less than 1%, except for the samples irradiated in test group H. The change in transmission for the samples in test group H was about 1.12% on average.

QUALIFICATION TEST RESULTS FOR THE BRR/SILICON COVERS

The matrix of qualification test groups for the BRR/silicon (BRR/s-0213) covers is identical to the matrix for the BRR/g-0213 covers shown in Table 1. All parts were measured for transmittance, UV reflectance, and NIR reflectance before test and met the OCLI Product Specification No. 6067001-09. As with the other test sets, the before and after measurements of transmittance were done for all test groups except group F. Group F only included observations of the surface quality and coating orientation for the samples. Measurements of reflectance are included in the data after testing for completeness, but no data was taken for this group before.

Table 2 Transmittance & Emittance for the BRR/g-0213 Samples Before Testing.
(Summary - Set 1* Run Numbers 466-1686/1688)

Test Group		50% Trans Lower	Cuton Upper	Peak 200-230	at	Avg 400-900	Avg 600-800	Emitt
A	Average	359.86	960.96	0.61	200.60	96.42	97.62	
	Std Dev	1.25	5.91	0.05	0.55	0.21	0.05	
B	Average	360.02	949.34	0.57	201.00	96.36	97.70	
	Std Dev	1.66	5.43	0.01	0.00	0.04	0.04	
C	Average	357.96	975.82	0.60	200.60	96.53	97.69	
	Std Dev	0.64	15.02	0.06	0.55	0.10	0.12	
D	Average	358.60	975.66	0.52	200.20	96.41	97.68	
	Std Dev	0.31	12.59	0.02	0.45	0.47	0.10	
E	Average	359.24	989.92	0.54	200.00	96.52	97.83	
	Std Dev	1.67	4.67	0.05	0.00	0.03	0.05	
F	Average		No Data	Taken				
	Std Dev							
G	Average	358.38	958.58	0.54	200.00	96.65	97.68	
	Std Dev	0.96	7.17	0.05	0.00	0.11	0.03	
H	Average	359.25	961.33	0.58	200.00	95.47	96.68	86.57
	Std Dev	0.52	3.26	0.02	0.00	0.28	0.24	0.27

Table 3 Transmittance & Emittance for the BRR/g-0213 Samples After Testing.
(Summary - Set 1* Run Numbers 466-1686/1688)

Test Group		50% Trans Lower	Cuton Upper	Peak 200-230	at	Avg 400-900	Avg 600-800	Emitt
A	Average	360.16	960.28	0.13	320.00	96.28	97.57	
	Std Dev	1.32	5.87	0.03	0.00	0.03	0.03	
B	Average	361.60	948.88	0.09	320.00	96.31	97.69	
	Std Dev	2.47	5.90	0.02	0.00	0.06	0.03	
C	Average	358.02	976.14	0.14	320.00	96.46	97.67	
	Std Dev	0.46	15.65	0.02	0.00	0.10	0.11	
D	Average	TBD	TBD	TBD	TBD	TBD	TBD	
	Std Dev							
E	Average	359.44	990.32	0.12	320.00	96.28	97.59	
	Std Dev	1.58	4.38	0.00	0.00	0.23	0.25	
F	Average	359.50	971.08	0.47	320.00	96.37	97.62	
	Std Dev	0.31	1.20	0.01	0.00	0.23	0.19	
G	Average	358.48	958.40	0.15	320.00	96.49	97.57	
	Std Dev	0.97	7.76	0.00	0.00	0.10	0.03	
H	Average	364.48	962.00	0.25	320.00	94.27	96.39	86.25
	Std Dev	0.45	.030	0.00	0.00	0.12	0.03	0.19

* Set 1 of two sets. Second set not displayed to save space. Data and conclusions are the same for Set 1 and Set 2. For an explanation of the TBD's in group D see the text.

Table 4 Changes in Transmittance and Emittance for the BRR/g-0213 Samples

Set 1* Run Numbers 466-1686/1688							
Test Group		50% Trans Lower	Cuton Upper	Peak 200-320	Avg 400-900	Avg 600-800	Emitt
A	Average	-0.30	0.68	0.49	0.14	0.05	
B	Average	-1.58	0.46	0.48	0.06	0.01	
C	Average	-0.06	-0.32	0.46	0.06	0.02	
D	Average	TBD	TBD	TBD	TBD	TBD	
E	Average	-0.20	-0.40	0.42	0.24	0.24	
G	Average	-0.10	0.18	0.39	0.16	0.10	
H	Average	-5.23	-0.67	0.33	1.21	0.29	0.32

A negative number signifies an increase in value

Space Environmental Tests

The BRR/s-0213 test group H was also the sample set sent to Boeing for particle irradiation. This test group was measured before and after test for emittance as well as for the transmittance values. The values for the emittance for the covers are calculated as one minus the reflectance in the range 5 μ m to 50 μ m.

Summaries of the before measurements of transmittance for the BRR/s-0213 test samples are shown in Table 5. The arithmetic average transmission for various wavelength ranges are shown in the table. (as mentioned before, the thermal cycle tests - Group D - have not been completed as of this writing).

The values for the reflectance of the covers in the UV and the position of the maximum value are also given. Data is presented for each of the test groups (the test group I has not been completed as of this writing.) Values for the emittance of the covers calculated as one minus the reflectance in the range 5 μ m to 50 μ m, are also shown for each cover in the H test group, as measured before testing.

The after exposure transmittance measurements for each of the BRR/s-0213 test groups are shown in Table 6. Again the values are the average or minimum transmittances in the selected wavelength ranges. In this data set, the values for the transmittance of the group F samples are also included, as measured after test, for reference. The change in transmittance, absorbance, reflectance and emittance for the test sample sets in each group are given in Table 7.

The surface quality of all BRR/s-0213 test parts in the test groups is \leq 80-50 per MIL-Q-13830A.

All parts were measured for transmittance before test and met the OCLI Product Specification No. 6067001-09.

The normal spectral emittance for the BRR/s-0213 covers was found to be unaffected, well within the accuracy of determination of the emittance value, by the combined effects testing. Nominal values for the normal spectral emittance as determined by these measurements was in the range of 86% to 87%. The average transmittances in the 450 nm to 1100 nm wavelength band were also unaffected by the normal environmental exposures.

The 50% cut-on wavelengths (transmission) of all BRR/Silicon coatings were 359.5 (\pm 15) nm at the UV position and 1160 (\pm 10) nm at the near infrared position. BRR/s-0213 test covers were placed into a test chamber at a controlled temperature for 72 hours at a temperature of 49°C \pm 2.5°C and > 95%

* Set 1 of two sets. Second set not displayed to save space. Data and conclusions are the same for Set 1 and Set 2.

relative humidity per MIL-C-675A (test group A). After humidity all parts were tested for 20 rub eraser abrasion resistance per MIL-C-675A and slow tape adhesion per MIL-M-13508B. No physical degradation was observed on any part and the change in transmission for the wavelengths 450 nm to 1100 nm was less than 0.57% on average. The change in the 50% transmittance cut-on edge was less than about 0.4 nm to 1.2 nm on average at the UV position.

The BRR/s-0213 parts in test group H were subjected to combined UV exposure to 300 AM0 UV sun days equivalent at 6x sun intensity, followed by 0.5 MeV proton irradiation to $5 \times 10^{14}/\text{cm}^2$ in a vacuum of 10^{-6} torr and then 1.0 MeV electron irradiation to $10^{15}/\text{cm}^2$. The average transmission from 450 nm to 1100 nm was lowered an average of 0.36%. The change in the cut-on edge at the UV was about 3.4 nm on average and at the NIR edge was about 5 nm on average.

It is interesting to note that the design of the BRR/silicon coating is the same as the design for the BRR/GaAs design, with the exception of the increase in the red reflector coating thickness to shift the reflectance band out beyond 1.1 μm . This represents a thickening of all of the layers in the design by about 15%. If the changes shown are compared between the two designs, however, it is not clear why the GaAs version should have changed so much while the silicon version changed so little.

Summary of Qualification for the BRR/Silicon

For all qualification test groups in the silicon BRR evaluations, the change in transmission was less than 1%. This is within the specification for the BRR covers and the BRR/s-0213 covers can therefore be qualified for space applications.

QUALIFICATIONS BY SIMILARITY

Based on the results of this testing and flight experience with other cover/coating combinations, it is possible to qualify other specific products by similarity. These include the blue-red reflecting solar cell covers using fused silica as the substrate and an AR-red reflector cover.

Other Versions of The Red Reflecting Solar Cell Cover

Among the alternate product forms for red reflecting solar cell covers are products that substitute other substrate materials such as fused silica, and product forms that substitute an antireflective coating on the front surface for the UVR.

As noted in the Introduction, the version of the design that substitutes fused silica for the substrate is designated by appending an FS to the product code in place of the 0213. The difference between the BRR/g-FS and the BRR/g-0213 and between the BRR/s-FS and the BRR/s-0213 solar cell covers is the substrate material and the addition to a small amount of UV absorbing material in the front coating (the UV reflector). The 0213 glass, qualified in the testing described in OCLI report no. APD 89011, changes very little when exposed to the particle irradiation, the other tests described in that report, and in this series of tests. However, fused silica is even more stable in these same tests. Therefore, the use of fused silica as the substrate would result in an even more stable cover product.

The coating design and material used for the front surface coating on the BRR/x-FS product is also a space qualified product that has flown for many years. This coating on fused silica is the blue reflector used in the AR/BR design that was the staple of the solar cell cover market for the years prior to the introduction of the CeO_2 stabilized glasses such as Corning 0213.

The reflectance and transmittance for these product forms are nearly identical to the glass based products. The solar absorbance for the fused silica based BRR products is a little less than that for the glass based product.

Table 5

Transmittance and Emittance for the BRR/s-0213 Samples Before Testing.

Set 1* Run Numbers 466-1685/1688							
Test Group		50% Trans Lower	Cuton Upper	Peak 200-230	at	Avg 450-1100	Emitt
A	Average	363.36	(ND)	0.71	200.60	96.49	
	Std Dev	0.38		0.05	0.55	0.07	
B	Average	364.68	(ND)	0.73	200.40	96.57	
	Std Dev	1.11		0.05	0.55	0.08	
C	Average	363.02	(ND)	0.66	200.80	96.55	
	Std Dev	2.88		0.02	0.45	0.06	
D	Average	362.54	(ND)	0.70	201.00	96.64	
	Std Dev	1.85		0.04	0.00	0.14	
E	Average	366.72	(ND)	0.72	200.60	96.72	
	Std Dev	2.43		0.05	0.55	0.08	
F	Average	No Data		Taken	(ND)		
	Std Dev						
G	Average	365.84	(ND)	0.68	200.60	96.68	
	Std Dev	2.76		0.05	0.55	0.12	
H	Average	364.40	(ND)	0.59	200.00	95.84	86.28
	Std Dev	1.44		0.01	0.00	0.15	0.06

Table 6

Transmittance and Emittance for the BRR/s-0213 Samples After Testing.

Set 1* Run Numbers 466-1685/1688							
Test Group		50% Trans Lower	Cuton Upper	Peak 200-230	at	Avg 450-1100	Emitt
A	Average	363.78	1209.02	0.15	320.00	96.12	
	Std Dev	0.40	4.79	0.03	0.00	0.19	
B	Average	365.28	1212.28	0.10	320.00	96.35	
	Std Dev	1.03	10.79	0.02	0.00	0.43	
C	Average	363.10	1214.48	0.12	320.00	96.43	
	Std Dev	3.03	13.45	0.03	0.00	0.11	
D	Average	TBD	TBD	TBD	TBD	TBD	
	Std Dev						
E	Average	366.74	1202.72	0.12	320.00	96.67	
	Std Dev	2.46	1.32	0.04	0.00	0.09	
F	Average	364.40	1227.92	0.36	320.00	96.67	
	Std Dev	2.60	7.62	0.06	0.00	0.24	
G	Average	366.34	1228.08	0.10	320.00	96.59	
	Std Dev	3.08	10.32	0.03	0.00	0.15	
H	Average	368.45	1182.05	0.30	320.00	95.99	86.29
	Std Dev	2.47	1.16	0.01	0.00	0.11	0.50

* Set 1 of two sets. Second set not displayed to save space. Data and conclusions are the same for Set 1 and Set 2. For an explanation of the TBD's in group D see the text.

Table 7 Changes In Transmittance and Emittance for the BRR/s-0213 Samples

Set 1* Run Numbers 466-1685/1690							
Test Group		50% Trans Lower	Cuton Upper	Peak 200-320	Avg 450-1100	Avg 400-450	Emitt
A	Average	-0.42	(ND)	0.56	0.36	0.12	
B	Average	-0.60	(ND)	0.63	0.22	-0.30	
C	Average	-0.08	(ND)	0.55	0.11	-0.15	
D	Average	TBD	(ND)	TBD	TBD	TBD	
E	Average	-0.02	(ND)	0.60	0.05	0.27	
G	Average	-0.50	(ND)	0.58	0.09	-0.40	
H	Average	-4.05	(ND)	0.29	-0.15	5.45	-0.01

A negative number signifies an increase in value. ND indicates no data due to no before measurements of the cut on edge. For an explanation of the TBD's in group D see the text.

The second alternate product form with an AR on the front has the designation AR-RR/g-0213 when the coatings are on the Corning 0213 microsheet glass. This product differs from the BRR/g-0213 product because the front coating is the conventional single layer magnesium fluoride antireflection coating that has flown in space for many years. In the same manner, the difference between the AR-RR/s-0213 product and the BRR/s-0213 cover is the same single layer antireflection coating design.

It may be possible, because of the flight history for parts of these designs and the results of the testing discussed here, to consider these alternate product forms qualified by similarity. Due to the high cost associated with such testing and the time required for a test program, it is hoped that the similarity of the products to the BRR/g-0213 and BRR/s-0213 will be sufficient for qualification. However, if there is sufficient justification for the specific testing of any of these alternate product forms, OCLI will entertain the suggestion that a test series be conducted for the AR-RR.

CONCLUSION

Based on the testing discussed here, the blue-red reflecting solar cell covers can be considered qualified for space use.

* Set 1 of two sets. Second set not displayed to save space. Data and conclusions are the same for Set 1 and Set 2.

UV TESTING OF INTELSAT-VII, VIIA, AND VIII SOLAR CELLS¹

A. Meulenberg
COMSAT Laboratories
Clarksburg, Maryland

Extended Abstract

A 4000 hour experiment, conducted in late 1992 through mid 1993, confirmed earlier results on the ultraviolet damage effects in covered solar cells of various types being used, or proposed for use, in INTELSAT programs. Two different UV test systems were used to identify systematic errors and to study the effects of UV source-bulb age on degradation rate.

After correction for contamination and UV source-bulb aging, the extrapolated degradation rates for irradiated and unirradiated INTELSAT-5, -6 single AR (SAR) coated cells and INTELSAT-7, -7A, -8 double layer AR (DAR) coated cells² in both the 1993 tests confirm the following hypotheses resulting from the 1992 experiment.

- a. Irradiated cells display significantly more UV degradation than do the unirradiated cells for tests exceeding 2000 hours. [The new data indicates that degradation effects from electron irradiation are proportional to t^2 (the square of the UV hours), at least for times ≤ 3000 hours.]
- b. This difference does not depend upon antireflective coating, cell resistivity, or manufacturer within the sensitivity and reproducibility of the experiment.
- c. There is a clear difference in degradation rate between single AR coated cells (TiO_x) and double layer AR coated cells (SiO_x and Al_2O_3 ?). At 100,000 hours (11.4 years) the DAR coated cells display more degradation than do the SAR coated cells, even though at 1,000 hours the DAR cells display less degradation.
- d. UV degradation rates, to modern covered silicon solar cells, at the beginning of bulb life drop from ~ 2 times the average rate to near zero after 2000 hours (average end-of-life for the xenon short-arc lamps used in the tests).

The effects of 1 MeV electron irradiation ($10^{15} \text{ e}^-/\text{cm}^2$) prior to UV exposure are clearly indicated in the plot of percent change in cell open circuit voltage (V_{oc}) versus percent change in short circuit current (I_{sc}) during the UV test and post-test cleanup of the cells (Figure 1). The heavy lines indicate the trends of the data for both unirradiated and pre-irradiated cells (different cell types and resistivity show the same trend). The slopes of

¹ This work was supported by the International Telecommunications Satellite Organization (INTELSAT) and by COMSAT Corporation.

² The tested INTELSAT-5, -6, and -7 cells are German and the INTELSAT-7A and -8 cells are Japanese.

the trend lines differ between the unirradiated and irradiated cells during UV exposure but not during the post-test removal of contamination. Clearly, extended UV testing produces a permanent photo-induced redegradation of previously irradiated cells. However, this photo-induced redegradation may be caused by the long-wavelength light, not the UV light.

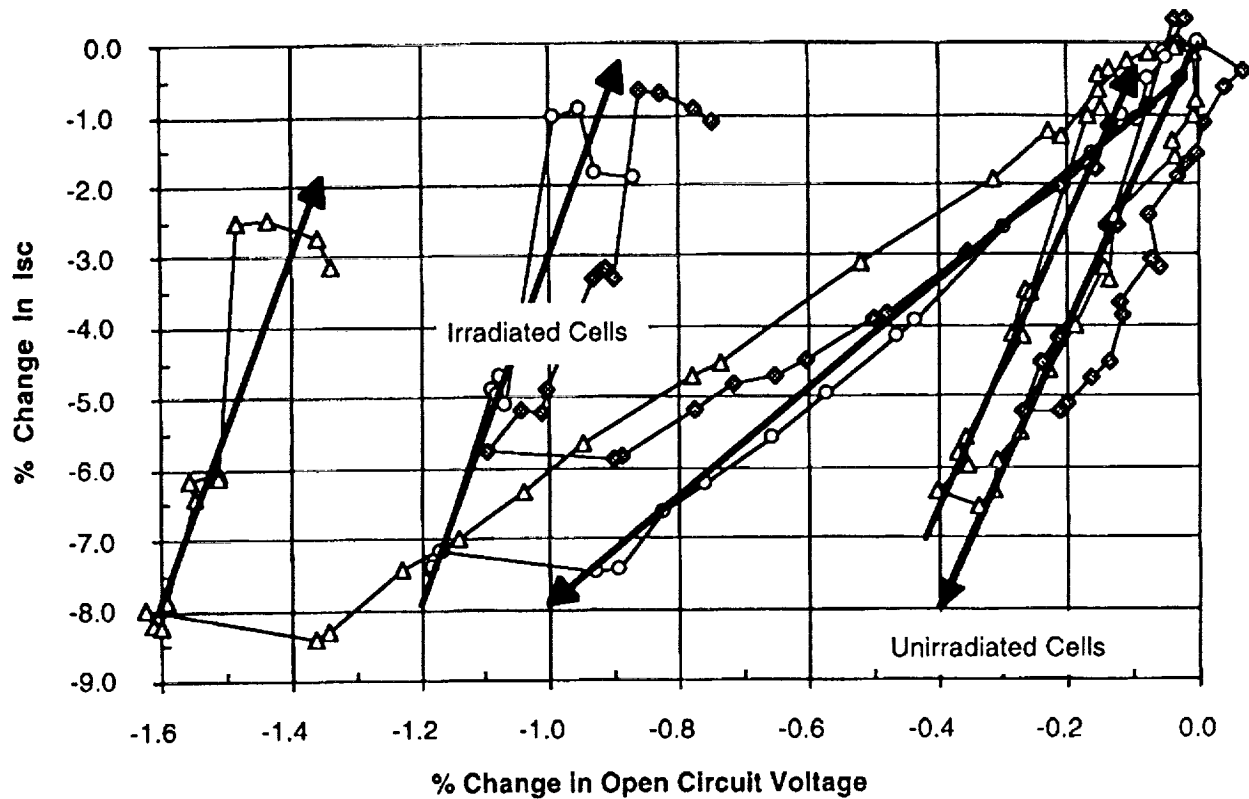


Figure 1. The % change in cell open circuit voltage versus % change in Isc during the UV test and post-test cleanup of unirradiated and irradiated (labeled), 2- and 10- ohm-cm (clear and filled symbols respectively) solar cells.

Figure 2 is representative of the reduced data obtained in the two 1993 tests reported here. The corrections to the data include: normalization against control cells, to adjust for any long-term intensity or spectral drift of the solar simulator; modification of the time base, to adjust for changes in the damaging portion of the UV test source spectrum; and, subtraction of the contamination that accumulated on both the quartz window and coverslides during the extended test.

A comparison of the results for SAR and DAR coated cells from the one 1992 and the average of two 1993 Tests (in the table) indicates their level of agreement and the spread in data and extrapolations of the tests. The very high degradation seen in the extrapolated result for irradiated DAR coated cells is partially an artifact of the assumption that photo redegradation of preirradiated cells does not saturate.

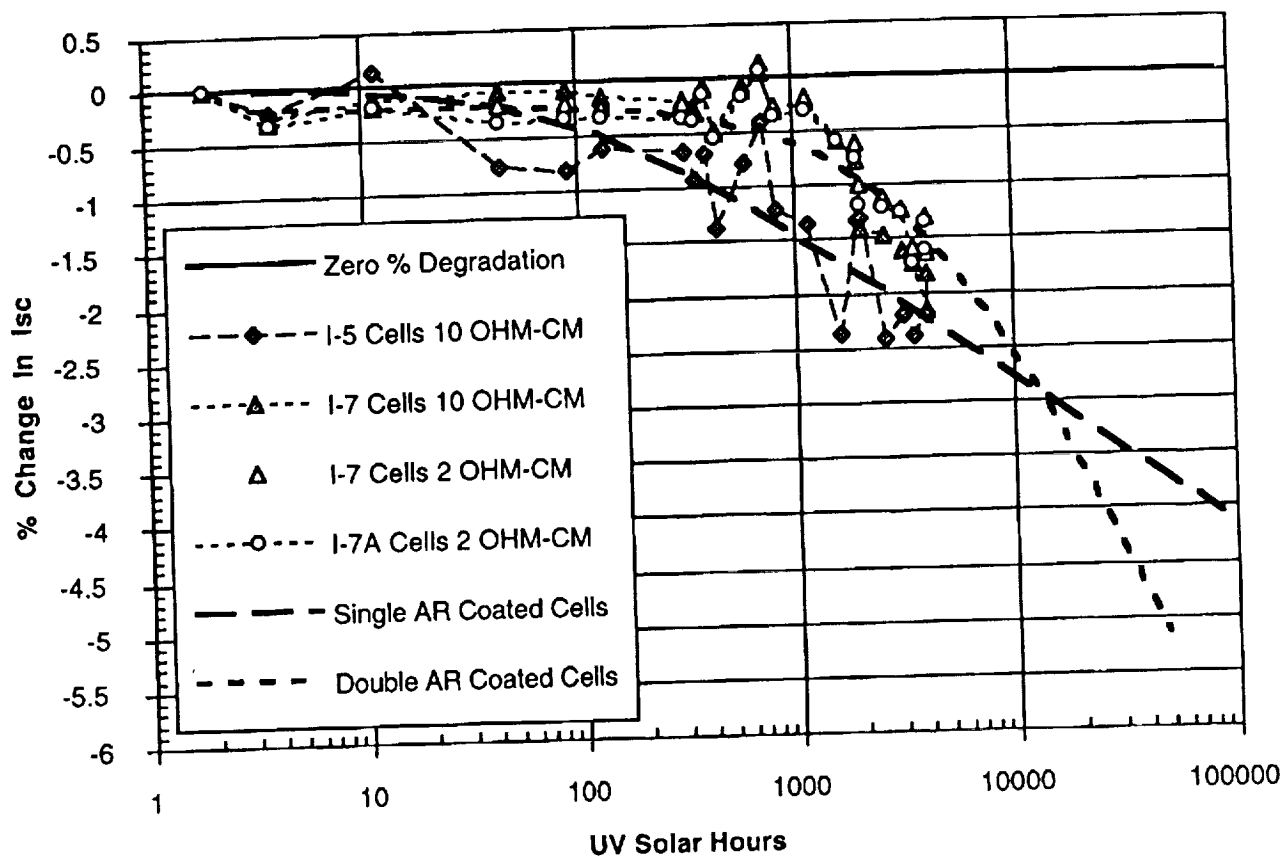


Figure 2. Corrected UV degradation, data and extrapolations, for the unirradiated cells of Test 1 in the 1993 experiment.

Comparison of 1992 and 1993 Test Results for SAR and DAR Coated Cells

Cell Configuration	% ΔI_{sc} at 1000 hours	% ΔI_{sc} at 10,000 hours	% ΔI_{sc} at 100,000 hours
UNIRRADIATED	1992 / 1993	1992 / 1993	1992 / 1993
SAR	-1.7 / -1.6 \pm 0.5	-3.8 / -2.5 \pm 1	-5.9 / -3.3 \pm 1.5
DAR	-0.5 / -1.5 \pm 0.5	-2.5 / -3.5 \pm 1	-6 / -6 \pm 2
IRRADIATED			
SAR	NA / -2.2 \pm 0.5	NA / -4 \pm 1	NA / -5.7 \pm 1.5
DAR	-0.8 / -1.5 \pm 0.5	-5 / -5.2 \pm 1	-14 / -10 \pm 2

Eleven years exposure to the space UV environment should degrade unirradiated I-5,6 cells by $4.5 \pm 1.5\%$ and I-7,8 cells by $6 \pm 2\%$. At 4000 hours, 10 and 2 ohm-cm, preirradiated cells display ~ 1.8 and $\sim 2.4\%$ greater loss than do the corresponding unirradiated cells. Therefore, degradation of the preirradiated cells at 100,000 hours should be $\geq 6.5 \pm 2\%$ for I-5,-6 cells and $\geq 8 \pm 2\%$ for I-7,-8 cells. It is not yet determined which set of laboratory data corresponds to space experience in a radiation environment.

PARASITIC CURRENT COLLECTION BY SOLAR ARRAYS IN LEO¹

Victoria A. Davis and Barbara M. Gardner
S-Cubed Division of Maxwell Laboratories
San Diego, California

SUMMARY

Solar cells at potentials positive with respect to a surrounding plasma collect electrons. Current is collected by the exposed high voltage surfaces: the interconnects and the sides of the solar cells. This current is a drain on the array power that can be significant for high-voltage arrays. In addition, this current influences the current balance that determines the floating potential of the spacecraft. One of the objectives of the Air Force (PL/GPS) PASP Plus experiment is an improved understanding of parasitic current collection. As part of the PASP Plus program, we are using computer modeling to improve our understanding of the physical processes that control parasitic current collection.

BACKGROUND

Solar arrays provide power for nearly all space systems. Traditionally, solar arrays have operated in the 30 V range to avoid complex interactions with the plasma environment. As space systems become more complex, more power, therefore higher voltages, is needed.

Typically, the negative side of each solar array is grounded to the spacecraft chassis. This makes the exposed metal and semiconductor of the arrays positive with respect to the spacecraft body. The equilibrium potential of a spacecraft with respect to the plasma is the potential at which there is no net current to the spacecraft. As illustrated in figure 1, there are several components of the current to a spacecraft. Portions of the solar array attract ions and other portions attract electrons, depending on the local potential. Ions are attracted to exposed conductors on the spacecraft surface, as the spacecraft body is negative with respect to the plasma. Particle beams and other emitters also contribute to the net current. Since electrons are more mobile than ions, spacecraft float negative unless the potential is actively controlled.

It may be necessary to keep the spacecraft body near zero potential with respect to the plasma. For example, an instrument to measure the low energy plasma environment may need to be near plasma ground. Anodization arcing and negative potential arcing are potentially disruptive at potentials greater than 50 to 100 V negative with respect to the plasma (refs. 1 and 2). Particle beams and plasma contactors are sometimes used to maintain the spacecraft potential. If the solar arrays are at 150 V and the spacecraft chassis is maintained at no more than 50 V negative with respect to the plasma, the most positive portions of the solar arrays are at 100 V, with respect to the plasma. Therefore, it is important to consider current collection by the portions of solar arrays at positive potentials.

A traditional solar array is an array of solar cells 2 to 8 cm in size and connected in series by millimeter-sized metal interconnects. The interconnects can be metallic meshes or sets of wires. Each solar cell is protected from the environment by a cover glass. Figure 2 shows the regions between cells in a typical array. Current is collected by the portions of the metallic interconnects and the semi-conducting solar cells exposed to the plasma environment.

¹ This work is supported by the Air Force Materiel Command.

At low potentials, a barrier forms that prevents electrons from reaching the high voltage surfaces. The barrier is created by the surrounding insulating surfaces, primarily the coverglass, that float slightly negative. The current collected is the high energy tail of the distribution and therefore depends exponentially on the barrier height. The barrier height depends on the potential, the plasma, and the geometry.

At high potentials, typically over 200 V, the current rapidly rises due to a phenomena called snapover. Snapover was first observed at NASA/LeRC (refs. 3, 4, and 5). Snapover can occur whenever there is a biased surface adjoining an insulating surface and the bias is above the first crossover of the secondary yield curve of the insulating surface (refs. 6 and 7).

When the solar cell potential is below the first crossover of the secondary yield curve, the insulating surface floats slightly negative (a few times the electron energy) and collects as many ions as electrons from the ambient plasma. If the potential of the insulating surface is above the first crossover, each electron generates more than one electron. The secondary electrons may either return to the surface or move across the surface under the influence of surface electric fields. The equilibrium potential at each location is the potential at which the net current of electrons from the plasma and secondary electrons arriving at and leaving the location balance. The exposed conductor is a sink for the secondary electrons. The surfaces adjust so that a potential gradient exists across the insulating surface attracting the secondaries to the conductor at the highest potential. The net effect is that the high potential area and the collecting area increase. There is a range of applied bias values for which the insulating surface may either float slightly negative or be snapped over. Experimentally, hysteresis is observed. The size of the snapped over region, and therefore the current, depends on the local geometry as well as the potentials and the plasma.

The Photovoltaic Array Space Power Plus Diagnostics (PASP Plus) flight experiment will explore high voltage current collection by solar arrays (ref. 8). PASP Plus is the principal experiment integrated onto the Advanced Photovoltaic and Electronics Experiments (APEX) satellite bus. APEX will be launched this summer into a 70° elliptical orbit from 360 to 1950 km. The spacecraft attitude is such that the solar array test panels will always face the sun. The experiment will test twelve different solar array designs. The experiment will investigate negative potential arcing, parasitic current collection, and long term radiation damage. Parasitic current collection will be measured for eight of the designs under various operational and environment conditions. The arrays will be biased from 75 to 400 V. Previous space experiments that examined parasitic current collection include PIX I (ref. 9), PIX II (refs. 10 and 11) and SAMPIE (ref. 12).

OUR APPROACH

The computation of the current collected by a specific solar array can become intractable. The gap size is of the order of tens of mils while the solar cells are a few centimeters and the entire array can be meters. Each solar cell is at a slightly different potential. The current depends on the geometry of the gap, the geometry of the entire array, the spacecraft, and the plasma conditions.

We are interested in improving our understanding of which aspects of the problem are most important and developing a tool or at least an algorithm to assist spacecraft designers. Our approach is to look in detail at current collection at a single cell gap. Using the computer we can vary each parameter independently. We then develop formulas that estimate the current collected by a single gap. We then incorporate the formulas into a tool that can add up the current from all the gaps to give the current collected by an array. Information on the array geometry and how it influences the current can also be added to the tool.

To compute the current to a single gap, we are using the Gilbert computer code. Gilbert is a general-purpose, two-dimensional, plasma analysis code. It can be used to solve for the electrostatic potential about an object, with flexible boundary conditions on the object and with space charge computed either

fully by particles, fully analytically, or in a hybrid manner. For this study Gilbert is used to first compute the electrostatic potentials in space around the solar cells and then to compute the electron trajectories in the previously computed potentials. The space charge was computed using an analytic formulation. The analytic formula includes charge density variation due to acceleration and convergence (ref. 13).

Figure 5 shows a typical grid for the Gilbert calculations. The gap and the space above the gap are gridded. The surfaces provide the boundary conditions. This grid represents solar cells with mesh interconnects. An idealized geometry was chosen because we are interested in understanding the relationship between the variables. The interconnect is modeled as a diagonal line extending across the bottom of the gap. The side of one solar cell is at a high potential along the left side of the gap. The sides of the coverglass on both sides of the gap are included. All the insulating surfaces have a special boundary condition that represents the snapover condition when appropriate.

Figure 6 shows potential contours and a few trajectories for a typical case. The potentials are computed using an analytic representation of the charge density. Macroparticles are emitted from several locations along each sheath segment. At each location, a set of particles with a thermal distribution of velocities is created. These macroparticles are tracked. The collected current is the current carried by the macroparticles reaching the high potential surfaces.

Current collection can be either orbit limited or space charge limited, depending on the debye length of the plasma and the size of the collecting area.

There are two serious limitations to computing the current in this way. Implicit in the technique of drawing a sheath edge and tracking current from this sheath edge is the assumption of a sharp sheath edge. This assumption is not necessarily valid when the sheath size is of the order of a debye length. The computed sheath sizes are smaller than a debye length for some geometries under some plasma conditions, particularly for geometries without an interconnect and at low potentials.

The other limitation is the assumption that current can reach the sheath. At lower cell potentials, the coverglass surface potential dominates the long distance potential. To reach the "sheath edge," an electron must pass through a negative potential region. Only the electrons in the high energy tail of the distribution are collected. A different technique is needed to compute the current in this regime.

A different approach is also needed at the highest potentials. When the entire surface of the array is snapped over, the sheath is dominated by three-dimensional effects.

RESULTS

We have done calculations for three geometries: cell-to-cell gap region with an interconnect, without an interconnect, and a single cell edge. The calculations span the space of anticipated plasma conditions, applied potential, and first crossover potential. The current rises rapidly when the applied bias is four to five times the first crossover potential. Figure 7 shows how the current varies as a function of the applied bias for a single solar cell edge.

We now have analytic formulas for the dependence of the current on the primary problem variables: applied voltage, plasma conditions, and, to some extent geometry. These formulas have been incorporated into the EPSAT computer code.

EPSAT is an analysis tool for determining the performance of power systems in both naturally occurring and self-induced environments (ref. 14). EPSAT is an engineering spreadsheet that allows rapid "what if" analysis of the effect of parametric changes on a space-based system's performance. EPSAT provides information on the plasma and neutral environment anticipated on orbit. The code presently models many of the interactions of the space environment with a power system, including sheath

formation, $v \times B$ potentials, particle beams, and sheath ionization. The code permits the user to do mission studies and evaluate the importance of the various interactions with a specific spacecraft design. The user can then adjust the design and examine the effect of the change on the ability of the system to operate in natural or hostile environments. EPSAT uses a unique architecture for integrating analysis models that allows modeling capabilities to evolve with changing needs.

A new solar array module for EPSAT has been developed. The current to a solar array is computed by summing the current to each solar cell edge, interconnect, and gap without interconnect, while not double counting. The current to a single edge or gap is computed using a fit to the two-dimensional computations.

Figure 8 shows the current to PASP Plus array #1, mesh interconnect design, under typical space conditions for different values of the first crossover potential. Figure 9 shows the current to PASP Plus array #3, space station design, under typical space conditions for different values of the first crossover potential.

Figure 10 shows how the current computed in this manner compares with laboratory measurements made on the PASP Plus array #8. Array 8 has a wrap-thru interconnect design.

CONCLUSIONS

We are refining our two-dimensional calculations and examining their limitations. As needed, we will use other techniques to extend the range of our calculations. The results are continuing to be incorporated into EPSAT. We look forward to comparing the flight measurements with the calculations. Once our understanding is validated, the formulas developed can be used to improve the design of solar cells to minimize complications due to this interaction.

REFERENCES

1. Vaughn, J.A., et al.: Extrapolation of Electrical Breakdown Currents from the Laboratory to Space Station. AIAA 92-0822, AIAA 30th Aerospace Sciences Meeting, Reno, Nevada, 1992.
2. Ferguson, D.C.: The Voltage Threshold for Arcing for Solar Cells in LEO - Flight and Ground Test Results. NASA TM 87259, 1986.
3. Purvis, C.K.; Stevens, N.J.; and Berkopce, F.D.: Interaction of Large High Power Systems with Operational Orbit Charged-Particle Environments. NASA TM X-73867, 1977.
4. Stevens, J.N.: Interactions Between Spacecraft and the Charged-Particle Environment. Spacecraft Charging Technology - 1978, NASA Conference Publication 2071, AFGL-TR-79-0082, 1978, pp. 268-294.
5. Kennerud, K.L.: High Voltage Solar Array Experiments, NASA Rep. CR-121280, 1974.
6. Chaky, R.C.; Nonnast, J.H.; and Enoch J.: Numerical Simulation of Sheath Structure and Current-Voltage Characteristics of a Conductor-dielectric Disk in a Plasma. J. Appl. Phys., vol. 52, 1981, pp. 7092-7098.
7. Katz, I.; and Mandell, M.J.: Differential Charging of High-Voltage Spacecraft: The Equilibrium Potential of Insulated Surfaces. J. Geophys. Res., vol. 87, 1982, pp. 4533-4541.

8. Guidice, D.A.: PASP Plus: An Experiment to Measure Space-Environment Effects on Photovoltaic Power Subsystems. Fifth Annual Workshop on Space Operations Applications and Research (SOAR '91), NASA Conference Publication 3127, vol. II, 1991, pp. 662-668.
9. Grier, N.T.; and Stevens, N.J.: Plasma Interaction Experiment (PIX) Flight Results. Spacecraft Charging Technology - 1978, NASA Conference Publication 2071, AFGL-TR-79-0082, 1979, pp. 295-314.
10. Grier, N.T.: Plasma Interaction Experiment II (PIX II): Laboratory and Flight Results. Spacecraft Environmental Interactions Technology, 1983, NASA Conference Publication 2359, AFGL-TR-85-0018, 1985, pp. 333-347.
11. Ferguson, D.C.: RAM/WAKE Effects on Plasma Current Collection of the PIX II Langmuir Probe. Spacecraft Environmental Interactions Technology, 1983, NASA Conference Publication 2359, AFGL-TR-85-0018, 1985, pp. 349-357.
12. Hillard, G. B.; and Ferguson D.C.: Solar Array Module Plasma Interactions Experiment (SAMPIE): Science and Technology Objectives. J. of Spacecraft and Rockets, vol. 30, 1993, pp. 488-494.
13. Mandell, M.J.; and Davis, V.A.: User's Guide to NASCAP/LEO. LEW-15641, SSS-R-85-7300-R2, 1990. (Available as LEW-15641 from COSMIC, U of Georgia.)
14. Kuharski, R.A., et al. High Voltage Interactions of a Sounding Rocket with the Ambient and System-Generated Environments. IEEE Transactions on Nuclear Science, vol. 37, 1990, pp.2128-2133.

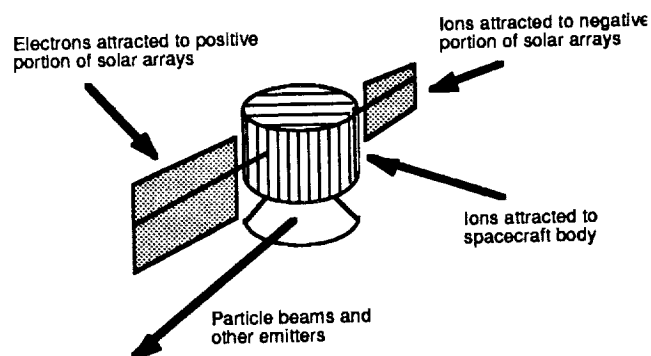


Figure 1.—At the spacecraft floating potential the net current is zero. This current has several components.

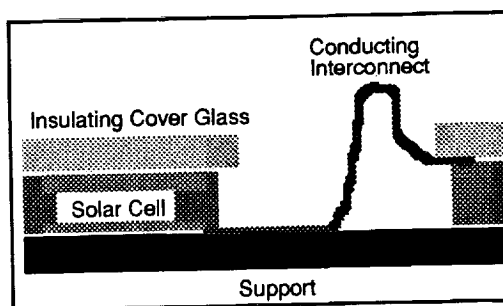


Figure 2.—Cross section of the region between traditional solar cells.

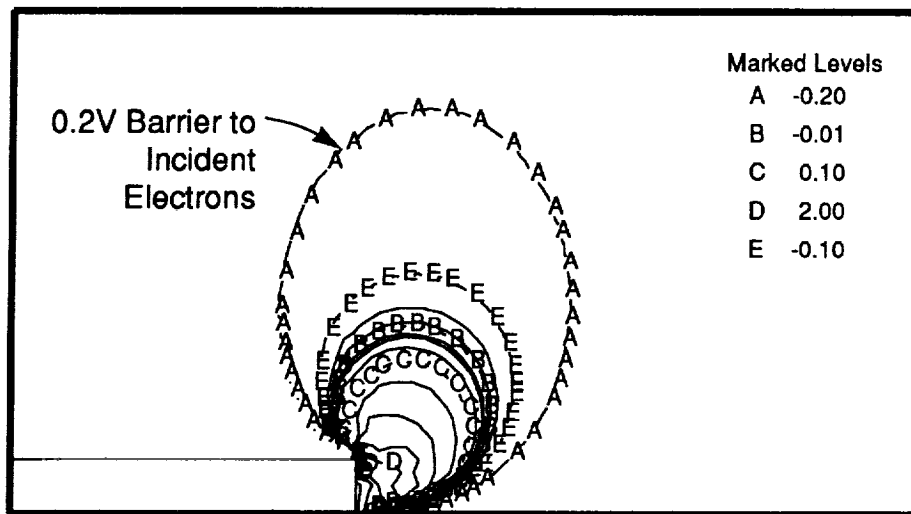


Figure 3.—At low potentials, barrier formation dominates current collection. Plasma of 10^{12} m^{-3} and 0.1 eV. Cell potential of 25 V, surface potential of -0.1 V . First crossover above 25 V.

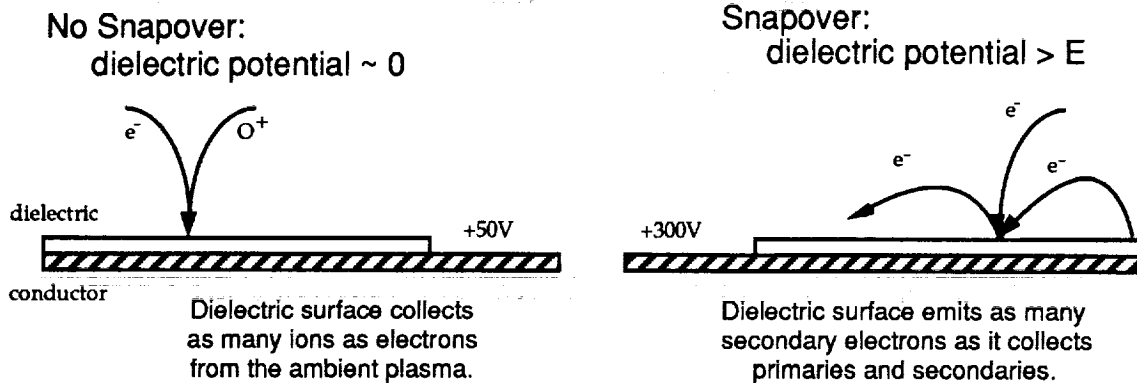


Figure 4.—When a conductor is at a potential above the first crossover of the secondary yield curve of an adjoining insulator, the insulator surface can develop positive potentials in a phenomena known as snapover.

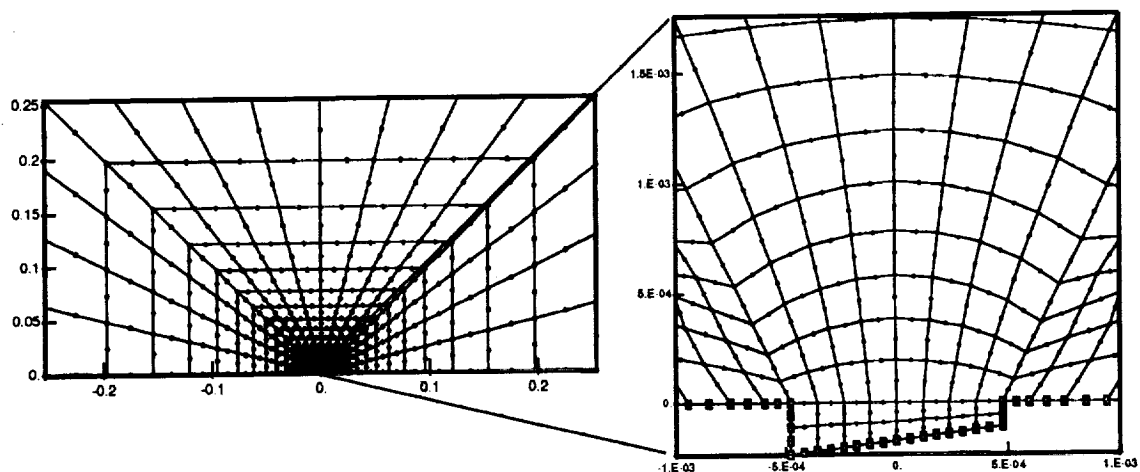


Figure 5.—Grid for two-dimensional Gilbert calculations.

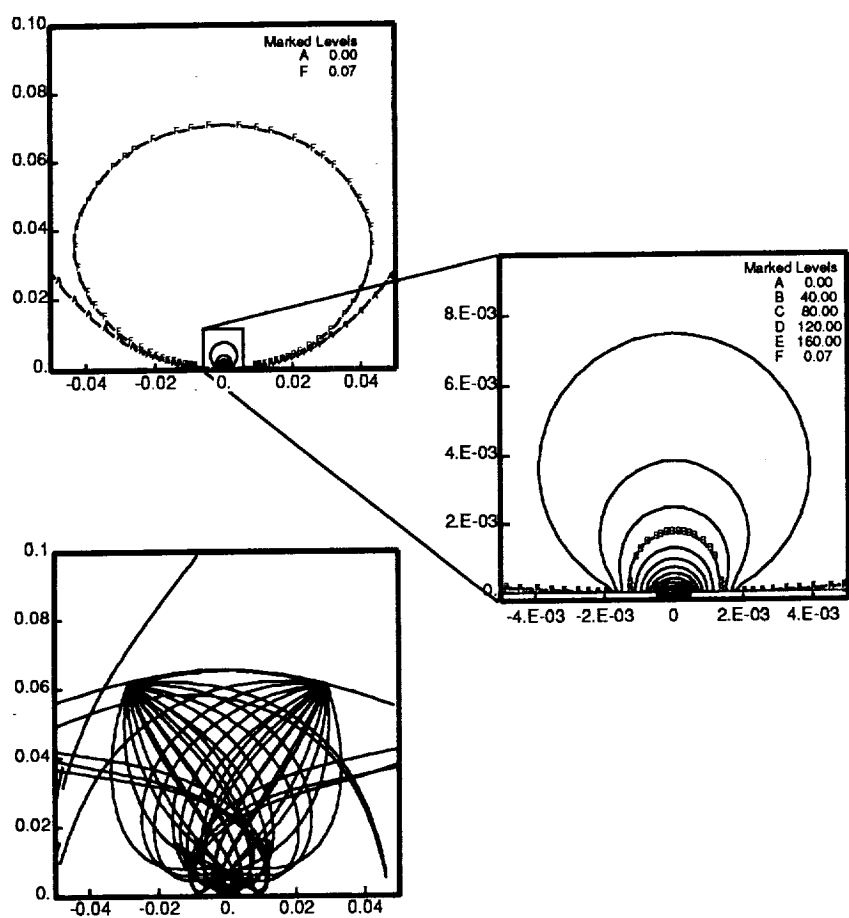


Figure 6.—Potential contours and a few representative trajectories. Plasma of 10^{11} m^{-3} and 0.1 eV. Cell potential of 150 V, surface potential of -0.5 V , first crossover of 40 V.

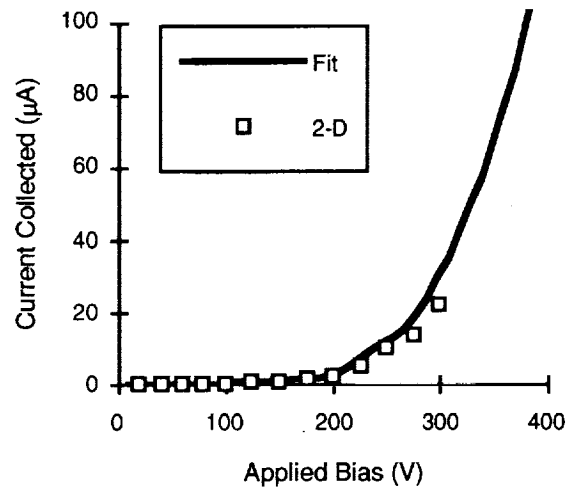


Figure 7.—Current to 1 m along 5 mil thick solar cell edges as a function of applied bias. Plasma of 10^{10} m^{-3} and 0.1 eV. First crossover of 40 V and surface potential of -0.5 V . The points are the results of Gilbert calculations and the line is a fit.

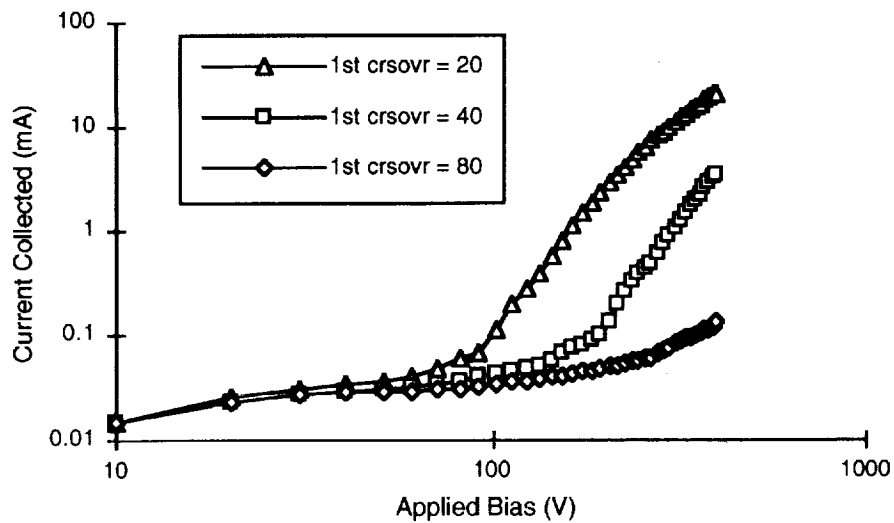


Figure 8.—Current to PASP Plus array #1, mesh interconnect design, as a function of applied bias. Plasma of $1.9 \times 10^{11} \text{ m}^{-3}$ and 0.088 eV. Surface potential of -0.5 V . Three value of the first crossover of the secondary yield.

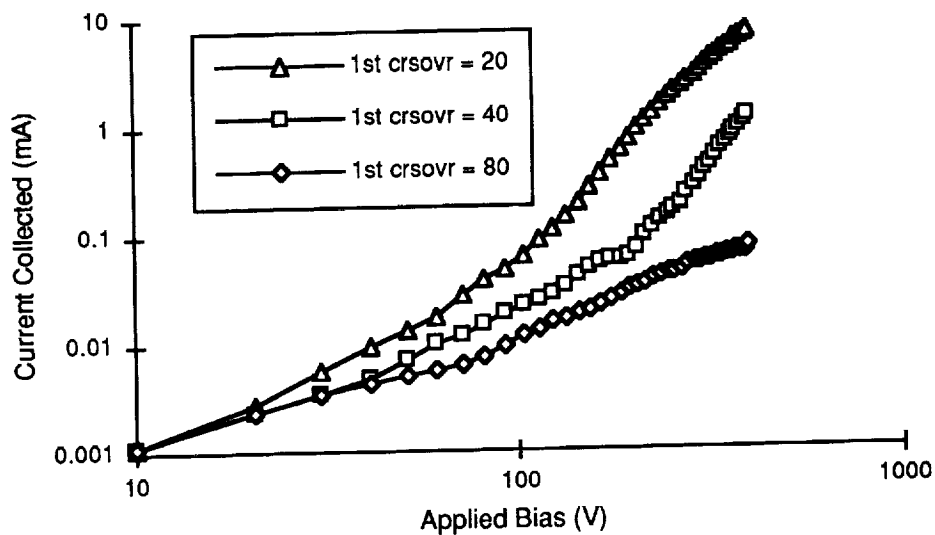


Figure 9.—Current to PASP Plus array #3, space station design, as a function of applied bias. Plasma of $1.9 \times 10^{11} \text{ m}^{-3}$ and 0.088 eV. Surface potential of -0.5 V . Three value of the first crossover of the secondary yield.

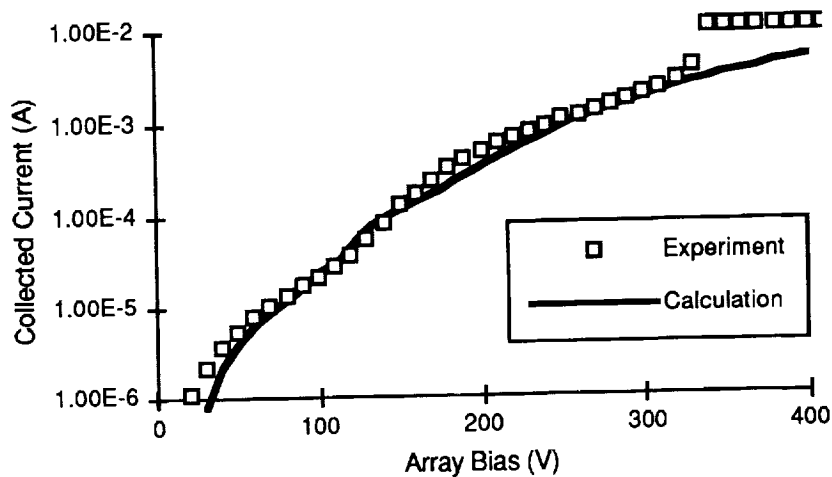


Figure 10.—Comparison of model of parasitic current collection with laboratory measurements for PASP Plus array #8. The environment is $4 \times 10^{11} \text{ m}^{-3}$ at 0.5 eV. The first crossover potential is assumed to be 25 V. (Unpublished experimental data courtesy of N. T. Grier of NASA/LeRC.)

SESSION IV

FLIGHT RESULTS

FINAL RESULTS OF THE ADVANCED PHOTOVOLTAIC EXPERIMENT

David J. Brinker
NASA Lewis Research Center
Cleveland, Ohio

and

John R. Hickey
The Eppley Laboratory, Inc.
Newport, Rhode Island

SUMMARY

The Advanced Photovoltaic Experiment was designed to generate laboratory reference standards as well as to explore the durability of a wide variety of space solar cells. In addition to the cells, it was equipped with an absolute cavity radiometer to measure solar intensity, a spectroradiometer to measure the spectral content of this radiation and a sun angle sensor. Data from the solar cells and various sensors was obtained on a daily basis during the first eleven months of the 69 month flight. In this paper we compare pre-flight and post-flight laboratory measurements with on-orbit calibration data. Pre-flight and post-flight calibration data of the cavity radiometer as well as on-orbit data demonstrated the accuracy and durability of the Eppley Labs. instrument flown on APEX.

INTRODUCTION AND EXPERIMENT DESCRIPTION

The Advanced Photovoltaic Experiment (APEX) is a space flight test designed to provide reference cell standards for laboratory photovoltaic performance measurements as well as to investigate the solar spectrum and the effect of long term exposure of solar cells to the space environment. Toward this end, 155 solar cells of the widest available variety of design and material were incorporated into the experiment along with sensors to measure total solar irradiance and sun angle. Experimental measurements were made on a daily basis, dependent upon the achievement of proper sun angles, and recorded on an on-board magnetic tape recorder. The experiment was designed around the original flight time of one year, with battery capacity the principal lifetime limiting factor. Useful data was in fact obtained for 325 days, at which time the voltage of the batteries supplying the data acquisition system fell below the threshold necessary for calibrated operation. Details of the design and operation of APEX have been previously published (ref. 1,2).

When the announcement of opportunity for LDEF experiments was released in 1976, a launch of about 1980 was envisioned. As a result, the solar cell samples prepared for APEX represented the state-of-the-art in space cell technology as of 1979, as well as samples of cells in use on a variety of satellites. A Shuttle-caused delay in the launch of LDEF by several years provided both the opportunity and necessity for updating the sample set, to one including the most recent advances in technology. The cell investigators were invited in mid-1982 to submit new cells. Of the 136 calibration cells (120 Isc and 16 IV cells), 69 were replaced. Many of those which were not replaced were either standards previously calibrated by other techniques or representative of cells in use on a variety of satellites.

These APEX solar cell investigators and the number of cells each supplied are:

A.F. Wright Aeronautical Laboratory	8
Applied Solar Energy Corporation	14
COMSAT Laboratories	7
European Space Agency	9
Jet Propulsion Laboratory	34
NASA Lewis Research Center	56 (Includes 19 sensor cells)
NASA Marshall Space Flight Center	11
Solarex Corporation	7
Spectrolab, Inc.	9

Each group provided cells representative of technologies which were either in development or production. The experiment was designed to accommodate a total of 155 such cells, including the silicon cells which were employed as sensors for the spectral radiometer portion of the experiment. All cells were permanently mounted on aluminum plates with a thermistor in contact with the rear of the cell. 139 cells were designated as Isc cells, 120 to be calibrated as reference standards and returned to the investigators, eighteen for use as spectral radiometer sensors and one as a night sensor to signal the data acquisition system that conditions were correct for the requisite periodic calibration of the cavity radiometer. For these cells, the short-circuit current was converted to a voltage through the use of a precision load resistor. In most cases a 0.1 Ω value was used. The remaining sixteen cells were designated IV cells, that is the entire current - voltage characteristic was measured through the loading of the cell by a series of five appropriately sized resistors.

At that time, Si cells were the only type in production, with the development of gallium arsenide in its early stages. This is reflected in the distribution of these semiconductor types in the APEX complement, which is summarized by cell type and size below:

Silicon:	105	2 x 2 cm	Gallium Arsenide:	10	2 x 2 cm
	21	2 x 4 cm		<u>1</u>	1.3 x 1.6 cm
	2	5 x 5 cm		11	
	15	5.9 x 5.9 cm			
	<u>1</u>	6 x 6 cm (module)			
	144				

The cells were mounted on 127 aluminum plates of twelve different sizes and configurations. 28 of the mounts each held two 2 x 2 cm cells. Each mount was equipped with a Yellow Springs Instruments Type 16429 thermistor (10,000 Ω @ 25 °C). An additional thermistor monitored the Eppley absolute cavity radiometer.

SENSOR RESULTS

A detailed examination and recalibration of the various sensors and instruments on APEX was performed. The Eppley Type HF absolute cavity radiometer was of particular interest in that it is the only radiometer ever returned from an extended stay in space. It is identical to an instrument that has provided over 12 years of data as part of the Earth Radiation Budget experiment on Nimbus 7. After detailed examination at the Eppley

Laboratories, it was intercompared with standards at the World Radiation Center in Davos, Switzerland (ref. 3). As seen in Table 1, the 69 months in-orbit had little effect on the radiometer. Its sensitivity was essentially unchanged, as was the its reflectance, in agreement with the results of visual inspections.

A spectroradiometer was included in APEX to measure the spectral content of the extraterrestrial sunlight. After return, it was intended that the instrument be used for calibration of laboratory solar simulators. The spectroradiometer consisted of sixteen identical silicon cells with narrow bandpass optical filters. The wavelength center of the filters ranged from 325 nm to 1100, with the last filter covering the infrared out to 2000 nm. Figure 1 compares values of solar irradiance from the APEX flight data with the World Meteorological Organization (WMO) standard. A comparison of pre-flight and post-flight transmittance of the first thirteen filters is seen in Figure 2. The drastic change in transmittance in many filter is clearly seen, although there was no major shift in wavelength band. This degradation was, of course, unexpected and has made the instrument unsuitable for further use in the laboratory. An explanation of the effect or its probable cause has not been forthcoming from the filter manufacturer (ref. 4).

The Digital Sun Angle Sensor (DSAS) was removed and returned to the manufacturer, Adcole Corporation, for recalibration. Its performance was unchanged due to the flight. One of the two gratitudes was cratered from a collision with a debris/micrometeoroid particle. Shadowing from the crater was evidence at the extreme angle limit of the DSAS (32°), but did not otherwise effect its performance. The instrument operated flawlessly during the data taking portion of the flight.

SOLAR CELL RESULTS

The overall condition of the cell sample set was excellent. A contaminating film seen over much of LDEF was present to a varying degree on APEX, the thickness of the layer dependent upon location. No loss of cell coverglass nor significant changes in color or appearance was observed. Several of the cells were cratered from micrometeoroid and/or debris impacts, with the range of damage spanning from microscopic craters in the coverglass surface to penetration of the coverglass and cell and cratering of the underlying aluminum mounting plate. However, even the few cells in which the cratering extended into the solar cell itself, or caused a crack in the coverglass and cell, electrical continuity was maintained. Loss in current proportional to the damage area and increase in fill factor due to cell cracking was observed. The electrical leads from the mounting plate feedthrough to the cell front and rear contacts were found to open in six cells. A silver ribbon of about 3 mil thickness was used for these cells. Where the flat portion of the ribbon faced the ram direction, the ribbon was severely eroded, creating an open circuit. In most cases the ribbon twisted through 90° at the feedthrough so that the narrow (3 mil) edge faced the ram direction; here the silver ribbon remained intact. Examination of the flight data indicates that the erosion did not occur to any extent that would affect cell performance during the data recording portion of the flight, the first eleven months. Post-flight performance testing of these cells was accomplished by direct probing of the cell contacts, no significant change from pre-flight performance was seen.

The first post-flight electrical test performed was measurement of the short-circuit

current utilizing the precision load resistor mounted on each cell for the flight. The resistors were soldered to the cell mounting plate electrical feedthroughs on the underside of the cell mounting plates. These measurements, as well as subsequent current-voltage (I-V) tests, were carried out in the Solar Cell Evaluation Laboratory at Lewis Research Center using a Spectrolab X-25L solar simulator. This simulator employs a short-arc xenon lamp as the light source and provides uniform, collimated illumination. The intensity of the simulator was set using an aircraft calibrated silicon standard which is identical to the standard used at Eppley Laboratory for pre-flight testing, where a xenon arc lamp simulator was also utilized. Cell temperature was monitored using the flight thermistors. One thermistor was found to be open. An examination of the flight data showed abnormal readings from it, indicating that the failure occurred before launch. With this sole exception, all of the thermistors functioned properly, providing values in close agreement with a temperature sensor used in controlling the laboratory test fixture. The short-circuit current values obtained in these test are useful in comparison with both pre-flight performance and flight data. The values obtained were in most cases in good agreement with pre-flight values, with the exception of those cells without a coverglass.

Upon completion of the measurement of short-circuit current, the load resistor was removed from the circuit by cutting one of its two leads. If LDEF had been retrieved on schedule and the value of the cells as calibration standards was retained, the load resistors could not have been removed. However, the absence of data from the last five years on-orbit negates their usefulness as standards. The complete I-V characteristic of all cells were then measured at 25 °C and recorded. Table II compares flight data with pre- and post-flight simulator data for a small representative sampling of the silicon cells. All data presented here is corrected to 25 °C and one AM0 sun (136.7 mW/cm²). All of these cells are n-p type, as were most of the silicon cells flown. Also included is the value of short-circuit current as measured on-orbit.

The loss in voltage and current in the unglassed cells (cells ISC 63 and ISC 83) was consistent with the proton radiation flux of the 250 nm, 28° inclination orbit. The variation in pre-flight to post-flight Isc for the last four cells of Table II is typical of the entire cells set; the variation was within about ±2%. It is believed that this variation was due to inherent differences in the LeRC simulator and data acquisition system used for post-flight testing and those at Eppley Labs used for pre-flight testing. Pre-flight testing was not performed at LeRC as it was expected that the APEX cells would be used as calibrated reference cells; the evolution of the experiment into a long term durability test was neither expected nor ever contemplated. The I-V characteristic of 16 cells was measured by first recording the open-circuit voltage and then switching in five load resistors and recording cell current and voltage for each. The excellent agreement of the on-orbit I-V data (black squares) with the post-flight laboratory data of a Solar Maximum Mission cell is shown (Figure 3).

A summary of results from GaAs cells is shown in Table III. Of the eleven GaAs cells flown, ten were made by Hughes Research Laboratory using liquid phase epitaxy, the only type of GaAs cells then available. These cells had junction depths of either 0.35 μm or 0.50 μm and were flown with either a 12 mil fused silica coverglass or unglassed. The performance degradation, particularly in open-circuit voltage, of the uncovered cells is consistent with the known radiation characteristics of these cells and the mostly proton flux of the orbit. The eleventh GaAs cell was a metal-oxide-semiconductor design which was

under study at that time as a low fabrication cost alternative to epitaxial growth for III-V compounds. It has a very thick coverglass of unknown thickness and material and degraded significantly in short-circuit current. The accuracy of the preflight Isc value is suspect.

Detailed discussion of other cells in the set, particularly those which sustained physical damage from micrometeoroids/debris, can be found in references 2 and 5.

CONCLUSION

The solar cells and sensors flown on APEX survived well their nearly six years in low earth orbit. Post-flight testing of the Eppley cavity radiometer shows that it is essentially unchanged from its pre-flight condition. The solar cell set survived equally well, with no evidence of electrical or physical changes except in those cases where debris or micrometeoroids cratered the cells. Pre-flight and post-flight performance measurements are in very good agreement.

REFERENCES

1. Brinker, D.J.; Hart, R.E. and Hickey, J.R.: Preliminary Results from the Advanced Photovoltaic Experiment Flight Test, 21st IEEE Photovoltaic Specialists Conference, 1990, pp 1213-1218.
2. Brinker, D.J.; Hickey, J.R. and Scheiman, D.A., Advanced Photovoltaic Experiment, S0014: Preliminary Flight Results and Post-Flight Findings, 1st LDEF Post-Retrieval Symposium, June 1991, NASA CP 3134, pp 1395-1404.
3. Hickey, J.R., Passive Exposure of Earth Radiation Budget Experiment Components, LDEF Experiment AO-147: Post-Flight Examinations and Tests, 1st LDEF Post-Retrieval Symposium, June 1991, NASA CP 3134, pp 1493-1510.
4. Hickey, J.R.; Brinker, D.J. and Jenkins, P.P., Studies of Effects on Optical Components and Sensors: LDEF Experiments AO-147 (ERB Components) and S-0014 (APEX), 2nd LDEF Post-Retrieval Symposium, June 1992, NASA CP-3194, pp. 1375-1388.
5. Brinker, D.J.; Hickey, J.R. and Scheiman, D.A., The Effect of the Low Earth Orbit Environment on Space Solar Cells: Results of the Advanced Photovoltaic Experiment (S0014), 2nd LDEF Post-Retrieval Symposium, June 1992, NASA CP-3194, pp. 1291-1302.

Table 1 - Cavity Radiometer Tests and Comparisons

	Pre-Flight	Post-Flight	% Change
Heater Resistance (Ω)	152.2	152.2	0.00
Thermopile Resistance (Ω)	354.4	354.7	0.08
Power Sensitivity Ratio (Vac/Atm)	1.2146	1.2126	-0.16

Intercomparison With World Radiation Reference

APEX Instrument 1.00069

EPLAB Reference Instrument 1.00002

Reflectance Measurement (WRC)

APEX Instrument 250 \pm 80 ppm

New cavity 270 \pm 80 ppm

Table 2 - Silicon Cell Data

Cell Number	Description	Coverglass	Pre-Flight	Isc (mA) Flight	Post-Flight
ISC 63, NA-10	Solarex, BSF/R	No Cover	146.9	144.6	133.5 ($\Delta V_{oc} = -65$ mV)
ISC 83, B-21R	LeRC A/C AStand.	No cover	150.1	152	145.4 ($\Delta V_{oc} = -46$ mV)
ISC 86, B2SOF	COMSAT, Intsat 5	6 mil F.S.	288.2	300.9	292.3
ISC 95, M-5	ASEC, 6x6 W/A	6 mil F.S.	1199	881.3	1195
ISC 112, B-2R	COMSAT Blue	30 mil V-Groove	160	178.6	163.7
ISC 114, B-4R	COMSAT Non-Refl.	12 mil F.S.	193.1	202.7	189.3

Table III - Gallium Arsenide Cell Data

Cell Number	Description	Coverglass	Pre-Flight	Is _c (mA) Flight	Post-Flight
ISC 71, NB-15L	HRL, D _j =0.5 μm	12 mil F.S.	122.5	116.1	108 (ΔV _{oc} =10 mV)
ISC 76, NB-29R	HRL, D _j =0.5 μm	No cover	117.2	111.6	95.5 (ΔV _{oc} =-65 mV)
ISC 77, NB-29L	HRL, D _j =0.35 μm	No Cover	117.3	113.1	93.6 (ΔV _{oc} =-85 mV)
ISC 111, A-2	JPL, AMOS	Unknown	17.6	33.6	22

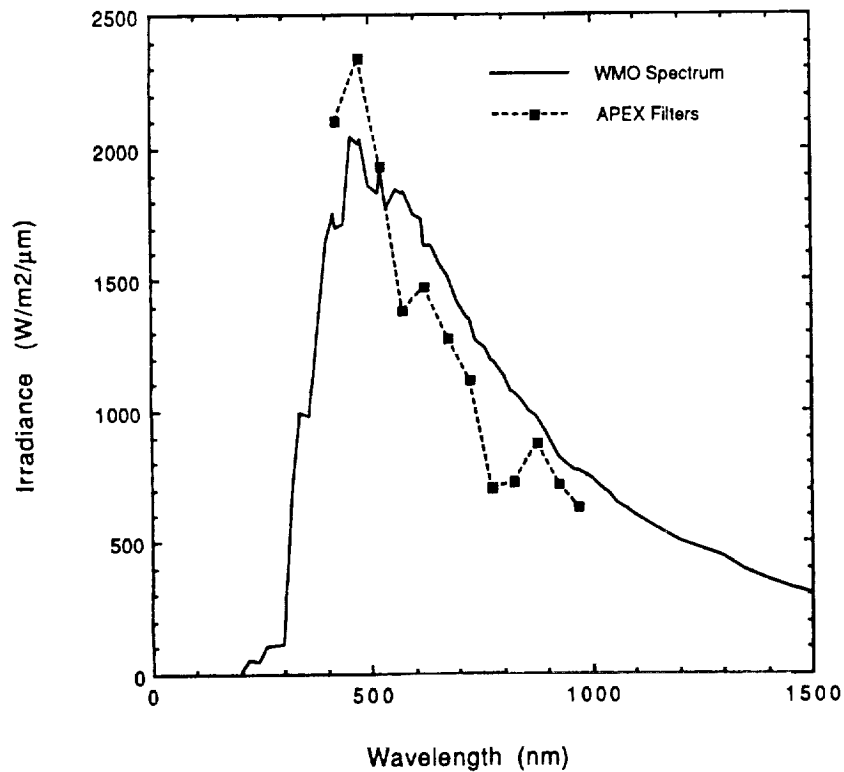


Figure 1 - APEX Filter Data Compared With WMO Spectrum

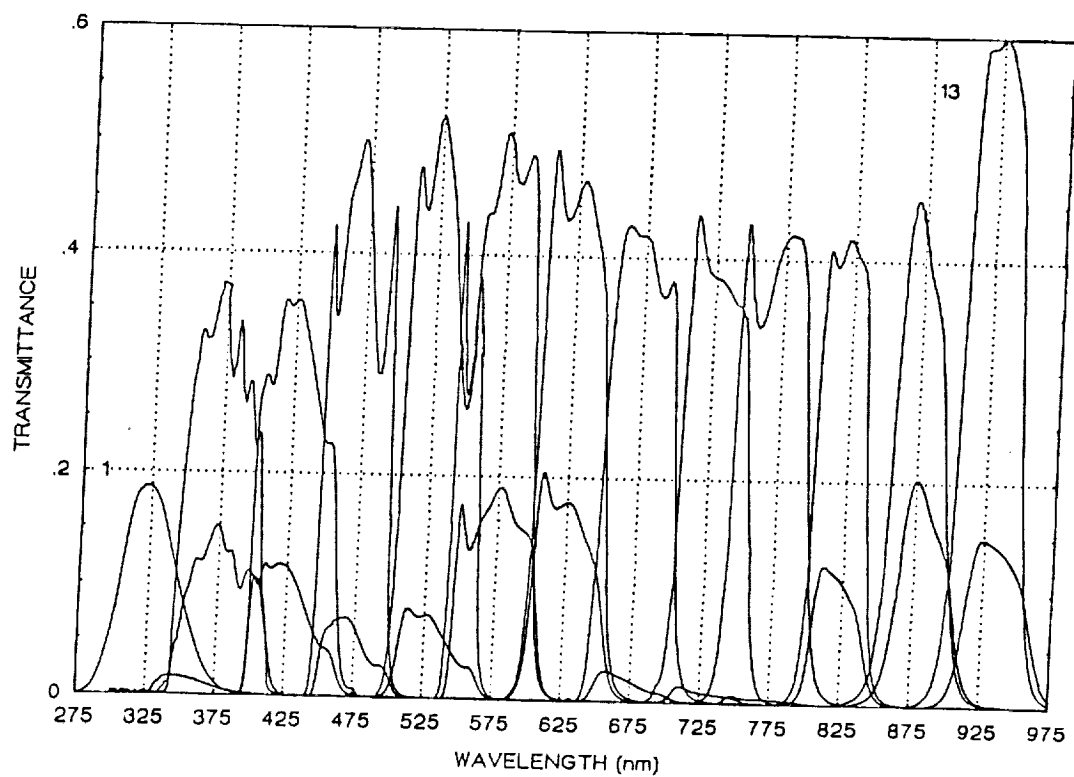


Figure 2 - Transmittance of APEX Filters 1 to 13

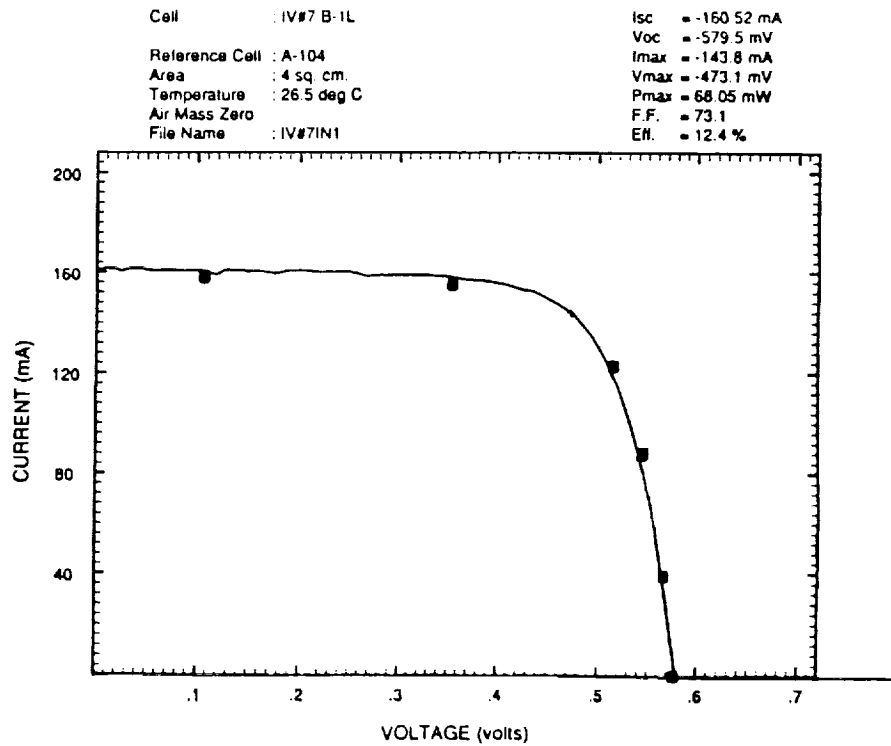


Figure 3 - I-V Curve of Solar Maximum Mission Cell

PRELIMINARY RESULTS FROM THE FLIGHT OF THE SOLAR ARRAY MODULE PLASMA INTERACTIONS EXPERIMENT (SAMPIE)

Dale C. Ferguson and G. Barry Hillard
NASA Lewis Research Center
Cleveland, Ohio

SAMPIE, the Solar Array Module Plasma Interactions Experiment, flew in the Space Shuttle Columbia payload bay as part of the OAST-2 mission on STS-62, March, 1994. SAMPIE biased samples of solar arrays and space power materials to varying potentials with respect to the surrounding space plasma, and recorded the plasma currents collected and the arcs which occurred, along with a set of plasma diagnostics data. A large set of high quality data was obtained on the behavior of solar arrays and space power materials in the space environment. This paper is the first report on the data SAMPIE telemetered to the ground during the mission. It will be seen that the flight data promise to help determine arcing thresholds, snapover potentials and floating potentials for arrays and spacecraft in LEO.

INTRODUCTION

Solar cells in low Earth orbit (LEO) environments have been shown to arc into the surrounding plasma when they are at a potential highly negative of the plasma (Ref. 1) and to collect anomalously large currents from the plasma (to "snapover") when at high positive potentials (Ref. 2). The space flight experiments PIX and PIX II showed that these phenomena are not confined to a laboratory environment, but occur naturally in space plasmas. Using data from these experiments and ground tests, Ferguson (Ref. 3) derived a threshold potential for plasma arcing from standard silicon solar cells, which has been the object of several theoretical treatments (Refs. 4 through 6). Based partly on these treatments, several means of mitigating the arcing phenomenon have been proposed (see Ref. 7). In addition, it has been shown that the currents collected by high voltage array strings in LEO will force negatively grounded power systems to "float" at high negative potentials relative to the plasma, where solar array arcing and/or breakdown of dielectric coatings may occur, causing possible power disruptions, EMI, and surface damage (Ref. 8). To prevent such occurrences, a plasma contacting device (a plasma contactor, or "PC") has been baselined for the International Space Station (ISSA), and operates by actively controlling the ISSA floating potential. This complex and expensive solution to a simple problem makes one desire simpler, cheaper methods of predicting and/or controlling spacecraft floating potentials or arcing thresholds. SAMPIE was flown to investigate the arcing and current collection phenomena in space, to enable the understanding and mitigation of arcing and other undesirable plasma effects.

SAMPIE

Figure 1 shows the electronics box and sample tray of the SAMPIE experiment. It was mounted on the top of a Hitchhiker cross-bay experiment carrier in the payload bay of the Space Shuttle Columbia. Inside this box (Figure 2) were the electronics that controlled the experiments, biased samples on the sample tray to high potentials, measured, stored and telemetered the resulting data, and measured the surrounding plasma conditions. On the side of another Hitchhiker attachment plate were two plasma diagnostic probes (a Langmuir probe and a vehicle potential, "V-Body", probe) to determine the plasma conditions during the biasing experiments. A pressure gauge monitored the payload bay pressure at one end of the electronics box.

Figure 3 shows a blowup of the electronics box and sample tray (experiment plate) assembly. On the sample tray were the samples which were biased in the LEO plasma conditions (Fig. 4). In all, there were 37 different experiment configurations which were tested in LEO. Two high voltage power supplies (HVPS-1 and HVPS-2) in the electronics box biased the experiments to predetermined voltages relative to the Orbiter. An electrometer in the HVPS-1 circuit measured the currents collected, and transient current detectors on both power supply circuits counted the arcs that occurred, on the biased samples. Both ion and electron collection currents were measured at the appropriate biases. The maximum biases attained were -600 V and + 300 V, relative to the Shuttle chassis. Thanks to the large collecting area of the Shuttle main engine nozzles, Columbia stayed within a few volts of the surrounding plasma during all of the bias and plasma conditions encountered.

Of interest to the Space Photovoltaic Power community were several solar array experiments. A twelve cell series coupon of the Advanced Photovoltaic Solar Array (APSA) was flown. A four cell string of Space Station technology cells were also flown. As the backs of these ordinarily flexible arrays are covered with Kapton, precluding significant plasma interactions from the array backs in LEO, the array backs were attached to the experiment plate by adhesive. These arrays were loaded to near their maximum power points by load resistors. In addition, three separate concentric strings of standard 2x2 cm silicon solar cells (similar to those flown on PIX and PIX II) were flown to serve as a control, and to investigate the dependence of current collection on the presence of surrounding solar cells.

Three sets of modified quarter-cells of Space Station design were flown to investigate the dependence of arc rate and current collection on solar cell parameters such as the presence or absence of adhesive on cell edges, the degree of adhesive coverage, and the overhang of cell coverslides past the cell edges. Previous work by many authors (Refs. 9 through 11) had predicted that by varying these parameters, cell arcing and/or current collection would be modified or prevented. To determine the dependence of arcing on exposed conductor properties, samples of pure metals were flown, with insulator strips or adjacent ground rods to encourage arcing. Since the floating potential of ISSA will depend to a great degree on the possibility of current collection by its radiator thermal control paint (Z-93), which had been shown by Hillard to be non-conductive in ground plasma tests (Ref. 12), a small sample of Z-93 was also flown. To investigate the arcing behavior of the ISSA structural material (anodized aluminum), a sample prepared to ISSA truss specifications was flown. The snapover effect, where insulators surrounding exposed conductors at high positive potentials start collecting currents as if they were conductors, was investigated by biasing conductors behind insulation pinholes of various sizes. Finally, a sun sensor on the sample tray confirmed the vehicle attitude. A more complete description of SAMPIE's experiments may be found in Ref. 13.

Preliminary data were telemetered back through the OAST-2 payload operations control center at Goddard Space Flight Center. During the experiment, an anomaly with the HVPS-1 circuit midway through the 37 hours of scheduled data-taking necessitated reconsideration of the experiment timeline, and new instructions were telemetered up to SAMPIE on orbit. In all, about 62 hours of data were obtained, stored on-board, and recovered after Columbia returned to Earth. Data were taken in the bay-to-earth, bay-to-ram, and bay-to-wake orientations. Initial inspection of the data show that they are surprisingly noise-free, and easily constitute the largest and best set of data on the interactions of solar arrays and space power materials with the LEO environment ever obtained.

PRELIMINARY RESULTS

Inspection of Figure 5 shows just how noise-free the SAMPIE data are. These curves of data on the electron collection of the APSA and SS (Space Station) arrays in the bay-to-earth orientation represent

comparison of not just the two array types, but also of the maximum and minimum measured currents at each bias step. Because they were obtained at plasma densities that varied by as much as a factor of ten, and because the Langmuir probe data have not yet been reduced, the different array types can't be naively directly compared or calibrated, but it is clear that the APSA array, with a smaller array area, collects significantly more current than does the array of Space Station cells at all potentials less than about +100 volts. Both arrays go into snapover at voltages between +200 V and +300 V, and at +300 V nearly the entire kapton-covered surface of the sample tray is snapped over in both cases. In Figure 6, the increase in APSA electron current at comparable voltages may be due to increased ram collection or to increased plasma densities. When the Langmuir probe data are reduced, the answer will be known.

Figure 7 shows the electron current collected in the ram condition, near the time of maximum orbital plasma density, for the Space Station array. It is believed that the plasma densities shown in this figure are overestimates by about a factor of 3.6. These data show that the Space Station cells, despite their lack of exposed interconnectors, can collect significant currents from the plasma, and thus influence the Space Station floating potential. It has been estimated that to prevent large negative potential excursions on ISSA, an exposed conducting area of 1000 to 2000 square meters would be required, were the plasma contactor not baselined for ISSA. The data also support the conclusion that the maximum current presently being considered for ISSA PC operation (10 A) will be sufficient to control the ISSA potential at all times. Space Station cells that have been modified to have varying degrees of coverslide overhang do indeed collect different amounts of current, as shown in Figure 8. Preliminary looks at the data seem to imply that a coverslide overhang of 11 mils would reduce the electron current collection of the ISSA arrays by at least an order of magnitude, reducing the need for a plasma contactor. Similar effects may be obtained by ensuring complete coverage of the cell edges with adhesive, although this paradoxically may increase their arc rates (Ref. 7). Reduction of the SAMPIE data on arcing of cells without exposed adhesive may help settle this question. Comparison of the data with those taken in ground plasma tests (Ref. 14) will also be instructive.

Figure 9 shows some of the arcing data on the anodized aluminum sample. As is typical of dielectric breakdown, the arc rate shows a strong dependence on the potential (in this case, we have fit the dependence by a power-law). Although these data have been normalized to a standard plasma condition and plate area, absolute rates must await reduction of the Langmuir probe data. It may be possible to determine an arcing threshold for this thickness of anodized aluminum in a plasma by further reduction of the complete data set.

During the SAMPIE arcing experiments, every sample biased to high negative potentials arced at least once, except for a sample of gold nearby a grounded rod. It may be hypothesized that the lack of surface oxides and/or contaminants prevented arcing in this case, although this is still speculation. In proximity to insulating Kapton strips, even gold showed arcs.

In addition to the experiments conducted to further our knowledge of arcing and current collection, SAMPIE also obtained payload bay pressure measurements to aid in the interpretation of the Experimental Investigation of Shuttle Glow (EISG) experiment data. Figure 10 shows some of the pressure data obtained for EISG, including times when the thrusters fired and gas releases took place. These events are clearly seen in the pressure record.

SUMMARY AND CONCLUSIONS

SAMPIE obtained excellent data on the arcing and current collection characteristics of solar arrays and space power materials in LEO. Further analysis of these data may furnish us with a better

understanding of, and better means to control, arcing on solar arrays and spacecraft in the LEO environment. The result could be better solar array or power system designs, ensuring years of safe and reliable operation in the harsh LEO plasma.

In order to determine the behavior of even newer and more diverse materials and solar arrays in the LEO environment, it is planned to reflly SAMPIE with different samples on the sample tray. This low-cost reflight may be one of our best near-term opportunities to learn more about LEO arcing and current collection behavior.

ACKNOWLEDGEMENTS

The authors would like to thank the Office of Advanced Concepts and Technology for footing the bill for SAMPIE. Their foresight and forbearance led to the great success that SAMPIE has become. Our thanks also go to the great SAMPIE team, all the way from technicians to project management, who built SAMPIE and ensured that it would work on-orbit. Like any great team, the watchword for the SAMPIE team was teamwork. Individual egos notwithstanding, the SAMPIE team worked cooperatively and selflessly to see the project through to completion. Thanks to Thomas L. Morton for his fine reduction of the SAMPIE Langmuir probe and modified Space Station cell data. We would also like to acknowledge the contributions of Steven C. Zook, a brilliant young software and electronics engineer who met an untimely death before SAMPIE was completed. We will miss him. Finally, we acknowledge the excellent OAST-2 mission control team at Goddard Space Flight Center. We could not have asked for a more responsive and supportive team during our real-time reprogramming of the SAMPIE timeline.

REFERENCES

1. Grier, N.T. (1983). "Plasma Interaction Experiment II: Laboratory and Flight Results," in NASA CP-2359, p. 333, 1985.
2. Gabriel, S.B., Garner, C.E. and Kitamura, S. (1983). "Experimental Measurements of the Plasma Sheath Around Pinhole Defects in a Simulated High-Voltage Solar Array," AIAA Paper 83-0311.
3. Ferguson, D.C. (1986). "The Voltage Threshold for Arcing for Solar Cells in LEO - Flight and Ground Test Results," NASA TM-87259.
4. Jongeward, G.A. et al (1985). "The Role of Unneutralized Surface Ions in Negative Potential Arcing," IEEE Trans. Nucl. Sci., vol. NS-32, no. 6, Dec., pp. 4087-4091.
5. Hastings, D.E., Weyl, G., and Kaufman, D. (1990). "Threshold Voltage for Arcing on Negatively Biased Solar Arrays," J. Spacecraft and Rockets, 27, p. 539.
6. Mong, R.L. (1993). "Arcing Mitigation and Predictions for High Voltage Solar Arrays," Master's Degree Thesis, Massachusetts Institute of Technology.
7. Ferguson, D.C. (1993). "Interactions Between Spacecraft and their Environments," AIAA Paper 93-0705.
8. Ferguson, D.C., Snyder, D.B., and Carruth, R. (1990). Final Report of the Joint Workshop on Evaluation of Impacts of Space Station Freedom Grounding Configurations, NASA LeRC,

August 21, 1990.

9. Upshulte, B.L. et al (1991). "Significant Reduction in Arc Frequency of Negatively Biased Solar Cells: Observations, Diagnostics, and Mitigation Technique(s)," in NASA CP-3121, p. 32-1.
10. Cho, M. and Hastings, D.E. (1991). "Dielectric Charging Processes and Arcing Rates of High Voltage Solar Arrays," J. Spacecraft and Rockets, 28, pp.698-706.
11. Hillard, G.B. and Ferguson, D.C. (1993). "The SAMPIE Flight Experiment Final Technical Requirements Document," NASA TM-106224.
12. Hillard, G.B. (1993). "Experimental Measurement of the Plasma Conductivity of Z93 and Z93P Thermal Control Paint," NASA TM-106284.
13. Hillard, G.B. and Ferguson, D.C. (1993). "The Solar Array Module Plasma Interactions Experiment (SAMPIE): Science and Technology Objectives," J. Spacecraft and Rockets, 30, p. 488.
14. Bozich, R.C. (1994). "Characterization of Solar Cells and Metal Samples in a Plasma Atmosphere Using the SAMPIE Proto-type Model System," Master's Degree Thesis, Cleveland State University.

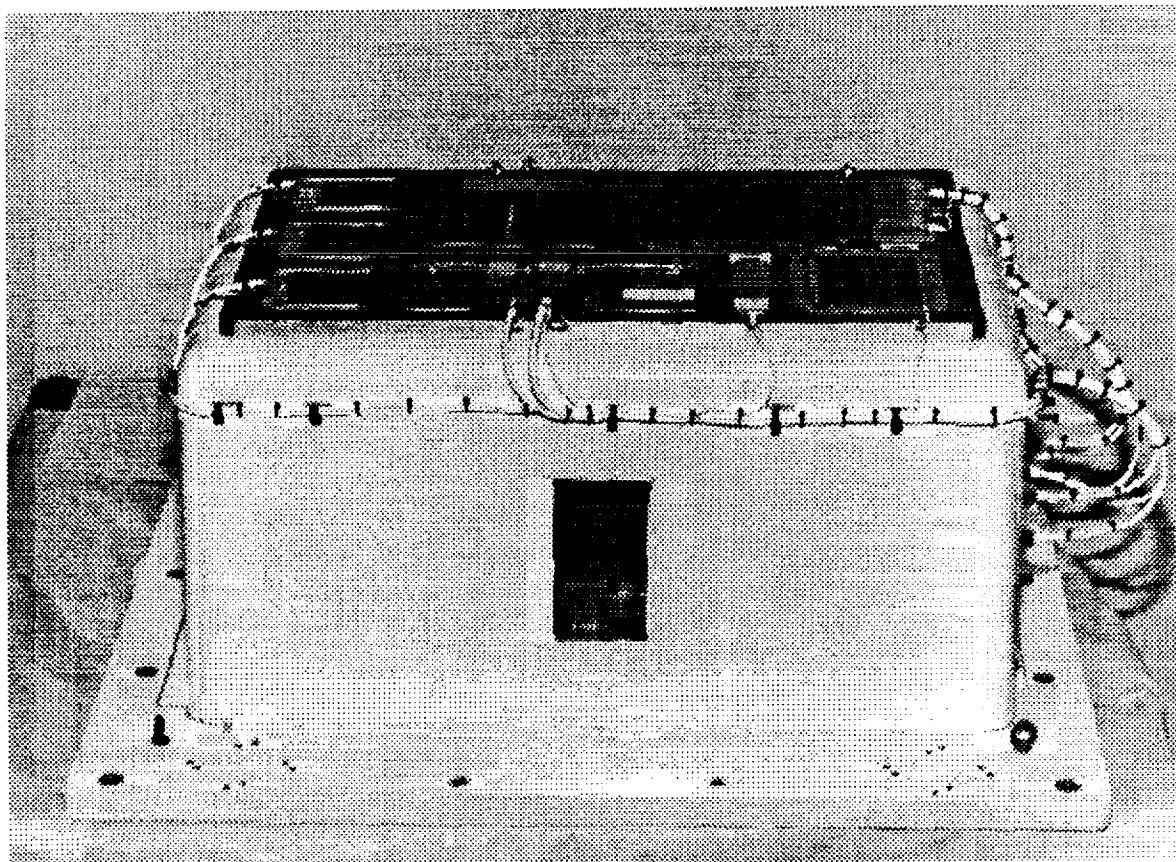


Figure 1. The Solar Array Module Plasma Interactions Experiment (SAMPIE) electronics box and sample tray.

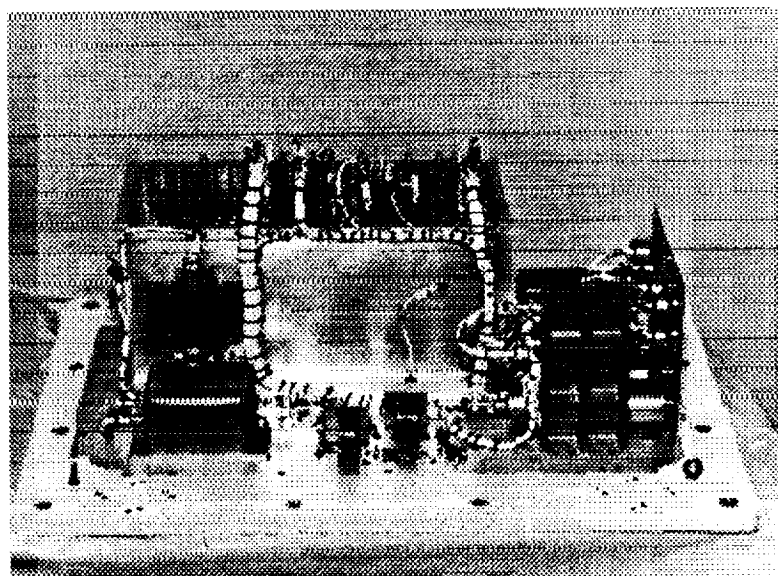


Figure 2. The SAMPIE electronics box card cage and interior components.

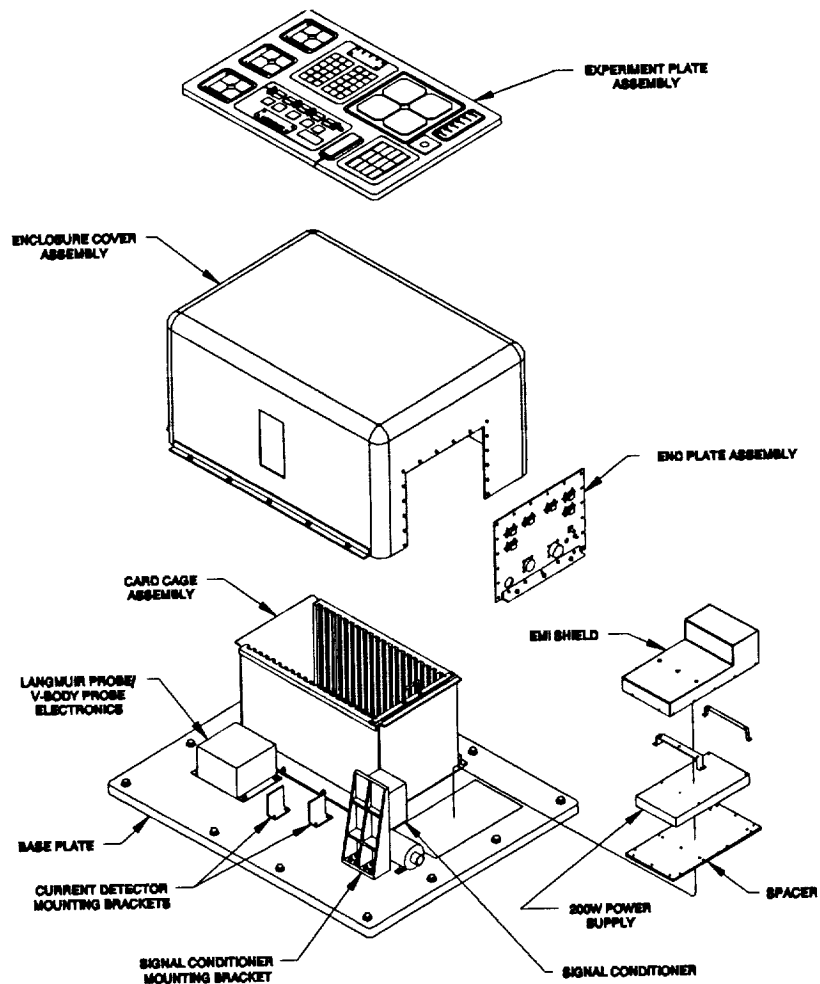


Figure 3. An exploded view of the SAMPIE electronics box and sample tray.

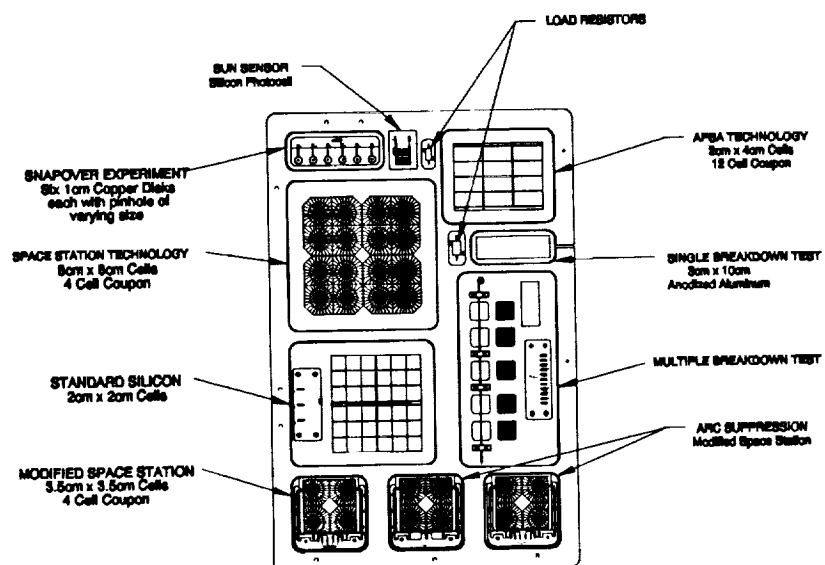


Figure 4. The SAMPIE sample tray.

APSA and SS Currents, Bay-to-Earth

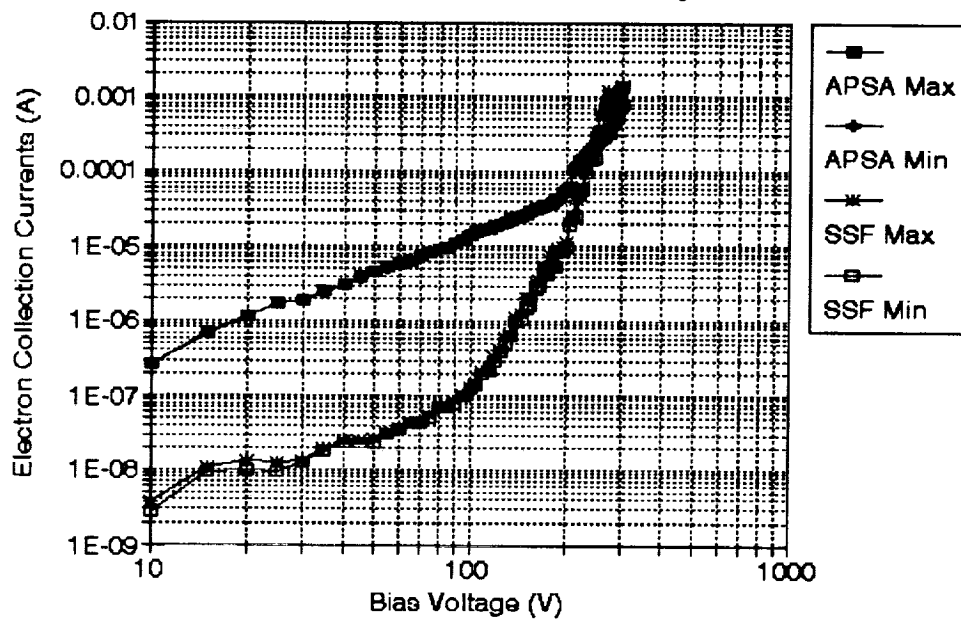


Figure 5. Electron currents collected by the APSA and Space Station arrays in the bay-to-earth orientation.

APSA Currents, Bay-to-Ram

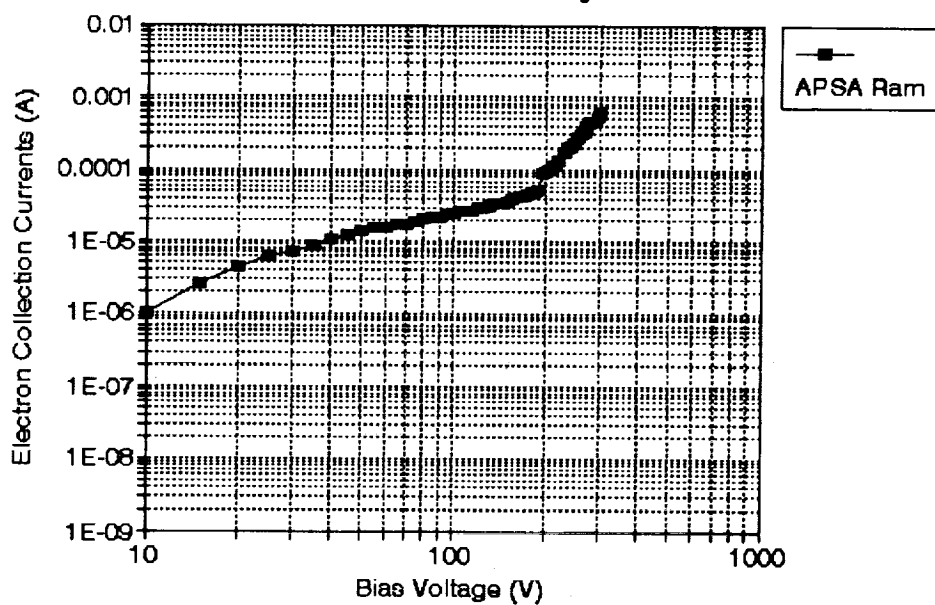


Figure 6. Electron currents collected by the APSA array in the bay-to-ram orientation.

Space Station Currents, Bay-to-Ram

Experiment 20

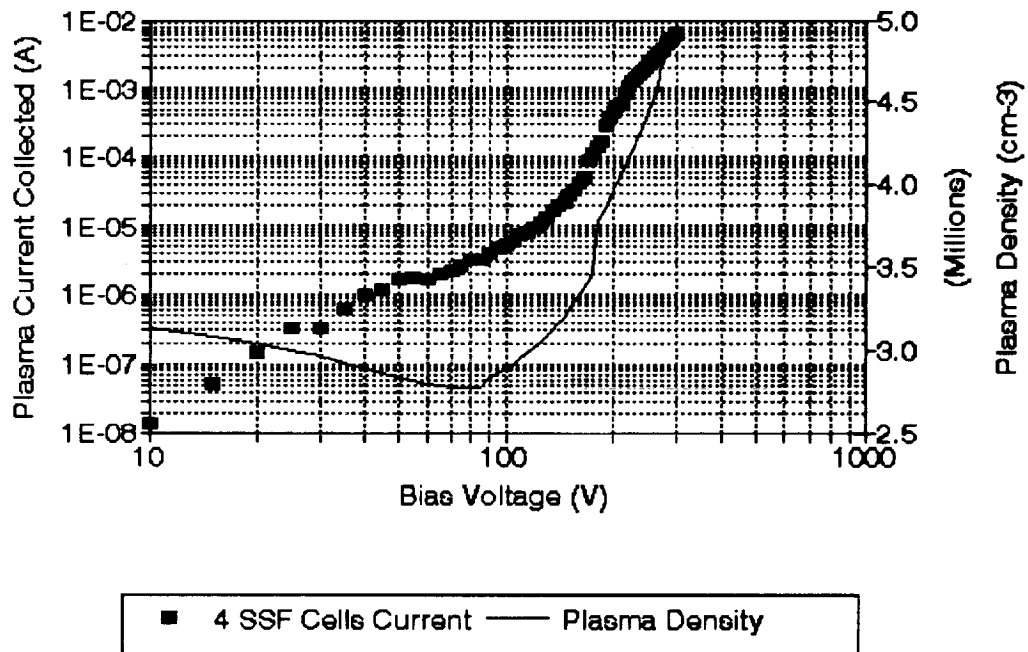
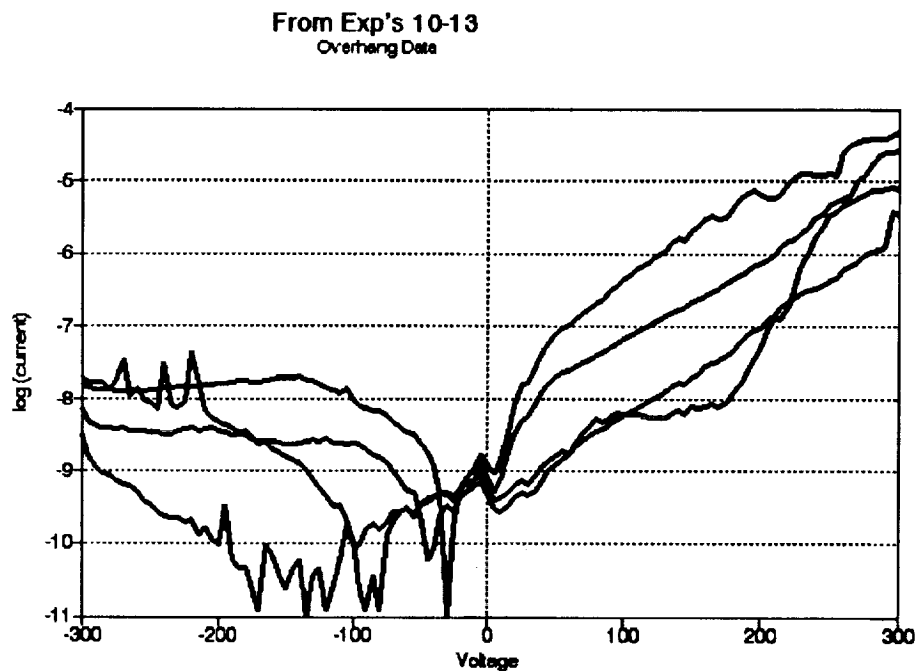


Figure 7. Electron current collection by the Space Station array in the bay-to-ram orientation. Plasma densities are overestimated (see text).



Courtesy of T. Morton

Figure 8. Electron currents collected in the bay-to-ram orientation by Space Station type cells modified to have varying amounts of coverslide overhang.

SAMPIE DATA - ANODIZED AL

Ram data #2

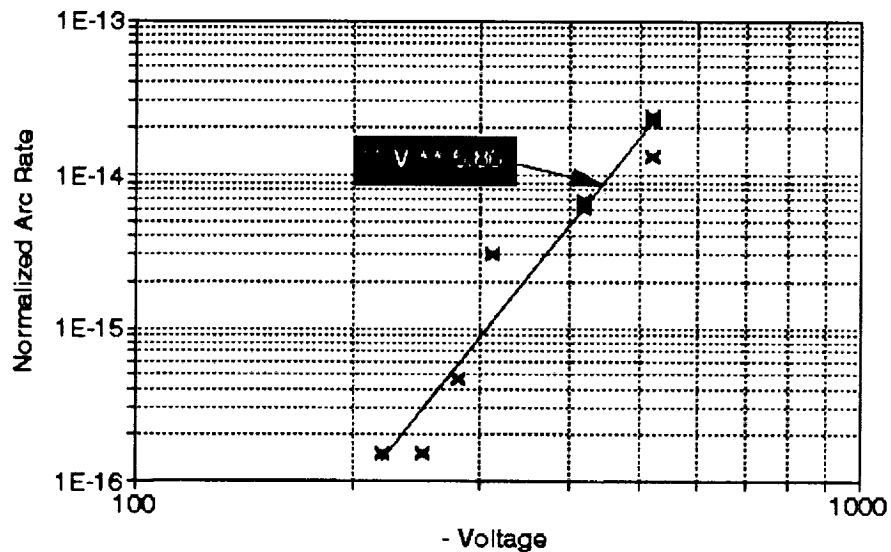


Figure 9. One set of normalized arcing data on the SAMPIE anodized aluminum sample in the bay-to-ram orientation.

Raw Pressure Data - SAMPIE

MET day 11

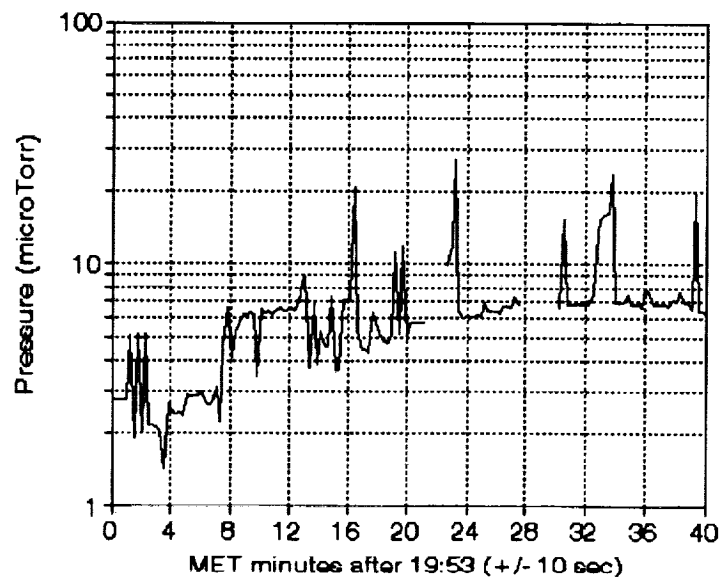


Figure 10. Raw telemetered pressure data taken during EISG experiment operation.

PHOTOVOLTAIC ELECTRIC POWER APPLIED TO UNMANNED AERIAL VEHICLES (UAV)

Jack Geis
Wright Patterson Air Force Base
Dayton, Ohio

and

Jack H. Arnold
Rockwell International
Canoga Park, California

ABSTRACT

Photovoltaic Electric-Powered Flight is receiving a great deal of attention in the context of the United States' Unmanned Aerial Vehicle (UAV) program. This paper addresses some of the enabling technical areas, and their potential solutions. Of particular interest are the long-duration, high-altitude class of UAVs whose mission it is to achieve altitudes between 60,000 and 100,000 feet, and to remain at those altitudes for prolonged periods performing various mapping and surveillance activities. Addressed herein are studies which reveal the need for extremely light-weight and efficient solar cells, high-efficiency electric motor-driven propeller modules, and power management and distribution control elements. Since the potential payloads vary dramatically in their power consumption and duty cycles, a typical load profile has been selected to provide commonality for the propulsion power comparisons. Also, since missions vary widely with respect to ground coverage requirements, from repeated orbiting over a localized target, to long-distance routes over irregular terrain, we have also averaged the power requirements for on-board G&C power, as well as ground control and communication link utilization.

In the context of the national technology reinvestment program, wherever possible we modeled components and materials which have been qualified for space and defense applications, yet are compatible with civilian UAV activities. These include, but are not limited to solar cell developments, electric storage technology for diurnal operation, local and ground communications, power management and distribution, and control servo design.

And finally, the results of tests conducted by Wright Laboratory on ultra-light, highly efficient MOCVD GaAs solar cells purchased from EPI Materials Ltd. (EML) of the UK are presented. These cells were also used for modeling the flight characteristics of UAV aircraft described in Section 3.0 and Table I.

1.0 Solar-Electric UAV Background and History: Solar powered human flight has been accomplished, and needs no elaborate historic

overview. It evolved from the ultra-light technology of AeroVironment's human-powered aircraft, and evolved from retrofitting similar vehicles with single-crystal silicon solar cell arrays and electrically-driven propellers. They sustained low-level flight for limited periods, and remained airborne largely at the whim of prevailing weather conditions. In fact, as a class they can be described as propeller-augmented sail planes. Later, in the fall of 1991, Eric Raymond's Sun Seeker aircraft, using Sanyo amorphous silicon cells deposited on polymeric film, logged a cross-country flight of 2,467 miles during a series of hops which totalled 119 hours of electrically-augmented flight. But again, at the risk of under-emphasizing the significance of these remarkable accomplishments, this aircraft was controlled more by the weather than the pilot, and the aircraft electrical propulsion system.

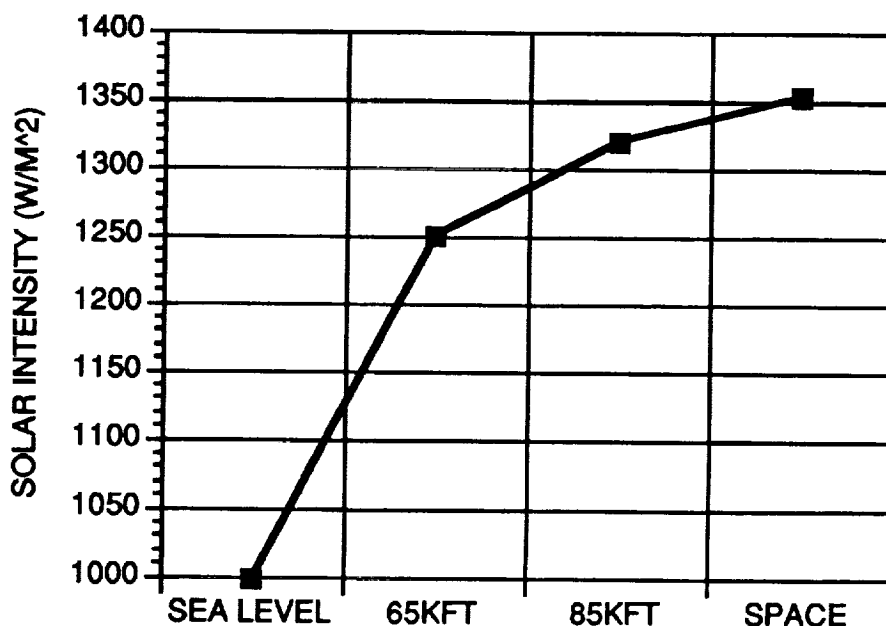


Figure 1: Relationship between altitude and solar intensity

2.0 Insolation vs Altitude: If the extended mission UAV must takeoff and achieve operational altitude as a conventional aircraft, it must operate through a wide spectrum of solar intensity which varies with altitude. On the ground, even though the batteries are fully charged, the array must be sized to operate the propulsion subsystem at Air Mass 1 (AM-1.0). However, as the vehicle climbs higher, and begins to rise above the near-ground atmosphere, it will eventually be receiving solar insolation which is 80-90% of AM-0.

Figure 1 depicts a general spectrum of solar intensity vs altitude, and shows an approximate gain of 25% in solar intensity at operating altitude. This prompts the designer to seek various means of hybrid or aircraft-assisted takeoff and climb-out augmentation, but in this paper, only electrical storage and solar power were modeled.

3.0 Impact On Aircraft Performance of Solar Cell Efficiency and Weight: As a general observation, until recently the efficiency of solar cells was inversely proportional to their weight. Space-qualified single crystal silicon cells, which are moderately efficient (14-16%,) are comparatively heavy, and require large wing-surface mounting areas in order to achieve a given power level. In later developments, when engineers were enticed by amorphous silicon cells deposited on thin, flexible films, because they were dramatically lighter in weight, it was necessary to devote 60% more surface area because of their lower efficiency. The applicability of using standard GaAs-on-Ge technology for higher efficiency (18% @ 28°C, AM-0)) will not improve the aircraft weight due to the fact that the resulting array weighs even more than single-crystal silicon of a comparable thickness. It should be noted that certain U.S. companies are working on 3-mil GaAs-on-Ge technology, but this was considered too far term to use for a near-term comparison. However, in the present timeframe, a British company is demonstrating high-efficiency, thin-film GaAs solar cells which are comparable in weight with a-Silicon-on-Kapton blanket material, or conventional blanket consisting of GaAs deposited on germanium substrates, then bonded to a Kapton blanket. The relative merits of cost for per watt for the various options are not addressed in the paper.

It was considered useful in our analysis to review an existing UAV experimental aircraft (Pathfinder) and the associated weight and power algorithms that are derived from it, then calculate aircraft performance over a range of solar cell efficiencies and array mass densities. We then revised or updated aircraft component characteristics such as propulsion and storage conversion efficiencies, and solar cell/ wing area ratios, then compared the new over-all airplane performance using state-of-the-art solar cells with the new model using vastly improved solar cells.

For this purpose, the authors interfaced with EPI Materials Ltd (EML) of the UK and used their ultra thin, ultra-lightweight MOCVD GaAs solar cells modeled for application to the new "Pathfinder" baseline aircraft. The results of this modeling are presented in Table I.

TABLE I

EFFECT OF PHOTOVOLTAIC OPTIONS ON ELECTRIC AIRPLANE
PERFORMANCE USING EPI MATERIAL LTD. (EML) THIN FILM GAAS
CELLS

FLIGHT CONDITIONS* • 60 KFT • Winter Solstice • 24 Hr. Operation	NEW BASELINE PATHFINDER	EML STANDARD THIN-FILM GAAS	EML BIFACIAL THIN-FILM GAAS (ALBEDO=.24)
Cell Efficiency (%)	21	21	24.6
Cell Mass Density (lbs/ft ²)	.0457	.0228	.0228
Payload Wt. (lbs)	100	100	100
Propulsion Wt. (lbs)	233.9	179.6	153.1
Misc. Wt. (lbs)	117.4	89.5	76.3
Solar Cell Wt. (lbs)	132.5	51	43.5
Energy Storage Wt. (lbs)	1060.4	822	701.1
Airframe Wt. (lbs)	274.9	233.7	197.6
Total Aircraft Wt. (lbs)	1919.1	1465.8	1271.6
Wing Area (ft ²)	3636.3	2790.5	2339
Wing Span (ft)	208.9	183	169
Storage Energy Density (Whrs/lb)	126	126	126
Payload Power (w)	250	250	250
Misc. Power (w)	115.5	88	75
Propulsion Power (w)	8352.7	6413.8	5467.9
Total Power (w)	8718.2	6751.8	5792.9

* Wright Laboratory Spreadsheet Model

It should be noted that the UAV design challenge is not merely sustaining marginal near-ground flight conditions. It involves the optimization of an un-piloted aerodynamic vehicle and electrical propulsion system which will permit the UAV to operate completely under the control of the ground station, at extremely high altitude, for extended

periods, bearing a payload, which for purposes of our comparison, weighs 100 pounds.

The aircraft, depending on mission requirements and design restrictions, may be capable of taking off conventionally on its own power and climbing out to design altitude, or if practical, it may be assisted by auxilliary propulsion, or carried aboard a larger mother aircraft where it is released at altitude. A computerized ground-control system will then "pilot" the aircraft robotically on a prescribed course over specified surface targets on a real-time basis. The electric propulsion and control systems would be capable of maneuvering the vehicle on an accurate, pre-specified flight plan during normal environmental conditions, thus requiring an adequate margin of power for all-weather aerodynamic stability.

It is clear from examining Table I that the use of EML ultra-lightweight, single-sided (high efficiency) solar cells reduces the present weight of a "Pathfinder" type aircraft significantly. Please note that Table I does not include performance for an aircraft with the type of solar cells currently used on the LLNL "Pathfinder" (mass density of 0.103 lbs./ft.².) For winter solstice flight conditions, this aircraft would weigh in excess of 6000 lbs., and have a wing area greater than 10,000 ft.², which is clearly an impractical design.

Column No.1 of the table is for a hypothetical baseline aircraft, similar to "Pathfinder," but with significant changes and/or improvements to aircraft component performance characteristics, as follows:

- A. Propulsion efficiency is increased from 64% to 70%, which is considered feasible using available technology
- B. Energy storage efficiency has been increased from 45% to 65%, which by today's space and aircraft technology standards is quite conservative
- C. Solar cell/ wing area ratio has been upgraded from 0.55 to 0.799 by mounting solar cells on surfaces inside a transparent wing (see Fig.3)
- D. Wing aspect ratio has been changed from 25 to 12
- E. Cell performance has been increased from 19.5% to 21% efficiency, and cell density decreased from 0.103 to 0.0457 lbs./ft², which the authors note is presently unsurpassed by several potential domestic options other than the cells produced by EML

F. The lift coefficient has been reduced from 1.0 to 0.78 to assure that the airplane travels at 20 ft./sec above the theoretical stall speed

In addition, the analyses were made for planes flying at worst optical conditions (winter solstice,) rather than summertime conditions.

It should be noted that despite an arbitrary increase in "pathfinder" solar cell efficiency from 19.5 to 21%, and reducing the cell mass density by 55%, the weight of this model could be reduced even further if EML cell technology were employed. For example, if the present cells were replaced by the EML single-sided cells, another 453 pounds could be saved, and if EML bifacial cell technology were employed, almost 650 pounds could be saved. It is also shown that the power requirements can be reduced from 8.7 kW to 6.7 kW using the EML single-sided cells, and to 5.8 kW for the bifacial cells.

SOLAR-POWERED UAV'S

21% SOLAR CELL EFFICIENCY

126 W-HR/LB STORAGE EFFICIENCY

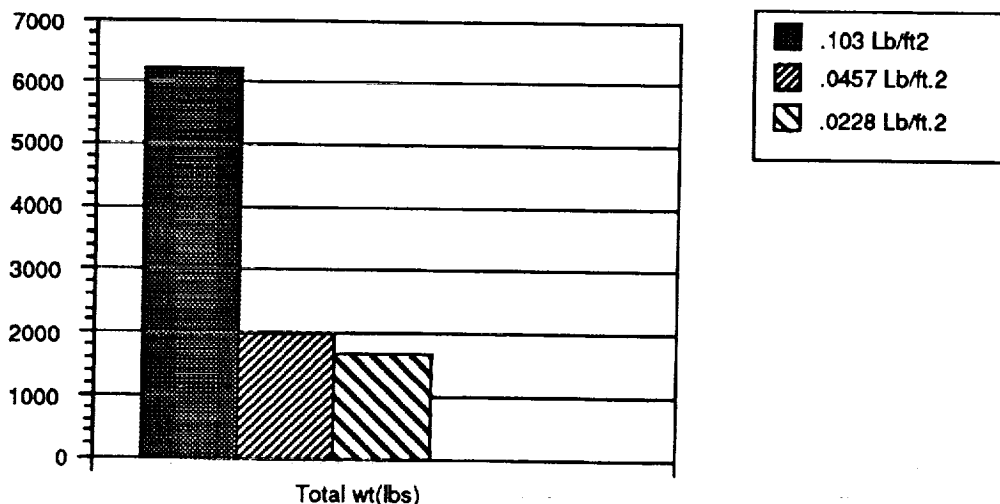


Figure 2: Impact of improved solar cell weight densities on total aircraft weights

Figure 2 illustrates graphically the effect of cell mass density on aircraft total weight for a 21% efficient cell. It is also evident from Table I that significant gains in energy storage round-trip efficiency will dramatically reduce the overall aircraft weight. For example, present advances in space technology now yield upwards to 80% charge/discharge efficiency, which when coupled to improved storage capacity density in watt-hrs./lb, could

make a profound impact on total aircraft weight. Clearly, each small improvement in aircraft component weight results in a cascade effect on total aircraft weight, and the end performance the aircraft can achieve.

A reduction in cell mass density means that the aircraft wing will weigh less, and the propulsion power (and weight) will be reduced to maintain the aircraft at nominal flying speed. Therefore, the aircraft can be proportionately downsized, including reduced wing area, resulting in still additional weight savings. For example, if the solar cell mass density is reduced by only 1 %, the aircraft weight drops by over 9 lbs. Similarly, when the solar cell efficiency is raised by 1 %, the aircraft weight drops by almost 54 lbs.

4.0 WRIGHT LAB TESTING OF EML SOLAR CELLS : A 3.98 cm X 3.98 cm, 16-volt, high-efficiency, thin film GaAs solar cell substring was delivered to Wright Laboratory for performance verification. The general configuration of the cells are shown in Figure 3. The substring is produced by creating a single solar cell which is 4 cm square, and then photolithographically dividing it into sixteen 1 cm square solar cells which are interconnected in series to provide the 16-volt nominal output. Clearly, the device could be left as a single solar cell, with even higher efficiency, but in most UAV applications the higher voltage substring would provide a convenient electrical building block.

The conversion efficiency was measured and recorded at the Air Force Institute of Technology by PhD candidate Kitt Reinhardt using a 1-kW Oriel Xenon solar simulator at AM-0 conditions, calibrated using a JPL balloon-flown standard GaAs cell. The I-V curve and the efficiency calculations are presented as Figure 4. As can be seen, the conversion efficiency of the planar solar cell was 20.3%. The Voc was 16.25 V, while the Isc was 31.85 mA, resulting in a fill factor of 0.84.

The general structure of the cell is shown in Figure 5. The cell has a significant weight advantage over standard cells inasmuch as bonding the cell to a 1-mil coverglass will result in a cell mass density of less than .03 lbs/square foot, which represents a factor of 3.5 improvement when compared with the current "Pathfinder" cell.

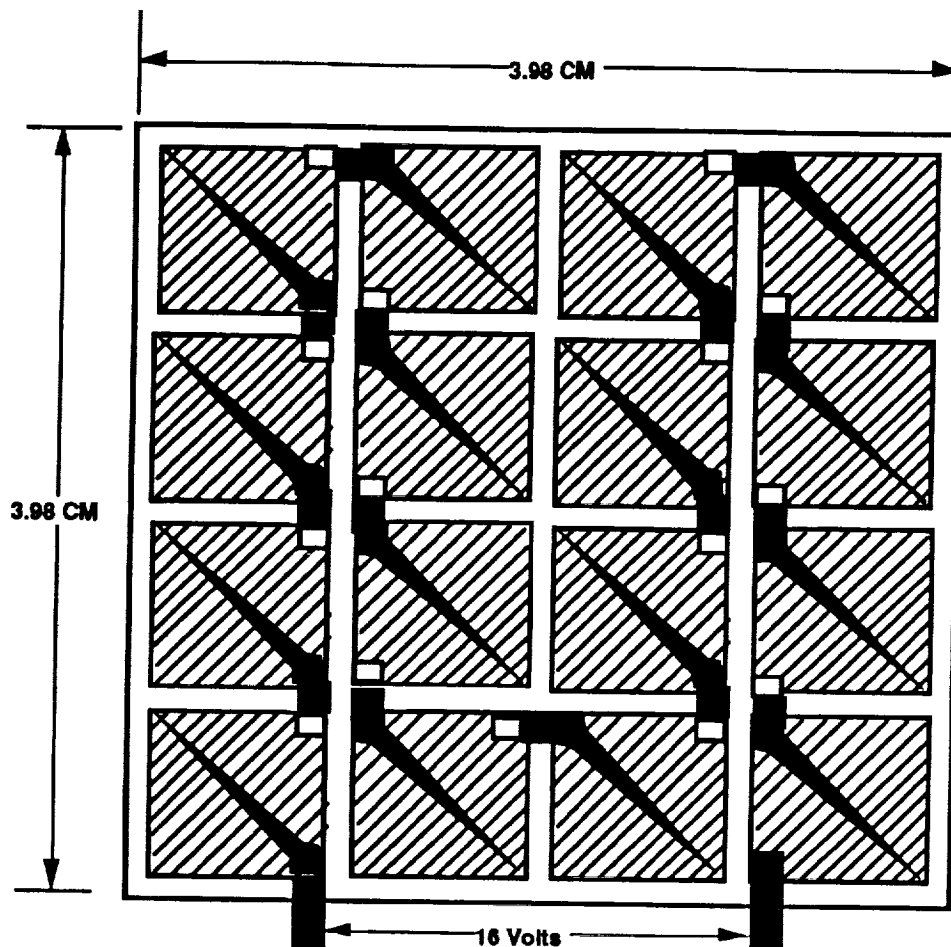


Figure 3: General Configuration of EML GaAs Solar Cell Substring

Ultrathin 16 V EML GaAs Solar Cell AMO **Conversion Efficiency Test Results & Calculations**

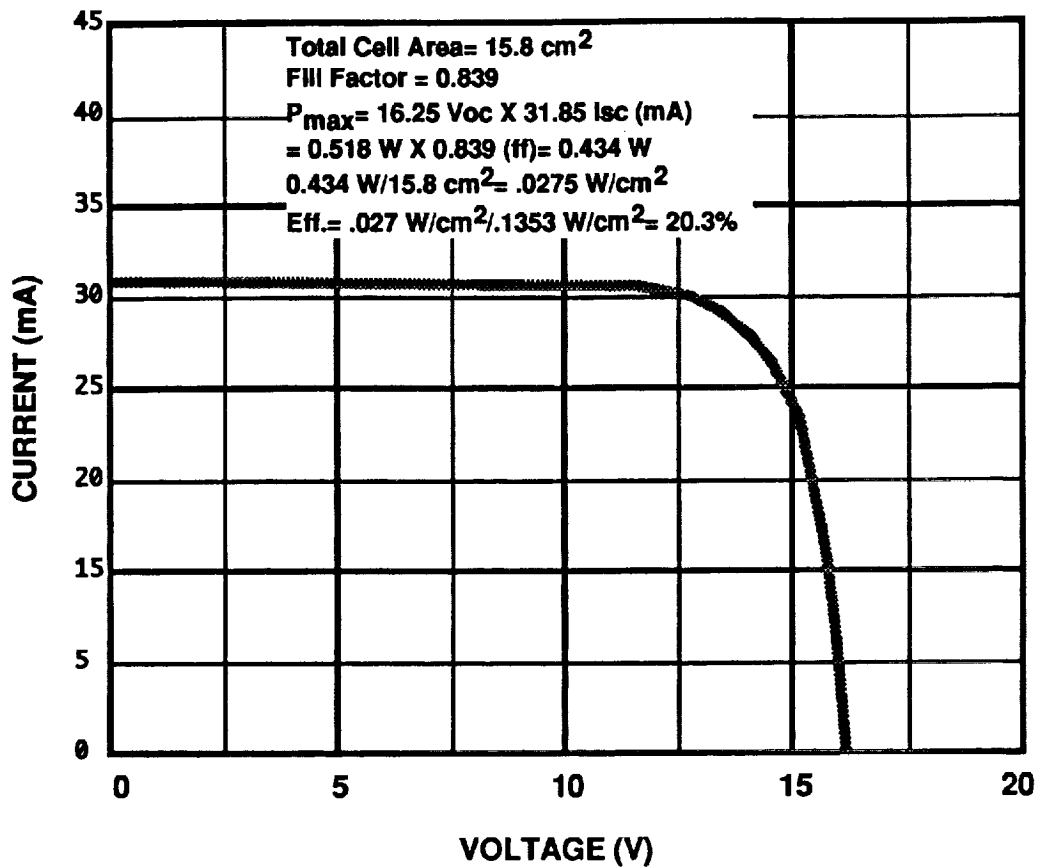


Figure 4: Current vs Voltage curve for EPI Ultrathin GaAs Cell

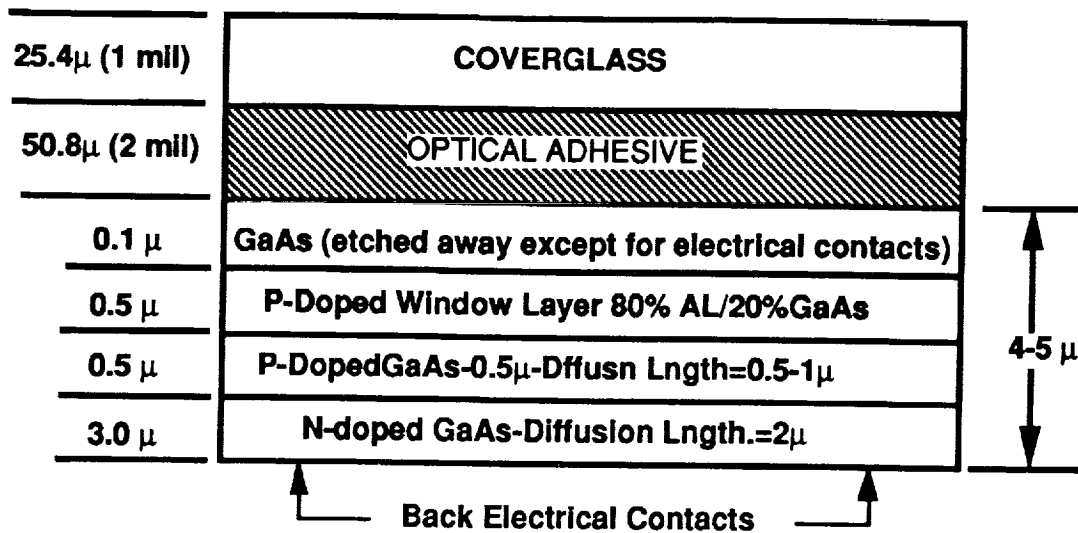
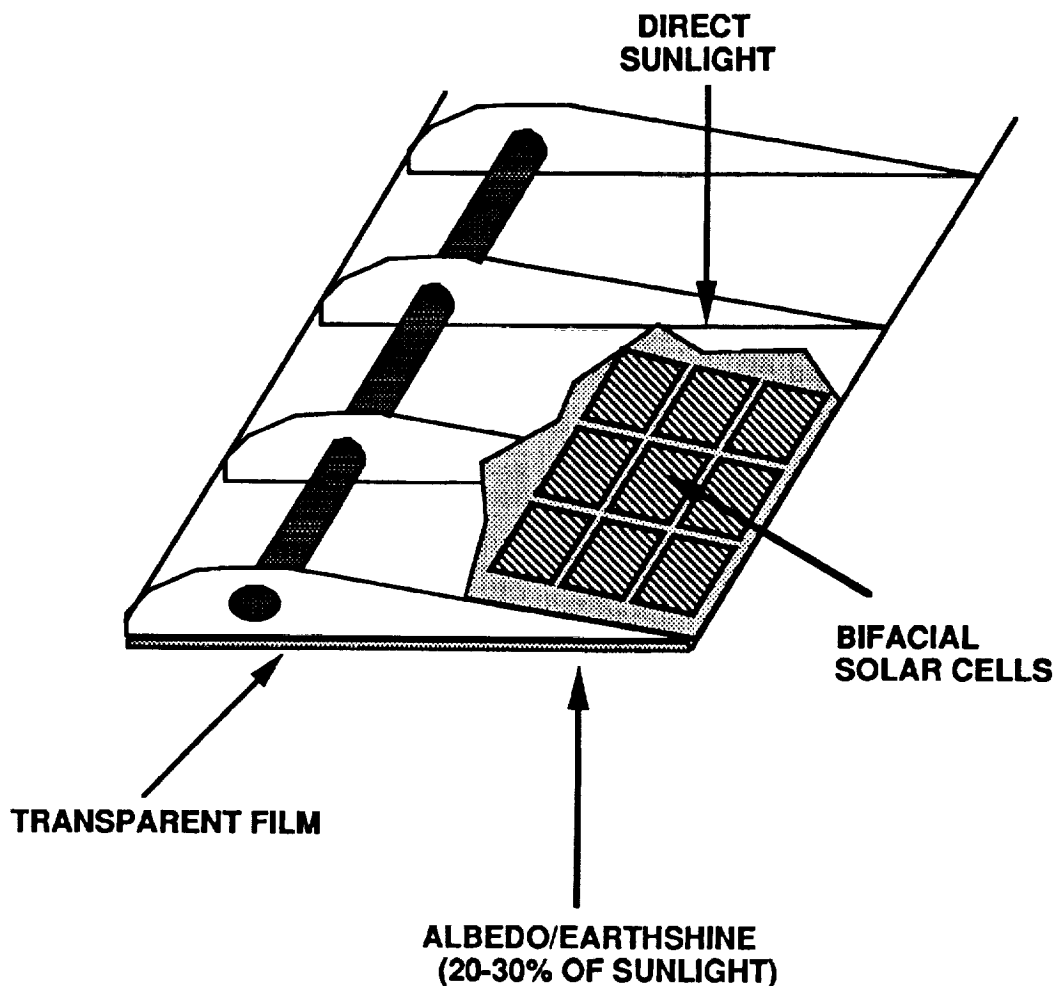


Figure 5: General structure of EML Ultrathin GaAs Solar Cell

5.0 Bifacial Solar Cell Sunlight Conversion: As previously described, bifacial solar cell performance is achieved when the solar cell is designed in such a way that it can receive and convert solar energy to electricity on either surface. In a UAV application, the wing-mounted solar arrays could be constructed in a manner that would allow the Earth's albedo, which is 20-30% of direct sunlight, to illuminate the lower surfaces of the solar cells, while the direct sunlight illuminates the upper surfaces.

The level of albedo intensity is a function of the Earth's local surface radiometric properties, but it is significant up to an altitude of 1000 miles, and intensified by snow and other highly reflective surface conditions. If employed, this "bifacial" feature could add about 20 to 30% to the conversion efficiency of the solar cell array, thus permitting it to be proportionately smaller and lighter in weight. Conversely, this makes the design of the wing structure more complex, thus requiring a trade study to determine the relative merits of bifacial power generation and its impact on construction complexities. Figure 8 illustrates how bifacial solar cell technology could be applied to a UAV wing construction.

**EML GaAs BIFACIAL SOLAR CELLS ARE
ULTRA-LIGHT AND EFFICIENT (24%)**



**Fig. 6: UAV Wing Construction Can Support Bifacial Solar
Cell Insolation**

6.0 Advanced Control and Sensing System: An advanced solid state control and sensing system would monitor the sunlight and maneuver the aircraft, when permitted, to maximize the solar-electric conversion process. Another feature of the automatic sensing/control system will monitor current loading and tachometer rotational speeds of the propeller motor drives. When the motors are developing higher torque than necessary to maintain the prescribed flight characteristics, more of the power delivered by the solar arrays will be switched to the battery recharging system for night operation. Under these conditions, when the battery reaches a fully charged state, portions of the solar arrays can either be automatically

switched off the load buses, or shunted to a thermal rejection radiator.. In this manner, during favorable weather conditions, the propeller motor life will be extended by minimizing over-current and voltage conditions. In summary, the solar power/control system will (1) drive the propeller motors during daylight hours; (2) replenish the battery to a fully charged capacity; (3) provide required power to the housekeeping and payload buses, and (4) optimize the torque of the propeller drive motors to conform to the conditions of maintaining the flight plan under variable weather conditions.

7.0 Summary: In summary, the use of extremely light-weight, highly-efficient, MOCVD GaAs solar cells, as described herein, represents an enabling technology which, in fact, allows solar-electric UAV aircraft to perform their mission, bearing reasonably heavy payloads, and of taking off in a conventional manner, climbing to high-altitude, and remaining aloft for long durations, whereas when they previously employed standard Si or GaAs cells they could not achieve these goals.

8.0 Conclusions and Recommendation: Although the adaptation and retrofitting of existing ultra-light aircraft to unmanned solar-electric flight is perhaps the most economic and expeditious method of near-term demonstrations, it will not bring the UAV community nearer to achieving the goals of high-altitude, long duration, stable and reliable flight. What seems to be required to realize these goals is designing an aircraft from scratch, using existing 1994 aerostructure, control, and propulsion technology transferred from the space and advanced aircraft industry, that can takeoff from the ground, climb to high altitude, and remain there in stable and reliable flight for extended periods. This, of course, requires the enthusiastic support and dedication of a strategic government/industrial alliance in which key national Superlabs and industrial firms not only identify desirable mission architectures, but fully collaborate in these efforts in a comprehensive national, and perhaps international, UAV solar-electric initiative.

POST-FLIGHT INVESTIGATION PROGRAMMES OF RECENTLY RETRIEVED SOLAR GENERATORS

Lothar Gerlach
European Space Agency—ESTEC (XPG)
Noordwijk, The Netherlands

Abstract

In 1993 two ESA solar power generators were successfully retrieved from Space.

- EURECA with its 10 panel rigid array in August 93, after 11 months in a 500 km orbit.
- One of the two flexible Hubble Space Telescope (HST) arrays in December 93, after almost 4 years in a 600 km orbit.

Both solar generators are undergoing separate Post-Flight Investigation Programmes (PFIP). These programmes cover investigations of all solar array (SA) components and mechanisms. Since both programmes have much in common, most of the component and material investigations are the same. Extremely valuable information on numerous essential subjects, such as atomic oxygen, radiation, meteoroid and space debris environment resulting damage, low cycle fatigue, material degradation etc. are expected to be obtained for both types of arrays. We will also be able to explain and understand the anomalies experienced on both solar arrays in orbit. The paper will outline both Post-Flight Investigation Programmes and will concentrate on reporting the first results and findings.

Keywords: Solar Arrays, Post-Flight Investigations, Thermal Fatigue, Power Degradation, Meteoroid Damage, Space Debris, Material Degradation

1 Introduction

The EURECA and the HST solar generators are the first solar arrays brought back from space after being exposed to the LEO environment for a significant duration (EURECA: 10.8 months, HST: 43.3 months) in a well known orbit and orbit orientation.

After its first mission the Eureka-SA was originally not planned to be investigated in detail. EURECA-SA was designed for 5 missions and the plan was to immediately refurbish it and prepare for a re-launch. However due to excessive power degradation during the first mission a post-flight investigation programme (PFIP) has been defined on short notice. EURECA-SA PFIP benefited from the work already done to prepare the HST-SA PFIP. Already in 1992, its preparation started and the content was optimised during the remaining period until retrieval. Unfortunately only one of the two HST-SA wings could be retrieved during the HST's first servicing mission (Dec. 1993) and brought back to Europe for investigation.

This paper is intended to give an insight into what is being investigated, reports on the preliminary results and what kind of results are expected, but concentrating on photovoltaic related issues only.

2 Post-Flight Investigation Programmes

It is of prime importance to the ESA to study these generators in detail. This provides a unique opportunity to study in depth the mechanical and electrical integrity of a retractable rigid panel array as well as of the flexible HST generator, following exposure to the severe LEO environment. It is expected to obtain extremely valuable and reliable information on numerous aspects, such as atomic oxygen (ATOX), meteoroid and space debris damage, low cycle fatigue, material degradation etc. It will also be possible to explain and understand the anomalies experienced in orbit. It will help to improve future solar arrays for both the rigid panel concepts and flexible arrays resulting in more reliable design and better protection against damaging effects such as random failures (e.g. short/open circuits) etc. The in-orbit performance of future arrays will be more predictable, the predictions more reliable and consequently the SA's can be designed and operated more cost effectively. The knowledge gained from the investigations is also important for the space debris and meteoroid community. The total surface of the retrieved HST wing and the EURECA solar-array is about 170 m², and provides a unique opportunity to study the craters of

impacting particles, also to assess the impacts and potential damage and to refine the current meteoroid, and debris models.

Both PFLIPs are co-ordinated and managed by ESA. The investigation team for the HST SA-PFLIP consists of all parties who were involved in the development and manufacturing of the solar arrays, i.e.: ESA/ESTEC, British Aerospace (BAe), Dornier, Contraves and DASA (formerly TST). For the EURECA-SA the team consists of Fokker Space & Systems, DASA Wedel and the same ESTEC team as for HST. They have the expertise for disassembly of the parts they have developed, minimising the risk that evidence is destroyed when handling or investigating the hardware. Where required, institutes and universities (i.e. for meteoroid and debris investigations) as well as the European Space Tribology Laboratory (ESTL) will be involved in the investigations and evaluations of the flight hardware. Most of the material investigations are planned to be done in the ESTEC Materials division.

The key guidelines of these investigations are to ensure that no evidence is destroyed during SA storage and handling, or when samples are being removed. Both PFIPs are now in progress. The EURECA-SA activities will be completed in Aug. 94. The HST-SA PFIP is expected to be completed in the first half of 1995. In May 95, the results will be presented at an HST-SA PFIP symposium at ESTEC.

Although both generators are different in their mechanical construction (rigid panels and flexible roll-out blankets) they have a lot in common. The solar cell assemblies are the same (only cell dimensions are different, table 1) and most of the materials and components used for the electrical network are the same.

Base material	- Crucible crown silicon	Silicon thickness	- HST: 250 μ m, EUR 150 μ m
Base resistivity	- 10 Ohm cm	BOL SCA efficiency	- 14% (1AMO, 25°C)
Junction	- n-on-p shallow diffused	SCA absorptivity	- 0.75 (unloaded)
Back surface field	- p+ doping	SCA emissivity	- 0.83 (hemispherical)
Back side reflector	- Aluminium layer	Cover slide material	- Soft Boro-silicate base glass (CMX)
Contact system	- Ti(Pd)Ag	Cover slide thickness	- 150 microns
Anti reflective layer	- TiOx	Adhesive for cell bonding	- Silicon, DC 93500 + Primer
Surface roughness	- ≤ 1.5 microns	Cover dimensions	HST - 21.0 mm x 40.5 mm
Solar cell dimensions	HST - 20.8mm x 40.2mm	Eureca, Charge	- 21.0mm x 59.7mm
	Eureca, Charge - 20.8mm x 59.4mm	Eureca, Load	- 27.1mm x 50.4mm
	Eureca, Load - 26.8mm x 50.1mm		

Table 1: Solar cell assembly (SCA) characteristics

YEARS	Isc	Voc	Pmax	Vmax	Imax	I(350)	fluence
0	0.33317	0.60480	0.15409	0.50500	0.30513	0.33217	BOL
1	0.32930	0.59330	0.14911	0.49540	0.30099	0.32802	8.480e+12
2	0.32644	0.58480	0.14554	0.48834	0.29803	0.32470	1.589e+13
3	0.32417	0.57950	0.14329	0.48390	0.29611	0.32220	2.222e+13
4	0.32261	0.57580	0.14181	0.48080	0.29494	0.32071	2.748e+13
5	0.32141	0.57340	0.14075	0.47870	0.29402	0.31965	3.166e+13

Table 2: SCA performance data (HST size)

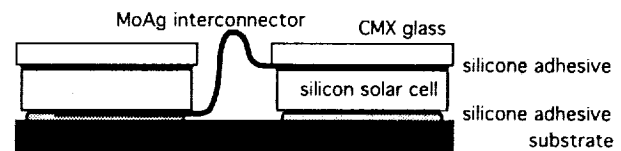


Figure 1: Interconnected SCA

Compared to EURECA, HST SA-1 investigations have the advantage that sufficient hardware can be provided for tests and investigation because there are no plans to re-use the first HST solar array. It is foreseen to completely disassemble and study the mechanisms. All blanket buffers and at least one SPA are planned to be completely dissected and analysed. The remaining parts will be subject to specific examination with small areas cut out as required.

The first activities in the programmes were the in-orbit inspections. Great emphasis was given to the photographic and video coverage during retrieval covering all SA areas and special close-ups of SA-highlights. A similar intensive photographic coverage were carried out after shuttle landing as well as initial insulation and continuity checks. Special attention will be given to the relative position of moving parts and other key features.

Based on previous experience and knowledge the investigation began at the earliest possibility at KSC, where reference samples were cut from both solar arrays, sealed in dry nitrogen and hand-carried to Europe for test and immediate investigation.

A further objective of the PFIP is to study changes of material properties and effects having a direct influence on SA power generation.

Silicon adhesive has largely been used for the blanket protection against ATOX. Those protective layers will experience changes in their material properties and their thermo optical characteristic. This is caused by the radiation environment including UV radiation, thermal cycling and attack by ATOX. Corresponding material investigations will study these type of synergistic effects.

As may be seen from the design description HST-SA has identical substrate surface coatings (DC 93500, fig. 6) on the front and rear side of the flexible blankets. Since the solar cell side was always sun oriented, the effect of the contribution of UV radiation to the synergistic environmental effects can be evaluated.

UV radiation also tends to cause darkening or reduction in transparency of the transparent silicone adhesives if they are not shielded. DC 93500 is used for gluing the cover slides to the solar cells and a darkened adhesive will reduce the power generated. One important question is, did the CMX cover glass sufficiently shield the adhesive from UV radiation?

Due to the low operation solar-cell string voltage of 37 volts (\approx 100 volts in Voc) plasma interaction or plasma sputtering is not expected to have an influence on the solar array hardware, but nevertheless it will be checked.

It is of interest to check the silicone adhesives for surface hardening and embrittlement, including depth effects, and to which degree the polymerisation chains have been changed, and also if changes caused the unbonding of the glass-fibre cloth from the Kapton foil (fig. 6 and 11).

How well the MoAg interconnector and its interconnections withstood the aggressive environment will be investigated. Are they showing signs of thermal fatigue (loop and weld areas) and to what extent did the silver erode in the ATOX exposed areas?

Comparison between shielded areas (e.g. inside stress relief loop) with respect to the surfaces exposed to the ram direction of the ATOX flux, and how the thermal movement of the interconnector influences the silver erosion are important questions to be answered. The clamped and embedded parts of the interconnectors (e.g. between cover slide and cell) will allow the study of possible creep erosion effects.

Further investigations being performed in the framework of the PFIPs are presented in section 4 together with preliminary results.

3 Solar-Array Design Description

The build-up of the two solar generators are only described to the extent which is needed to understand this paper or expected to be of interest to the SPRAT community. This implies that details of the deployment and retraction mechanisms are not discussed in this paper. For more design details refer to [ref. 1 to 6].

3.1 HST Solar-Array Design

The Hubble Space Telescope (HST) was launched into a 614 kilometre low earth orbit (LEO) on 24 April 1990. The HST is a joint NASA/ESA project. ESA provided two major elements towards the project one being the Solar Arrays (SA). Under the prime responsibility of the European Space Agency, a group of European contractors led by BAe, with DASA (formerly TST) providing the flexible blankets, have developed and built the largest flexible solar generator to date.

It comprises two double roll-out solar array wings (fig. 2, 3) which are deployable and retractable. Each wing is equipped with two solar array blankets (2.4m x 6.34m) carrying the solar cells which are protected from each other by an embossed Kapton cushion whilst they are stowed on a common storage drum.

To unfurl the blankets an actuator motor for each wing drives the four bi-stem booms out (two per blanket, fig. 4), which in turn draw the blanket from the drum by means of a spreader bar fixed between the ends of the two bi-stem booms. The first set of solar array wings were successfully deployed on 25 April 1990 with the Space Shuttle Discovery and HST in a 614 km orbit.

The HST-SA is designed to survive intact for at least five years in a \approx 600 km low earth orbit (30000 cycles, \pm 100°C). HST-SA is required to deliver at least 4.4 kilowatts of electrical power at 34 volts after two years in orbit. On 5 Dec. 93 (day of SA retraction) the solar array delivered 4.8 kW which is 6 % above predictions. Each of the four solar array blankets is made up of five identical power generating sections, known as the Solar Panel Assemblies (SPA, figure 8, 11) and four Buffer Assemblies which act as mechanical and electrical interface to the deployment mechanism.

Each of the power-generating SPAs (1.1m x 2.4m) are equipped with 3 solar cell strings, each having 106 solar cell assemblies (SCAs) in series, two of them with 8 single solar-cell rows in parallel and one of them with 7 single cell rows in parallel. The single cell rows for each string are connected via MoAg tapping bars in groups of 14, 15 or 16 cells. All of these groups are protected by flat solar cell shunt diodes (Si wafer 2 cm x 2 cm with Au coated Ag in-plane interconnector and CMX cover) for shadow protection. They are

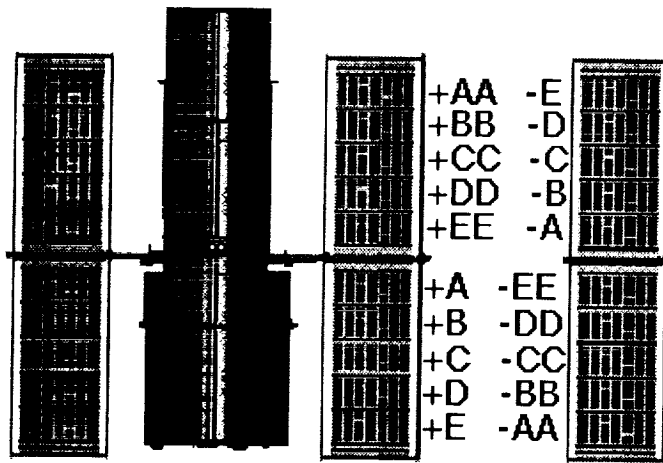


Figure 2: Solar array hot case configuration

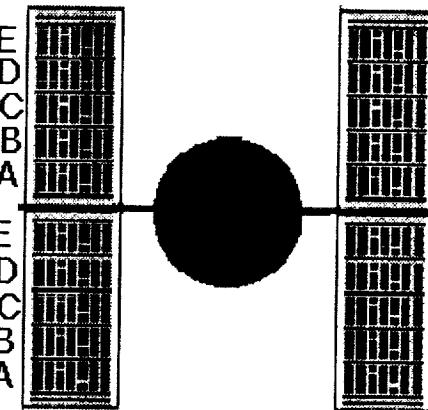


Figure 3: Solar array in cold case configuration

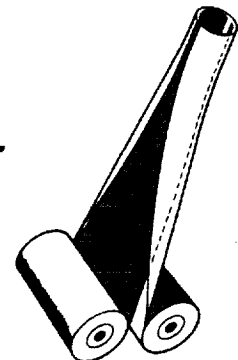


Fig. 4: Bi-Stem Boom

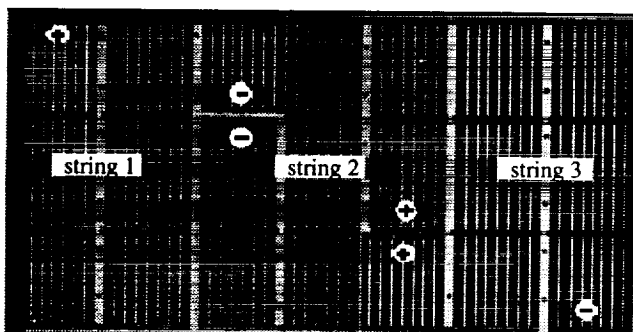


Figure 5: Solar-panel assemblies (SPA)

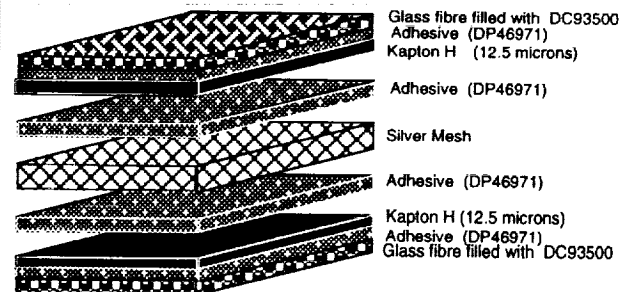


Figure 6: Exploded view of the 0.21 mm - thick, flexible carrier substrate of the SPA, including 50 micron-thick silver mesh for power transfer

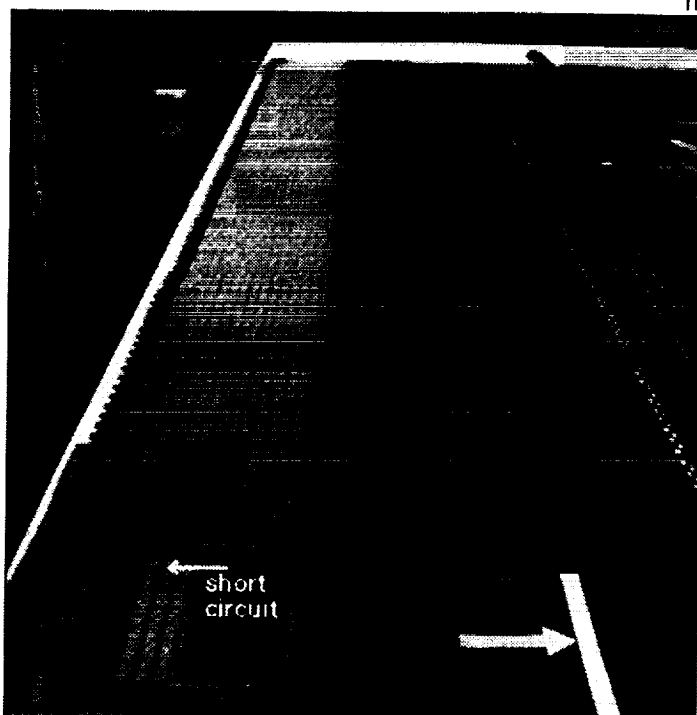


Figure 7: Upper IBA of STSA-1 with Ag power tracks for string connection, discolouration due to UV and location of anomaly

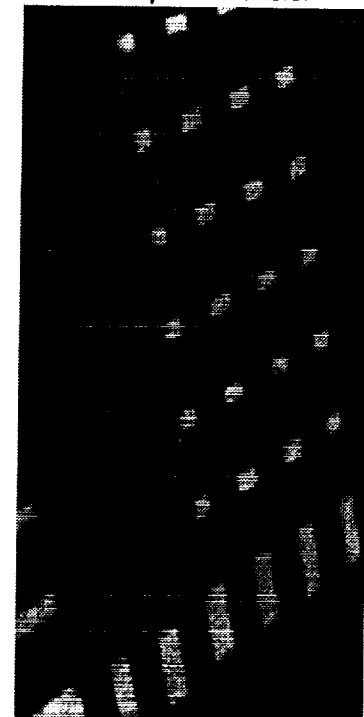


Figure 8: Close-up of short circuit location (rear side)

mounted in the tooling gaps between the solar cell strings. On the Inner Buffer Assembly (IBA), figure 7, the individual solar cell strings are electrically connected by means of 75 micron thick silver foil strips to main and redundant connections for each SPA. They are routed to a flexible printed circuit board which serves as the interface to the harness attached to the deployment mechanism.

The basic carrier substrate of the flexible blankets consists of a 210 μm thick atomic oxygen (ATOX) resistant glass fibre/Kapton compound (Fig 12).

The power is provided by 48760 solar cell assemblies (table 1, 2 and fig. 1) consisting of silicon cell, cover and MoAg interconnector. They are bonded with silicone adhesive RTV-S 691 to the 20 SPA substrates.

3.2 EURECA Solar-Array

The European Retrievable Carrier (EURECA) is a unique, re-usable, user oriented space facility developed to meet the needs of both scientific and application oriented users. The Eureka solar array consists of 2 fully interchangeable wings of 5 panels each (fig. 9, 10).

The panels consist of a rigid aluminium honey comb structure with carbon fibre face sheets of 1.4 m width and 3.4 m length. The thickness of the substrate is ≈ 22 mm (fig. 11).

The panel size requires 6 hold down points of 100 mm diameter in-side the panel area for stowed conditions and 4 edge brackets for the deployment mechanism. On the front side the panels are equipped with the solar cell network bonded with the standard silicone adhesive RTV S-691 to an insulation layer (fig. 11) which protects the structure against the atomic oxygen environment. For the solar cell layout ATOX resistant MoAg interconnector (Ag-coating required for welding) have been chosen. In the area exposed to the environment the silver has been removed from the cell interconnector (except Panel F5 which was planned to be a qualification panel). On the rear side an Aluminium/Kapton/ITO layer is bonded to the panel for protection against ATOX erosion and to improve the thermo-optical behaviour of the panels.

The power conditioning design required that the panels are split into a load (main bus) array part and a charge array part as shown in figure 12.

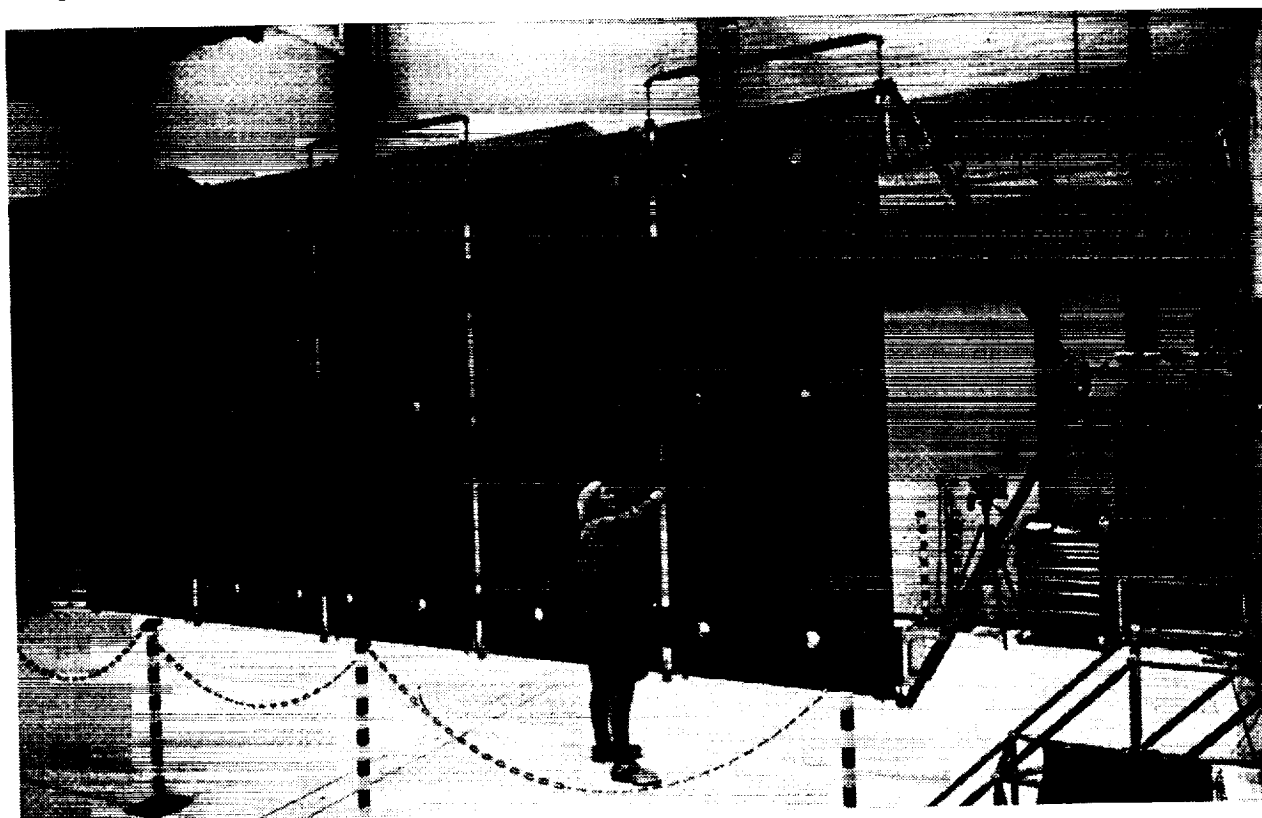


Figure 9: EURECA-SA wing after retrieval at Fokker Space & Systems

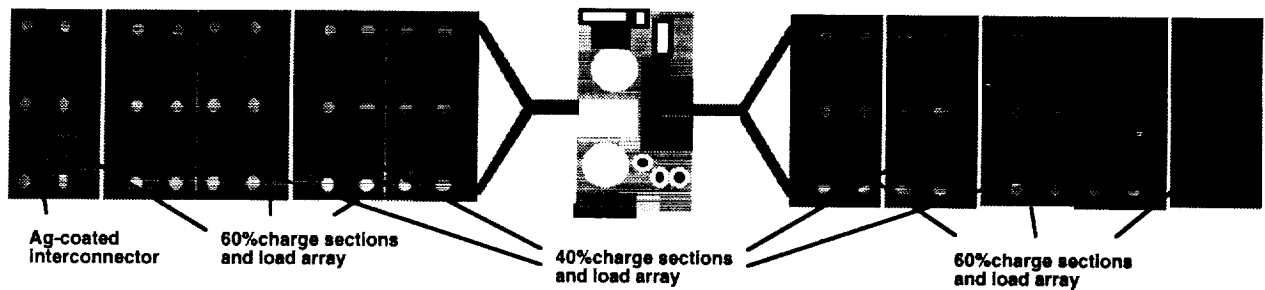


Figure 10: EURECA solar-array configuration (deployed: 1 Aug. 92, retracted: 24 Jun. 93)

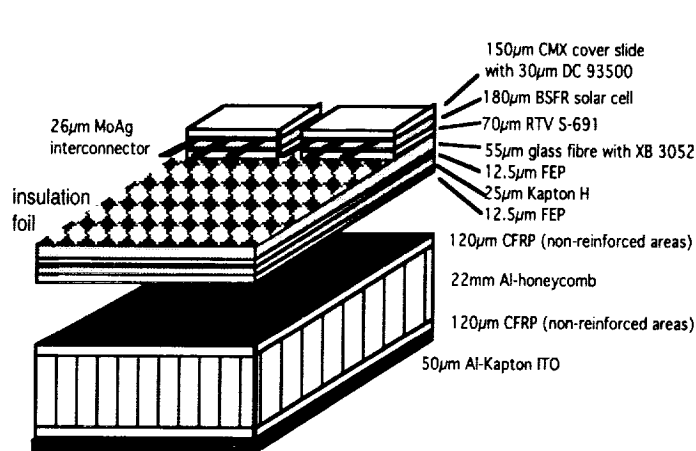


Figure 11: Panel cross-section

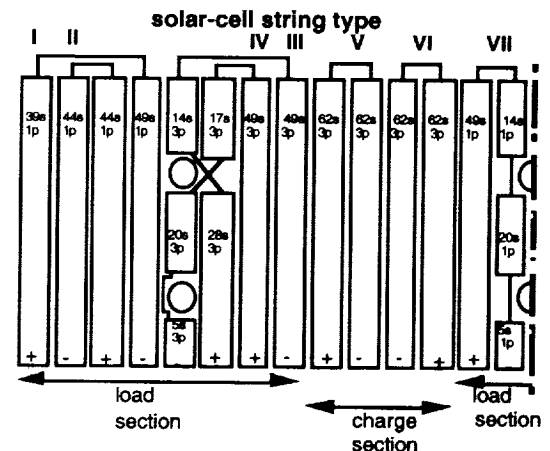


Figure 12: Solar cell string layout of solar array panel (panel half)

Each panel is equipped with 4 charge strings with 124 cells in series (124s). These charge strings are built up of 3 single cell rows with intermediate parallel connection via MoAg - tapping bars in groups of 6 to 12 cells. All these groups or shunt intervals on panels F1, F5, F6 and F10 are protected by flat solar cell shunt diodes (0.2mm x 20mm x 40mm) against local hot spots since shadows were possible on those panels. To reach the optimum cell packing factor the shunt diodes are located on the rear side of the panels.

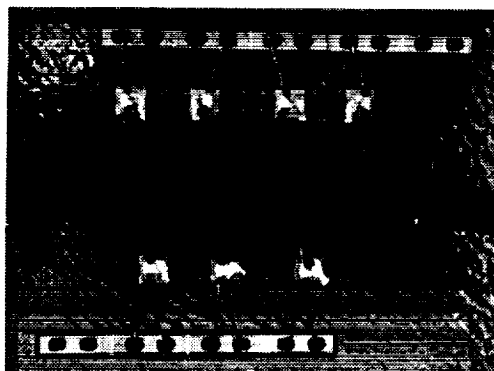
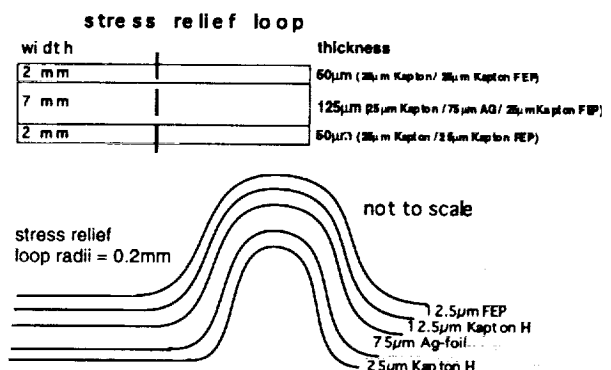


Figure 13: Wiring Collecting Panel (WCP) arrangement - Figure 14: Design details of WCP



The build-up of the load array is following the same shadow protection concept with its shunt intervals but different number of cells per string in parallel. Due to geometrical constraints the cell dimensions for the load array are different to the charge array type.

Load array string are build-up with 91 and 88 solar cells (26.8 mm x 50.1 mm), respectively, connected in series to provide the required power of 2500W after 1 year at 30 V at any condition during the sun-lit phase.

Each of the solar cell sub-strings (Fig. 5) or cell matrices is equipped with silver bus bars (coated with RTV S-691 for ATOX protection) at their ends to form a solar cell string. The solar array strings of the load- and charge array are separately wired through holes in the panel to a wiring collection panel (WCP) on the panel rear side where the individual solar cell strings are connected in parallel (solder connections) to form electrical sub-sections. The WCP design and wiring connection concept is given in figures 13 and 14.

4 Post-Flight Investigation Programme - First Results

4.1 HST-SA In-Flight Power Generation Anomalies

During its almost 4 years in-flight operation there were 5 power generation related anomalies on the 4 blankets. Two disconnected solar cell strings from which one recovered, a short within a solar cell string of SPA -CC (fig. 3) which also recovered, a short between a power circuit and a temperature sensor circuit and a short between two SPAs and structure. The intermittent short circuit on SPA -CC and the last anomaly are on the retrieved wing (-wing or -V2 wing).

Until now there are no results available on the -CC anomaly, however the last failure seems to be traced. The failure appeared on 5 December 1993 while astronauts attempting to close the -V3 Aft Shroud door during HST's First Servicing Mission (FSM), EVA-1.

Having reviewed the anomaly history of both solar array wings together with the recent in-flight data it was concluded that there was a short from the positive rail of SPA-C (SA section 4) to the return rail of SPA-E (SA section 3) and a short from the newly formed SPA -C/-E circuit to structure (fig. 15).

The above shorts are theoretically possible at several locations, due to the physical layout of the blankets. This is limited to SPA-C and the IBA of the upper blanket (-wing). Other theoretically possible failure locations (PCU, diode box, harness) were investigated but the in-flight data was never in agreement with possible failure scenarii.

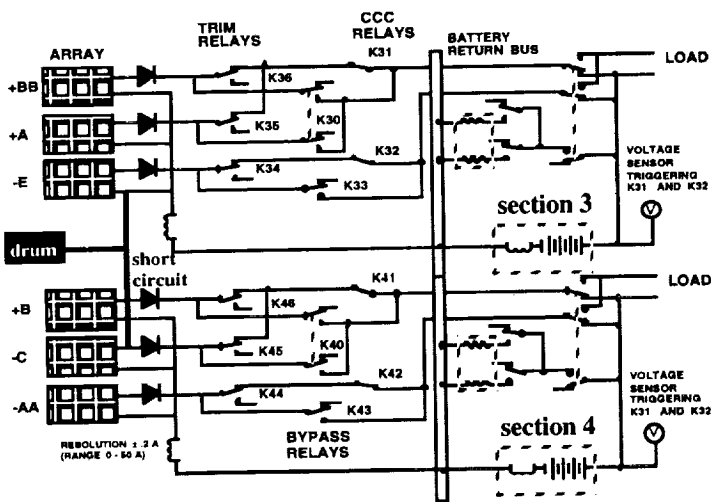


Figure 15: STSA-1 Section 3 and 4 logic with short circuits indicated



Figure 16: Drum with cut-out and burn mark

After HST SA-1 retrieval electrical health checks were performed at KSC and at BAe. There was a short circuit between SPA-C and -E as well as low resistance between SPA-E to ground. The visual evidence was only available after completion of flash testing and after disassembly of the blankets from the drum. There was a burn mark on the IBA where the SPA-C positive rail crosses the return rail of SPA-E (fig. 7 & 8). The cross-section of the IBA substrate is the same as for the SPAs (fig. 12), except that the Ag-mesh is replaced by: 75µm thick silver strip/ 25µm Kapton/ 75µm Silver strip. The location of the burn mark on the IBA is more visible on the rear side of the blanket at the interface to the flexible harness. This flexible harness is routed to a printed circuit board (PCB) located in a cut-out slot of the drum (fig. 16). Where the IBA is in contact with the edge of the cut-out, the burn mark on the IBA coincides with a burn mark on the drum.

This indicates that the observed shorts during FSM are on the upper blanket at the expected locations, showing also that both shorts (between SPAs and the short to ground) were caused by a single failure.

Presently the following failure modes and conditions (single and combined) are being investigated:

- a) Sharp edges on silver wiring strips due to manufacture by guillotine.
- b) Manufacturing induced effects (e.g. pre-damaged, torn/bent silver bars, foreign metal inclusion)
- c) Wear of IBA, and flexible harness and cushion surfaces caused by cut-out edge and PCB cover.
- d) Creep of Kapton (25 micron insulation between power tracks) due to local pressure on the IBA and by the interface to the PCB cover.
- e) Thermal cycling effects.
- f) Electrical fields.

All non electrical anomalies which were observed are not discussed here but most of them (e.g. tension sensor failure, SA jitter and stick-slip effect) are described in ref. 7.

4.2 EURECA-SA In-Flight Anomalies

Since 14 Aug. 92 (day 227) the solar array has continuously experienced anomalous power degradation due to unexpected in-orbit failures (one short circuit and numerous open circuits). Two examples are given in the following:

On day 263 of 1992 it was observed that during the first minutes after entering eclipse the current sensor of section 2.2 indicated a current from the battery to the solar array (no blocking diodes were put between the SA and battery circuits). Figure 17 shows the actual current profile. The current profile with its obvious sensitivity to temperature changes is typical for a short circuit. An evaluation of the in-orbit data indicated that the short is present at about half the string length of a solar cell string (40% branch of section 2.2) with three solar cells in parallel and 124 cells in series.

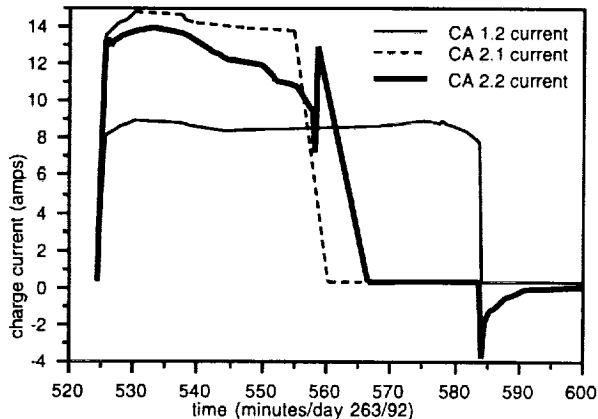


Figure 17: Charge current profile at time short circuit

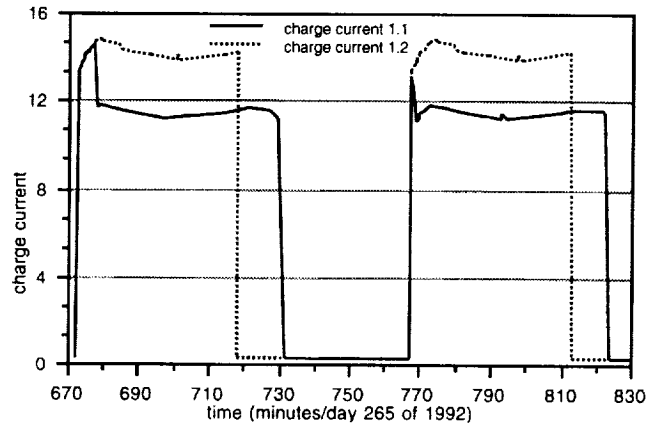


Figure 18: Orbit with first open circuit failure

After retrieval a large burn mark was found at the expected short circuit location on panel F7 (fig. 19). The size of the burn-out area is unexpectedly large and indicates that very high temperatures must have occurred at this spot ($>2000^{\circ}\text{C}$). In some areas the glass from the cover and the silicon is melted. Adhesives and insulation foil are carbonised. X-ray photographs also reveal that the honeycomb of the panel has locally been damaged below this area. Experts on arc progression are involved in the investigation of this unusual burn mark. The triggering mechanism(s) of the burn mark is not yet found. Tests are planned to reproduce this anomalous event.

Between 21 Sept. 92 (day 265) up to the end of the mission a certain number of open circuits were observed, first in the charge array sections and later also in the load array. From 21 Sep. 92 onwards sudden drops of ≈ 1.5 and ≈ 3 amps were observed in the charge current profile (1.5 amps corresponds to the current generated by one solar cell charge string). In the beginning wing 1 charge sections were affected and only towards the end of mission wing 2 solar cell strings started to fail. In some cases the loss was immediate, in other cases the string toggled before the single or double string was lost. In all cases the first drop in current generation was within the first three minutes after entering orbit day. A typical sample of recorded current profiles, showing an open circuit failure is provided in figures 18. The cumulative charge array power loss during the mission is given in figure 21.

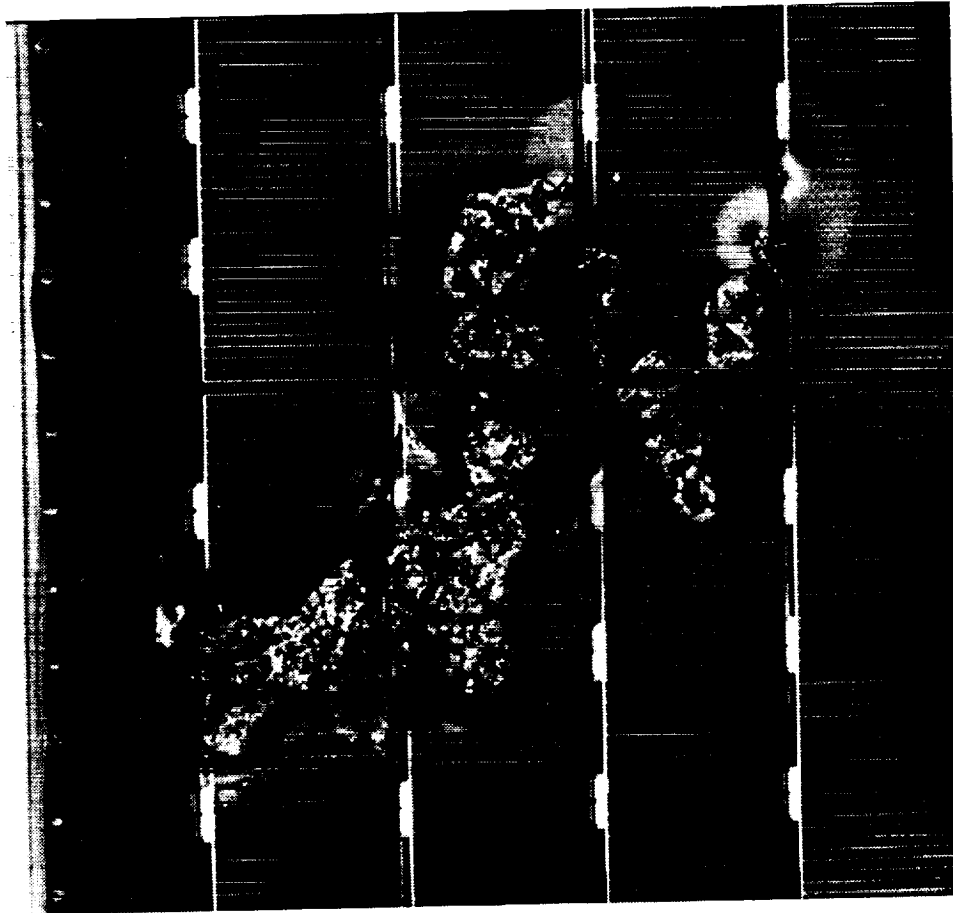


Figure 19, left: Burn mark at short circuit location (shown area is $\approx 10 \text{ cm} \times 10 \text{ cm}$)

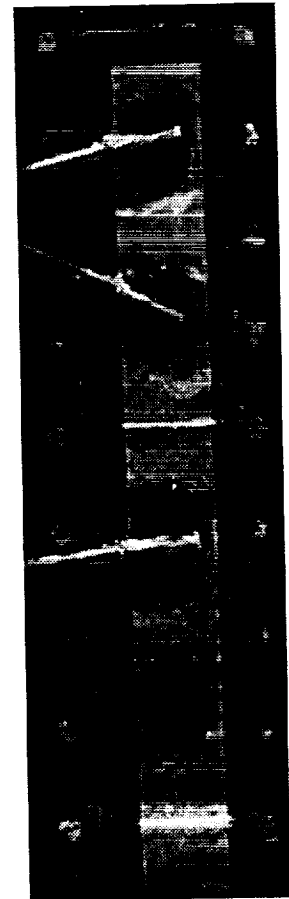


Figure 20, right: Part of a WCP showing early effects from arcing in stress relief loop

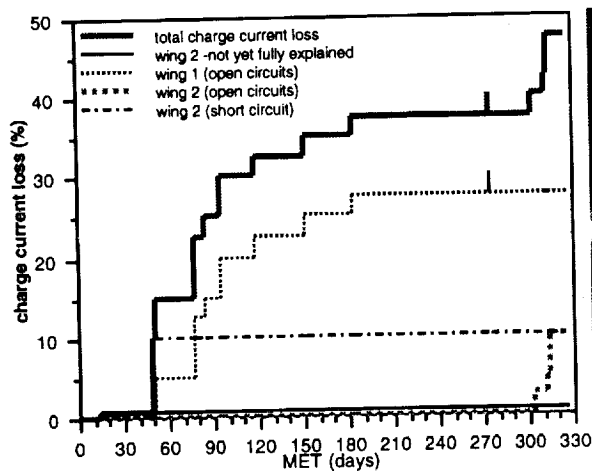


Figure 21: Cumulative charge array power loss during the mission



Figure 22: Completely destroyed WCP

Due to the numerous anomalies in the charge array it was also expected that in the load array several solar cell strings could be lost. There is no easy method to measure the load array output because the required power from the load is most of the time below the actual capabilities of the load array and the string/section currents are not measured. Only at times of high power consumption, above the capabilities of the load array, the actual load array performance can be roughly calculated using the total load current and the delta

current to be provided by the batteries. The last possibility was in Jan. 93, shortly before all payload experiments were successfully completed. It could be calculated that at this time about 24 % of the load array capability has been lost.

From the investigation into the loss of solar cell strings it was found that the power loss is a result of failures in the wiring collecting panels (silver bus bars) located on the rear side of the panels connecting solar cell strings in parallel. The failure is a common mode failure occurring in all WCPs. The failure occurred in the stress relief loop and all parties involved in the investigation agree that the failure is a fatigue problem due to inadequate bend radii in the stress relief loop. Figure 20 and 22 give an indication from the degree of damage seen on the WCPs. It covers the complete range of damage from broken loops (only detectable with X-rays) still conducting current, first sign of arcing until complete destruction of the WCPs with short to panel structure. Plasma and arcing experts will also study this type of arc progression.

The reason why this has not been detected prior to launch is, that the WCPs were neither tested in a fully flight representative configuration nor were the loops inspected after test to the required detail (X-ray). However, this failure would be easy to correct for a re-flight. The failed components can easily be removed and replaced by reliable WCPs.

Another clear early conclusion from the WCP related investigation is that the acoustic test performed only on wing 1 cannot be made responsible for any of the failures. If a proper design would have been chosen the effects from the acoustic test would not be visible. In our case, we are only "lucky" that we had this weak design allowing us to correlate the acoustic test and the launch environment with fatigue effect as a result of in-orbit thermal cycles. This helps us for the future to better consider the total mechanical stress on the electrical network.

However, in light of the extent of the failures, all payload and mission objectives were met. The flexible nature of the mission planning and payload together with adaptable operational methods allowed work around solutions to be incorporated as the mission and failures progressed.

4.3 Power / Solar-Cell Degradation Studies

For all satellites, reliable solar-array power degradation studies are needed, and it is important that all damaging mechanisms are considered in the power budget predictions. The goal is to fully understand these power degradation effects. This gives us the chance to minimise their effects on the solar array during the design phase, or even eliminate them in some cases. For this reason great emphasis will be put in studying all the negative impacts on electrical power generation.

Extensive radiation studies and tests will be performed to predict the total accumulated fluence and evaluate the effects of electron, proton and photon radiation on the solar-cell assemblies.

The most interesting parameters for the Space Telescope cell type, in combination with the 150 micron thick cover and resulting degradation characteristic for 1MeV electrons/cm² are shown in table 2.

These are well known and well established characteristics for solar cells radiated with 1MeV electrons. The radiation environment is also well known, but the uncertainty is, if the proton and electron spectrum is correctly converted to the 1MeV electrons. Ground tests for comparison will be done refining the power predictions and power verification method for future solar arrays.

When, solely the effects of radiation are used to evaluate the power during lifetime the resulting total degradation would be under-estimated.

The monitoring of in-flight generated power at the operation voltage does not allow to differentiate between power degradation caused by radiation and other damaging effects. Thus only a total power reduction is observed. The solar cell efficiency also changes with the solar cell operation temperature. Parameters which alter the array temperatures are the cell efficiency itself and the thermo optical properties of the materials used on the outer surfaces of the array.

In addition to the natural environment (radiation temperature, ATOX) further potential impacts on the power output have to be considered. These are solar cell orientation errors, solar cell mismatch, meteoroid and space debris bombardment and random failures, which include open circuits as well as short circuits (not caused by meteoroid and space debris). These effects are considered in the form of current and voltage loss factors applied to the solar cell network. Except for the sun intensity the individual current or amperage

loss factors typically considered were based on ground tests and best engineering estimate, but worst case and never expected to occur. Those used for the HST solar generator are summarised in table 3.

Years in Orbit	BOL	1	2	3	4	Table 3: Current or amperage loss factors for HST-SA deployment on 25th Apr. 1990
Calibration Error	.980	.980	.980	.980	.980	
SCA mismatch	1.00	.998	.996	.994	.992	
Orientation Error	.996	.996	.996	.996	.996	
Random Failure	1.00	.982	.970	.960	.950	
Meteoroid/Debris	1.00	.995	.990	.985	.980	
Total	.976	.952	.934	.917	.901	

The power profile prediction for one typical SA section and actual in-flight data are given in figure 23. After 43.3 months in orbit in-flight data show currents 6% above the prediction.

The in-flight power generation of HST-SA is continuously monitored and recorded. However, only readings taken in "cold case" configuration (fig. 3) are suitable for the power degradation studies. Others solar array slew angles or HST off-nominal roll angles result in undefined reflections or shadows on the solar array. Due to the numerous reorientations of the HST this for the power verification ideal configuration is not frequently approached and also angles close to this configuration had to be used to monitor the power degradation. Additional power generation due to reflections can reach 4 % (total array output).

It is getting increasingly important for economic reasons to adjust these worst case factors, which normally cover all solar array eventualities, to more realistic degradation factors. STSA-1 offers us the possibility to investigate which losses were considered too pessimistic or too optimistic, or may be there are others to be considered in the future.

For example, the effect of particle impacts on the power generation can be checked by a laser scanning the surface of the SCA. The distribution and number of impacting particles can be provided by the corresponding numerical models.

A darkening of cover slide and its adhesive by UV, if any, will be verified by means of spectral response measurements

Reliable power/solar-cell degradation studies can only be performed with the in-flight results from HST-SA because there was no measurable degradation on the EURECA-SA when measuring on solar cell string level using the Flasher Test Equipment. Eureka power output measurements compared to pre-flight data were between +5% and -1.6%. With the known uncertainty due to electrical contact difficulties, all results are within the measurement accuracy of flash test (+/- 1%).

For HST a LAPSS (flash-test) was performed on the integrated solar array blankets. The results are shown in figures 24 to 26 together with the pre-flight data. The Pmax data were intentionally left out because at this test level they are not suitable for power degradation studies. There are too many unknowns due to blanket wiring and harness. The results for the currents are very homogeneous. There are insignificant small variations between the SPAs. The measured degradation for the two operation points (short circuit and at 34 volts) is 3%. This is including all cell damages (particle impacts etc.). The results are as expected, but not in line with the worst case predictions. The worst case relative degradation outlines 10% for these operation points.

For the open circuit voltages the degradation is smaller than expected. It varies between 0.2% and 0.7% (fig. 25, due to the short in SPA -C no measurement available for SPA -C).

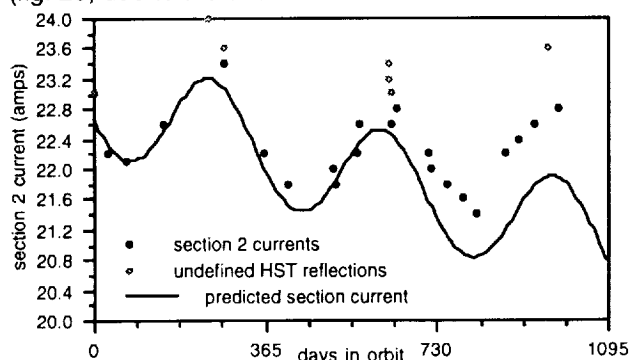


Figure 23. Power profile of SA section 2

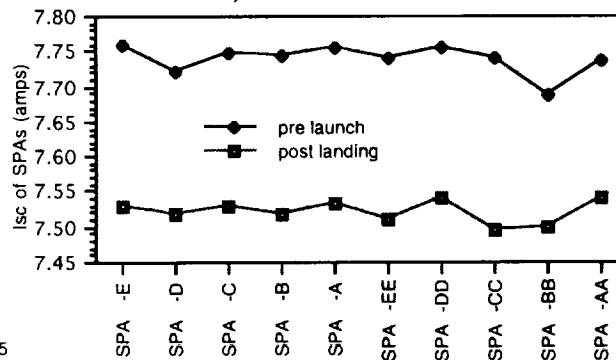


Figure 24. Short-circuit current comparison

Although above results give already a clear indication of the much smaller cell performance degradation when compared with the worst case predictions, more detailed power measurements are planned on SPA level, string level and on individual single cell rows in shunt intervals. The results will be compared with pre-flight data which partly consider the initial matching classes distribution for individual single cell rows in shunt intervals.

Two different standards (JPL ST-05, and Telecom 10/5) were used in parallel during the HST-SA1 programme. Because of the low degradation it will be difficult to reliably assess the actual level, but it will be attempted. To evaluate the relative degradation is much easier.

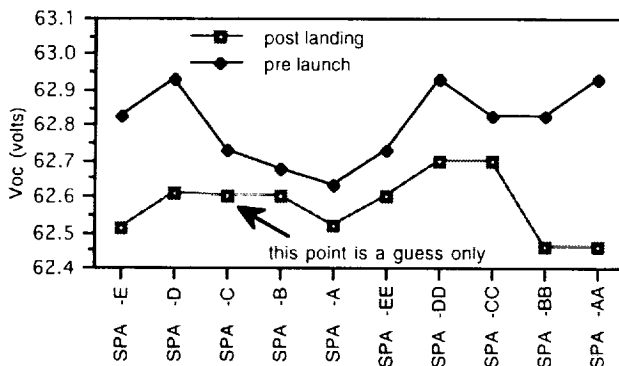


Figure 25. Open-circuit voltage comparison

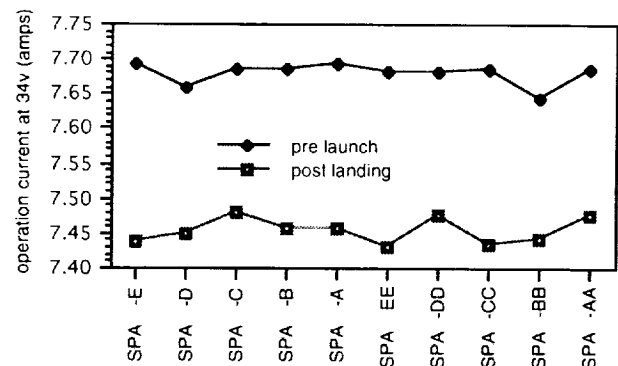


Figure 26. Operation (34v) current comparison

4.4 Results from Material Investigations and General Observations

HST-SA

The blanket compound seems to be in a good bonding state. No delaminations of the carrier substrate were visible from the front side. This is planned to be verified by a vacuum test on a small coupon sample.

The piano hinges are in good shape. No rupture of hinge loops were observed. In one case the hinge rod penetrated the sliding protection substrate (≈ 1 cm). There will be a detailed inspection of the contact point of the hinge rod and the protection substrate, and a measurement of the force needed to push the hinge rod through the restraint tab.

No delamination of the GFRP stiffeners have been observed.

The RTV S-691 coatings show different degrees of discolouration. This is very obvious where the stiffeners and meander bars are next to each other. The coatings on the stiffeners are generally much darker than the coatings applied on the silver bus bars or meander bars. A thickness measurement of the coating might explain this difference.

The SCA interconnectors are in good shape. The colour when inspected with unaided eye is similar to the interconnectors seen on EURECA. Since Eureka had the silver removed in the ATOX exposed areas it would be no surprise when on STSA the silver in the ram direction is completely gone. ESTEC Materials division is taking care of this investigation.

The shunt diode assemblies are in good shape. There is no obvious darkening of the DC 93500, but spectral response measurements will still have to be made (i.e. on SCAs). Considering that the gold coated in-plane diode interconnectors were exposed to almost 4 years in the LEO environment they are looking very good. The gold coating was obviously efficient and provided sufficient protection against ATOX.

DC 93500 was also used as ATOX protection for the flexible substrate (fig. 6). Its darkening under UV light is known and it was no surprise to see a strong discolourations of the blankets. The most pronounced discolouration can be seen on the upper IBA (fig. 7). The portion which was exposed to UV light is very dark over a short stripe of ≈ 10 cm, at a location where there were reflections from the cushion roller. Temperature effects on the discolouration are also seen at the location on top of the power tracks. Other areas were less dark. The unexposed areas were almost as new and had the original colour.

Contrary to the Eureka-SA, no effects from arcing have been observed on the front side (unaided eye inspection). The rear side is not yet accessible. In the frame work of our PFIP potential arcing areas will be investigated in detail.

EURECA-SA

As for HST-SA there are no further special observations concerning the bonding integrity to report. There was no significant change of thermo optical properties on solar cell assemblies (SCAs) other power generation related surfaces (i.e. aluminised Kapton ITO).

The investigation has also revealed that the bus bars and their connection method are containing weaknesses in the design which will fail after a re-launch. Some have failed already. However, the total extent of the bus bar failures can only be established after evaluation of the X-ray photographs taken from all critical and accessible areas. To date only the worst areas are visible, since all bus bars are coated for ATOX protection with a non transparent adhesive (RTV-S691). Metallurgical investigations are also foreseen. But from initial observations it can be concluded that the bus bar design is not fully reliable. In addition, the external forces induced from the cables soldered to the bus bars have been underestimated. For EURECA-SA the conclusion is that without correcting the bus bar problem with its interconnection method, a re-launch of the solar array is not possible and a reliable repair method must be found. The results from the material investigations have not yet been completed, except for the reference samples cut at KSC from panel F5 having silver coatings exposed to ATOX. The results have already been published in reference 3. Different types of silver erosion have been found. Changes of surfaces are discussed which includes contamination (see also reference 8).

4.5 Investigation of mechanisms

HST-SA

After completion of the first checks (at KSC and BAe, Bristol) and a deployment and retraction cycle all three mechanisms (Primary Deployment Mechanism, Secondary Deployment Mechanism, Solar Array Drive) will be dismounted for detailed inspection and investigations. In general all moving parts will be checked against their pre-flight performance, for evidence of wear and damage.

Torques and frictions will be measured where applicable.

The state of lubricant in each bearing will be assessed. Fluid reservoirs and possible fluid creep will be examined as well as surface treatments. Wavy washers/preload devices will be checked for deformation, adhesion etc. Gears will be investigated for state of lubricant gear wear and wear of ceramic gear carriers.

Static adhesion or fretting will be examined on all clamps/end stops.

Electrical contacts will be checked. Motor currents including speed/torque characteristic will be studied as well as brushes and commutator surfaces.

The above list is not exhaustive but reflects the detail to which we intend to study the mechanisms.

EURECA-SA

The EURECA-SA deployment/retraction mechanism worked like a clockwork. All deployment - tensioning-retraction cycles, prior to launch, in-orbit and post-flight were in excellent agreement. No adjustments are needed for a re-flight.

4.6 Meteoroid and space debris investigations

The investigation of space debris and meteoroid particles and their distribution is one of the major tasks and of great help to the space debris and meteoroid community in refining their models and knowledge on damaging effects of impacting particles.

EURECA-SA

The meteoroid survey on both wings have been completed in Dec. 93 and the evaluation of the craters is under way. So far it is known that on the outer panel of +X wing 165 out of 3108 solar cells have been hit of which 68 have a larger impact feature than 200µm (see also ref. 9). No particle has penetrated the panels completely. Figure 27 shows typical impact craters from the HST and Eureka solar array.

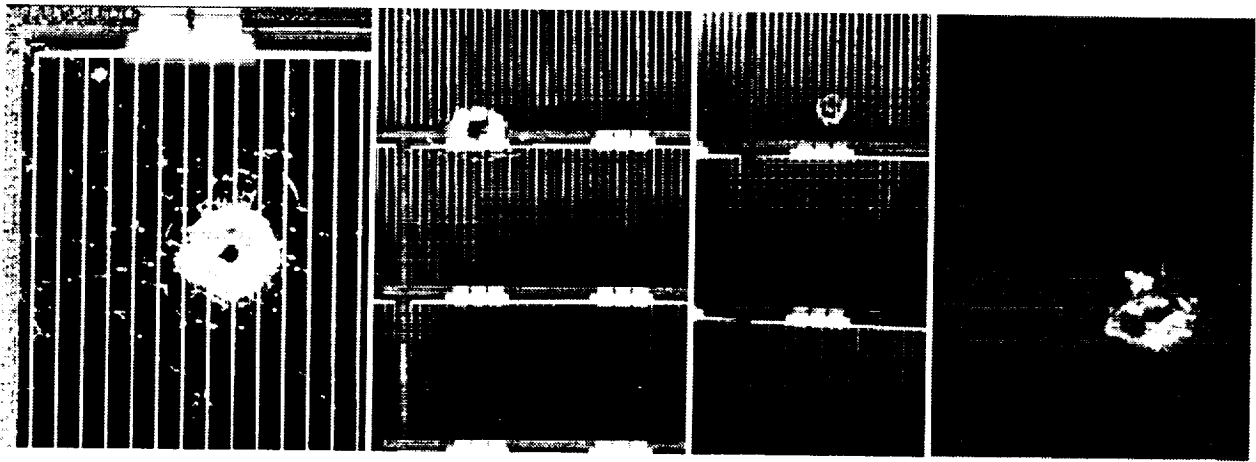


Figure 27. Typical particle impacts

Left: Largest impact feature on EURECA-SA (solar-cell grid finger spacing for all cells = 1.2 mm)
 Centre left: Impact on HST blanket with particle penetrating the blanket at the cell interconnector
 Centre right: Impact feature on HST blanket (rear side hit, no particle penetration)
 Right: Impact feature (≈ 4 mm) of particle penetrating the HST blanket (rear side view)

HST-SA

After an exposure time of almost 4 years in orbit about 40000 particles greater than 10 microns are expected on the ≈ 70 m² of the HST-SA1 wing (counting both sides of the array) from which several hundred will penetrate the blankets.

It is foreseen to examine all solar array units for highlights and use only the two blankets (still ≈ 60 m²) for the systematic documentation of crater and impacting particles. The survey of both blanket front sides have just been completed (10 June 94). Based on the high number of impacts the plan is to document on the 2 blankets impact features ≥ 100 microns only. The cataloguing and investigation of smaller particles will be limited to one SPA (≈ 5 m²) and one buffer assembly (≈ 3 m²). As already mentioned, we will not exclude special highlights and the thermal covers on the mechanisms.

General

The solar array front sides with the solar cell cover slides are an ideal surface to record particle impacts. Depending on speed and size of the impacting particles, the diameter of impact features can be up to 30 times bigger than the particle size.

Through dedicated "in-situ" experiments on spare material calibration measurements are performed to study crater size versus particle size etc.

With some luck we may find a sufficient number of trapped particles allowing us to perform a chemical analyses in order to distinguish meteoroids from man-made objects, with a statistically significant distribution.

A major goal of this investigation is to study which size of craters have an influence on the power generation caused by particles hitting the SCA surfaces. Also if particles can cause short or open circuits between the electrical network and the carrier substrate or trigger some other failure mechanism.

Until now, there is no evidence that any meteoroid or debris impact has caused any of the observed failures. Some of the particles hitting the solar cells have damaged locally the silicon, but the resulting effect is that the chipped off portion or broken portion of the cell simply does not contribute anymore to the power generation. Power measurements on wing level indicate that the remaining cell area functions normally.

5 Conclusion

The solar-array Post-Flight Investigation Programmes for EURECA and HST have already proven to be very valuable for ESA and its future solar-array projects.

The mechanical performance of the retrieved hardware was in excellent agreement with the pre-flight data. The selected materials and coatings for the protection against atomic oxygen are suitable for long duration missions in LEO with high concentrations of atomic oxygen.

Design weaknesses due to thermal fatigue could be identified and design improvements were implemented into the running Polar Platform and ISO project.

The electrical degradation of solar cells was somewhat less than expected.

Ten thousands of particle impacts are recorded on the arrays with several penetrating the flexible blankets. Despite the numerous clearly visible impacts there is no indication that any meteoroid or debris impact has caused any of the observed failures or other unusual power degradation. The loss of power due to local damage of the silicon is not measurable on panel level.

All PFIP activities will be completed by May 1995, and above findings are only a snap shot. The results from the PFIPs will significantly extend the technical knowledge that will lead to better solar-arrays in the future, and are a great help in refining the environmental models and the understanding of damaging effects of impacting particles.

References

- 1 K. Adamson, L. Gerlach, P. Birot, 1994, Electrical Performance, Anomaly Investigation and Operational Implications for the EURECA Solar Generator, *ESA WPP-069, EURECA Symposium, 26-29 Apr. 94, ESTEC, Noordwijk, The Netherlands*
- 2 L. Gerlach, E. Bongers, T. Mende, 1994, Post-Flight Investigation Programme for the Eureka Solar Generator and First Results *ESA WPP-069, EURECA Symposium, 26-29 Apr. 94, ESTEC, Noordwijk, The Netherlands*
- 3 A. de Rooij, L. Gerlach, 1994, First Investigation Results from EURECA Solar-Array Samples Cut after Retrieval at NASA-KSC *ESA WPP-069, EURECA Symposium, 26-29 Apr. 94, ESTEC, Noordwijk, The Netherlands*
- 4 Laurance R.J. 1990, The History of the Hubble Space Telescope and ESA's Involvement, *ESA Bulletin No. 61, February 1990*
- 5 Henson B.W. 1990, ESA's First In-Orbit Replaceable Solar Array, *ESA Bulletin No. 61, February 1990*
- 6 Gerlach L. 1990, The Solar-Power Generator for the Hubble Space Telescope, *ESA Journal 1990/2, Vol. 14*
- 7 Henson B.W., Jackson B., Gerlach L. 1991, In-Orbit Performance Overview of the HST Solar-Generator *European Space Power Conference, Florence, Italy, 2-6 Sep. 1991, ESA SP-320*
- 8 M. v. Eesbeek et al, 1994, Post Flight Investigation of EURECA - Preliminary Findings and Recommendations *ESA WPP-069, EURECA Symposium, 26-29 Apr. 94, ESTEC, Noordwijk, The Netherlands*
- 9 G. Drolshagen, 1994, EURECA Meteoroid/Debris Impact Analysis *ESA WPP-069, EURECA Symposium, 26-29 Apr. 94, ESTEC, Noordwijk, The Netherlands*

SESSION V

BLANKET AND ARRAY DEVELOPMENT

HIGH-PERFORMANCE, FLEXIBLE, DEPLOYABLE ARRAY DEVELOPMENT FOR SPACE APPLICATIONS¹

Russell N. Gehling, Joseph H. Armstrong, and Mohan S. Misra
Martin Marietta Astronautics
Denver, Colorado

SUMMARY

Flexible, deployable arrays are an attractive alternative to conventional solar arrays for near-term and future space power applications, particularly due to their potential for high specific power and low stowage volume. Combined with low-cost flexible thin-film photovoltaics, these arrays have the potential to become an enabling or an enhancing technology for many missions. In order to expedite the acceptance of thin-film photovoltaics for space applications, however, parallel development of flexible photovoltaics and the corresponding deployable structure is essential. Many innovative technologies must be incorporated in these arrays to ensure a significant performance increase over conventional technologies. For example, innovative mechanisms which employ shape memory alloys for stowage latches, deployment mechanisms, and array positioning gimbals can be incorporated into flexible array design with significant improvement in the areas of cost, weight, and reliability.

This paper discusses recent activities at Martin Marietta regarding the development of flexible, deployable solar array technology. Particular emphasis is placed on the novel use of shape memory alloys for lightweight deployment elements to improve the overall specific power of the array. Array performance projections with flexible thin-film copper-indium-diselenide (CIS) are presented, and Government-sponsored solar array programs recently initiated at Martin Marietta through NASA and Air Force Phillips Laboratory are discussed.

INTRODUCTION

It is evident that a strong trend towards smaller, lighter spacecraft launched on smaller launch vehicles has developed, and presently all spacecraft subsystem components are being scrutinized for improved performance. Along these lines, the power subsystem, and more specifically, the solar array and associated structure, has been receiving significant attention, particularly in terms of higher specific power and reduced stowed volume. The reason the solar array plays such a significant role in this activity is that solar array structures are often physically the largest subsystem, and any reduction of weight on an extended boom can have significant impact on spacecraft operations. To achieve overall specific power levels greater than 100 W/kg, and stowage volumes less than 0.10 m³ for arrays as large as 1 kW, a complete system approach must be taken. In most cases, aggressive goals such as these cannot be met with evolutionary technologies. Rather, revolutionary advancement of technologies must be accomplished to meet or exceed these goals.

Both reduced array weight and higher photovoltaic conversion efficiency have an effect on spacecraft design in terms of increased payload size/weight. Dynamics of arrays in the kilowatt range can adversely affect spacecraft performance. Presently, PV arrays are nominally 20 W/kg to 40 W/kg, where most of the array weight is associated with the rigid substrate upon which the cells are mounted. As a result, a great deal of effort has been placed on improving efficiency to reduce array size, but low manufacturing yield and increased complexity drives device and installation cost significantly. Other efforts to improve specific power are related to lightweight structures, including fold-up and roll-up technologies. An additional advantage of these lightweight substrate approaches is the promise of smaller stowage volume.

¹ This Work Sponsored by Martin Marietta Independent Research and Development (IR&D) Project D-17R and Other Internal Funding.

The following paragraphs introduce the incorporation of revolutionary technologies currently under development at Martin Marietta in both thin-film flexible photovoltaics and in lightweight, reliable deployment/structural elements.

Stowage and Deployment of Flexible Arrays - While use of composite materials in array structures to improve specific power for reduced weight is becoming more commonplace, they cannot easily accommodate small stowage volume, particularly for large arrays. One of the ideal configurations is a flexible array, although implementation of such technology has been limited due to the lack of a commercially-available flexible solar cell design. Some flexible deployable arrays have been flown, most notably on the Hubble Space Telescope and the Solar Array Flight Experiment (SAFE) on the Space Shuttle. In both cases, the fragile nature of the solar cells (Si and GaAs) demanded significant attention to structural support. As a result, no array which has flown was truly flexible; at best, the array consisted of numerous array segments housing the rigid cells hinged together in flexible joints.

Due to the advent of flexible solar cells and modules, many flexible array concepts are now possible. For example, issues regarding the stowage and deployment of a rollup array similar to that used in the Hubble Telescope can be more easily addressed. Difficulty in rolling up rigid, fragile solar cells in a compact stowage volume is eliminated by completely flexible solar arrays and photovoltaics. Because the blanket is completely flexible, it is possible to integrate the deployment mechanism and the blanket for improved rigidity, thereby eliminating the possibility of buckling noted in the latest Hubble repair mission.

Martin Marietta is investigating a variety of techniques to deploy flexible PV blankets. One promising concept utilizes shape memory alloy (SMA) elements to achieve both weight and performance advantages over other technologies, including self-rigidizing inflatable technologies. Furthermore, because the shape memory effect can be activated both electrically and by passive solar heating, structural deformations caused by unanticipated spacecraft maneuvers exceeding design parameters can be autonomously repaired in orbit. This key advantage over every deployment scheme can ensure array repair and continued high-level performance over a significant array lifetime.

In addition to the blanket and deployment schemes, a key aspect in the overall specific power goals is the pointing subsystem. Martin Marietta IR&D funding has developed a shape memory gimbal mechanism capable of two-axis tracking with a weight savings of approximately 50% compared to conventional technology.

Photovoltaics - An attractive alternative to conventional crystalline and amorphous silicon PV is polycrystalline thin-film devices. Polycrystalline thin-film PV, such as copper-indium-diselenide (CIS), offer an alternative to Si for most space power applications. These devices have the highest tolerance for radiation damage of any crystalline PV material in proton and electron environments because their short diffusion length (compared to conventional Si and GaAs) makes them less susceptible to damage caused by radiation. Furthermore, polycrystalline thin-film PV have proven themselves far more stable than single-junction a-Si [1,2]. Polycrystalline thin-film devices, which nominally do not exceed 5-8 μm thickness (excluding substrate), have been reported with efficiencies as high as 15.5% (NREL - 1993) in Air Mass (AM) 1.5 insolation. Also in a joint Martin Marietta/NREL effort to supply a PV test article, an active area efficiency exceeding 13.5% in AM0 was observed. The CIS Technology is discussed in an accompanying paper: "Advances in Polycrystalline Thin-Film Photovoltaics for Space Applications".

LIGHTWEIGHT ARRAY TECHNOLOGIES

Integral Deployment / Structural Elements - The achievement of high overall specific power places a premium on subsystem mass allocations. Current deployable solar arrays generally use motor driven mechanisms to extend rigid panels or deployable structural support elements (Astromasts, STEMs, telescoping booms, etc.). While structurally efficient, the mass of the deployment drives and mechanisms penalizes the overall solar array specific power. For non-retractable applications, inflatable deployment sys-

terms are one approach to eliminating the motors and mechanisms, but must include a pressurization system and an envelope or collapsed structure that holds pressure during deployment. Inflatables generate reliability concerns from the standpoint of assuring that the integrity of the pressure envelope is not lost during final stowage prior to the mission.

In order to achieve the most reliable, lowest mass system, Martin Marietta has developed a concept which combines deployment and structural elements of the solar array into an integral system. We are developing integral deployment / structural support elements composed either entirely of SMA, or SMA-composite laminates. Deployment will be accomplished by one of two methods; 1) heating of the SMA member, or 2) using heated SMA to control deployment of an elastic member. The integral deployment / structural elements, combined with a fully flexible array blanket will allow the attainment of array specific power levels greater than 100 W/kg.

Design Using Shape Memory Alloys - Shape memory alloys such as Nitinol (a Nickel-Titanium intermetallic discovered by the Naval Ordnance Laboratory in 1963) provide attractive engineering properties for use in lightweight actuator designs and adaptive composite structures. SMAs undergo a reversible crystalline phase transformation that is the basis of the "shape memory effect". The low temperature phase is a twinned, martensitic structure which is capable of large strain deformation (in excess of 10% in some alloys) with relatively little stress (approx. 70 MPa). The high temperature phase is a cubic based, austenitic structure with mechanical behavior more similar to conventional metals. When the martensite is deformed, and then heated, the original heat-treated shape is recovered. However, if the deformed martensite is constrained during heating, high recovery stresses evolve (>690 MPa is possible in some alloys). A combination of the two effects allows SMAs to produce mechanical work with the application of heat. Using wire as an example, Figure 1 demonstrates the shape memory effect.

Despite their attractive capabilities, the utility of SMAs in the past has been limited due to a lack of understanding of their very interdependent force-length-temperature response and associated non-linear and hysteretic behavior, as well as the effects of creep, fatigue, and material property drift which results from transformational cycling. These effects have been under study at Martin Marietta to provide the basis for effective alloy processing and "training" before incorporation in applications. Moreover, recent development of analytic modeling theory has made possible effective engineering of optimized mechanisms and devices based on experimentally derived parameters from property-stabilized SMA material.

Shape memory alloys are an ideal solution to the deployment of a flexible lightweight solar array. Because the array has an extremely low mass and is deployed in a 0-G environment, the load carrying demands placed on the shape memory deployment system will be very manageable. In addition, since the system requires one mission cycle (and 5 to 10 test cycles) SMA stability and non-linearity is not a major issue. However, several design challenges remain, including the use of the SMA material as structural elements in a martensitic state, and forming the required support geometries. As shown in Figure 2, the yield strength for a typical NiTi SMA is much lower for martensite than for austenite. As a result, SMAs are seldom used in their martensitic state as structural members. However, because lightweight arrays experience minimal on-orbit loads, using the SMA elements in their martensitic state is feasible. Benefits of reduced mechanism mass and associated interfacing hardware must be traded against the increased structural mass associated with the shape memory elements. Our studies indicate that an integral SMA structure provides the lowest mass deployment/support system.

Structural and Deployment Concepts - Our deployment concept employs a novel expansive roll-out approach. In the stowed configuration the array blanket and support elements are rolled-up together in a bundle approximately 30 cm in diameter. Activation of the primary deployment elements causes the bundle to expand and un-roll. The fully flexible solar blanket (including flexible solar cells) allows a smooth deployment with very little resistance applied to the deployment elements. When the deployment elements fully straighten at their full activation, this stage of deployment is complete.

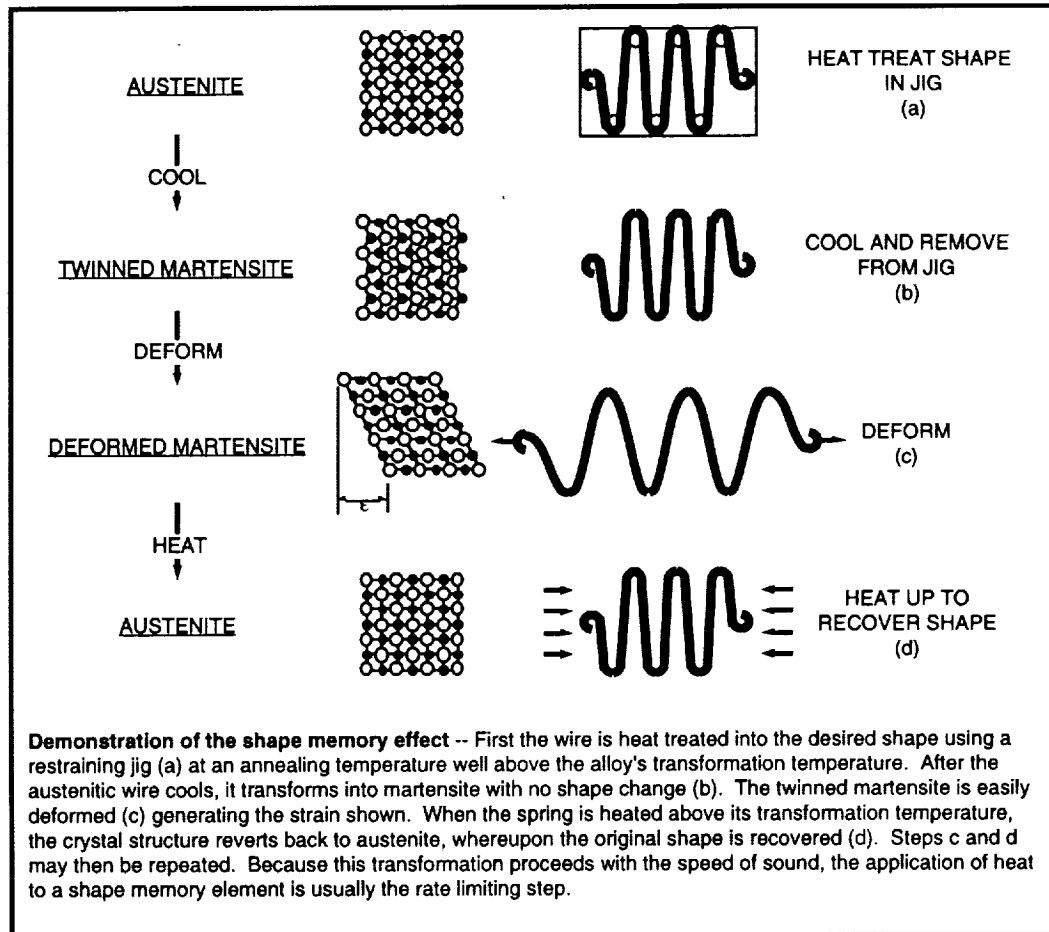


Figure 1 Description of the Shape Memory Effect

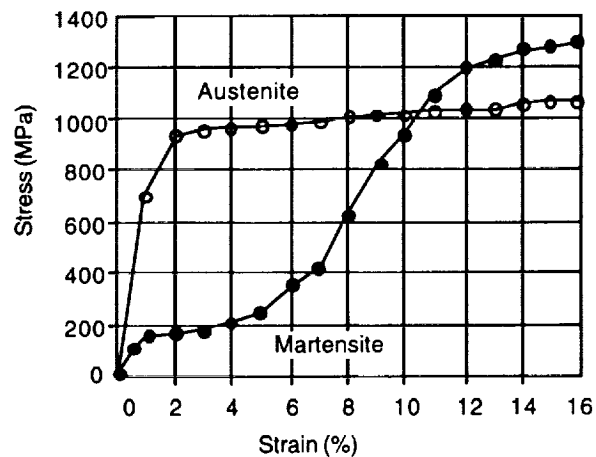


Figure 2 NiTi Stress/Strain Curve

The expansive roll-out deployment concept has several inherent advantages over other deployment approaches. High reliability can be achieved since there are no moving parts, drive mechanisms, or latches (except for launch restraint). Also, the absence of these components and associated interface hardware leads to the lowest mass deployment and structural support system achievable. Further, unlike systems using deployable masts or other elaborate deployable truss works, the low part count lends itself to rapid and efficient production. Finally, the concept allows manual restowage for repeated deployments using the actual mission hardware. This feature further improves the reliability of the system by allowing functional ground testing of all hardware.

In order to obtain the greatest structural efficiency, yet maintain a single spacecraft attachment point, the array configuration should be approximately square rather than rectangular. However, to achieve reasonable maximum dimensions in the stowed configuration, a nearly square array must use a two stage deployment sequence. While a two-stage deployment adds some complexity and risk, use of SMA hinges for the secondary deployment makes the additional deployment step simple and reliable. The overall deployment sequence is shown in Figure 3.

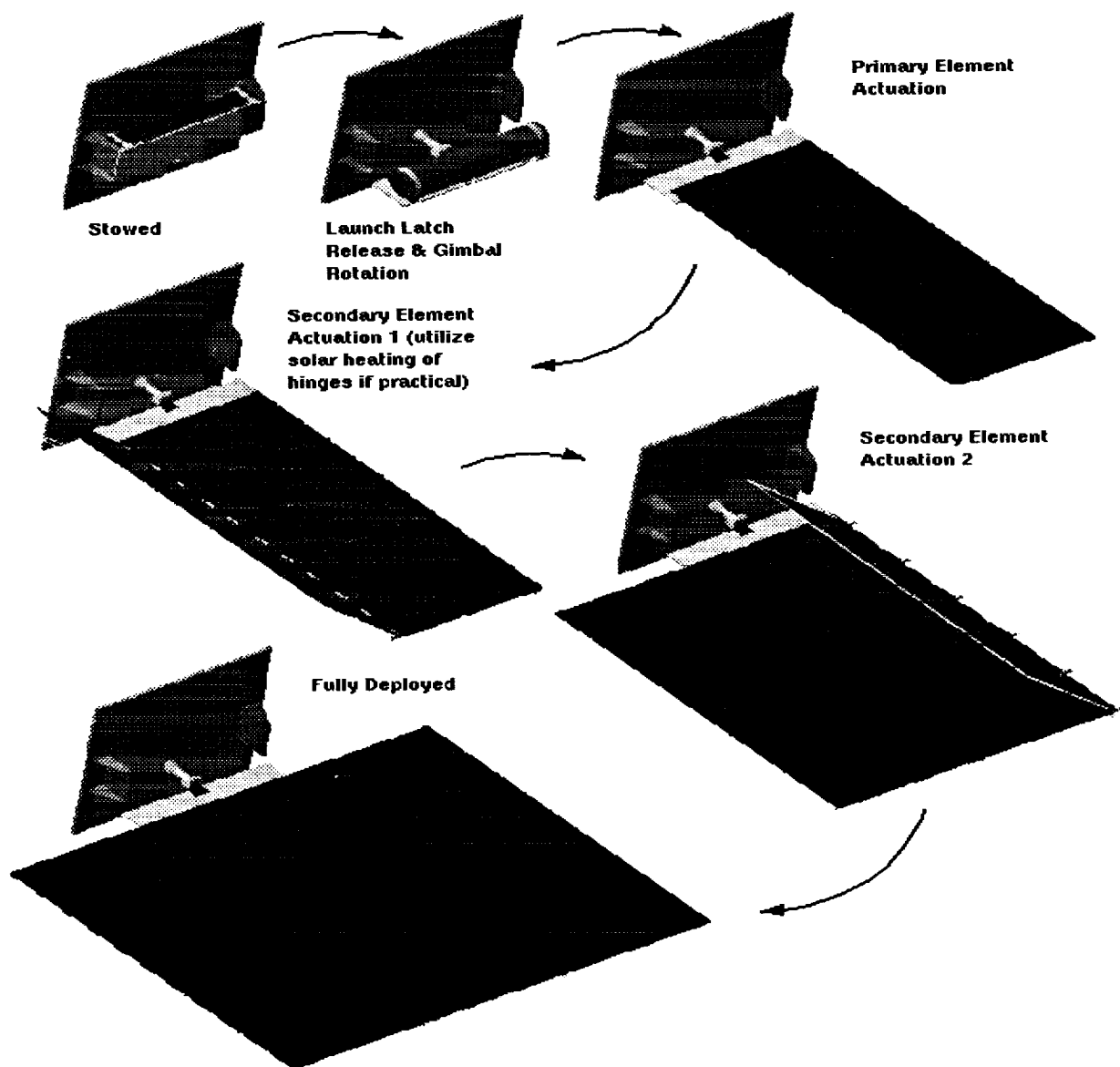


Figure 3 Array Development Sequence

A variety of primary support element geometries are under development and evaluation. These include the deployable element cross-sections shown in Figure 4. Initial analysis of potential cross-sections suggests that while the SMA tube configuration is most structurally efficient, it may be difficult to package repeatedly. Alternatively, while the arc cross-section is most easily fabricated and packaged, lateral / torsional buckling of arc cross section makes a suitable design difficult to achieve unless additional lateral support is provided. The array blanket interface could provide the necessary lateral support to make use of the arc cross-section viable. The two-part, joined cross section is also a candidate, but requires attention to the joint design and reliability, as well as requiring more assembly time.

SMA Support Element Concepts

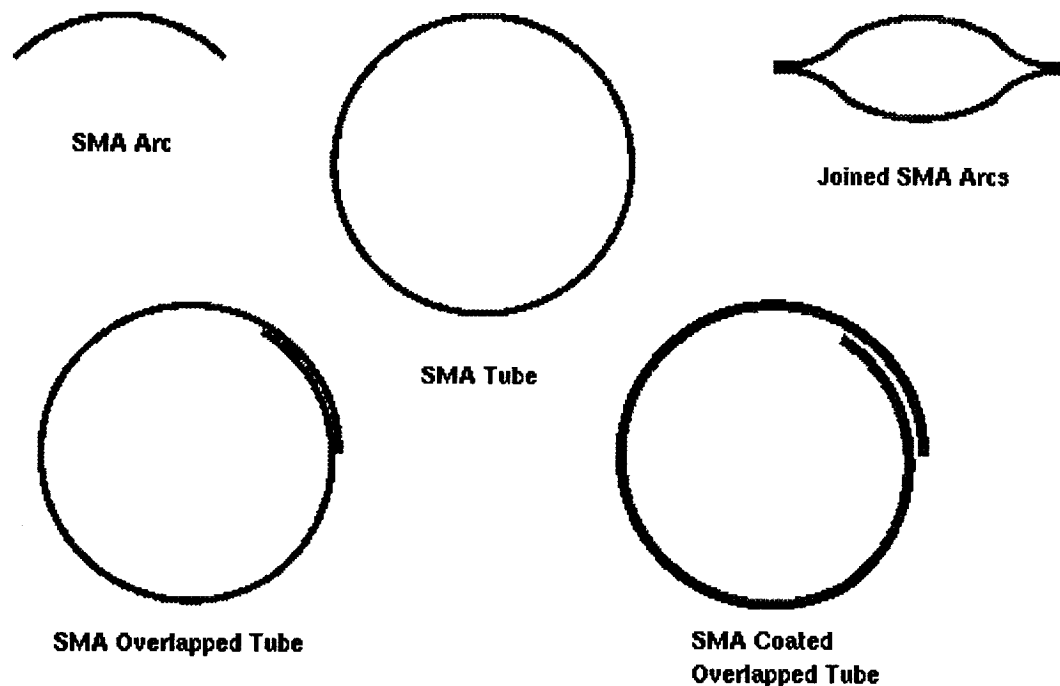


Figure 4 Primary Support Member Concepts

If deployed loading and natural frequency requirements are greater than about 0.2 G and 0.25 Hz respectively, an SMA coated STEM-type element must be implemented. In this concept, the deployment force is generated by elastic energy stored in the STEM. An SMA foil layer sputtered on the STEM serves to control the deployment. Without an SMA control layer, the STEM would spring out in a violent and unpredictable fashion, thereby disturbing the spacecraft and possibly damaging the array blanket. Prior to blanket release, the SMA would be heated to hold the STEM rolled-up. With gradual cooling, the STEM would overcome the force generated by the SMA coating and deploy in a smooth, predictable fashion. In order to evaluate the viability of this concept, the required SMA coating thickness and thermal control to avoid post deployment deflection due to solar heating must be determined.

Secondary deployment can be accomplished using SMA activated flexural hinges. These hinges may be all SMA or a coated beryllium-copper flexure (Fig. 5). This approach enjoys the same advantages as those discussed for the primary deployment elements. A potential advantage of the SMA hinges is the capability to achieve passive deployment from solar heating. This would further simplify the system but requires a better knowledge of the thermal environment.

SMA actuated deployment is accomplished by inducing a temperature change in the "as stowed" shape memory elements. Increasing temperature causes the element to experience a phase transformation

SMA HINGE

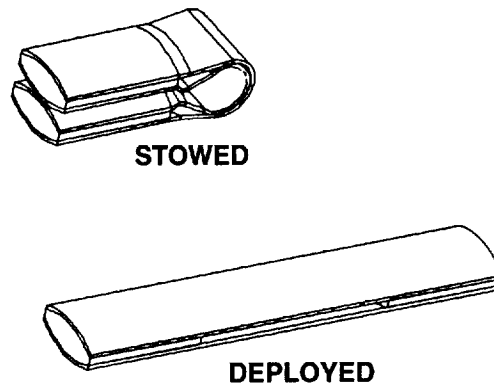


Figure 5 SMA Flexure Hinge

from a fully martensitic condition to an austenitic state generating the necessary deployment force and displacement. The change in temperature can be generated by passively exposing the array to solar radiation or using a control system which regulates current flow to a thin film heater placed in intimate thermal contact within the actuation element

Lightweight Gimbal Technology - The burgeoning demand for lightweight spacecraft and solar array technology requires development of an ultra-lightweight two-axis gimbal drive for solar array positioning. In response to this requirement, Martin Marietta's Mechanical Research & Technology Group has developed a new design for a lightweight gimbal to meet small spacecraft solar array pointing requirements.

The basic requirement for the SMA gimbal was to position a small rigid panel with a slow and smooth motion during a fixed orbit with a two-axis rotation of $\pm 90^\circ$ in elevation and $\pm 175^\circ$ in azimuth. Owing to small orbital loads, the torque requirement was determined to be 1 N-m; primarily due to the bearings and cable management system. In order to keep a 2:1 torque margin the cable management system had to be smooth and consistent. As always, weight was an important consideration and a 1 kg maximum was set as a design goal. Power and drive efficiency was also considered and limited to 3.0 watts average and 5.0 watts peak. The gimbal was required to maintain position and stiffness with the power off.

The gimbal design that was developed to meet these requirements uses shape memory alloy springs in a unique way to obtain a smooth rotary positioning. Figure 6 shows a photograph of the gimbal engineering development unit. A proprietary SMA drive technique, used for both the azimuth and elevation drives, results in significant reduction of the control electronics associated with brushless motor drives.

Another requirement that must be addressed is gimbal stiffness and holding torque. We have incorporated a brake into the design which passively releases when the SMA drive is activated, and then engages after power is removed. There are two brakes per axis and they act as a "no-backdrive" mechanism which stabilizes the gimbal position.

During the evolution of this design, many methods to reduce structural weight were implemented. The gimbal housings are constructed using graphite polycyanate composite material combined with the high performance composite plastic, Torlon. These two materials are used together, and in some cases co-cured, to produce a unique hybrid housing that is strong and very lightweight. This technique allows housing design without complex composite lay-ups or inefficient weight reduction machining.

Flexible Blanket Design - The photovoltaic blanket subsystem for our solar array concepts will be fully flexible. Blanket layout consists of a laminate printed circuit, adhesive, and monolithically-integrated CIS

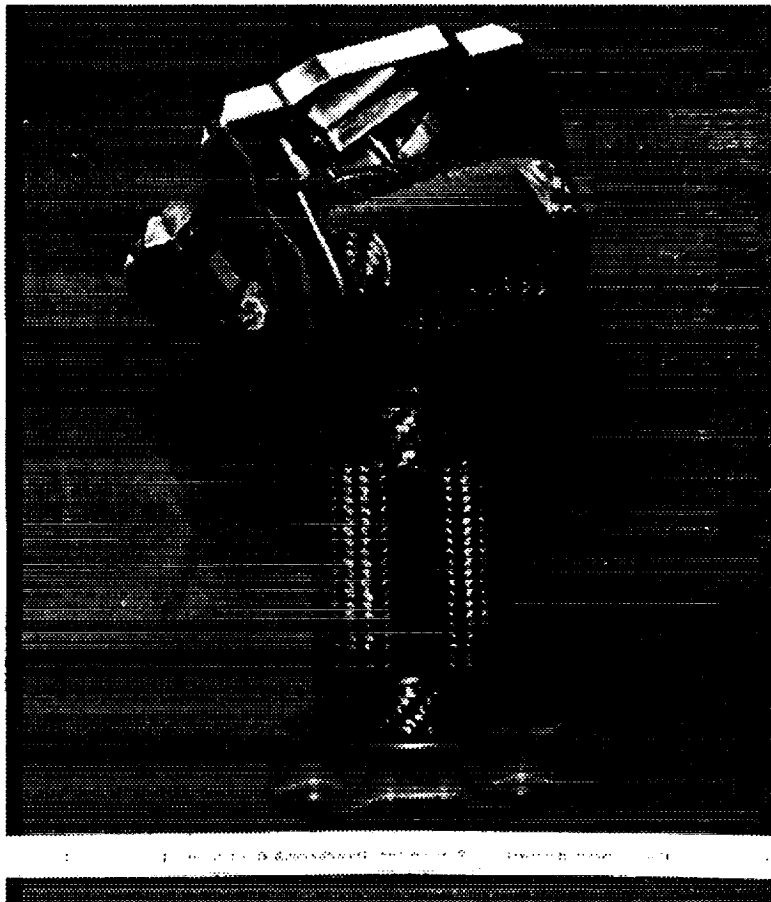


Figure 6 SMA Gimbal Engineering Development Unit

modules which already include thin-film replacement for conventional coverglass. Because the large size of the modules (nominally 30 x 30 cm) allows for passing circuitry underneath while still maintaining electrical connections, it is possible to lay-up the printed circuit in a single layer. Electrical interconnects are made from the module to the interconnect pads via soldered flexible jumpers parallel to the rolling axis. The printed circuits laminated into the blanket are used to convey array power to a flexible bus connector at the edge of each blanket section

ARRAY FUNCTIONAL AND ENVIRONMENTS TESTING

Extensive functional and operational testing of flexible arrays is planned. Tests include power generation, deployment, thermal vacuum, and random vibration. The following paragraphs summarize key aspects of the planned testing.

Power Generation - While array mass can easily be measured, solar simulation requires specialized equipment. Individual development modules up to 15 cm x 15 cm (6.0 in. x 6.0 in.) will be tested in a computer-controlled facility capable of testing these modules in AM0 and AM1.5 insolation while monitoring temperature as the modules and array are heated/cooled. I-V and quantum efficiency characteristics will be measured by sweeping in both directions, as well as standard test methods developed for space arrays by NASA Lewis Research Center. Standard solar cells will also be measured to provide a reference signal. Modules up to 30.5 cm x 122 cm, as well as the complete array, can be tested in Martin Marietta's large space chamber/space simulator laboratory. Continuous solar spot size of 4.9 m (16 ft) diameter from 0.35 to 1.4 sun insolation can be realized. In addition, because of the uncertainty in time-

dependent phenomenon observed in some polycrystalline materials, modules and array components will also be tested in the Large Area Pulsed Solar Simulator (LAPSS) which can accommodate 5.2 m (17 ft) spot diameter and the data will be used to develop a standard comparison between the test methods.

Deployment Testing - A critical aspect of the solar array system is reliable deployment. In order to assure high reliability, deployment must be demonstrated using the actual hardware destined for the mission. To this end, we plan to design and conduct deployment tests of the assembled solar array. An advantage of our integral SMA structure is the capability to re-stow (manually) the array and repeat the deployment sequence multiple times. However, due to the highly flexible nature of our array concept, all aspects of the deployment cannot be tested simultaneously. We therefore plan to use a relatively simple gravity off-load suspension to test the primary and secondary deployment using separate test setups. This will require a test approach utilizing long (> 35 m), lightweight suspension wires supporting the array in two alternate test configurations; a primary deployment test, and a secondary deployment test.

Thermal Vacuum Testing - Thermo-structural array response is of critical importance to successful operation in the space environment. The low mass and stiffness of the structure makes it susceptible to thermal distortion and buckling. Our planned testing includes subjecting flexible arrays and components (in deployed configuration) to anticipated low and high temperature extremes (as shown in Figure 7, typical extremes are -200°C to 80°C, although actual values will depend upon the optical characteristics of the modules) and measuring the thermo-structural response and power output.

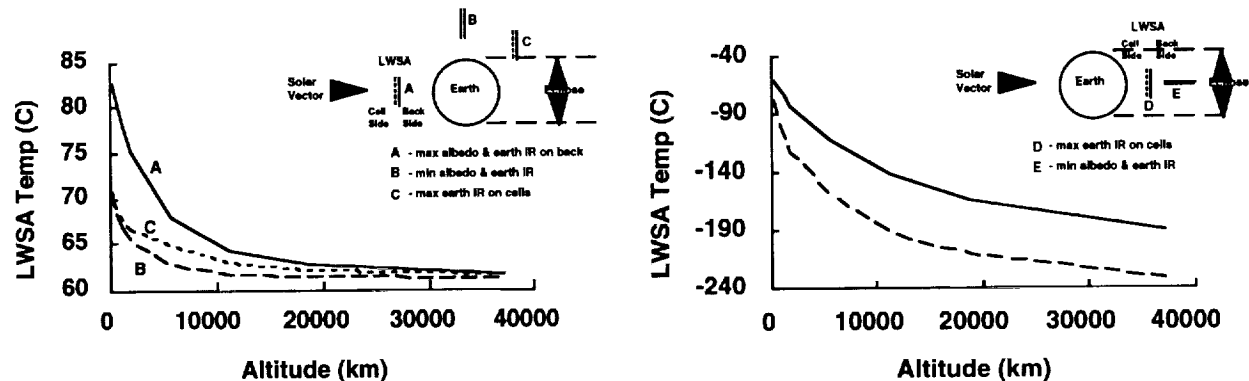


Figure 7 Array Temperature Versus Altitude

Launch Vibration Testing - Vibration and quasi-static loading during launch will produce the highest load levels experienced by the solar array in its stowed configuration. Typically, stresses due to random vibration response far exceed those caused by quasi-static accelerations. Therefore, we plan to conduct a random vibration test on the stowed solar array system to proto-flight levels using a Delta or Pegasus input spectrum. Analyses will be performed to predict peak load levels and verify that combined launch quasi-static and random loads are enveloped.

PLANNED ARRAY DEVELOPMENT

Martin Marietta has recently been awarded two Government sponsored solar array programs; a Phase A INSTEP study (NASA) to define a thin-film, deployable array flight experiment, and an Air Force Phillips Lab contract to develop a prototype lightweight, deployable solar array.

Our INSTEP program will focus on the thermo-structural and electrical performance of flexible thin-film solar arrays. The experiment, as proposed, is summarized in Figure 8.

The Phillips Lab / Martin Marietta LWSA program will combine the technologies discussed above to meet

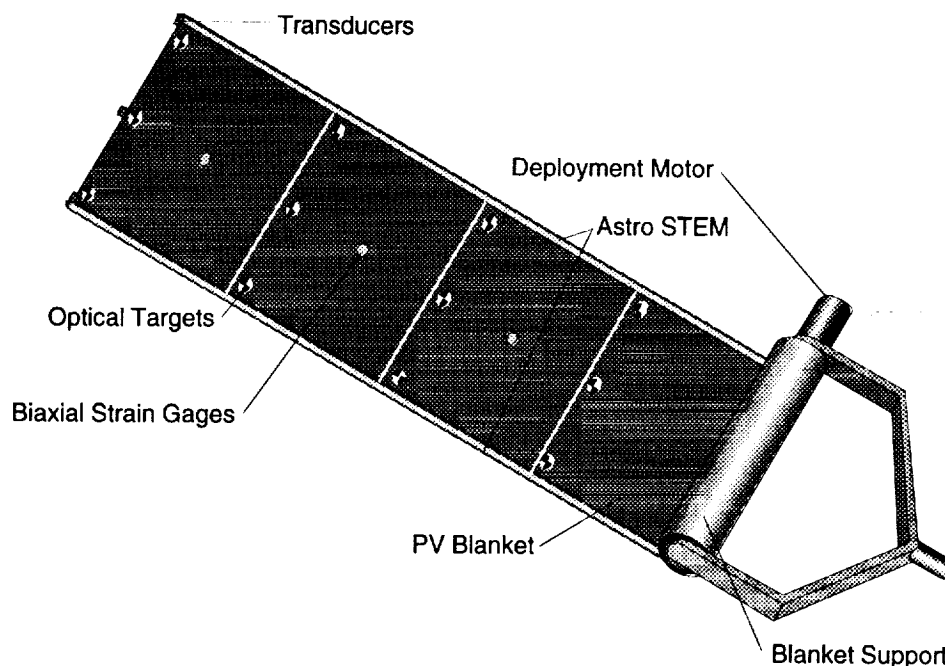


Figure 8 INSTEP Flexible Thin-Film Solar Array Experiment

the needs of future Air Force spacecraft. We have developed an initial configuration for our concept that employs integral deployment/structural elements, an ultra-lightweight gimbal, and a fully flexible blanket using flexible CIS solar cells. This configuration, shown in Figure 9, is sized for at least 750 W EOL power generation. The integral deployment/structural elements are sized for 0.1 G load in the deployed configuration. Use of the structural innovations previously described, together with the lightweight and flexible blanket, allow our concept to achieve a specific power of 160 W/kg EOL under nominal LEO operating conditions.

Estimated total system mass for achieving 500 W, 750 W, and 1000 W power levels is listed in Table I for the LEO and GEO environments at both 28°C and 60°C operating temperatures. These mass estimates were derived from our 750 W baseline concept. Note that the EOL specific power output exceeds 150 W/kg after 7 years in the LEO environment and can approach that level after 10 years in the GEO environment if operating temperatures can be kept relatively low.

REFERENCES

1. L. Mrig: "PV Reliability Issues," Photovoltaics Workshop, Denver, CO 1990.
2. J.H. Armstrong, C.O. Pistole, M.S. Misra, V.K. Kapur, and B.M. Basol: "Flexible Copper-Indium-Diselenide Films and Devices for Space Applications," Proc. SPRAT XI, 1991.

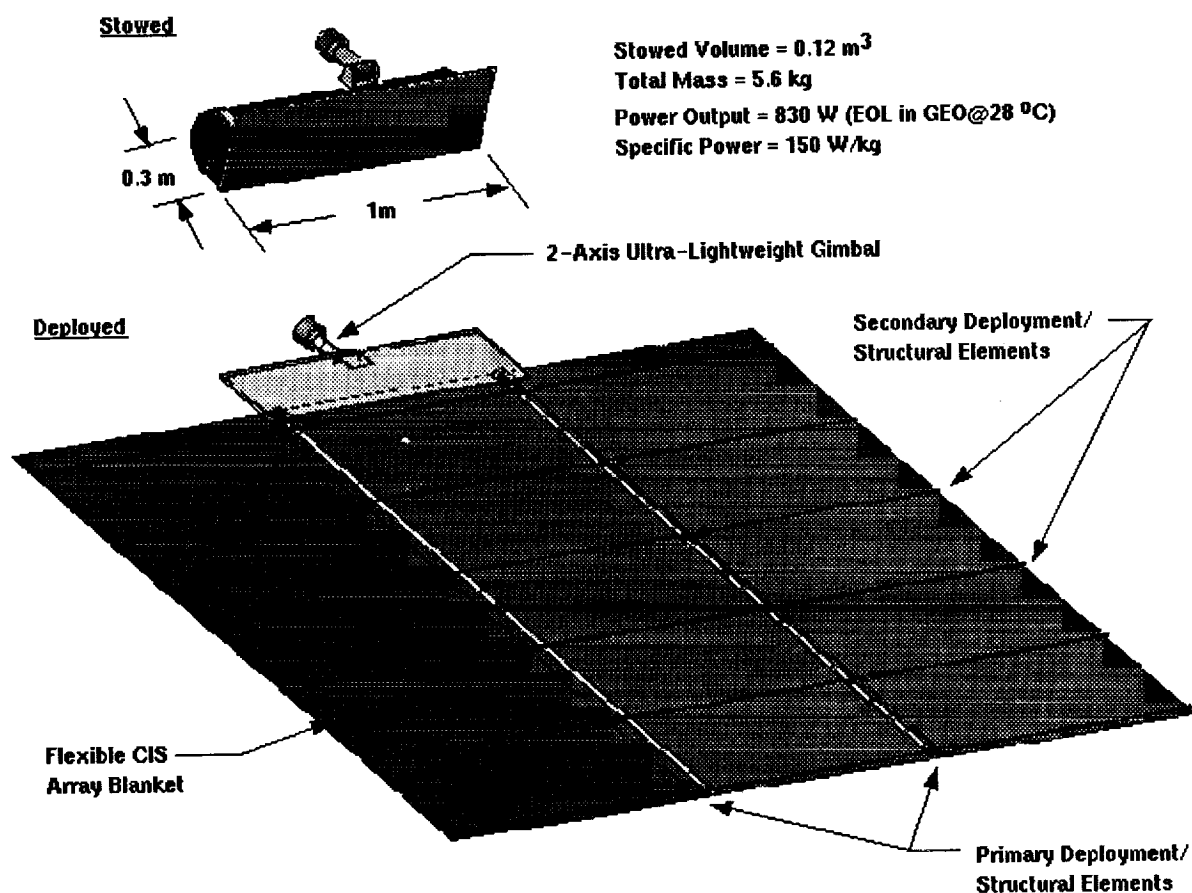


Figure 9 LWSA Baseline Design Concept

Table 1 EOL Specific Power Estimates for LEO and GEO Mission Profiles

Power (W)	Temp (°C)	Low Earth Orbit (7 yrs, 1000 km)						Geosynchronous Orbit (10 yrs, 36000 km)					
		Area (m ²)	Blanket (kg)	Structure (kg)	Gimbal (kg)	Total (kg)	Specific Power (W/kg)	Area (m ²)	Blanket (kg)	Structure (kg)	Gimbal (kg)	Total (kg)	Specific Power (W/kg)
500	28	4.0	1.6	0.5	1.0	3.1	160	4.6	1.8	0.7	1.0	3.5	140
	60	4.4	1.8	0.6	1.0	3.4	150	5.1	2.0	0.8	1.0	3.8	130
750	28	6.0	2.2	1.2	1.0	4.4	170	6.8	2.6	1.5	1.0	5.1	150
	60	6.7	2.3	1.4	1.0	4.7	160	7.5	2.8	1.8	1.0	5.6	130
1000	28	8.1	3.0	2.1	1.0	6.1	160	9.1	3.4	2.6	1.0	7.0	140
	60	8.9	3.3	2.5	1.0	6.8	150	10.1	3.7	3.3	1.0	8.0	130

STATIC STABILITY OF A THREE-DIMENSIONAL SPACE TRUSS

John F. Shaker
NASA Lewis Research Center
Cleveland, Ohio

Abstract - Space Station requirements for power have resulted in a need for photovoltaic solar arrays possessing large blanket surface area. However, due to the limited Shuttle payload volume solar array designers have been driven to a deployable concept that by nature is extremely flexible. The principal support for this array system is the **Folding Articulating Square Truss Mast (FASTMast)**. In order to accommodate service loads the FASTMast is expected to exhibit nonlinear behavior which could possibly result in structural instability. Presented herein are the results of the Lewis Research Center test and analysis efforts performed in an effort to characterize the FASTMast structural behavior in terms of stability. Results include those obtained from recent nonlinear testing and analysis involving a 1/10 segment of the FASTMast flight article. Implications of these results as they relate to expected behavior of the flight unit will also be discussed.

INTRODUCTION

In order to characterize complex structures with any degree of accuracy it is necessary to update finite element (FE) models using appropriate test data. In general the approach involves a two-fold process whereby a structural model is optimized utilizing FE modeling methods and response data obtained from characterization tests. Test data is used to either validate or modify original assumptions used when creating an idealized computational model. In many cases the finite element method (FEM) is limited in terms of representation of structural behavior that deviates from linear-elastic response regime. In addition to improving the accuracy of response predictions this approach also reduces the cost of structural characterization by minimizing the amount of required testing. Once a FE model has been test verified it can be exercised repeatedly until all desired response information has been obtained. Although computational costs can also be expensive they are generally much less than those associated with structural testing. Due the complex nature of the FASTMast structure and the limited resources available, this approach was taken to identify the load states at which the structure becomes unstable. The objective of this initial study was to create a FE model of the FASTMast structure and attempt to correlate response states to those obtained from a static structural test involving various applied loads. Utilizing the test results as a guide, appropriate model parameters were updated and analyses repeated until agreement between test data and FE results was achieved. It is clear from the results that this methodology can be used to effectively treat the stability characterization of this structure.

In order to deploy large flexible space structures it is necessary to develop support systems that are strong and lightweight. The most recent example of this aerospace design need is vividly evident in the Space Station solar array assembly. In order to accommodate both weight limitations and strength performance criteria, ABLE Engineering has developed the (FASTMast) support structure. The FASTMast is a space truss/mechanism hybrid that can provide system support while adhering to stringent packaging demands. However, due to its slender nature and anticipated loading, stability characterization is a critical part of the design process. Furthermore, the dire consequences surely to result from a catastrophic instability quickly provide the motivation for careful examination of this problem.

Shown in figure (1) is the solar array assembly of the Space Station Freedom. Once fully deployed the FASTMast structure will provide structural support for the solar array system. A unique feature of this

structure is that the system responds linearly within a certain range of operating loads and nonlinearly when that range is exceeded. However, this study involves the nonlinear large displacement problem only since it yields the lowest load levels leading to a state of instability. A complete examination of the FASTMast stability problem is given in reference (1).

HARDWARE DESCRIPTION

Due to electric power demands of the Space Station user community it was necessary to provide solar array assemblies much larger than normally used for space flight. Limited by the modest payload volume of the Space Shuttle, designers were immediately driven to a deployable concept that could accommodate packaging and weight constraints. In order to support the solar array blanket it was necessary to design a support structure that possessed the strength characteristics of a space truss with the mechanistic features of a deployable structure. The answer to this problem was provided by ABLE Engineering with the FASTMast deployable mast assembly.

The FASTMast structure is comprised of thirty-two interconnected **bays** of mast. A complete flight unit will stand approximately 104 feet in length and supports two solar arrays which are a total of 40 feet in width. The total weight of this structure including the mast canister and blanket boxes required for launch support is 2500 pounds. It is designed to provide 18KW of electrical power to the Space Station user community. Shown in figure (2) is a detailed description of the primary components that make up a single bay of mast structure. The longhorns are the primary axial and moment load carrying elements of the structure. In order to provide additional buckling resistance the longerons in the lower twenty bays possess a tapered cross-section. The engineering properties of all major structural components are given in tables (1) and (2).

The principal elements providing resistance to shear and torsional loading are the prestrained stainless steel 7X7 wire rope diagonals. In addition to the shear resistance provided by this structural member it also provides flexibility that is required of a deployable structure. The current design preload level in this element is 31 pounds. Supplying the load required for diagonal prestrain is the fiberglass flex batten. In order to create the necessary force the flex batten is installed in a post-buckled state. The buckled shape of this element is clearly visible from the top view of the mast given in figure (3). A direct analogy to this design concept is the energy transmitted to a string from a buckled bow.

In addition to reacting the preload of the flex batten, the elbow joints provide a pivot point required for mast stowage and deployment. Therefore, it was necessary to design this joint with a dual-function end fixity. In order to facilitate the folding action of the mast the elbow joints act as a hinge in the direction of rotation required for stowage. Shown in figure (4) is the manner in which the elbow joint, flex batten, and diagonal elements are connected to the mast. Figure (5) shows the diagonal to longeron connection which is made with a bracket and two 4-40 socket-head cap screws. Also given in this drawing is a clear view of the folding direction of the longeron/flex batten interface. The pinned and hinged boundary conditions at this joint are associated with the Euler buckling and large displacement failure modes respectively. The pinned condition exists at this interface when hinge action is not taking place.

At the top and bottom of each bay of FASTMast are the rigid battens and the corner fittings. These structural elements provide a pivot point for the longeron at the top of the bay and anchor the rigid battens to the space lattice. Rigid battens provide shear and torsion load resistance by restraining corner fitting motion. The taper feature of the rigid batten was incorporated in order to reduce weight and increase strength of the element. The diagonals are mounted at the top of the bay in a manner similar to that described above.

Although the individual elements of the FASTMast structure do not possess large strength capability the integrated unit appears capable of withstanding service loads. However, in order to achieve the required strength to weight ratio this type of structure presents an obvious stability problem. Further complicating this problem is the fact that there exists both a local and global instability modes each influenced by deformed mast geometries and applied loading conditions.

NONLINEAR FAILURE MODE IDENTIFICATION

The allowable load of a structure is a function of its design and the anticipated failure mode. Determination of allowable load requires a clear understanding of structural behavior during loading events and identifying the appropriate mode of failure. Once these two goals have been achieved a valid analytical model can be constructed and the allowable load of the structure can be determined.

The FASTMast will be subjected to a combined state of moment (M), axial (A), shear (V), and torsion (T) load as graphically depicted in figure (6). From a simple static assessment of the mast it is clear that applied shear torsion loads are reacted in essentially the same manner. This figure merely attempts to present a simplified representation of all possible applied loads at a system level. Nonlinear behavior of the FASTMast structure is due principally to the changing stiffness state of the structure that results from slack diagonals. As was previously stated shear and torsion loading is reacted internally by the diagonals and battens. An attempt to illustrate mast reaction to shear load is given in figures (7) and (8). Shown in this figure is the action of the flex batten and diagonals due to the action of preload P and shear load V. The shear and torsional stiffness of the mast is a result of the post-buckled flex batten force P inducing a tensile preload in the wire diagonals. The load state in figure (7) is a result of only preload P while the manner in which the mast will react shear load V is illustrated in figure (8). The sum of figures (7) and (8) represents the combined action of V and P. It is assumed that each diagonal is prestrained to the same level while resisting shear load equally. The flex batten reaction to the shear load is zero because it is in a post-buckled state and cannot take additional load. Although figure (8) indicates that a set of diagonals would be in "compression", physically this equates to a reduction of the force P supplied by the flex batten. The limiting state is reached when the load in the "compressed" diagonal becomes zero (slack condition), at which time the flex batten begins to pick up additional compressive load and the mast begins to move into a fold-up mode required for mast retraction (figure 9). The applied shear level at which unwanted mast stowage occurs is that required to overcome the preload in the wire diagonals. A shear load of this magnitude is much lower than that required for material yield in either the diagonal or flex batten. Therefore the principal failure mode for applied loads involving shear and torsion is structural instability.

Based upon the preliminary failure mode assessment above it is clear that an evaluation of FASTMast stability should be undertaken. From initial instability considerations it was determined that the deformed state during instability would be either a local or global deformation as given in figure (10). A global or system failure event would correspond to the fold-up mode that results from excessive shear/torsion and axial load. Fold-up in this instance is defined to be mast action which occurs during a solar array restowing event. The instability event involving mast fold-up is mechanistic in nature and is due to the nature of the FASTMast design which involves both truss and mechanism elements. Furthermore, due to mast stiffness changes which occur during large deflections of the elbow joint, this form of instability is nonlinear in nature. On the other hand, the local failure mode involves the classic general instability of a pinned-pinned column subjected to an axial load which would occur during excessive moment and axial loading on the mast. The local instability event involves Euler buckling of a single longeron as is shown in figures (10) and (11) and is a linear response event. The principal difference between these two failure modes is that the system event is kinematic in nature. Also, the local event does not involve nonlinear behavior indicative of the system type failure mode.

APPROACH

After considering both problem physics and resource limitations it was decided that a one-tenth segment of FASTMast structure could be used to meet study objectives. This one-tenth model of the flight hardware is referred to as the 3-bay FASTMast unit. Furthermore, due to the symmetric nature of the structural load paths extending the test verified 3-bay theory to the 32-bay flight unit configuration was considered plausible. Based upon these initial assumptions parallel test and analysis efforts involving FASTMast nonlinear stability assessments were design and executed.

THREE-DIMENSIONAL NONLINEAR LARGE DISPLACEMENT ANALYSIS

The source of nonlinearity in this case is due to the changing system stiffness as the structure experiences large deflections. This particular large displacement problem includes the effects of large translations and rotations while strains remain small. However, in order to accurately predict nonlinear behavior it is extremely important the FE model closely match the nonlinear elements of the hardware. Therefore, accurate modeling of the flex battens, wire diagonals, and mast joints was deemed critical for generation of accurate and valid data.

The model used for this analysis was created with the ANSYS finite element code. ANSYS was selected due to its proven nonlinear capabilities. The entire model consisted of 312 elements, 225 nodes, and an estimated 1330 degrees of freedom. Shown in figure (12) is the undeformed preloaded ANSYS model. In order to define the entire model five element types and ten real constant sets were required. All mast structural properties were based on the most-up-to-date information available.

The longerons were modeled using three-dimensional tapered beams thus reflecting the design of the lower twenty bays of the flight unit. Each rigid batten frame required three-dimensional truss elements to model the batten tube and three-dimensional tapered beams to model the corner fittings. The wire diagonals were represented by two-dimensional tension only spar elements which included an initial prestrain equal to that prescribed by the required tensile preload. Finally, the fiberglass flex battens were also represented by three-dimensional beam elements.

In order to represent joint flexibilities at the elbow and corner fittings hinge elements were introduced to these parts of the structure. The ANSYS hinge joint provides translational and rotational stiffness in all six degrees of freedom at the point of application. At each elbow joint there are four hinge elements and at each corner fitting there are two. A hinge element consists of a coincident node pair that are connected in all but one rotational degree of freedom. Shown in figure (13) is an example of an elbow joint modeled using hinge elements. In this example the coincident node pairs are (5,45), (5,35), (5,25), and (5,15). At each longeron end there is a hinge that allows for ninety-degree rotation plus a 0.6 degree back rotation required to model stopping action of the deploying mast. After engaging the stop the hinge is no longer free to rotate and instead behaves as a torsional spring with a rotational stiffness of 1×10^6 in-lb/rad. The hinges on flex batten ends do not have rotational limits and possess very high translational stiffnesses. An identical connection process is carried out at the corner fittings without the inclusion of the flex batten.

The ability to identify instability points during a geometric nonlinear large displacement analysis is not straightforward. Unlike linear static analyses, the structure is loaded incrementally and the equations of motion are solved in a piecewise linear manner over subintervals of the response regime. Over each loading increment the equations of equilibrium are solved iteratively until the solution converges within some specified tolerance band. During this analysis both force and moment convergence criteria were

used to evaluate the adequacy of the solution before proceeding to the next load step. Solution iterations continue until either convergence is achieved or the analysis is terminated by user request. Upon successfully satisfying the equations of equilibrium the stiffness matrix is updated and the analysis moves to the next interval of applied load. This process is repeated over the entire range of applied load. The fact that the solution is derived in a piecewise manner introduces the first analytical difficulty which involves bypassing the point of instability due to an interval selection that is too broad. This situation can occur for instabilities such as "snap through" buckling. Furthermore, even if the proper interval has been identified there still remains the question of at which point in the interval instability will actually occur. For example, if an instability occurred between ten and twenty pounds the failure load level possibilities include eleven, twelve, ... , and twenty pounds. The only explicit conclusion presented by code output is that a failure occurred somewhere between the end points of the applied load interval. Also, identification of instability points from output data can be accomplished by identifying radical changes in output values at some predefined characteristic point. In this case large displacements at the top of the mast due to a load of smaller or equal magnitude than the preceding step was taken to infer a point of instability. An analytical consequence of such an event may result in a set of equilibrium equations that prove to be nonconvergent. This type of nonconvergence is due to the fact that the structure has undergone a shape change that will not satisfy conditions of equilibrium. However, convergence problems may also result from modeling errors that have no relationship to a possible state of instability. Therefore, prior to reporting large displacements and nonconvergent behavior as indications of instability points structural response must be judged appropriate. The analyst must ensure that the FE model is accurately representing nonlinear behavior and results reflect problem physics. In general this is accomplished by utilizing engineering insight and structural test data during the data reduction process.

The focus for this particular model correlation activity resided with the hinge elements. At each node involving a hinge element there are six degrees of freedom five of which must be assigned stiffness values. The sixth degree of freedom is that of the primary hinge rotational direction which for this study was taken to be frictionless. Of the remaining five degrees of freedom only the lateral and axial stiffnesses were updated with the aid of results from stiffness testing. Stiffness values were obtained by performing a longeron axial load test and a system level lateral load test. The model hinge stiffness parameters were then updated and a nonlinear analysis of the configuration given in figure (14) was performed and compared to test results. The remaining translational and rotational hinge stiffnesses were assumed to be either zero or very large and that fact is reflected in the FE model.

STIFFNESS TESTING

In order to generate the required stiffness values an axial stiffness of the longeron/elbow joint was performed in addition to a tip shear stiffness test. The test configurations are shown in figures (16) and (17). Stiffness testing was performed by agents of the Engineering Directorate of Lewis Research Center (LeRC) and details are available in references (2) and (3).

The first model update was performed using stiffness data from an axial stiffness test which was configured as shown in figure (17). The test specimen consisted of an elbow fitting and two square longerons and was loaded in a series of ten load steps to final level of 4200 lbs. As the load level reached 3000 lbs nominal yielding of the structure had occurred. Yielding of the specimen increased dramatically over the range of 3000 to 4500 lbs at which point the test was terminated. Linear behavior was observed throughout the 2400 lb load case with yield occurring at approximately 2500 lbs. A linear fit of the test data resulted in the load/displacement curve with a slope of 4.3×10^5 lb/in which represents the axial stiffness of the hinge.

Updating of the lateral elbow joint stiffness was made using results from the 3-bay lateral loads test. The system level lateral load test was performed in a manner that allowed for sequential loading of the truss

structure until a limit value was achieved. A lateral load of 120 lbs was applied to the structure in a stepped fashion and the displacements were recorded at locations given in figure (15). The nonlinear behavior of the FASTMast is clearly evident in figure (18) which gives the deflection of the mast top as a function of lateral load. The system response becomes nonlinear as the applied load reaches a level of 83 pounds. This bilinear behavior is due to the fact that the diagonal tension has been reduced to zero and the flex battens begin to react the applied load. The mast stiffness up to the 83 lb inflection point is approximately 332 lbs/in and decreases to 28 lbs/in at the onset of nonlinear behavior. In order to achieve model correlation an attempt was made to match analytically the test results given in figure (18) by adjusting the lateral stiffness of the elbow joint.

RESULTS AND DISCUSSION

The results of the structural testing and nonlinear large displacement analyses are given graphically in figure (19). In this figure the lateral displacement of the 3-bay FASTMast is plotted as a function of lateral load. The top curve represents the system response identified during the 3-bay lateral load test and the remaining curves show results from the nonlinear analyses. A total of three FE model updates were made in support of this study. For each analysis the lateral load was equal to 120 lbs applied in twelve equal load steps of 10 lbs. In all three cases there was no evidence of a structural instability. As a starting point all hinge stiffnesses were modeled as rigid connections. As expected this resulted in a mast stiffness much higher than that observed in test. System performance with rigid hinge connections is shown in the lower-most in curve of figure (19). The results indicate a system stiffness of 796 lb/in in the linear regime, and 34 lb/in during nonlinear response. The first update of the model consisted of modifying the axial stiffness of the hinge joint to a value 4.3×10^5 lb/in. This change resulted in a linear system stiffness of 667 lb/in, and a nonlinear stiffness of 33 lb/in. Finally, the lateral stiffness of the hinge elements was updated to a value of 400 lb/in. This value was determined from a recent hinge joint test of the 3-bay unit. From figure (19) it is clear that this change results in a dramatic increase in system flexibility. The slope of the curve depicting these results indicates a linear stiffness of 515 lb/in and nonlinear stiffness of 24 lb/in. Therefore, the final updated model possess a 54% error in linear stiffness and -14% error in nonlinear stiffness. For this study a negative error rate implies excessive flexibility exists in the model as compared to test results. Although model results improved over the updating process more work will be required to obtain a better model correlation.

A second interesting result shown in figure (19) is that the onset of nonlinear behavior given by analysis differs from that found during testing. The test results indicate that nonlinear behavior begins at an applied lateral load level of 84 lbs while the analytical level is approximately 100 lbs. This discrepancy could be the result of several possible test and/or model anomalies which may include: (1) variation in anticipated test article diagonal preload, (2) model hinge stiffness inaccuracies, (3) excessively stiff model of the rigid batten, and (4) inaccurate value of Young's modulus for the flex batten. Each of these items will be examined during the remainder of the model correlation effort in order to identify the source of this discrepancy.

In terms of structural performance it is clear that resistance to applied loads will decrease dramatically when the FASTMast enters a nonlinear response regime. Furthermore, if the predominant failure mode is instability collapse will be sudden and catastrophic. Therefore, it would prudent to restrict mast operations to the linear regime.

SUMMARY

The results presented herein indicate that FE model updating techniques can be successively employed when analyzing large flexible structures. However, reliable updates to complex elements such as rotating hinges and preloaded elements can only be achieved utilizing test data and sound updating procedures. Once the FE model has been test verified, characterization of system responses can be achieved with greater levels of accuracy and validity.

REFERENCES

1. Shaker, John F., Static Stability of a Three-Dimensional Space Truss, M.S. Project, Case Western Reserve University, 1994.
2. 3-Bay FASTMast Shear Test and Analysis, Lewis Research Center Engineering Report No. SAB 93-003, April 1993.
3. PV Structural Analysis Space Station Tension Test of FASTMast Elbow Joint, Lewis Research Center Engineering Report No. 93-3.

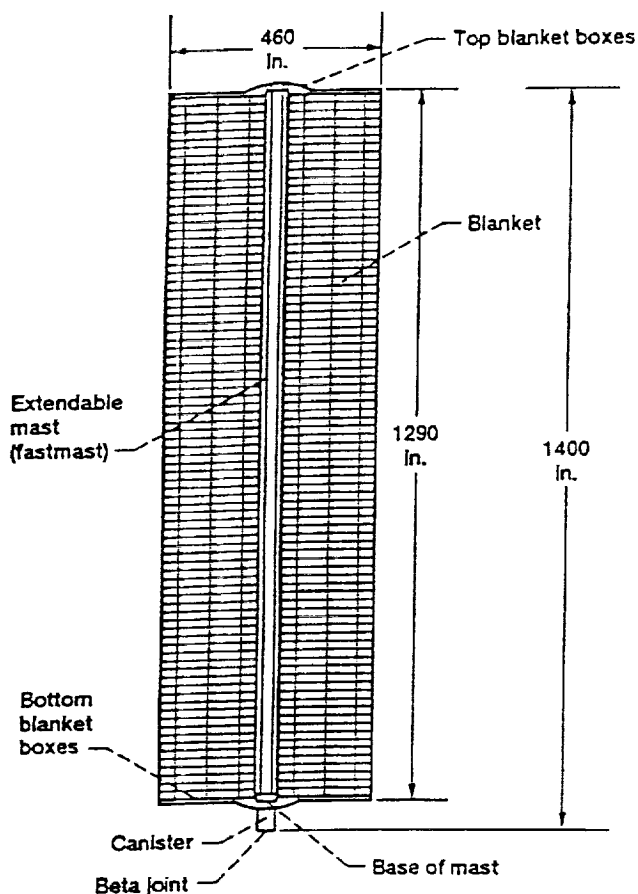


Figure 1 - Space Station Solar Array

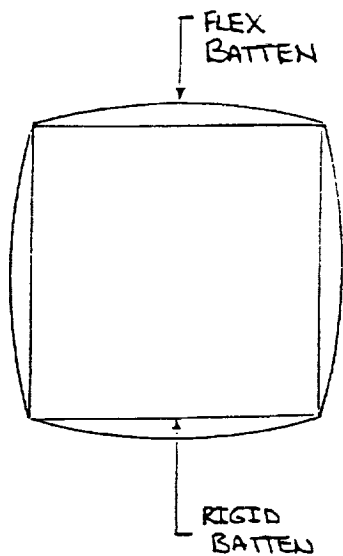


Figure 3 - FASTMast (top view)

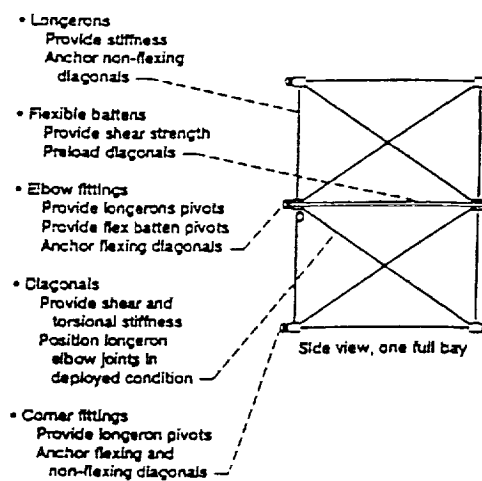


Figure 2 - FASTMast Structure

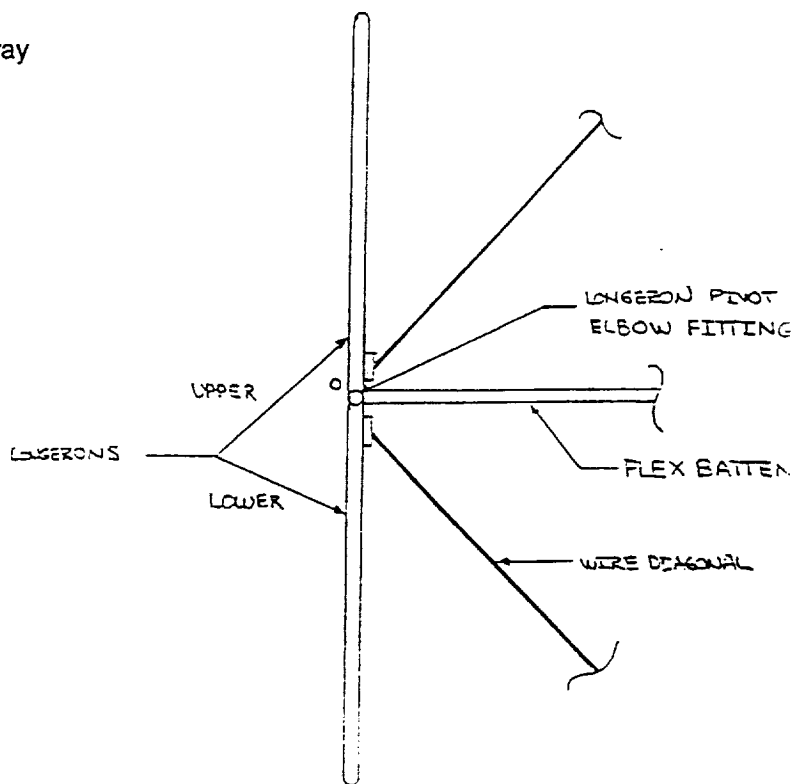


Figure 4 - Flex Batten / Longeron Interface

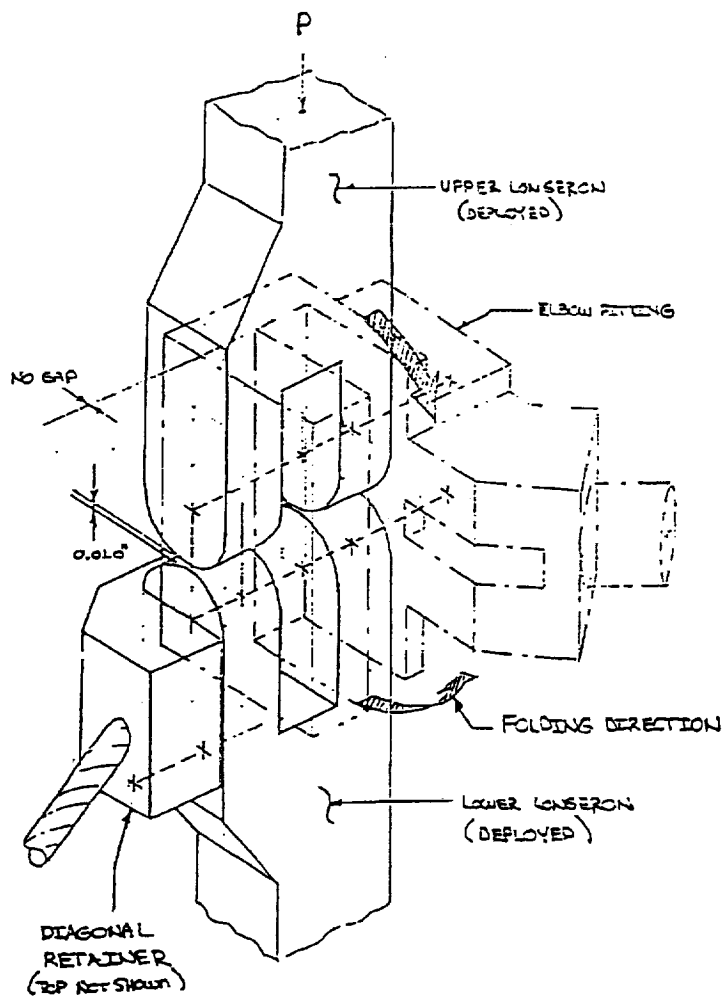


Figure 5 - Elbow Fitting Longeron Interface

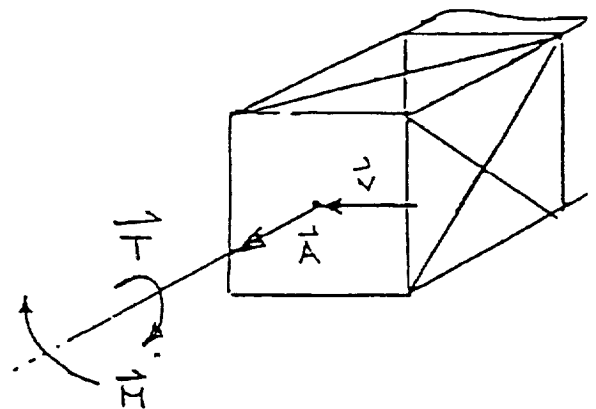


Figure 6 - FASTMast System Loading

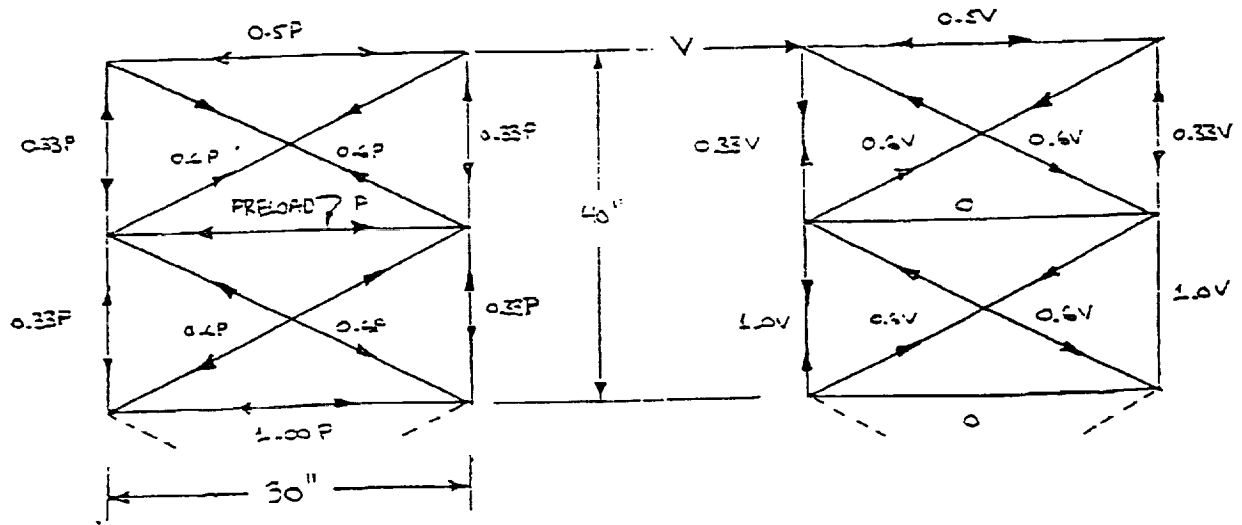


Figure 7 - FASTMast Preload Reactions

Figure 8 - FASTMast Shear Load Reaction

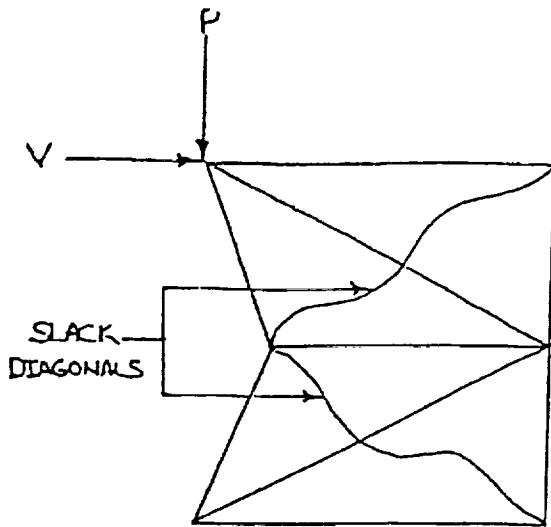


Figure 9 - FASTMast Fold-up Action

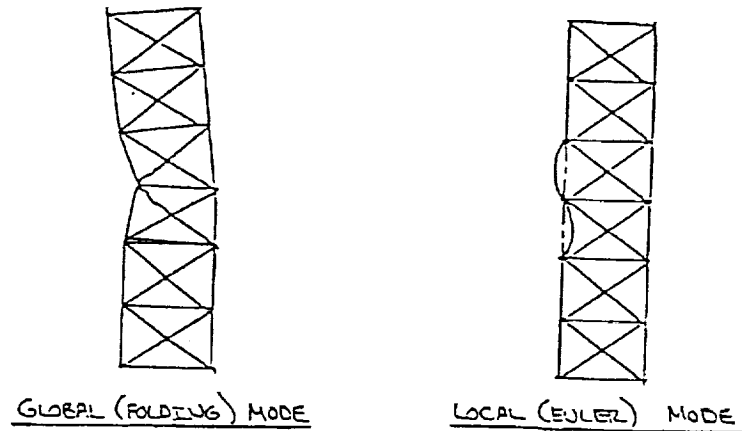


Figure 10 - FASTMast Failure Modes

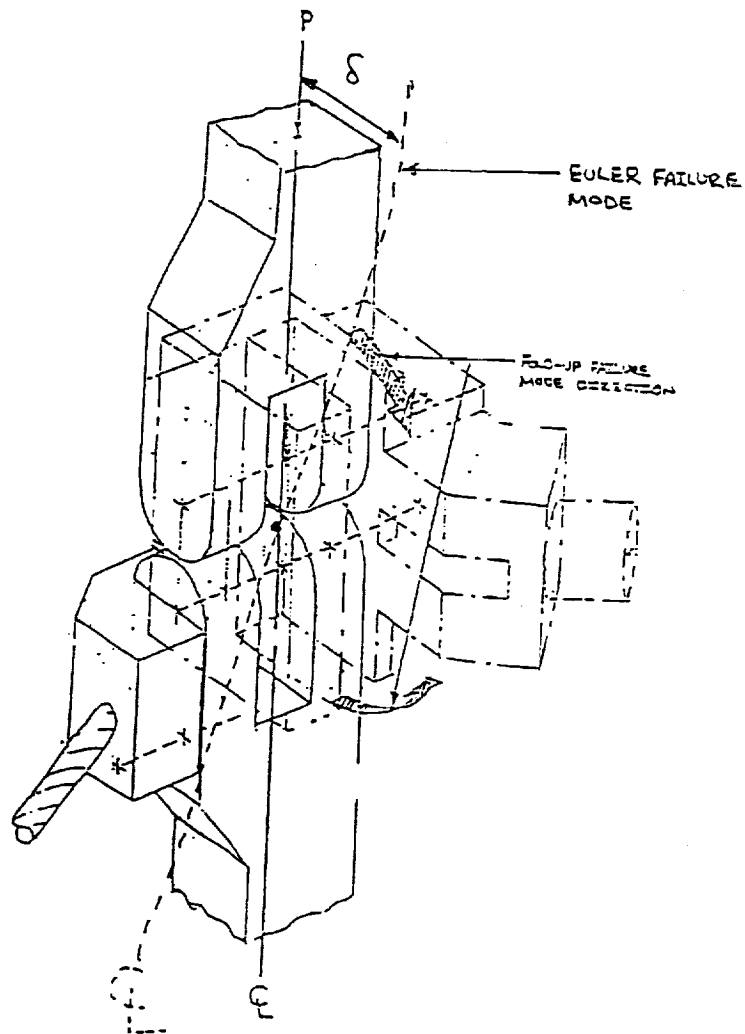


Figure 11 - Longerons Motion During Failure Modes

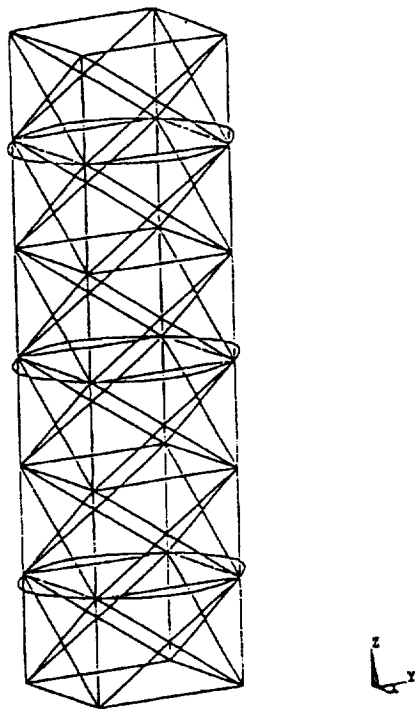


Figure 12 - FASTMast Nonlinear Finite Element Model

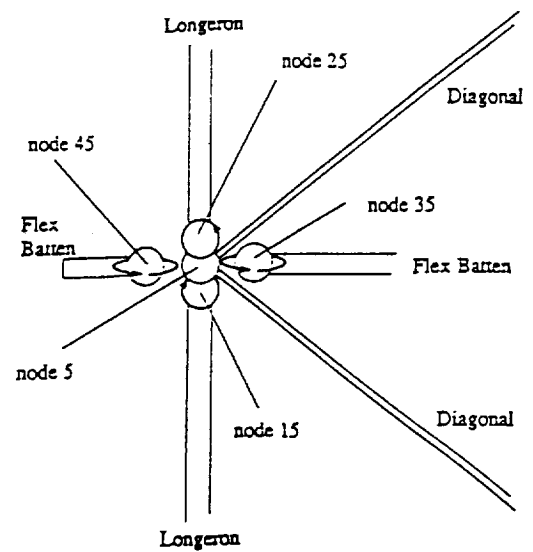


Figure 13 - FASTMast Hinge Joint

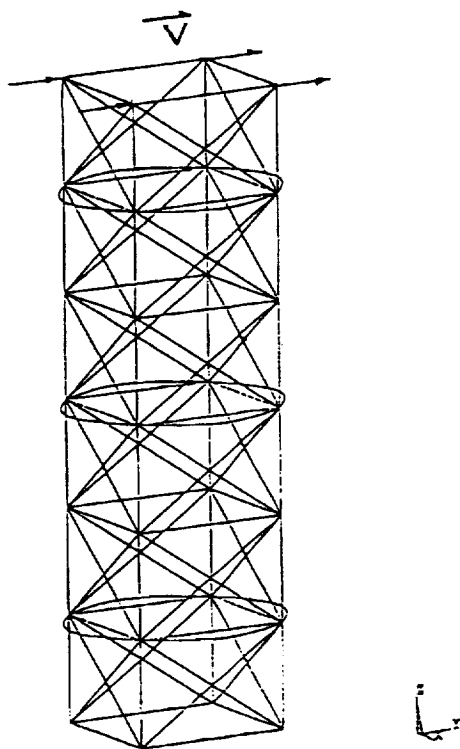


Figure 14 - Nonlinear Finite Element Model Tip Shear Case

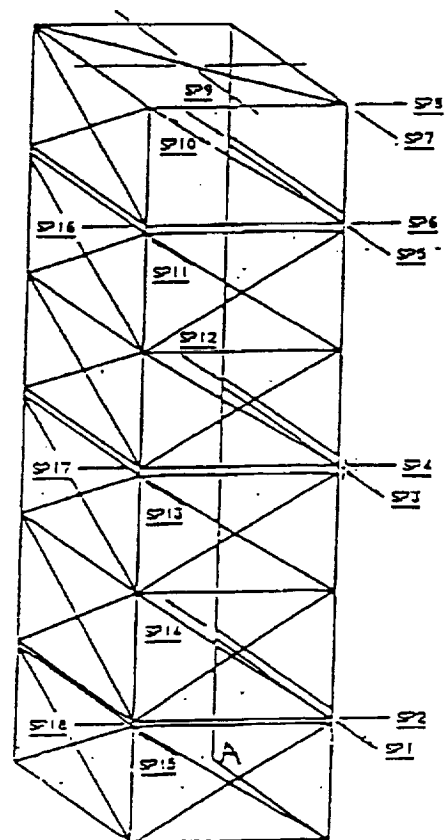


Figure 15 - Displacement Transducer Locations for Tip Shear Test

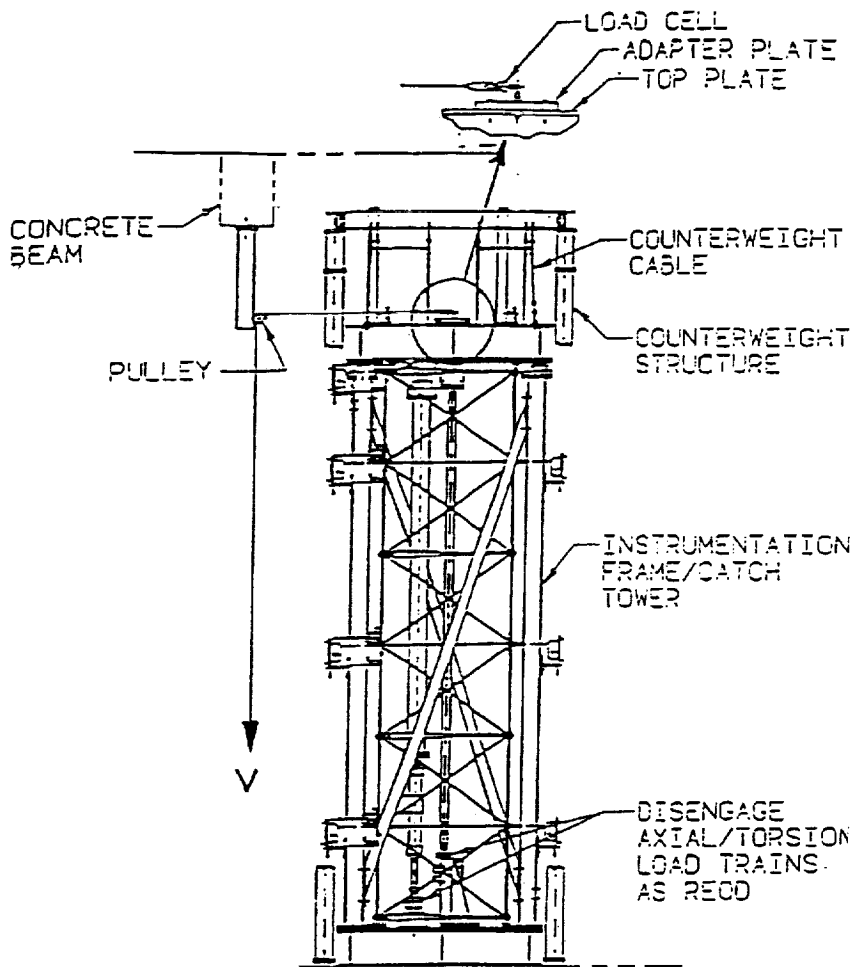


Figure 16 - 3-Bay Tip Shear Test Configuration

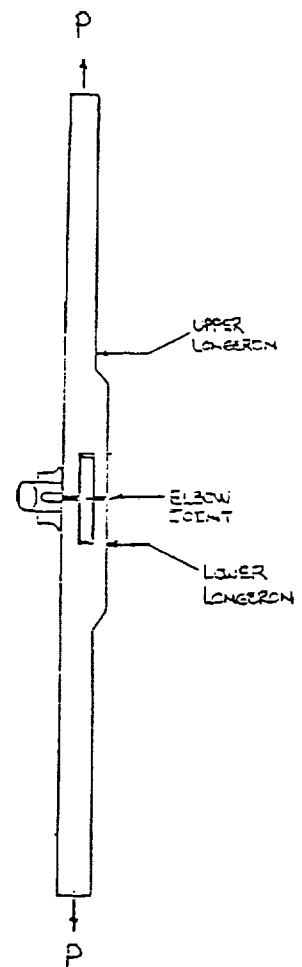


Figure 17 - Longeron Axial Stiffness Test Configuration

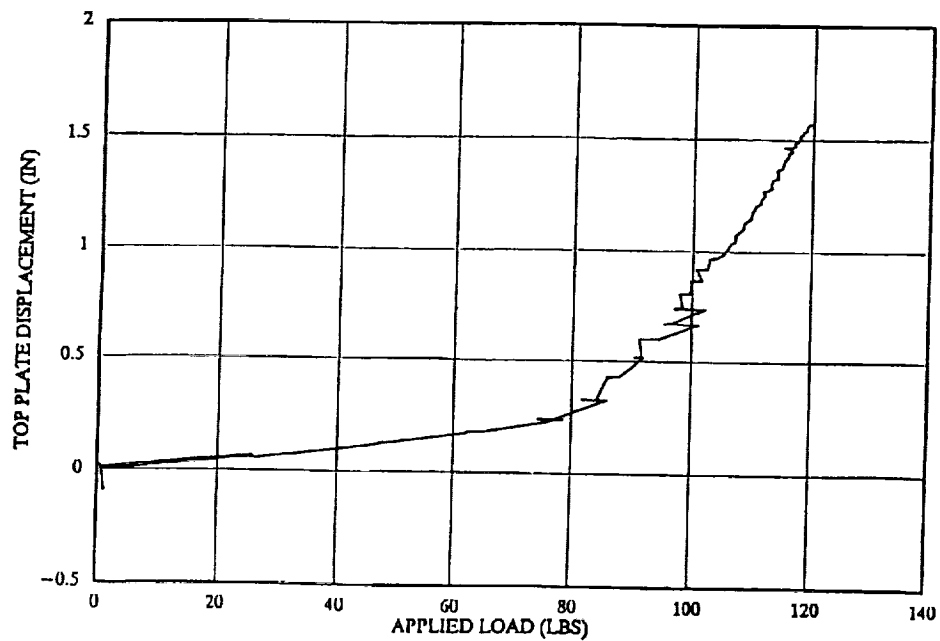


Figure 18 - FASTMast Top Deflection vs. Lateral Load from LeRC Shear Test

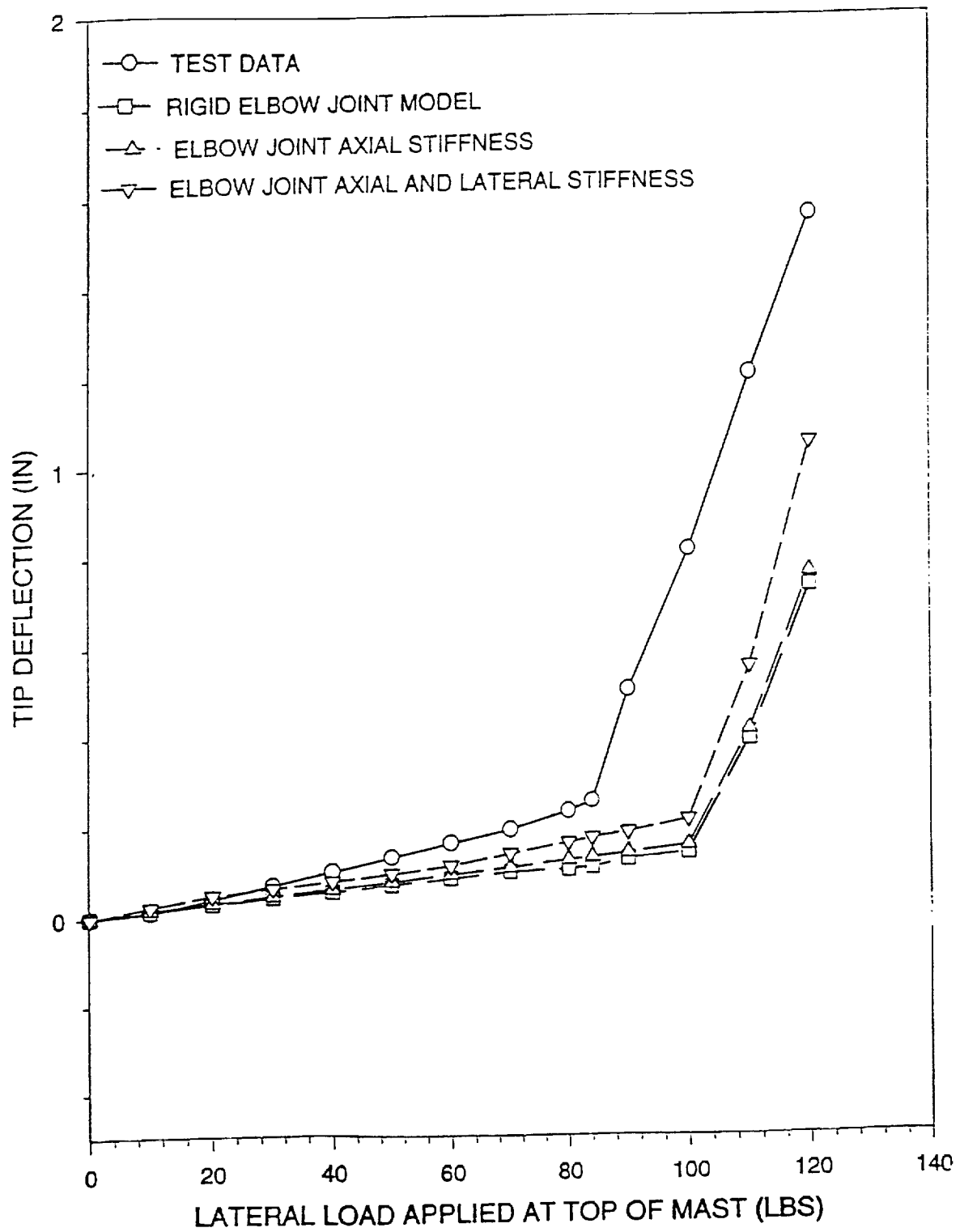


Figure 19 - Test and Analysis Mast Top Deflection vs. Applied Load

Mast Element	Material	Length	Area	Young's Modulus	Movement of Inertia I_w^1	Movement of Inertia I_w^2
		IN	IN ²	LB/IN ²	IN ⁴	IN ⁴
Tapered Longeron	Aluminum 6061-T6	19.750000	0.348100	10×10^9	0.010100	0.010100
Straight Longeron	Aluminum 6061-T6	19.750000	0.250000	10×10^9	0.005210	0.005210
Rigid Batten	Aluminum 6061-T6	19.300000	0.063900 ² 0.036200 ⁴	10×10^9	0.017400 ¹ 0.001440 ²	0.000436 ¹ 0.000316 ²
Batten Tube	Aluminum 6061-T6	11.200000	0.051110	10×10^9	0.001390	0.001390
Flex Batten	Fiberglass	31.750000	0.103000	8×10^9	0.001210	0.000591
Diagonal	Stainless Steel	36.000000	0.002313	29×10^9	—	—

1. Element y-axis oriented such that with x-axis along length of element right-hand rule is satisfied
2. Element z-axis vertical to cross-section
3. Wide end of tapered section
4. Narrow end of tapered section

Table 1 - Engineering Properties of Principal FASTMast Components

Structural Element	Material	Young's Modulus	Poisson's Ratio	Area	Moment of Inertia	Coefficient of Thermal Expansion
		LB/IN ²		IN ²	IN ⁴	IN/IN ² F ³
Longeron	Al-6061	10×10^9	0.33000	0.25000	0.00521	0.0
Flex Batten	Fiberglass	8×10^9	0.33000	0.10300	0.00121	1.0×10^{-3}
Diagonal	Stainless Steel	30×10^9	0.33000	0.00231	N/A	0.0

Table 2 - Properties for Two-Dimensional Nonlinear Planar Truss Study

AN UPDATE ON THE DEVELOPMENT OF A LINE-FOCUS REFRACTIVE CONCENTRATOR ARRAY

Michael F. Piszczor
NASA Lewis Research Center
Cleveland, Ohio

Mark J. O'Neill
Entech, Inc.
DFW Airport, Texas

and

Lewis M. Fraas
JX Crystals
Issaquah, Washington

ABSTRACT

Concentrator arrays offer a number of generic benefits for space (i.e. high array efficiency, protection from space radiation effects, minimized plasma interactions, etc.). The line-focus refractive concentrator concept, however, also offers two very important advantages: (1) relaxation of precise array tracking requirements to only a single axis and (2) low-cost mass production of the lens material. The linear refractive concentrator can be designed to provide an essentially flat response over a wide range of longitudinal errors for satellites having only single-axis tracking capability. New panel designs emphasize light weight, high stiffness, stowability and ease of manufacturing & assembly. This paper will address the current status of the concentrator program with special emphasis on the design implications, and flexibility, of using a linear refractive concentrator lens as well as detail the recent fabrication of prototype hardware.

INTRODUCTION

During the past two years, NASA Lewis, ENTECH and JX Crystals have been working on a refractive line-focus PV concentrator array for space applications (ref. 1). The linear-focus concentrator array for space is directly comparable to ENTECH's current line of terrestrial PV concentrator systems, and benefits from the operational and manufacturing knowledge gained by years of experience in this field. This concentrator concept is based on the same general principles as the point-focus mini-dome Fresnel lens concentrator (ref. 2,3) and offers many of the same advantages of the point-focus system. In addition to the generic benefits offered by PV concentrator systems for space (i.e. high array efficiency, inherent protection from space radiation effects, minimized interactions with the space plasma, etc.), the linear concept offers two very important advantages: (1) relaxation of precise array tracking requirements to only a single axis and (2) low-cost mass production of the concentrator lens material.

While the program is still pushing to maintain high array performance (i.e. high efficiency, low weight & volume, etc.) as its primary goal, greater emphasis is being put on manufacturability and overall array and spacecraft system cost reductions. Since the last report on this technology, low-cost, roll-to-roll production of the concentrator lens material has been demonstrated. New array structure designs are also being developed. The new array designs emphasize light weight, high stiffness, low thermal distortions and ease of manufacturing & assembly.

LINEAR CONCENTRATOR LENS DESIGN

As mentioned previously, the linear concentrator is based upon the same general lens design as the mini-dome Fresnel lens concentrator. The lens, currently made from silicone, has a curved, smooth outer surface with individually tailored linear Fresnel facets along the inner surface. (Refer to Fig. 1). The curvature of the outer surface and the Fresnel facets are designed such that the angles at which the light enters and exists the lens are equal, producing a condition that maximizes optical efficiency while minimizing the effects of radial shape errors. Thus, the lens is very tolerant to shape errors due to manufacturing, assembly or operational thermal distortions. The lens can also be easily designed to adjust the desired flux profile on the cell. (A double-hump design is currently used). This design flexibility has minimal impact to the overall design of the panel and array structure.

One of the major concerns facing photovoltaic concentrator systems is the precision of sun-pointing required. A key advantage of the linear refractive concentrator is the ability to modify the lens/cell design to obtain the necessary off-track design profile required for a specific mission without significantly affecting the basic array design. Because of the linear nature of the lens design, pointing errors along the longitudinal (length-wise) axis of the lens are much more tolerant to off-tracking than errors along the lateral (critical) axis. Errors along the critical axis are on the order of a few degrees and are highly dependent upon the lens/cell configuration, concentration ratio and the use of optical secondaries.

Fig. 2 demonstrates what happens when a linear lens is off-pointed along the longitudinal axis for the current lens design (40 degree rim angle). In Fig. 2a, light rays from the sun enter the curved lens and are then focused on to the cell within a specific flux profile. As the array begins to off-track along the longitudinal axis the focal length begins to effectively "shorten" (in a two-dimensional visualization). As this happens, some of the outer rays begin to move off the cell. Fig. 2b shows what happens for a 10 degree longitudinal error. At this angle the focal "shortening" is small and most of the light still hits the cell. The effective loss on lens optical efficiency is minimal. As the off-tracking error is increased (Figs. 2c. & 2d.), the effective "shortening" becomes more pronounced and the lens optical efficiency begins to decrease.

To illustrate the flexibility of the linear refractive concentrator lens, the effects of both lateral and longitudinal errors are plotted in Fig. 3 for two different lens designs. Lens optical efficiency refers to the amount of sunlight that actually falls on the photovoltaic cell and includes all reflection losses associated with the lens. Please note that these plots are for two specific designs and that optical secondaries were not included. (The use of optical secondaries will significantly increase tolerance along the lateral (critical) axis and cell concentration ratio along the longitudinal axis). The purpose of Fig. 3 is to qualitatively illustrate the variability of off-tracking tolerance as a function of the combined lens/cell design.

Fig. 3a shows a 3-dimensional plot of lens efficiency as a function of tracking error for the current lens design (40 degree rim angle). Note the much greater degree of tolerance along the longitudinal axis for a line-focus design. Still, the decrease in lens efficiency is fairly symmetric about the "on sun" position. Fig. 3b shows the same plot for a lens/cell design that is "single-axis tracking" (i.e. can accommodate errors of ± 23.5 degrees along the longitudinal axis without significant power loss). Note the difference in the shape of the plots. Also note that, unlike certain point-focus concentrator systems, there is still a significant amount of power available as the array begins to move off the sun. The "single-axis tracking" design could be used to provide an essentially flat response over a wide range of longitudinal errors for those satellites having only single-axis tracking capability. However, the cost of this added off-tracking capability is usually a decrease in concentration ratio (i.e. increased cell area). Thus, a true optimization of the lens/cell design is dependent upon a number of array, system and mission level factors (i.e. cell cost, array cost, radiation damage, single axis vs. double-axis tracking, contingency requirements, etc.). The plots in Fig. 3 represent the start of a detailed analysis to evaluate and quantify these relationships.

Fig. 4 illustrates how the design calculations compare to actual measured performance. Fig. 4 shows the calculated curve of geometric concentration ratio as a function of sun-pointing error tolerance along the lateral axis. As noted previously, to effectively improve the sun-pointing tolerance of the array, the geometric

concentration ratio on the cell must decrease (i.e. cell area must increase). Also plotted on the chart are measured data points from both the current linear lens design for space and one of ENTECH's production level terrestrial concentrators. (The range on the measured values correspond to optical lens efficiencies in the range of 90 to 95%.) Note that the measured points follow the predicted values quite well, being slightly above the predicted curve in all cases.

PROTOTYPE HARDWARE DEVELOPMENT

Fig. 5 shows some of the early prototype hardware developed under the linear concentrator program. The photograph shows a single linear lens with a cell receiver assembly that uses gallium arsenide/gallium antimonide (GaAs/GaSb) tandem cells (ref. 4) and molded optical secondaries. Further optimization and fabrication of the cell receiver assembly is currently under way at JX Crystals.

The lens in Fig. 5 was one of the first lenses produced and was fabricated by hand using a single tool to mold the unit. Since that time, low-cost, mass production of the lens material has been demonstrated. Because the Fresnel facets run linearly along the inner surface of the lens, the linear lens is very easy to fabricate and lends itself to roll-to-roll fabrication techniques. (The lens can be fabricated in a flat form and then curved to the proper shape upon integration with the array structure). Fig. 6 shows a 200 ft. roll of lens material fabricated by 3M to ENTECH specifications. The lens fabrication process is similar to that used by ENTECH on their large terrestrial linear modules. The roll contains five linear lenses side-by-side, which, by proper design of the spacing between lenses, could be mounted to the array structure as a single unit.

Significant progress has also been made on the development of an array structure. Fig. 7 shows different views of an array panel that was recently fabricated. The structure was made from carbon composite material to minimize weight and the effects of thermal distortions. An important point to note is that the structure achieves its stiffness from the honeycomb panel on the back of the structure, while the lenses are held accurately in place above the cell plane with a minimal amount of supporting structure. This design allows for a number of options with regard to reducing the stowed panel thickness by rotating the lenses down.

Optimization of the panel structure indicates that a total panel weight of $< 2 \text{ kg/m}^2$ is readily achievable. Estimates for both the panel mass and performance are given in Table I. With a cell operating efficiency of around 25% and an optical lens performance of 90%, an array efficiency corresponding to 300 watts/m^2 is achievable. This provides a panel specific power of 150 watts/kg . Based on this, a specific power of $> 100 \text{ watts/kg}$ at the array level should be achievable in the near-term.

SUMMARY

The line-focus refractive concentrator array is a novel photovoltaic array concept that offers two very important advantages compared to some other concentrator concepts: (1) relaxation of precise array tracking requirements to only a single axis and (2) low-cost mass production of the lens material. This means that the linear refractive concentrator can be designed to provide essentially constant power for satellites using only single-axis tracking. Low-cost, roll-to-roll production of the lens material has been demonstrated and new panel designs, emphasizing light weight, high stiffness, stowability and ease of manufacturing & assembly, are currently being fabricated and tested.

REFERENCES

1. M.F. Piszczor et al., "A Novel Space Photovoltaic Module Using a Linear Fresnel Lens and a Line-Focus Tandem Cell Receiver," *Proc. of 23rd IEEE Photovoltaic Specialist Conf.*, Louisville, KY, May 1993, pp. 1386-1391.
2. M.F. Piszczor and M.J. O'Neill, "Development of a Dome Fresnel Lens/Gallium Arsenide Photovoltaic Concentrator for Space Applications," *Proc. of 19th IEEE Photovoltaic Specialist Conf.*, New Orleans, LA, May 1987, pp. 479-484.
3. M.F. Piszczor et al., "A High-Performance Photovoltaic Concentrator Array: The Mini-Dome Fresnel Lens Concentrator with 30% Efficient GaAs/GaSb Tandem Cells," *Proc. of 22nd IEEE Photovoltaic Specialist Conf.*, Las Vegas, NV, October 1991, pp. 1485-1490.
4. L.M. Fraas et al., "Over 30% Efficient Tandem Gallium Solar Cells for Use With Concentrated Sunlight," *Optoelectronics-Devices and Technology*, 3, 1990, p. 297.

Mass Estimate of the Line-Focus Fresnel Lens Concentrator Panel				
Element	Thickness (microns)	Density (g/cu cm.)	Part Area/Aperture Area	Mass/Aperture Area (kg/sq.m.)
Lens Glass Superstrate	50	2.50	1.20	0.15
Silicone Fresnel Lens	200	1.00	1.20	0.24
Composite Structure	375	1.80	1.60	1.08
Cells & Cover Glasses	1250	2.50	0.07	0.22
Miscellaneous				0.31
Total				2.00
Panel Performance Estimate				
Cell Efficiency at Operating Temp. (%)	Lens Efficiency (%)	Packing Factor (%)	Areal Power (W/sq.m.)	Specific Power (W/kg)
18	90	95	211	105
20	90	95	234	117
22	90	95	258	129
24	90	95	281	141
26	90	95	305	152
28	90	95	328	164
30	90	95	352	176

Table I. Mass & Performance Estimates for a Linear Refractive Concentrator Panel

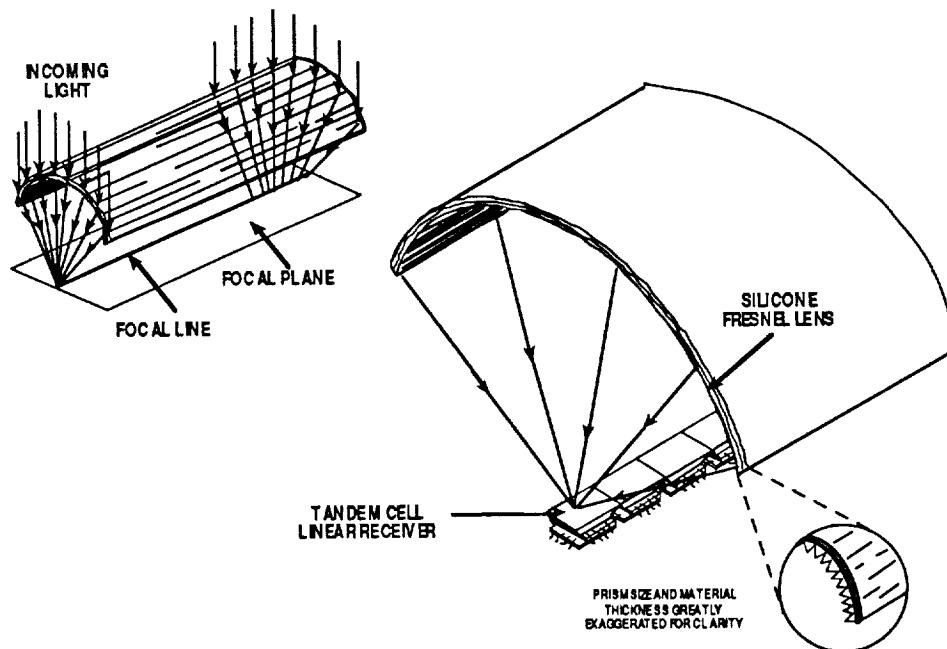
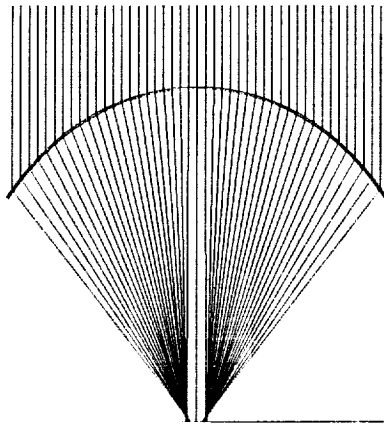
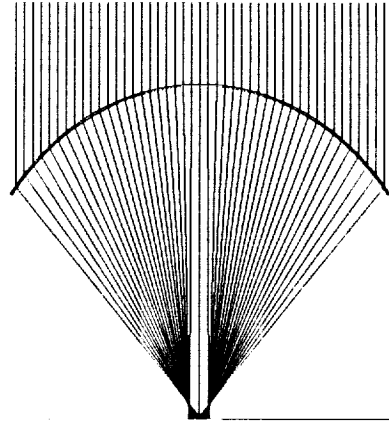


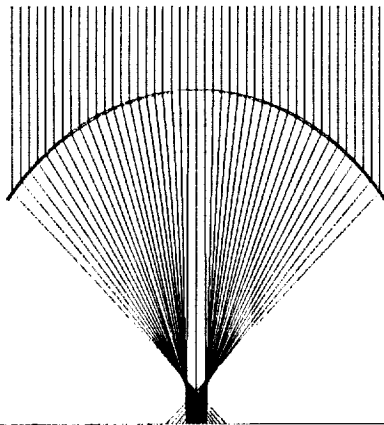
Fig. 1. Sketch of line-focus refractive concentrator components detailing operation and construction of the lens/cell element.



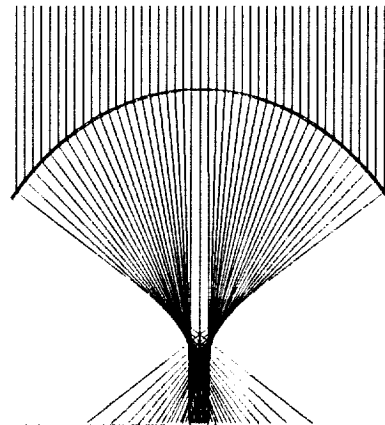
A. Zero
Longitudinal
Incidence



B. 10 deg
Longitudinal
Incidence



C. 20 deg
Longitudinal
Incidence



D. 30 deg
Longitudinal
Incidence

Fig. 2 - Effective 2-Dimensional Visualization of Focal Length Shortening Due to Off-Pointing Along the Longitudinal Axis

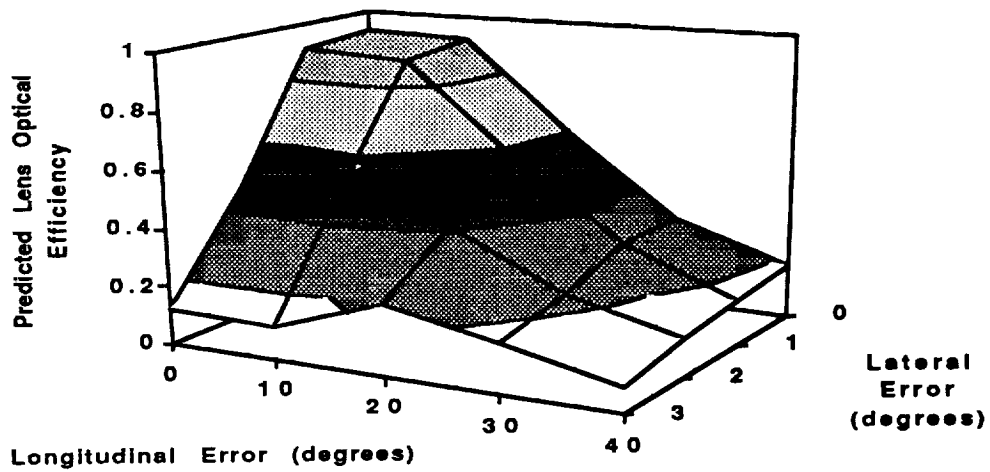


Fig. 3a. Predicted optical lens efficiency vs. off-pointing for a linear refractive concentrator. (Current lens design without an optical secondary.)

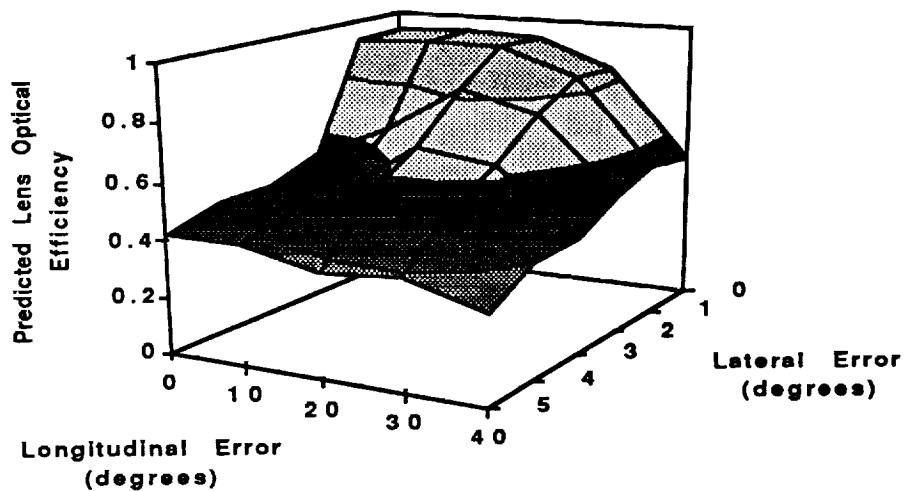


Fig. 3b. Predicted optical lens efficiency vs. off-pointing for a linear refractive concentrator. (Single-axis tracking lens design without an optical secondary.)

Calculated and Measured Geometric Concentration Ratio vs. Sun-Pointing Error Tolerance for Production-Version Line-Focus Lens (40 deg Rim, Designed for +/- 1 deg Tolerance at 15X) with No Secondary Optics

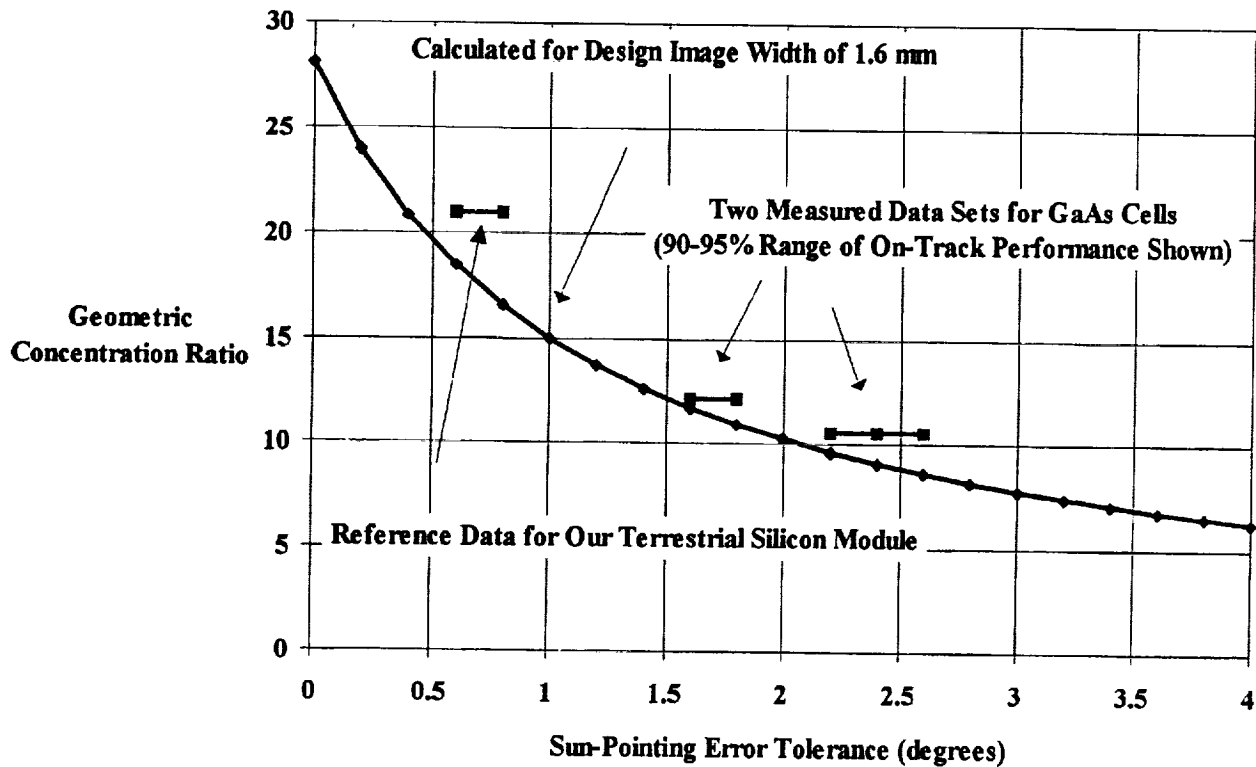


Fig. 4. Calculated vs. Measured Design Values for Linear Refractive Concentrators



Fig. 5. Early prototype of linear refractive concentrator element. Photograph shows a single linear lens and a GaAs/GaSb tandem cell receiver with optical secondaries.



Fig. 6. A 200 ft. roll of linear con.lens material. The 5-element wide roll was fabricated by 3M using a low-cost, roll-to-roll manufacturing process.

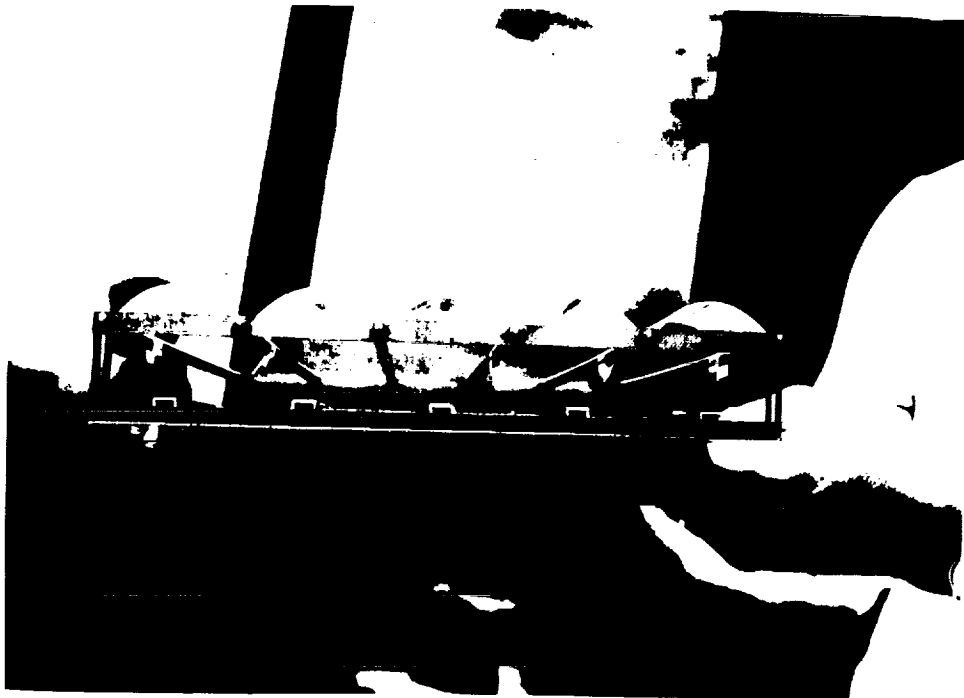


Fig. 7a. Prototype linear concentrator panel structure recently fabricated. Note that the stiffness of the carbon composite panel is achieved from the honeycomb panel on the back of the structure.



Fig. 7b. Prototype linear concentrator panel structure with linear lenses in place focusing light onto the back panel. Lens elements are a single unit cut from the 200 ft. roll of lens material.

AN INTRODUCTION TO THE ASTRO EDGE¹ SOLAR ARRAY

B.R. Spence and G.W. Marks
Astro Aerospace Corporation
Carpinteria, California

ABSTRACT

The *Astro Edge* solar array is a new and innovative low concentrator power generating system which has been developed for applications requiring high specific power, high stiffness, low risk, light weight, reliability, low stowed volume, negligible thermal snap, and affordability. The basic system is of modular construction which utilizes conventional materials and technology, and standard photovoltaic solar cells and laydown processes. Mechanisms, restraint/release devices, wiring harnesses, substrates, and support structures are designed to be simple, functional, lightweight, and modular. A brief overview of the *Astro Edge* solar array is discussed.

INTRODUCTION

The *Astro Edge* solar array is an innovative low cost, lightweight, compact, low concentrator solar array of modular construction which provides significant advancements in performance, reliability and affordability of solar array systems. A breadboard demonstration model is shown in Figure 1.

The *Astro Edge* solar array takes conventional materials and achieves a significant advance in efficiency by innovative packaging and incorporation of unique deployment systems. Mechanisms are designed to be simple and functional, tailored to the strength of lightweight substrates. Simplistic design and use of reflectors to decrease the number of solar cells enables an increase in efficiency while decreasing the system cost.

The *Astro Edge* solar array achieves low cost and low weight by using a lightweight reflector system to concentrate energy from the sun, obtaining the required output from 33 percent fewer solar cells than standard flat arrays. Net solar concentration is 150 percent (1.5 AM0), assuming a conservative 15 percent reflectivity, dimensional inaccuracy and thermal distortion loss. Specific powers for a 1000-watt EOL solar array wing of 150 W/kg with near-term multi-junction cells and 122 W/kg with existing GaAs/Ge cells are realistically achievable.

The deployed *Astro Edge* solar array forms a "channel" shaped configuration to provide very high stiffness allowing for the use of extremely lightweight substrate materials and hinges. Near-frictionless rolling tape type hinges and a simple damped spring-driven coordination sequence promote reliable deployment.

A more compact stowed package is achieved as a result of extremely thin substrates which are in contact when stowed. The cells are protected for launch by cushioned reflector surfaces. The reflective film is mounted to a thin foam cushion on the reflector panels. In the stowed configuration, the reflector panels are folded onto the solar cell panels, and the stack is compressed together for launch. The stowed configuration forms a compact package which is both secured and cushioned to provide a highly damped launch environment. In the deployed condition the reflector surfaces and structural configuration thermally decouple extreme temperature differentials to eliminate "thermal snap" phenomena resulting from exiting an eclipse.

The *Astro Edge* solar array is applicable to a broad power range and provides a low risk alternative for future spacecraft missions requiring high performance, light weight, reliability, low stowed volume and affordability. An overview of pertinent components is discussed in the ensuing paragraphs.

¹ Patent applied for.

DEPLOYMENT

The deployment sequence is shown in Figure 2. The array is preloaded against the spacecraft sidewall for launch and released with a lightweight hot wire cutter. On release, the hinge lines at the yoke/orientation drive, the yoke/panel, and the reflector panel/panel joints start to spring open. The motion is controlled by a system of lightweight graphite control rods and damped with a small viscous damper at the root hinge. When the reflector panel/panel hinges are fully open, the reflector to cell panel hinges will then spring open. This deployment is undamped, but because of the low torque springs and the lightweight reflectors, the energy involved is small. The reflector panels will deploy until terminated by diagonal tension lines. These lines will accurately determine the angle of the reflector. Preload from the hinges will be adequate to maintain the structural configuration through all spacecraft motions. A latch or locking mechanism is not required. In fact, latches are not necessary on the reflector panel/panel hinges because their geometry will prevent any bending.

The deployment forces associated with this lightweight solar array are very low. Spring designs are such that the array would survive an uncontrolled deployment. Control is required primarily to ensure that the array does not impact the spacecraft or any payloads. Control does not have to be precise and small errors in relative panel positions are acceptable.

The coordination linkage, shown in Figure 3, is a series of parallel linkages in which the panels form one part of the linkage and an assembly of 0.25-inch graphite composite tubes form the other. Because of the allowable inaccuracy, the hinges between the links need not be precision devices. In addition, because of the low drive torque involved, they can be of minimum strength.

CELL SUBSTRATES

The *Astro Edge* solar array geometry inherently provides a high degree of stiffness in the deployed position due to the reflector and cell substrate panels configured at steep angles to each other. By using the high in-plane stiffness of the flat panels, the out-of-plane bending stiffness requirements are much lower than typical deployable solar panels. This provides major opportunities for selection of lightweight materials and panel designs using thin sandwich construction for reducing volume and providing low weight. The solar cell substrates provide a dimensionally stable surface with sufficient stiffness and strength to support and prevent damage to the bonded solar cells. In addition, the substrate also electrically isolates the cells and provides an effective heat flow path for dissipation of waste heat. The substrates incorporated in the *Astro Edge* design are 1/8-inch-thick aluminum honeycomb core with 0.003-inch-thick Kevlar facesheets. The low CTE of the Kevlar laminate, combined with the low moisture absorption of the cyanate ester matrix, provides dimensional stability near that of a graphite facesheet at lower weight and cost. The Kevlar also provides an inherent electrical barrier for the solar cells without the added weight or the concern over pin holes of a Kapton film. The facesheet on the non-cell side of the panel incorporates a resin matrix loaded with graphite, resulting in a black Kevlar appearance which increases emissivity to 0.9 for higher heat dissipation from the panel.

REFLECTOR SUBSTRATES

Reflector substrate materials are identical to the cell substrate materials except for the additional mirrored surface and underlying foam. The back surfaces of the reflector substrates are not carbon loaded so that wiring harness can be directly bonded to the substrate. The integration of a 1/16-inch-thick polyurethane foam combined with a 0.002-inch-thick aluminized Teflon film comprise the remainder of the reflector panel. The layer of foam provides compliance for the reflective film and protects cells during launch.

HINGES

Hinging lightweight panels requires a different design from the traditional hinges and torsion springs commonly used. The panel to panel hinges employed are essentially frictionless, as they rely on rolling motion, and wrapping and unwrapping of metal tapes. Low torque and lightweight leaf springs, incorporated into each hinge, are used as the driving force for deployment. An engineering model of the

panel to panel hinge is shown in Figure 4. The hinge incorporates a female receptacle for easy assembly and changeout that becomes an integrated component of the substrate panels during lay-up.

The yoke to panel hinges are of the same rolling tape type as on the panels, but for this application incorporate a locking feature to maintain deployed position since geometry will not automatically lock it.

The orientation drive to yoke hinge, located at the root of the array, is the most heavily loaded and needs to lock out in a backlash-free manner. The baseline hinge is shown in Figure 5. At the root of the yoke structure, two journal bearings form a clevis hinge with the orientation drive flange. A leaf spring is mounted on the hinge axis to slow the whole deployment. The leaf spring is sized to provide the required margins over the damper and bearing friction, and the resistance from the stabilization link. The stabilization link is mounted to the orientation flange by a flexible pivot built of S-glass composite. It therefore will always have a tendency to move to the deployed position. At the other end of the link, rollers roll in the track mounted to the yoke and in the deployed position run over a spring latch which latches them against a hard stop eliminating any backlash in the joint.

WIRING HARNESS

Wiring harness has been designed such that at all times it assists deployment. Power is carried on flat beryllium copper strips attached to the backside of the reflector panels as shown in Figure 6. Beryllium copper cusps, preformed to deployed configurations, provide positive torque during deployment and bridge power between panels and other hinging points. The wiring harness is made from thin beryllium copper spring material, and is preformed along the hinge-lines to provide additional deployment force.

SUPPORT STRUCTURE

Because the array is an extremely lightweight device, all support structures are not required to be very stiff to achieve the common 0.1 Hz deployed system frequency.

The yoke structure is an extremely lightweight structure composed of high modulus graphite tubes with a 0.010-inch wall thickness. This member, as with all other support structures, is sized by the minimum practical manufacturable thickness and easily provides more than adequate stiffness.

STOWAGE SYSTEM

The stowed design concept, shown in Figure 7, preloads a sandwiched package of solar panels and cushioned reflector panels together against snubbers on the spacecraft sidewall. Shear load transfer is accomplished by features on the central snubber and selected external snubbers.

A preloaded structural load spreader, shown in Figure 8, is attached to the backside of an outboard panel which spreads the load from the central tie-down to attachments at the outermost panel edges. The attachments are at the feet of the structural load spreader and slide in a radial direction so that as load is applied to the hub the feet slide outward until the hub is in contact with the central preload stack. Upon release, the structure hub will jump up and clear the panel, but the feet will remain attached to the panel. As deployment takes place, the structure remains attached to an outer panel. The extra weight at the outboard end of the array has minimal effect because of the inherent stiffness of the deployed array, and the fact that the entire structure is at a minimum manufacturable thickness.

As mentioned previously, the solar array is preloaded against the spacecraft side wall and reacted at several snubbing points, but directly attached at the orientation drive and at a centrally located single restraint/release mechanism. Launch restraint/release is provided by a lightweight thermal cutter system as illustrated in Figure 8. The basic components are a Kevlar cord which is used to preload the array system and two cutting wires. The cutters are sequenced to give redundancy. Initially, the lower wire is heated. If this fails to cause release, then the upper wire is heated. The cutter wires are

preloaded against the Kevlar tie cord by a light torsional spring, sufficient to prevent vibration on launch, but not enough to cause damage to the Kevlar.

PERFORMANCE SUMMARY

The *Astro Edge* solar array can be adapted to a variety of applications ranging from Pegasus-class size to EOS-class size power ranges. Design studies have been performed to evaluate performance characteristics of an *Astro Edge* solar array modified for both a Pegasus-class size and EOS-size spacecraft. Table 1 shows a performance summary detailing mission requirements, EOL wing power, mass properties (including orientation drive), first deployed mode, first stowed mode, and stowed volume.

A preliminary COSMOS/M structural model of the deployed array is shown in Figure 9. The array forms into an inherently stiff configuration when deployed. As a result, the first deployed mode is driven primarily at the yoke structure root as shown. Deployed natural frequency can be tailored by simply modifying the yoke structure section.

A preliminary COSMOS/M structural model of the stowed array is shown in Figure 10. Stowed first mode is driven primarily by the stowage structure stiffness. Stowed natural frequency can be tailored by simply modifying the stowage structure section or by increasing the number of leg supports.

A conservative thermal analysis was performed to determine GaAs/Ge cell operating temperatures. Figure 11 shows the GaAs/Ge array temperature distribution for a sun synchronous Earth-oriented low-Earth orbit. The preliminary analysis indicates a maximum cell operating temperature of 89.1°C, and an average cell operating temperature of approximately 86°C. Additionally, a worst case thermal analysis was performed for an equatorial low-Earth orbit. Figure 12 shows the temperature profile for this worst case condition. The analysis indicates an average cell operating temperature of 94°C.

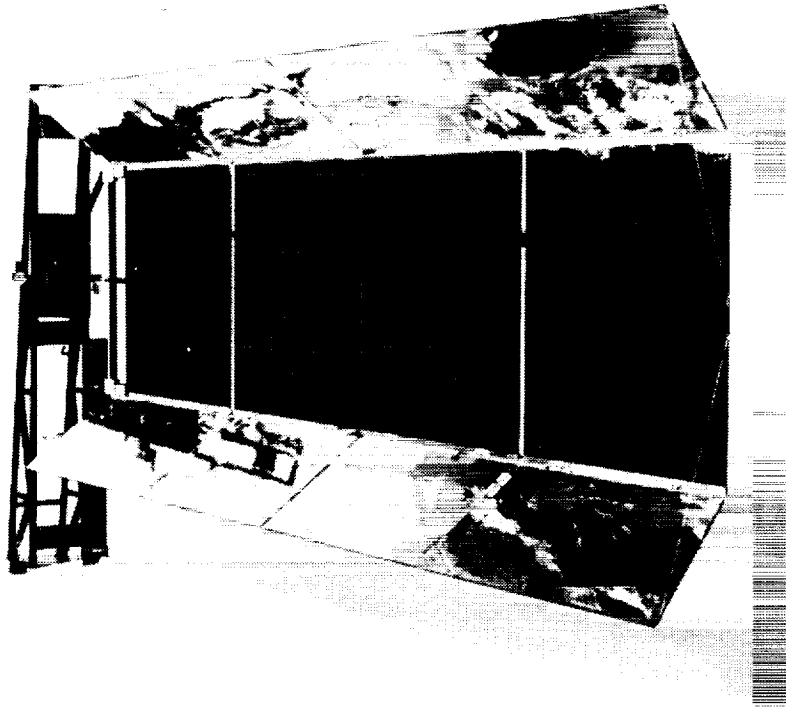
Another inherent advantage of the *Astro Edge* solar array lies in its ability to react large thermal differentials in a controlled manner without affecting overall spacecraft control. The reflective surface and foam interlayer on the reflector panels effectively thermally decouple extreme temperature differentials to eliminate thermal snap resulting from exiting an eclipse. The end result is a dynamically stable array during eclipse transition.

CONCLUSION

The *Astro Edge* solar array represents a unique technology applicable to a variety of power ranges and provides a low risk alternative for applications requiring high specific power, low weight, low stowed volume, reliability and affordability.

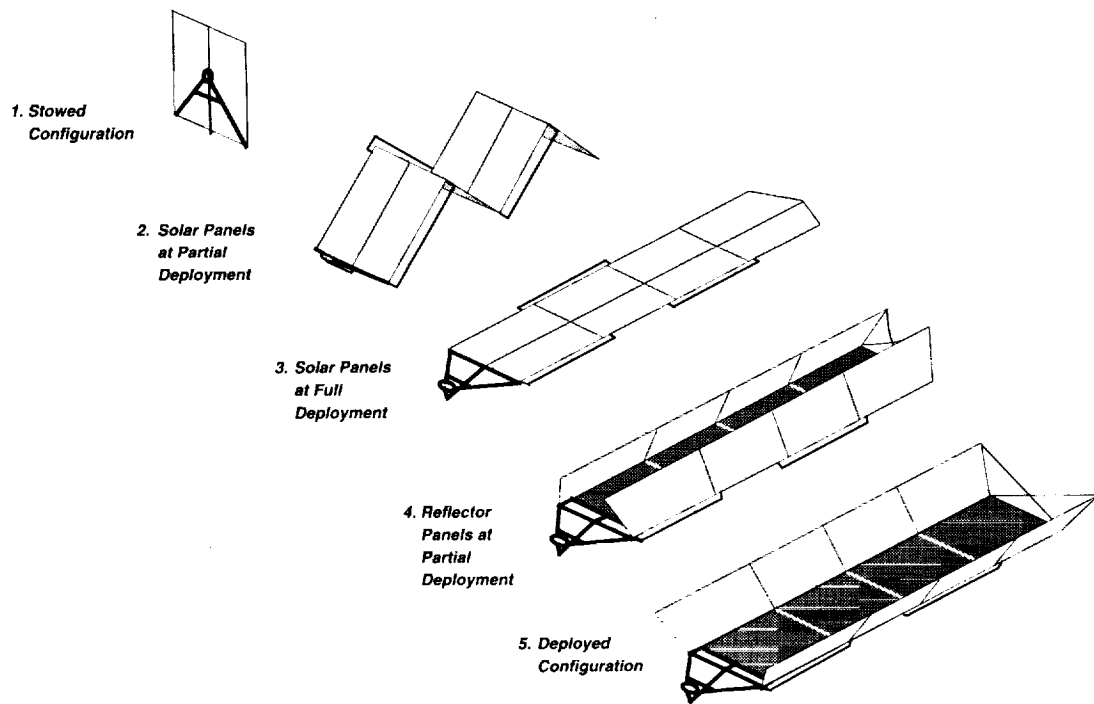
TABLE 1.—ASTRO EDGE SOLAR ARRAY PERFORMANCE SUMMARY
WITH 3.5-MIL-THICK GaAs/Ge SOLAR CELLS

Parameter	Pegasus-Class Size Performance	EOS-Class Size Performance
Mission	7 years LEO	7 years LEO
EOL Power	1364 W	5017 W
EOL Specific Power	113 W/kg	138 W/kg
Deployed First Mode (governed by yoke structure stiffness)	0.32 Hz	0.092 Hz
Stowed First Mode (governed by stowed structure geometry and stiffness)	25.1 Hz	25 Hz
Stowed Volume	~1.2 ft ³	~15 ft ³



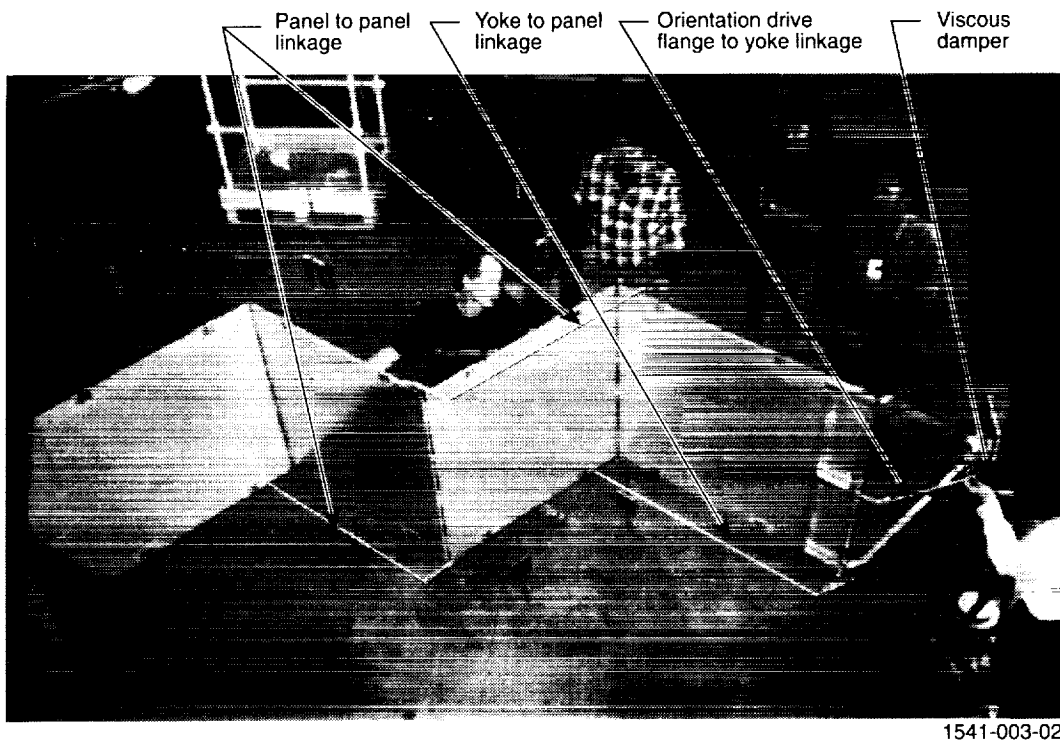
1541-004-02

Figure 1. *Astro Edge* Solar Array Breadboard Demonstration Model.



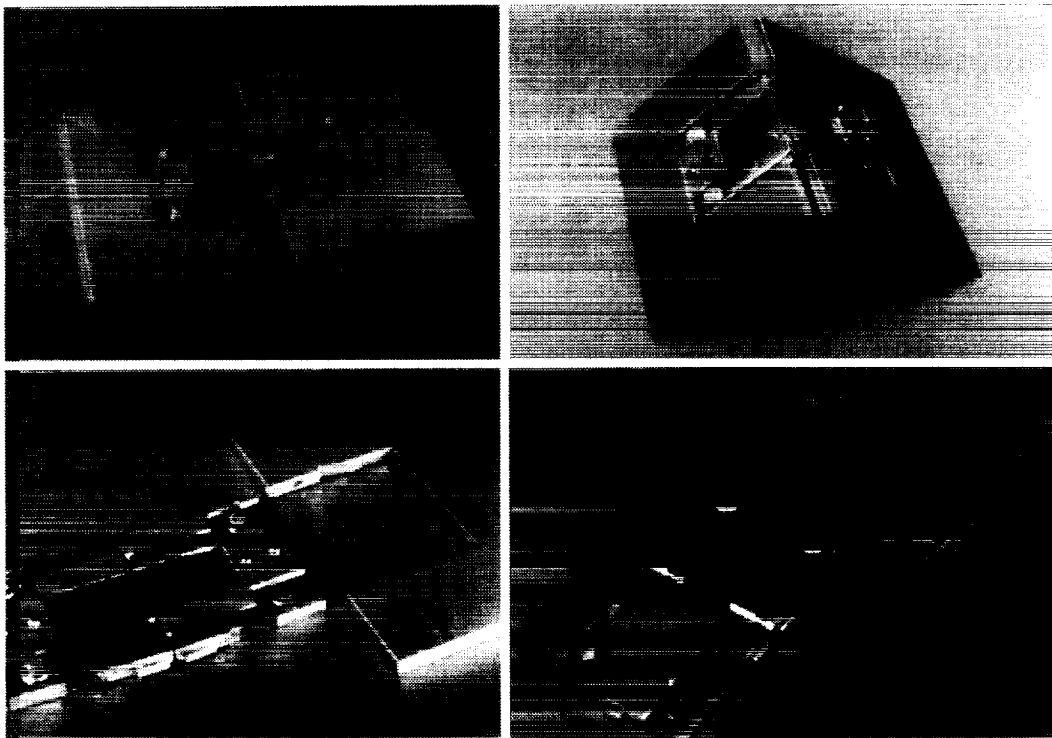
5813FH

Figure 2. *Astro Edge* Deployment Sequence.



1541-003-02

Figure 3. *Astro Edge* Coordination System.



1540-001

Figure 4. *Astro Edge* Panel to Panel Hinge Assembly.

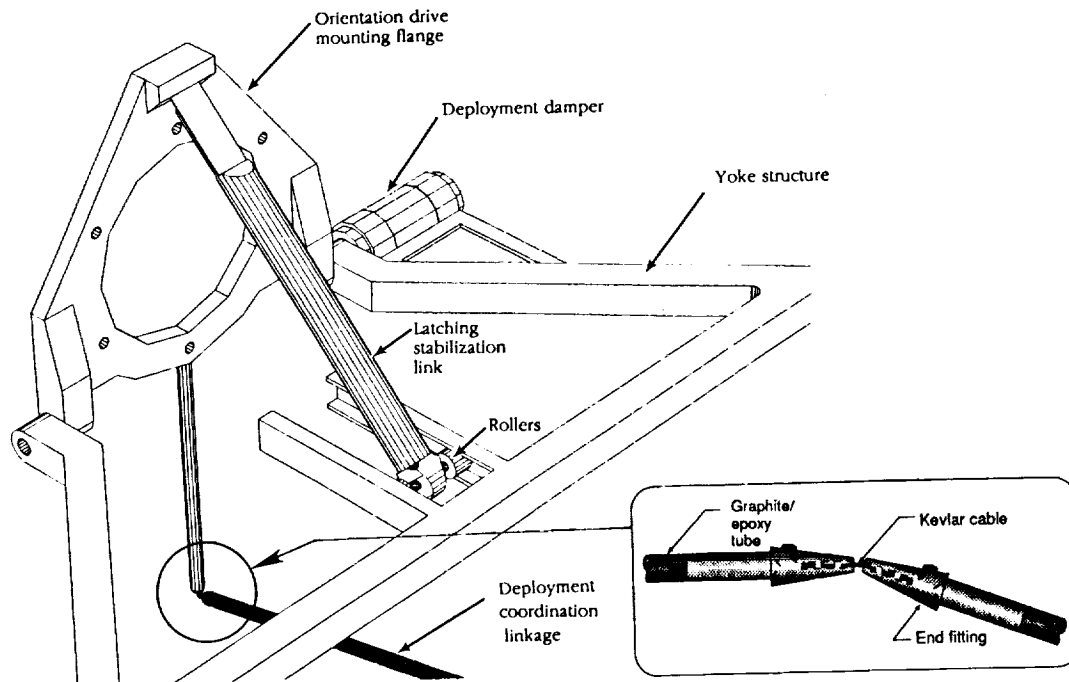
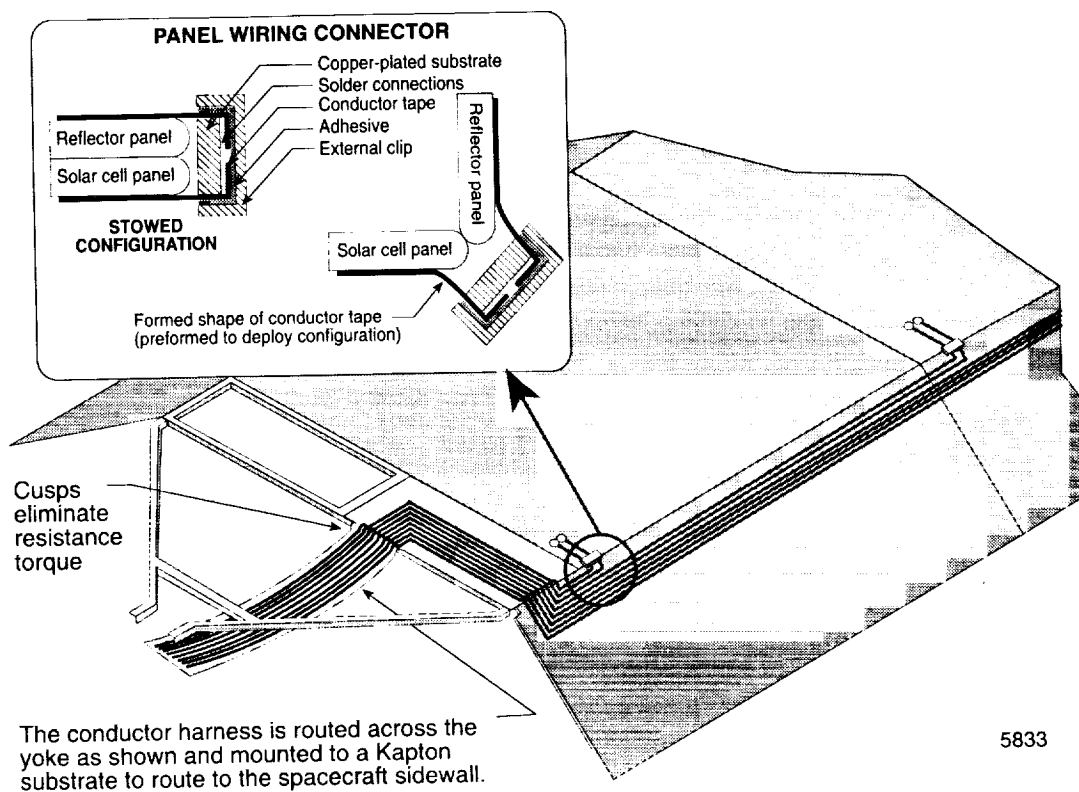


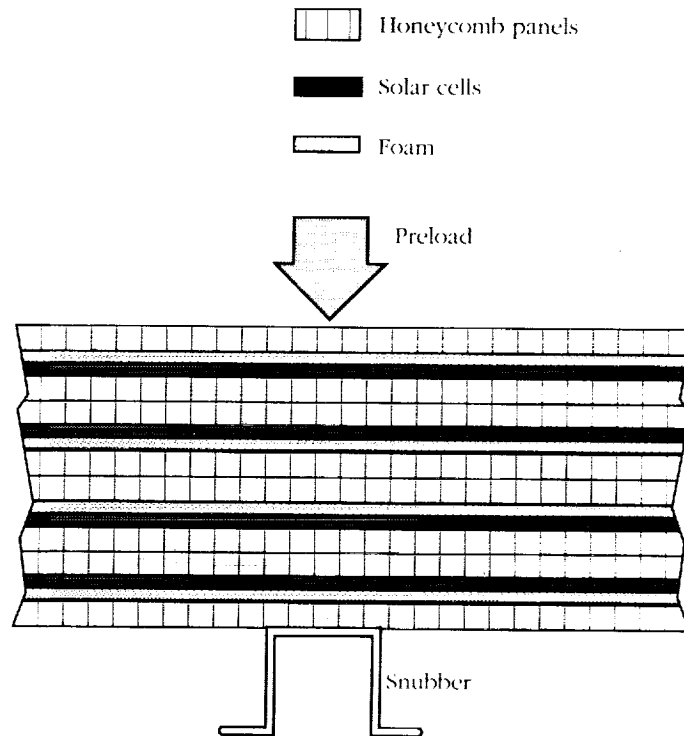
Figure 5. *Astro Edge* Yoke to Orientation Drive Hinge.

5835



5833

Figure 6. *Astro Edge* Wiring Harness.



5837

Figure 7. *Astro Edge* Stowed Package Concept.

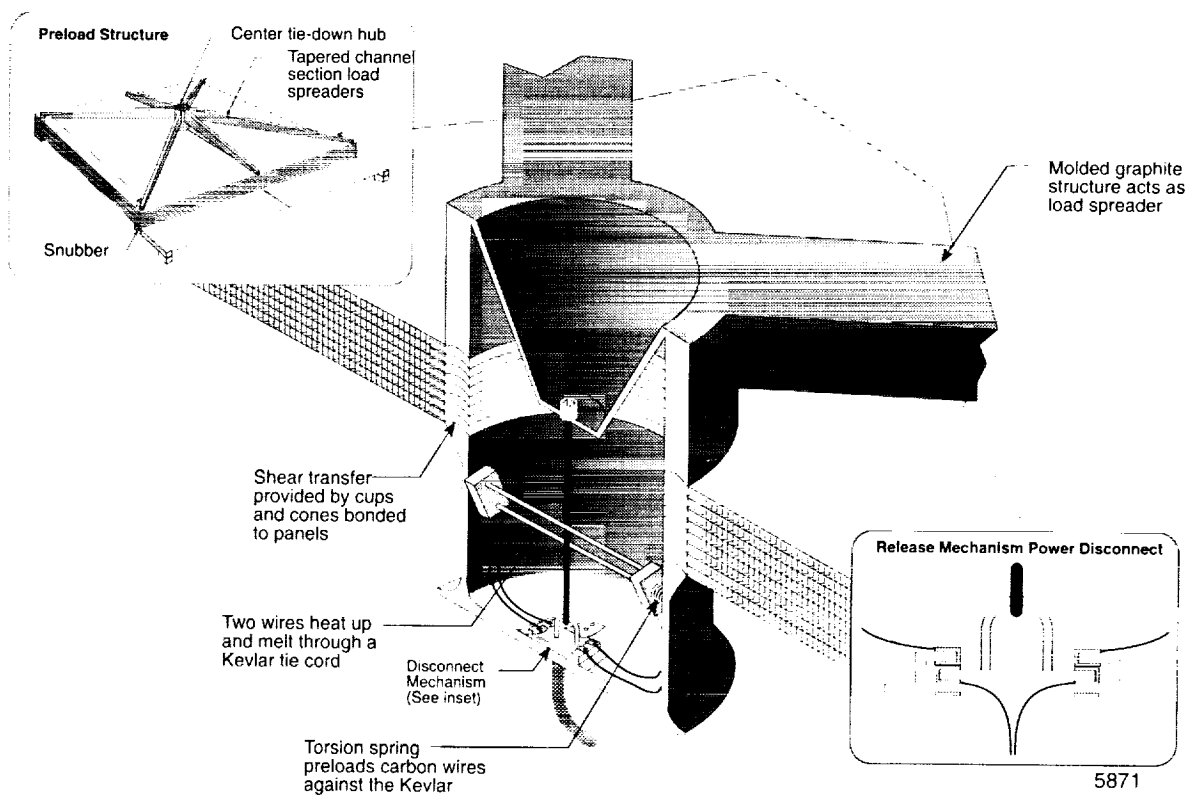
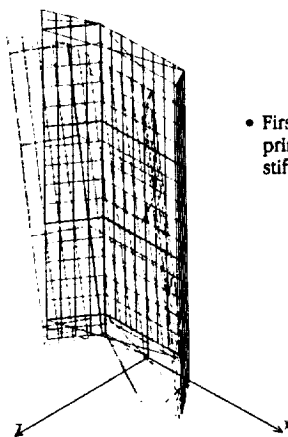


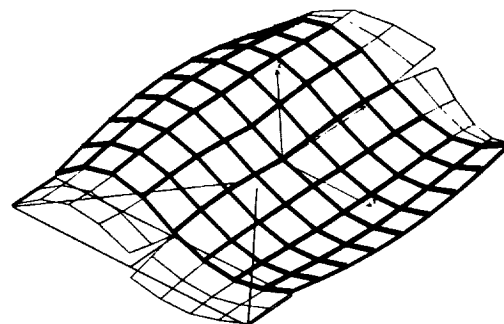
Figure 8. *Astro Edge* Solar Array Launch Restraint.



- First deployed mode driven primarily by yoke structure stiffness at root

5848

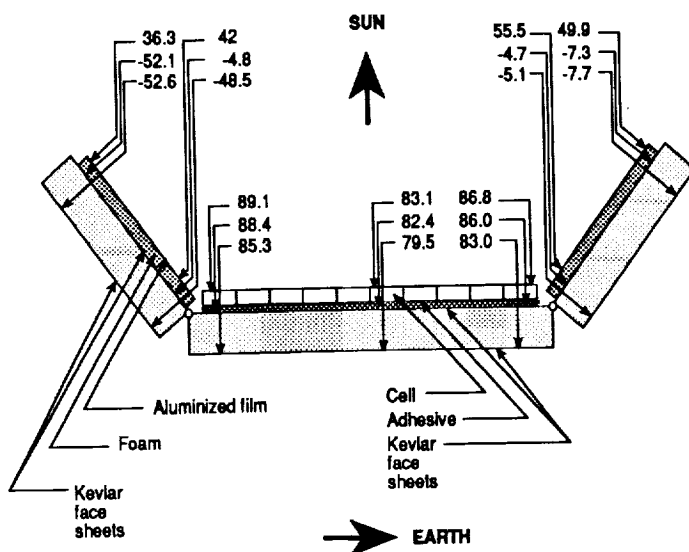
Figure 9. *Astro Edge* Solar Array First Deployed Mode.



- First stowed mode driven primarily stowage "spider" structure stiffness

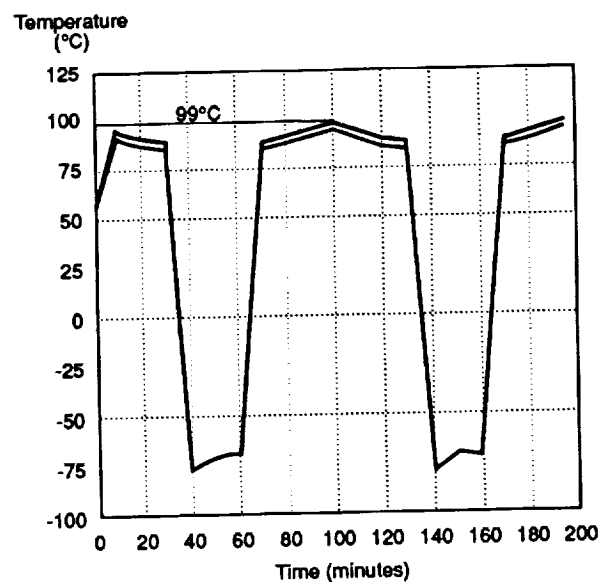
5851

Figure 10. *Astro Edge* Solar Array First Stowed Mode.



5904

Figure 11. *Astro Edge* Solar Array Temperature Distribution for Sun Synchronous Earth Oriented Orbit.



5905

Figure 12. *Astro Edge* Solar Array GaAs Cell Temperature Profile for Worst Case Equatorial LEO.

SESSION VI

NON-SOLAR ENERGY CONVERSION

RARE EARTH GARNET SELECTIVE EMITTER

Roland A. Lowe
Kent State University
Kent, Ohio

and

Donald L. Chubb, Serene C. Farmer, and Brian S. Good
NASA Lewis Research Center
Cleveland, Ohio

ABSTRACT

Thin film Ho-YAG and Er-YAG emitters with a platinum substrate exhibit high spectral emittance in the emission band ($\epsilon_\lambda \approx 0.75$, $^4I_{15/2} - ^4I_{13/2}$, for Er-YAG and $\epsilon_\lambda \approx 0.65$, $^5I_7 - ^5I_8$ for Ho-YAG) at 1500K. In addition, low out-of-band spectral emittance, $\epsilon_\lambda < 0.2$, suggest these materials would be excellent candidates for high efficiency selective emitters in thermophotovoltaic (TPV) systems operating at moderate temperatures (1200-1500K). Spectral emittance measurements of the thin films were made ($1.2 < \lambda < 3.0 \mu\text{m}$) and compared to the theoretical emittances calculated using measured values of the spectral extinction coefficient.

In this paper we present the results for a new class of rare earth ion selective emitters. These emitters are thin sections ($< 1\text{mm}$) of yttrium aluminum garnet (YAG) single crystal with a rare earth substitutional impurity. Selective emitters in the near IR are of special interest for thermophotovoltaic (TPV) energy conversion^{1,2}. The most promising solid selective emitters for use in a TPV system are rare earth oxides. Early spectral emittance work³ on rare earth oxides showed strong emission bands in the infrared (.9 - 3 microns). However, the emittance outside the emission band was also significant and the efficiency of these emitters was low. Recent improvements in efficiency^{4,5} have been made with emitters fabricated from fine (5-10 μm) rare earth oxide fibers similar to the Welsbach mantle used in gas lanterns. However, the rare earth garnet emitters are more rugged than the mantle type emitters.

A thin film selective emitter⁶ on a low emissivity substrate such as gold, platinum etc., is rugged and easily adapted to a wide variety of thermal sources. The garnet structure and its many subgroups have been successfully used as hosts for rare earth ions, introduced as substitutional impurities, in the development of solid state laser crystals⁷. Doping, dependent on the particular ion and crystal structure, may be as high as 100 at. % (complete substitution of yttrium ion with the rare earth ion). These materials have high melting points, 1940 C for YAG (Yttrium Aluminum Garnet), and low emissivity in the near infrared making them excellent candidates for a thin film selective emitter.

As previously stated, the spectral emittance of a rare earth emitter is characterized by one or more well defined emission bands. Outside the emission band the emittance (absorptance) is much lower. Therefore, it is expected that emission outside the band for a thin film selective emitter will be dominated by the emitter substrate. For an efficient emitter (power in the emission band/total emitted power) the substrate must have low emittance, ϵ_s . Within the emission band the spectral emittance is governed by the index of refraction, n_f , and the spectral extinction coefficient, α_λ (sum of the absorption coefficient, a_λ , and scattering coefficient, σ_λ), the emitter temperature, T_E , and thickness, d . In reference 6 the emitter emittance and efficiency are derived as a function of the optical depth, $K_\lambda = \alpha_\lambda d$, and the dimensionless emission-band energy, E_g/kT_E , where E_g is the photon energy at the center of the emission band. This analysis shows that maximum efficiency occurs for an optimum K_λ and $E_g/kT_E \sim 4$.

This paper presents normal spectral emittance, ϵ_λ , measurements of holmium, (Ho) and erbium (Er) doped YAG thin film selective emitters at (1500 K), and compares those results with the theoretical spectral emittance. The spectral extinction coefficient, which is required to calculate ϵ_λ , was also

calculated from transmission and reflectance measurements performed at room temperature.

Specimens were cut from Czochralski grown crystals and polished on both sides with 1 μ diamond abrasive. Spectral transmission, T_λ , and reflectance, R_λ , measurements were made at room temperature with a Perkin Elmer Lambda 19 UV/VIS/NIR spectrophotometer and a Nicolet Model 750 Magna-IR spectrometer. The spectral extinction coefficient, α_λ , was calculated⁸ using:

$$e^{-\alpha_\lambda d} = \frac{1}{2} \left\{ \sqrt{\left[\frac{(1-R_\lambda)^2 - T_\lambda^2}{T_\lambda^2} \right]^2 + 4} - \frac{1}{T_\lambda} [(1-R_\lambda)^2 - T_\lambda^2] \right\} \quad (1)$$

Fig. 1 shows the spectral extinction coefficient for 25 at. % Ho-YAG (.32 mm thickness) and 40 at. % Er-YAG (.65 mm thickness) specimens within the emission band. Relatively strong absorption is evident at the characteristic laser transitions in Er-YAG ($^4I_{15/2} - ^4I_{13/2}$) and Ho-YAG ($^5I_7 - ^5I_8$). Measurements with the Nicolet Model 750 Magna-IR spectrometer indicate the absorption is low compared to the emission band in the near infrared until approximately $\lambda = 6\mu$ where absorption increases greatly and continues through the far infrared.

Quantities such as emissivity and absorptivity are usually thought of as properties of an isothermal surface. However, for the thin film rare-earth YAG emitter emission from throughout the film contributes to the spectral emittance. Since significant temperature gradients (200 K) exist across the specimens the "emitter temperature", used to calculate emittance from the intensity measurements, is not the surface temperature but rather the average of the front and back surface temperatures in the center of the sample. Temperature measurements, made with type R thermocouples, had an accuracy of ± 6 K. Spectral intensity measurements were made with a monochromator and a temperature controlled PbS detector calibrated with a 1270 K blackbody reference. Measurement accuracy and repeatability with the blackbody standard at 1270 K were typically within 2%. Platinum foil was placed behind the samples as a low emittance substrate. The configuration shown in fig. 2 was used to eliminate reflected radiation from the furnace interior, a near blackbody radiator, from reaching the detector. Two sources of measurement error were identified. Alumina insulation, a nearly perfect diffuse reflector, reflects radiation originating from the perimeter of the sample (a), which is at a higher temperature than the viewed area, to the surface of the sample in the field of view of the detector. Also, emission from the hot alumina (b) is reflected directly from the viewed area to the detector. Comparison of ϵ_λ measurements of platinum foil under conditions identical to those required to produce an average emitter temperature of 1500 K (furnace @ 1664 K) and data from ref. 9 show the increase in ϵ_λ due to reflected radiation is $+0.09$ @ $2.0 \mu\text{m}$ and $+0.125$ @ $1.5 \mu\text{m}$. This will be the maximum measurement error for materials with high spectral reflectance ($\sim 80\%$) and low emittance such as platinum. However, in the Ho and Er-YAG specimens, reflectance in the emission band is less (20-70% for Ho-YAG). Therefore, an estimate for the maximum experimental error in measured values of ϵ_λ in the emission band is ± 0.1 .

Fig. 3 shows the measured and theoretical⁶ spectral emittance for different values of the scattering albedo, $\Omega_\lambda = \sigma_\lambda / (a_\lambda + \sigma_\lambda)$, of 25% Ho-YAG (.65 mm thickness) and 40% Er-YAG (1.04 mm thickness) at 1500 K. The theory assumes a uniform temperature for the film and the theoretical spectral emittance is independent of temperature. For theoretical calculations the extinction coefficients shown in fig. 1 were used. An index of refraction of $n_f = 1.9$ was used for the rare-earth YAG and the platinum substrate was assumed to have a constant spectral emittance⁹ of $\epsilon_s = 0.2$. Small changes in n_f (< 0.1) had a negligible effect on the theoretical results. In comparing the theoretical and experimental ϵ_λ results, several features should be noted. First, results with small scattering ($\Omega_\lambda < 0.5$) agree more closely with the measurements. Second, the measured emittance outside the emission band is considerably higher than the theoretical values. As stated earlier, emission outside of the band is primarily from the platinum substrate. Measurements of ϵ_λ of pure platinum foil under identical conditions required to produce an average emitter temperature of 1500 K provided a value of 0.28 @ $2.4\mu\text{m}$. This value corresponds well

with the out of band emission observed in fig. 3a,b. Values of experimental ϵ_λ for the platinum substrate are greater than ref. 9 due to reflected radiation seen by the detector. Finally, due to absorption in the rare-earth YAG, theoretical values for ϵ_λ outside the emission band are less than the substrate emittance, $\epsilon_s = 0.2$.

In conclusion, we have measured large emittance in the emission band of Ho-YAG, $\epsilon_\lambda \approx .65$, and Er-YAG, $\epsilon_\lambda \approx .75$, thin film selective emitters. Calculated spectral emittances for small scattering ($\Omega_\lambda < .5$) are in fairly good agreement with the measured emittances. However, accurate emittance calculations are possible only if the temperature gradient across the thin emitter is included. Finally, the large emittance in the emission band and low out-of-band emittance suggest that Ho-YAG and Er-YAG thin film selective emitters may make it possible to develop an efficient TPV energy conversion system at moderate temperatures (1500K).

The authors would like to acknowledge the assistance of Dr. David Hehemann of Kent State University in obtaining the FTIR data and Dr. Milan Kokta of Union Carbide Corporation Crystal Products Division for providing the Ho and Er-YAG crystals.

REFERENCES

1. R. E. Nelson and P. A. Iles, ASME/ASES/SOLTECH Joint Solar Energy Conference, (1993)
2. P. A. Iles, Conference Record of 21st IEEE Photovoltaic Specialists Conference, 420 (1990)
3. G.E. Guazzoni, Appl. Spectra **26**, 60 (1972)
4. R.E. Nelson, Proceedings of the 32nd International Power Sources Symposium, 95 (1986)
5. C.R. Parent and R.E. Nelson, Proceedings of the Twenty-First Intersociety Energy Conversion Engineering Conference, 1314 (1986)
6. D. L. Chubb and R. A. Lowe, J. Appl Phys. **74** (9), 5687 (1993)
7. L.G. DeShazer, S.C. Rand, and B.A. Wechsler, *CRC Handbook of Laser Science and Technology*, Vol. 5, Part 3, "Laser Crystals", (CRC Press) 1987
8. R. Siegal and J. R. Howell, *Thermal Radiation and Heat Transfer*, (Hemisphere, Washington, DC) 2nd ed. 1981, p. 722
9. Y.S. Touloukian and C.Y. Ho, *Thermophysical Properties of Matter vol. 7 "Thermal Radiative Properties Metallic Elements & Alloys"*, (IFI/Plenum, New York-Washington) 1970, p. 542 (curve 39)

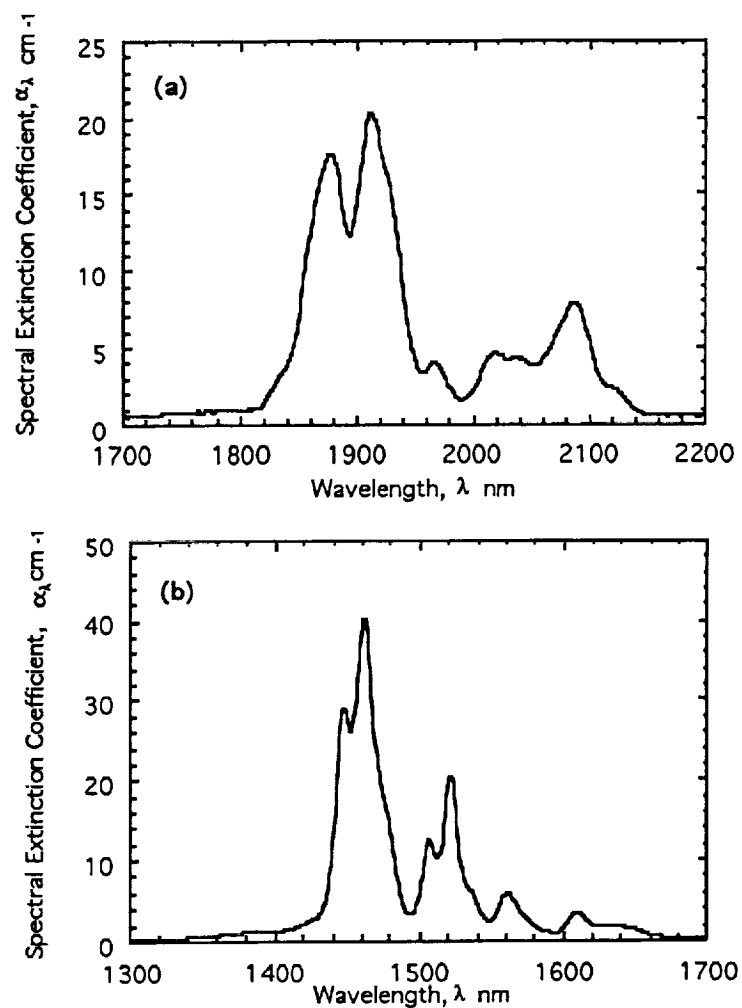


FIG. 1 Spectral extinction coefficient calculated from measured transmission and reflectance (a) 25% Ho-YAG (b) 40% Er-YAG

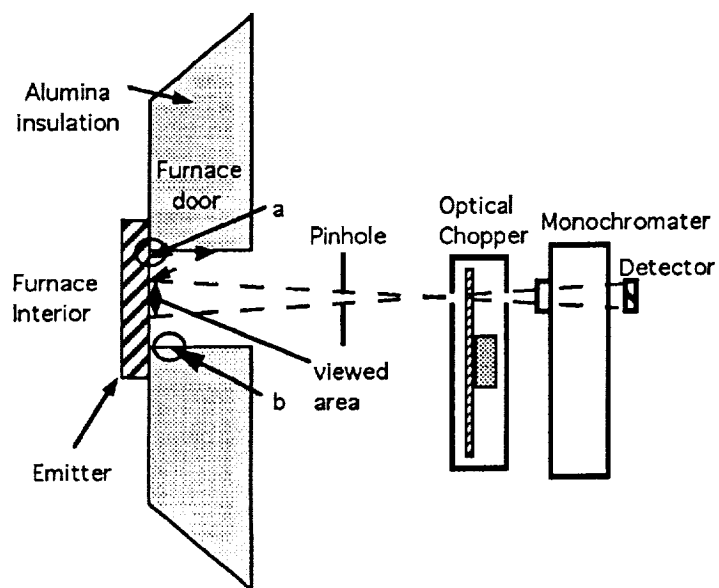
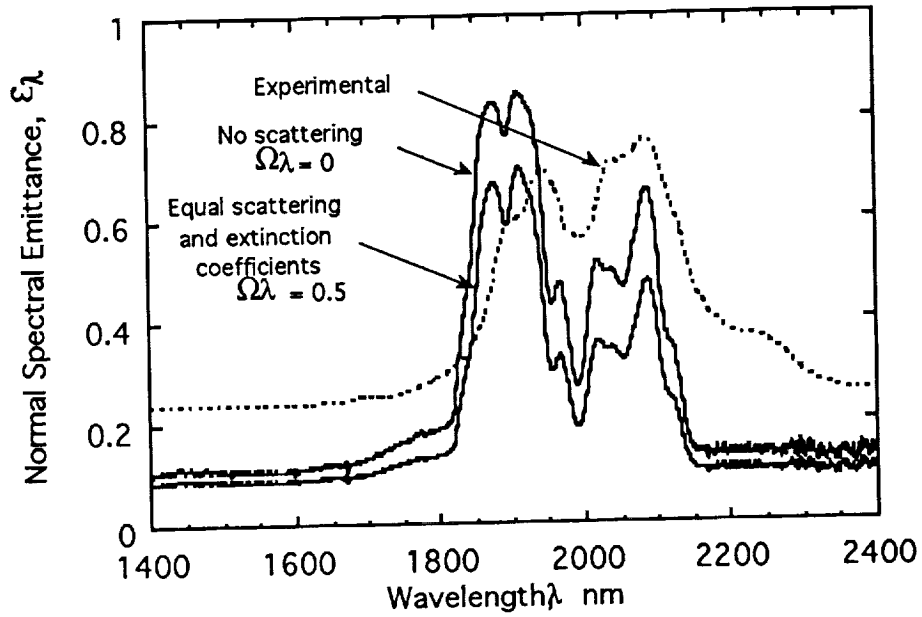
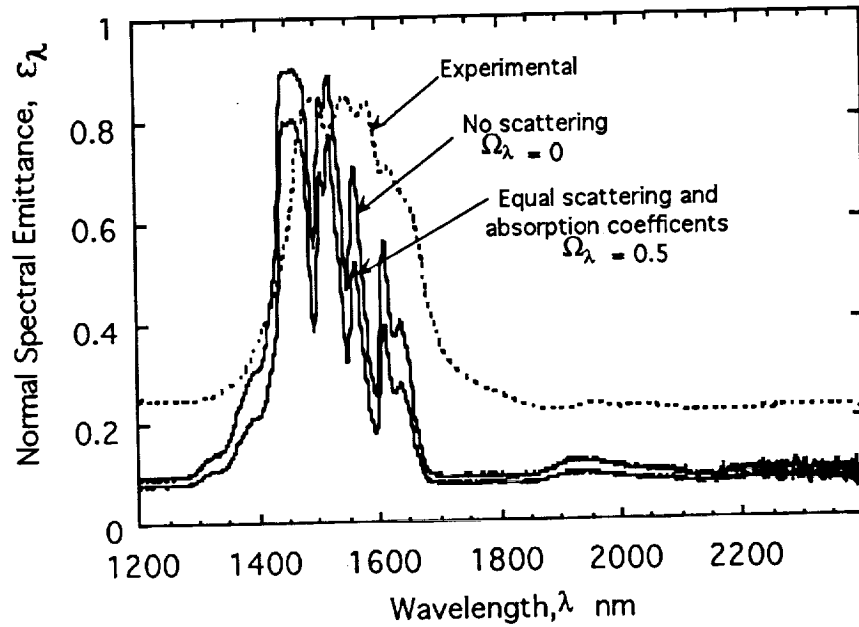


FIG. 2 Schematic representation of the experimental setup



(a)



(b)

FIG. 3 Theoretical and measured spectral emittance ϵ_λ with a platinum foil substrate (constant $\epsilon_\lambda = .2$) and index of refraction for YAG ($n_f = 1.9$) used for theoretical calculations (a) 25% Ho-YAG .65 mm thick; front surface temp. = 1389 K, back surface temp. = 1616K, average emitter temp. = 1500K (b) 40% Er-YAG 1.04 mm thick; front surface temp. = 1398K, back surface temp = 1606K, average emitter temp. = 1500K

InGaAs PV DEVICE DEVELOPMENT FOR TPV POWER SYSTEMS

David M. Wilt, Navid S. Fatemi, and Richard W. Hoffman, Jr.
Essential Research, Inc.
Cleveland, Ohio

Phillip P. Jenkins, David J. Brinker, and David Scheiman
NYMA, Inc.
Brook Park, Ohio

Roland Lowe
Kent State University
Kent, Ohio

and

Donald Chubb
NASA Lewis Research Center
Cleveland, Ohio

SUMMARY

Indium Gallium Arsenide (InGaAs) photovoltaic devices have been fabricated with bandgaps ranging from 0.75 eV to 0.60 eV on Indium Phosphide (InP) substrates. Reported efficiencies have been as high as 11.2% (AM0) for the lattice matched 0.75 eV devices. The 0.75 eV cell demonstrated 14.8% efficiency under a 1500°K blackbody with a projected efficiency of 29.3%. The lattice mismatched devices (0.66 and 0.60 eV) demonstrated measured efficiencies of 8% and 6% respectively under similar conditions. Low long wavelength response and high dark currents are responsible for the poor performance of the mismatched devices. Temperature coefficients have been measured and are presented for all of the bandgaps tested.

INTRODUCTION

Research in thermophotovoltaic (TPV) power systems has persisted for many years, driven by high projected thermal to electric system efficiencies.(ref. 1,2) Several variants of TPV systems have emerged with the principal difference being the method of thermal to radiant energy conversion. In blackbody based systems an emitter material is heated to produce broadband radiation. Unfortunately, much of the emitted energy is below the bandgap of the photovoltaic cell, therefore these systems must include some type of spectrum shaping element. This element must efficiently recycle the low energy photons back to the emitter in order to obtain high system efficiencies.

The other method of producing photons from thermal sources is based on selective emitters. These materials emit energy in a narrow spectral band when heated, eliminating the need for additional spectrum shaping elements. Chubb, et al, have demonstrated rare earth doped Yttrium Alumina Garnets (YAG) crystals with good selective emission properties.(ref. 3) Common to all TPV systems designed for operation at moderate temperatures ($< 1500^{\circ}\text{K}$) is the need for a low bandgap photovoltaic device. For blackbody based systems, the optimum bandgap is dependant upon the operating temperature of the emitter and of the cell. For an emitter temperature of 1500°K , Woolf (ref. 2) has calculated that the optimum bandgap ranges from 0.52 eV to 0.82 eV depending upon the cell temperature. The optimum bandgap for selective emitter based systems depends upon the composition of the selective emitter (ref. 1).

The original work in TPV utilized standard silicon solar cells. The high bandgap of silicon ($E_g = 1.1$ eV) limited the systems to very high emitter temperatures ($> 2000^{\circ}\text{K}$). Radio-isotope and conventionally fueled heat sources operate at much lower temperatures, requiring lower bandgap photovoltaic devices. Indium Gallium Arsenide ($\text{In}_x\text{Ga}_{1-x}\text{As}$) is a direct bandgap semiconductor material that has a bandgap ranging from 0.35 eV to 1.42 eV depending on the In/Ga ratio. $\text{In}_{.53}\text{Ga}_{.47}\text{As}$ solar cells ($E_g = 0.75$ eV), with efficiencies of up to 11.2% (AM0), have been fabricated on lattice matched indium phosphide (InP) substrates (ref. 4).

EXPERIMENT

$\text{In}_x\text{Ga}_{1-x}\text{As}$ device structures were grown by Organo Metallic Vapor Phase Epitaxy (OMVPE) in a horizontal, low pressure reactor designed and constructed at NASA Lewis. The source gases consisted of trimethyl gallium, trimethyl indium, arsine (100%), phosphine (100%), diethyl zinc, and silane diluted in hydrogen. Typical growth conditions were: 620°C growth temperature, 190 torr reactor pressure, V/III ratio of 75, and carrier gas flow rate of 3.5 std. l/min. The InP substrates were zinc doped ($p = 4 \times 10^{18} \text{ cm}^{-3}$), oriented (100) and used as received from the vendor. A co-flow of arsine and phosphine was used at the time of crossover from InP growth to InGaAs growth. The co-flow lasted 10 sec. and was used to protect the InP substrate from decomposition until the InGaAs had formed a continuous coverage. The growth rate of InP was 6.1 \AA/sec and the growth rate of InGaAs was 8.1 \AA/sec .

Device structures for the 0.75, 0.66 and 0.6 eV $\text{In}_x\text{Ga}_{1-x}\text{As}$ devices are shown in figure 1. The lattice matched InGaAs device (0.75 eV) incorporated a very thick ($1.5 \mu\text{m}$) InP window layer to reduce the series resistance. Modeling predicts a very high short circuit current density from this device (4.7 A/cm^2) under a 1500°K blackbody emitter (approximately equivalent to $170\times \text{AM0}$), therefore reduction of resistive losses through window layer design and front contact grid design will be very important. Losses due to absorption in the thick InP window layer are minimal under a 1500°K blackbody.

The lattice mismatched devices ($E_g = 0.66$ and 0.6 eV) incorporate step graded buffer layers between the InP substrate and the cell structure. These layers attempt to minimize the density of threading dislocations in the active device layers. An extensive examination of the effect of the grading structure on the performance of lattice mismatched devices is planned. Due to the lattice mismatch (0.74% and 1.2%) of the 0.66 and the 0.6 eV material, thin InP window layers were used in these devices. Alternate window layer materials based on InAsP and AlInAs are under development to allow the incorporation of thick window layers for the reduction of series resistance.

The devices were processed using standard thermal evaporation and photolithographic techniques. The lattice mismatched cells were processed with a higher coverage front grid pattern to partially offset the limitations imposed by the high sheet resistance of the devices. Single layer anti-reflective coatings of Ta_2O_5 were roughly matched to the expected illumination source.

RESULTS

Figure 2 shows the AM0 I-V data for the three different bandgap InGaAs devices without AR coatings. The large change in J_{sc} with bandgap is not directly related to bandgap, as might be thought. The 0.75 eV cell has a thick ($1.5 \mu m$) InP window layer that dramatically reduces the AM0 J_{sc} , which can be seen in the external quantum efficiency (QE) data of figure 3. Dark diode measurements of the devices demonstrated that they were all diffusion limited, with diode ideality factors of ~ 1 . The dark current showed a large dependence on lattice mismatch as can be seen in table 1.

The external QE measurements (figure 3) were taken after Ta_2O_5 AR coating deposition. Unfortunately, our equipment limits the measurements to $1.9 \mu m$, at which point the 0.6 and 0.66 eV cells are still operating. The roll off of the mismatched InGaAs devices at the longer wavelengths is expected due to the deep absorption depth of the low energy photons and the short minority carrier lifetimes expected in the heavily dislocated material. Optimization of base thicknesses, doping levels and lattice grading structures should improve the long wavelength response.

The test devices were mounted on fixtures to facilitate their testing under blackbody and selective emitter illumination. The test fixture incorporated 4-wire connections for independent current and voltage measurement and a thermocouple mounted under the cell to monitor the operating temperature. An electric furnace, used for selective emitter development, was used as a $1500^\circ K$ blackbody illumination source (fig. 4). Its emissivity had previously been determined to be > 0.95 . Calculations indicate that total emitted power from the black body should be $26.5 W/cm^2$, although measurements of the actual emitted power were only $3.0 W/cm^2$ where the cells were mounted. This difference is attributed to the reduction in view factor which results from the 3.6 cm separating the cell from the furnace viewport.

The 0.75 eV cell was also measured under the illumination of an Er-YAG selective emitter at 1500°K (fig. 4). The measured output power from the selective emitter was 1.9 W/cm² at the cell test distance. This value is down from the 5.7 W/cm² value calculated from the measured selective emitter (SE) spectral emissivity data. Difficulties were experienced in accurately determining the surface temperature of the SE and in keeping the entire exposed surface at a uniform temperature. Due to these errors we will not be reporting efficiencies for the InGaAs devices under SE illumination.

The results of the test devices under the blackbody illumination are listed in table 2. As expected, the cell efficiency without filters to recycle the sub-bandgap photons is very low. The 0.75eV cell is only able to absorb 16.8% of the total incident radiative energy. If the sub-bandgap portion of the spectrum is eliminated from the measurement, the efficiency increases to 14.8%. An efficiency of 29.3% was predicted for this device. Those predictions assumed the illumination of the cell by a perfect black body (emissivity =1) at 1500°K with a view factor of 1, and used the measured SR and dark diode characteristics of the actual test device. The discrepancy in efficiencies is largely attributable to the low intensity of the actual measurement compared to the calculated spectrum. The actual cell generated 277 mA/cm² of short circuit current, whereas the integration of the SR with the perfect blackbody spectrum predicted a J_{sc} of 4.7 A/cm². Achieving this optical coupling in actual practice will obviously entail the incorporation of optical concentrating elements, given the necessity of separating the emitter from the cell for thermal management reasons. Another reason for the large difference in the predicted vs. measured cell efficiency was a slight degradation in the cell performance after mounting on the test fixture. The cell had a smaller shunt resistance after mounting, leading to a reduction in the fill factor. Additional experience in mounting devices should eliminate this problem. Calculated cell efficiencies for the 0.66 and 0.6 eV devices is not included due to the incomplete QE data for these devices.

Cell performance as a function of cell temperature is shown in figures 5-7 and table 3 under blackbody illumination. The temperature coefficients of V_{oc} were very constant at -1.6 mV/°C for all of the bandgaps tested. As expected, the J_{sc} increased with increasing cell temperature, due to bandgap narrowing. An interesting feature of the lattice mismatched devices is the peak in the J_{sc} at a cell temperature of ~70°C. We believe that this is caused by increased recombination in the bulk as the temperature increases. The effect is more pronounced in the greater lattice mismatched 0.60 eV cell compared to the 0.66 eV cell. This indicates that the recombination mechanism may be related to the misfit and threading dislocations present in the mismatched InGaAs.

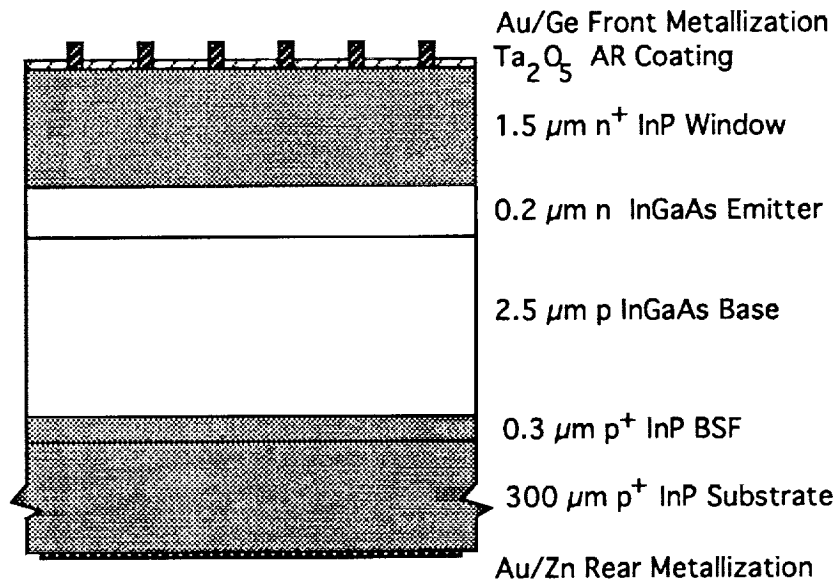
Figure 8 shows the temperature dependence for the 0.75 eV cell under the Er-YAG selective emitter. The small change in J_{sc} with increasing temperature indicates that the SE has very little emission outside of the Er related emission band.

CONCLUSIONS

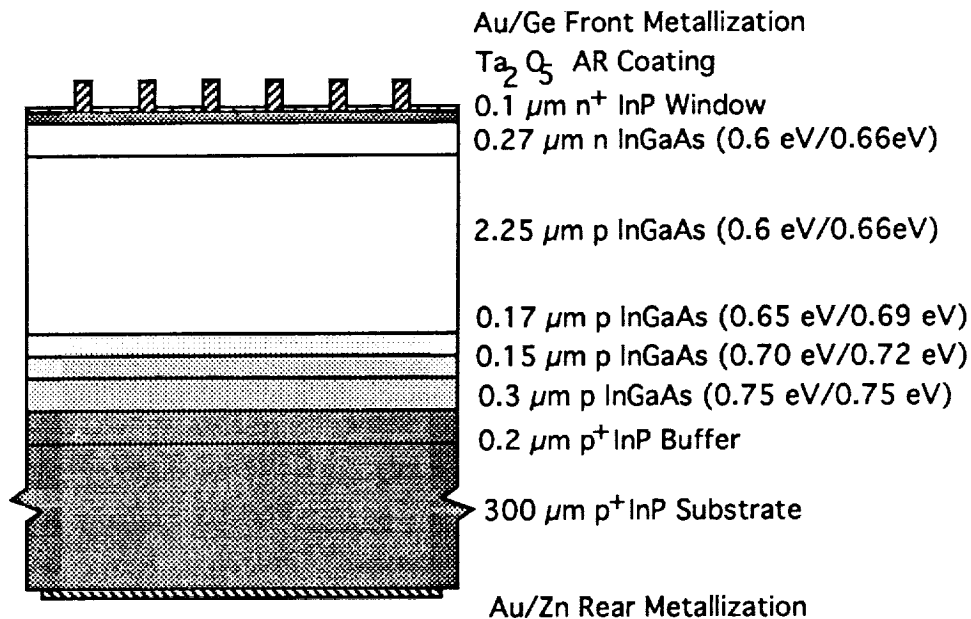
Lattice matched InGaAs has been demonstrated to have excellent potential for application in TPV power systems. Non-optimized device structures have projected efficiencies approaching 30% under 1500°K blackbody illumination. Lattice mismatched InGaAs devices offer the ability to "tune" the photovoltaic device response to correspond to the emission band of the illumination source. Initial results indicate that poor long wavelength response and high dark currents need to be addressed before these devices are feasible. The effect of buffer layer design on device performance must be examined for lattice mismatched devices. We are also planning to examine the effectiveness of hydrogen passivation for reducing the deleterious effects of threading dislocations. Design of an actual TPV system will require many trade off studies. It may turn out to be preferable to use an efficient photovoltaic device which is not optimally tuned to the emission source rather than a poor performance device that is tuned to the source.

REFERENCES

1. D. Chubb, R. Lowe and D. Flood, NASA TM 105755 (1992)
2. L.D. Woolf, Solar Cells **19**, 19 (1986).
3. R.L. Lowe, D.L. Chubb, S.C. Farmer and B.S. Good, "Rare Earth Garnet Selective Emitter", Submitted to Appl. Phys. Lett. (1994)
4. D.M. Wilt, N.S. Fatemi, R.W. Hoffman, Jr., et al, Appl. Phys. Lett. **64** (18), p. 2415 (1994)



0.75 eV InGaAs Cell Structure



0.60 eV/0.66eV InGaAs Cell Structure

Figure 1 - InGaAs TPV cell Structures

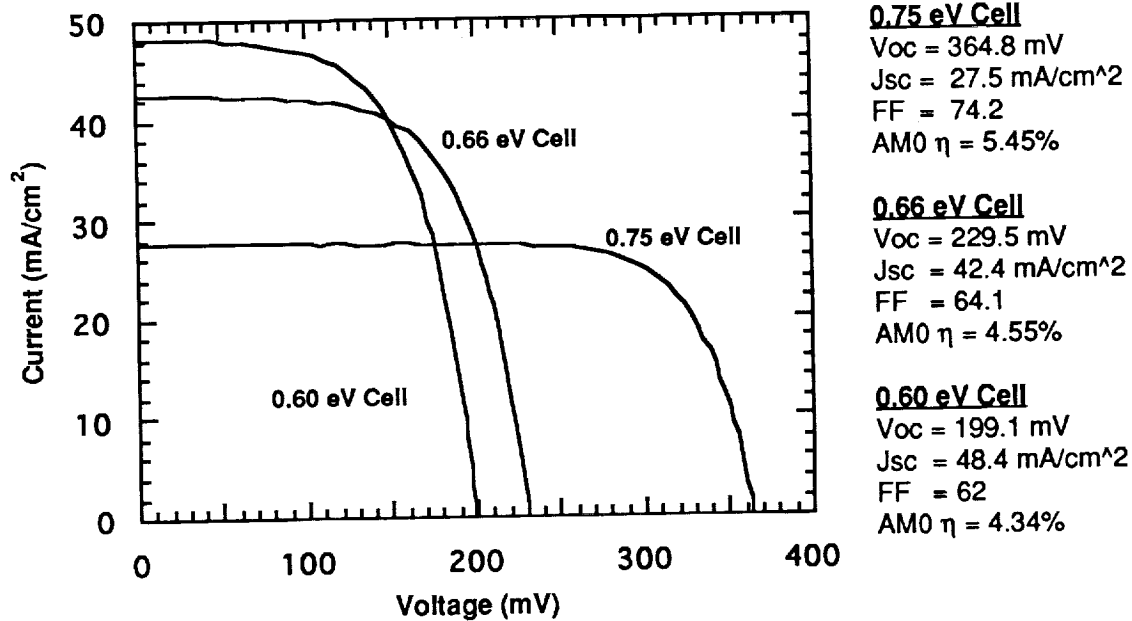


Figure 2 - AM0 I-V data for InGaAs solar cells without AR coatings.

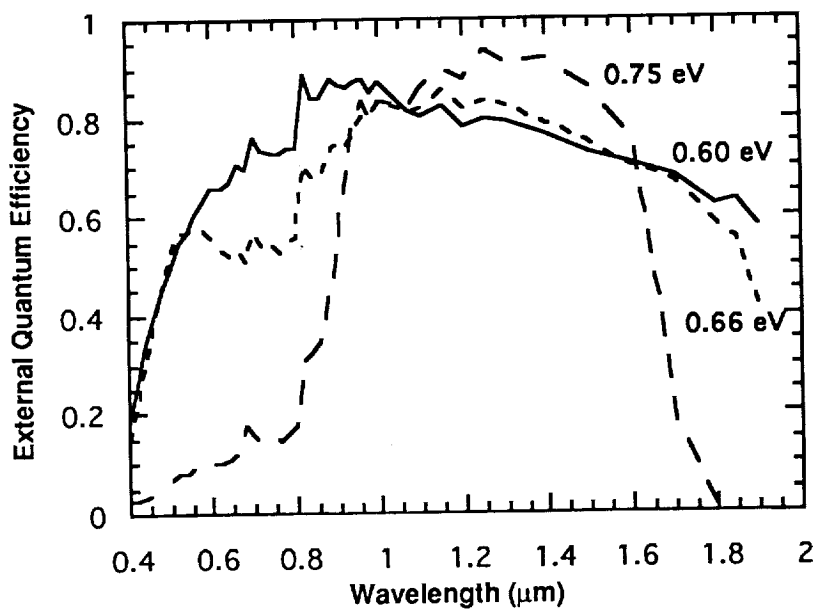


Figure 3 - External QE measurements of AR Coated InGaAs Devices

Bandgap (eV)	A	J01 (A/cm ²)	Rs (Ω)	Rsh (Ω)
0.75	1.01	3.6e-8	0.453	3.4e3
0.66	0.99	6.5e-6	0.431	2.5e3
0.60	0.96	2.2e-5	0.387	8.0e2

Table 1 - Dark diode data for InGaAs devices at 25 °C

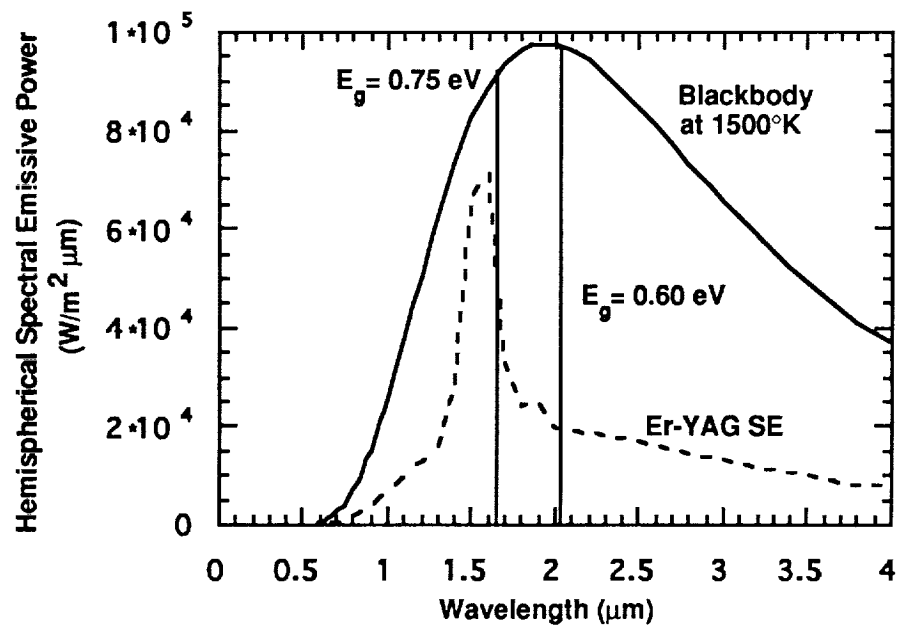


Figure 4 - Blackbody and Er-YAG Selective Emitter Spectrum at 1500 °K.

Bandgap (eV)	Measured Cell Efficiency w/o filter	Measured Cell Efficiency assuming a perfect filter	Calculated Cell Efficiency using Measured SR
0.75	2.5% #	14.8%	29.3%
0.66	1.9% #	8.0%	
0.60	1.9% #	6.0%	

Cell Temperature = 34°C

Table 2 - Performance of InGaAs Devices under Blackbody Illumination

Bandgap (eV)	$(1/J_{sc})(dJ_{sc}/dT)$ (x e-3/°C)	$(1/V_{oc})(dV_{oc}/dT)$ (x e-3/°C)	$(1/FF)(dFF/dT)$ (x e-3/°C)	$(1/P_{max})(dP_{max}/dT)$ (x e-3/°C)	Linear Temperature Range (°C)
0.75	1.99	4.20	2.32	4.67	30-60
0.66	3.18	7.44	6.39	1.01	30-60
0.60	3.04	6.97	5.87	9.46	30-70

Table 3 - Temperature Coefficients for InGaAs Cells Under 1500°K Blackbody Illumination

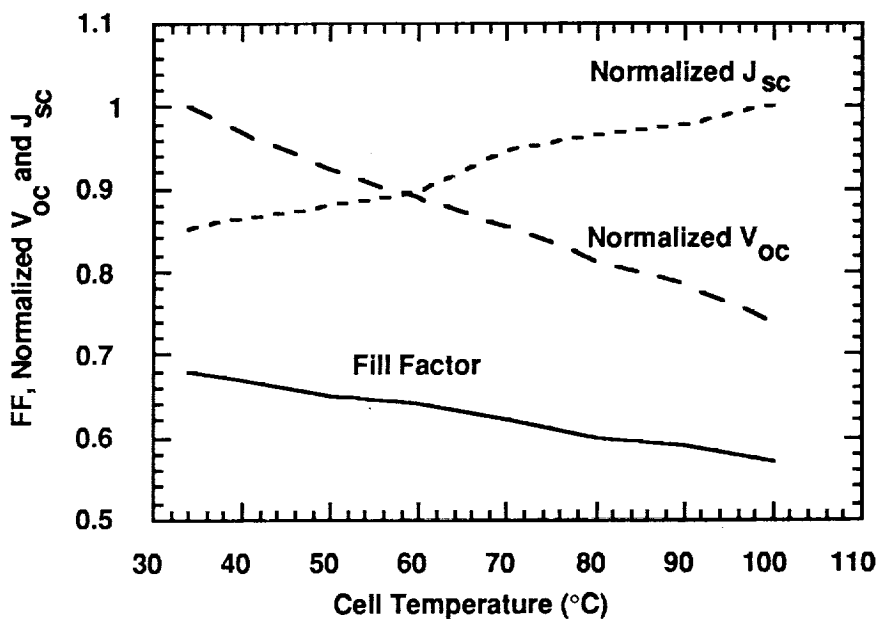


Figure 5 - 0.75 eV InGaAs Cell Performance vs. Temperature Under 1500°K Blackbody Illumination

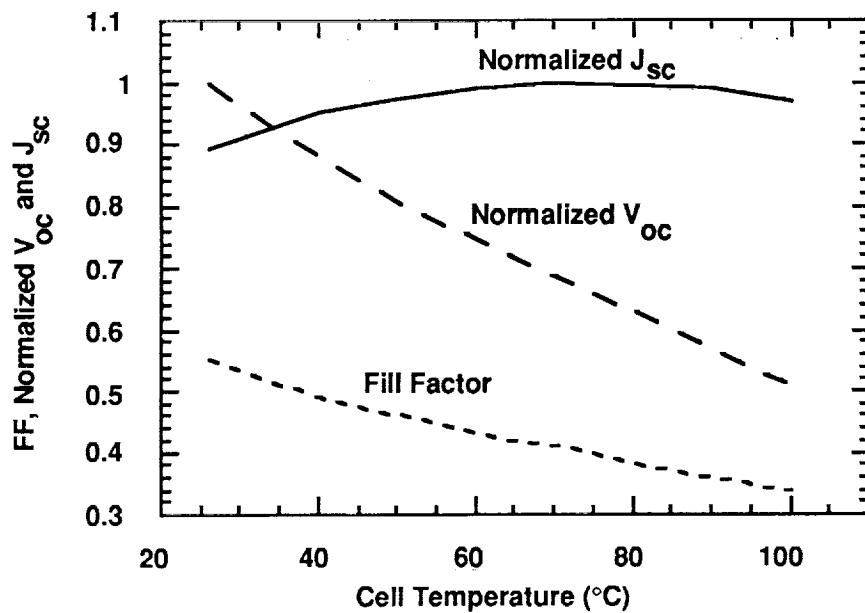


Figure 6 - 0.66 eV InGaAs Cell Performance vs. Temperature Under 1500°K Blackbody Illumination

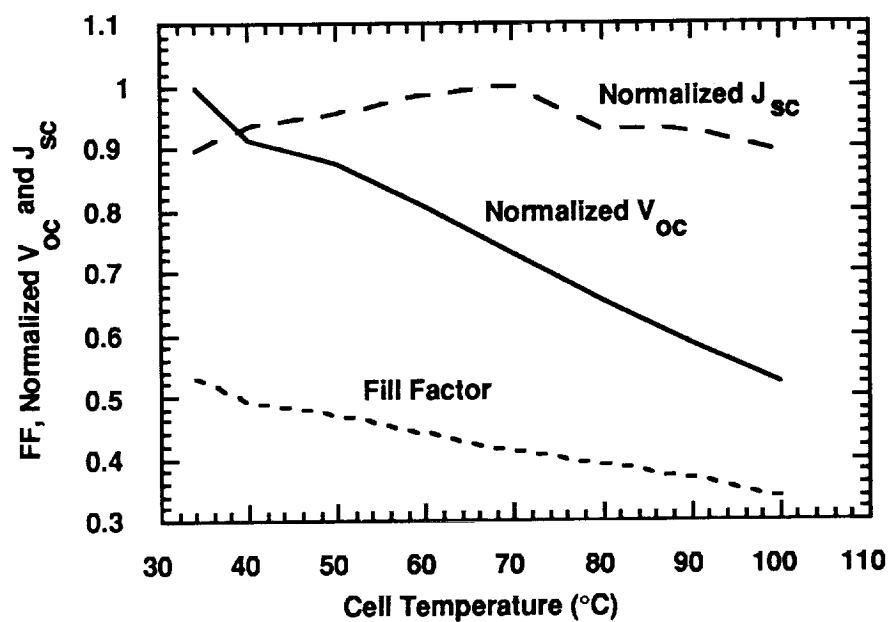


Figure 7 - 0.60 eV InGaAs Cell Performance vs. Temperature Under 1500°K Blackbody Illumination

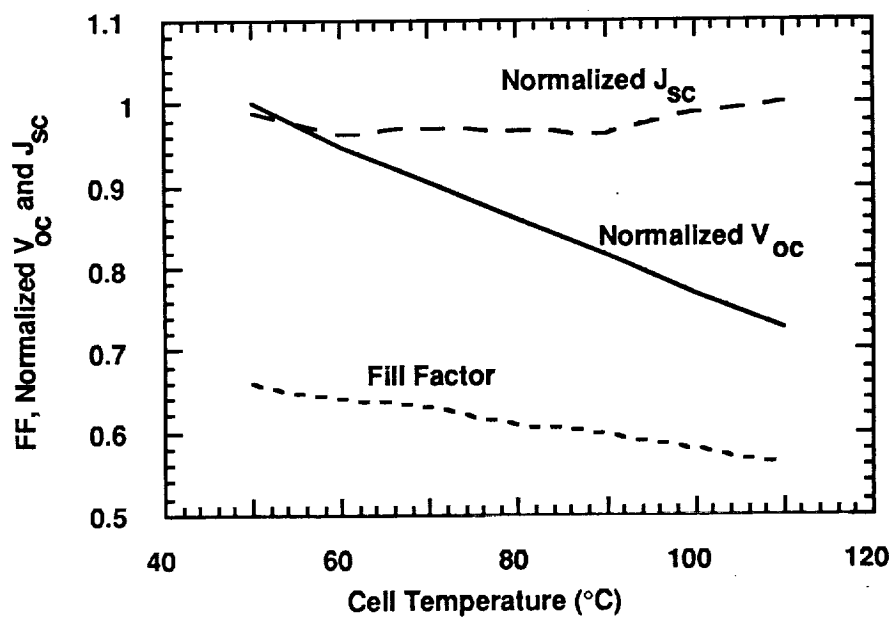


Figure 8 - 0.75 eV InGaAs Cell Performance vs. Temperature Under 1500°K Er-YAG Selective Emitter

PULSED LASER ILLUMINATION OF PHOTOVOLTAIC CELLS

Jane A. Yater¹
NASA Lewis Research Center
Cleveland, Ohio

Roland Lowe
Kent State University
Kent, Ohio

and

Philip Jenkins and Geoffrey A. Landis
NYMA, Inc.
Brook Park, Ohio

SUMMARY

In future space missions, free electron lasers may be used to illuminate photovoltaic array receivers to provide remote power. The induction FEL and the radio-frequency (RF) FEL both produce pulsed rather than continuous output. In this work, we investigate cell response to pulsed laser light which simulates the RF FEL format, producing 50 ps pulses at a frequency of 78 MHz. A variety of Si, GaAs, GaSb and CdInSe₂ (CIS) solar cells are tested at average incident powers between 4 mW/cm² and 425 mW/cm². The results indicate that if the pulse repetition is high, cell efficiencies are only slightly reduced by using a pulsed laser source compared to constant illumination at the same wavelength. Because the pulse separation is less than or approximately equal to the minority carrier lifetime, the illumination conditions are effectively those of a continuous wave laser. The time dependence of the voltage and current response of the cells are also measured using a sampling oscilloscope equipped with a high frequency voltage probe and current transformer. The frequency response of the cells is weak, with both voltage and current outputs essentially dc in nature. Comparison with previous experiments shows that the RF FEL pulse format yields much more efficient photovoltaic conversion of light than does an induction FEL pulse format.

INTRODUCTION

The use of high power lasers has been proposed for beaming power to remote photovoltaic arrays in space. Power beaming during eclipses, for instance, would eliminate the need for batteries on satellites in Geosynchronous Earth Orbit, thus reducing the mass of the satellite power system (ref. 1). Night operation of a moon base can also be facilitated through earth-based laser illumination of photovoltaic arrays, again simplifying the power system requirements of the moonbase (ref. 2). Photovoltaics can have very high efficiencies under monochromatic illumination compared to solar light (ref. 3), creating another advantage for use of laser power beaming. Many of the issues involved in designing an appropriate laser and optical system have been discussed elsewhere (refs. 4 and 5) and will influence the ultimate selection of lasers and cell materials.

The free electron laser (FEL) is an attractive choice of power source. It can produce megawatts of power and can be tuned to wavelengths appropriate for atmospheric transmission as well as

¹ National Research Council Postdoctoral Associate.

the solar cell requirements. Two FEL designs have been proposed, the induction FEL and the radio-frequency (RF) FEL (refs. 6 and 7). Both produce pulses of light with high power rather than continuous output. The induction laser produces pulses ranging from 10 to 50 nanoseconds wide at frequencies of 20 to 50 kHz. The RF FEL operates at MHz frequencies, producing 10 to 40 picosecond "micropulses" which are spaced tens of nanoseconds apart. While the average laser power reaching the cell must be sufficient to generate the required output power, the peak pulse power is hundreds or thousands of times higher than the average level. The response of the photovoltaic receiver to the input pulses depends on the minority carrier lifetime of the solar cell material (refs. 8 and 9). Carriers created by the incident pulses have a finite lifetime before being collected at the junction and thus produce an elongated output signal. When the pulses arrive in rapid succession relative to the lifetime, the cells effectively see the input as a continuous source. However, if the pulse separation is greater than the minority carrier lifetime, the cell must respond to the peak power of each pulse. For Si cells, lifetimes range from 10 to 100 μ s for undamaged material, while radiation damage can lower the value to 1 μ s. Direct bandgap semiconductors such as GaAs have a much shorter minority carrier lifetime, in the range of 10 to 100 ns (ref. 10). Hence, the ability to convert FEL pulses to power depends on the particular laser format and the cells being used.

Previous experimental studies and 1-D computer simulations have focused on the induction FEL format (refs. 11-15). Cell efficiencies are significantly reduced, especially for direct bandgap semiconductors. Issues such as minimizing series resistance and designing cells to avoid LC oscillations are challenges that must be met to successfully utilize the induction FEL. However, studies of cell efficiency and behavior must also be made using other laser pulse formats. In this work, we investigate the response of conventional PV cells to laser light with the RF FEL format. Using a laser with a pulse separation of about 10 ns, we expect the cells to respond to the average illumination power. The results are compared with those of a previous experiment where a copper vapor laser was used to simulate the induction FEL pulse format (ref. 12).

EXPERIMENTAL PROCEDURE

A Coherent Antares mode-locked Nd:YAG laser with 50 ps pulses at a frequency of 78 MHz is used to simulate the output of an RF FEL. As illustrated in figure 1, the duty cycle of the laser, with pulses separated by 13 ns, is 1:260. The peak power per pulse is therefore 260 times higher than the average laser power. In contrast, the copper vapor laser used in the previous induction-format experiment produced 511 nm pulses which were 38 ns wide and spaced 116 μ s apart. The corresponding duty cycle of 1:3000 was significantly larger.

The experimental apparatus is depicted in figure 2. The laser is focused by a microscope objective into a 300 μ m optical fiber and then collimated upon exiting the fiber. PV cells are mounted on an electrically isolated vacuum chuck which moves on a rail aligned normal to the optical path. A calibrated power meter, also mounted on the rail, is slid into the laser path to measure the time averaged power. Apertures block out all but the portion of the laser beam which illuminates the PV cell. The spatial uniformity of the beam over the area of the cells is within 10%.

The frequency doubled 532 nm wavelength is used to illuminate the collection of solar cells listed in Table 1, many of which were tested in the induction FEL experiment (ref. 12). Use of the 532 nm wavelength facilitates comparison with the data taken using the 511 nm Cu-vapor laser. Si, an indirect bandgap semiconductor, and several direct bandgap materials are included in order to examine the dependence of cell efficiency on minority carrier lifetime. All are planar cells, except for several Si and the GaSb concentrator cells. Since concentrator cells are designed with low series

resistance in order to respond to high illumination intensities and peak currents, they may yield a better efficiency in converting high power laser pulses.

The cells are tested at average illumination intensities between 4 mW/cm² and 425 mW/cm². The measurement circuit is shown in figure 3. The average dc output power ($P_{out} = I_{out} \times V_{bias}$) is determined by applying a constant dc voltage across the cell with a variable bipolar power supply that can sink and source current. The average dc current is measured with a digital ammeter. The average power is a measure of the output available in an operational situation. Because of pulse to pulse variation in the laser energy, the readings are averaged over several hundred laser pulses. The conversion efficiency is calculated at the maximum power point using the relation

$$\eta = \frac{P_{out}}{P_{in}A}, \quad (1)$$

where A is the total cell area, P_{in} is the average incident laser power and P_{out} is the output power as defined above. The time dependence of the cell voltage and current is measured using a Tektronix 11802 digital sampling oscilloscope equipped with a 200 MHz inductive current pickup and a 3.5 GHz high-impedance sampling head. Lead lengths are kept to below 3 cm to minimize induced voltage caused by current transients during each laser pulse.

RESULTS

The time dependence of the voltage and current under pulsed illumination is one indication of the solar cell response to the short pulses. The voltage waveform observed on the oscilloscope shows the time evolution of the bias voltage across the cell, which is maintained at a nominally constant level through feedback control. However, current transients during the laser pulses can force the voltage towards the open circuit value. Figure 4a shows voltage and current waveforms for a Si concentrator cell illuminated with Nd:YAG pulses at 425 mW/cm². With an applied bias voltage of almost 400 mV, the resultant voltage waveform is essentially a dc signal, with a small sawtoothed ac component repeating every 13 ns as the laser pulses hit. The corresponding current waveform also shows a small response, with 10 mA current transients also following the laser pulses. Similar behavior is seen for all the cells tested. The ac signal is largest at short circuit conditions, and under the highest laser intensities. At the maximum power point where cells are generally operated, the peak response is negligible, as seen in figure 4a.

In contrast, figure 4b shows the voltage and current waveforms for the same cell and bias voltage, but illuminated with the copper vapor laser pulses at 279 mW/cm². With a significantly higher duty cycle and pulse separations of over 100 μ s, the cell obviously exhibits a strong frequency response. The voltage rises in a spike as a laser pulse hits, with a slow decay over tens of microseconds down to the dc bias level. The current transients of over half an amp decays equally slowly as carriers diffuse to the depletion region. With these voltage and current pulses occurring every 116 μ s, the cell output can hardly be maintained at a constant dc level. The response to the induction format pulses varied considerably from cell to cell, with the most dramatic LC oscillations occurring with the GaAs concentrator cells (ref. 12). However, every cell exhibited a strong frequency response and a corresponding reduced conversion efficiency. The RF-type pulses produce a very weak frequency response and, as the data will show, good efficiencies.

Figure 5 shows current-voltage curves for a 10 Ω -cm planar Si cell illuminated with both the RF (Nd:YAG) and induction (Cu-vapor) type pulses. While the laser wavelength is comparable, the incident intensity is not identical. However, the cell performs better at 170 mW/cm² under the RF-simulated pulses than at the higher average power of 263 mW/cm² with the induction pulses. Both

the fill factor and efficiency are significantly better, while J_{sc} is comparable for both cases. The Si cell is able to convert the incoming Nd:YAG pulses more efficiently than the Cu-vapor pulses, as already suggested by the ac waveforms discussed above. Even for Nd:YAG pulses at 470 mW/cm^2 (peak power = 800 suns), where series resistance limiting of the current might cause deterioration of the cell performance, the fill factor and efficiency are essentially constant. Comparisons of direct bandgap cells illuminated with both pulse formats, though not shown here, are even more striking. The GaAs and CIS cells perform well under the Nd:YAG illumination (although the 532 nm wavelength is far from optimal, especially for GaSb and CIS), whereas efficiencies are exceedingly low for the Cu-vapor pulse experiments. J_{sc} is several milliamps for the induction case but hundreds of milliamps under RF pulse conditions at comparable average intensities.

Efficiencies are calculated at the maximum power point, indicated by a cross on the I-V curves, and are compiled in table 2 for AM0, cw (514 nm), and pulsed illumination conditions using both the Nd:YAG (532 nm) and Cu-vapor (511 nm) laser pulses. An Argon ion laser was used in the previous experiment to collect cw data (ref. 12). Efficiencies for the Si and GaAs cells tend to be a bit higher under monochromatic cw light than the solar spectrum, an effect which would be even more noticeable at the optimum wavelength of each semiconductor material. A comparison of results from the 532 nm pulses and the 514 nm continuous illumination, both at 170 mW/cm^2 , shows that the pulsed laser efficiency is slightly lower for the planar cells but higher for the concentrator cells. However, while the PV conversion efficiency remains 70% to 99% of the cw value using RF-type pulses, the detrimental effect of induction-type pulses is more extreme. Si cells show an additional reduction in efficiency, while direct bandgap efficiencies drop to almost zero.

Typical I-V curves of Si and GaAs cells are shown in figure 6 for 532 nm pulsed illumination at 425, 170 and 41 mW/cm^2 . These average power levels correspond to approximately 3.1, 1.25 and 0.3 suns, respectively, while the equivalent peak powers are 810, 325 and 80 suns. The dependence of cell efficiency on average laser power is plotted in figure 7 for several different cells, while table 3 compiles the power dependence for all cells tested. Some variation in efficiency with laser power is evident, with a maximum tending to occur at 170 mW/cm^2 . However, the curves at 425 mW/cm^2 show no sign of current saturation due to series resistance limiting at the highest peak pulse powers and the fill factors remain constant. Previous results with the induction formatted laser indicated current saturation at the highest laser intensities, where the peak power increased to 6000 suns.

DISCUSSION

As noted previously, the efficiencies tabulated in this paper do not represent the peak efficiencies expected at laser wavelengths matched to the PV bandgap. The 532 nm light used in this experiment is chosen so that previous results can be compared and trends noted. The wavelength of peak monochromatic efficiency for undamaged Si is about 950 nm (shorter for damaged material), 850 nm for GaAs, 1600 nm for GaSb and 1000 nm for CIS. Corrections to the efficiency can be estimated by using the equation (ref. 4)

$$\frac{\eta(\lambda_{\text{peak}})}{\eta(\lambda_{532\text{nm}})} = \frac{\lambda_{\text{peak}}}{\lambda_{532\text{nm}}} \times \frac{QE(\lambda_{\text{peak}})}{QE(\lambda_{532\text{nm}})}, \quad (2)$$

where QE is the quantum efficiency of the cell at the selected wavelength. Assuming that the quantum efficiency is nearly constant with wavelength over the range of interest below the bandgap (confirmed by measurements of external quantum yield), the correction factor is approximately the ratio of the chosen wavelengths. This wavelength term simply describes the inverse proportionality between incident laser power and wavelength.

For the 532 nm Nd:YAG laser pulses, no substantial difference in efficiency is evident between the various materials, with all planar cells performing at 70% to 99% of the cw level. The minority carrier lifetime, significantly longer for Si than the other semiconductors, is not a limiting factor in the ability of the cells to respond to the short pulses. The I-V curves show no evidence of current saturation at the highest pulse intensity, where peak output currents due to individual pulses would be 260 times larger than the average current. Consider the limiting equation

$$I < V_{oc}/R_{series}, \quad (3)$$

where the series resistance of the cells was measured previously (ref. 12). If the incident laser pulses were spaced sufficiently far apart so that generated carriers were all collected before the next pulse, every cell tested should have displayed current saturation at the higher laser powers. Such is not the case, indicating approximately continuous wave illumination conditions. The Si concentrator cells, designed to respond to higher current densities than planar cells, exhibit a modest increase in efficiency under the RF-type laser pulses. Despite temporal stretching of the incident pulse due to minority carrier diffusion, carrier concentrations rise above the average value as each pulse arrives. The concentrator cells are better able to collect these carriers than are the planar cells, as the results confirm. All the PV cells, however, convert the incident laser pulses to nearly dc output power with little or no loss compared to cw laser results.

The time dependent current and voltage waveforms also indicate that the cells see quasi-cw illumination conditions. For GaAs, the peak to peak amplitude is never more than 20 mV, with corresponding current variations of about 10 mA. Si cells sometimes exhibit larger voltage amplitudes, up to 125 mV under short circuit conditions, but the waveform at the maximum power point decreases to values similar to those indicated for the GaAs. As the bias voltage is increased, the load impedance (at the voltage supply) also increases, thereby reducing the current transients. The oscilloscope shows essentially dc output with a small ac signal. Analysis of the waveforms is not pursued given the small magnitude of the peaks and the noise often obscuring the exact shape. Some observations, such as a slight rounding off at the peak of the sawtooth-like voltage signal or the non-linear decay of some curves, could give insight into cell design for maximum efficiency under these pulses. However, a detailed discussion of the many factors affecting cell response to individual pulses can be found in the referenced studies (refs. 11-15), while the main result of this work is that conventional PV cells yield almost dc outputs when illuminated with high frequency pulses.

CONCLUSIONS

Experimental results indicate that the conversion efficiency of conventional PV cells illuminated with high frequency laser pulses is not reduced significantly. The 532 nm wavelength of a mode-locked Nd:YAG laser is used to simulate the RF FEL pulse format, with the resultant cell performance improved compared to previous results using a Cu-vapor laser to simulate the induction FEL format. Direct bandgap cells exhibit the most significant enhancement in cell efficiency for incident laser intensities up to 425 mW/cm². The ac frequency response of the cells to the short pulses is weak, while time averaged currents and fill factors are comparable those under cw illumination conditions. Because the pulse separation is as short as the minority carrier lifetime, the cells respond as if the incident illumination is quasi-continuous in nature.

REFERENCES

1. Landis, G.A.: Satellite Eclipse Power by Laser Illumination. *Acta Astron.*, 229-233.
2. Landis, G.A.; Bailey, S.G.; Brinker, D.J.; and Flood, D.J.: Photovoltaic Power. *Acta Astron.*, vol. 22, 1990, pp. 197-203.
3. Olsen, L.C.; Huber, D.A.; Dunham, G.; Addis, F.W.; and Anheier, N.: High Efficiency GaAs Solar Cells. IEEE 22nd Photovoltaic Specialists Conference, Oct. 1991, pp. 1494-1502.
4. Landis, G.A.: Photovoltaic Receivers for Laser Beamed Power in Space. IEEE 22nd Photovoltaic Specialists Conference, Oct. 1991, pp. 1494-1502.
5. Weichel, H.: Laser Beam Propagation in the Atmosphere. SPIE Optical Engineering Series, Vol. 3, Bellingham, WA, 1990.
6. De Young, R.J.; Lee, J.H.; Williams, M.D.; Schuster, G.; and Conway, E.J.: Electrically Driven Lasers for Space Power Transmission. NASA Technical Memorandum 88-215, 1988.
7. Burke, R.: SELENE Laser Power Beaming Applications Workshop. NASA Marshall Space Flight Center, AL, March 24, 1992.
8. Rose, B.H.: Minority Carrier Lifetime Measurements on Si Solar Cells Using I_{sc} Decay. IEEE Trans. on Electron Devices, vol. ED-31, 1984, pp. 559-565.
9. Iles, P.A.: Non-solar Photovoltaic Cells. IEEE 21st Photovoltaic Specialists Conference, 1990, pp. 420-425.
10. Ahrenkiel, R.K.; Dunlavy, D.J.; and Hanak, T.: Photoluminescence Lifetime in Solar Cells, vol. 24, 1988, pp. 339-352.
11. Anspaugh, B.; Mueller, R.; Lowe, R.; and Landis, G.A.: Results of Illuminated Solar Cells with Pulsed Laser Beams. JPL Publication 92-95, Nov. 1992.
12. Lowe, R.; Landis, G.A.; and Jenkins, P.: The Efficiency of Photovoltaic Cells Exposed to Laser Light. 12th Space Photovoltaic Research and Technology Conference, NASA CP 3210, Oct. 1992, pp. 129-146.
13. Willowby, D.; Alexander, D.; Edge, T.; and Herren, K.: Response of Silicon Solar Cells to Pulsed Laser Illumination. 12th Space Photovoltaic Research and Technology Conference, Oct. 1992, pp. 147-154.
14. Landis, G.A.; and Jain, R.K.: Approaches to Solar Cell Design for Pulsed Laser Illumination. 12th Space Photovoltaic Research and Technology Conference, NASA CP 3210, Oct. 1992, pp. 166-175.
15. Jain, R.K.; and Landis, G.A.: Modelling of High Efficiency Concentrator Solar Cells. SPIE Laser Power Beaming Conference, vol. 2121, Jan. 1994, pp. 264-273.

Cell Type	Type	Material	Area (cm ²)
ASEC #10	Planar	Si	4.0
ASEC 10 Ω -cm BSR	"	"	"
ASEC 0.2 Ω -cm	"	"	"
MSFC - ATM	"	"	"
ASEC 10 Ω -cm BSR	Rad. Damaged	"	"
ASEC string	Planar	"	1.25
Sunpower HECO 250	Concentrator	Si	1.44
ASEC 10 Ω -cm	"	"	1.0
ASEC 0.15 Ω -cm	"	"	"
Varian	Planar	GaAs	4.0
ASEC MANTEC	"	"	"
ASEC #2	"	GaAs/Ge	"
ASEC #16	"	"	"
BOEING #6701	Concentrator	GaSb	0.196
BOEING A096A	Planar	CIS	4.0

Table I. Cells Tested Under Pulsed Laser Illumination Using Nd:YAG Laser

		RF		Induction
	AM0	cw 514 nm	Pulsed 532 nm	Pulsed 511 nm
Average Intensity, mW/cm ²	137	170	170	250
Cell Type	Cell Efficiency, %			
Silicon				
ASEC #10	15.0		13.3	
ASEC 10 Ω -cm BSR	11.0	14.5	10.1	5.6
ASEC 0.2 Ω -cm	15.6	19.0	14.5	7.2
MSFC - ATM	10.4	12.6	10.8	
ASEC 10 Ω -cm (rad. damaged)	10.5	13.9	13.4	1.9
ASEC planar string	11.1		7.5	
Sunpower HECO 250 (conc.)	17.2		19.2	
ASEC 10 Ω -cm (conc.)	13.0	13.7	15.3	7.6
ASEC 0.15 Ω -cm (conc.)	15.2	15.3	19.0	12.1
GaAs				
Varian	17.2	29.0	20.5	0.15
ASEC MANTEC	16.5	28.3	23.0	
ASEC #2	17.5		24.1	
ASEC #16	18.0	26.0	25.7	
KOPIN Super (conc.)	20.7	26.6		1.3
GaSb				
BOEING #6701 (conc.)	5.8	1.26	2.9	0.25
CIS				
BOEING A096A	8.2	5.5	5.3	0.01

Table II. Cell Efficiencies Under Illumination with AM0, cw Laser, and RF and Induction FEL Laser Format

	Pulsed Nd:YAG Laser at 532 nm (simulating RF FEL format)			
Average Intensity, mW/cm ²	425	170	41	4
Cell Type	Cell Efficiency, %			
Silicon				
ASEC #10	12.2	13.3	13.1	9.9
ASEC 10 Ω-cm BSR	9.5	10.1	10.3	8.5
ASEC 0.2 Ω-cm	12.6	14.5	14.3	10.6
MSFC - ATM	10.2	10.8	9.8	5.2
ASEC 10 Ω-cm (rad. damaged)	12.1	13.4	13.3	9.8
ASEC planar string	7.5	7.5	6.5	5.1
Sunpower HECO 250 (conc.)	19.2	19.2	18.0	14.3
ASEC 10 Ω-cm (conc.)	13.4	15.3	15.3	11.5
ASEC 0.15 Ω-cm (conc.)	19.0	19.0	18.8	14.9
GaAs				
Varian	14.0	20.5	17.8	
ASEC MANTEC	21.7	23.0	21.7	17.5
ASEC #2	25.0	24.1	21.8	15.4
ASEC #16	26.3	25.7	23.5	
GaSb				
BOEING #6701 (conc.)	3.9	2.9	1.5	1.9
CIS				
BOEING A096A	3.7	5.3	5.3	3.3

Table III. Cell Efficiencies at Different Laser Powers for RF FEL Simulated Format

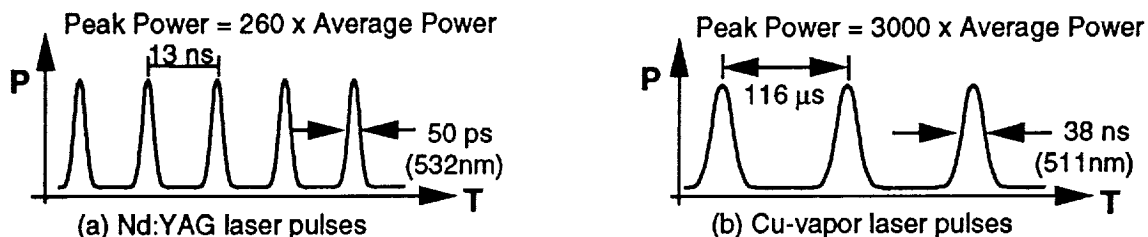


Figure 1. RF (a) and Induction (b) FEL pulse formats

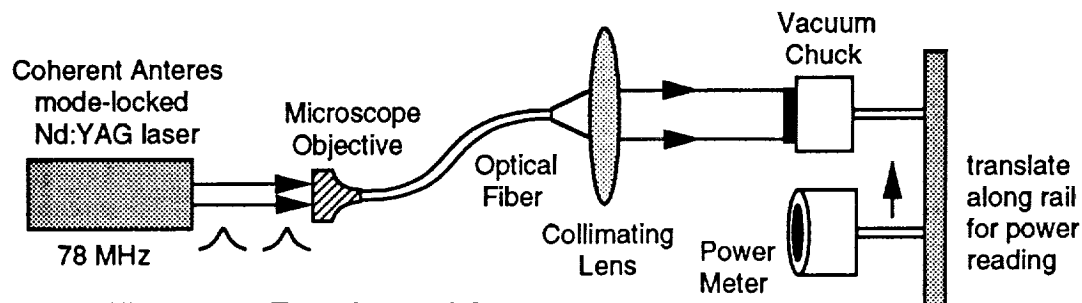


Figure 2. Experimental Apparatus

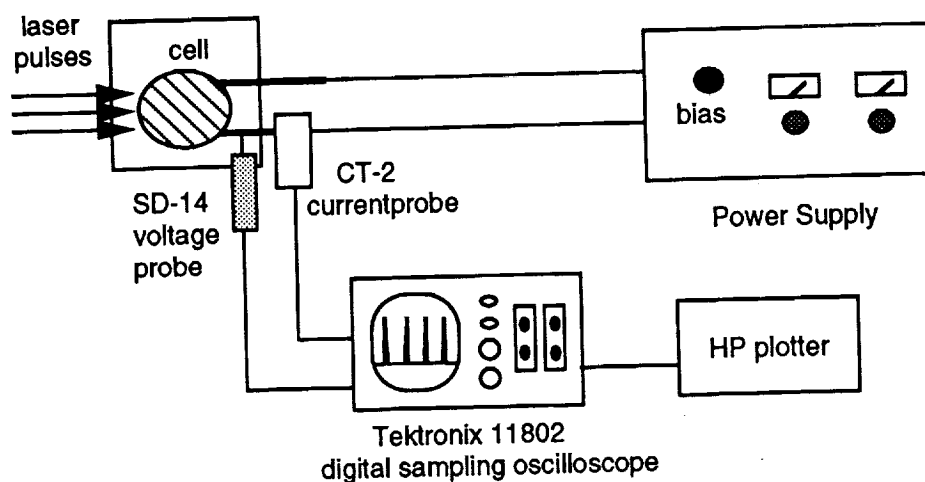


Figure 3. Schematic of Measurement Circuit

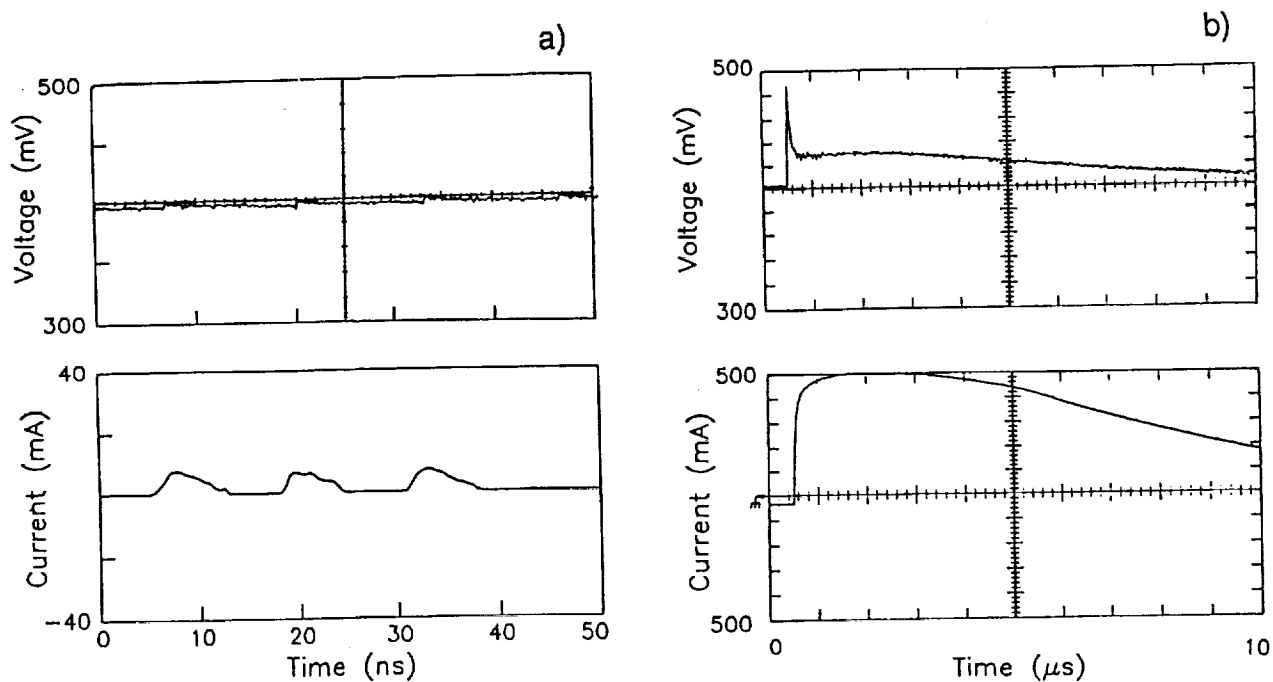


Figure 4. Voltage and Current Waveforms for Si Concentrator Cell. a) Illumination is with 532 nm Nd:YAG Pulses at a Repetition Rate of 13 ns. Average Power is 425 mW/cm². b) Same Cell Illuminated with 511 nm Copper Vapor Laser Pulses Arriving at 116 μ s Intervals. Average Power is 263 mW/cm².

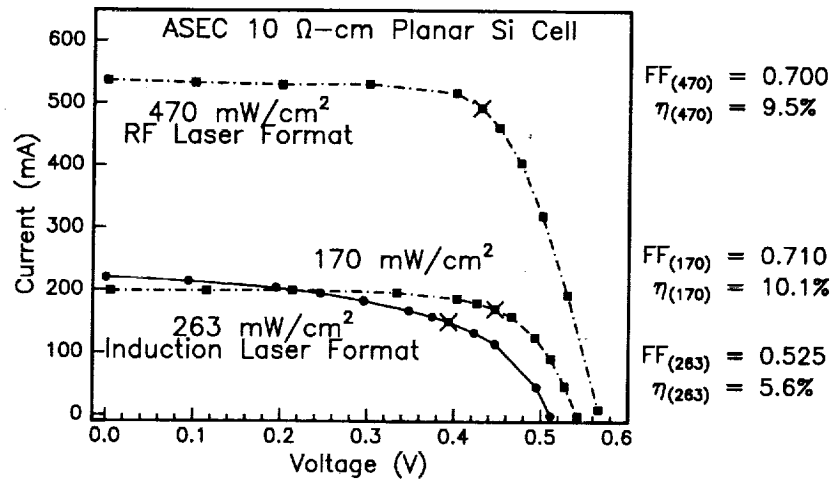


Figure 5. I-V Curves for Planar Si Cell as a Function of Pulse Format and Average Laser Power. Maximum Power Points are Indicated by an X.

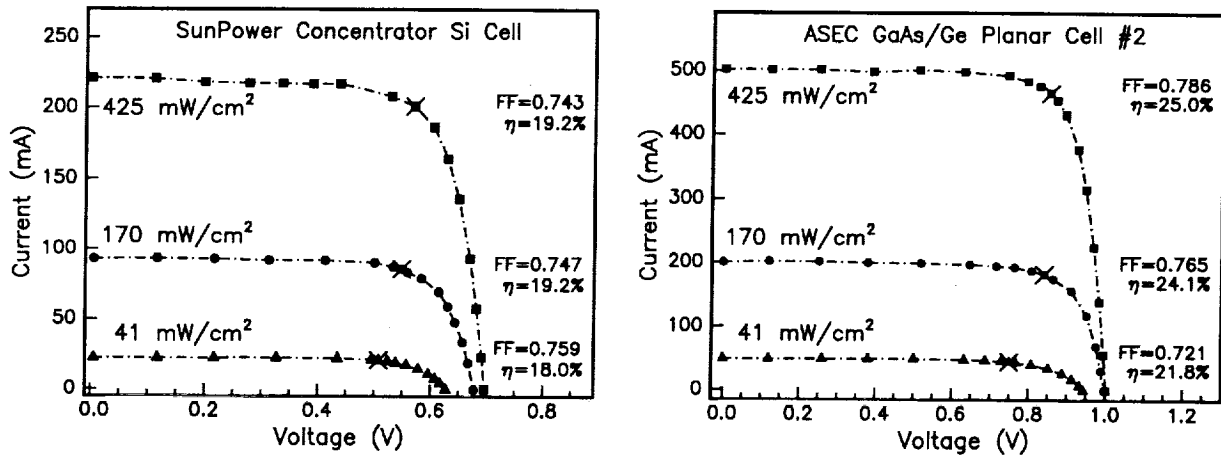


Figure 6. I-V Curves for Si Concentrator and GaAs Planar Cell. The Fill Factor and Efficiencies Correspond to Each of the 3 Powers.

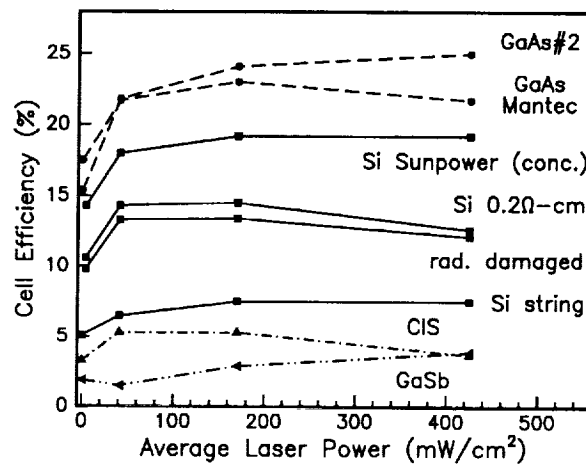


Figure 7. Efficiency as a Function of Nd:YAG Laser Power for Various Cells.

P/N In(Al) GaAs MULTIJUNCTION LASER POWER CONVERTERS

Steven Wojtczuk and Themis Parodos
Spire Corporation
Bedford, Massachusetts

and

Gilbert Walker
NASA Langley Research Center
Hampton, Virginia

SUMMARY

Eight In(Al)GaAs PN junctions grown epitaxially on a semi-insulating wafer were monolithically integrated in series to boost the $\sim 0.4\text{V}$ photovoltage per typical In(Al)GaAs junction to over 3 volts for the 1 cm^2 laser power converter (LPC) chip. This is the first report of a multijunction LPC for the 1.3 to $1.5\text{ }\mu\text{m}$ wavelength range. This wavelength range is optimum for laser power transmission over low-loss single-mode silica optical fiber, and is also useful with high efficiency $1.315\text{ }\mu\text{m}$ iodine lasers in free-space power transmission.

Advantages of multijunction LPC designs include the need for less circuitry for power re-conditioning and the potential for lower I^2R power loss. As an example, these LPC's have a responsivity of $\sim 1\text{ amp/watt}$. With a single junction LPC, 100 watts/cm^2 incident power would lead to about 100 A/cm^2 short-circuit current at $\sim 0.4\text{V}$ open-circuit voltage. One disadvantage is the large current would lead to a large I^2R loss which would lower the fill factor so that 40 watts/cm^2 output would not be obtained. Another is that few circuits are designed to work at 0.4 volts, so DC-DC power conversion circuitry would be necessary to raise the voltage to a reasonable level. The multijunction LPC being developed in this program is a step toward solving these problems. In the above example, an eight-junction LPC would have eight times the voltage, $\sim 3\text{V}$, so that DC-DC power conversion may not be needed in many instances. In addition, the multijunction LPC would have $1/8$ the current of a single-junction LPC, for only $1/64$ the I^2R loss if the series resistance is the same.

Working monolithic multijunction laser power converters (LPCs) were made in two different compositions of the $\text{In}_x\text{Al}_y\text{Ga}_{1-x-y}\text{As}$ semiconductor alloy, $\text{In}_{0.53}\text{Ga}_{0.47}\text{As}$ (0.74 eV) and $\text{In}_{0.5}\text{Al}_{0.1}\text{Ga}_{0.4}\text{As}$ (0.87 eV). The final 0.8 cm^2 LPCs had output voltages of about 3 volts and output currents up to about one-half amp. Maximum $1.3\text{ }\mu\text{m}$ power conversion efficiencies were $\sim 22\%$. One key advantage of multijunction LPCs is that they have higher output voltages, so that less DC-DC power conversion circuitry is needed in applications.

INTRODUCTION

Laser power converters (LPCs) efficiently transform the optical power of a laser beam into electrical power (ref. 1). Myriad applications exist for this technology:

Powering planetary "rover" vehicles - The original goal of this program was to develop an efficient converter of $1.315\text{ }\mu\text{m}$ light that would be supplied by a high-power solar-pumped iodide laser (ref. 2) in orbit around a planet. This laser would be aimed at a "rover" vehicle on the planet's surface, so that heavy batteries or other vehicular power sources would not be needed.

Powering orbital transfer vehicles - Powerful ground-based lasers could deliver more optical power to an array of LPCs on a space platform than sunlight could deliver optical power on an array of

solar cells of similar weight to the LPC array (ref. 3). As an additional advantage, because the LPC system is optimized to the single laser wavelength, it will also be more efficient at converting the laser light than a solar cell array would be at converting the multiple-wavelength sunlight.

Safe explosive fuses - Explosives for both commercial and military uses are often detonated remotely by an electrical signal sent over wires to a blasting cap attached to the explosives. The wires can act as antennae, and a passing radio transmitter (*e.g.* a CB radio) can induce a voltage which prematurely detonates the explosive, with unfortunate consequences. If the wires are replaced by optical fiber, the system becomes immune to this hazard. LPCs are used to convert the light signal sent over the fiber into electricity to trigger the explosion safely.

Powering remote sites - The $\text{In}_{0.53}\text{Ga}_{0.47}\text{As}$ LPCs developed in this Phase II are ideally suited for use with low-loss silica optical fiber transmission systems. Such optical fiber has an attenuation minimum at 1.5 μm (power lost is only 0.2 decibels per kilometer). Undersea cable telecommunications repeater stations power is one possible application.

Power for telephones - Telephone lines superimpose weak voice signals on a steady 48V DC potential. This potential is used to power the phone ringer, *etc.* When optical fiber comes into the home, LPCs will most likely come with it to mimic the present system. A steady high intensity laser beam present on the fiber would be superimposed with weaker optical voice signals; the LPC would supply power to the phone ringer.

This program (ref. 4) was undertaken since efficient photovoltaic converters did not exist for use with 1.3 μm light. For example, silicon (Si) and gallium arsenide (GaAs) solar cells, the most popular types, have semiconductor bandgaps too high to absorb any of the 1.3 μm laser light. The 0.94 eV photon energy is smaller than the 1.1 eV bandgap of silicon or the 1.4 eV bandgap of gallium arsenide and passes through these materials without absorption. The quaternary (four-component alloy) compound semiconductor indium aluminum gallium arsenide $\text{In}_x\text{Al}_y\text{Ga}_{1-x-y}\text{As}$ was selected as the cell epitaxial material because it had three desirable characteristics:

- 1) The bandgap was tunable in the range from 0.36 eV to 2.2 eV. Material with any bandgap in this range could be obtained by epitaxially growing the right material composition.
- 2) A small subset of material compositions, with bandgaps ranging from 0.74 eV to 1.52 eV, was available having the same crystal lattice constant as an available wafer, indium phosphide (InP). This would allow defect-free (*i.e.* dislocation-free) material to be grown with better performance than would otherwise be possible.
- 3) The $\text{In}_x\text{Al}_y\text{Ga}_{1-x-y}\text{As}$ system is a (periodic table) group III-III-III-V material. Because there is only one group V hydride, arsine, the material composition should theoretically be easier to control than, for example, InGaAsP, a group III-III-V-V with much the same bandgap range as $\text{In}_x\text{Al}_y\text{Ga}_{1-x-y}\text{As}$. When growing $\text{In}_x\text{Al}_y\text{Ga}_{1-x-y}\text{As}$, there can be a great excess of the group V arsine gas present; it does not have to be tightly controlled. Since the three group III materials (indium, aluminum, gallium) should incorporate into the growing epitaxial film similarly, the composition should be easy to adjust.

LASER POWER CONVERTER EPILAYER STRUCTURE

Table I shows the epilayer structure for the LPCs. Both $\text{In}_{0.53}\text{Ga}_{0.47}\text{As}$ and $\text{In}_{0.5}\text{Al}_{0.1}\text{Ga}_{0.4}\text{As}$ LPCs used the same overall structure shown in Table I, the only difference being the $\text{In}_x\text{Al}_y\text{Ga}_{1-x-y}\text{As}$ composition. The epitaxial layers were grown in a Spire 100S low-pressure metalorganic chemical vapor deposition (MOCVD) reactor at a temperature of 690°C, using trimethylindium, triethylgallium,

trimethylaluminum, and arsine. Dimethylzinc and silane were the P and N type dopants, respectively. The 690°C growth temperature was a compromise between better $\text{In}_x\text{Al}_y\text{Ga}_{1-x-y}\text{As}$ material lifetime (better at higher temperatures due less aluminum bonding with oxygen) and better compositional uniformity (better at low temperatures since indium has a low vapor pressure).

Table I *P-on-N laser power converter epilayer structure.*

Layer	Material	Doping cm^{-3}	Thickness μm	Comments
Emitter	$\text{In}(\text{Al})\text{GaAs}$	P, 10^{19} (max)	0.3	> Thickness tradeoff - QE (thin better) vs. low series resistance (thick better) > InGaAs is a good contact layer
Base	$\text{In}(\text{Al})\text{GaAs}$	N, 2×10^{17}	2.5	> ~3 absorption lengths thick; absorbs 95% of 1.3 μm light > ~4 hole diffusion lengths thick
B.S. Field Etch Stop	InP	N, 10^{19} (max)	0.1	> Minority carrier mirror enhances QE > InGaAs mesa etch does not etch InP
Buried Layer	InGaAs	N, 10^{19} (max)	3	> Thick, hi-doped to lower I^2R loss > Bottom contact layer
Substrate	InP	Semi-insulating	500	> Fe-doped semi-insulating wafer to isolate the LPC multi-junctions

LASER POWER CONVERTER FABRICATION

The laser power converters (LPC) we have fabricated are a series connection on a semi-insulating InP wafer of $\text{In}(\text{Al})\text{GaAs}$ P on N mesa photodiodes. Similar devices for 800 nm use have been made on semi-insulating GaAs (ref. 5). The main challenge in multijunction LPC fabrication was establishing a process to interconnect the individual junctions.

The first step in fabrication was isolation of the individual mesas required to form the LPCs. A positive photoresist process was used to pattern the mesas. Care was taken to insure the mask was aligned to the substrate such that any orientation dependent etches would result in profiles which could easily be covered by subsequent thin film depositions. A 3:4:1 $\text{H}_3\text{PO}_4\text{:H}_2\text{O}_2\text{:DI}$ etch, selective to $\text{In}(\text{Al})\text{GaAs}$, was used to remove the junction layers to the InP etch-stop. Typical etch rates were 400 Å/s. Etching to completion was achieved by observing a color change while the samples were immersed in the solution. Continuing for an additional 10s beyond this point insured total removal of the $\text{In}(\text{Al})\text{GaAs}$ junction layers. With the same photoresist in place, a 10s HCL dip removed the InP etch stop exposing the N^+ $\text{In}(\text{Al})\text{GaAs}$ buried layer. To complete isolation of the mesas, the 3:4:1 $\text{H}_3\text{PO}_4\text{:H}_2\text{O}_2\text{:DI}$ etch was used to remove the InGaAs buried layer down to the semi-insulating InP substrate. Since the etch is selective, a protruding overhang of the InP etch-stop resulted as the 3:4:1 solution removed the $\text{In}(\text{Al})\text{GaAs}$. To insure continuity of the films to follow, we used a 5s HCl dip to remove the InP . Initially we were concerned that this final dip would undercut the InGaAs buried layer, however, examination of several cleaved cross sections proved that there was no undercut. In fact we found a transition between the InGaAs and InP which was favorable for film continuity.

Once the mesas had been formed, the next step was exposure of the N^+ InGaAs buried layer to form the back contact. Once again, positive resist was used. Care was taken to insure coverage of the mesa edges. The 3:4:1 solution was used to remove the junction layers to the etch stop and an HCl dip removed the InP .

A 2000Å of Si_3N_4 was deposited on the wafers by plasma assisted chemical vapor deposition (PACVD). The Si_3N_4 was then patterned to cover one side of the interconnect from the P⁺⁺ top contact to the bottom of the via. The BHF used to pattern the Si_3N_4 undercut the photoresist and reduced the width of the final pattern. Therefore to correct for the undercut, we adjusted alignment of the Si_3N_4 etch mask to insure coverage of the step. In addition, the BHF bubbled vigorously as it etched the Si_3N_4 . Any bubbles which adhered to the surface acted as masks, leaving some Si_3N_4 underneath as the film etched. To minimize the amount of Si_3N_4 residue caused by the bubbles, we removed them at the midpoint of the etch using flowing DI water. Upon completion of this process, both the N and P sides of the junctions were ready for metallization.

Based on supporting experimental data indicating good contact resistance, we chose to use the same metal system for ohmic contact to both the N and P type materials. Image reversal photolithography and lift-off was used to pattern the 3 µm thick metallization.

The last step in LPC fabrication was deposition and patterning of the anti-reflection (AR) coating. A single-layer, quarter-wave PACVD Si_3N_4 film tuned for minimum reflectance at 1.315 µm was deposited on the wafers. A final photolithographic step removed the Si_3N_4 from the bonding regions. Figure 1 shows a top view of a completed two-inch wafer. Figure 2a shows a single multijunction LPC and Figure 2b shows one of the test sites. Figures 3a shows details of the grid lines too fine to see in Figure 2a, and Figure 3b shows details of the interconnect.

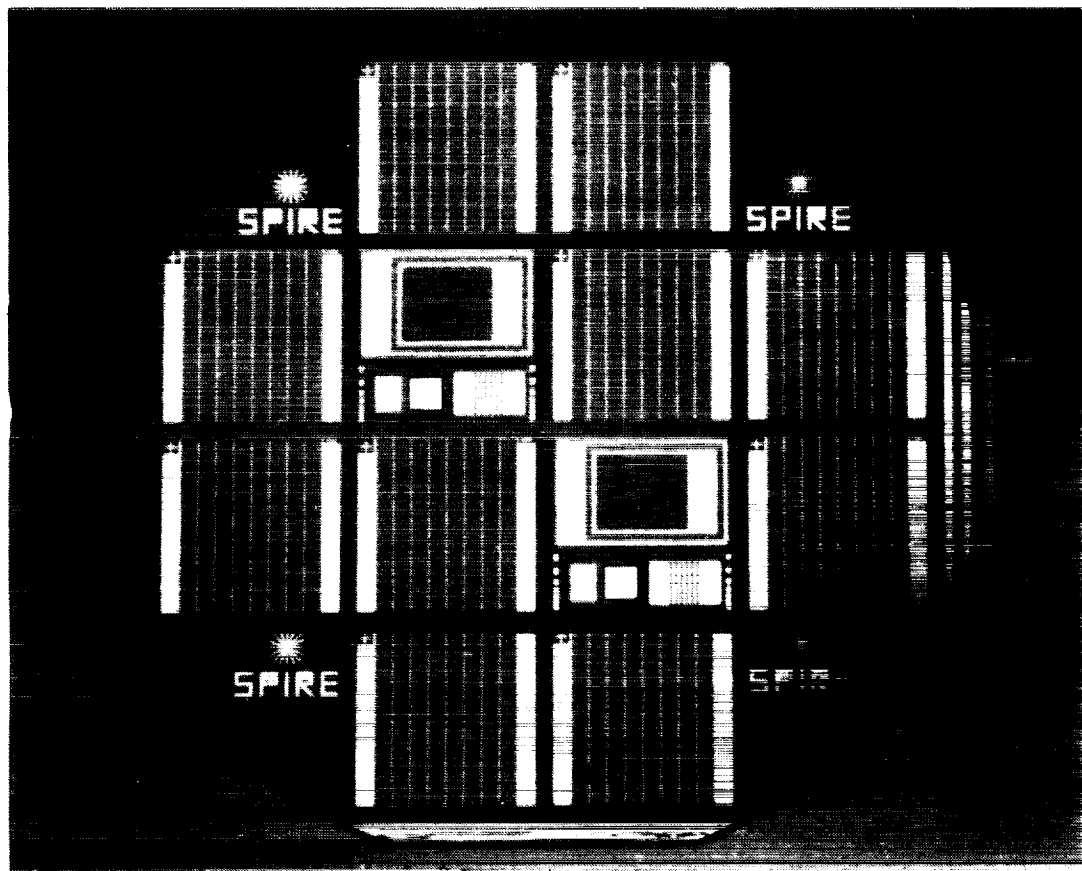
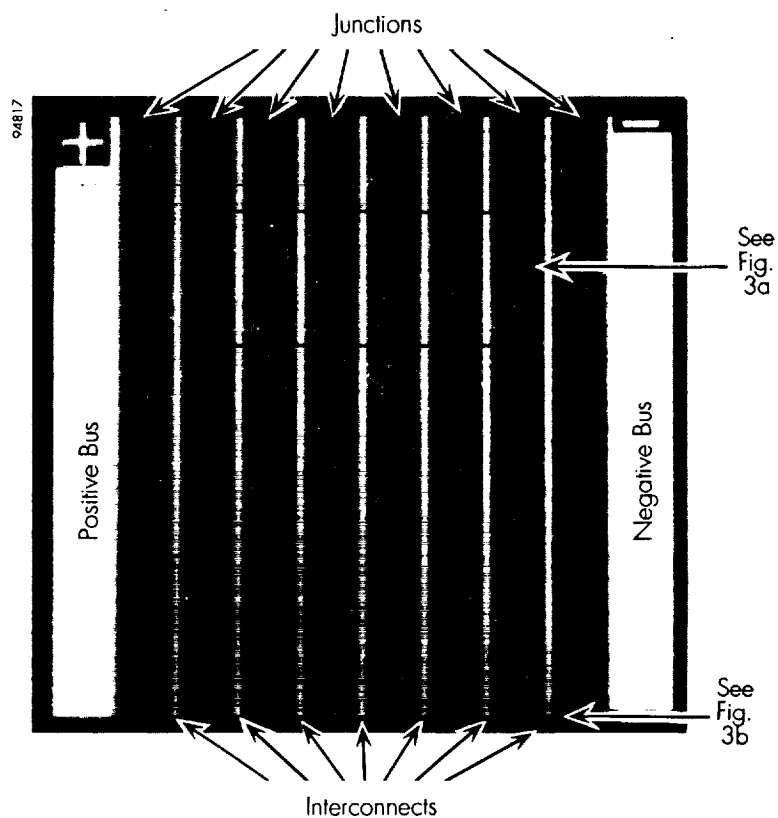


Figure 1 Two-inch InP wafer with ten LPCs and two test sites. These square devices are designed for uniform illumination over the photoarea from a distant laser. LPCs for optical fibers or for free-space transmission with small diameter laser beams should have pie-shaped circular photoareas.

2a)



2b)

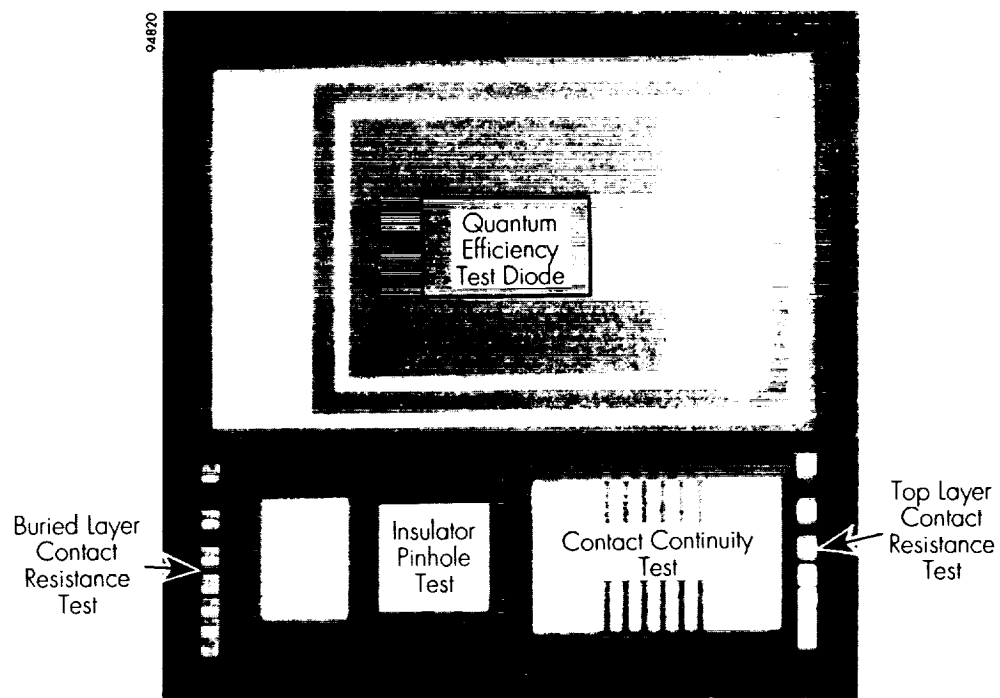
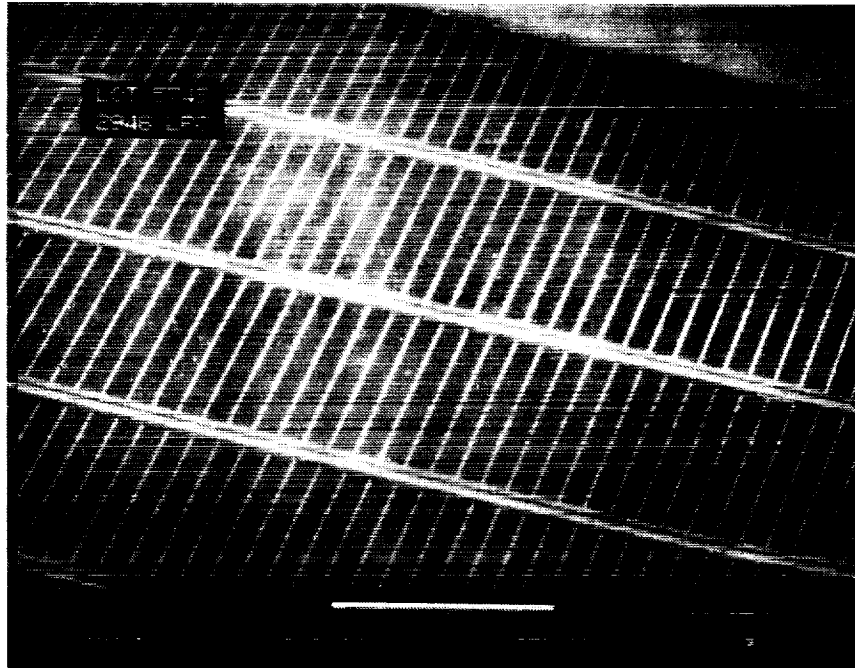


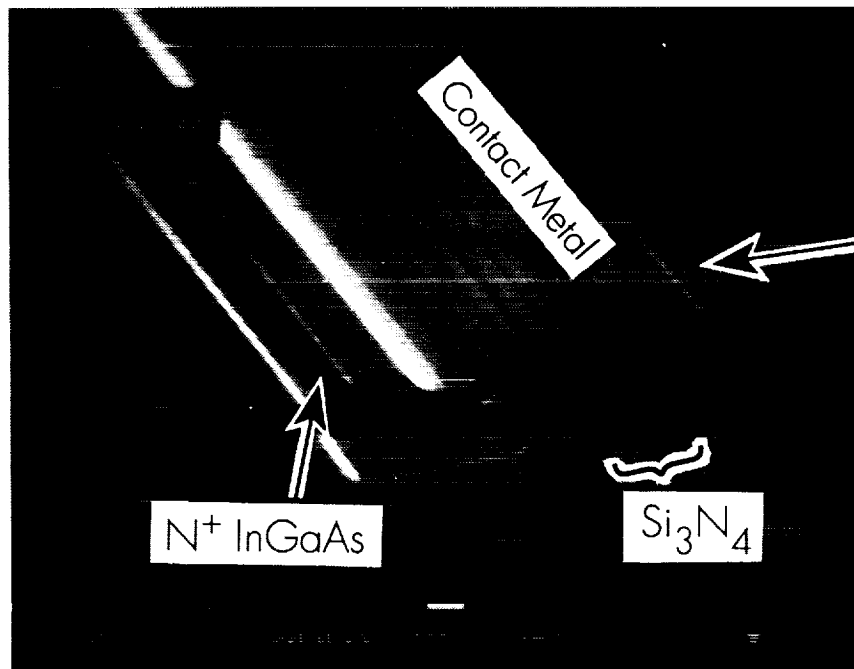
Figure 2 a) Multijunction 1 cm² LPC (0.8 cm² photoarea); b) test site containing large single-junction photodiode for QE measurement, contact resistance test patterns for both the top (P) and bottom (N) contact layers, and an insulator test pattern.

3a)



94818

3b)



94819

Figure 3

a) SEM detail of top contact 5 μm gridlines (100 μm centers) too fine to see in Fig. 2a.
 b) SEM detail of 100 μm wide metal interconnect from bottom N^+ $\text{In}(\text{Al})\text{GaAs}$ layer of one junction over a silicon-nitride-protected mesa edge onto the upper P^+ InGaAs layer of the next junction. The number of junctions per cm for the LPC is limited by this "dead" interconnect area to about 10 per cm (100 μm dead to 900 μm active width).

MEASUREMENTS

Figure 4 shows measured absolute quantum efficiencies of $\text{In}_{0.53}\text{Ga}_{0.47}\text{As}$ and $\text{In}_{0.5}\text{Al}_{0.1}\text{Ga}_{0.4}\text{As}$ single junction test diodes.

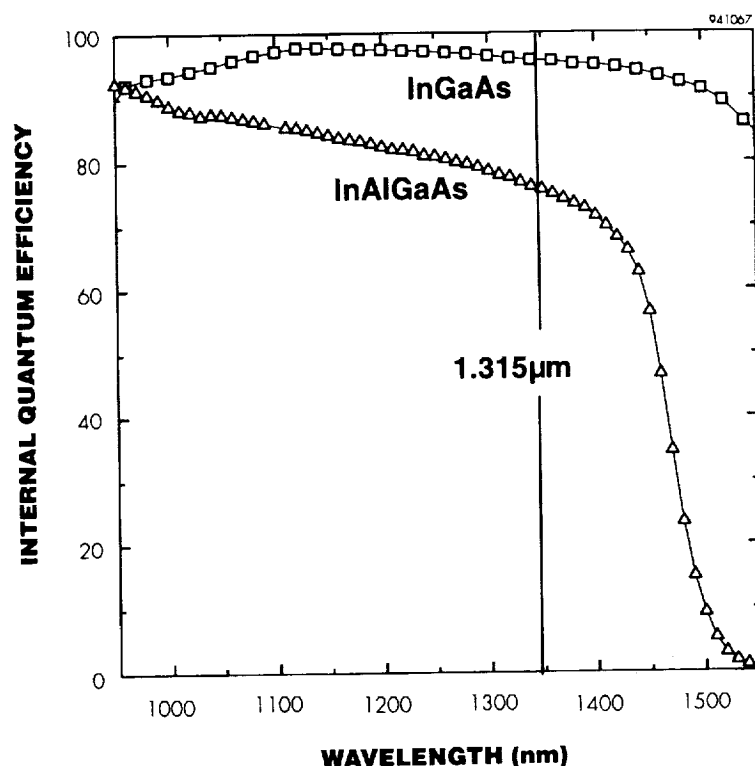


Figure 4 Quantum efficiency of 0.74 eV InGaAs and 0.85 eV InAlGaAs test diodes. The InGaAs results are typical, but InAlGaAs results vary considerably depending on lattice-mismatch and MOCVD reactor growth conditions; the InAlGaAs device here is from a better MOCVD growth run.

In general, the $\text{In}_{0.53}\text{Ga}_{0.47}\text{As}$ devices performed better than the $\text{In}(\text{Al})\text{GaAs}$ LPCs, even though the $\text{In}_{0.53}\text{Ga}_{0.47}\text{As}$ LPCs bandgap was not as favorable for this application. The quaternary $\text{In}(\text{Al})\text{GaAs}$ devices are harder to lattice-match during epitaxial growth repeatably than the ternary InGaAs devices. In addition, the aluminum in the InAlGaAs devices scavenges oxygen very readily. In general, quantum efficiencies were considerably lower for In(Al)GaAs LPCs than for InGaAs LPCs. The dark currents for In(Al)GaAs LPCs were often better than the InGaAs devices, presumably because of the higher bandgap, and the photovoltages were as good or slightly better than InGaAs devices; however, the lower photocurrent and quantum efficiency of the In(Al)GaAs devices always meant the InGaAs devices were better performers.

Figure 5 below shows two illuminated I-V curves of an eight junction $\text{In}_{0.53}\text{Ga}_{0.47}\text{As}$ LPC. An equivalent 1.3 μm single wavelength power density is shown for each curve. The measurements were actually taken with a solar simulator (concentrated white light). We now explain how we arrived at an equivalent 1.3 μm light power density with the simulator. The devices were illuminated and driven to an arbitrary photocurrent. The 1.3 μm quantum efficiency measured previously (similar to Figure 4) from the test site single junction diode is used to determine how much 1.3 μm light would need to be incident on the LPC to produce the simulator photocurrent:

$$\text{Equivalent } 1.3 \mu \text{ power} = \frac{hc}{q\lambda\eta} * (\text{simulator photocurrent})$$

where h is Planck's constant (J/s), c is light's velocity (m/s), q is the electron charge (C), λ is 1.3×10^{-6} m, and η is the $1.3 \mu\text{m}$ quantum efficiency from the test site diode for the wafer. The above formula is a simple re-arrangement of the standard formula for the photocurrent from a photodetector. The dead interconnect area (10%) and gridline shadow loss (5%) of the LPC, which is not present or part of the test site diode, is included in this calculation. This is the power density indicated on the graph. The open-circuit voltage and fill-factor are exactly the same for either white light or single $1.3 \mu\text{m}$ wavelength illumination as long as the total photocurrent is exactly the same, as it is by definition here.

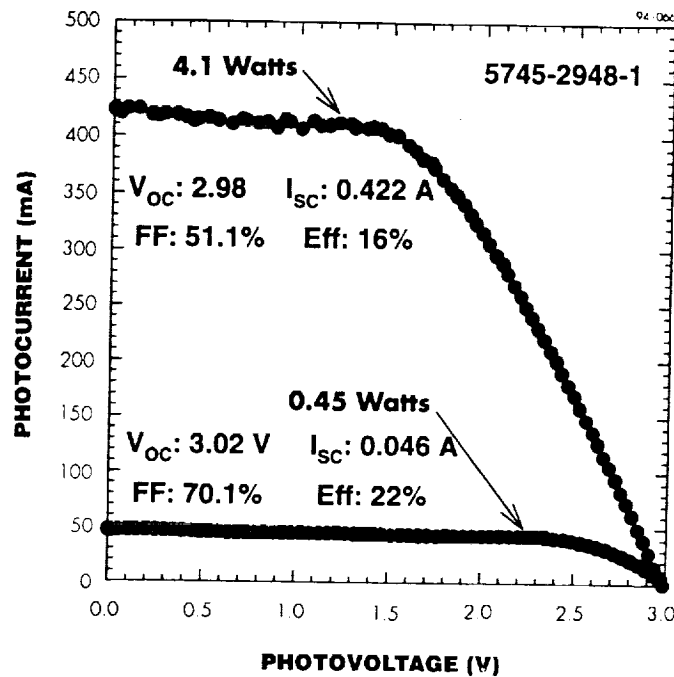


Figure 5 *I-V curves of an eight-junction $\text{In}_{0.53}\text{Ga}_{0.47}\text{As}$ laser power converter under two $1.3 \mu\text{m}$ equivalent illumination levels. At higher photocurrents the device becomes series resistance limited*

CONCLUSIONS

We have demonstrated working monolithic multijunction (eight-junction) $\text{In}_x\text{Al}_y\text{Ga}_{1-x-y}\text{As}$ LPCs with $1.3 \mu\text{m}$ power efficiencies up to 22%. Although the (0.85 eV) $\text{In}_{0.5}\text{Al}_{0.1}\text{Ga}_{0.4}\text{As}$ LPCs should have been superior to the (0.74 eV) $\text{In}_{0.53}\text{Ga}_{0.47}\text{As}$ LPCs for converting $1.315 \mu\text{m}$ light (0.94 eV), additional material dislocation defects and oxygen recombination sites limit the current performance of the more complex $\text{In}_{0.5}\text{Al}_{0.1}\text{Ga}_{0.4}\text{As}$ LPCs. The simpler $\text{In}_{0.53}\text{Ga}_{0.47}\text{As}$ LPCs in all cases had better power conversion efficiencies. LPCs of both types are currently limited by series resistance to incident optical power densities below 10 W/cm^2 . Some additional redesign of the contact grid and emitter and buried layers may result in some improvement of the series resistance. However, to improve the operating power density by an order of magnitude, more junctions are needed to lower the photocurrent and I^2R loss. Additional development of photolithographic processing of non-planar device is needed in order to successfully pattern the photoresist in the small trenches between LPC junctions.

REFERENCES

1. G.H. Walker and J.H. Heinbockel, "Mathematical Modeling of a Photovoltaic-Laser Energy Converter for Iodine Laser Radiation," NASA Tech. Memo. 100482.
2. R.J. De Young, G.H. Walker, M.D. Williams, G.L. Schuster, and E.J. Conway, "Preliminary Design and Cost of a 1-Megawatt Solar Pumped Iodide Laser Space-to-Space Transmission Station," NASA Tech. Memo. 4002.
3. G.A. Landis, "Photovoltaic Receivers for Laser Beamed Power in Space," *Proc. of 22nd IEEE PVSC*, pp. 1494-1502, (1991).
4. S. Wojtczuk, S. Vernon, and E. Gagnon, "InGaAs Concentrator Cells for Laser Power Converters and Tandem Cells," *Proc. of the 12th NASA SPRAT, NASA Conf. Pub. 3210*, pp. 119-128, (1992).
5. M.B. Spitzer, R.W. McClelland, B.D. Dingle, J.E. Dingle, D.S. Hill, and B.H. Rose, "Monolithic Series-Connected GaAs Converter Development," *Proc. of 22nd IEEE PVSC*, pp. 142-146, (1991).

HIGH EFFICIENCY GaP POWER CONVERSION FOR BETAVOLTAIC APPLICATIONS¹

Paul E. Sims, Louis C. DiNetta, and Allen M. Barnett
AstroPower, Inc.
Newark, Delaware

SUMMARY

AstroPower is developing a gallium phosphide (GaP) based energy converter optimized for radio luminescent light-based power supplies. A "two-step" or "indirect" process is used where a phosphor is excited by radioactive decay products to produce light that is then converted to electricity by a photovoltaic energy converter. This indirect conversion of β -radiation to electrical energy can be realized by applying recent developments in tritium based radio luminescent (RL) light sources in combination with the high conversion efficiencies that can be achieved under low illumination with low leakage, gallium phosphide based devices. This tritium to light approach is inherently safer than battery designs that incorporate high activity radionuclides because the beta particles emitted by tritium are of low average energy and are easily stopped by a thin layer of glass. GaP layers were grown by liquid phase epitaxy and p/n junction devices were fabricated and characterized for low light intensity power conversion. AstroPower has demonstrated the feasibility of the GaP based energy converter with the following key results: 23.54% conversion efficiency under $968 \mu\text{W}/\text{cm}^2$ 440 nm blue light, 14.59% conversion efficiency for $2.85 \mu\text{W}/\text{cm}^2$ 440 nm blue light, and fabrication of a working 5 V array. We have also determined that at least $20 \mu\text{W}/\text{cm}^2$ optical power is available for betavoltaic power systems. Successful development of this device is an enabling technology for low volume, safe, high voltage, milliwatt power supplies with service lifetimes in excess of 12 years. One potential application for the RL-power supply system concept is illustrated in Figure 1.

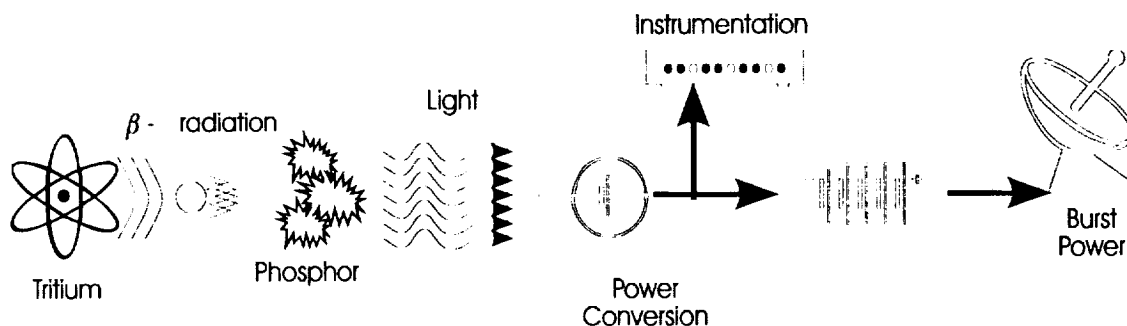


Figure 1. Two step betavoltaic conversion.

There are three major product sectors that the development of betavoltaic technology enables:

- 1) 10 to 20 year milliwatt power sources for medical implants, remote instrument packages, deep space probes, or security devices
- 2) 10 to 20 year nanowatt "static" voltage sources for on circuit board (or on chip) illumination and power cogeneration, and
- 3) integrated illumination and power generation for portable computers and embedded roadside/road sensors for the Intelligent Vehicle Highway System.

¹ Work funded by National Science Foundation Contract III-9261713

INTRODUCTION

The approach of this research is to utilize the tritium fueled two step method to develop cost effective betavoltaic-batteries (β -batteries). The betavoltaic effect was discovered by Rappaport in 1953 (ref. 1). Soon after, the Elgin-Kidde (ref. 2) two-step, 5 year atomic battery was developed. This was based on $^{147}\text{Pm}/\text{ZnS}/\text{Si}$. Conversion efficiencies were low, and the subsequent development of Li based batteries quickly made the Elgin-Kidde cell obsolete. Olsen (ref. 3, ref. 4) has reported on the conversion efficiency of direct betavoltaic power supplies. A review of this technology reveals that there are three major limitations to the direct conversion approach.

Direct Conversion

- the activity and range of the beta emitter must be coupled to the diffusion length of the semiconductor material
- the power flux produced by a beta emitter cannot be concentrated
- the effective ionization energy of the converter material limits the efficiency of the device

Indirect Conversion

- the activity and range of the beta source is coupled to a phosphor which is chosen so that the light emitted is optimal for conversion by the semiconductor material.
- the use of down converting phosphors allows for a volumetric concentration of the beta energy in the form of light flux.
- energy loss is transferred to the phosphor which has experimentally demonstrated radioluminescent conversion efficiencies from 10 to 30%, depending on phosphor type and material quality.

Light emission has been accomplished with an areal power flux greater than that which has been considered to be the maximum possible for tritium gas (ref. 5). The available power density from the tritium/phosphor light is at least $23 \mu\text{W}/\text{cm}^2$. Device modeling results indicate that the light to electricity converter of a β -battery system can have a 20 to 30% conversion efficiency. The modeled efficiency for identical devices with indirect and direct conversion configurations are displayed in Figure 2. The efficiency of the direct conversion configuration is much less than the conversion efficiency of the "indirect" process.

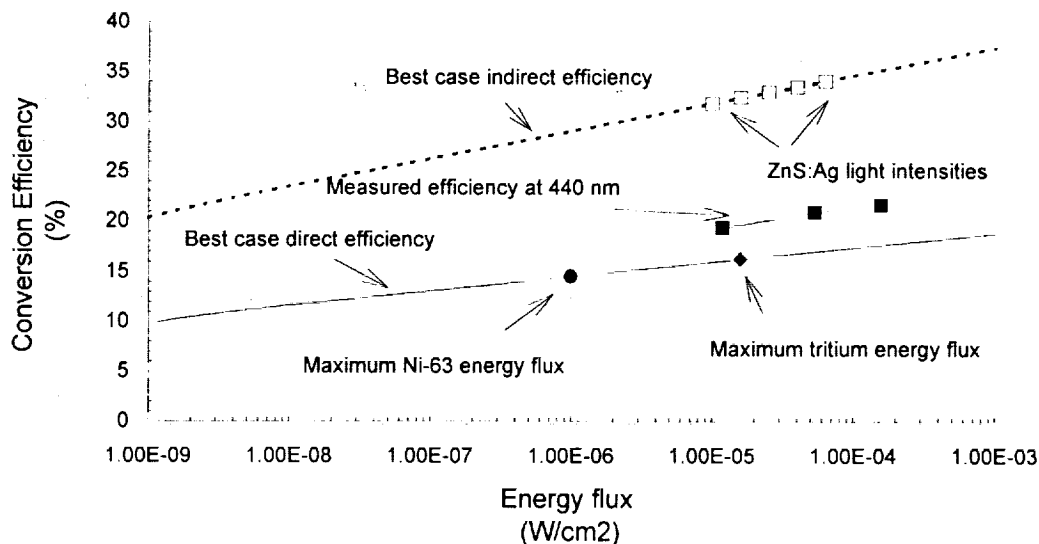


Figure 2. Best case conversion efficiency of GaP.

EXPERIMENTAL RESULTS

Blue Phosphors

The absorption edge for gallium phosphide extends from 549 nm to 520 nm, consequently only the higher photon energy blue and UV phosphors are of interest. Blue phosphors consist of a high bandgap semiconducting or semi-insulating material doped with mid-bandgap luminescent center impurities. These impurities provide midband energy levels for the radiative recombination of a carrier that has been excited by impact ionization to an energy state within the conduction band. In principle, phosphors can be highly efficient because the light is emitted within a non-absorbing lattice. In practice, phosphor efficiencies are lower, mainly due to non-radiative recombination mechanisms dependent on the material quality and material processing. It is important to note that phosphor generated light cannot be intensified by simply increasing the thickness of the phosphor layer. Optical effects such as scattering, absorption, and light trapping will determine the optimum thickness for maximum brightness of a phosphor at a given level of excitation.

For this application, power generation efficiency depends on beta-to-optical and optical-to-electrical conversion efficiencies, therefore, a literature search for phosphor conversion efficiency was conducted. The most comprehensive source of this type of data has been found in Brill (ref. 5). Table 1 gives a summary of the available phosphors.

Table 1. Blue Phosphors

Phosphor	Emission (nm)	Bandwidth (fwhm)	e ⁻ -beam Quantum Efficiency*	UV Quantum Efficiency**
Ca ₃ (PO ₄) ₂ :Tl	300	40 nm	$\eta_R = 0.2\%$	$\eta_R = 49\%$, QE = 56%
BaSi ₂ O ₅ :Pb	351	90 nm	$\eta_R = 4\%$	$\eta_R = 55\%$, QE = 75%
SrB ₄ O ₇ :Eu	371			
Sr ₂ P ₂ O ₇ :Eu	420			
CaWO ₄ :Pb	446	120 nm	$\eta_R = 3\%$ $\eta_L = 5 \text{ lm/W}$	$\eta_R = 42\%$, QE = 75% $\eta_L = 65 \text{ lm/W}$
Sr ₅ Cl(PO ₄) ₃ :Eu	447			
BaMg ₂ Al ₁₆ O ₂₇ :Eu	450			
ZnS:Ag	450	55 nm	$\eta_R = 21\%$ $\eta_L = 22 \text{ lm/W}$	
Sr ₂ P ₂ O ₇ :Sn	460			
MgWO ₄	473	160 nm	$\eta_R = 2.5\%$ $\eta_L = 7 \text{ lm/W}$	
ZnS:Tm	477	10 nm		
Ca ₅ F(PO ₄) ₃ :Sb	482			

* e⁻-beam efficiency is determined at 20 keV.

η_R = radiant efficiency

** UV efficiency is determined at 260 nm.

η_L = luminous efficiency

From these data, it appears that silver doped zinc sulfide is a superior phosphor for this application. The majority, 99%, of the light emission from ZnS:Ag is above the bandgap of gallium phosphide (2.26 eV) and 75% of the light emission is in the spectral region where GaP has a high spectral response. Silver doped zinc sulfide also has demonstrated a high radiative conversion efficiency when excited by 20 keV mono-energetic electrons (ref. 6) and the highest conversion efficiency (20.1%) of the phosphors found in the literature search. Since the phosphor must be stable for 10 to 20 years under betavoltaic irradiation, lifetime studies under high energy electron irradiation need to be performed for the appropriate phosphors.

Phosphor packaging

There are currently four options for packaging light generating phosphors for the β -battery. These are: the commercially available tritium/phosphor tube; microspheres; aerogels; and, tritirated polymers.

The standard commercial tritium/phosphor light is basically a fluorescent light bulb where the UV excitation by an ionized gas is replaced by beta excitation from tritium gas. This technology is compatible with all of the commercially available powdered phosphors. "The maximum light power flux from a standard tritium gas tube RL light has been experimentally shown to be limited to $\sim 2.3 \mu\text{W}/\text{cm}^2$ {1 Footlambert (fL) @ 520 nanometers} because of beta self-absorption in the gas"(ref. 5).

The second possible light source is "Self-Luminous Microspheres" (ref. 7). Microspheres consist of a phosphor and T_2 gas enclosed in a hollow glass sphere. This is similar to the standard commercial package with some important differences. The spheres are very small, 0.1 mm in diameter, and each contains less than $3.6 \times 10^{-5} \text{ cm}^3$ of T_2 at STP. The possible light intensity is estimated at 1 to 10 ft.-lamberts. Since the glass sphere completely absorbs beta emission, no external shielding or high pressure containment is required for a battery assembly. The use of microspheres solves the design issues of safety and containment of the tritium gas, and is compatible with any phosphor. In principle, this type of light source can be concentrated by suspending the glass balls in a transparent matrix. However, there is currently no experimental evidence of the degree of concentration that can be achieved. Some of the items that must be considered are that the glass used to encapsulate the tritium and phosphor will have some absorption and that the scattering mechanisms that limit the brightness of commercial T_2 /phosphor lights still applies.

The third possible light source is the use of aerogels. Phosphors may be suspended in a transparent matrix such as a silica aerogel. The advantage to this type of approach is that volumetric light concentration can be achieved since the aerogel is an open pore structure and tritium completely infiltrates the matrix. Preliminary experiments at Sandia National Laboratories (SNL) have determined that this type of light source can achieve an intensity of at least $23 \mu\text{W}/\text{cm}^2$ (ref. 8). This technology is promising and seems to have the best potential for producing a high luminous flux.

The fourth possible technology is a completely organic, optically clear polymeric matrix demonstrated by Renschler et al. (ref. 9) at SNL in 1989, and Naumann (ref. 10) at E.F. Johnson in 1991. This technology is based on an all-organic, clear system where tritium is covalently bound within a transparent polymeric matrix containing a set of soluble organic scintillant dyes. All of the components are distributed on a molecular scale and reside within angstroms of each other for efficient conversion. However, research by Webb (ref. 7) indicates that there are inherent problems with this technology; exposure to its own radiation causes the tritirated polymer to lose gas. Therefore, the tritirated gas compounds readily diffuse through the polymer leading to radiation hazards and degradation of the transparency of the polymer. Walko (ref. 8) comments that the overall conversion efficiency of this technology is less than 5%. American Atomics, Inc., Self Powered Lighting, Inc., the Oak Ridge National Laboratories, and the 3M company have investigated self-luminous signs and self-lumination based on the tritirated polymer.

The only technology that is immediately available is the standard commercial package. The two more promising technologies, the microsphere concept and the aerogel concept, are both in developmental stages. The microsphere is being developed by Encapsulight, Inc. The aerogel concept has been evaluated by SNL and some preliminary investigations have been done at AstroPower using aerogel material supplied by CF-Technologies, Inc. The organic matrix approach does not seem to be interesting for this application at the current state of development.

Device Modeling

In order to develop a cost-effective β -battery system, a conversion efficiency of 30% at $20 \mu\text{W}/\text{cm}^2$ is desired. The modeling results indicate that this is possible. A 30% efficient device imposes stringent requirements on both the device design and on the quality and reproducibility of the growth and fabrication process. The device must both collect the maximum amount of current and generate power with minimal losses. The pertinent factors are the shunt resistance of the diode (R_{sh}), the depletion region recombination reverse saturation current (J_{02}), the external quantum efficiency of the device (EQE), and the photodiode's fill factor (FF). Figure 3 displays the effects that each of these parameters has on the device conversion efficiency.

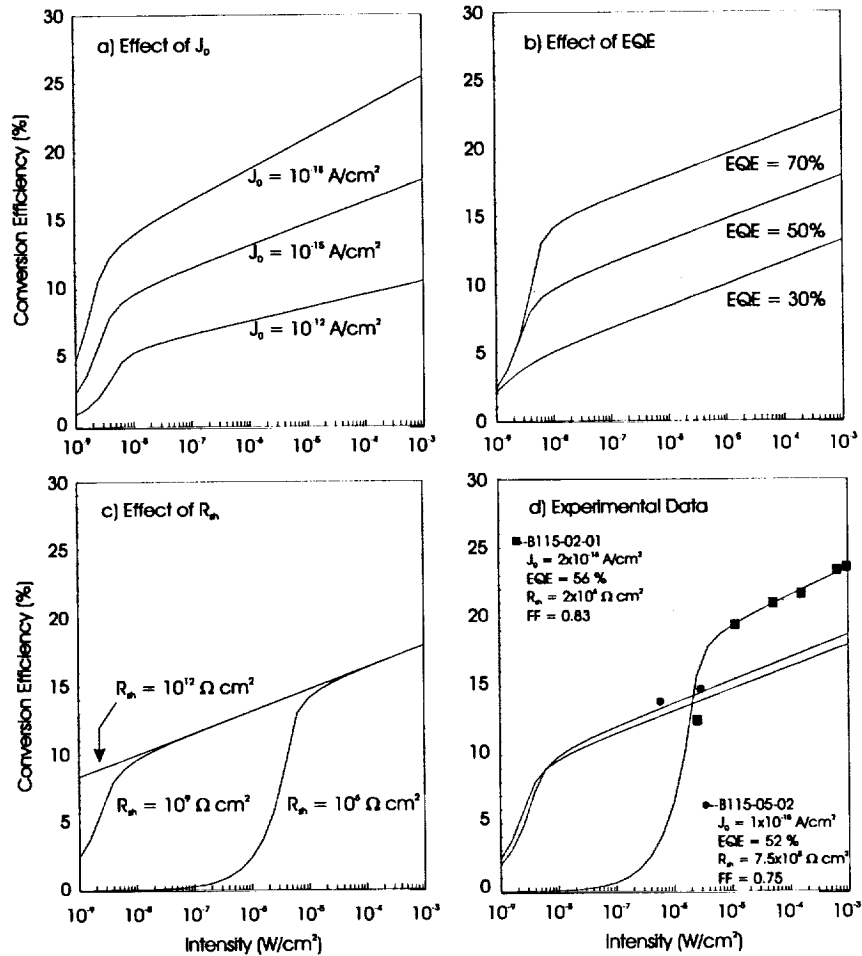


Figure 3. Effects of model parameters on predicted device conversion efficiency.

At a given light intensity conversion efficiency is linearly proportional to the external quantum efficiency (EQE) of the device. The fill factor also affects conversion efficiency linearly. The EQE is affected by surface recombination, the diffusion length of the emitter and base material, and the depth of the junction. For this application, the fill factor is mainly affected by the quality of the contacts at low current levels. Reducing J_{02} increases the voltage of the device at a given light intensity. The efficiency increase is less, it is log-linear (i.e. $\Phi \cdot \ln \Phi$) with the flux. The reverse saturation current depends on the carrier concentration of the material and the diffusion length in the material. The shunt resistance of the diode determines a threshold intensity for efficient conversion. The shunt resistance of the device seems to be mainly determined by the isolation technique utilized, and the depth of the junction.

The results of this modelling were used to determine the device parameters necessary to achieve 30% conversion efficiency for the "indirect conversion" β -battery. These are summarized in Table 2. For reference, parameters corresponding to the middle curves in the Figure 3 graphs are also shown.

Table 2. Device Modeling Results

Device Parameter	Middle Curves	30% Conversion Efficiency
Reverse Saturation Current	10^{-15} A/cm ²	10^{-18} A/cm ²
External Quantum Efficiency	50%	80%
Shunt Resistance	10^9 Ω -cm ²	10^9 Ω -cm ²
Fill Factor @ 10^{-6} watts/cm ²	70%	80%

Device Results

Gallium phosphide layers were grown by liquid phase epitaxy and p/n junction devices were fabricated and characterized for low light intensity power conversion. AstroPower has demonstrated GaP based energy conversion efficiency of 440 nm blue light of 23.54% at 968 μ W/cm² and 14.59% at 2.85 μ W/cm².

Representative quantum efficiency curves of devices produced during this program are displayed in Figure 4. The external quantum efficiency (EQE) of GaP devices can be increased up to 20% by the application of an optimized AR coating, resulting in 70 to 80% EQE in the 380 to 480 nm spectral range.

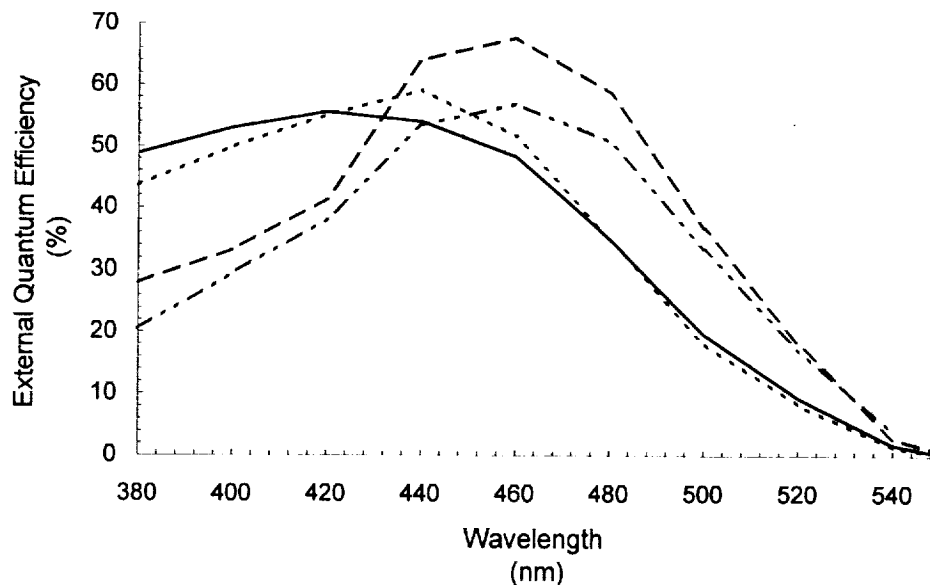


Figure 4. Quantum efficiency of some devices produced during the research program (no AR).

The J-V curves of device B115-05 illuminated by different wavelengths of light are displayed in Figure 5. This device has good shunt resistance, but the reverse saturation current is higher so that the photogenerated voltages are lower. Note that the conversion efficiency of 2.85 μ W/cm² 440 nm light is 14.59%. This color and intensity of light is barely visible to the naked eye.

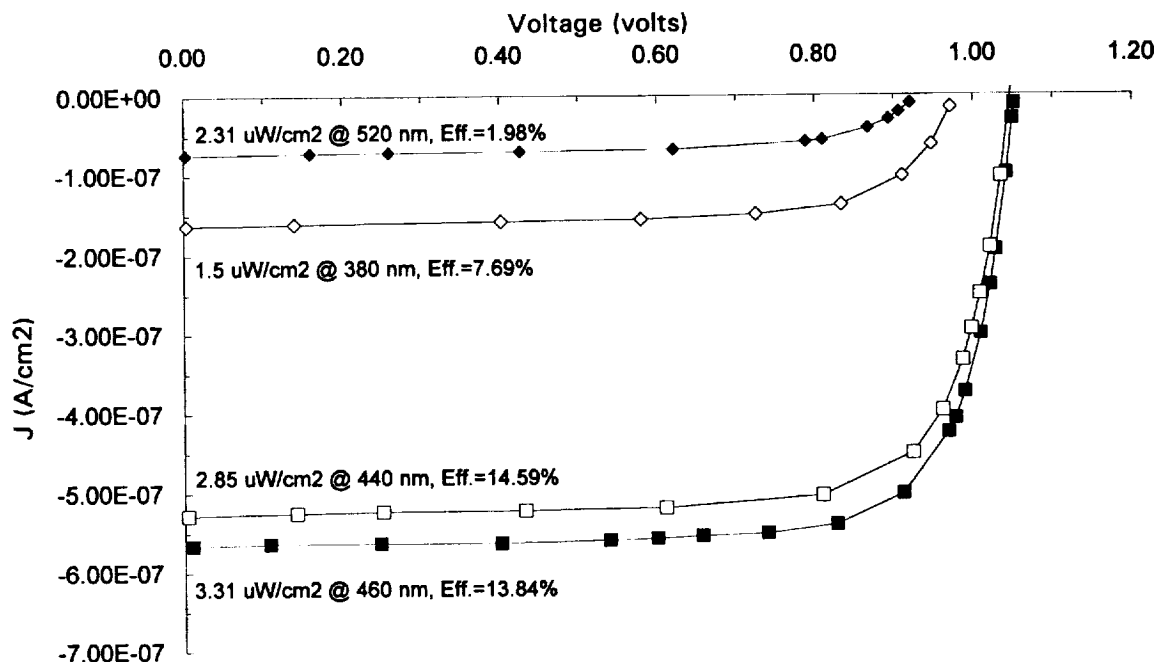


Figure 7. Conversion efficiency of device B115-05 for different wavelengths and intensities of monochromatic light.

At the low operating current levels for this type of device, a high series resistance can be disregarded, although the contacts must be ohmic. However, high shunt resistance is critical for low energy conversion efficiency.

A window layer was incorporated in the device design to passivate the surface of the device. The growth of a thin layer of AlGaP on the surface of the diode has also been found to significantly reduce surface recombination. This can be attributed to a combination of band bending effects and the possible formation of a passivating oxide.

A measurement of V_{oc} vs. J_{sc} , Figure 6, at varying light intensities is used to determine J_{02} and the shunt resistance of the device. This technique eliminates the effects of series resistance on the J-V characteristic and permits a straight forward determination of the diode ideality factor n and saturation current density J_0 . In general, such a plot will exhibit several distinct regions with characteristic values of n and J . Under low forward bias, $n \approx 2$ and J_0 is the depletion region

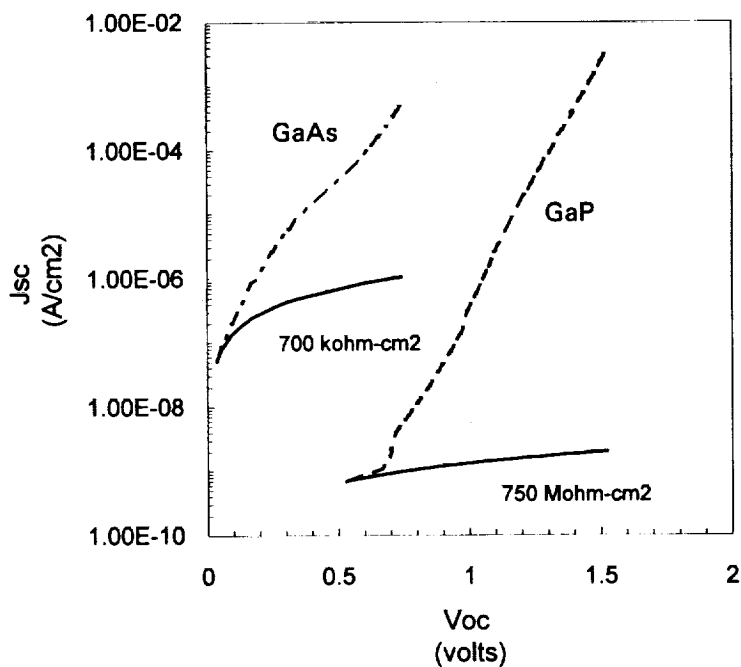


Figure 6. $\log J_{sc}$ versus V_{oc} for GaAs and GaP devices.

recombination current. Under high forward bias, $n \approx 1$ and J_0 is due to the recombination of injected minority carriers in the quasi-neutral region of the base layer. High bandgap materials rarely display $n = 1$ behavior. Figure 6 displays $\log J_{sc}$ vs. V_{oc} for a GaAs solar cell and a GaP energy converter. The light intensity varies from $\sim 1 \mu W/cm^2$ to $100 mW/cm^2$. There is no evidence of $n = 1$ behavior for either device. R_{shunt} is extracted from Ohm's Law. J_{02} is determined by the y-intercept. At room temperature, the $n = 2$ slope is 120 mV/decade of current.

The diffusion length of the base material is estimated from the absorption edge portion of the quantum efficiency curve. Due to some details in the experimental process, the values obtained are "characteristic" of the true value of the diffusion length. A proprietary growth enhancement has been found to both increase the short wavelength current generation of the device by promoting good window layer formation and to increase the long wavelength response of the device by increasing the diffusion length of the material. The "diffusion lengths" of the enhanced growth devices measured during this program are twice those of non-enhanced growths.

A twelve cell array was fabricated using GaP devices grown by the non-enhanced technique. This array consisted of devices in a two-string configuration. The cells were current matched at an operating point of 0.8 volts while illuminated by an $8.24 \mu W/cm^2$ ZnS:Ag light source. The fabricated array had a better performance than the predicted values from the individual cell test data due to a current boost from the reduced shading for wire bonded interconnects compared to the probe station. The details of the current matching data are in Table 2. Figure 7 displays the J-V and P-V curve of the array illuminated by the phosphor light source. Since this array was fabricated from devices without growth enhancement, it is expected that an array with at least double the efficiency could be fabricated. Two devices (B115-50-01 and B-115-05-02), from enhanced growth runs, that were not incorporated into the array are included to show the efficiency achievable with this material at its present state of development. Array efficiencies above 20% should be achievable. For reference a GaAs cell is also included.

Table 3. Cell data for array elements illuminated by $\approx 8.24 \mu W/cm^2$ ZnS:Ag light

Array Position	Cell	V_{oc} (V)	I_{sc} (nA)	V_{mp} (V)	I_{mp} (nA)	I at 0.8V (nA)	FF	η (%)
A1	B114-14-05	0.99	51	0.8	45	45	0.72	4.37
A2	B114-10-05	1.03	54	0.8	48	48	0.69	4.66
A3	B114-10-07	0.95	52	0.8	48	48	0.78	4.66
A4	B114-12-05	1.00	51	0.9	44	49	0.77	4.81
A5	B114-10-04	1.03	51	0.8	50	50	0.76	4.86
A6	B114-14-01	1.04	53	0.8	50	50	0.73	4.86
B1	B114-12-04	1.06	52	0.9	46	51	0.75	5.03
B2	B114-12-02	1.01	52	0.9	47	52	0.80	5.14
B3	B114-12-01	1.12	53	0.9	53	52	0.76	5.46
B4	B114-14-02	1.14	54	1.0	50	53	0.81	6.07
B5	B114-10-01	1.08	55	0.9	52	54	0.79	5.68
B6	B114-10-03	1.16	55	1.0	51	55	0.80	6.19
Array		6.27	145*	5.25	116	121 @ 4.8 V	0.56	5.52
	B115-02-01	1.19	106	0.9	100	104	0.71	10.93
	B115-05-02	1.11	111	0.9	108	109	0.79	11.8
	GaAs cell	0.24	251	0.2	159		0.52	3.86

* Current boost is due to the elimination of probe shading after array fabrication.

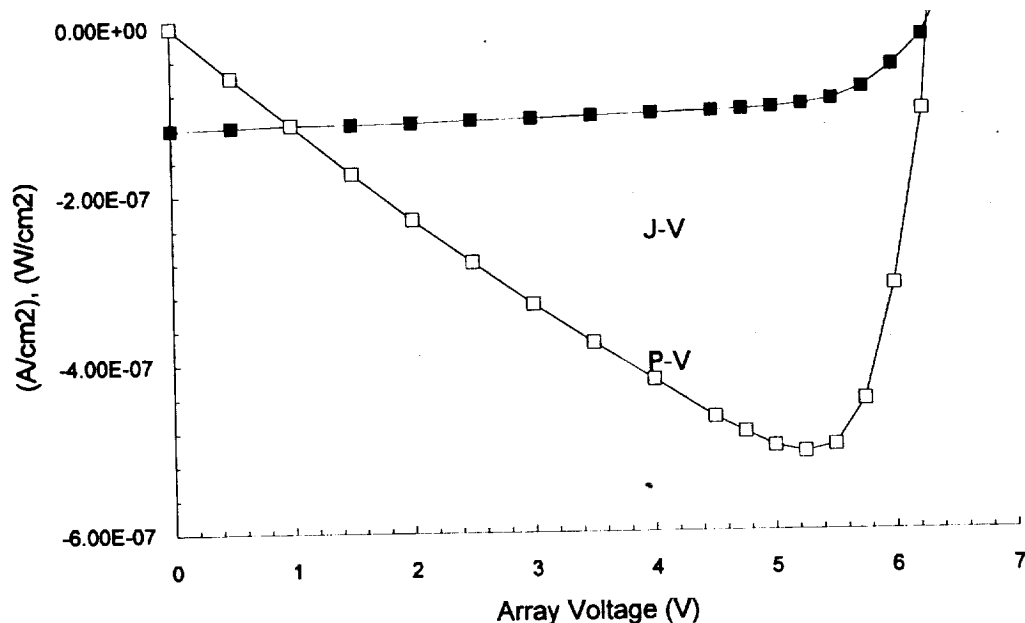


Figure 8. Prototype array illuminated by the ZnS:Ag phosphor.

CONCLUSIONS

Completion of the Phase I program resulted in a prototype 5 volt array based on a non-optimized photodiode structure for the indirect conversion of tritium beta decay to electrical power. Future programs will concentrate on β -battery system design, optimization of the photodiode energy converter, and the manufacturing solutions required for the economic production of the large semiconductor material quantities needed for the β -battery.

The β -battery design encompasses unique advantages. For low power applications, the proposed beta battery has six times less volume than LiSO_2 batteries. An optimized β -battery requires 60 cm^3 per mW while a lithium battery requires 360 cm^3 per mW (ref. 8). These batteries can be used in applications where an instrument package is to be left unattended for years in a remote location (such as at the bottom of the ocean or embedded in a roadway for the Intelligent Vehicle Highway System) with an intermittent telemetry stream or a low power housekeeping load. This type of battery will also prove useful in deep space probe power systems. The beta battery also has widespread commercial potential as an on-board power supply to maintain non-volatile memory.

REFERENCES

1. Rappaport, "THE ELECTRON-VOLTAIC EFFECT IN P-N JUNCTIONS INDUCED BY BETA-PARTICLE BOMBARDMENT," PHYSICAL REVIEW, 93, 1954, PP. 246.
2. Elgin-Kidde ATOMIC BATTERY, "MINIATURE ATOMIC POWERED BATTERY", RADIO AND TV NEWS, V.57, PAGE 160, MAY 1957.
3. Olsen, "BETAVOLTAIC ENERGY CONVERSION", ENERGY CONVERSION, 13, 117 1973.

4. Olsen, "REVIEW OF BETAVOLTAIC ENERGY CONVERSION", PROCEEDINGS OF THE XII SPACE PHOTOVOLTAIC RESEARCH AND TECHNOLOGY CONFERENCE (SPRAT XII), NASA LEWIS, OCT. 1992.
5. Walko, R.C. Lincoln, W.E. Baca, S.H. Goods, AND G.H. Negley, "TRITIUM-FUELED BETACELLS", IECEC 1991.
6. Bril, "ABSOLUTE EFFICIENCIES OF PHOSPHORS WITH ULTRAVIOLET AND CATHODE-RAY EXCITATION", LUMINESCENCE OF ORGANIC AND INORGANIC MATERIALS, H.P. KALLMANN AND G. MARMOR SPRUCH ED., JOHN WILEY AND SONS, 1962.
7. Webb, "SAFE AND EFFICIENT SELF-LUMINOUS MICROSPHERES", U.S. PATENT 4,677,008, JUNE 30, 1987.
8. Walko, C.S Ashley, C.J. Brinker, S.T. Reed, C.L. Renschler, T.J. Shepodd, R.E. Ellefson, J.T. Gill, AND L.E. Leonard, "ELECTRONIC AND PHOTONIC POWER APPLICATIONS", RADIOLUMINESCENT SPECIALISTS CONFERENCE, ANNAPOLIS, MD, 1990.
9. Renschler, R.L. Clough, AND T.J. Shepodd, "DEMONSTRATION OF COMPLETELY ORGANIC, OPTICALLY CLEAR RADIOLUMINESCENT LIGHT", JOURNAL OF APPLIED PHYSICS, 66 (9), NOVEMBER 1987.
10. Naumann, "COLD LIGHT BECOMES LONG-LIFE ELECTRIC GENERATOR", SENSOR, DEC. 1990.

SESSION VII

CELL/MATERIAL PROPERTIES

REVIEW OF SOLAR CELL TEMPERATURE COEFFICIENTS FOR SPACE

Geoffrey A. Landis
NYMA, Inc.
Brook Park, Ohio

INTRODUCTION

Energy conversion efficiency is an important parameter for solar cells, and well reported in the literature. However, solar cells heat up when in sunlight, and the efficiency decreases. The temperature coefficient of the conversion efficiency is thus also extremely important, especially in mission modeling, but is much less well reported. It is of value to have a table which compiles into a single document values of temperature coefficient reported in the literature.

In addition to modeling performance of solar cells in Earth orbit, where operating temperatures may range from about 20°C to as high as 85° C, it is of interest to model solar cells for several other recently proposed missions. These include use for the surface of Mars, for solar electric propulsion missions that may range from Venus to the Asteroid belt, and for laser-photovoltaic power that may involve laser intensities equivalent several suns. For all of these applications, variations in operating temperature away from the nominal test conditions result in a significant changes in operating performance.

In general the efficiency change with temperature is non-linear, however, in the range from negative 100 °C through room temperature to a few hundred degrees C, efficiency is usually quite well modeled as a linear function of temperature (except for a few unusual cell types, such as amorphous silicon, and for extremely low bandgap cells, such as InGaAs). Typical curves of efficiency versus temperature are shown in figure 1, from Reference [9].

TEMPERATURE COEFFICIENTS

This is a compilation of data reported in the literature on a variety of cell types. Not all literature values were reported. Some of the literature is ambiguous (for example, not listing whether reported values are normalized), or lacks required information (for example, reporting power variation in mW/°C without reporting cell power, or reporting I_{sc} variation without listing cell area). This compilation is also biased toward more recent cell types and cell types currently in production, and data on several old cell designs no longer in use has been left out.

These parameters are reported in terms of the normalized coefficients, that is, the fractional change in value per degree Celsius, $1/\eta \, d\eta/dT$. Clearly, the same coefficients apply to both efficiency and power, $1/\eta \, d\eta/dT = 1/P \, dP/dT$. A negative coefficient indicates a decrease in efficiency as temperature rises. Thus, given the efficiency at the nominal measurement temperature T_0 , the efficiency at T is:

$$\eta(T) = \eta(T_0) [1 + (1/\eta \, d\eta/dT)(T_0 - T)] \quad (1)$$

The temperature coefficient can be resolved into the sum of the variations of the open circuit voltage, V_{oc} , the short circuit current, J_{sc} , and the fill factor, FF:

$$1/\eta \, d\eta/dT = 1/V_{oc} \, dV_{oc}/dT + 1/J_{sc} \, dJ_{sc}/dT + 1/FF \, dFF/dT \quad (2)$$

The V_{oc} variation contributes the majority of the change in efficiency. The V_{oc} and FF variations can be found in the references and are not tabulated here. The short circuit current temperature coefficient, $1/J_{sc} \, dJ_{sc}/dT (= 1/I_{sc} \, dI_{sc}/dT)$ is reported, for reasons discussed below.

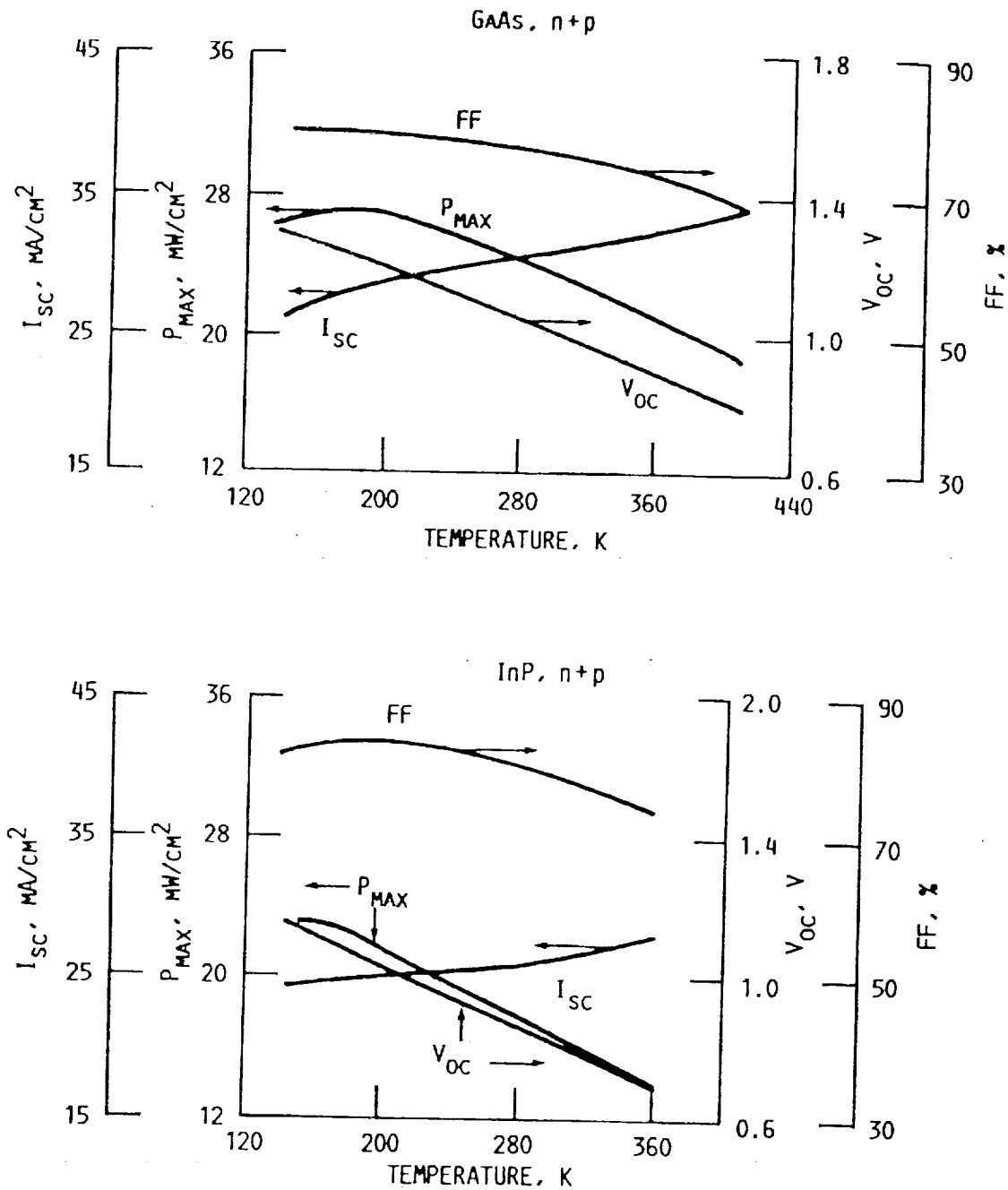


Figure 1

Variation of maximum power (P_{max}) and V_{oc} , I_{sc} , and fill factor with temperature for gallium arsenide solar cell (top) and indium phosphide solar cell (bottom) (data from Weinberg et al. [9], used with permission of the author).

The wide variability in the quoted values of the J_{sc} temperature coefficient for cells of the same general type deserves discussion. The values differ not only from each other, but from the actual value measured under space conditions. This can be seen, for example, in a comparison of temperature coefficients measured using simulated sunlight compared with measurements made in space on the NTS-1 mission [table 4-12 of reference 32, reproduced as figure 2]. The temperature coefficients of voltage match to well within the error bars of the measurement. Measured temperature coefficients of J_{sc} , on the other hand, are incorrect by an average of 340 percent.

Variation of short circuit current with temperature is primarily due to the change in bandgap energy with temperature. As the cell heats up, the bandgap decreases, and hence the cell responds further into the infrared portion of the spectrum. Hence, the J_{sc} variation term is roughly proportional to the incident spectral intensity at wavelengths near the band edge. Solar cells are not typically tested under actual sun illumination, however, but under a solar simulator, often a Xenon lamp. While a Xenon lamp has a spectrum that approximates that of the solar spectrum on the average, the intensity does not duplicate the solar spectrum in detail [31]. This is shown in figure 3. In particular, the spectral intensity near the semiconductor band edge (the range from about 800 to 1100 nm for silicon and GaAs cells) is significantly different from that of the sun, and in general different simulators (even of the same type) will have differences in the detailed structure. Thus, the variability of J_{sc} temperature coefficient is due to variations in the solar simulator, and not differences in the cells.

Measurements of J_{sc} temperature coefficient made with simulated sunlight cannot be trusted. Fortunately, the J_{sc} variation accounts for only about 10-20 percent of the efficiency variation. For greatest accuracy, it is suggested that the measured $1/J_{sc} dJ_{sc}/dT$ term should be subtracted from the normalized power temperature coefficient to cancel this variation, and a calculated value appropriate to the cell material should be substituted. For Si and GaAs cells, use of values from flight experiments (last lines of tables 1 and 2) are suggested.

Tables 1-2 give the compiled values of temperature coefficients from the solar cell literature, along with the temperature range of the measurement and the cell efficiency when listed, for silicon and GaAs space solar cells. The first three values in the list show current production cells for space. Table 3 compiles temperature coefficient data for various emerging materials not yet being used for space power. Table 4 shows values for low-bandgap TPV cells under 1500° blackbody illumination. Note that since 1500° blackbody radiation contains considerably higher amounts of infrared than the solar spectrum, the J_{sc} temperature coefficient is much higher than under solar spectrum illumination.

As expected, the temperature coefficients varies with the bandgap of the material, with the highest temperature dependence shown by the materials with lowest bandgaps. For comparison, table 5 shows the theoretical values of temperature coefficient for idealized GaAs, Si, and Ge cells [24]. The efficiencies of these idealized cells are higher than that of those achieved today, and hence the temperature coefficients are slightly lower. However, the theoretical values for efficiency coefficient agree rather well with the measured values for the GaAs and the Ge cells, as well as for the best of the silicon cells. For reasons discussed above, the short-circuit current coefficients do not agree very well.

The emphasis here is for space operation (Air Mass Zero spectrum). However, since the V_{oc} and FF coefficients are not dependent on spectrum, most of this data is also usable for terrestrial calculations.

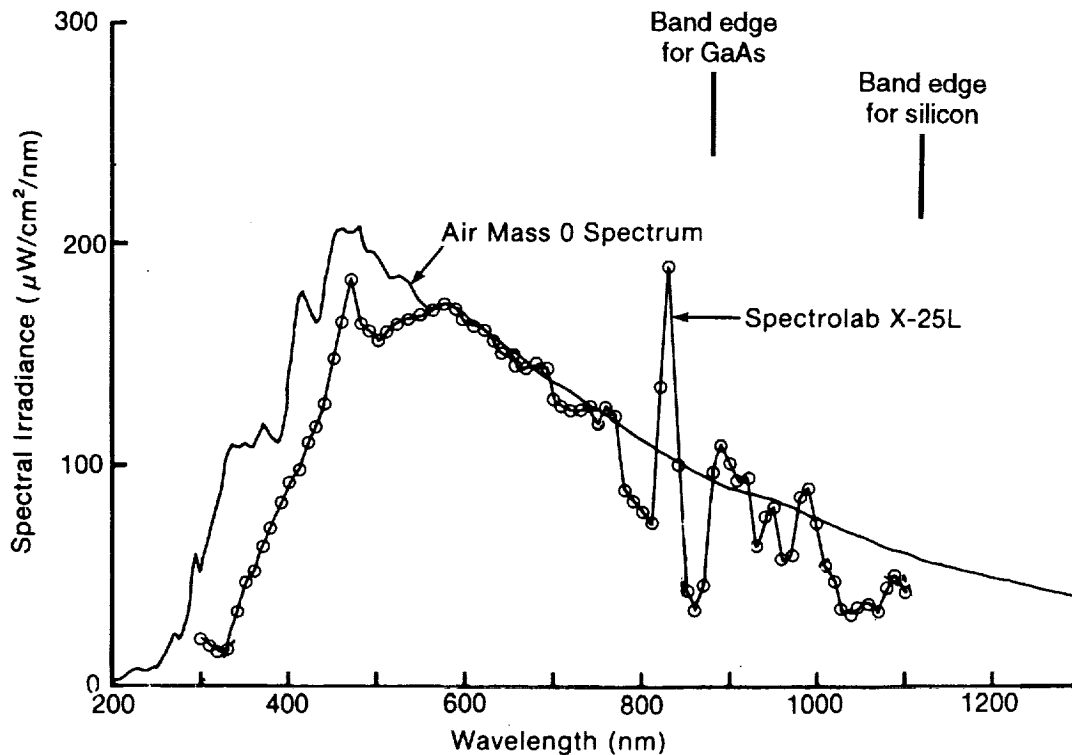
Reference [24] discusses the theoretical basis for the variation of performance with temperature. The largest term in the temperature dependence is the voltage term, which is:

$$dV_{oc}/dT = (V_{oc} - E_g/q)/T - 3k/q - d(E_g/q)/dT + kT/q(1/J_{sc} dJ_{sc}/dT) \quad (3)$$

Exp. No.	$\frac{dV_{oc}}{dT}$ (mV/°C)		$\frac{dI_{sc}}{dT}$ (mA/°C/4 cm ²)	
	Ground Measurement	Space Measurement	Ground Measurement	Space Measurement
1	2.114	2.139 ± .178	.045	.197 ± .064
2	2.082	2.144 ± .113	.058	.213 ± .137
4	1.941	1.871 ± .149	.096	.271 ± .093
5	2.191	2.098 ± .117	.046	.139 ± .047
6	2.082	1.989 ± .140	.058	.170 ± .041
7	1.973	2.089 ± .149	.076	.231 ± .055
8	2.082	2.098 ± .127	.058	.225 ± .061

Figure 2

Measure of voltage and current temperature coefficients for 8 silicon solar cell experiments flown on NTS-1 satellite, comparing measurements made on the ground with those made in space [from ref. 32].



SOURCE: Seaman et al. 1980

Figure 3

Spectral comparison of Spectrolab X-25 Xenon-Arc Solar Simulator with AM0 solar spectrum

where E_g/q is the bandgap in volts, T the temperature, and k/q the thermal voltage, equal to 0.086 mV/°C. Parameters to calculate the bandgap change with voltage for GaAs, Si, and Ge are given in [24], and for InP in [16].

The largest contribution comes from the first term, proportional to the difference between the bandgap and the open circuit voltage. Temperature coefficient thus decreases nearly linearly as voltage increases. Since higher efficiency cells typically have higher open circuit voltages, higher efficiency cells tend to have lower temperature coefficients than low efficiency cells of the same material. This can be clearly seen in table 1.

Temperature coefficient is rarely considered as a design parameter for solar cells. From the standpoint of temperature coefficient, increasing open circuit voltage, even at the expense of decreases in other cell parameters (for example, by increasing base doping of the cell) may result in higher power under actual space operating conditions.

Since open circuit voltage increases logarithmically with short circuit current, temperature coefficient decreases as the log of the intensity. This is shown in the graph of temperature coefficient versus intensity for GaAs solar cells [from Swartz and Hart, [11]]. For cells with low bandgap, such as Ge, the fractional rise in voltage is higher, and thus the decrease in the coefficient with intensity larger. Since temperature coefficient is a function of illumination level, these tables do not report temperature coefficients for concentrator solar cells [33-36].

At low temperature, the linear approximation is less valid. The increase in efficiency as temperature decreases tends to level off, reaching a plateau typically around -80°C for silicon cells [see figures 4-57 through 4-60 of reference 32]. At low illumination intensity and low temperature ("LILT" conditions), some solar cells are subject to additional degradation in performance. References [39], [40], and [41] discuss operation of silicon solar cells at low temperatures and low intensity.

OPERATING TEMPERATURE AND EFFICIENCY

Operating temperature can be calculated from equating the power incident on the array, P_{in} , with the power produced plus that radiated away, P_{out} . Here

$$P_{in} = \alpha_{solar} P_{sun} + \alpha_{albedo} P_{albedo} + \alpha_{thermal} P_{thermal} \quad (4)$$

and

$$P_{out} = \eta(T) P_{sun} + \epsilon_{front} \sigma T^4 + \epsilon_{rear} \sigma T^4 \quad (5)$$

where T is in degrees Kelvin and σ is the Stefan-Boltzmann constant, $5.67 \cdot 10^{-8} \text{ W/m}^2 \cdot \text{K}^4$. For the case of a laser-illuminated array there are additional terms corresponding to the laser incident power and the laser conversion efficiency [47]. Equating these and inserting η as a linear function of T results in a fourth-order equation, which is typically solved by Newton's method.

Note that in calculating temperatures in low Earth orbit, the contribution of sunlight reflected from the Earth ("albedo") and thermal infrared radiated from the Earth must be accounted for. The Earth's albedo varies with cloud cover and season. Average values for P_{albedo} are quoted as "up to 30%" [31], "about 0.3" [28], and 0.35 [1]. Note that albedo increases significantly at high latitudes in winter due to snow cover; this can be important for polar orbits. The worst (highest temperature) case is at orbital noon, when the albedo illumination is directly on the back of the array; for this reason, the rear-surface alpha is an important parameter and is listed in table 6 for the cases where it has been reported.

Thermal radiation also varies with position over the Earth and time of year. Typical thermal estimates use a thermal load in low Earth orbit (LEO) of about $P_{thermal}=0.17$ solar intensity [28,31], with

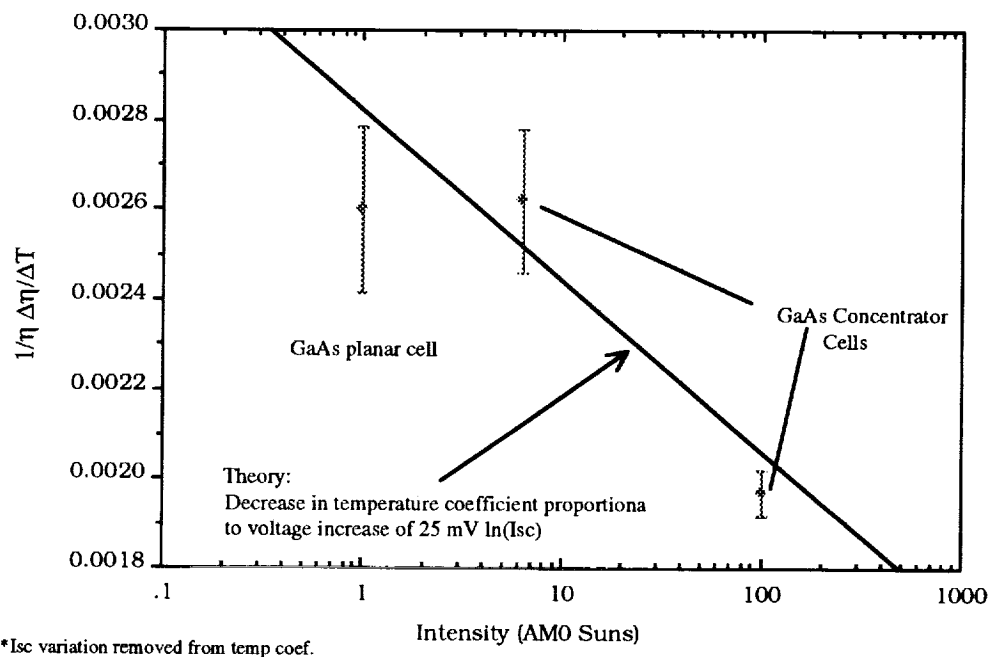


Figure 4

Normalized temperature coefficient (with I_{sc} variation subtracted) of GaAs solar cells at various incident solar intensities. Line shows the expected variation if the only factor in temperature coefficient is the variation of V_{oc} .

the spectrum of a 288 °K blackbody [31]. The absorption constant for thermal radiation α_{thermal} is the same as the thermal emissivity, ϵ , rather than the solar absorptivity α . Higher orbits reduce albedo and thermal loading proportionately to the solid angle subtended by the Earth. Hence (as can be seen in table 6) operating temperatures tend to be lower for GEO orbit (40,000 km altitude) than in LEO (800 km altitude).

The solar absorptivity, α , is a characteristic of the solar cell, subject to some modification by ultraviolet and/or infrared rejection filters on the coverglass. To reduce the solar absorptance, silicon cells may have back-surface reflectors ("BSR") to reflect unabsorbed infrared radiation back to space, or even gridded back contacts to transmit unused infrared directly through the array. Cells with textured surfaces have higher absorptance than cells with planar surfaces, and hence higher operating temperature. In the infrared, the glass cover on the solar array is typically opaque, and hence the thermal emittance ϵ is characteristic of the glass and independent of the cell type.

Table 6 gives some quoted values of the thermal parameters, α and ϵ , and also shows the calculated equilibrium operating temperatures in orbit for several cells.

Future cells may have advanced covers which more efficiently reflect undesired IR and UV radiation [43,44]. This can reduce the solar alpha for silicon cells to 0.75 for cells without back-surface reflectors or gridded back contacts [43], and to 0.72 to 0.79 [43, 44] for GaAs/Ge cells.

TEMPERATURE COEFFICIENTS FOR NON-SOLAR SPECTRA

There has recently been some interest in use of photovoltaic cells for converting laser radiation [45,46]. Equation 2 shows the components of the variation of efficiency with temperature. Of the three terms, only the J_{sc} term should depend on spectrum. Hence, the normalized temperature coefficient under laser illumination can be calculated from the efficiency and J_{sc} terms:

$$[1/\eta \, d\eta/dT]_{\text{laser}} = [1/\eta \, d\eta/dT]_{\text{solar}} - [1/J_{sc} \, dJ_{sc}/dT]_{\text{solar}} + [1/J_{sc} \, dJ_{sc}/dT]_{\text{laser}} \quad (5)$$

Since the J_{sc} term typically contributes 10-20% of the efficiency variation with temperature, to single-digit accuracy the normalized efficiency temperature coefficient should be roughly the same for laser or solar illumination [47]. The V_{oc} term will have a slight dependence on spectrum because the laser wavelength may be chosen to be close to the cell spectral response maximum, and hence the current output for a given intensity input will be higher, resulting in a logarithmic increase in voltage and a slight decrease in temperature coefficient.

Under solar illumination the short circuit current increases with temperature. Under monochromatic illumination this may or may not be true. There are two regions of operation, depending on the wavelength of the laser and the shape of the cell spectral response (in A/W). The two regions are: (1) wavelength shorter than the spectral response peak, or (2) wavelength longer than the spectral response peak.

For wavelengths shorter than the spectral response peak, the semiconductor absorbs essentially all of the incident light, and this does not change as the bandgap changes with temperature. Changes in short circuit current are only due to changes in quantum efficiency, which should be close to unity for high efficiency cells. Since the number of incident photons is not dependent on the bandgap, the current is nearly independent of temperature, and the temperature coefficient of J_{sc} is near zero. Hence, for this region of operation, the monochromatic temperature coefficient can be approximated by subtracting the (solar) normalized J_{sc} temperature coefficient from the normalized efficiency coefficient.

For a cell operating at wavelengths longer than the peak of the spectral response this will not be

true. At long wavelengths the laser light is only weakly absorbed, and hence a small change in the bandgap will result in a large change in absorption. For such cells the J_{sc} will increase with temperature. This effect may be especially important in indirect bandgap materials, such as a silicon cell operated at 1.06μ . For such regimes of operation the change of absorption with temperature will be very significant, and the cell may even increase in efficiency with temperature.

The theoretical monochromatic J_{sc} temperature coefficient is:

$$[1/J_{sc} d J_{sc}/dT]_{laser} = \lambda/Eg (dQE/d\lambda)(dEg/dT) \quad (6)$$

where QE is the cell quantum efficiency at the laser wavelength λ . The variation in bandgap energy with temperature for most materials, dEg/dT , can be found in the literature [16,24].

Solar cells can be used for spectra other than solar or laser. Wilt et al [47] discusses the temperature coefficient of 0.6 to 0.7 eV InGaAs cells under 1500 °C blackbody radiation; these results are shown in table 4. Note that, for these cells, the J_{sc} component of the temperature coefficients is a much larger component of the total. This is because of the low bandgap of the cell and the fact that the 1500° C blackbody has a large amount of its radiation in the infrared. The fact that these cells are operated under high intensity also means that the V_{oc} component of the temperature coefficient is somewhat reduced by the logarithmic dependence of V_{oc} .

For blackbody spectra, as for laser spectra, the temperature coefficient can be computed from the solar temperature coefficient by subtracting out the measured J_{sc} coefficient and replacing it with the J_{sc} coefficient for the spectrum desired.

CONCLUSIONS

The variation of solar conversion efficiency with temperature has been reviewed. The efficiency is assumed to be linear with temperature. This is correct for temperatures near 25° C for most cell types, but the behavior is nonlinear at extremely high and low temperatures. Typically the increase of efficiency with reduction of temperature flattens out below ~200 °K. Also, at extremely high temperatures, the efficiency does not go to negative values, but levels off near zero. References 32 and 33 have data on (1967 vintage) silicon cells to temperatures down to 82 °K. The *Design Handbook* has data on later vintage silicon cells at low intensity and low temperatures [32].

Table 1: Silicon Cell Temperature Coefficients

The first cell listed, SSF gridded back, is the large-area silicon cell developed for the space station Freedom project. This, and the Applied Solar Energy Corporation (ASEC) Back Surface Field/Reflector (BSFR) and ASEC Back Surface Field (BSF) cells, may be taken typical of silicon cells currently used in flight, however, they are not significantly different in performance from the other silicon cells listed, with the exception of the last two.

The University of New South Wales (UNSW) cells are recently developed laboratory cells with improved open-circuit voltage and high efficiency. Cells of this design are not yet qualified for use in space.

Cell Type	Temp (°C)	η (28°C)	<u>normalized temp. coefficients</u>		Ref.
			$1/\eta \, d\eta/dT$ ($\times 10^{-3} \text{°C}^{-1}$)	$1/J_{sc} \, dJ_{sc}/dT$ ($\times 10^{-3} \text{°C}^{-1}$)	
SSF grid back	0-95	.13	-4.5		[1]
ASEC BSFR	28-60	.135-.148	-4.60		[2]
ASEC BSR	28-60	.125-.134	-4.45		[2]
2Ω High E.	0-140	.122	-4.62	+0.74	[3]
10Ω Helios	0-140	.116	-4.72	+0.59	[3]
10Ω BSF	0-75	.140	-5.0		[4]
2Ω K5	0-75	.136	-5.0		[4]
"Violet"	0-120	.14	-4.2	+0.65	[5]
CNR (text.)	10-70	.148	-4.35	+0.34	[5]
AEG 10Ω BSR		.122	-3.79	+1.14	[6]
UNSW MINP	5-60	.1870	-3.443	+0.650	[7]
UNSW PESCS	5-60	.1907	-3.202	+0.650	[7]
NTS-1 space measurement (avg. 7 types)				+1.12	[32]

Table 2: GaAs Cell Temperature Coefficients

The ASEC GaAs/Ge cells listed on the first two lines can be taken as typical of cells that are currently flown in space.

Cell Type	Temp (°C)	η (28°C)	<u>normalized temp. coefficients</u>		Ref.
			$1/\eta \, d\eta/dT$ ($\times 10^{-3} \text{°C}^{-1}$)	$1/J_{sc} \, dJ_{sc}/dT$ ($\times 10^{-3} \text{°C}^{-1}$)	
ASEC GaAs/Ge	20-120	.174	-1.60	+0.830	[8]
ASEC GaAs/Ge	28-60	.18-.185	-2.23	+0.56	[2]
ASEC /GaAs	28-60	.18-.185	-2.32	+0.56	[2]
Spire /GaAs	10-80		-1.47	+0.246	[38]
Varian	60	.195	-2.2	+0.6	[9]
EEV LPE		.174	-1.90	+0.92	[10]
Hughes LPE	0-415	.157	-2.09	+1.1	[11]
French LPE	40-200	.212	-2.53		[12]
LPE	25-350	.156	-2.64	+0.37	[13]
DH	15-80		-2.74	+0.30	[14]
Hughes p/n	0-80	.164	-2.0	+0.714	[15]
LL n/p homo.	0-80	.166	-2.6	+0.71	[15]
Japan LPE p/n	0-100	.175	-2.10	+0.63	[37]
Varian	10-80 (high altitude test)			+0.508	[31]

Table 3: Temperature Coefficients from Cells of Other Materials

<u>normalized temp. coefficients</u>					
Cell Type	Temp [°C]	η (28°C)	$1/\eta \, d\eta/dT$ ($\times 10^{-3} \text{°C}^{-1}$)	$1/J_{sc} \, dJ_{sc}/dT$ ($\times 10^{-3} \text{°C}^{-1}$)	Ref.
<u>1.7eV AlGaAs</u>					
AlGaAs	15-80		-1.55	+0.95	[14]
<u>1.93 eV AlGaAs</u>					
Varian	25-96	(high altitude test)		+0.761	[31]
<u>InP</u>					
diffused (best)	60	.132	-3.45	+0.767	[16]
diffused (wrst)	60	.103	-3.56	+0.966	[16]
RPI	60	.136	-2.8	+0.8	[9]
MO-CVD	0-150	.195	-1.59	+0.890	[17]
ITO/InP	15-80		-3.80	+0.515	[14]
<u>Ge</u>					
RTI	20-80	.090	-10.1	+0.617	[18]
<u>CuInSe₂</u>					
Boeing CIS	-40-80	.087	-6.52		[19]
ISCT CIS	-40-80	.088	-6.03		[19]
Boeing CIS	25	.08	-5.26	+0.43	[20]
CIS/CdZnS	15-80		-5.87	+0.260	[14]
CIS/CdS			-6.880	+0.057	[21]
<u>Amorphous Si alloys</u> Reported a-si cells have nonlinear response with temperature. Data reported here is for the region listed.					
<i>(single junction)</i>					
Solarex	0-40	.066	-1.11*	+0.74	[19]
ECD a-si:H,F	15-80		-0.98 to -1.97*	0.83 to 0.95*	[14]
ECD aSiGe:H,F	15-80		-1.02 to -1.97*	1.01 to 1.36*	[14]
*nonlinear					
<i>(two junction)</i>					
Fuji	22-60	.089-.10	2.0		[42]
<u>GaAs/Ge Tandem</u>					
low temp.*	35-100	.194	-2.85	+1.02	[22]
high temp.*	100-180	~.18	-2.0	+1.02	[22]
Spire	25-80	.189	-1.54	+0.94	[23]
[see also ref. 38]					
*nonlinear					

Table 4: Temperature Coefficients For Thermophotovoltaic (TPV) Cells under 1500°C blackbody radiation

Note that J_{sc} temperature coefficient will be much higher under 1500° blackbody radiation than under the solar illumination.

Cell Type	Temp (°C)	<u>normalized temp. coefficients</u>		Ref.
		$1/\eta \, d\eta/dT$ ($\times 10^{-3} \text{°C}^{-1}$)	$1/J_{sc} \, dJ_{sc}/dT$ ($\times 10^{-3} \text{°C}^{-1}$)	
0.6eV InGaAs	30-70	-9.46	+3.04	[48]
0.66eV InGaAs	25-60	-10.12	+3.18	[48]
0.75eV InGaAs	30-60	-4.67	+2.00	[48]

note: the J_{sc} temperature coefficients for these cells are highly non-linear above 60°C.

Table 5: Calculated Values of Temperature Coefficients

These values are for theoretical cells with performance at or near the theoretical limit. Numbers are not representative of actual cells in use today.

Cell Material	Temp (°C)	η (28°C)	<u>normalized temp. coefficients</u>		Ref.
			$1/\eta \, d\eta/dT$ ($\times 10^{-3} \text{°C}^{-1}$)	$1/J_{sc} \, dJ_{sc}/dT$ ($\times 10^{-3} \text{°C}^{-1}$)	
GaAs (calc.)	27	.277	-2.40	+0.34	[24]
Si (calc.)	27	.247	-3.27	+0.293	[24]
Ge (calc.)	27	.106	-9.53	+0.125	[24]

Table 6: Other Thermal Parameters

Cell	Front		Rear		Operating		Orbit	Ref.
	α	ϵ	α	ϵ	temp. (°C)			
Silicon Cells/Arrays								
8x8 (SSF)	0.62	0.85	0.25	0.85	60	($\eta=13.5$)	LEO	[1]
ASEC grd back	0.65					($\eta=14.2\%$)		[2]
ASEC BSR	0.68					($\eta=12.5-13.4\%$)		[2]
ASEC BSFR	0.72-0.74					($\eta=13.5-14.8\%$)		[2]
Si (HST) (BSFR Si)	0.75 _(cell) 0.54 _(array)	0.83	0.54	0.70	50-61		LEO	[25]
Silicon	0.80-0.84	0.81-0.84		0.81				[26]
Si K4, K6 (planar Si, gridded back)	0.63				23	($\eta=14\%$)	LEO	[4]
Si K5, K7 (textured Si, gridded back)	0.81				43	($\eta=14\%$)	LEO	[4]
Si BSFR	0.757	0.83	0.54	0.898	71	($\eta=8\%$)	LEO	
					44	($\eta=8\%$)	GEO	[27]
Si bifacial	0.66	0.83	0.57	0.78	57	($\eta=9\%$)	LEO	[27]
Si BSF 0.82	0.82			0.86	42	($\eta=14.2\%$)		[28]
Thin Si	0.72	0.86		0.86	27	($\eta=13.5\%$)		[28]
IR refl. Si	0.69	0.86		0.86	22	($\eta=14.4\%$)		[28]
IR transp. Si	0.67	0.86		0.86	21	($\eta=13.3\%$)		[28]
ASEC BST	0.65	0.88						[29]
Sharp BSFR Si	0.75	0.82		0.80	37	($\eta=14.3\%$)		[30]
textured cell	0.93	0.77						[5]
(textured Si, no BSR)								
textured cell	0.905	0.75						[5]
(above, with conductive coated coverglass)								
GaAs Cells								
ASEC /Ge	0.870					($\eta=18-18.5\%$)		[2]
ASEC/GaAs	0.83					($\eta=18-18.5\%$)		[2]
thin GaAs	0.82	0.86		0.86	36	($\eta=16.0\%$)	LEO	[28]
Sharp GaAs	0.86	0.82		0.80	45	($\eta=18.0\%$)		[30]
GaAs/Ge	0.88	0.80	0.20	0.85	84	polar 5600nm		[22]
GaAs	0.84	0.83	0.54	0.898	72	($\eta=9\%$)	LEO	
*					48	($\eta=9\%$)	GEO	[27]

REFERENCES

- [1] J.F. Baumeister and S. Morren, Space Station Solar Thermal Analysis Presentation, 6/23/88, NASA Lewis.
- [2] Applied Solar Energy Corporation; product data sheets (1993).
- [3] Jet Propulsion Laboratory, *Solar Array Design Handbook, Volume II*, section 3.2 (Oct. 1976). Data shown is from cell types manufactured in 1974 and 1975.
- [4] G.F.J. Garlick and D.R. Lillington, "Design Study of Large Area 8x8 cm Wrapthrough Cells for Space Station," *Space Photovoltaic Research and Technology 1986, NASA CP-2475*, pp. 87-97 (1987).
- [5] L.W. Slifer, Jr., "The Goddard SFC High Efficiency Cell Development and Evaluation Program," *Solar Cell High Efficiency and Radiation Damage, NASA CP-2020*, pp. 7-23 (1977).
- [6] H. Bebermeier, "Design and Qualification of BSR- Solar Cells for Future Solar Arrays," *Proc. 14th IEEE Photovoltaic Specialists Conf.*, pp. 1144-1147 (1980).
- [7] M.A. Green, A.W. Blakers, and C.R. Osterwald, "Characterization of High-Efficiency Silicon Solar Cells," *J. Appl. Phys.* **58** (11), pp. 4402-4408 (1985).
- [8] B. Anspaugh, Jet Propulsion Laboratories, private communication, Mar. 1992; data set 10-11 Oct. 1990 RSW.
- [9] I. Weinberg, C.K. Swartz, R.E. Hart, and R.L. Statler, *Radiation and Temperature Effects in GaAs, InP, and Si Solar Cells, NASA Technical Memorandum 89870*, presented at the 19th IEEE Photovoltaic Specialists Conference, 1987.
- [10] R. Cross, J. Burrage, C. Hardingham and A. Potts, "GaAs Space Solar Cells Pilot Production Experience...", *Proc. European Space Power Conference, ESA SP-294, Vol. 2*, Oct. 1989, pp. 525-529.
- [11] C.K. Swartz and R.E. Hart Jr., "Temperature and Intensity Dependence of the Performance of an Electron Irradiated (AlGa)As/GaAs Solar Cell," *Solar Cell High Efficiency and Radiation Damage - 1979, NASA CP-2097* pp. 217-226 (1979).
- [12] E. Fanetti, G. Fiorito, and C. Flores, "Concentration and Temperature Performances of GaAs-GaAlAs Solar Cells", *Proc. 2nd EC Photovoltaic Solar Energy Conf.*, Berlin, April 1979, 447-454.
- [13] G.H. Walker, E.J. Conway, K.H. Hong and J.H. Heinbockel, "High Temperature Properties of GaAlAs/GaAs Heteroface Solar Cells," *Proc. 14th IEEE Photovoltaic Specialists Conf.*, pp. 1098-1101 (1980).
- [14] C.R. Osterwald, T. Glatfelter and J. Burdick, "Comparison of the Temperature Coefficients of the Basic I-V Parameters for Various Types of Solar Cells," *Proc. 19th IEEE Photovoltaic Specialists Conf.*, pp. 188-193 (1987).
- [15] I. Weinberg, C.K. Swartz and R.E. Hart, "Performance and Temperature Dependencies of Proton Irradiated n/p and p/n GaAs and n/p Si Cells," *Proc. 18th IEEE Photovoltaic Specialists Conference*, 344-349 (1985).
- [16] I. Weinberg, *et al.*, "Comparative Radiation Resistance, Temperature Coefficient and Performance of..." *Solar Cells, Vol. 22*, pp. 113-123 (1987). Data from table 4 corrected to 28°C.
- [17] R.J. Walters, R.L. Statler, and G.P. Summers, "Temperature Coefficients and Radiation Induced DLTS Spectra of MO-CVD Grown n+p InP Solar Cells," *Space Photovoltaic Research and Technology 1991, NASA CP-3121*, May 1991, 42-1.

- [18] R. Venkatasubramanian *et al.*, "High Temperature Performance and Radiation Resistance of High Efficiency Ge and Si(0.07)Ge(0.93) Solar Cells on Lightweight Ge Substrates," *Proc. 22nd IEEE Photovoltaic Specialists Conf.*, Vol. 1, pp. 85-89 (1991)
- [19] J. Boswell, B. Anspaugh and R. Mueller, "Thin Film Photovoltaic Development at Phillips Laboratory," *Proc. 23rd IEEE Photovoltaic Specialists Conference*, 1324-1329 (1993).
- [20] R.M. Burgess, W.E. Devaney and W.S. Chen, "Performance Analysis of CIS and GaAs Solar Cells Aboard the LIPS-III Flight Boeing Lightweight Panel," *Proc. 23rd IEEE Photovoltaic Specialists Conference*, 1465-1468 (1993).
- [21] C.R. Osterwald, "Translation of Device Performance Measurements to Reference Conditions," *Solar Cells*, Vol. 18, pp. 269-279 (1986).
- [22] E.L. Ralph and E.J. Stofel, *Advanced Hardened Array, Vol. I, Preliminary Design, WRDC-TR-90-2098*, Nov. 1990, pp. 156-182.
- [23] S. Wojtczuk *et al.*, "Monolithic Two-terminal GaAs/Ge Tandem Space Concentrator Cells," *Proc. 22nd IEEE Photovoltaic Specialists Conf.*, Vol. 1, pp. 73-79 (1991).
- [24] J.C.C. Fan, Theoretical Temperature Dependence of Solar Cell Parameters, *Solar Cells* 17, 309-315 (1986).
- [25] L. Gerlach, "HST Solar Generator Electrical Performance During the First Year in Orbit," *Proc. European Space Power Conference, ESA SP-320*, Aug. 1991, pp. 725-731.
- [26] P.A. Iles and S. Khemthong, "The Alpha Factor: Controlling Solar Cell Absorptance," *Proc. 13th IEEE Photovoltaic Specialists Conf.*, pp. 327-332 (1978).
- [27] F. Reissman and M. Baumgart, "Application of Gallium Arsenide Solar Cell Arrays for Long Duration Low Earth Orbit Missions Like Columbus," *Proc. European Space Power Conference, ESA SP-294, Vol. 2*, Oct. 1989, pp. 525-529.
- [28] TRW, *Advanced Photovoltaic Solar Array Design Final Technical Report CDRL-008*, 3 November 1986, JPL Contract 957358, p. 3-65 to 4-69.
- [29] S. Khemthong, P. Iles, M. Roberts, C. Karnopp and N. Senk, "Performance of Large Area, Thin Silicon Cells," *Proc. 20th IEEE Photovoltaic Specialists Conf.*, Vol. 2, pp. 960-963 (1988).
- [30] M. Uesuegi *et al.*, "High Efficiency Silicon Solar Cells for Space Use," *Proc. 22nd IEEE Photovoltaic Specialists Conf.*, Vol. 2, pp. 1521-1524 (1991).
- [31] G.F. Virshup, B-C Chung, and D. Brinker, "Temperature Coefficients of Multijunction Solar Cells," *Proc. 21st IEEE Photovoltaic Specialists Conf.*, pp. 336-338 (1991).
- [32] H.S. Rauschenbach, *Solar Cell Array Design Handbook*, Van Nostrand Reinhold Company New York, 1980, "Solar Cell Performance Data," pp. 196-241.
- [33] H.B. Curtis and R.E. Hart, Jr., "Temperature Coefficients for Concentrator Cells at Various Electron and Proton Fluence Levels", paper 889048, Intersociety Energy Conversion Engineering Conference 1988, 85-89.
- [34] R. Loo and G.S. Kamath, *High Efficiency GaAs Concentrator Cells*, Report Final report HAC REF F4356 for NASA Lewis Research Center, contract NAS3-23877, p. 5-7, Mar. 1988.
- [35] L. Fraas *et al.*, *Optoelectronics Devices and Technologies*, Vol. 5, No. 2, 297-310 (1990).
- [36] M.W. Wanlass, T.J. Coutts, J.S. Ward, and K.A. Emery, "High-Efficiency Heteroepitaxial InP Solar Cells," *Proc. 22nd IEEE Photovoltaic Specialists Conf.*, Vol. 1, pp. 159-165 (1991).

- [37] N. Takata, *et al*, "Space Proven GaAs Solar Cells - Main Power Generation for CS-3," *Proc. 21st IEEE Photovoltaic Specialists Conf.*, Vol. 2, pp. 1219-1225 (1990).
- [38] S.P. Tobin *et al.*, "High Efficiency GaAs/Ge Monolithic Tandem Solar Cells," *Proc. 20th IEEE Photovoltaic Specialists Conf.*, Vol. 1, pp. 405-410 (1988).
- [39] R.J. Lammert, "Characteristics of Solar Cells at Low Temperatures," *Proc. 7th IEEE Photovoltaic Specialists Conference*, 97-100 (1968).
- [40] C.H. Liebert, "Solar Cell Performance at Jupiter Temperature and Solar Intensity," *Proc. 7th IEEE Photovoltaic Specialists Conference*, pp. 92-96 (1968).
- [41] IEEE, session 2B, "Temperature-Illumination Studies," *Proc. 8th IEEE Photovoltaic Specialists Conference*, pp. 110-168 (1970)
- [42] Y. Ichikawa, "Large-Area Amorphous Silicon Solar Cells With High Stabilized Efficiency," *Proc. 23rd IEEE Photovoltaic Specialists Conf.*, pp. 27-33 (1993).
- [43] K. Mullaney *et al.*, "Infra-Red Reflective Coverglasses: the Next Generation," *Proc. 23rd IEEE Photovoltaic Specialists Conf.*, pp. 1363-1368 (1993).
- [44] W.T. Beauchamp, T.T. Hart and M.L. Sanders, "Blue/Red Reflecting Solar Cell Covers for GaAs Cells," *Proc. 23rd IEEE Photovoltaic Specialists Conf.*, pp. 1487-1490 (1993).
- [45] G.A. Landis, "Satellite Eclipse Power by Laser Illumination" (paper IAF-90-053), *Acta Astronautica*, Vol. 25 No. 4, 229-233 (1991).
- [46] G.A. Landis, "Space Power by Ground-based Laser Illumination," *IEEE Aerospace and Electronics Systems*, Vol. 6 No. 6, 3-7, Nov. 1991; presented at 26th Intersociety Energy Conversion Engineering Conf., Aug. 1991, Vol. 1, pp. 1-6.
- [47] G.A. Landis, "Photovoltaic Receivers for Laser Beamed Power," *Journal of Propulsion and Power*, Vol. 9 No. 1, 105-112 (1993); presented at 22nd IEEE Photovoltaic Specialists Conference, Las Vegas NV, Oct. 1991, Vol. II, 1494-1502.
- [48] D. Wilt, N. Fatemi, R. Hoffman, P. Jenkins, D. Brinker, D. Scheiman, R. Lowe, D. Chubb, M. Faur, and F. DeAngelo, "High Efficiency, Low Bandgap InGaAs PV Device Development for TPV Power Systems," *13th Space Photovoltaic Research and Technology Conference*, NASA Lewis, June 14-16 1994 (proceedings in press).

EFFECTS OF PLASMA HYDROGENATION ON TRAPPING PROPERTIES OF DISLOCATIONS IN HETEROEPITAXIAL InP/GaAs¹

S.A. Ringel and B. Chatterjee
The Ohio State University
Columbus, Ohio

ABSTRACT

In previous work, we have demonstrated the effectiveness of a post-growth hydrogen plasma treatment for passivating the electrical activity of dislocations in metalorganic chemical vapor deposition (MOCVD) grown InP on GaAs substrates by a more than two order of magnitude reduction in deep level concentration and an improvement in reverse bias leakage current by a factor of ~ 20 (refs. 1-2). These results make plasma hydrogenation an extremely promising technique for achieving high efficiency large area and light weight heteroepitaxial InP solar cells for space applications. In this work we investigate the carrier trapping process by dislocations in heteroepitaxial InP/GaAs and the role of hydrogen passivation on this process. It is shown that the charge trapping kinetics of dislocations after hydrogen passivation are significantly altered, approaching point defect-like behavior consistent with a transformation from a high concentration of dislocation-related defect bands within the InP bandgap to a low concentration of individual deep levels after hydrogen passivation. It is further shown that the "apparent" activation energies of dislocation related deep levels, before and after passivation, reduce by ~ 70 meV as DLTS fill pulse times are increased from 1 μ sec. to 1 msec. A model is proposed which explains these effects based on a reduction of Coulombic interaction between individual core sites along the dislocation cores by hydrogen incorporation. Knowledge of the trapping properties in these specific structures is important to develop optimum, low loss heteroepitaxial InP cells.

INTRODUCTION

Dislocations within InP layers grown on lattice mismatched substrates such as GaAs, Si and Ge are currently a major limitation for the development of efficient heteroepitaxial InP solar cells for space applications. The $\sim 8\%$ mismatch in lattice constant for InP/Si, and 4% for both InP/Ge and InP/GaAs, typically result in threading dislocation densities in the range $1\text{--}10 \times 10^8 \text{ cm}^{-2}$ in the InP layers which has severely reduced heteroepitaxial InP cell efficiencies thus far (ref. 3). This has prompted investigations of a number of approaches to reduce threading dislocation density toward $1 \times 10^5 \text{ cm}^{-2}$, the theoretically predicted value necessary to achieve efficiencies comparable to homoepitaxial InP/InP (ref.3). These approaches include the use of compositionally graded buffer layers, thermally cycled growth and hydrogen passivation (refs. 1-5).

For the case of hydrogen passivation, where the focus is on reducing the electrical activity of dislocations rather than total dislocation concentration, it has been shown that exposure of p-InP grown on GaAs substrates to a hydrogen plasma at 250°C reduces the dislocation related deep level concentration from $\sim 6 \times 10^{14} \text{ cm}^{-3}$ to $\sim 3 \times 10^{12} \text{ cm}^{-3}$ in the InP layer (ref. 1). This passivation was found to be stable up to $\sim 550^\circ\text{C}$, which combined with dopant reactivation occurring at 380°C , opens a 170°C post-passivation processing window for cell completion. Furthermore, it was shown that reverse leakage currents of heteroepitaxial InP diodes on GaAs were significantly improved as the result of dislocation passivation. These results are summarized in Figures 1 and 2.

¹ Work supported by NASA under grant no. NAG-1461.

In addition to reducing the concentration of deep levels resulting from dislocations, hydrogen incorporation is found to change the mechanisms of the actual carrier trapping process. Knowledge of the dislocation trapping properties is critical to understand current transport characteristics of heteroepitaxial cells and must be accounted for in heteroepitaxy-specific cell design optimization. In this paper we present a study of the charge trapping properties of dislocations in p-type InP grown by MOCVD on GaAs substrates, both prior to and after hydrogen passivation.

EXPERIMENTAL

InP was grown on (100) GaAs substrates by low pressure MOCVD. Growth details have been reported elsewhere (ref. 1). The InP structure consisted of a 2 μm thick layer of Zn doped p-type ($1 \times 10^{17} \text{ cm}^{-3}$) InP grown on a 0.5 μm thick n⁺ InP layer on n⁺ GaAs substrates. Ohmic contacts were formed by electron beam evaporation and patterning of Au/Zn/Au and Ni/Ge/Au on the p-type InP and n-type GaAs substrate, respectively, followed by a 380° C anneal in N₂. This device structure, shown in Figure 3, allows us to probe the depletion region as measured from the buried junction and up toward the InP surface.

Hydrogenation was performed in a Technics Planar Etch II 30 kHz parallel plate plasma reactor. Hydrogen exposure was performed using a 30 sccm flow rate of semiconductor grade H₂, chamber pressure of 530 mTorr, power density of 0.08 W/cm² and a substrate temperature of 250° C. Hydrogen exposure time was either 1.5 or 2 hours, as noted. Immediately prior to hydrogen exposure, all samples were capped with a thin, hydrogen-permeable, ~ 20 nm layer of SiN_x to prevent surface degradation by preferential loss of phosphorous during hydrogenation. The nitride layer was etched off in dilute HF before metallization. DLTS measurements were performed using a Biorad DL4602 DLTS spectrometer, respectively based on the double boxcar data acquisition method. Fill pulse times were controlled using the Biorad pulse timing circuit and by an external pulse generator.

Note that all data of hydrogenated samples discussed in this paper received a post hydrogenation dopant reactivation anneal for 380 °C for 5 minutes.

RESULTS AND DISCUSSION

Figure 4 shows the DLTS spectra for non-hydrogenated heteroepitaxial InP measured at a rate window of 1000/sec. as a function of fill pulse time. The fill pulse time dependence of the three main peaks (T1, T2 and T3) is more quantitatively depicted in Figure 5a (before hydrogenation) and 5b (after hydrogenation) where it is seen that the peak height variation of T1 and T2 display a linear relationship with the natural logarithm of the fill pulse time. Such behavior is consistent with earlier reports for charge capture by extended defects and dislocations in other semiconductors which has been described by a rate equation given as (ref. 6)

$$dp_T/dt = [(c_p + e_n)(N_T - p_T(t)) - (c_n + e_p)p_T(t)]\exp(-q\phi(t)/kT) \quad (1)$$

where $c_{n,p}$ are capture rates for electrons and holes, $e_{n,p}$ are emission rates for electrons and holes, p_T is the concentration of traps filled with holes, N_T is the total trap concentration, and $\phi(t)$ is a time dependent potential barrier associated with the charging of a dislocation. Note that this differs from the usual point defect rate equation only by the presence of the exponential term which acts to slow the trap filling rate. The solution of this equation, after some simplification and in terms of the trap fill pulse time, t_p , used in the DLTS experiment is given by (ref. 6)

$$p_T(t_p) = \sigma_p \langle v_p \rangle n \tau N_T \ln[t_p/\tau] \quad (2)$$

The term τ in equation (2) is proportional to the height of this potential barrier and p_T is proportional to $\Delta C/C$ as given in Figure 5. Note that in each of these plots of Figure 5, T1 and T2 follow the logarithmic behavior

and extended fill pulse time dependence predicted for dislocations, whereas T3 follows the usual point defect behavior. In fact, we have earlier shown that T3 was indeed associated with a point defect since it was the only level evident in the DLTS spectra of homoepitaxial InP/InP structures (ref. 7). By comparing Figures 5a and 5b, it can be seen that hydrogen passivation results in a significant change in the slope of the plotted data. Calculations have shown that the slope for the T1 and T2 curves reduce by approximately two orders of magnitude after hydrogenation, indicating that the trap state density is decreased as expected, and that the barrier to carrier trapping, $\phi(t)$, has been lowered.

While the logarithmic capture kinetics is one characteristic of the unusual trapping properties of dislocations in heteroepitaxial InP, it is also clear from Figure 4 that T1 and T2 broaden on the low temperature side of the DLTS peaks as the fill pulse time is increased, resulting in a shift toward lower temperatures of the peak maximum with fill pulse time. This is shown more quantitatively for T2 in Figure 6 where the FWHM/T_p is plotted against the fill pulse time (T_p is the temperature at which the DLTS peak is maximum). It can be shown that for a single deep level, $\text{FWHM}/T_p = 0.104$ for a rate window of 1000/sec., which should not vary with fill pulse time. As seen in the figure, T2 is clearly broadened compared to this value and furthermore, varies with fill pulse time until it saturates at $t_p \sim 0.1$ msec. This behavior can be understood if one first considers that dislocations are generally thought to cause a band of deep levels, rather than non-interacting isolated levels, due to wavefunction overlap of closely spaced dislocation core states. In this case, only the lower energy states within the band are filled for very short fill pulse times. As fill pulse time increases, higher energy states can trap carriers, eventually saturating as the band becomes filled. It can be shown that the higher energy states for holes (this corresponds to states closer to the valence band), which result in lower activation energies ($E_T - E_v$), will always contribute DLTS peaks at lower temperatures for the same rate window and cross section, compared to lower energy states (higher activation energies). This would explain why the DLTS peaks broaden only on their low temperature sides. It should be noted here that a similar analysis was performed for T1. A complete analysis will be presented elsewhere.

Figure 6 also includes FWHM/T_p data for hydrogen passivated samples. Note that in comparison to non-hydrogenated data, the FWHM/T_p characteristic of peak T2 after hydrogen passivation is much closer to that of an ideal point defect, although it is still somewhat broadened. This is likely the result of a reduction in the active core site density which causes an increase in the average active core site spacing and a change in the dislocation density of states.

The result of the peak broadening and shifting for DLTS interpretation is most striking in Figure 7, which shows the measured trap activation energy for T1, T2, and T3 as a function of fill pulse time following the usual Arrhenius method. First consider the non-hydrogenated data. As can be seen, the measured activation energy shifts by approximately 80 meV for T1, from ~ 880 eV for a 1usec. fill pulse time, to ~ 800 eV for a 10 msec. fill pulse time. T2 shows a shift of similar magnitude. In contrast, the point defect level, T3, shows no such dependence, as would be expected. For the complicated case of dislocations, the Arrhenius method for DLTS activation energy actually yields the *weighted average energy of the filled states within the dislocation energy band that contribute to carrier emission*. For short fill pulse times, only those states farthest from the valence band are filled with holes, resulting in larger activation energies. One would therefore expect a more "point defect-like" behavior due to reduced dislocation charging. This is corroborated by Figure 6 which shows less peak broadening for short fill pulse times. For longer fill pulse times, the band fills downward with higher energy holes (toward the valence band edge). Therefore the average energy of the re-emitted holes is higher and the measured average activation energy decreases, as observed. Eventually, for longer fill pulse times, the band will saturate with trapped holes. At this point, the measured activation energy is indicative of the weighted average over the entire band. Note that the variation of activation energy in Figure 7 is completely consistent with the FWHM/T_p variation shown in Figure 6. These results suggest that care should be taken when comparing DLTS measured activation energies for dislocations, with particular attention to the fill pulse time used in the experiment.

The effect of hydrogen passivation on the activation energy behavior is also shown in Figure 7 for each DLTS peak. Again, negligible change in activation energy is observed for the point defect level, T3,

while a significant change of activation energy with fill pulse time is still evident for both T1 and T2. However, from the figure it is clear that the activation energies of T1 and T2 are consistently higher for all fill pulse times after hydrogenation. It should be noted that the shape of the activation energy dependence on fill pulse time also changes after hydrogen passivation. This is likely a result of reduced density of states at certain energies due to passivation, which allows a faster change, or response, to fill pulse time. This suggests that such a plot of activation energy versus fill pulse time may provide information about the actual shape of the dislocation density of states. This is currently being looked at in more detail.

CONCLUSIONS

Hydrogen passivation by plasma hydrogenation has been shown to be effective in reducing the electrical activity of dislocations in p-type InP grown on GaAs substrates. Deep level concentrations were reduced by more than 2 orders of magnitude and diode leakage currents were suppressed. These beneficial effects were found to be stable up to a post hydrogenation annealing temperature of 550 °C. Detailed analysis of the dislocation trapping kinetics prior to hydrogenation showed the expected logarithmic trapping kinetics as reported for dislocations in other materials. Furthermore, it was shown that this was related to the observed DLTS peak broadening toward lower temperatures with fill pulse time and a large dependence of measured trap activation energy on fill pulse time. It was found that hydrogen passivation significantly altered the fundamental trapping properties of the dislocations, resulting in a decrease in the broadening of the dislocation related DLTS peaks in addition to a shift in the average energy of the dislocation density of states away from the valence band. These effects suggest that hydrogen passivation reduces the interaction between adjacent dislocation core sites and results in a trapping behavior that approaches that expected for point defects.

REFERENCES

1. B. Chatterjee, S.A. Ringel, R. Sieg, R. Hoffman and I. Weinberg, "Hydrogen Passivation of Dislocations in InP on GaAs Heterostructures," *Appl. Phys. Lett.*, vol. 65, pp. 1-3, 1994.
2. B. Chatterjee, S.A. Ringel, R. Sieg, R. Hoffman and I. Weinberg, "Deep Level Characterization and Passivation in Heteroepitaxial InP," *Mat. Res. Soc. Symp. Proc.*, vol. 325, pp. 125-130, 1994.
3. R.K. Jain and D.J. Flood, "Influence of the Dislocation Density on the Performance of Heteroepitaxial Indium Phosphide Solar Cells," *IEEE Trans. Electron. Dev.*, vol. 40, pp. 128-134, 1993.
4. C.J. Keavney, S.M. Vernon, V.E. Haven, S.J. Wojtczuk and M.M. Al-Jassim, "Fabrication of n⁺/p InP Solar Cells on Si Substrates," *Appl. Phys. Lett.*, vol. 54, pp. 1139-1141, 1989.
5. I. Weinberg, C.K. Swartz and D.J. Brinker, "Heteroepitaxial InP Solar Cells on Si and GaAs Substrates," *Tech. Digest Int. PVSEC-5*, pp. 81-84, 1990.
6. P. Omling, E.R. Weber, L. Montelius, H. Alexander, and J. Michel, "Electrical Properties of Dislocations and Point Defects in Plastically Deformed Silicon," *Phys. Rev. B*, vol. 32, pp. 6571-6581, 1985.
7. B. Chatterjee, S.A. Ringel, R. Sieg, R. Hoffman and I. Weinberg, "Identification and Passivation of Mismatch Related Deep Levels in Heteroepitaxial InP on GaAs Substrates," *Proc. 184th Meeting Electrochem. Soc.*, New Orleans, 1993 (in press).

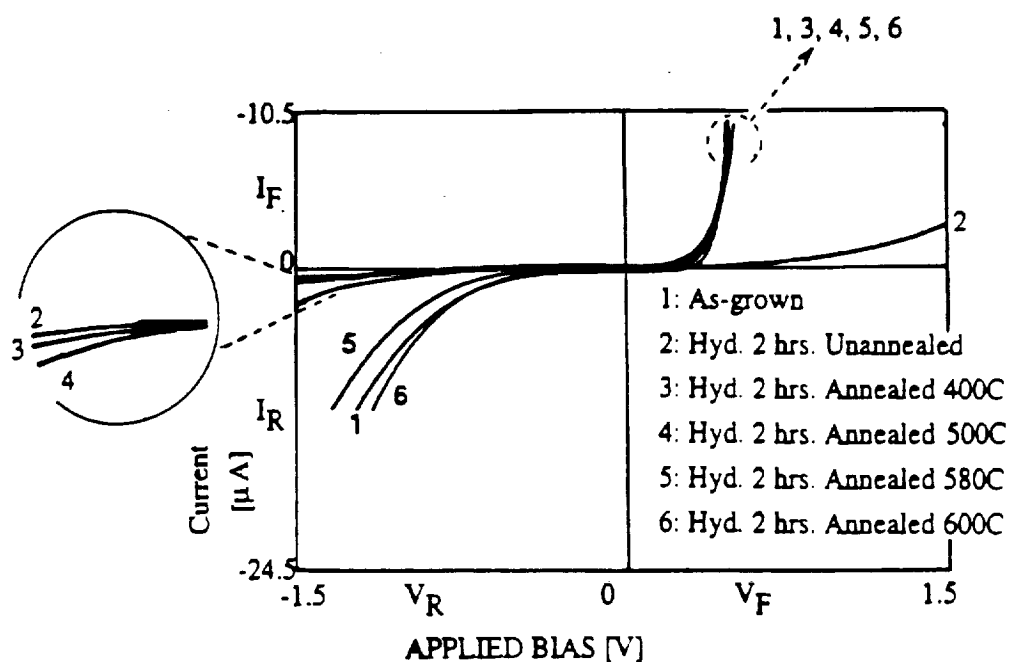


Figure 1. Current-voltage characteristics of p-InP/n⁺-InP diode grown on GaAs, measured before and after hydrogenation and after various post-hydrogenation anneals at the temperatures indicated.

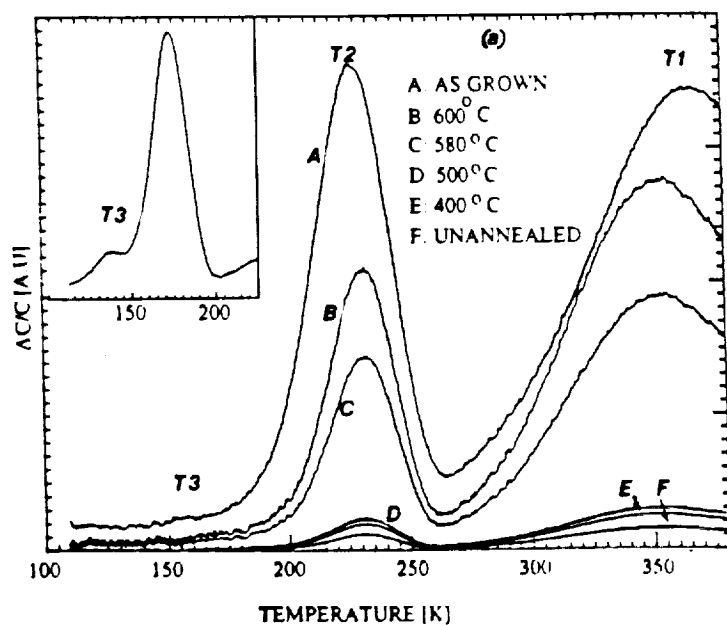


Figure 2. Effect of hydrogenation and post-hydrogen anneals on DLTS spectra for InP/GaAs, measured at a rate window of 1000/sec. The inset measured at 50/sec rate window, clearly shows trap T3, which is prominent at higher rate windows.

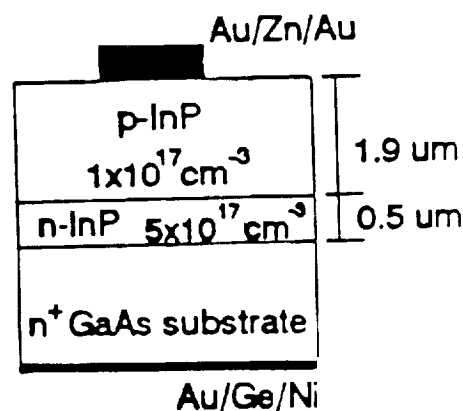


Figure 3. Device structure used for this study.

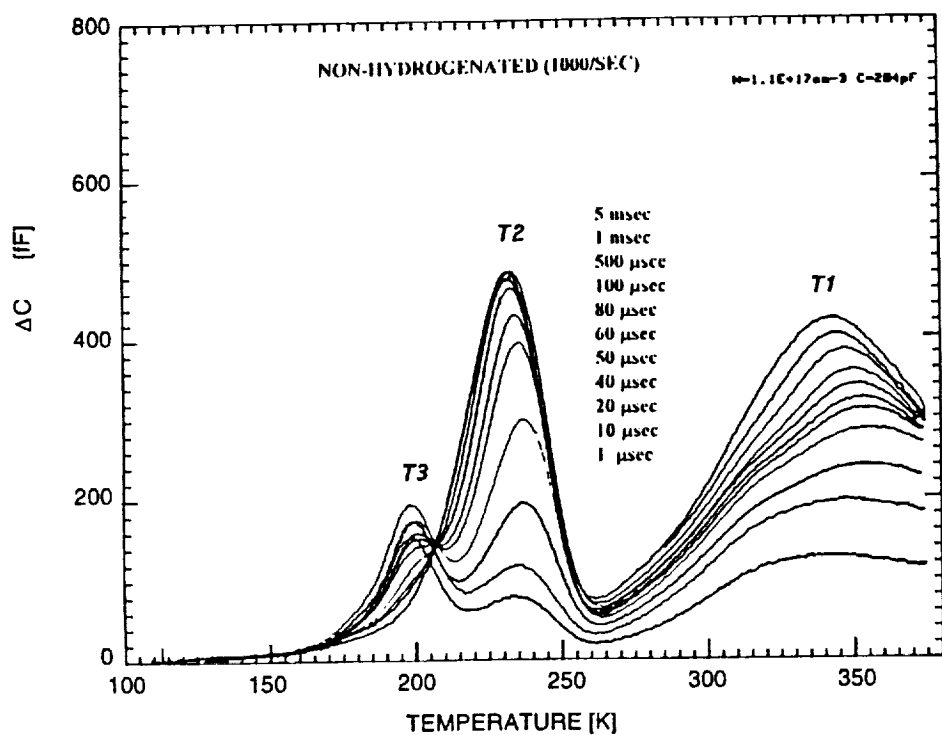


Figure 4. DLTS spectra measured at 1000/sec. rate window for the different fill pulse times as shown.

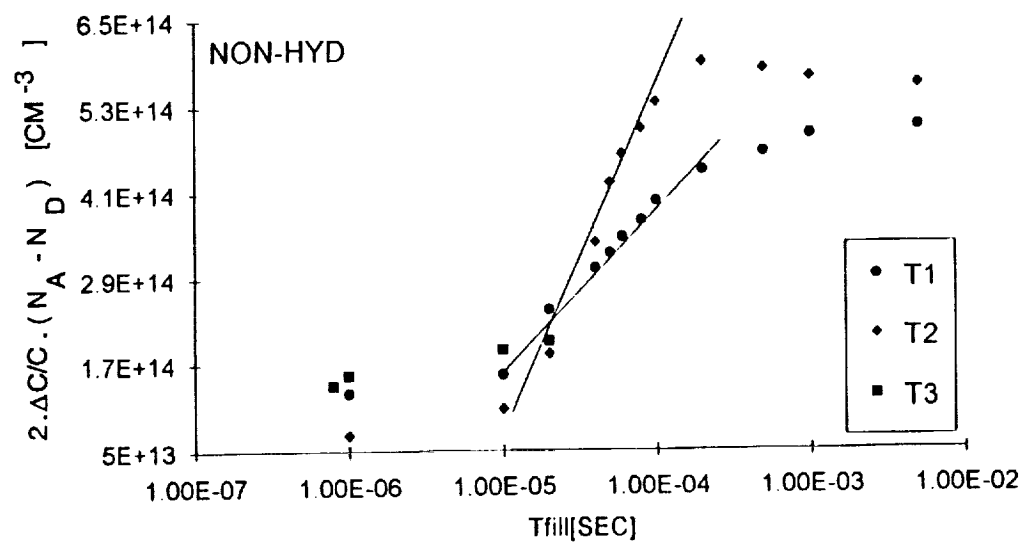


Figure 5(a). Capture characteristics for traps T1, T2 and T3 before hydrogenation. T1 and T2 exhibit extended dependence on fill pulse time that is characteristic of dislocations and follows eqn. (2).

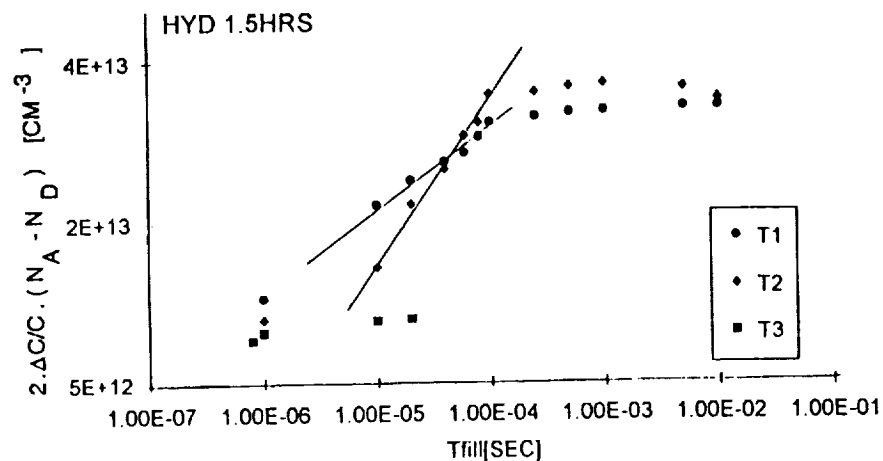


Figure 5(b). Capture characteristics for traps T1, T2 and T3 after hydrogenation. Note the reduction in slope for T1 and T2 compared to figure 5(a).

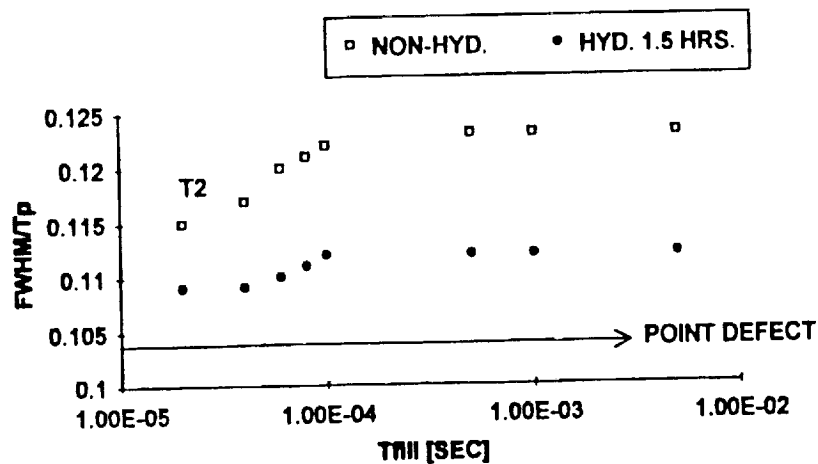


Figure 6. FWHM/ T_p data for T2, as a function of fill pulse time measured before and after hydrogenation. The line at FWHM/ T_p = 0.104 is calculated for an ideal point defect.

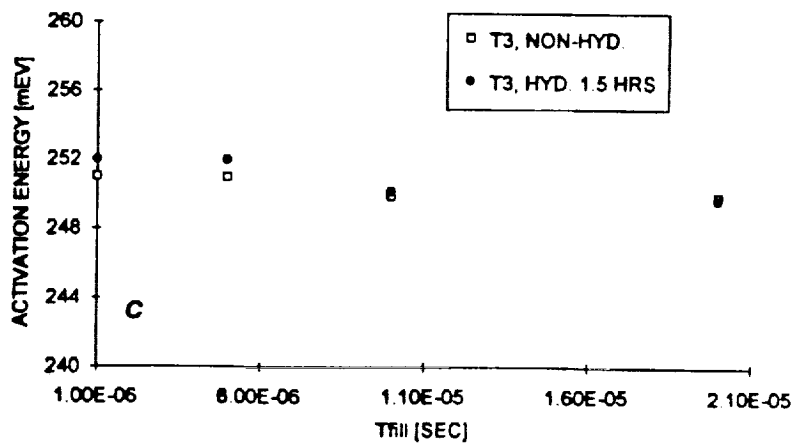
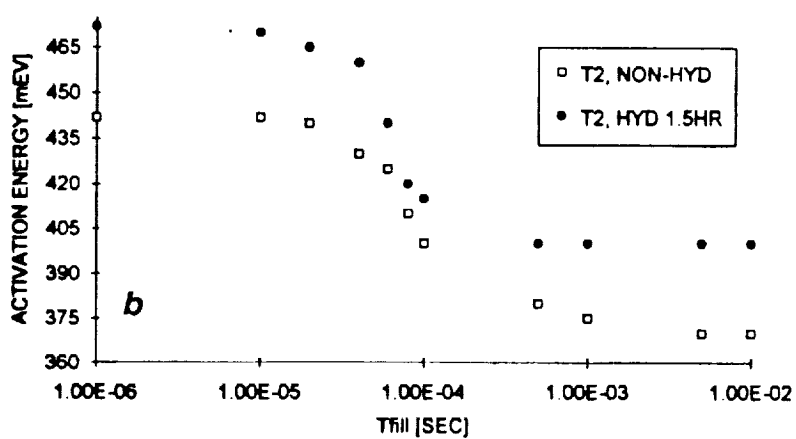
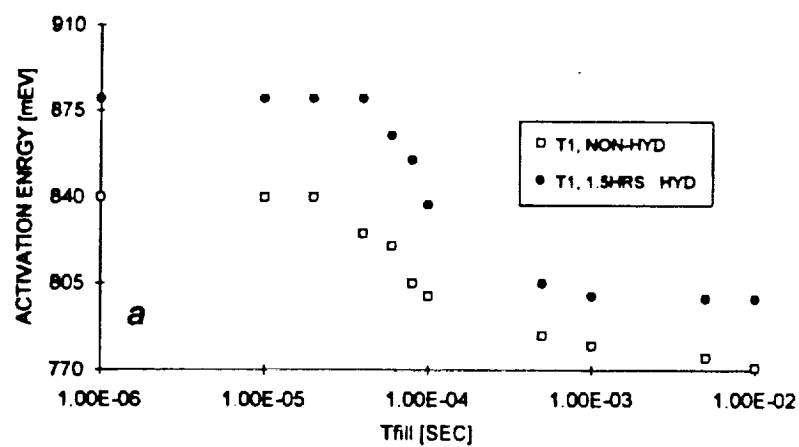


Figure 7. Variation of DLTS activation energy with fill pulse time, measured by the Arrhenius method for as-grown and hydrogenated samples for (a) T1, (b) T2, and (c) T3.

NUCLEATION, GROWTH, AND STRAIN RELAXATION OF LATTICE-MISMATCHED III-V SEMICONDUCTOR EPITAXIAL LAYERS¹

R.E. Welser and L.J. Guido
Yale University
New Haven, Connecticut

Summary

We have investigated the early stages of evolution of highly strained 2-D InAs layers and 3-D InAs islands grown by metal-organic chemical vapor deposition (MOCVD) on (100) and (111)B GaAs substrates. The InAs epilayer / GaAs substrate combination has been chosen because the lattice-mismatch is severe ($\sim 7.2\%$), yet these materials are otherwise very similar. By examining InAs-on-GaAs composites instead of the more common $\text{In}_x\text{Ga}_{1-x}\text{As}$ alloy, we remove an additional degree of freedom (x) and thereby simplify data interpretation. A matrix of experiments is described in which the MOCVD growth parameters -- susceptor temperature, TMI flux, and AsH_3 flux -- have been varied over a wide range. Scanning electron microscopy, atomic force microscopy, transmission electron microscopy, and electron microprobe analysis have been employed to observe the thin film surface morphology. In the case of 3-D growth, we have extracted activation energies and power-dependent exponents that characterize the nucleation process. As a consequence, optimized growth conditions have been identified for depositing ~ 250 Å thick (100) and (111)B oriented InAs layers with relatively smooth surfaces. Together with preliminary data on the strain relaxation of these layers, the above results on the evolution of thin InAs films indicate that the (111)B orientation is particularly promising for yielding lattice-mismatched films that are fully relaxed with only misfit dislocations at the epilayer / substrate interface.

Introduction

In comparison with Si and Ge, III-V semiconductor alloys are well-suited for space photovoltaic applications because of improved radiation hardness and the potential for heterostructure devices with high power conversion efficiency. Unfortunately, the choice of starting substrate for the subsequent growth of III-V epitaxial layers is limited by the practical requirements of a large strength-to-weight ratio and low cost. The single crystal materials that satisfy these constraints -- Si, Ge, and, to a lesser degree, GaAs -- also possess lattice constants that differ significantly from those of the III-V semiconductor alloys of interest (fig. 1). Consequently, the lattice-mismatched epitaxial layer / substrate composite undergoes an elastic deformation that (1) causes a transformation from the desired 2-D layer-by-layer growth mode to a 3-D island mode and (2) provides the driving force for dislocation generation and propagation. The result is a rough surface and a high density of defects in the overlying epitaxial layers (fig. 2a). What is needed instead for device applications is a smooth 2-D surface with misfit dislocations at the epitaxial layer / substrate interface which relieve the strain caused by the lattice-mismatch, but do not thread the epitaxial layer and consequently degrade the device quality (fig. 2b).

Several different multi-step fabrication schemes have been attempted to improve the structural properties of lattice-mismatched epitaxial layers. In fact, the practices of using either a low-temperature buffer layer or a vicinal substrate to initiate growth, and of incorporating a compositionally graded layer or a superlattice dislocation filter between the substrate and active region, have all met with limited success (ref. 1 -4). Post-growth annealing techniques have also been explored but have proven less effective (ref. 5). Despite some encouraging results, even these multi-step methods have failed to yield defect densities low enough for high-performance minority carrier devices ($< 10^4 \text{ cm}^{-2}$).

¹ The authors gratefully acknowledge the financial support of the National Science Foundation via the Presidential Faculty Fellowship Program (Grant # ECS-9253760) and of the NASA Graduate Student Researchers Program (Grant # NGT-50832).

Recent reports suggest that epitaxial growth conditions may strongly influence the kinetics of strain relaxation (ref. 6). Although the *minimum energy* configuration of a highly strained material is characterized by a rough, three-dimensional surface morphology, the exact nature of this *equilibrium* configuration, or even whether or not it develops at all, also depends on kinetic limitations. By implication, the efficacy of a particular buffer layer technique depends upon the experimental conditions during each step of the deposition process. In this paper, we describe the influence of the kinetic pathways of nucleation, growth, and strain relaxation on the surface morphology and the defect structure of highly-strained epitaxial thin films.

The Initial Stages of Deposition

While a comprehensive theoretical description of III-V heteroepitaxy which incorporates the complexities of MOCVD is lacking at present, a generic model of atomic deposition provides a useful reference (ref. 7). Figure 3 illustrates the initial stages of film deposition from single atoms which arrive at the substrate at a rate R and diffuse across the surface with diffusion coefficient D . The surface density of these single atoms (n_1) is then determined primarily by the competition between the arrival rate and the rate at which single atoms are lost to re-evaporation and incorporation into a growing island or pre-existing step edge. During the nucleation stage, single atoms can also couple to other atoms (binding energy E_j) to form sub-critical clusters of atoms whose density (n_j) is inversely proportional to the number of atoms in the cluster. Above a critical size i^* , the sub-critical cluster is more likely to grow into a stable island than to disintegrate. The density (n_x) and the geometry of these growing islands are the two most important parameters determining the surface morphology and defect structure of thicker epitaxial layers.

The three traditional modes of growth (ref. 8) can be described in terms of the island width-to-height ratio (w/h). In the limit of large w/h , the islands are two-dimensional even at the point of coalescence, and growth proceeds in a layer-by-layer fashion (Frank-van der Merwe). In the limit of small w/h , on the other hand, islands grow in a three-dimensional or islanding mode (Volmer-Weber). If the w/h ratio changes from a large to a small value as the islands evolve, then layer-by-layer growth is followed by islanding (Stranski-Krastanov). Growth may also proceed in a more complicated fashion for intermediate values of w/h . Specifically, as the island density increases and island coalescence begins, there is a range of w/h values which produces films that are nearly indistinguishable from those grown via the layer-by-layer mode.

As stated above, the density of growing islands is proportional to the density of critical clusters, which is inversely proportional to the number of atoms in the critical cluster and directly proportional to the density of single atoms and their binding energy. The processes depicted in Figure 3 can be quantitatively described by rate equations which govern the density of single atoms, sub-critical clusters, and stable clusters (growing islands) on the substrate surface and highlight the interrelation between nucleation and growth. Solving this set of equations in a self-consistent manner yields a nucleus saturation value (N_s)

$$N_s \sim N_0^{-1} P R^p \exp(E_a/kT),$$

where N_0 is the density of absorption sites, E_a is an activation energy, and the exponent p is proportional to the critical cluster size (ref. 7).

In many cases, the stress in thick lattice-mismatched films is large enough to drive dislocation nucleation and propagation (ref. 2). However, the thickness at which dislocations nucleate and propagate in 2-D films is very sensitive to the kinetic pathways of epitaxial growth (ref. 9) and to heterogeneities in material properties (ref. 10). For example, recent work has shown that islands can form before the onset of dislocation generation (ref. 11). As these coherent islands grow, there is an increase in the driving force for dislocation generation. Thus, there is a direct connection between the evolving surface morphology and defect generation in highly-strained epitaxial layers.

Experimental Approach and Summary of Results

The InAs samples have been deposited in a horizontal-geometry MOCVD reactor at a base pressure of 100 torr, with an H₂ carrier gas flow of 12 slm and TMIn and AsH₃ sources. All growths have been performed simultaneously on (100) and (111)B Si-doped GaAs substrates. After a standard oxide desorption process, the substrate temperature (T_s) and AsH₃ flow (f_{AsH_3}) are adjusted to the desired values, and the growth of InAs is initiated directly on the substrates by switching in a pre-stabilized TMIn flow (f_{TMIn}). The surface morphology has been observed by Nomarski optical microscopy (NOM), scanning electron microscopy (SEM), and atomic force microscopy (AFM). Transmission-electron microscopy (TEM) has also been performed to determine structural quality of the films. The constancy of the island density with time indicates that, except for the eventual decrease in density because of coalescence, the measured values are indeed the nucleus saturation densities. The pertinent results of these experiments are summarized in the following discussion.

The impact of substrate temperature, TMIn flow, and AsH₃ flow on InAs nucleation has been examined in a 2³ factorial experiment on nominally 250-Å thick films. This approach is designed to efficiently evaluate the principal and interactive effects of a large set of variables (ref. 12). There are several noteworthy trends evidenced in the data of Table I. First, the island density on the (100) substrate is approximately 100x larger than that for the (111)B case. In addition, the island density on both substrates increases with either a decrease in T_s or an increase in f_{TMIn} , as shown in more detail in Figures 4a and 4b. An increase in f_{AsH_3} also has a modest effect, but with the opposite sense for the two orientations. Next, the island geometry is completely different in the two cases (fig. 5a and 5b). For the (100) substrate, AFM reveals pyramids with a rectangular base aligned to the <011> crystallographic directions and side-walls best fitted by {111} planes. In contrast, the islands on the (111)B substrate are flat polygons with the base aligned to <211> directions, and extremely abrupt side-walls which are most likely {011} cleavage planes. The w/h values of the islands are also very different on the two substrate orientations, with a value of ~ 2 on the (100) substrate and ~ 50 for the (111)B case. The exponential dependence of N_s with T_s and the power dependence of N_s with f_{TMIn} agrees qualitatively with the conventional picture of nucleation. The lower densities on the (111)B substrate can be explained by assuming that the critical cluster size is larger than on the (100) substrate. However, the effect of AsH₃ flow on the nucleus saturation density cannot be accounted for via this simple single-species nucleation model.

Using these results, the surface morphology can be transformed from a 3-D into a 2-D surface. Figure 6 shows that lowering the temperature to 525 °C, increasing the TMIn flow to 720 sccm, and *increasing* the AsH₃ flow to 500 sccm leads to a nearly featureless 250 Å thick InAs layer on the (111)B substrate. Conditions were also found for a similar occurrence on (100) substrates. Figure 7 shows that the morphology transition on the (100) substrate is achieved by lowering the temperature to 475 °C, increasing the TMIn flow to 950 sccm, and *lowering* the AsH₃ flow to 82 sccm. While the films shown in 6b and 7b are both "specular," a more quantitative analysis has been obtained via AFM. The surface roughness of the strained (100) InAs layer (< 50 Å) is higher than that of (100) GaAs (< 10 Å) grown under similar conditions. However, in comparison to a (111)B GaAs layer, the surface roughness of the strained InAs is 30x lower. The flat surface and large w/h ratio of InAs islands on (111)B GaAs substrates is consistent with the observation that 2-D films form more readily (at higher temperature and lower TMIn flow) than on (100) substrates. The small w/h ratio of InAs islands on (100) substrates also accounts for the relatively large surface roughness. While TEM analysis indicates that both films are fully relaxed, the (100) film exhibits a large density of threading dislocations. However, for the (111)B InAs film, preliminary analysis reveals misfit dislocations only; no threading dislocations are observed in cross-sectional TEM images.

Conclusions

Using InAs-on-GaAs as a model high-strain system and a factorial design of experiments approach, we have demonstrated that the thin-film surface morphology is quite sensitive to epitaxial growth parameters. The temperature and TMIn effects can be described, at least qualitatively, by traditional one-species nucleation theory. However, a more complex model is needed to account for the effects of AsH₃ flow. Two-dimensional morphologies have been demonstrated on both (100) and (111)B substrate orientations; however, the (111)B orientation is more promising because only misfit dislocations are present at the epilayer / substrate interface.

References

01. M. S. Abrahams, L. R. Weisberg, G. J. Busocchi, and J. Blanc, *J. Mater. Sci.* **4**, 223 (1969).
02. J. W. Matthews and A. E. Blakeslee, *J. Cryst. Growth* **32**, 265 (1976).
03. M. Akiyama, Y. Kawarada, and K. Kaminichi, *J. Cryst. Growth* **68**, 21 (1984).
04. R. Fisher, D. Neumann, D. Zibel, H. Morkoc, C. Choi, and N. Ostuka, *Appl. Phys. Lett.* **48**, 1223 (1986).
05. J. W. Lee, H. Shichijo, H. L. Tsai, and R. J. Matyi, *Appl. Phys. Lett.* **50**, 31 (1987).
06. E. A. Fitzgerald, Y-H. Xie, D. Monroi, P. J. Silverman, J. M. Kuo, A. R. Kortan, F. A. Thiel, and B. E. Weir, *J. Vac. Sci. Technol. B* **10**, 1807 (1992).
07. J. A. Venables, G. D. T. Spiller, and M. Hanbucken, *Rep. Prog. Phys.* **47**, 399 (1984).
08. E. Bauer, *Z. Kristallogr.* **110**, 372 (1958).
09. B. W. Dodson and J. Y. Tsao, *Appl. Phys. Lett.* **51**, 1325 (1987).
10. E. A. Fitzgerald, *J. Vac. Sci. Technol. B* **7**, 782 (1989).
11. D. J. Eaglesham and M. Cerullo, *Phys. Rev. Lett.* **16**, 1943 (1990).
12. G. E. D. Box, W. G. Hunter, and J. S. Hunter, *Statistics for Experimenters*, John Wiley & Sons, 1977.

Table I : Matrix of Growths of InAs on GaAs - A 2^3 Factorial Design

Run Number	Growth Temp. ($^{\circ}\text{C}$)	H_2 Flow In TMin (sccm)	V/III	Island Density (cm^{-2})	
				(100) Substrate	(111) Substrate
1	525	140	100	5.6×10^8	coalesced
2	600	140	100	1.4×10^8	1.9×10^6
3	525	720	100	1.0×10^9	coalesced
4	600	720	100	1.7×10^8	4.5×10^6
5	525	140	400	4.3×10^8	coalesced
6	600	140	400	4.9×10^7	2.7×10^6
7	525	720	400	6.7×10^8	coalesced
8	600	720	400	1.0×10^8	7.8×10^6

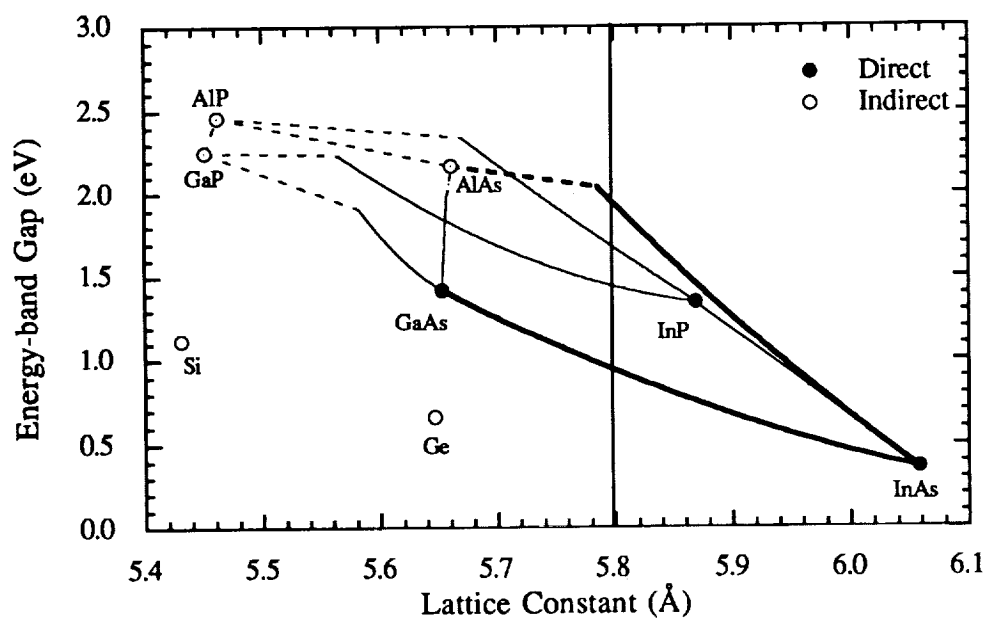


Figure - 1 Plot of energy-gap vs. lattice constant for elemental and III-V compound semiconductors and alloys. Note that InP has a lattice constant that is 3.8 % larger than that of GaAs and 8.1 % larger than Si. Also note that the $(\text{Al}_x\text{Ga}_{1-x})_{0.65}\text{In}_{0.35}\text{As}$ alloy with a lattice constant of 5.8 Å covers an energy-gap range from 1 eV to 2 eV, which is the optimum energy-gap spectrum for a multijunction solar cell configuration.

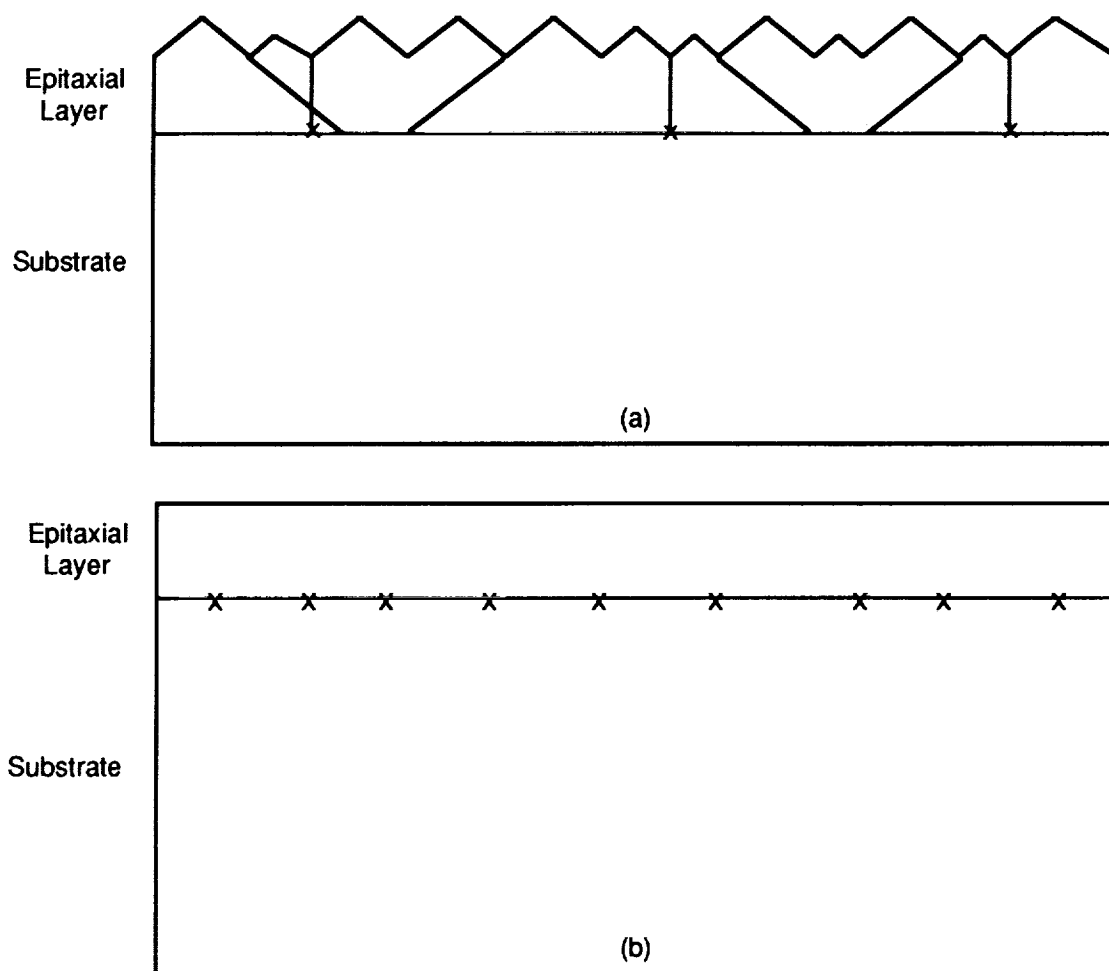


Figure - 2 (a) Relaxed epitaxial layer with a rough surface morphology and high threading dislocation density. (b) Relaxed epitaxial layer with only misfit dislocations.

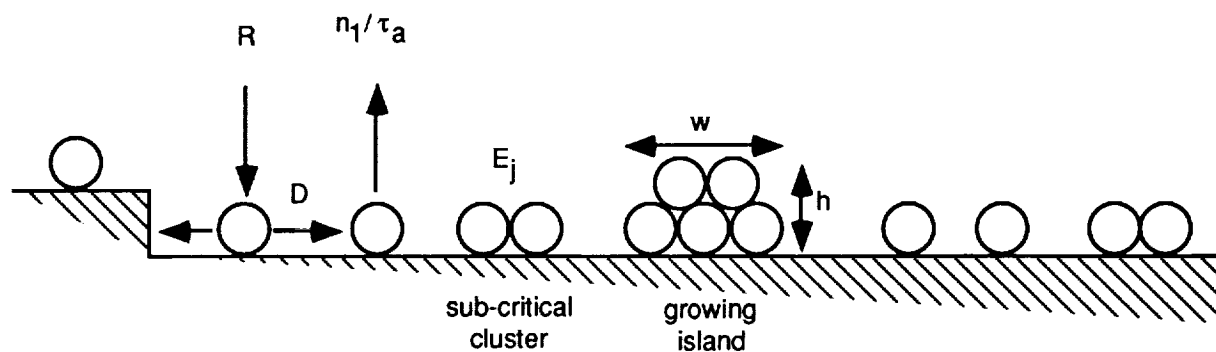


Figure - 3 A stepped surface with a sub-monolayer deposit consisting of single atoms, sub-critical clusters of atoms, and growing islands. Single atoms arrive at the substrate at a rate R , move across the surface with diffusion coefficient D , and can either re-evaporate at a rate n_1 / τ_a , form sub-critical clusters of atoms which are finally transformed into growing islands, or incorporate directly into a pre-existing step edge.

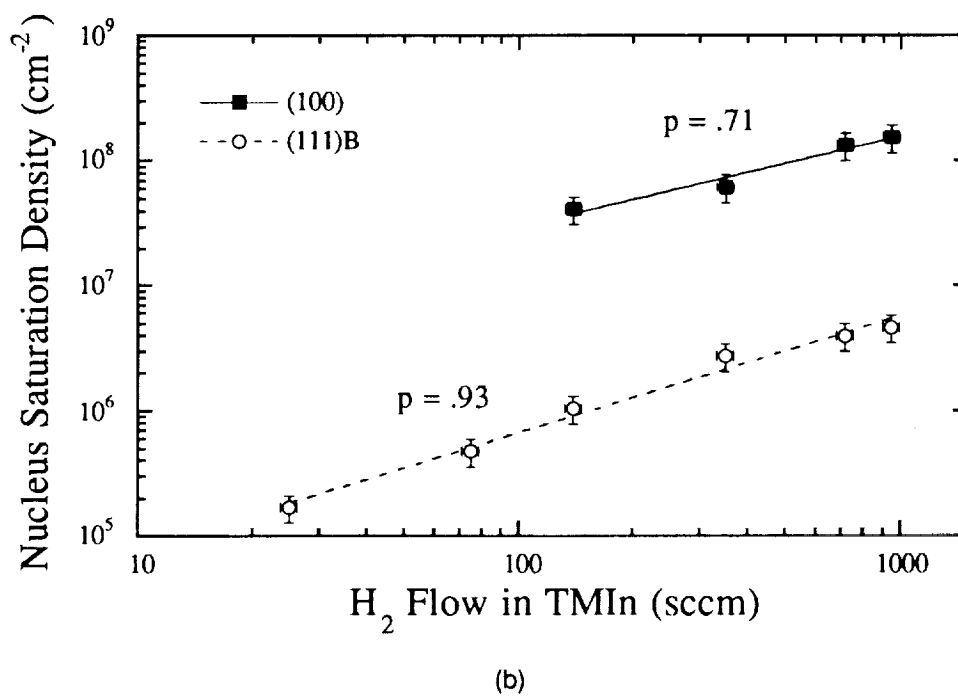
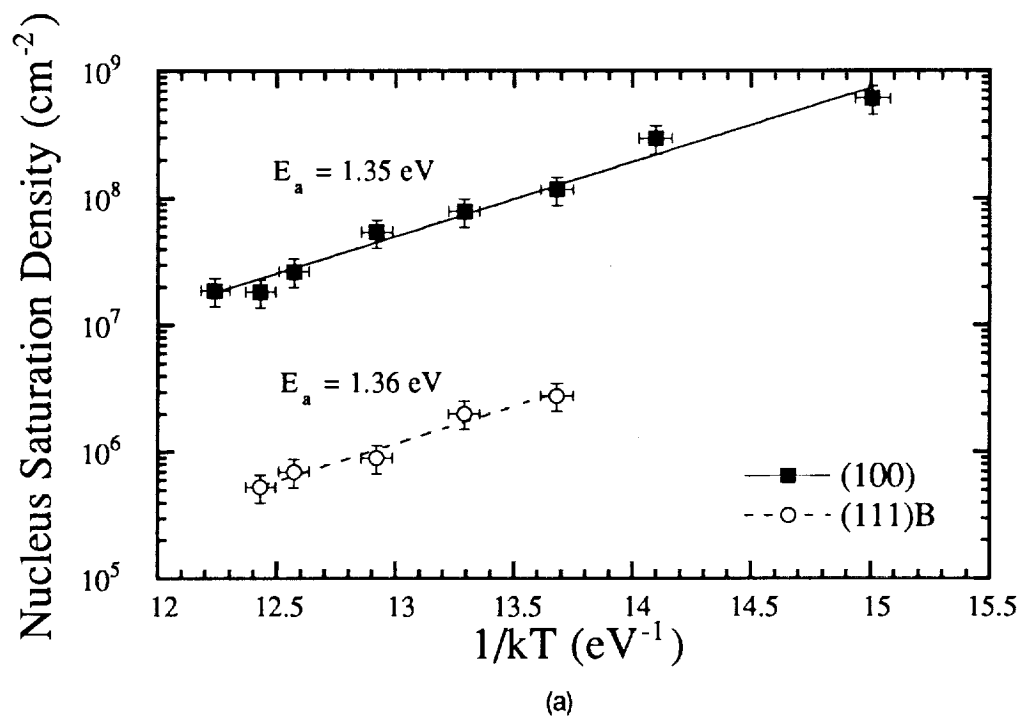


Figure - 4 Nucleus saturation density as a function of temperature in (a), and TMIn flow in (b).

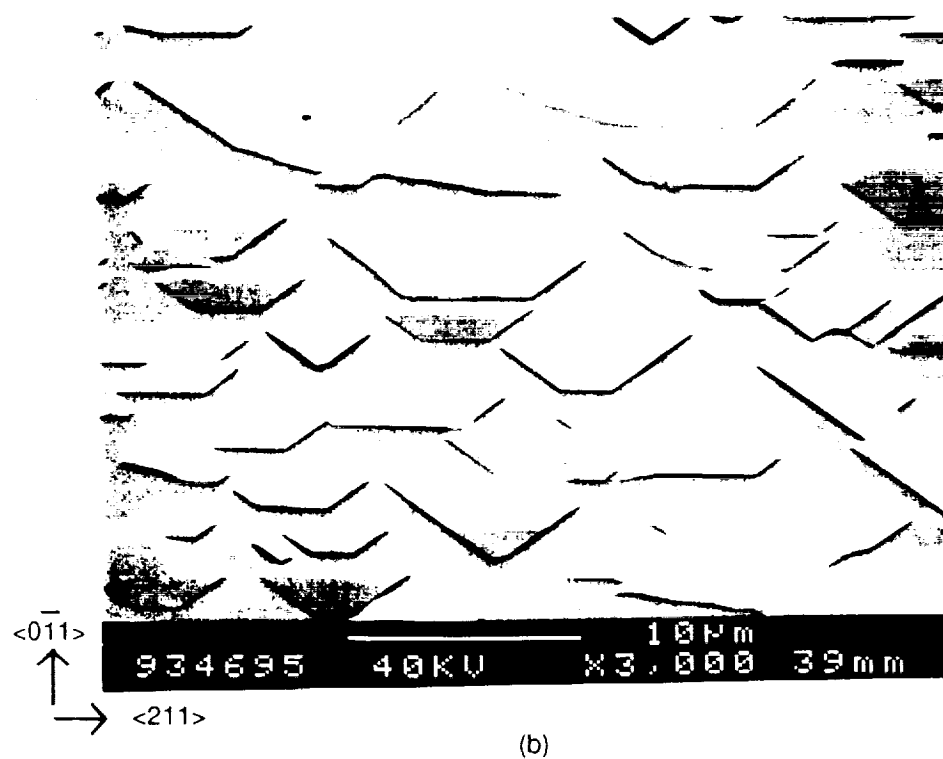
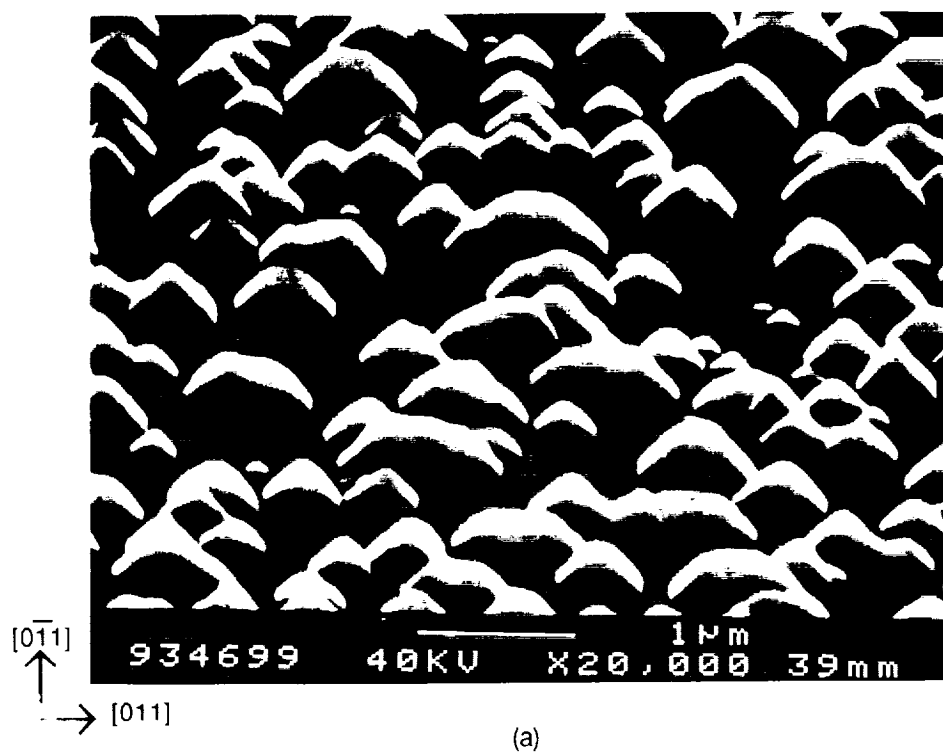
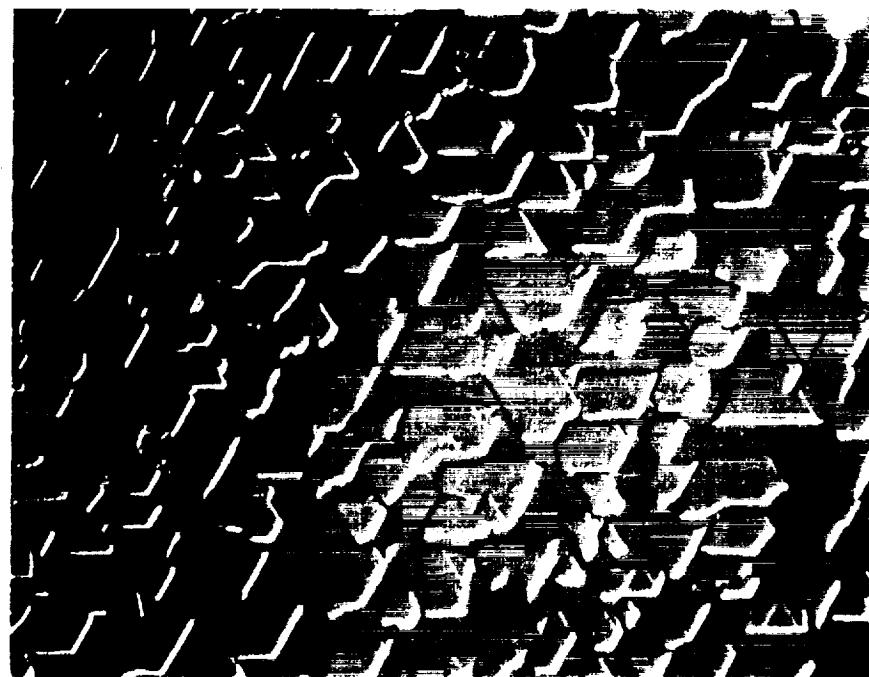
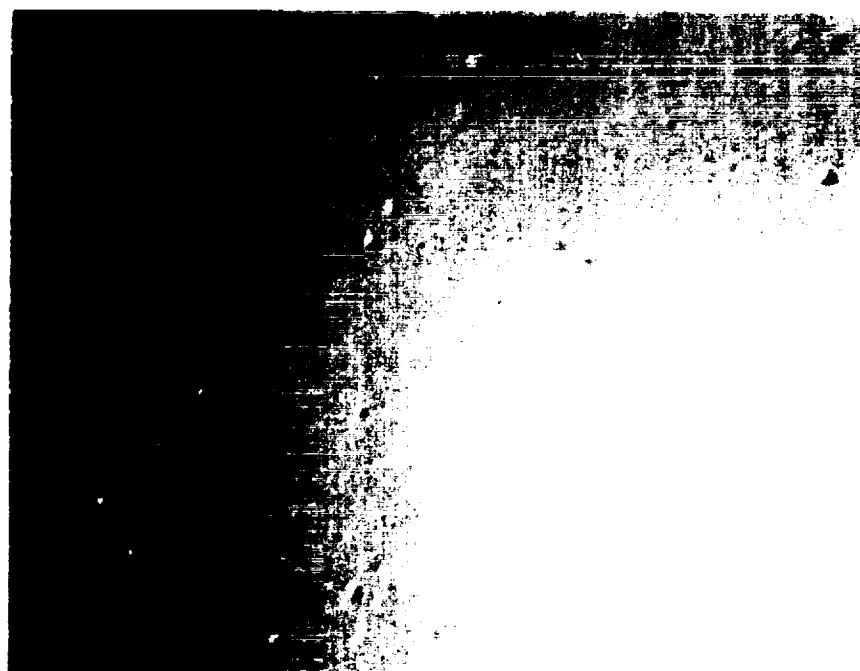


Figure - 5 InAs islands on a (100) oriented GaAs substrate in (a), and a (111)B substrate in (b). Growth conditions are $T = 600\text{ }^{\circ}\text{C}$, $f_{\text{TMIIn}} = 140\text{ sccm}$, $f_{\text{TMGa}} = 100\text{ sccm}$, $t_{\text{avg}} \sim 100\text{ \AA}$.



(a)

10 μm



(b)

10 μm

Figure - 6 Optical micrographs for the (111)B GaAs substrate depicting the transition from a 3-D morphology in (a) to a nominally 2-D InAs surface in (b). Growth conditions are $T = 600\text{ }^{\circ}\text{C}$, $f_{\text{TMIIn}} = 140\text{ sccm}$, $f_{\text{AsH}_3} = 100\text{ sccm}$, $t_{\text{avg}} \sim 250\text{ \AA}$ for (a), and $T = 525\text{ }^{\circ}\text{C}$, $f_{\text{TMIIn}} = 720\text{ sccm}$, $f_{\text{AsH}_3} = 500\text{ sccm}$, $t_{\text{avg}} \sim 250\text{ \AA}$ for (b).

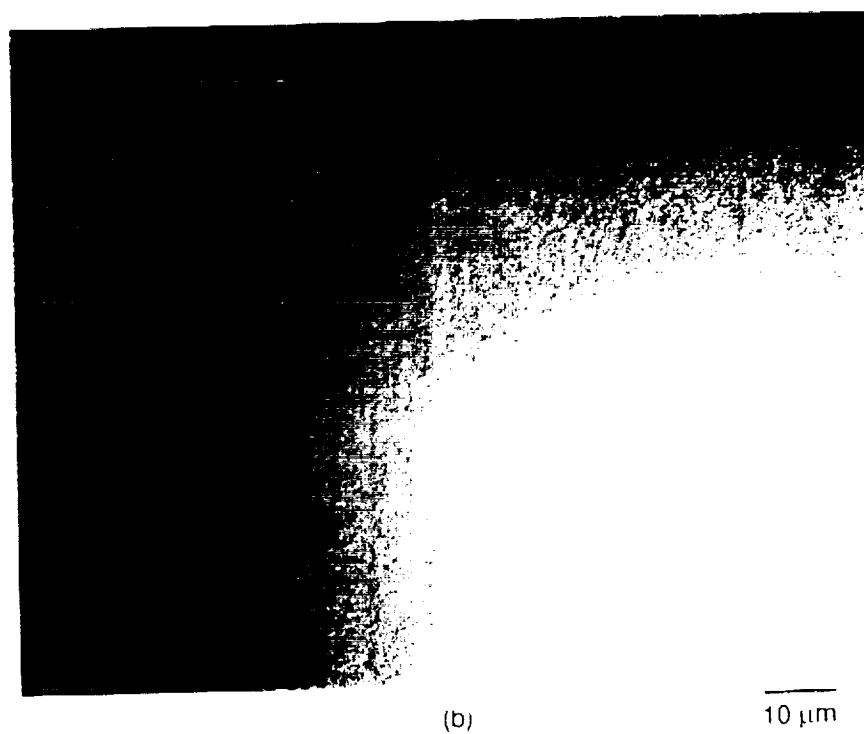
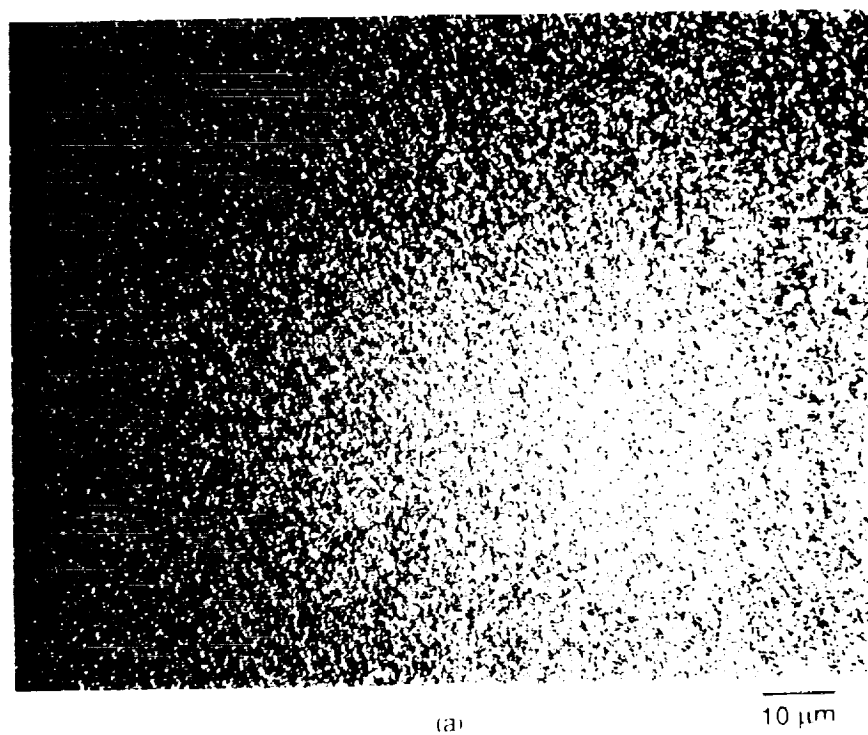


Figure - 7 Optical micrographs for the (100) GaAs substrate depicting the transition from a 3-D morphology in (a) to a nominally 2-D surface in (b). Growth conditions are $T = 525^\circ\text{C}$, $f_{\text{TMIIn}} = 720$ sccm, $f_{\text{AsH}_3} = 125$ sccm, $t_{\text{avg}} \sim 250$ Å for (a), and $T = 475^\circ\text{C}$, $f_{\text{TMIIn}} = 950$ sccm, $f_{\text{AsH}_3} = 82.5$ sccm, $t_{\text{avg}} \sim 250$ Å for (b).

SUMMARY OF WORKSHOP ON InP: STATUS AND PROSPECTS

R.J. Walters
U.S. Naval Research Laboratory
Washington, DC

and

I. Weinberg
NASA Lewis Research Center
Cleveland, Ohio

This paper presents a summary of the workshop on InP solar cells. The overall purpose of this workshop was to:

- 1) determine the primary objective of the present InP research programs
- 2) establish the immediate prospects for use of InP solar cells
- 3) state the current status of the various InP research projects
- 4) identify the current major problem areas in the development of InP cell technology

This report address each of these topics in turn.

1) OBJECTIVES

The primary objective of most of the programs in InP solar cells is the development of the most radiation hard solar cell technology. In the workshop, it was generally agreed that the goal is a cell which displays high radiation tolerance in a radiation environment equivalent to a 1 MeV electron fluence of about 10^{16} cm^{-2} . Furthermore, it is desired that the radiation response of the cell be essentially flat out to this fluence - i.e. that the power output of the cell not decrease from its beginning of life (BOL) value in this radiation environment.

It was also agreed in the workshop that the manufacturability of InP solar cells needs to be improved. In particular, since InP wafers are relatively dense and brittle, alternative substrates need to be developed. Research on hetero-epitaxial InP cells grown on Si, Ge, and GaAs substrates is currently underway. The ultimate goal is to develop hetero-epitaxial InP solar cells using a cheap, strong, and lightweight substrate.

2) PROSPECTS

The prospects for use of InP solar cells are primarily in high radiation earth orbiting satellites. There has been an expressed need in the Navy and in commercial interests (particularly in the communication industry) to fly satellites in orbits where the equivalent 1 MeV electron fluence for a five year mission is greater than $3 \times 10^{15} \text{ cm}^{-2}$. Calculations made at the Naval Research Laboratory (NRL) and NASA Lewis have shown hetero-epitaxial InP cells grown on Si wafers to be the most cost-effective technology for these missions. Also, even low-earth-orbits (LEO), especially polar orbits, can be a severe radiation environment due to solar flares. A satellite power system based on radiation hard InP

solar cells would be relatively insensitive to solar flares. Also, extending geostationary mission lives to beyond 10 years has been considered. Such a mission would experience a significant amount radiation. Radiation hard InP solar cell technology has the potential to significantly improve the performance of these missions.

Another area where InP solar cell technology has been considered is in the alpha and beta voltaic power sources. By there very nature, such devices are very sensitive to radiation effects. The radiation hardness of InP seems well suited for this application.

Although the focus of the present conference is space photovoltaics, the possibility of terrestrial applications for InP solar cells was identified. One particular application was that of a concentrator array. While no space system has ever used a concentrator array, terrestrial systems make ample use of this technology. Modeling results reported by the National Renewable Energy Laboratory (NREL) have shown the InP/Ga_{0.47}In_{0.53}As tandem cell to be the best band gap combination for concentrator applications.

3) STATUS

The status of the present research in InP solar cells is best described by summarizing the current programs:

at NRL:

1) Hetero-epitaxial InP on Si cells

This is an SBIR program with Spire Corporation. Phase I was recently completed and phase II is currently underway. The goal of this project is to produce a large number (> 100) 2x2 cm cells with BOL efficiencies of 16% (1 sun, AM0, 25 C) which virtually do not degrade after an equivalent 1 MeV electron fluence of 10¹⁶ cm⁻².

2) InP/Ga_{0.47}In_{0.53}As Tandem Solar Cells

This program includes NREL for the cell growth and NRL for the cell characterization. The current best cell efficiency is 22%. The program was not funded in FY 94 but has good chances for funding in FY 95. The next step in the program is to grow the tandem on a Si substrate.

3) Basic Research - Annealing of Radiation Damage

NRL has a basic research program studying displacement damage effects in InP solar cells. At present, the main research topic is the annealing characteristics of irradiated InP cells.

at NASA Lewis:

1) Hetero-epitaxial InP on Si

NASA is funding Matrix Sciences to grow InP cells on Si substrates. This is a phase two contract.

2) Hetero-epitaxial InP on Ge

NASA Lewis funded Spire Corporation to grow InP cells on Ge. This was a phase I

SBIR and has been completed.

3) **Hetero-epitaxial InP on Ge**

NASA Lewis also has an "in-house" program to develop InP cells on Ge substrates.

4) **Hydrogen Passivation**

NASA Lewis is funding Ohio State to study the effects of hydrogen on the dislocations which occur in a hetero-epitaxial cell.

at Space Vacuum Epitaxy Center, University of Houston:

The research at Space Vacuum Epitaxy Center is developing chemical beam epitaxy as a growth technique for photovoltaic devices. As part of this development, these researchers are growing InP/Ga_{0.47}In_{0.53}As tandem cells.

4) PROBLEM AREAS

The main problem area encountered in the present research is that the heteroepitaxial cells must be p⁺n cells while most cells grown to date have been n⁺p cells. Therefore, the major research focus is in optimizing homojunction p⁺n cells to the level of the n⁺p cells.

Another research focus is the reduction of the deleterious effects of the dislocations which form in InP cells grown on Si, Ge, or GaAs substrates. The use of graded and possibly strained layers as an intermediating layer between the substrate and the cell active layers to prevent the propagation of the dislocations into the active region is being investigated. Also, the research at Ohio state is investigating the possibility of passivating the defect levels created by the dislocations with hydrogen.

SUMMARY

In general, the workshop concluded that the InP solar cells are being developed as an *enabling* technology which, by virtue of its superior radiation resistance, will allow space flights in high radiation orbits which are not possible with Si or GaAs solar cell technology.

SYSTEMS, ARRAYS AND APPLICATIONS WORKSHOP 1

G.J. Pack
Lockheed Missiles and Space Company
Sunnyvale, California

and

Lothar Gerlach
ESA/ESTEC
Chelmsford, Essex, United Kingdom

The charter of this workshop was to evaluate photovoltaic technologies from the broad perspective of future mission needs and operational requirements. We were given a set of six questions listed in Figure 1 to start the discussion, however; these were viewed as sample questions which didn't constrain our deliberations.

Our primary objective in discussing the provided questions and other items of interest to the group was to answer the question: How should NASA spend its scarce space power resources? It was clear from the papers presented in the main session and the depth of technical talent present in the audience, that there are significantly more good projects available than there is funding for. Thus NASA is faced with the problem of deciding whether to allocate their resources across a range of projects or to focus on a small subset of tasks that are mission enabling.

Our discussion arrived at two primary findings:

- NASA management has failed to articulate a vision of where the agency is going.
- Consequently, the questions listed in figure 1 are irrelevant.

The failure of management to provide leadership and a consistent direction is apparent in the space power arena. Photovoltaics has been the mainstay power source for U. S. space missions for the past thirty years. However, for the last decade, NASA (and the Air Force) has continually wasted more money on frivolous pursuits of nuclear, solar dynamic, and other poorly justified energy sources than they have invested in the photovoltaic arena. We must therefor face up to the reality that space photovoltaics research has slipped out of the mainstream and into the eddies.

We have seen the mission emphasis change yearly from missions to Mars, to missions to Earth. It has thus become traditional for the research centers to try to fund a little something for everybody and keep all options open. The subset of questions posed for this group follows that path ranging from interplanetary to near term LEO commercial missions and everything in between. Insufficient funding to make significant progress in a timely manner renders these efforts irrelevant to the ultimately selected mission.

The R&D technical community cannot expect to redefine the agency. The following suggestions can reposition space power to take maximum advantage of the resources that are available.

- **Set technology improvement goals at 100% minimum.**

The key word for the 90's should be focus. Since the resources will be very limited go for the gold. Select only high risk, high payoff, mission enabling technologies for consideration. Anything less than 100% improvement at the system level is evolutionary and will not achieve rapid market acceptance.

- **Time to market (Faster) is just as important to technology efforts as commercial efforts.**

The advantage scientists and engineers have over artists is that we shouldn't have to be dead to see our work applied and appreciated. Focus!

- **Efficiency**

Efficiency drives everything: weight, volume, cost, etc.

- **Look for revolutionary, mission enabling systems.**

In order to tackle this suggestion, researchers and NASA center personnel will have to get out of their labs and offices and go talk to the users. Kind of a novel suggestion? Just remember, the customer is always right. Go find out what would generate new programs and public support. Tackle those problems. Focus!

- What should the maximum operating voltage of a solar array be?
- Are arc-proof arrays required for future space PV?
- Do we need new array technology for the next generation of commercial satellites? If so, what is required?
- Expendable arrays for complex missions -- Should arrays be expendable?
- What is the operational range of PV in the solar system -- PV for Pluto?
- Do we need new array technology for intermediate orbit applications?

¹The following paper presents the general results of the workshop and does not necessarily represent the views of any individual participant or company.

FUTURE DIRECTIONS IN PV CELL DEVELOPMENT: SUMMARY OF THE WORKSHOP AT SPRAT-XIII

Geoffrey A. Landis
NYMA, Inc.
Brook Park, Ohio

Workshop co-chairs: Geoffrey A. Landis (NYMA/NASA Lewis) and Ed Gaddy (NASA Goddard)

MISSIONS

The "mission" of this workshop was to identify what areas of PV cell development would be most fruitful to direct NASA's scarce research money toward in order to have the greatest impact on future space power systems.

Before analyzing what advances customers need, it is necessary to decide who are the customers for improved solar cells will be, and what orbits the cells will be required to operate in. The following list of customers was generated:

<i>NASA:</i>	Earth orbit missions:	Low Earth Orbit (LEO) Intermediate Earth Orbit Geosynchronous Earth Orbit (GEO)
	Solar-system exploration:	Inward (Sun, Mercury, Venus) Outward (Mars, Asteroids, Outer Planets)
<i>Commercial</i>	communications	LEO Molniya orbit GEO
<i>Military</i>	communications, navigation, observation	
<i>Other Government Agencies</i>	weather, navigation, observation	

It was decided that NASA research should be directed toward applications by NASA and commercial users. Representatives of the military and other government agencies at the workshop made no comment. Workshop co-leader Ed Gaddy of NASA Goddard Spaceflight Center suggested that there will be only a small number of NASA missions devoted to solar system exploration, and a large number of future missions to LEO and GEO orbits, where LEO missions will include many polar- and near-polar (sun synchronous) orbits. [The representatives from NASA JPL were all in the other session on array technology, so no one challenged this statement.] The consensus of the workshop was that commercial missions will also be primarily to LEO and GEO orbits. Thus, the overall consensus of the group was that the most important applications for future solar cells will be for satellites in the orbits which are important today: LEO and GEO.

Two strong trends were identified, with important implications for the future: a trend toward small satellites (less than a few kilowatts, as opposed to the 10 kW+ projects envisioned just a few years ago), and an industry-wide trend toward fast cycle times for development of new technology.

GOALS

The next question is: in which solar cell parameters are advances most needed by the user community?

The answer is: cost. Array volume and reliability of interconnects were mentioned, but the overwhelming answer of the participants was that cost is critical. However, in the ensuing discussion, it became clear that the important cost is not *cell* cost, but life-cycle *system* cost.

The typical purchase cost to users of solar arrays ranges from \$1000 to \$2000 per watt today. Some of this is non-recurring cost, since power requirements are different for each satellite. One vendor said that they are providing arrays for \$800 per watt to a military customer, where the non-recurring cost is amortized over many satellites. Frank Ho provided the following "typical" numbers. For a GaAs array of a few kilowatts, roughly 25% of the cost of the power system is the cost of the solar panels. Of the panel cost, roughly half of the cost is cell cost (for GaAs/Ge cells). Thus, about 12% of the cost of a power system is attributable to the cost of the cells for (relatively expensive) GaAs cells, and a few percent for (relatively cheap) silicon cells. From this we conclude that cutting the cell cost can have at most a 12% impact on the power system cost, and, considering launch costs and other system costs, is likely to have a much lower impact. In itself, *cell cost is not a major issue*.

To achieve low system cost, the workshop participants suggested that the single most important factor is conversion efficiency, since an increased efficiency reduces the entire array cost. In addition, in order to get a new technology into the marketplace, investors require a low development cost, and a fast cycle time.

Lew Fraas emphasized that low development cost is critical. He said that Boeing estimated that the development cost to bring their 30% efficient tandem GaAs/GaSb concentrator system to market would be \$100 M, and that this high cost made it impossible to attract investors. Representatives of the space-cell industry said that development of the GaAs on Ge cell [1,2] required "lots of millions of dollars" and took over three years, but that it had a strong selling point in that the cells already had a customer, since they were direct replacements for existing GaAs on GaAs cells developed for an unnamed (presumably military) customer.

It was also mentioned that low development cost means that the capital cost for production has to be reasonably low as well. There was a discussion of what low capital cost means, applied to space solar arrays. George Vendura of TRW pointed out that amorphous silicon may have a high capital cost if a new production facility must be built for the space product, but that TRW was pursuing a low capital cost approach for a-Si arrays by leveraging the huge (many megawatt) a-Si production capability in place for terrestrial markets. On the other hand, it was pointed out that a typical amorphous silicon production facility has a capital cost of about \$10M. If this were expensed over a year's production of 50 kW, the cost would be \$200 per watt. This is only a small fraction of the current space-cell production cost, and if other costs (such as the cost of assembling the array) were reduced, it might be acceptable.

The current industry trend is toward extremely fast cycle time: getting a product to market as swiftly as possible. Several of the participants suggested that for a new produce to fly, development time ought to be three years or less. Frank Ho said that getting MO-CVD GaAs cells to market took four years from the 1982 manufacturing technology (mantech) program. GaAs on Ge cells took three years after the mantech. Lew Fraas said that his experience at Boeing was that they had their research breakthrough in GaSb in 1989, found a flight opportunity in 1992 for a flight in 1994-- and the program was terminated by Boeing in 1992. The time scale of 5 years from technology to flight test was too long.

It was debated whether a 3 year cycle time was possible. It was concluded that it may be possible for developments with low technical risk and the ability to use existing system heritage, as the GaAs/Ge cell did, where system components other than the cell can be transferred unchanged.

It was concluded that space experience was the big stumbling block to short cycle times. It is important for NASA to use advanced cells on actual missions, in order to get the space heritage demanded by mission designers. A scientific satellite, for example, could be designed so that one of the panels of an array is made with advanced cells.

SOLAR CELL TECHNOLOGIES

Seven different advanced cell technologies were discussed in some detail.

Amorphous silicon, copper indium diselenide, and cadmium telluride thin films were discussed as systems that could have lower cost at the cell and array levels, and have the potential for very low mass and good radiation tolerance [3,4]. However, it was expected that to take maximum advantage of these systems, new array technologies would be needed. The workshop was divided on this issue.

Ultra-thin (5 micron) gallium arsenide was discussed. The costs were considered higher, but the reduced cell mass would improve the specific power of arrays.

High-efficiency monolithic tandem cells, such as GaInP₂ on GaAs/Ge [5], and GaAs on active germanium, were discussed as ways of improving efficiency. Since these cells could be used directly as replacement for existing GaAs/Ge cells in existing arrays, this was considered a very promising approach.

Indium phosphide was discussed, as well as the heteroepitaxial InP approaches such as InP/Ge and InP/Si. The cost is high today, but it was agreed that ultimately the cost of InP/Si or InP/Ge could be made competitive. It was agreed that these cells may have an application in orbits which see high radiation environments.

The concentrator approach was discussed. This is not a direct replacement into existing arrays, and may find some resistance from program managers due to pointing requirements. However, they have the potential for high efficiency and good radiation tolerance [6].

Finally, it was mentioned that new generation silicon cells with efficiency of 20% have performance as good as GaAs cells. However, the radiation tolerance of these cells is yet to be determined, and they are not yet space qualified.

Thermophotovoltaic (TPV) cells were mentioned as a promising new use for photovoltaics, but since there was a separate workshop on these concepts, they were not discussed in detail.

DISCUSSION SESSION

In the summary session, Geoffrey Landis took issue with the consensus that future systems will be primarily LEO and GEO. He suggested that the most significant commercial space system in the next decade will be the emplacement of a worldwide communications satellite network for portable telephone systems, with an investment of tens of billions of dollars, and that these satellite systems may be significantly different from currently operated GEO satellites. He presented results from an unpublished study [7] that shows that the number of satellites required to provide global phone coverage can be reduced by a factor of four if an intermediate orbit of 3200 kilometers is chosen instead of the low Earth orbit proposed. A page from these results is shown in figure 1.

Andrew Meulenberg agreed with this conclusion. He said that a study done by Comsat on behalf of Inmarsat concluded that Inmarsat could save nearly a billion dollars on their worldwide telephone satellite constellation "Inmarsat-P" due to the reduced number of satellites required if they went to intermediate orbits instead of low orbit. According to articles in *Space News* [8], the price of the Inmarsat-P system reduces from 3 billion dollars to 2 billion, and the number of satellites is reduced from 54 to 12-15, if intermediate orbit of 10,300 km is chosen instead of LEO. (This data point is shown to the right of the curve shown in figure 1). A recent study published in *Space News* indicated that there will be a market for as many as four of these worldwide communications satellites systems, and that these will produce a revenue of \$9 billion per year [9].

These intermediate orbits see an intense radiation environment. At 3200 km, the radiation dose received from trapped protons in one day is approximately the same as that seen in geosynchronous orbit in a year! This implies that radiation tolerant solar cells may be critical components of future communications satellite networks, and thus could have considerable commercial value. Data presented by Landis showed that InP cells (and possibly other radiation-resistant cell types as well) may be able to stand up to this environment.

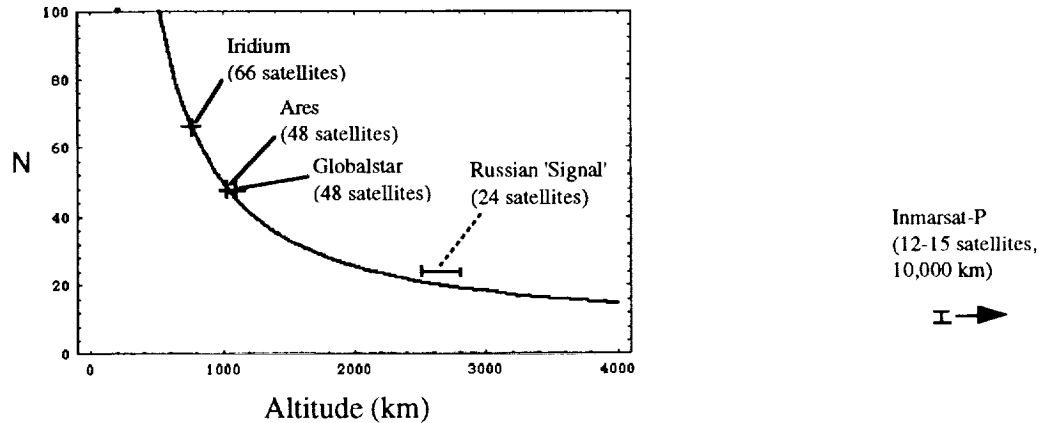


Figure 1. Number of satellites required for a phone network to provide worldwide continuous coverage, as a function of altitude (data from Bailey and Landis [1]). Solid line is theoretical curve, for polar-orbit satellite constellations; data points shown are for proposed American and Russian global coverage systems.

Some further comments of note from the discussion of the workshop summary:

Geoffrey Sommers said that telephone satellites will not have a lot of fancy electronics; they will be simple relays, and could be built so that the electronics will be (relatively) radiation tolerant. Thus, if the solar arrays could be made radiation tolerant, it would indeed be possible to utilize high-radiation orbits.

Irving Weinberg said that radiation-tolerant cells such as InP are important for commercial applications in GEO, not just intermediate orbits. He said that a satellite in GEO accumulates a radiation dose of 10^{15} electrons over ten years, and that this results in degradation in power of 30 to 40 percent. Further, he notes that the next generation of commercial satellites are going to extended lifetimes of fifteen years and longer, making radiation-limited lifetime important.

Finally, Lew Fraas concluded by reminding us that research aimed at near-term markets is a job for industry. The government should think in the long term, and fund technology development, so that we maintain a technology base for industry to draw on in the future.

CONCLUSIONS

Cost is the main issue for space photovoltaics, but *cell* cost is only a minor (10%) component of the cost. The parameter that is most desired out of next-generation photovoltaic technology is high conversion efficiency. To get a product to market required fast cycle time and a low development and qualification cost. One thing that aids low development cost the ability to directly replace existing cells in existing array designs, so that a new array design doesn't have to be developed.

There is a good argument that development of radiation tolerant cell technology could open up a new range of intermediate orbits, with potentially high commercial value. This may be a strong argument for continued development of InP and other radiation tolerant cell designs.

REFERENCES

- [1] B. Smith, M. Gillanders, P. Vijayakumar, D. Lillington, H. Yang and R. Rolph, "Production Status of GaAs/Ge Solar Cells and Panels," *Space Photovoltaic Research and Technology 1991*, NASA CP-3121, 9-1 (1991).
- [2] C.L. Chu, P.A. Iles, and W. Patterson, "Recent Advances in GaAs/Ge Solar Cells," *Space Photovoltaic Research and Technology 1991*, NASA CP-3121, 8-1 (1991).

- [3] G.A. Landis and A.F. Hepp, "Thin-Film Photovoltaics: Status and Applications to Space Power," *Proc. European Space Power Conf.*, 2-6 Sept. 1991, Florence Italy; pub. ESA SP-320, 517-522 (1991).
- [4] R.L. Mueller and B.E. Anspaugh, "Results of Some Initial Space Qualification Testing on Triple Junction α -Si and CuInSe₂ Thin Film Solar Cells," *Proceedings of the XII Space Photovoltaic Research and Technology Conference*, 108-117 (1992).
- [5] M.F. Piszczor and M.J. O'Neill, "Recent Developments in Refractive Concentrators for Space Photovoltaic Power Systems," *Proceedings of the XII Space Photovoltaic Research and Technology Conference*, 206-216 (1992).
- [6] J.M. Olson, S.R. Kurtz, A.E. Kibbler, K.A. Bertness, and D.J. Friedman, "GaInP₂/GaAs Tandem Cells for Space Applications," *Space Photovoltaic Research and Technology 1991*, NASA CP-3121, 12-1.
- [7] S.G. Bailey and G.A. Landis, submitted to 1st World Conference on Photovoltaic Energy Conversion, Hawaii, December 1994.
- [8] P. deSelding, "Inmarsat Drops LEO Concept," *Space News*, Aug. 2-8 1993; page 3 and "Inmarsat Takes First Step to Privatization," *Space News*, May 16-22 1994, page 1.
- [9] "Study Claims LEO Market Can Support Four Systems," *Space News*, June 13-19, 1994.

ARRAY TECHNOLOGIES WORKSHOP I

Douglas Allen
W.J. Schafer Associates
North Olmsted, Ohio

and

Andrew Meulenberg
Comsat Laboratories
Clarksburg, Maryland

The following is a summary of responses to questions posed to the workshop and related discussions. Approximately 40 people attended the workshop and included representatives of satellite design and fabrication companies, cell development and manufacturing companies, panel development and manufacturing companies, Universities, and several government organizations. Commercial, DoD, and civil applications were all well represented by workshop attendees, as were rigid, flexible, and concentrator array technologies. Most of the time in the workshop was spent discussing questions 1 and 2, the remaining questions received only minimal deliberation.

Question 1. What will determine the selection of a specific array type (rigid, flexible, concentrator)?

Workshop attendees all agreed that the first criteria for selecting an array on any satellite program is past use. This is because of the cost of designing and qualifying any new technology, which can add about \$15M to the cost of a satellite program and add risk. Any time a new technology is integrated into a spacecraft design, there are many "what ifs" that must be studied and answered which is the cause of the high cost.

There are only two ways that a new array technology will be used on a spacecraft in nearly all circumstances: 1) the technology "enables" the mission or 2) The technology provides system level benefits that overcome the extra cost and risk. Enabling technology means that the new technology allow the mission to be accomplished when no existing technology will. For example, concentrator array technology may be enabling for some non-nuclear deep space missions or for orbital missions in the radiation belts. The second criteria allows spacecraft builders to take advantage of new technology if the risk/benefit analysis shows significant system level payoff for integrating a new array technology. In general, the new array technology must provide about a 2X improvement in an important parameter (volume, cost, mass, etc.) to meet this criteria. Otherwise, spacecraft builders do not feel it is worthwhile to accept the extra cost and risk of integrating a new technology.

One positive sign that was discussed is that there appears to be a growing number of opportunities for space experiments and demonstrations that will help new array technologies overcome the past use criteria.

After past use, the next issue for a new array technology is schedule. Many satellites are being designed, built, and launched on a 2-3 year schedule now and if a technology option can not meet the schedule for a program, the program will not wait. Another similar go/no go criterion on many satellite programs is stowed volume and configuration. The array must be able to be packaged into the planned launch vehicle or it will not be considered.

After passing through the above gates, the criteria for selecting an array technology are cost, then area, then mass. It was noted that array mass tends to be much less important than the other criteria for most satellites. Area is important due to several considerations like the

spacecraft moment of inertia's impact on the attitude control subsystem and the need for drag makeup propellant in low orbits.

The workshop also spent time discussing the growing importance of small satellites in the marketplace and the need for new technologies to be compatible with this trend. There was no consensus on the definition of what is a "small satellite." Some of the definitions offered included power below 1 kW, program cost below \$50M, and a satellite that can be launched on a Pegasus. It was also noted that there may be an misperception about the importance of small satellites in the marketplace. For example, many of the new LEO communications constellations will include large numbers of satellites, but the satellites do not come close to any of the above definitions of small satellites. Teledesic at 11 kW (BOL) and Ellipsat at about 5 kW (EOL) were cited as examples.

Other topics discussed in the course of answering the first question included the variety of possible concentrator arrays (concepts with concentration ratios of anywhere from 1.5X to 1000X have appeared recently in the literature), the relationship between array stiffness and pointing tolerance, the ability of concentrator arrays to perform under spacecraft error conditions, and the fact that the number of satellites in a constellation and other constellation parameters changes the criteria for selection and the importance of each criteria.

A concentrator array's ability to locate and track the sun when a spacecraft tumbles was the highlight of the other topics, as it followed up on discussion started in the morning session. Significant comments included suggestions about using hybrid arrays or body mounting a backup panel to overcome this problem. It was also noted that the degree of the potential problem was spacecraft dependent contingent on factors such as what percentage of the spacecraft's power is necessary to keep the spacecraft alive until the attitude problem is solved and the relative cost of losing one spacecraft (critical in a one of a kind science mission, but somewhat less important in a large constellation). It was also noted that a program may be willing to take the risk if the concentrator array provides enough system level cost and mass benefits.

Finally, the workshop attendees agreed that the team that developed GaAs/Ge should be congratulated as it is an excellent model of how to achieve wide use of a new spacecraft technology in a short time span. The downside of this success is that any new technologies might require the same size budget and commitment to be successful.

Question 2. Are 300 W/kg, 300 W/m², and \$300/W achievable goals for rigid, flexible, and concentrator arrays? If not, what is practically achievable for each array type?

Many of the workshop participants were very hesitant to specify numbers for these parameters for any of the array types. Many reasons were given:

- Specific numbers vary greatly depending on orbit, design life, what's included (whole array or panel), amount of funding to be invested, timeframe, design of the spacecraft, etc.
- Many times, it is not smart to optimize the mass or other parameters at the panel or array level - trades must be done at the spacecraft level and include other parameters such as reliability, cost, etc.
- Performance predictions depend on what assumptions are made including how good predicted performance is, assumed investment to be made in the technology, etc. (can result in "fantasy" predictions)

- Some of the parameters may be possible, but can not be practically achieved on a real spacecraft due to real world considerations (e.g. APSA technology was demonstrated at 130 W/kg, but implemented on EOS at 32 W/kg)

With the above qualifiers, the group did fill out the table below to specifically answer the question. The column of "300 days" was added to stress the growing importance of delivering array hardware in less than one year (from receipt of the specification and order) to meet short spacecraft program schedules. In each box in the table, there are two sections. The upper section is the capability of each technology today. The lower section is the workshop's assessment of what is practically achievable in the foreseeable future for each array type, for each parameter. If the word "yes" appears, it means that 300 is achievable, if not, the number or range represents what is achievable.

Array Type (Now/ _{Possible})	300 W/m ²	300 W/kg	300 \$/W	300 Days
Rigid	150 - 200 Yes	50 - 75 (20) 150 - 250	1500 (Si) 2-3000 (GaAs) 1500	Yes Yes
Flexible	150 + Yes	16 - 66 200 - 250	1700 - 6000 Yes	Yes Yes
Concentrators	>200 (exper.) Yes	150 200 - 250	4-500 (Proj.) Yes	N/A Yes

Several observations were made about the table once it was completed. First, there is surprisingly little difference between the array types for some of the parameters such as in W/m². After reflection, this is probably due to the ability of each array type to use similar photovoltaic cell technology, although implementing advanced cell technology is different for each array type. Another observation that got a lot of discussion is that flexible array mass is strongly dependent on satellite integration. Some examples quoted were Hubble at 16 W/kg, Hubble technology available today at 24 W/kg, EOS at 32 W/kg, SAFE at 66 W/kg, and APSA at 130 W/kg.

Flexible array mass is also very dependent on the power level. For any satellite design, there is a crossover power level above which flexible arrays are lighter than rigid arrays and below that point they are heavier. However, where this point is depends strongly on the assumptions you make and on the spacecraft design. Two studies were quoted: an ESA study

that set the crossover at 7 kW (later updated to 15 kW) and a JPL study that placed the crossover at 700 W. This shows the importance of studying options for a specific satellite with available technology to select the optimum array type.

A final comment was made about the reality of the numbers. Even though 50+ W/kg is possible with current rigid array technology, the actual specific power is usually 20 - 25 W/kg on real satellites. Therefore, all the numbers on the table should be taken with the disclaimers listed at the beginning of this section in mind.

Question 3. Why is there no general consensus amount the industry with regard to the future trends in array technology and is there (or should there be) a trend toward standardizing array technology to be applicable to a variety of missions?

As was evident in the answer to question 2, different missions and spacecraft designs drive the design trades. This results in different types of arrays (rigid or flexible) being the best solution for different programs. Another important point from question 2 is that some parameters for the different types of arrays tend to be similar, which results in no one type of array standing out over the others for a wide variety of missions.

With regard to standards, it was generally agreed that there will never be a "standard solar array." This is because mission requirements vary significantly and because individual aerospace companies want to advertise an edge or a benefit with their design. However, there essentially are already several mini-standards, as each major aerospace company uses their own standard array design when they bid most programs.

It was noted that in lieu of standard arrays, the best way to reduce program costs would be to standardize an all-encompassing set of requirements to minimize the non-recurring testing required for each program. This could have a major impact on program costs since the recurring cost of the solar arrays is typically a small part of the total cost to a program.

Question 4. What are the operational pointing requirements for concentrator arrays? Is two axis tracking worth the effort or are linear concentrators better?

In general, at least $\pm 2^\circ$ of sun acceptance angle at the individual concentrator level should allow the use of standard, off-the-shelf array components such as sun sensors and array tracking gimbals. The exact requirement for this angle is dependent on several factors including manufacturing precision of the concentrator elements, positioning accuracy of the concentrators into the panel, panel to panel alignment, gimbal pointing accuracy, sun sensor accuracy, thermal distortions, and tolerance of defects in the concentrator concept. A well managed error budget taking all these factors into account will result in determination of the allowable acceptance angle for a given concentrator design.

For a linear concentrator, a sun acceptance angle of at least ± 20 to 30° in the linear axis allows easy integration into a wide range of satellites, as this is a typical requirement on satellites that only track the sun in one axis (mission design and attitude control result in maintaining nominal pointing in the other axis).

As was discussed in question 1, it was again noted that minimizing the time for sun acquisition is an important consideration in designing a satellite concentrator array. This is important to minimize the impact of possible attitude control subsystem problems and to

minimize the required battery size for initial operation of the spacecraft when deployed from the launch vehicle.

Regarding 2 axis vs. 1 axis tracking concentrator arrays, the trade on which will better meet a spacecraft's requirements is very mission dependent. However, in general there is more applicability for single axis tracking concentrators. One reason for this is the cost and reliability of a 2 axis tracker. Another is that many spacecraft now use only a single axis tracker and changing to a two axis tracking system can have significant impact on other spacecraft subsystems and the overall design concepts. DoD and NASA have decided to move forward with the single axis systems first due to several factors including lower development and recurring costs, applicability to a wider range of satellites (any satellite that can use a two axis concentrator can also use a one axis system, but the reverse is not true), and lower risk for flight testing a full size array. Once the technology is demonstrated, an individual program may decide that the benefits of two axis technology is worth the added investment to optimize that spacecraft.

Question 5. What are the advantages of integrating the solar array into the overall satellite to further optimize the satellite and is there interest in doing this?

(Due to time limitations, there was not a lot of discussion about this question.) The advantages of complete integrated design of the array into a satellite vary by the individual satellite and mission. Some examples include direct drive of high voltage (300V) electric propulsion thrusters to eliminate the power conditioners and optimizing the voltage to match high load users to minimize cable and electronics mass. It was generally agreed that every company is already looking for ways to do this for every satellite, and it is really required for companies to stay competitive.

WORKSHOP SUMMARY
THERMOPHOTOVOLTAICS AND NON-SOLAR ENERGY CONVERSION

Donald L. Chubb
NASA Lewis Research Center
Cleveland, Ohio

and

Larry C. Olsen
Washington State University
Richland, Washington

The workshop was well attended (about 20) with the discussion limited to alpha/betavoltaics and thermophotovoltaics (TPV). TPV was the major part of the discussion. Both space and terrestrial applications were presented for TPV at various power levels. However, alpha/betavoltaics appear to be limited to very low power (mw) level applications. Reference 1 lists several low power applications for betavoltaics.

ALPHA/BETA VOLTAICS

In an alphavoltaic or betavoltaic energy converter charge carriers are produced in a p-n junction semiconductor by alpha particles or beta particles rather than photons as in a conventional photovoltaic energy converter. One of the key issues discussed for these devices was radiation damage. For a betavoltaic device the threshold for damage begins for beta particles with energies greater than 200-300 KEV. Promethium (P_m^{147}) and tritium (H^3) were mentioned as possible beta sources with energies less than the damage threshold. For beta sources with energies greater than the damage threshold, strontium (Sr^{90}) and thallium (Tl^{204}) were mentioned. Since the half life for each of these sources is long, the potential lifetime for an alpha/betavoltaic device is long. Both InP and SiC were discussed as possible semiconductor materials suitable for alpha/betavoltaics. To make these devices feasible, the radiation damage problem must be solved.

THERMOPHOTOVOLTAICS (TPV)

The TPV discussion centered around possible applications and the key research areas.

TPV Applications

TPV has both low power (≤ 100 w) and high power space applications. The low power applications are for deep space missions such as the Pluto flyby where the thermal energy is supplied by radioisotope decay. For higher power applications such as earth orbit or a moon base, solar energy can be used as the thermal source. In this case TPV has an advantage over the conventional PV-battery system since thermal energy storage can be used. The TPV system thus will have a lower mass, especially for a moon base if the lunar soil can be used as a storage material.

It is the commercial applications of TPV that has caused the great interest in TPV in the last several years. Although the discussion was limited on this subject the following applications were mentioned: portable power supplies for recreational vehicles and Army field units, cogeneration of electrical power for natural gas appliances such as electrical power for furnace blowers, and hybrid electrical vehicles.

TPV Research

Two important developments have made efficient TPV energy conversion at moderate temperatures (< 2000 K) possible. One is low bandgap energy ($< 1\text{eV}$) PV cells such as GaSb and InGaAs and the other is efficient selective emitters. Research in these areas was thus the main topic of discussion. For high temperature ($\geq 2000\text{K}$), high efficiency can be attained using Si PV cells.

There are two approaches to attaining an efficient TPV emitter. First of all a selective emitter that emits mainly in the wavelength region where the PV cells have maximum efficiency and secondly a grey body emitter with a band pass filter to make the emitter behave like a selective emitter. Discussion was centered on rare earth selective emitters. The mantle type emitter² made of small (5-10 μm) diameter rare earth oxide fibers, such as Yb_2O_3 , has demonstrated good efficiency. Research is continuing on the fiber emitter with different geometry than the mantle. Also, a new rugged, rare earth-garnet emitter shows promising spectral emittance.³

Currently there is considerable research on low bandgap energy PV cells. Probably the most developed low bandgap energy, E_g , cell is GaSb with $E_g = .72$ eV. Also being actively researched is $\text{In}_x\text{Ga}_{1-x}\text{As}$ on InP substrates. This system yields $.36 \leq E_g \leq 1.42$ eV depending on the value of x . Also, just beginning is research on $\text{In}_x\text{Ga}_{1-x}\text{Sb}$ which has $.17 \leq E_g \leq .72$ eV depending on the value of x and $\text{In}_x\text{Ga}_{1-x}\text{As}_y\text{Sb}_{1-y}$, which has $.17 \leq E_g \leq 1.42$ eV depending on the value of x and y . This later quaternary system will allow lattice matched growth on GaSb substrates in the energy range $.3 \leq E_g \leq .72$ eV. Two other PV materials that are not currently being considered, but should be considered, are $\text{Hg}_x\text{Cd}_{1-x}\text{Te}$ and Ge. The HgCdTe system allows lattice matched growth for $0 \leq E_g \leq 1.56$ eV. The main advantage of Ge ($E_g = .66$ eV) is that it potentially should be the lowest cost.

Most people felt that low bandgap energy PV cell development will occur before an efficient emitter is developed. The main reason for this is the large amount of cell research compared to emitter research. For an efficient TPV system both an efficient emitter and PV cell are required.

CONCLUSION

Both low bandgap energy PV cell research and emitter research are required to make efficient TPV energy conversion possible. The many potential applications of TPV more than justify the research effort. Alpha/betavoltaic energy conversion will be viable if the radiation damage problem can be solved.

References

1. P. W. Sims, L. C. DiNetta and A. M. Barrett, "High Efficiency GAP Power Conversion for Betavoltaic Applications," Proceedings of the XIII Space Photovoltaic Research & Technology Conference (SPRAT XIII), Cleveland, Ohio, June 1994.
2. R. E. Nelson, in "Proceedings of 32nd International Power Sources Symposium," (Electrochemical Society, Pennington, NJ, 1986), pp. 95-101.
3. R. A. Lowe, D. L. Chubb, S. C. Farmer and B. S. Good, "Rare Earth-Garnet Selective Emitter," *Appl. Phys. Letts.*, 64, 3551 (1994).

REPORT DOCUMENTATION PAGE			Form Approved OMB No. 0704-0188	
Public reporting burden for this collection of information is estimated to average 1 hour per response, including the time for reviewing instructions, searching existing data sources, gathering and maintaining the data needed, and completing and reviewing the collection of information. Send comments regarding this burden estimate or any other aspect of this collection of information, including suggestions for reducing this burden, to Washington Headquarters Services, Directorate for Information Operations and Reports, 1215 Jefferson Davis Highway, Suite 1204, Arlington, VA 22202-4302, and to the Office of Management and Budget, Paperwork Reduction Project (0704-0188), Washington, DC 20503.				
1. AGENCY USE ONLY (Leave blank)		2. REPORT DATE September 1994		3. REPORT TYPE AND DATES COVERED Conference Publication
4. TITLE AND SUBTITLE Proceedings of the XIII Space Photovoltaic Research and Technology Conference (SPRAT XIII)			5. FUNDING NUMBERS WU-233-01-0A C-NAS1-19592 C-NAS3-26703 C-NAS3-27004 G-NAG3-1466	
6. AUTHOR(S)				
7. PERFORMING ORGANIZATION NAME(S) AND ADDRESS(ES) National Aeronautics and Space Administration Lewis Research Center Cleveland, Ohio 44135-3191			8. PERFORMING ORGANIZATION REPORT NUMBER E-9083	
9. SPONSORING/MONITORING AGENCY NAME(S) AND ADDRESS(ES) National Aeronautics and Space Administration Washington, D.C. 20546-0001			10. SPONSORING/MONITORING AGENCY REPORT NUMBER NASA CP-3278	
11. SUPPLEMENTARY NOTES Responsible person, George C. Rybicki, organization code 5410, (216) 433-8473.				
12a. DISTRIBUTION/AVAILABILITY STATEMENT Unclassified - Unlimited Subject Category 33			12b. DISTRIBUTION CODE	
13. ABSTRACT (Maximum 200 words) The Thirteenth Space Photovoltaic Research and Technology (SPRAT) Conference gathered representatives from 26 commercial corporations, 8 universities and 7 governmental agencies, including Europe, for two and a half days of presentations and discussions regarding the status and future of space photovoltaics. The conference was well attended, with over 100 attendees, and included 38 technical papers, 6 program reviews and 5 workshop discussions. The effects of shrinking research and development budgets were evident in the focus and tone of this SPRAT. Most attendees appeared to be oriented toward near term, system oriented projects and fewer were involved in long term, high risk research. It was generally agreed that space power requirements would continue to move toward smaller (<2kW) power levels. Most future applications are believed to be in traditional orbits (LEO, GEO) although interesting opportunities may be found in high radiation, mid-altitude orbits useful for global communication networks. New solar cell devices and materials will be difficult to introduce unless they are mission enabling, or offer significant cost and/or performance benefits. The attendees were unable to come to a consensus regarding the type of array (eg. rigid, concentrator, flexible) suitable for specific missions. Many factors outside the realm of photovoltaics influence the selection process. These topics and many more are covered in the following pages of this record.				
14. SUBJECT TERMS Photovoltaics; Space power; Solar cells			15. NUMBER OF PAGES 452	
			16. PRICE CODE A20	
17. SECURITY CLASSIFICATION OF REPORT Unclassified	18. SECURITY CLASSIFICATION OF THIS PAGE Unclassified	19. SECURITY CLASSIFICATION OF ABSTRACT Unclassified	20. LIMITATION OF ABSTRACT	